AD

230 333

1 OF 7

"NOTICE: When Government or other drawings, specifications or other data are used for any purpose other than in connection wi a definitely related Government procurement operation, the U.S. Government thereby incurs no responsibility, nor any obligation whatsoever; and the fact that the Government may have formulat furnished, or in any way supplied the said drawings, specifications or other data is not to be regarded by implication or otherwise a in any manner licensing the holder or any other person or corpo tion, or conveying any rights or permission to manufacture, use or sell any patented invention that may in any way be related there

SWR-TM-59-2

HEADQUARTERS

AIR FORCE SPECIAL WEAPONS CENTER

AIR RESEARCH AND DEVELOPMENT COMMAND

KIRTLAND AIR FORCE BASE, NEW MEXICO

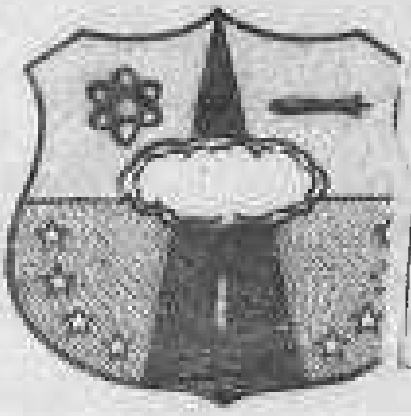

PROCEEDINGS

of

THIRD SHOCK TUBE SYMPOSIUM

10 - 12 March 1959

Sponsored by
Air Force Special Weapons Center

SWR-TM-59-2

PROCEEDINGS
OF
THIRD SHOCK TUBE SYMPOSIUM
10 - 12 March 1959

Research Directorate
AIR FORCE SPECIAL WEAPONS CENTER
Air Research and Development Command
Kirtland Air Force Base
New Mexico

Approved:

LEONARD A. EDDY
Colonel USAF
Director

Project No. 1080

Tuesday and Wednesday, 10 and 11 March 1959
Old Point Comfort, Fort Monroe, Virginia

PROGRAM OF THIRD SHOCK TUBE SYMPOSIUM

Sponsored by
Air Force Special Weapons Center

AGENDA

Tuesday, 10 March - Moderator: James Shreve,
Sandia Corporation

"Official Welcome" - Colonel L. A. Eddy, AFSWC
Director of
Research Directorate

"Resumé of Experiments Conducted in the High Pressure Shock Tube of Gas Dynamics Laboratory at NASA"
Jim J. Jones, NASA

"A Probe for Determining Flow Conditions in a Short Duration Hypersonic Stream"
Arthur V. Farmer, Lockheed Aircraft Corporation

"Calculation of the Flow Phenomena in the CONVAIR Free Jet Shock Tunnel Facility"
Karl A. Faymon, CONVAIR

"An Explosive Driven Conical Shock Tube for the Study of Spherical Shock Waves"
William S. Filler, U. S. Naval Ordnance Laboratory

LUNCH

"Shock Tube Investigation of Hydrogen Dissociation"
V. Metzler, Rocketdyne, North American Aviation, Inc.

"Observations of Ultra-Violet Absorption Behind Strong Shock Waves in Oxygen"
John S. Evans, Jr. and Charles J. Schexnayder, NASA

"Diffusion Effects on Shock Structure in a Plasma"
H. K. Sen, O. W. Greenberg, and Y. Treve, Air Force Cambridge Research Center

"Technique of Pressure Measurement on an Airfoil in a Shock Tube"
J. Ray Ruetenik, Massachusetts Institute of Technology

"Application of Pressure and Force Transducers in Hypersonic Shock Tunnel Aerodynamic Experimentation"
Clarence J. Harris, General Electric

EVENING SESSION - Moderator: Roman Birukoff, AFSWC

"Biological Experiments Utilizing a Closed-end Shock Tube"
Donald R. Richmond and Rinaldo V. Taborelli, Lovelace Foundation

"Program for the NCEL Blast Simulator"
Sterling L. Bugg, Navy Civil Engineering Laboratory

"Structural Integrity of Spread Foundations Subjected to Extreme Horizontal Impulses"
D. B. Singer and C. A. Miller, Armour Research Foundation

"The Shock Chamber: A Device for Producing High Strength, Spherically Expanding Shock Waves"
A. B. Willoughby and Kenneth Kaplan, Broadview Research Corporation

Wednesday, 11 March - Moderator: Jack Kelso, AFSWP

"A One-inch Force Gage for Drag Measurements in the Shock Tube"
William. Zuke, U. S. Naval Ordnance Laboratory

"Changes in Pressure Drag Caused by Shielding"
George A. Coulter, Ballistics Research Laboratories

"Correlation Between Shock Tube and Wind Tunnel Drag Coefficients"
Captain Marcus L. Whitfield, AFSWP

"Interaction of Blast Waves with Wings" - Part I, "Ten-Foot Diameter Free Jet Shock Tube"
Harold B. Pierce, NASA

"Interaction of Blast Waves with Wings" - Part II, "Wave-Table Studies"
Donald R. McFarland, NASA

LUNCH

"Experiments and Theory on Explosive Decompression in the Six-foot Shock Chamber"
Theodore Schiffman, Armour Research Foundation

"Theory on Filling Process in Chamber, Shock Tube, and Field Tests"
A. Wiedermann, Armour Research Foundation

"Diaphragm Calibration Techniques in a 2.00-inch Diameter Shock Tube"
George H. Tweney, Boeing Airplane Company

Closing Remarks - Roman Birukoff, AFSWC

Thursday, 12 March 1959

A Tour of the National Aeronautics and Space Administration Facility at Langley Research Center

VISIT TO THE LANGLEY RESEARCH CENTER OF THE NASA

12 March 1959

Welcome and Introductory Remarks

Description of the 9 × 6-foot Thermal Structures Tunnel
Donald H. Trussell

Demonstration of the 9 × 6-foot Thermal Structures Tunnel

Gas Dynamics Laboratory

1. Blast wave table
2. Dissociation rate study shock tube
3. Magnetohydrodynamics Laboratory
4. Hypersonic high pressure shock tube
5. Small pressure transducers

Attendance at the

THIRD SHOCK TUBE SYMPOSIUM

Sponsored by the

Air Force Special Weapons Center

10 and 11 March 1959
Old Point Comfort, For. Monroe, Virginia

Armed Forces Special Weapons Project
Washington 25, D. C.

Andrews, James D., LCDR USN
Whitfield, Marcus L., Captain, USA
Batson, Richard T., Lt. Col., USA
Kelso, Jack R., Physicist

Commander, Field Command
Armed Forces Special Weapons Project
Sandia Base, Albuquerque, New Mexico

Gulick, C. W., Lt. CEC, USN

Corps of Engineers, USA
Research & Development Division
Office Chief of Engineers
Washington 25, D. C.

Hutchison, Russell J., Major USA

Ballistic Research Laboratories
U. S. Army Ordnance
Aberdeen Proving Ground, Maryland

Coulter, George A., Physicist
Grauath, Benjamin A., Physicist
Kingery, Charles N., Physicist
Clark, Robert O., Physicist
Taylor, William J., Physicist
MacAllister, Leonard C.,
Chief of Engineers Section
Fru Flight Br. EBL
Kahl, George D ,
Cohen, Arthur,

Engineers Research & Development Laboratories
Fort Belvoir, Virginia

Paca, Francis B., Chief Appl Research Section, Mine warfare
Walsh, Thomas G., Physicist
Maloney, James W., Captain CE
Sievers, Ralph H., Jr., 1st Lt.

Office of the Director
Waterways Experiment Station
Corps of Engineers, USA
Vicksburg, Mississippi

Kirkland, Jesse L., Physicist

Headquarters
Quartermaster Research & Development Command
US Army
Natick, Massachusetts

Zagieboylo, Walter, Mechanical Engineer

U. S. Army Medical Research Laboratory
Fort Knox, Kentucky

Odell, Dr. Floyd A., Technical Director of Research

Navy Department
Bureau of Ships
Washington 25, D. C.

Park, Yip' H., Naval Architect

U. S. Naval Research Laboratory
Washington 25, D. C.

Scherrer, V. E., Physicist

Aeronautical Structures Laboratory
Philadelphia 12, Pennsylvania

Jankiewicz, E. J., Research Engineer

Naval Air Material Center
Philadelphia 12, Pennsylvania

Fonash, Raymond L., Aero. Research Engineer

Navy Civil Engineer Laboratory
Port Hueneme, California

Bugg, S. L., Dir. Struct. Div.

Commander,
U. S. Naval Ordnance Laboratory
White Oak, Silver Spring, Maryland

Pomerantz, Jacob
Echemman, Dr. Jeromo, Physicist
Fussell, William B., Physicist
Noonan, Barry, Aeronautical Engineer
Dawson, Victor, C. D., Supervisory Research Engineer
Bixler, David N., Physicist
Lundquist, George A., Research Engineer
Filler, William S., Physicist
Triolo, Jack J., Physicist
Zerke, William, Physicist

Headquarters, United States Air Force (AFCIN-3B)
Washington 25, D. C.

Burberk Jr., George R., Engineer
Lehman, Hugh R., Lt. Col. USAF

Air Force Cambridge Research Center
Hanscom Field
Bedford, Massachusetts

Karandikar, Ramachandra V., Physicist
Greenberg, O. W., 1st Lt.

Air Force Special Weapons Center
Albuquerque, New Mexico

Birukoff, R. R., Research Engineer
Player, Jr., Richard L., Project Engineer

ARDC - United States Air Force
Langley, Air Force Base

Roche, J. A., Aero Dev. Engineer

United States Atomic Energy Commission
Washington 25, D C.

McCalley, Robert B , Reactor Containment Engineer

AERO
Diamond Ordnance Fuze Laboratories
Washington 25, D. C.

Curcheck, Herb, AERO Engineer

National Aeronautics and Space Administration
Langley Research Center
Langley Field, Virginia

Trimpi, Robert L., Aero. Research Engineer
Cooper, Morton, Aero. Research Engineer
Ellis Jr., Macon C., Hd. Gas Dynamics Branch
Patterson, J. L., Research Engineer
Keafer Jr., Lloyd S., Research Engineer
Evans, John S., Aeronautical Research Engineer
Frvchtman, Irving, Research Aero Engineer
Gooderum, Paul B., Aero Research Engineer
McFarland, Donald R., Aero Research Engineer
Huber, Paul W., Aero Engineer
Collins, Dennis F., Aero Research Engineer
Stainback, P. C., Aero Research Engineer
Jones, Jim J., Aero Research Engineer
Jones, William B., Research Engineer
Manning, James C., Aero Research Engineer
Pierce, H. B., Aero Research Engineer
Peterson, Sheldon T., Head, Pressure Measurement Section
Pilny, M. J., Research Engineer
Morton, Richard W., Research Engineer
Schexnayder, Charles J., Aero. Research Engineer
Muller, Joseph A., Research Engineer
TaSack, Irrael, Mechanical Engineer
Hermad, Mark, Aero Research Engineer
Lauver, Milton R., Aero Research Engineer
Burlock Joseph, Research Engineer

National Bureau of Standards
Washington 25, D. C.

Beckett, Dr. C. W., Chief Thermodynamics Sec.
Lederer, Paul S., Research Engineer
Smith, R. O., Physicist
Thompson, Robert C., Physicist
Davis, Harry J., Physicist

Office of Civil and Defense Mobilization
Battle Creek, Michigan

Lynch, John P., Structural Research Engineer

Picatinny Arsenal
Dover, New Jersey

Ling, R. C., Supervisory Physicist (Solid State)

American Science and Engineering, Inc.
12 Norfolk Street
Cambridge, Mass.

Carpenter, Jack W., Scientist

Armour Research Foundation
Illinois Institute of Technology
Chicago 16, Illinois

Wiedermann, Arne H., Supervisor
Nagumo, George, Research Engineer
Schiffman, Theodore, Asst. Manager Division of Fluids
Dickens, R. G., Supervisor
Lieberman, Paul, Associate Research Engineer
Zaker, Thomas A., Research Engineer
Gallagher, Edward V., Research Engineer
Singer, David B., Asst. Supervisor, Structural Analysis Div.

Atlantic Research Corporation
Alexandria, Virginia

Bryant, R. C. Director, Electromechanical Division

AVCO
Wilmington, Massachusetts

Offenhacto, Edward, Group Leader

Beckman and Whitley
973 San Carlos Avenue
San Carlos, California

Patterson, Jack M., Installation Engineer
Teeple, Laurence R., Manager Camera Products

Boeing Airplane Company
Systems Management Office
P. O. Box 3915
Seattle 24, Washington

Tweney, George H., Senior Group Engineer
Harris, William G., Aero Engineer
Brown Jr., E. A., Research Specialist

Broadview Research Corporation
1811 Trousdale Drive
Burlingame, California

Kaplan, Kenneth, Physicist

Chesapeake Instrument Corporation
Shady Side, Maryland

LaFevre, Leland M., Head Electro acoustic Div.

Convair, San Diego
San Diego, California

Lous, John F., Thermodynamics Engineer
Fayman, Karl A., Aerodynamics
Hankin, Norbert N., Physicist

Cornell Aeronautical Laboratory
Cornell University
4455 Genesee Street
P. O. Box 235
Buffalo 21, New York

Wittliff, Charles E., Research Engineer
Reece, J. W. (Bill), Staff Engineer
Martin, James T., Hypersonic Branch

University of Dayton Research Institute
Dayton, 9, Ohio

Luthman, Robert R., Director, Special Projects Division
Wurst, John, Research Engineer

Douglas Aircraft Company, Inc.
Santa Monica, California

Young, Joseph F., Research Engineer
Murphy, James S., Design Specialist
Davis, Charles L, Designer

General Electric Company
Defense Electronics Division
Court Street
Syracuse, New York

Molello, Sam, Systems Engineer
Kaegi, Emil M., Aerodynamics Specialist – MSVD
Philadelphia, Pennsylvania

Grumann Aircraft
Bethpage, New York

Hopkins, Jr., Harold B., Group Leader
Leng, Jarvis, Research Engineer

Hayes Aircraft Corporation
2525 7th Street N. E.
Birmingham 15, Alabama

Scott, R. C., Scientist B

University of Illinois
Aeronautical Engineering Department
Urbana, Illinois

Barthel, Harold O., Research Assistant Prof.

Lehigh University
Bethlehem, Pennsylvania

Weimer, D.,

Lockheed Missile and Space Division
Palo Alto, California

Farmer, Arthur V., Senior Scientist

Lovelace Foundation
Albuquerque, New Mexico

Richmond, D., Project Officer
Taborelli, R. V. Head, Engineering Department

Martin Company
Denver, Colorado

Davis, Theodore, Group Engineer
Chapin, S. G., Design Engineer

Massachusetts Institute of Technology
Department of Aeronautical Engineering
Cambridge 39, Massachusetts

Ruetenik, J. R. Senior Engineer
Clay, W. G., Engineer)
Murphy, Edward L., Physicist) Lincoln Lab. Lexington, Mass.

McDonnell Aircraft Corporation
St. Louis, Missouri

Sivier, Kenneth R., Senior Engineer

Norair
A Division of Northrop Corporation
Hawthorne, California

Quinville, James A., Engineering Specialist

Missile Division
North American Ave.
Downeym, California

Faulders, Charles R., Res. Specialist
Leef, C. R., Specialist

Pratt and Whitney Aircraft
East Hartford, Connecticut

Roberts Jr., Frank, Project Engineer

Republic Aviation Corporation
Farmingdale, New York

Lu, H. R., Chief Fluid Mechanics
Pappas, C. E., Asst. Dir. Sci, Research
Nomicos, George N., Associate Scientist

Rocketdyne
A Division of North American Aviation, Inc.
Canoga Park, California

Metzler, C. V., Senior Research Engineer

Sandberg - Serrell Corporation
2550 E. Foothill Blvd
Pasadena, California

Ying - Nien Yu, Design Specialist

Sandia Corporation
Albuquerque, New Mexico

Chabai, Albert J.,
Shreve Jr., J. D. Supervisor, Burst Simulation Div.

Space Technology Lab
Los Angeles, California

Lamb, Lawrence, Y., Member of Technical Staff
Schaffer, Allen, Member of Technical Staff

Senucon Arsor Incorporated
P. O. Box 832
Lexington 12, New York

Kippins, Otto G., Pres

Sun Oil Company
Research and Engineering Department
Marcus Hook, Pennsylvania

Malmberg, Earl, Research

United Aircraft Corporation
400 S. Main Street
E. Hartford, Connecticut

Patch, Richard Walker, Research Engineer
Foley, William M., Engineer
Anderson, Olof L. Research Engineer
Taylor, William E., Research Engineer

University of Virginia
Charlottesville, Virginia

Parker, Herman M., Head Theoretical Div. ORL

Westinghouse Electronic Corporation
East Pittsburg, Pennsylvania

Donald, Jack M., Senior Engineer

TABLE OF CONTENTS

WELCOMING ADDRESS

Scheduled to be given by Colonel Leonard A. Eddy, Director of Research of the Air Force Special Weapons Center, the welcoming address was made by Mr. Roman R. Birukoff of AFSWC, who briefly explained the work load situation precluding Col Eddy's presence at this Symposium. In behalf of the Air Force Special Weapons Center he welcomed the attending group, and expressed the wish that the event would be an interesting and successful undertaking.

RESUMÉ OF EXPERIMENTS CONDUCTED IN THE HIGH-PRESSURE SHOCK TUBE OF THE GAS DYNAMICS LABORATORY AT NASA

Jim J. Jones
NASA Langley Research Center

This talk describes several investigations performed at the gas dynamics laboratory of the Langley Research Center, NASA. Most of the experiments described were conducted in the gas dynamics high-pressure shock tube. It is a constant-area tube, 3-3/4 inches in diameter. The high-pressure chamber is 14 feet long and the low-pressure chamber has a working length of about 70 feet, although at the time that attenuation was studied it was considerably longer.

Shock-Wave Attenuation

Shock-wave attenuation has been studied in this tube for some time, largely from the standpoint of shock-tube technology rather than the basic flow physics. That is, what are practical drivers to use to produce the desired shock strengths, what is the relative shock attenuation for each driver, and, what is the resultant flow behind the shock wave like?

Those drivers which have been investigated are helium, hydrogen, constant-volume combustion of H_2 and O_2 diluted with helium, and a constant pressure combustion of a similar mixture. In all cases, air was the driven gas. Some consideration was also given to a double diaphragm, or three-chamber arrangement.

Figure 1 summarizes the attentuation rate for these various drivers. The low pressure p_1 was the same for each run. Notice that, except for the helium driver, each of the runs has about the same shock Mach number at about 225 diameters. Very high helium pressure would be required to generate a shock wave of the same strength at 225 diameters as the others shown, so a weaker shock is presented for comparison.

The constant-volume and constant-pressure combustion drivers were identical except for the strength of the diaphragm used. Constant-pressure drivers have been shown by Hertzberg and others to have rather poor reproducibility.

Hydrogen-rich mixtures, that is, mixtures of, say 8 percent or 10 percent O_2 and the balance of H_2, have been attempted but the tendency of the combustion to become a detonation has caused us to abandon this type driver.

The difference in shock-wave attenuation is quite marked for the various drivers and follows the general rule that the more efficient drivers in producing strong shock waves display the higher attenuation rates.

Measurements of the time history of the static pressure immediately behind the primary shock also show characteristics associated with each particular driver. (See Figure 2.) These pressure records were all made some 200 diameters from the diaphragm and are therefore influenced by the very sizeable amount of attenuation which the shock has undergone. Pressure level and shock strength influence the pressure history, of course, but comparisons show that, in general, cold gas drivers, hydrogen and helium, show a short period of nearly constant pressure and then a rising pressure. One can see, for example, that for the helium driver case shown, the pressure has about doubled in the first millisecond.

The higher attenuation rate of the combustion driven shocks indicates that stronger downstream expansion waves are overtaking the shock. These expansion waves are present largely because of the cooling of the hot combustion gases. The effect of this increased strength of the expansion waves is to cancel the tendency of the pressure to increase with time. Thus, as illustrated in Figure 3, combustion-driven shock waves show a nearly constant pressure and in some cases a decrease in pressure. This is not to infer that other flow properties are constant with time. For example, it can be inferred that the stagnation enthalpy increases rapidly with time. Another rule seems to exist here: the more efficient drivers, although possessing higher attenuation rates, show a more constant-pressure history in the driven gas.

The attentuation for hydrogen and helium drivers in this shock tube was reported in reference 1. The combustion driver studies have not been reported.

The gas dynamics laboratory has one rather small three-chamber shock tube. It is described in more detail by Mr. Evans in his talk. The driver and buffer chambers are 4-inch diameter and the low-pressure chamber is 1-inch diameter. Hydrogen-helium-air and helium-helium-air combinations are used in this tube. The maximum shock strengths attained are compared with the theoretical values in Figure 4. In all cases the middle, or buffer gas, was adjusted to its theoretical optimum pressure for the particular over-all pressure ratio. It may be seen that agreement with theory is somewhat better for the helium driver than for the hydrogen driver. A single diaphragm, H_2-air curve for a constant-area tube is presented for comparison. Two effects account for the superiority of the three-chamber configuration curves - the area change and the addition of the buffer gas. This figure does not show the relative importance of each. The shock attenuation rate is approximately the same in the three-chamber tube as in the 3-3/4-inch tube for like drivers. This work has been reported by Mr. C. J. Schexnayder (reference 2).

The three-chamber shock tube just discussed has an area reduction by a factor of 16 at the second diaphragm. The effect of this area change on maximum attainable shock strengths has been recognized. It becomes important, however, from another viewpoint as well. Most theoretical discussions neglect the attenuation in the buffer chamber. It is not, in the general case, negligible as may be seen in Figure 5. A few runs made in the constant 3-3/4-inch-diameter tube with a three-chamber arrangement showed that the attenuation in the center chamber cancelled the beneficial

effects of the double-diaphragm configuration. The driver was constant-volume combustion and the buffer gas was helium. The attenuation of the shock wave from $M_s = 3\text{-}1/4$ to $M_s = 2.4$ lowered the maximum shock strength in the air from a theoretical $M_s = 9\text{-}1/4$ to an experimental value just over 7. This indicates the importance of maximizing the buffer chamber diameter.

Heat Transfer

An investigation has been made of flat-plate heat transfer for a range of Reynolds numbers from 10^4 to over 10^7. The model configurations used are shown in Figure 6. The surfaces to which the heat-transfer rate was measured were pyrex. Hanovia paste resistance thermometers were used to measure the surface temperature. A wedge was used for the lower Reynolds number range. It was necessary to have a steel leading edge on the wedge to avoid chipping so there was a steel-to-glass joint ahead of the measuring stations.

In order to obtain a long run of boundary layer with a minimum of interference effects, a hollow cylinder was utilized. Again a steel leading edge was necessary. The cylinder was 50-millimeter pyrex tubing, 24 inches long.

An estimation of the boundary-layer-displacement thickness at the trailing edge of the cylinder indicated that it was 4 percent or less of the radius of the cylinder. The slight pressure gradient induced by the area change has been neglected in reducing the data.

Figure 7 shows the data obtained for a range of shock Mach numbers from 4.6 to 10.5. The wedge data are based on conditions behind the oblique shock wave.

The data correlate quite well with the incompressible relations if the heat-transfer parameter is based on stagnation-to-wall enthalpy difference. Rose, Probstein, and Adams (reference 3) have proposed this relation for the turbulent case.

These data, although obtained at high static temperature and low stream Mach number, as is typical of all data obtained in a constant-area shock tube, can be shown to be directly applicable to hypersonic flight in the atmosphere. If one considers the case of a wedge, or compression surfaces, with a blunt leading edge, the conditions just outside the boundary layer some distance from the leading edge are very similar to the conditions of the present data. As an example, one run of the present data was selected ($M_s = 8.45$) and it was found that the stream and stagnation conditions matched those on a blunted 8° half-angle wedge flying at $M = 13.5$ at 70,000 feet.

Reference 4, which reports on the data obtained on the cylinder model, is expected to be published in the near future.

Probe Electrification

A phenomenon of some interest which appears in shock-tube investigations is the charge acquired by any probe placed in the flow.

Early efforts to obtain heat-transfer data in the shock tube with an evaporated thermocouple indicated that "hash" or extraneous signal predominated over the thermocouple signal for cases in which the shock Mach number was about 6 or greater. The hash could be reduced but not eliminated by balancing the resistance to ground of the two thermocouple leads. The trouble could be eliminated in a resistance thermometer by shunting across the thermometer and centertapping the shunt to ground. It was not possible to do this in the case of a thermocouple, of course, since the thermocouple requires a high-resistance circuit.

A detailed, systematic investigation of this phenomenon has not been made, but a few tests have brought some interesting results: First, any probe sufficiently insulated from ground (say, a megohm or greater) acquires a charge which may be of the order of a volt or greater when placed in the shock-tube flow and the polarity as well as the actual magnitude of the charge are dependent on the material of the probe. Figure 8 shows examples of the charge on brass and aluminum probes. The reproducibility of the signal for approximately similar running conditions is shown by the two brass probe examples on the figure. Copper and steel probes, as well as brass, show a positive charge in air; aluminum shows a negative charge.

The amplitude of the charge is rather surprisingly insensitive to the temperature level, as shown on Figure 9.

The charge is present when helium is the driven gas and the polarity was negative for all the probe materials tested in helium. Since very little of the helium is ionized at the temperature of this run, it is very possible that impurities are responsible for the presence of the signal here. High velocity of the flow is not necessary, since the charge is very similar for a probe placed at the end of a closed shock tube.

It is not to be expected that a probe will assume the potential of a partially ionized gas in which it is immersed even for the case when the gas is neutral, due to the greater mobility of the electrons. But simple probe theory does not account for the large effect of probe material. The effect of probe material suggests a phenomenon similar to contact electrification. While contact potential difference has been reported for liquids flowing in a pipe, none has been reported between a gas and a metal.

In conclusion, it might be mentioned that present and future work include studies in a small reflected-shock-type nozzle that is now attached to the high-pressure shock tube and somewhat more specific heat-transfer studies.

REFERENCES

1. Jones, Jim J.: Experimental Investigation of Attenuation of Strong Shock Waves in a Shock Tube with Hydrogen and Helium as Driver Gases. NACA TN 4072, July 1957.

2. Schexnayder, Charles J., Jr.: On the Performance of a Double-Diaphragm Shock Tube Using the Reflected-Shock Method and a Light-Gas Buffer. Journal of Aero/Space Sciences, Vol. 25, No. 8, Aug. 1958.

3. Rose, Peter H., Probstein, Ronald F., and Adams, Mac C.: Turbulent Heat Transfer Through a Highly Cooled Partially Dissociated Boundary Layer. Avco Research Laboratory Res. Rep't. 14, January 1958.

4. Jones, Jim J.: Shock Tube Heat-Transfer Measurements on the Inner Surface of a Cylinder (Simulating a Flat Plate) for the Stagnation Temperature Range 4100° to 8300° R. (Prospective NASA Memo.)

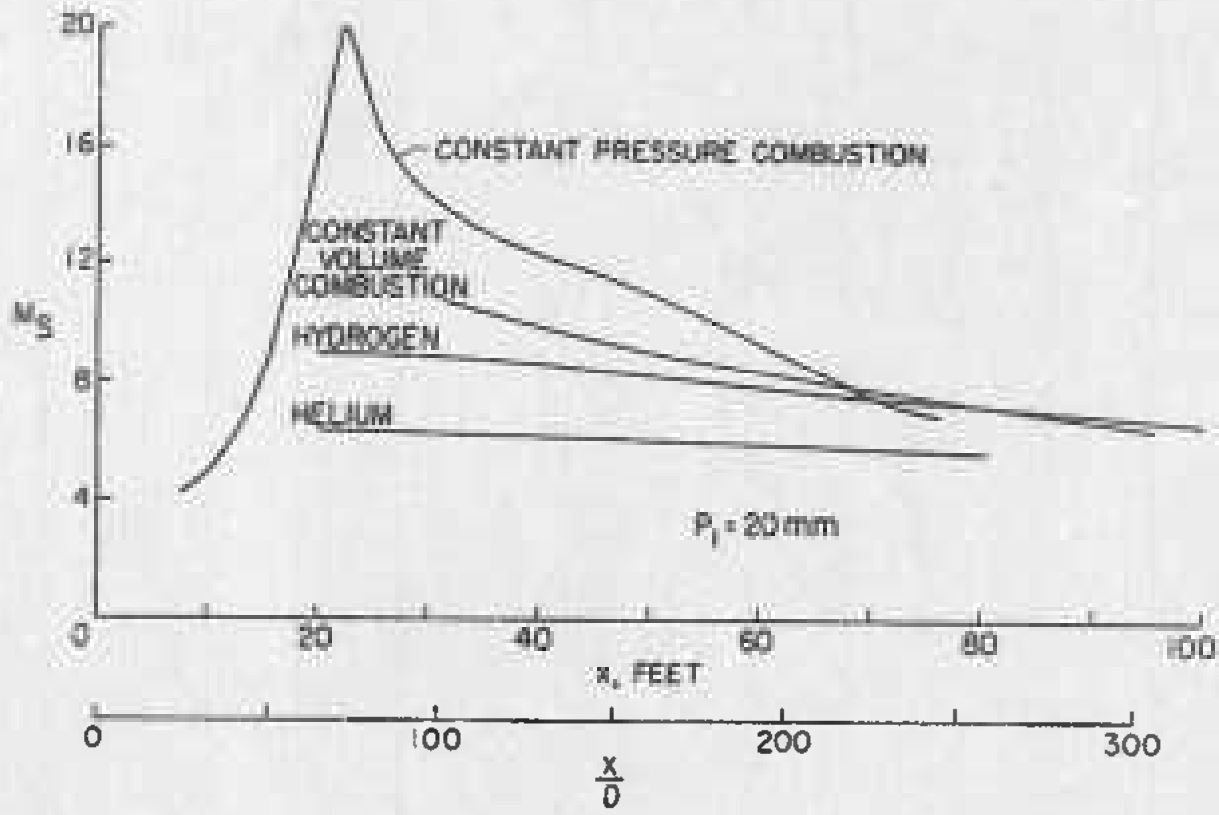

Figure 1 *Effect of Driver on Attenuation - NASA*

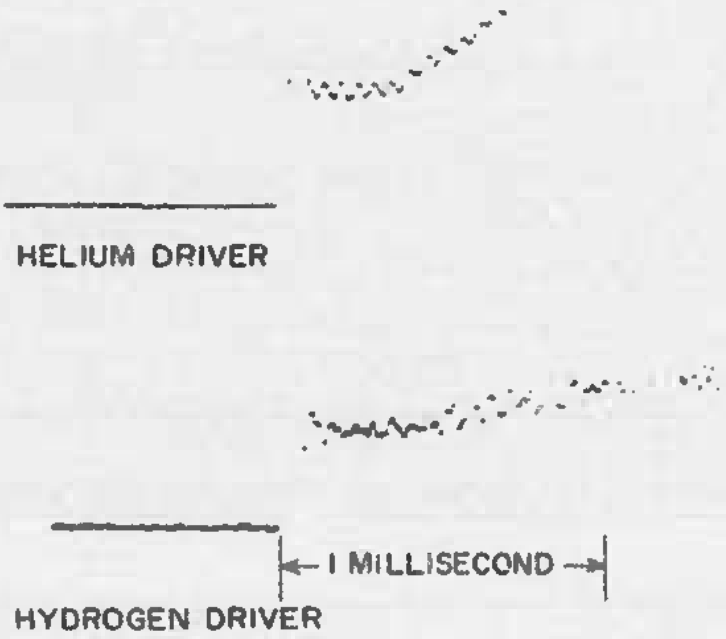

Figure 2 Typical Pressure Histories - Cold Gas Drivers - NASA

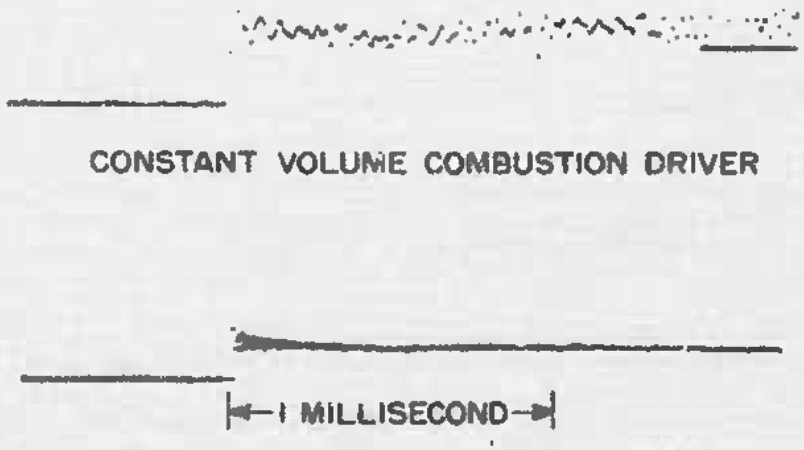

Figure 3 Typical Pressure Histories - Combustior Drivers - NASA

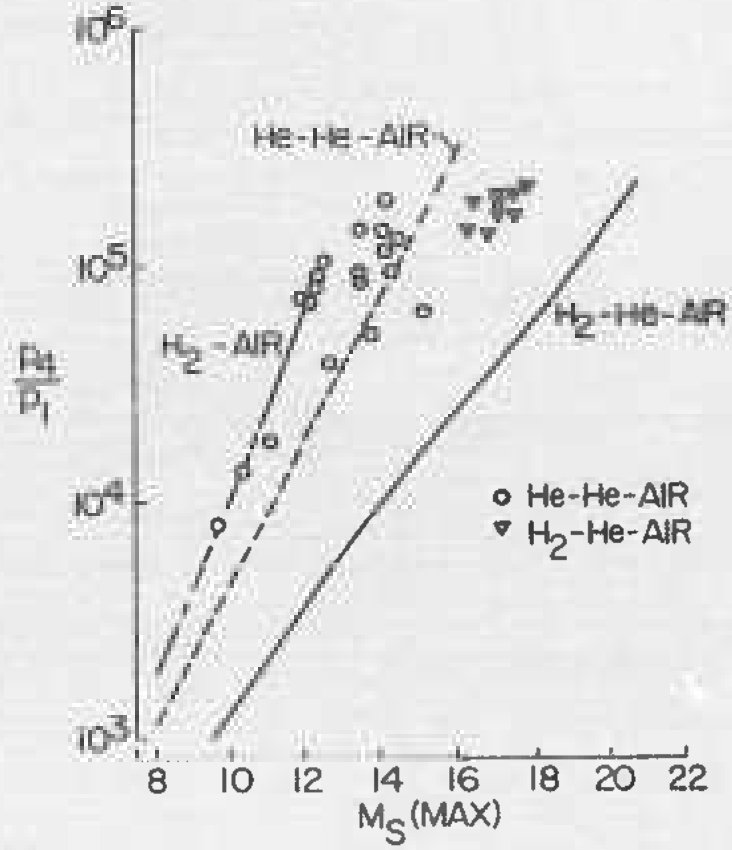

Figure 4 Double Diaphragm Shock-Tube Performance - NASA

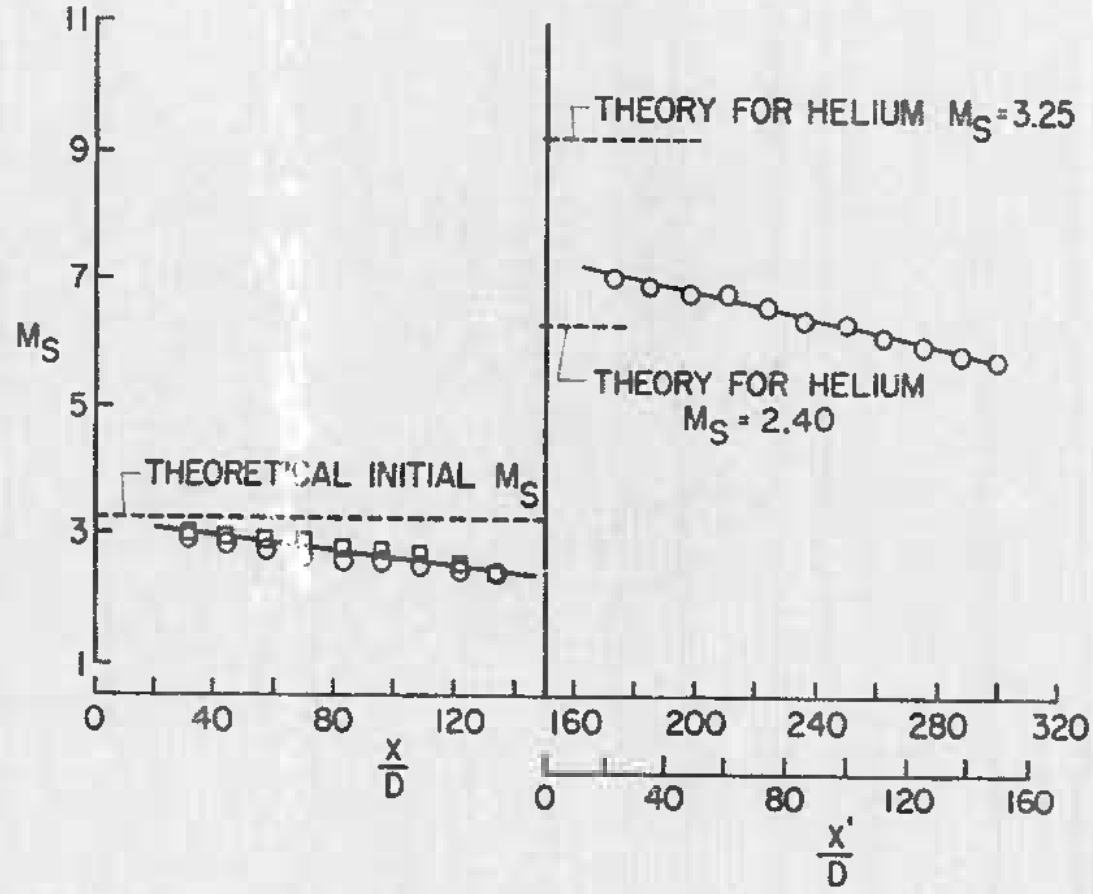

Figure 5 Effect of Buffer-Chamber Attenuation - NASA

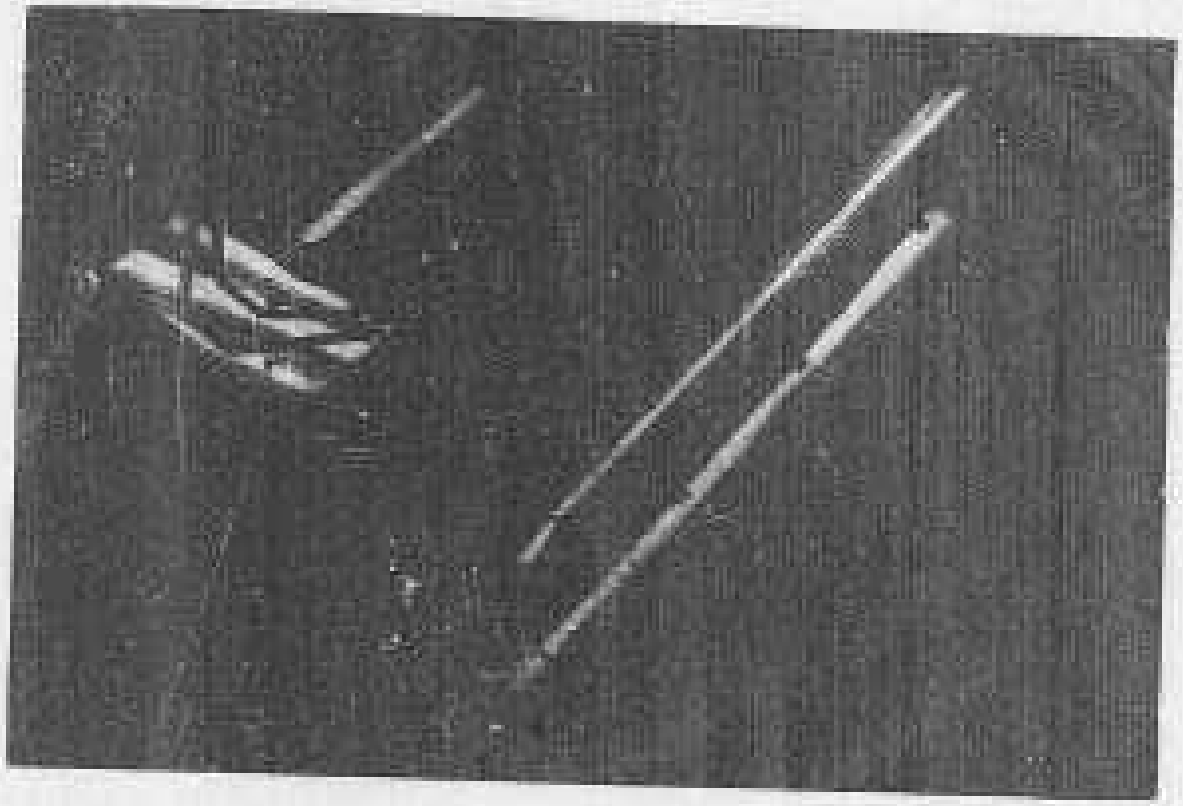

Figure 6 Heat-Transfer Models - NASA

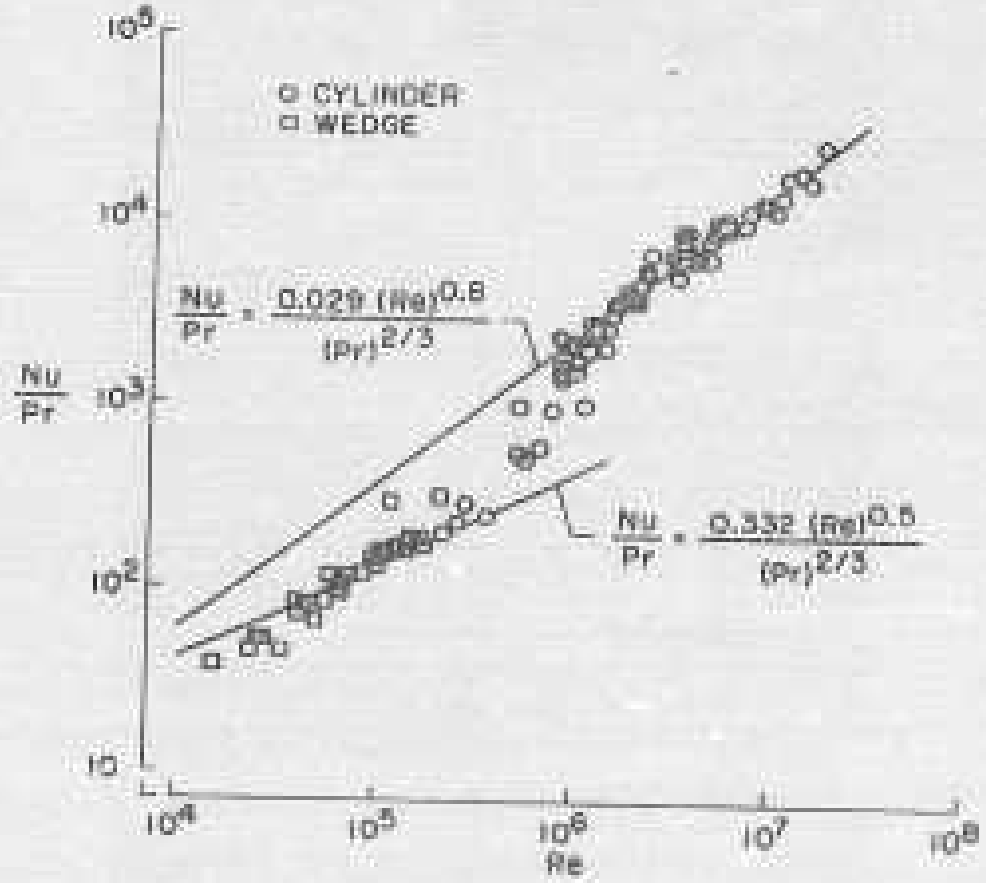

Figure 7 Flat-Plate Heat Transfer - NASA

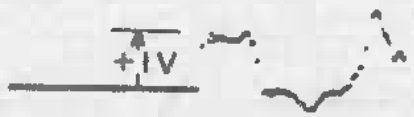

BRASS PROBE

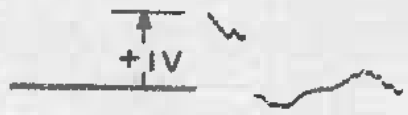

BRASS PROBE

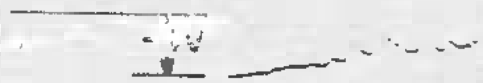

ALUMINUM PROBE

Figure 8 Probe Signals in Air - NASA

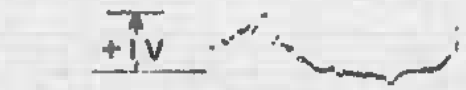

STEEL PROBE IN AIR – T_S = 5,900° R

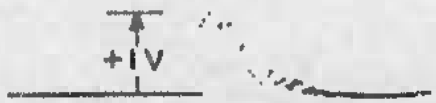

STEEL PROBE IN AIR – T_S = 12,800° R

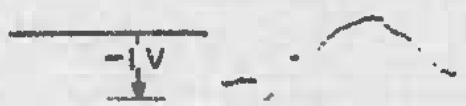

STEEL PROBE IN HELIUM – T_S = 9,420° R

Figure 9 Effect of Temperature and Gas on Probe Signal - NASA

A PROBE FOR DETERMINING FLOW CONDITIONS IN A SHORT DURATION HYPERSONIC STREAM*

A. V. Farmer
Lockheed Aircraft Corporation

ABSTRACT

A method is proposed for experimentally determining flow conditions in short-duration hypersonic flows, such as that found in hot-shot tunnels or shock tunnels. The method involves determination of the stagnation enthalpy of the flow by measuring the speed of sound and pressure in a probe and the determination of the rate at which the flow fills the cylindrical probe. By using these values in the flow equations, the free-stream conditions may be determined. The problems associated with the development of the instrumentation, and the progress already made are briefly described.

1. INTRODUCTION

The construction of the hot-shot tunnel at Lockheed (Reference 1 and 2) emphasized the need to develop instrumentation that would determine the flow conditions in such a facility. The conditions of this short duration flow are high velocity, high stagnation enthalpy, high Mach number, and low density. This type of flow is found also in shock tunnels. At present, only pressure and heat transfer are measured in these flows. Temperature measurements are precluded by the short duration of the flow. As the heat transfer measurements are a function of density, viscosity, velocity gradients, and enthalpy, only one state property, the pressure, is measured directly.

To determine the state of a gas at rest and in equilibrium, two state properties need to be known. In the hot-shot tunnel, the total energy content, or total enthalpy, is determined from the conditions in the arc chamber. The initial density loading, which remains constant during the arc discharge, and the peak pressure from the discharge provide the two state properties. The flow conditions are found by assuming an isentropic expansion from the arc chamber to the test section, making use of a corrected area ratio based on measured stagnation pressures in the test section. Thus, if there is no heat loss to the wall of the tunnel, and if the flow is in equilibrium, the flow may be determined in the test section. Both of these conditions are violated to some degree. Certainly, the erosion of the tungsten throat testifies to the heat transfer there, and Bray (Reference 3) states that the lack of dissociation equilibrium may be expected in the working sections of hypersonic wind tunnels. Therefore, it was the purpose of this work to develop instrumentation that would determine the stagnation enthalpy and the flow velocity, density, etc. in the test section of a hypersonic tunnel and would determine the profile of these conditions across the test section.

*The author would like to thank Professor Walter G. Vincenti of the Department of Aeronautical Engineering, Stanford University, for his encouragement in the development of this probe.

2. BASIC IDEAS

If the gas flow in a hypersonic facility is brought to rest in a small container in the test section, conditions found at the stagnation point of a model in the flow would be created inside this container. Using a hollow cylinder with one end closed as the container and aligning it so that its open end is presented to the flow, it is possible to use the time it takes for the flow to fill this cylinder to give the other flow information desired. This is akin to catching the flow of water in a bucket. By analogy, the reflected shock wave, moving back from the closed end, is the water level in this case. To be more explicit, by writing the equations of continuity, energy, and momentum relative to an observer moving with the reflected shock wave, it is possible, in theory at least, to find the flow velocity, density, and pressure, if the state of the gas in the container can be determined. If the gas flow is in equilibrium, this would also give the Mach number of the flow.

To find the state of the equilibrium gas at rest in the container, or probe, two state properties need to be measured. One, the pressure, is already being measured in this type of flow. Thus, this necessitates only one new-type measurement of a state property. Now, the speed of sound is a state property, but apparently its measurement had not been applied to this type of hypersonic flow.* The measurement of the speed of sound in the stagnation gas in the probe would be much easier than in the free stream where the lower density and high Mach numbers make the use of a sound-pulse-transmitter-and-receiver system or an optical measurement of the acoustic disturbance difficult. Because the gas in the probe is at rest and the density is increased an order of magnitude over that of the free stream, the use of a transmitter-receiver system is facilitated.

Since the space needed between transducers is small, a probe diameter of an inch would be adequate and thus would be small enough to make a profile of conditions in the two-foot test section of the hot-shot tunnel. The time interval required for a measurement would likewise be short, and thus many readings could be taken, continually monitoring the stagnation conditions as the energy in the reservoir is depleted during the twenty millisecond testing time. This is important in determining how much of the test data, such as heat transfer, to use. This report shall be used to introduce the theory of the probe and to discuss the problems associated with putting the probe into practice.

3. THEORY OF THE PROBE

The speed of sound for a gas in thermodynamic equilibrium is given by

$$a^2 = \left(\frac{\partial p}{\partial \rho}\right)_s \qquad (1)$$

*The author later found that Aronson and Marshall (Reference 4) of the NOL were attempting to determine the stagnation speed of sound in a shock tunnel by allowing the shock to resonate a tube, the end of which was a piezoelectric crystal. Assuming that all disturbances after the initial and reflected shock waves were weak ones, and hence sonic, they could determine the sound velocity by the frequency at which the crystal was driven.

where the partial derivative of the pressure in respect to the density is evaluated along an isentrope. For the range of stagnation conditions found in the hot-shot tunnel, this quantity is obtained from statistical mechanical calculations and is plotted on a Mollier diagram (Reference 5). It can be seen from this diagram that any two state properties in the equilibrium gas at rest will determine the state of the gas and, hence, the value of the other state properties at that condition. Thus, the measurement of the speed of sound and the pressure in the stagnation state gas, created by bringing the flow to rest in the probe (Fig. 1), will determine the stagnation state of the gas if it is in equilibrium.

The flow initially enters the probe with the same conditions as found in the free stream outside. Upon reaching the closed end, the flow in the probe must stop. Thus, a shock wave, which will be called the reflected shock wave, moves upstream in the probe to halt the oncoming flow. Now, the enthalpy of the stagnation gas in the probe behind this reflected shock wave is greater than the stagnation enthalpy of the free stream as found at the stagnation point of a model in the flow behind a stationary bow shock wave. This can be shown by writing the energy equation in a coordinate system fixed to the reflected shock front. Or it can be shown by simply consulting some tabulated shock tube performance data, e.g. Reference 5, and comparing the enthalpy of the gas in the tube after the reflected shock with that found at the stagnation point of a body in the flow. When the reflected shock moves outside of the mouth of the probe to become a detached bow shock, the enthalpy inside the probe is reduced to the stagnation enthalpy of the stream by means of an expansion wave which enters the probe.

The equations of continuity, energy, and momentum, written relative to the reflected normal shock wave in the probe, are

$$\rho(V + V_{SR}) = \rho_R V_{SR} \tag{2}$$

$$h + \frac{(V + V_{SR})^2}{2} = h_R + \frac{V_{SR}^2}{2} \tag{3}$$

$$p + \rho(V + V_{SR})^2 = p_R + \rho_R V_{SR}^2 \tag{4}$$

where ρ, V, h, and p with no subscripts denote the free stream density, velocity, enthalpy, and pressure, respectively, and those with the subscript "R" denote conditions after the reflected shock wave. V_{SR} is the reflected shock wave velocity. Both velocities are relative to the probe which is fixed in the laboratory system.

The terms on the right side of the three equations are all known if two state properties in the reflected region and the reflected shock velocity are measured and if equilibrium of the gas in this region is assumed so that an equation of state,

$$h_R = h_R(p_R, \rho_R) \tag{5}$$

can be used.

This gives three equations for four unknowns: V, ρ, h, p. Rather than assuming equilibrium upstream of the shock wave, i.e., $h = (p, \rho)$, the system is completed by use of the energy relation

$$h + \frac{V^2}{2} = h_s \tag{6}$$

where h_s is the stagnation enthalpy of the stream, found from measurements in the probe when the conditions have readjusted from those present after the reflected shock to those found at the stagnation point of a body in the flow. Equation (6) simplifies Eq. (3) to the form,

$$h_s + V V_{SR} = h_R \tag{7}$$

where only V is unknown. Thus, by determining h_R, the enthalpy while the reflected shock is in the probe; h_s, the enthalpy when the gas inside reaches stagnation point conditions; and V_{SR}, the reflected shock velocity relative to the probe, the free stream velocity of the flow can be determined from the energy equation, Eq. (7). In addition to determining h_R, the measurement of the speed of sound and pressure after the reflected shock also gives the other state properties, including the density ρ_R. Therefore, using the free stream velocity found from the energy equation and V_s and ρ_R, the free stream density, ρ, can be found from the continuity equation, Eq. (2).

Finally, use of the momentum equation, Eq. (4), with the terms determined above, yields the free stream pressure p. However, reservation must be placed on the use of this equation because of the order of magnitude of the various terms. This will be discussed in a later section of this report.

In no place in the preceding theory has any assumption been made as to the thermodynamic state of the gas ahead of the shock wave. Therefore, it is possible to use the probe theory in non-equilibrium flows.

4. DISCUSSION

Although the probe seems uncomplicated in theory, there are several problems that stand between the theory and actuality. This section discusses these problems and describes the progress already made on the probe (Fig. 1).

4.1 The Speed of Sound Measurement

The pressure in the probe can be measured by a commercial pressure transducer. The reflected shock velocity can be measured by using two pressure gages or two heat transfer gages mounted at different locations along the length of the tube. However, the measurement of the speed of sound is new and, thus, requires development. This velocity will be measured by dividing the distance between a sound pulse transmitter and its receiver by the time required for the pulse to traverse that distance.

In order that the distance traveled through the colder thermal boundary layer that will surround the hot gas in the probe be small compared to that traveled through the hot core of the gas, it was proposed that the sound be propagated lengthwise in the probe, with the transmitter near the open end and the receiver in the closed end. In this manner, the probe diameter can be kept small for a long distance between transmitter and receiver. The part of the sound pulse traveling through the hotter core of the gas will arrive at the receiver before the remainder of the pulse which is traveling along the boundary layer, since the speed of sound is greater in hot gas. Hence, the first of the pulse to arrive at the receiver will be an accurate determination of the true stagnation speed of sound. If a hole is placed in the end to allow a small flow to replenish the heat lost to the walls by the gas, the sound wave could be reflected off the closed end and received back near the source. Thus, the subsonic velocity of this small flow would be added to and subtracted from the sound velocity and would not affect the measurement. It was also proposed that piezoelectric crystals be used for the transmitter and receiver, although a spark could be substituted for the transmitter. A study of the complexities involved disclosed two main problems:

1. The transmitting of enough energy at these low densities to be seen by the receiver above the noise of the system.

2. The design of a receiver and high amplification system that would not be overloaded by the pressure pulse of the reflected shock wave and, hence, would be able to function shortly after passage of this shock.

To simplify the first problem, it was decided to transmit across the probe rather than lengthwise, temporarily ignoring the small effect of the thermal boundary layer. The development of the sonic measuring instrumentation will be reported in a later publication (Reference 6). This instrumentation has performed satisfactorily in a shock tube designed specifically to give the small pressure jump expected from the reflected shock in the hot shot tunnel. This shock tube was used rather than the hot shot because of the expense and the long-time duration between tests involved in using the larger facility. The speeds of sound measured in the shock tube correspond very closely to the values expected from use of the shock tube equations. The instrumentation now awaits testing in the hot-shot tunnel.

4.2 Equilibrium of the Gas in the Probe

Since the gas in the probe behind the standing normal shock remains in the tube for a long time, it will reach equilibrium. However, the stagnation enthalpy after the reflected shock is determined by measurements taken while the reflected shock is still in the probe, or at least before the subsequent expansion wave reaches the receiver. Thus, the time for a measurement is quite short. In order that the sound velocity and the pressure measured in the gas in that interval can be related to the other gas properties by use of the Mollier diagram, the gas must have reached equilibrium. Therefore, it is important to determine what can be expected for the relaxation time of the gas passing through the reflected normal shock.

Logan (Reference 7) has computed equilibrium distances behind a standing normal shock at 120,000-ft altitude versus Mach number. The 120,000-ft altitude is at the lower limits of the densities expected in the hot-shot tunnel. As the reflected shock in the probe is only slightly stronger than the standing normal shock wave in front of a body, the conditions after the reflected normal shock can be assumed to be roughly the conditions found after the standing normal shock in Logan's work for the same free-stream flow conditions. Likewise, the velocity at which the reflected shock moves away from the stagnant gas in the probe can be taken as equal to the velocity of the gas moving away from the standing normal shock. Thus, the relaxation distances determined by Logan apply to the distances required behind the reflected shock for the gas in the probe to reach equilibrium. This distance must be shorter than the length of the probe.

The relaxation path lengths for vibrational excitation, oxygen dissociation, and NO formation are found to be less than a tenth of a foot for the Mach numbers expected in the hot-shot tunnel. The path length required to achieve nitrogen dissociation equilibrium exceeds 1 ft below a Mach number of 16 but rapidly becomes shorter above this Mach number. However, only 5 percent of the total internal energy of the gas is in nitrogen dissociation at Mach 16, and this drops to 1 percent at Mach 14. Therefore, the lack of nitrogen dissociation equilibrium may be disregarded. It appears, then, that any length of probe will be adequate in hot-shot test conditions with densities comparable to 120,000-ft altitudes. Logan states that at higher altitudes dissociation equilibrium distances may be a foot or more for small values of dissociation. Thus, for the initial tests, a 6-in. probe length will suffice, but this may have to be lengthened at the upper range of hot-shot simulated altitudes. Lack of equilibrium in the flow ahead of the shock wave will mean that conditions the shock wave tends to produce, e.g., dissociation, are already present to some extent in the flow. The effect of this will be to shorten the equilibrium distances behind the shock wave.

4.3 Heat Loss from the Gas in the Probe

Since the probe brings the gas to stagnation conditions and, hence, high temperatures, there will be heat transferred from the gas to the probe walls. This means a loss of stagnation enthalpy and, therefore, an error in measurement of the true stagnation conditions. Theoretically, after the reflected shock, the gas should be brought to rest. However, there undoubtedly will be some eddy motion in this gas. Thus, it would be difficult to make an analysis of the convection heat transfer. It is easier to construct the probe and mount heat transfer gages on the walls, directly measuring the heat loss by all means of heat transfer to the wall. This will be done when the probe is tested in the hot-shot tunnel.

At the high stagnation temperatures encountered, there is some concern as to the magnitude of the radiation heat loss. It is possible to get a rough estimate of this loss by referring to the work done by Meyerott (Reference 8). He makes an estimate of the radiation heat transfer to the hemispherical nose of a ballistic missile re-entering the atmosphere, finding the peak heating to occur at an altitude of about 100,000 ft. Since the thickness of his shock layer is about the same as the probe diameter, the results

can be applied to the probe, although the temperature, about 8,000°K, exceeds those found in the hot-shot simulation of this altitude by 3,000°K. Accordingly, for this rough estimate, the radiant heat flux will be reduced by the fourth power of the temperature ratio. Although the missile's radiant heat transfer flux, 75 Btu/sq ft/sec, is only 10 percent of the convective heat flux, the lack of motion of the gas in the probe greatly reduces the convective heat flux, and the radiant flux becomes important. The radiant heat transfer flux in the probe is reduced to 11 Btu/sq ft/sec by accounting, as mentioned above, for the lower stagnation temperature. This makes the heat lost to the walls of the 1-in. diameter, 6-in. long probe 1.43 Btu/sec, i.e., 5.2 percent of the heat content of the gas in the probe is lost in 1 ms. But for the same time duration, 51 times the energy lost to the probe walls is delivered at the mouth of the probe by the gas flow. Thus, allowing a small flow through the probe by drilling a vent hole in the closed end, true stagnation conditions can be maintained. This flow is necessary also for continual monitoring of the decreasing stagnation conditions of the flow outside.

The heat contained within the probe is a function of the square of the diameter, whereas the heat loss depends linearly on this dimension. Therefore, variation of the probe diameter in tests will provide an estimate of the minimum probe size for a certain degree of accuracy.

4.4 The Effect of the Boundary Layer on the Conditions Behind the Reflected Shock

The beginning of flow into the probe brings with it the growth of a boundary layer in the tube. Thus, the assumed one-dimensional character of the flow is violated, and the conditions behind the reflected shock wave will vary from those expected by theory. The redistribution of velocity across the probe also will affect the reflected shock wave velocity. Therefore, an estimate of the effect of the boundary layer can be obtained by comparing the reflected shock velocity measured in shock tube experiments with the theoretically expected values. The few measurements made of this value at Lockheed agree within 10 percent of the theoretical values and an improvement in the measuring technique may indicate closer agreement.

4.5 Comparison of the Magnitudes of Terms in the Equations

In order to use the experimentally obtained values in Eqs. (2), (4), and (7) to determine the unknown quantities, the terms involving these unknown quantities must have values that are significant when compared to the terms containing the measured values. For instance, in Eq. (7), the term VV_{SR} must be large enough that the measured value of h_R is sufficiently greater than that of h_S so that the experimental accuracy of the measurements is a small percent of the difference. At large velocities and low static temperatures, conditions found in the hot-shot test section, h_S can be approximated by $\frac{V^2}{2}$. For the velocities and densities expected, V_{SR} will be about one-tenth of V. Therefore, VV_{SR} will be about 20 percent of h_S, or h_R will be 20 percent greater than h_S. This means the speed of sound and pressure readings will have to be quite precise to determine accurately the velocity. The progress on the speed of sound instrumentation indicates high accuracies, and this may prove less troublesome than the pressure and reflected shock velocity measurements.

In the momentum equation, Eq. (4), the ambient pressure term, p, in high-speed, low-density flows, is two orders of magnitude smaller than the dynamic pressure. Therefore, the experimental determination of the static pressure by finding the other terms in this equation is quite impossible. However, this might have some application near the throat of a hypersonic tunnel where the static pressure is still high. In the hot-shot tunnel, the flow is almost one-dimensional, and thus the static pressure on the wall of the test section can be assumed to exist across the flow at that location. Neglecting p, the momentum equation can serve as a check on the values determined from the energy and continuity equations.

4.6 Approximations

If the flow in the test section of a hypersonic facility has a high velocity and a low static temperature and is in equilibrium, or is not in equilibrium but has only a small percent of its energy in frozen degrees of freedom, then the steady state energy equation is approximated by

$$\frac{V^2}{2} = h_S \tag{8}$$

This means that the stagnation enthalpy, found from measurements in the probe when the bow wave is standing outside of the mouth, will determine the flow velocity.

If the free stream static pressure is small compared to ρV^2, it can be neglected. Thus, neglecting the pressure due to the small velocity after the bow wave, the momentum equation will yield

$$\rho = \frac{p_S}{V^2} \tag{9}$$

or

$$\rho = \frac{p_S}{2\,h_S} \tag{10}$$

where p_S is the pressure of the stagnation gas in the probe. Hence, the usual hypersonic assumptions will greatly simplify the measurements to be made in the probe. However, the assumption that the free stream enthalpy, h, is small compared to $\frac{V^2}{2}$ (from 1 to 5 percent at hypersonic velocities) may not be justified in the case of frozen flow and thus Eq. (7) must be used to find the flow velocity.

5. CONCLUDING REMARKS

In the preceding discussion, problems associated with the probe have been briefly investigated and, at present, do not look forbidding. Thus, it seems possible to calibrate short duration hypersonic flows by use of the probe. The flow must be of sufficient duration, however, so that conditions do not change significantly during the time required for the reflected shock

to move outside the probe and become the bow wave. This is necessary in order that h_S and h_R may be measured under the same flow conditions and may involve a time duration of 1 to 2 ms. By extending the probe some distance beyond the rear transducer, any transient flow that precedes the establishment of the quasi-steady state flow in the hypersonic facility will fill only that part of the probe and hence will not affect the measurements, provided that the pressure adjustment is rapid.

It may be possible to use a quick opening gate in front of an evacuated probe to produce the reflected and subsequent stagnation conditions at any given time in a steady or long duration flow. The probe should also make it possible to monitor the constancy of flow conditions over a period of time by determining the stagnation enthalpy at intervals of 0.5 ms.

By making some of the common assumptions of hypersonic flow, the problems of the probe are greatly simplified. For instance, the reflected shock velocity and the reflected conditions do not need to be measured. However, frozen flow may not allow one of these assumptions.

At present, it seems that the development of instrumentation to measure the speed of sound will be a success. The theory of the probe involves the measurement of two state properties in the probe but does not specify which these should be. Therefore, other possibilities, such as absorption measurements of the density, should not be overlooked in the event that the measuring of either pressure or sonic velocity becomes too difficult.

A program is in progress to apply the probe to the calibration of the Lockheed hot-shot tunnel, and the results of this program will testify as to the practicality of the probe theory.

REFERENCES

1. Smelt, Ronald and Turner, T. E., "Lockheed Arc-Heated Hypersonic Tunnel", paper presented at the SAE National Aeronatuic Meeting, Oct 1958.

2. Turner, T. E., " Design of the Lockheed Spark-Heated Wind Tunnel", Lockheed Missiles and Space Division Rept. No. LMSD-48467, March 1959.

3. Bray, K. N. C., Departure From Dissociation Equilibrium in a Hypersonic Nozzle, Aeronautical Research Council, ARC Report 19, 983, March 1958

4. Aronson, P. and Marshall, T., "Shock Tube Wind Tunnel Research at the Naval Ordnance Laboratory", paper presented at the Second Shock Tube Symposium sponsored by the Air Force Special Weapons Center, March 1958

5. Feldman, Saul, Hypersonic Gas Dynamic Charts for Equilibrium Air, AVCO Research Laboratory, AVCO Report, January 1957

6. Hollander, L. E., Vick, G. L., Hearns, C. B., Farmer, A. V., and Perls, T. A., "Velocity of Sound Measurements in High Temperature, Low-Density Gas Flows", LMSD-48477, (in preparation)

7. Logan, Joseph G. Jr., "Relation Phenomena in Hypersonic Aerodynamics", paper presented at the 25th annual meeting of the Institute of the Aeronautical Sciences, January 1957 (IAS Preprint No. 728)

8. Meyerott, Roland E., Radiation Heat Transfer to Hypersonic Vehicles, LMSD-2264, Sunnyvale, California, November 1957

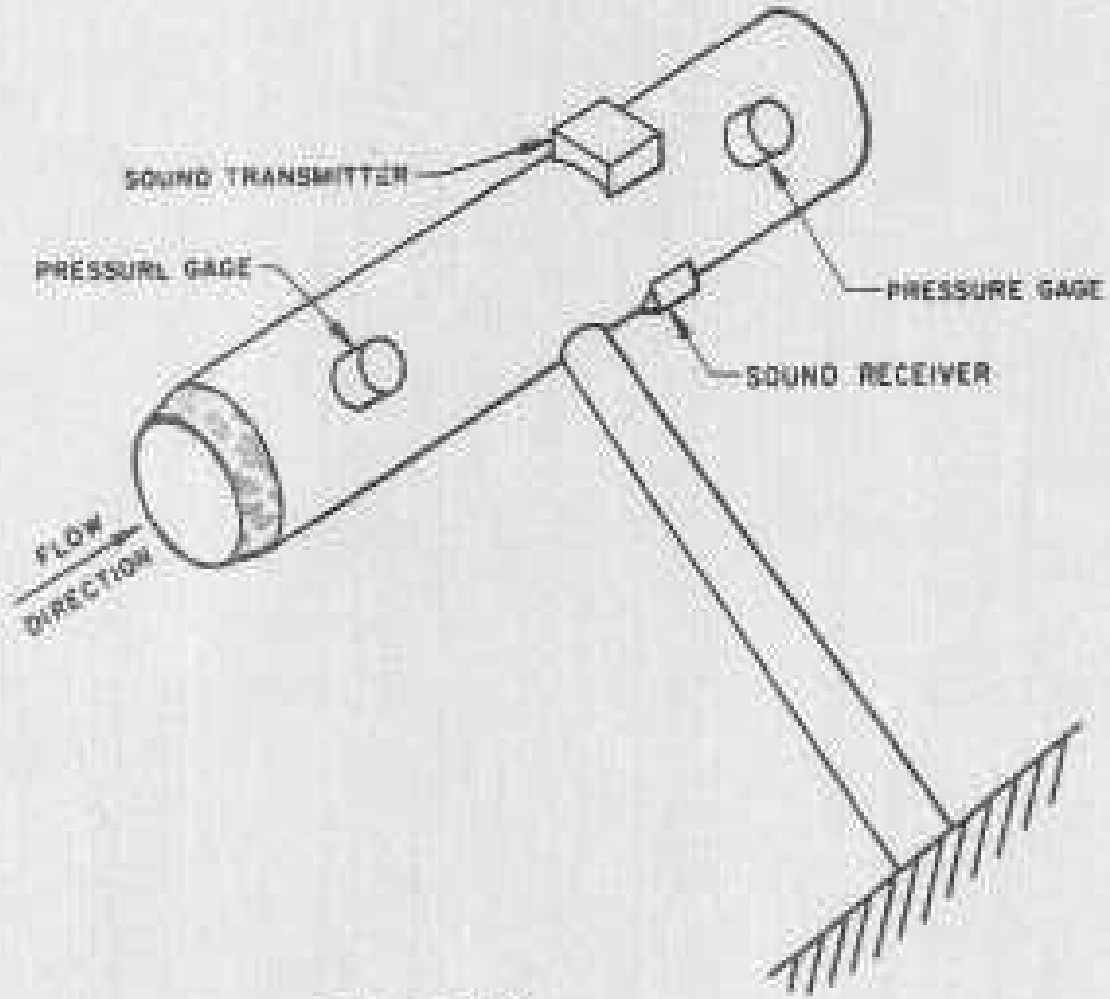

Figure 1 Probe

FLOW PHENOMENA IN THE CONVAIR FREE JET SHOCK TUNNEL

Karl A. Faymon
Theoretical Aerodynamics Group, Convair

The free jet shock tunnel is an aerodynamic facility wherein testing is carried out by directing a high velocity jet, which issues from a gun muzzle or the open end of a shock tube, against a model suspended in the path of this jet. In order to effectively utilize this tool as an aerodynamic test facility, it is necessary that the flow phenomena in the test area be accurately known. For this reason, calculations have been carried out to determine the state of the working gas in the gun barrel or shock tube, and to determine the flow field of the jet. The determination of the flow field includes the location and geometry of the recompression shock, and the resulting rotational flow behind this shock, which forms whenever a high pressure jet is expanded into a low pressure environment.

INTRODUCTION

The Convair Free Jet Shock Tunnel facility is basically an open end shock tube. The working, or driven, gas issues from the open end and is directed against the model. The model is suspended in a manner such that it has unrestrained freedom of motion. The jet, when it strikes and flows over the model causes model displacement. Time histories of this displacement, as recorded by high speed cameras, permit the calculation of the pertinent aerodynamic force and moment coefficients.

Figure 1 is a schematic diagram showing the essentials of the Convair facility. The motion, as in any shock tube, is initiated by the rupture of the diaphragm separating the high pressure driver gas section from the low pressure working or driven gas section.

The initial shock which originates at the time of diaphragm rupture travels down the barrel, or tube, and upon arriving at the end bursts the diaphragm which separates the driven or working gas from the test chamber where the model is suspended. The flow then expands into the test chamber which is evacuated to the desired pressure level.

The flow in the test chamber is no longer one-dimensional but has an axis-symmetric character. Thus the model is not immersed in a uniform stream, but in a flow with axial velocity gradients and radial velocity components. Actually, it is the Mach number gradients, both axial and radial, which are of interest rather than the velocity gradients. Therefore, in order to be able to evaluate the test data obtained by means of this facility, it is necessary to know these Mach number gradients and radial components.

Also, a recompression shock forms in the test chamber and behind it is the free jet boundary. It is necessary to have knowledge of the geometry and location of this shock to determine whether or not it will interfere with the flow in the region to be used for testing.

MOTION AND STAGE OF THE GAS IN THE SHOCK TUBE

The motion in the tube or barrel portion is a typical shock tube motion. It is the final phase of this motion which must provide the initial conditions for the solution of the free jet flow field. Thus, it is desirable to determine to as high a degree as possible, the state of the gas at the shock tube exit.

In a case where viscous effects are neglected, a typical shock tube motion consists of a steady initial shock, followed by a constant velocity contact surface which is in turn followed by a rarefaction wave centered at the diaphragm station. The portion of the flow bounded by the shock and the contact surface is a steady flow and it is this portion of the flow which is used for testing. Thus it is the state of this portion of the flow which is of interest here.

The driver gas which was considered was a mixture of hydrogen-oxygen-helium. The working gas was taken as air at 520°R, the pressure being varied to obtain various states behind the initial shock. The state of the driver gas at the moment of motion initiation was taken as 55,000 psia with a sound speed of 6,700 fps. The specific heat ratio γ in this gas was taken to be 1.5.*

It is a simple matter to determine the state behind a steady shock in a shock tube if the specific heat ratio γ does not change appreciably across the shock (see for instance, Reference 1). However, in the case of very strong shocks, the specific heat ratio cannot be considered to remain constant across the shock. For this reason iterative procedures were used in conjunction with the gas tables of Reference 2 to determine the thermodynamic state of the gas behind the shock. These results are given in Figure 2 plotted against the driver-driven gas diaphragm pressure ratio.

Also of interest are the chemical states and the electronic states of the gases. The electronic state (ionization), was found to be negligible and the chemical state (composition) was determined from the tables of Reference 4. All cases considered were for equilibrium air. The composition of the air is shown in Fig. 3.

FREE JET FLOW FIELD

A method of characteristics procedure was used to carry out an analysis of the flow field of the expanding jet of the high-velocity gas gun. The analysis includes the assumption of steady state flow and constant specific heat ratio but no restriction as to shock free irrotational flow is imposed.

The characteristic procedure for the flow field calculation was devised and programmed by J. Bowyer of the Aerophysics Group of Convair-Astronautics.

---

*These values were suggested by Dr. Z. Slawsky of NOL who serves as consultant for the Convair facility

The jet flow field calculation starts at the tube or barrel exit. This station serves as the initial data carrier of the initial value problem for the flow field calculation, the initial data being determined from the shock tube portion of the flow. The governing equations are the axisymmetric flow equations, and these are set up to treat the cases where the jet expands into an absolute vacuum environment or into a non-zero pressure environment.

Figure 4 is a schematic diagram showing the characteristic network in the neighborhood of the initial data carrier. The computation starts by assuming a Prandtl-Meyer type expansion at the nozzle corner. Whenever expansion takes place into a non-zero pressure environment a recompression shock forms. Figure 4 shows the characteristic geometry by which this shock is determined. The C_+ characteristics strike the constant pressure jet boundary and are reflected. These reflected characteristics are propagated into the flow field as C_- type characteristics and at some point will intersect the ray-like characteristics of the Prandtl-Meyer fan. At such points the solution loses its single-valuedness, and these points may be identified with shock points. At such a point the shock conditions must be fulfilled.

The shock must start at the tube corner with zero strength. It must start at this point with vanishing strength since in a sufficiently small neighborhood of the corner every direction is a characteristic direction and only a zero strength shock can coincide with a characteristic direction. Because of this, in a region close to the corner the shock is of such weak strength that it can be ignored, and the cross characteristics at this point can be assumed to have slope continuity until they reach the constant pressure boundary and are reflected. This allows a portion of the flow behind the shock to be determined and this is necessary for proceeding with the calculation when the shock can no longer be neglected. The entire flow field was then computed by a method of characteristics procedure. Since the shock is non-uniform the flow behind the shock has rotational components.

Figure 5 shows the Iso-Mach lines and the streamlines for the case of an incomplete expansion (expansion into a non-zero pressure environment). The initial conditions at the jet are: P = 4,530 psia, M = 1.80, T = 7,360°R, and the flow direction was everywhere parallel to the nozzle axis at the exit.

The jet expanded into an environment with an ambient pressure of one one-hundredth of an atmosphere (0.147 psia). The environment fluid was assumed to be air with $\gamma = 1.400$. This value of the pressure for the ambient air was chosen since it may represent an upper limit for desirable testing. Being an upper limit it presents the most severe case and will represent the case where the shock has progressed the farthest into the region that will be of interest for aerodynamic testing. This shock location is compatible only with these initial conditions, since the shock location and the location of the jet boundary depend upon the ratio of the static pressure in the jet before expansion to the ambient environment pressure. Thus, even though the environment pressure was to be held at one one-hundredth of an atmosphere both the

shock and the jet boundary could be caused to migrate further into the flow region of interest by lowering the static pressure in the jet before expansion.

As can be seen from Figure 5 the location of the shock and jet boundary are such that with these initial conditions, no interference with the flow in the region of interest is expected.

On Figure 6 are shown the various shock and jet boundary locations which result by varying the ambient to static jet pressure ratios. In all cases the pressure of the ambient environment was assumed to be 0.147 psia which may represent the maximum desirable for aerodynamic testing. The ambient medium was taken to be air with a γ-value of 1.400. In the case where the environment medium is at rest, which is the only case treated here, the γ-value of this medium has no effect upon the shock and jet boundary locations. Only the pressure of this medium can effect the shock and jet boundary locations if the local Mach number in the environment medium is zero.

Three separate cases with different initial conditions in the jet are shown here. The sets of initial conditions are: 1) P_{jet} = 4,500 psia, M = 1.80; 2) P_{jet} = 2,140 psia, M = 1.76; 3) P_{jet} = 1,350 psia, M = 1.78; and the flow direction in all cases was parallel to the jet axis at the exit. These sets of initial conditions for the jet correspond to the following sets of initial states of the driver and working gases at the instant motion is initiated: 1) driver gas pressure 55,000 psia, working gas pressure is three atmospheres; 2) driver gas pressure is 55,000 psia, working gas pressure is one atmosphere; and 3) driver gas pressure is 55,000 psia, and working gas pressure is one-half atmosphere. In all cases, the driver gas was taken to be a mixture of helium-oxygen-hydrogen and the working gas was at standard temperature before motion was initiated.

As can be seen from this plot, the location of the jet boundary and the shock is such in each case that no interference with the region to be utilized for aerodynamic testing is expected. No complete characteristics diagrams were obtained for the flows with jet static pressures of 2,140 psia and 1,350 psia due to difficulties with the machine program. However, the dimensionless quantities in the flow field such as Mach number and streamline direction depend only on the initial value of the Mach number given at the jet exit. Since this Mach number was very nearly the same for all three cases shown here, the streamline pattern and Mach lines shown on Figure 5 may be used with any of these cases.

Figure 7 is a comparison between the Iso-Mach lines for two different values of γ, the values chosen being 1.332 and 1.400. As mentioned previously, these constant Mach lines for the case γ = 1.332 are considered representative for all the flow conditions analyzed in this report.

Of particular interest, in the region of the jet which will be utilized for aerodynamic testing, are the Mach number gradients in both the axial and radial directions. As can be seen from Figure 7, these gradients do not change appreciably with a change in γ. The average axial Mach number gradient, (range $9 < M \leq 16$) for both values of γ is approximately 0.125 Mach number

per nozzle radius. The average radial Mach number gradient for the same range is of the same magnitude in the region near the axis which is of interest for testing.

SUMMARY

The analysis of the flow field has been carried out and it has been found that, under the conditions that will be present when this facility is used for aerodynamic testing, the Mach number gradients are very small, and the recompression shock geometry is such that it will not interfere with the testing region. However, this analysis did not take into account the possibility of reflection from container tank walls.

The size of the tank of the Hypersonic Gas Gun is about eight to ten feet in diameter or larger and this is large enough so that the reflections will be swept downstream before they can interfere with the flow in the test region. If these walls are not too far removed from the axis of the jet, this reflection phenomena could result in an interference with the flow in the test region. One way of preventing such interference would be to replace some streamline in the expanding jet by a conical wall section, the outer surface of which would absorb the reflections. Since such a conical section would be, in effect, a streamtube surface, no interference with the internal flow could take place.

This analysis has assumed a constant γ-value throughout the flow. In a real gas, γ is a function of the local thermodynamic state and therefore varies from point to point in the flow. A characteristic procedure which takes into account the local variation of γ is at present being studied and prepared for machine computation. When ready, the irrotational portion of the flow field will be computed to ascertain the effect of non-constant gamma on the flow field.

REFERENCES

1. Liepmann, H.W., and Roshko, A., "Elements of Gas Dynamics", John Wiley and Sons, New York, 1957.

2. Hochstim, A., and Arave, R.J., "Gas Properties Behind Shocks at Hypersonic Velocities", Convair Report ZPH-004, 6-14-57, San Diego, California.

3. Niblett, G.B.F., and Kenney, Anne, "An Approximate Calculation of Equilibrium Conditions Behind Shock Waves in the Noble Gases", Princeton University T.R. II-24, Princeton, New Jersey.

4. Gilmore, F. R., "Equilibrium Composition and Thermodynamic Properties of Air to 24,000 °K", Rand Report R.M. 1543, 24 Aug 1955, Santa Monica, Calif.

5. Faymon, K.A., "Determination of the State of the Working Gas Entering the Test Section of a Shock Tunnel", Theoretical Aerodynamics Note No. 15, Convair, San Diego, 3 Sept. 1958.

6. Faymon, K.A., "High Velocity Gas Gun Jet Analysis", Theoretical Aerodynamics Note No. 16, Convair, San Diego, 9 Oct. 1958.

7. Denton, J.C., "High Velocity Gas Gun Jet Analysis", Thermodynamics Report T-G-102, Convair, San Diego, 31 Jan 1958.

8. Faymon, K. A., "The Composition and Electronic State of the Working Gas Entering the Test Section of a Shock Tunnel", Theoretical Aerodynamics Note No. 18, 3 Nov. 1958.

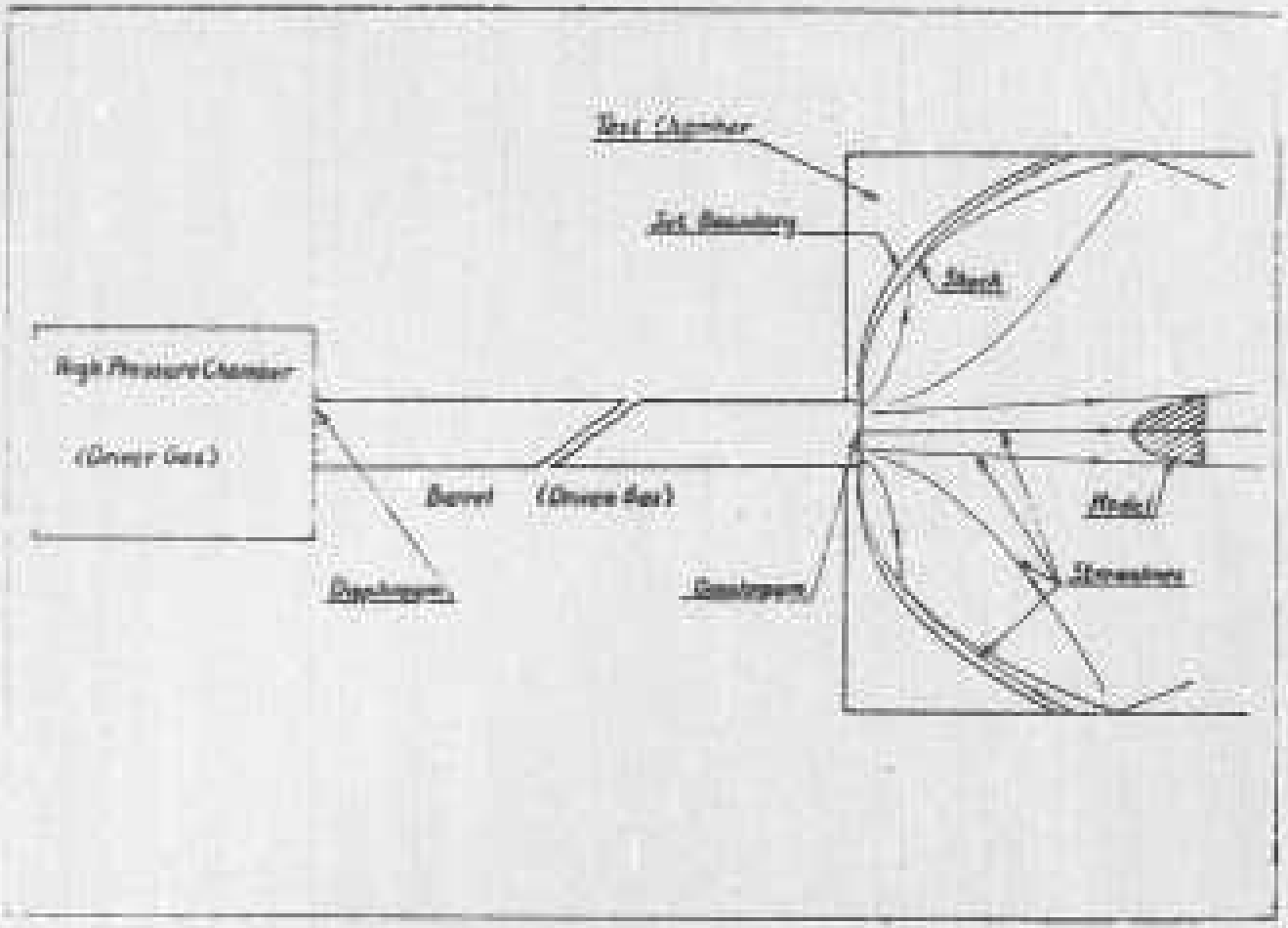

Figure 1 Schematic Diagram of Convair Free Jet Shock Tunnel

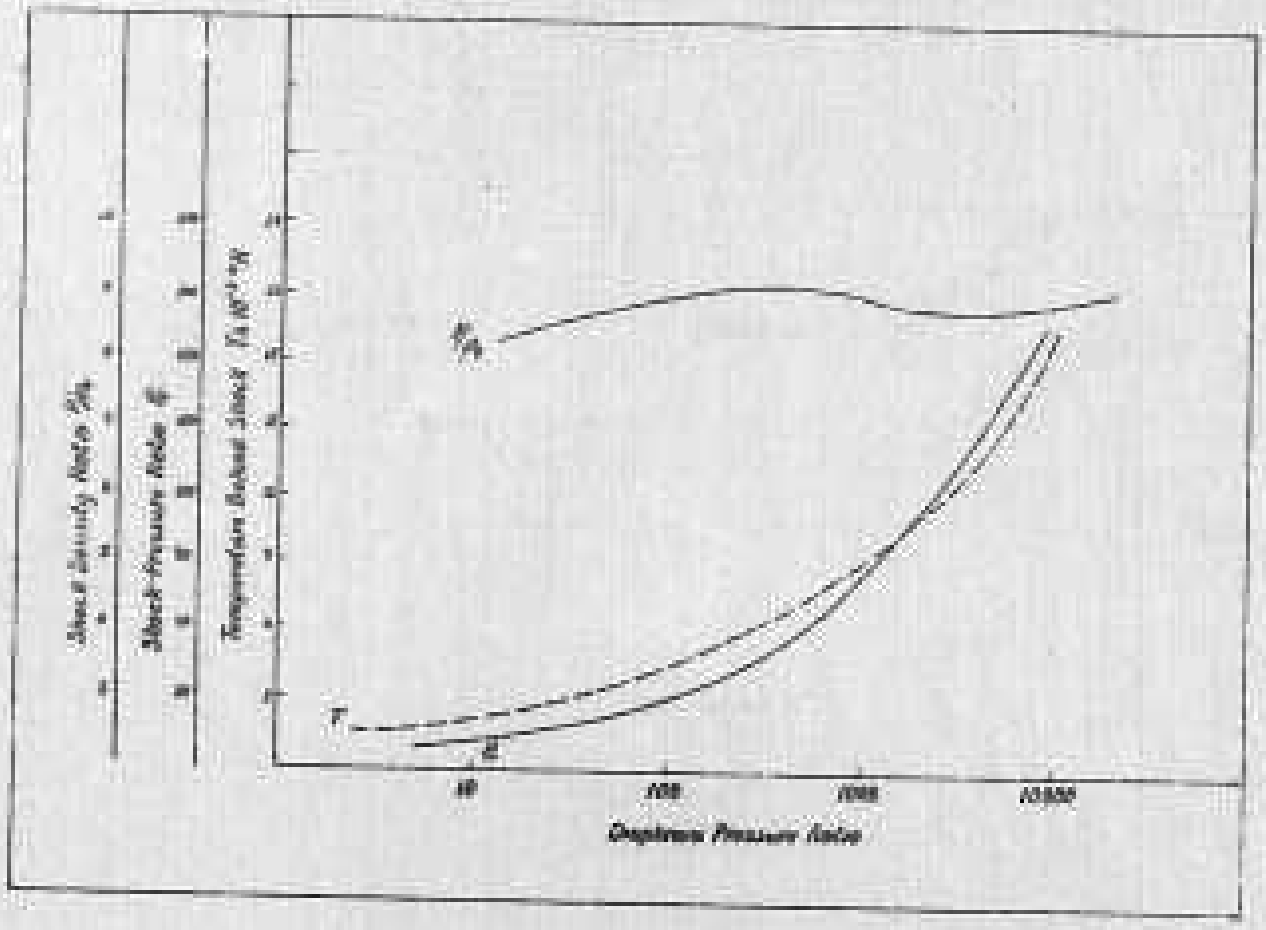

Figure 2 Thermodynamic State of Working Gas (Air) Entering Test Section

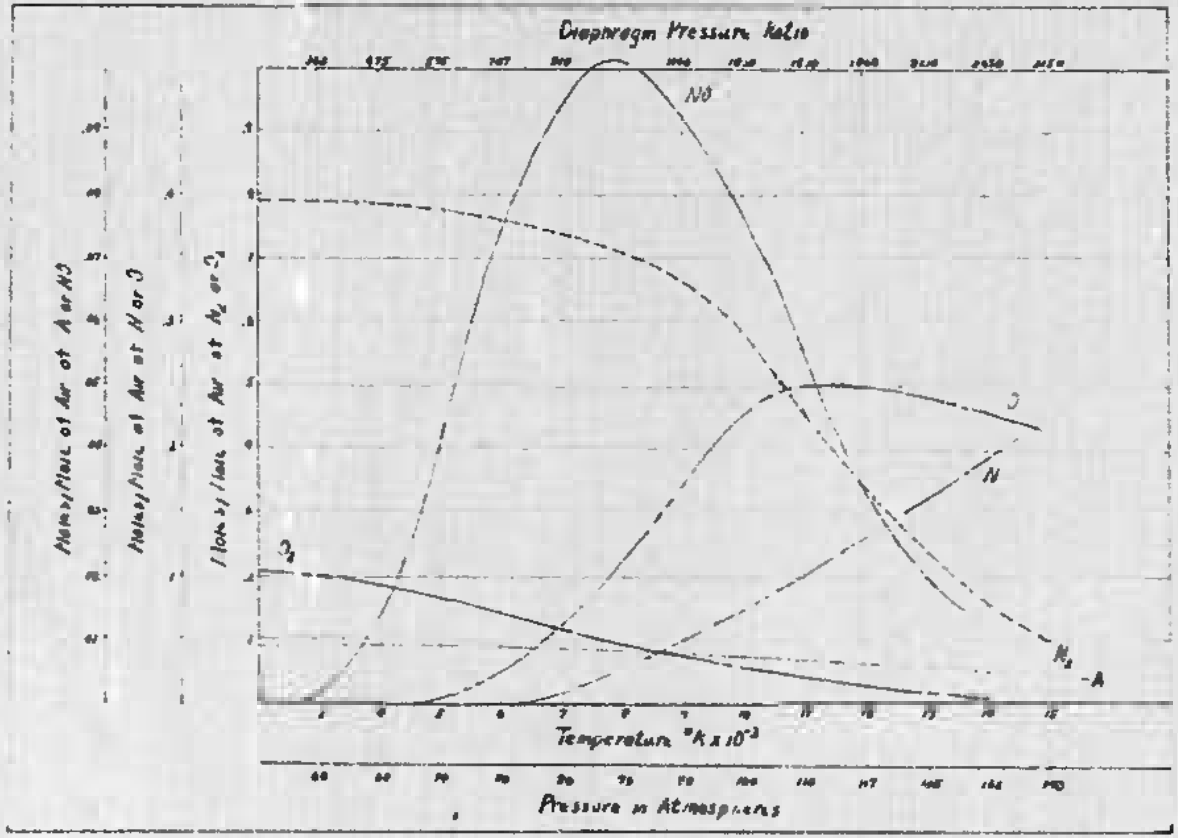

Figure 3 Composition of Equilibrium Air Entering Test Section

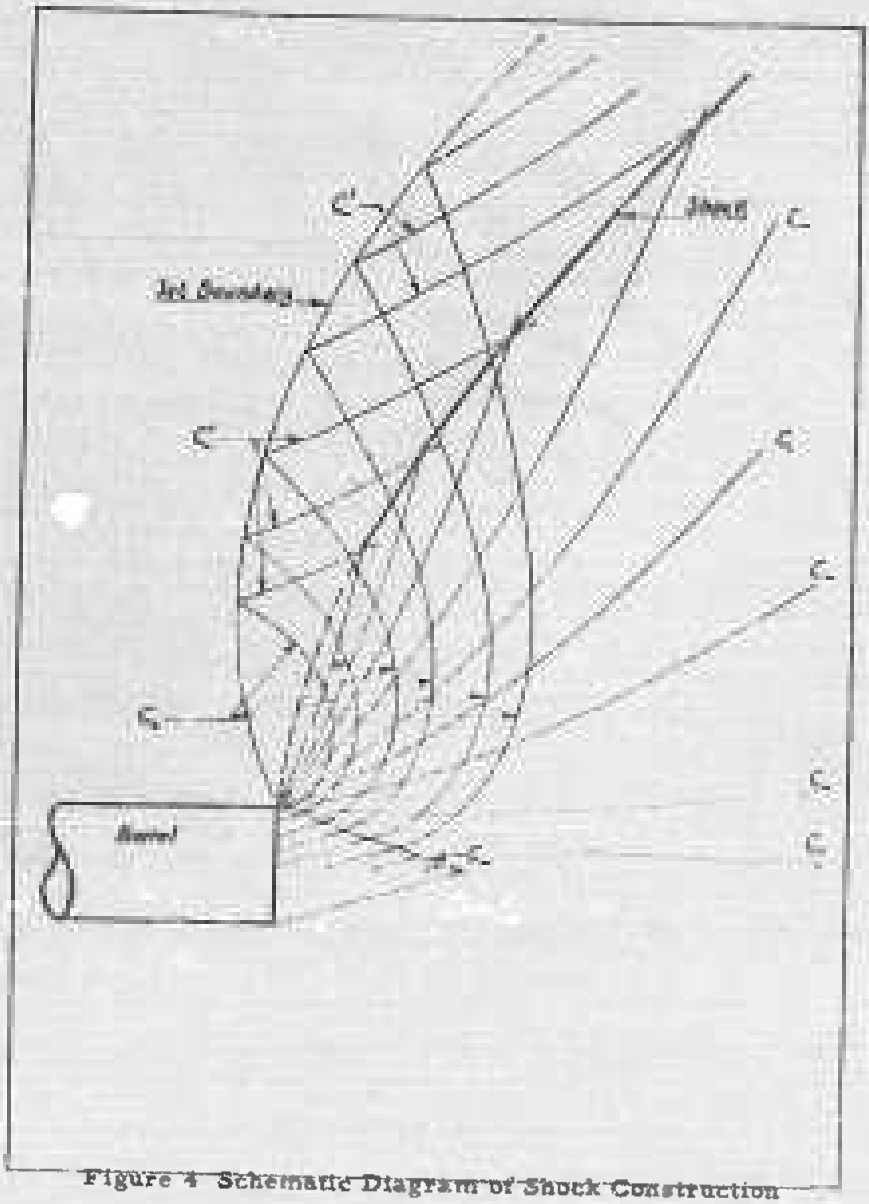

Figure 4 Schematic Diagram of Shock Construction

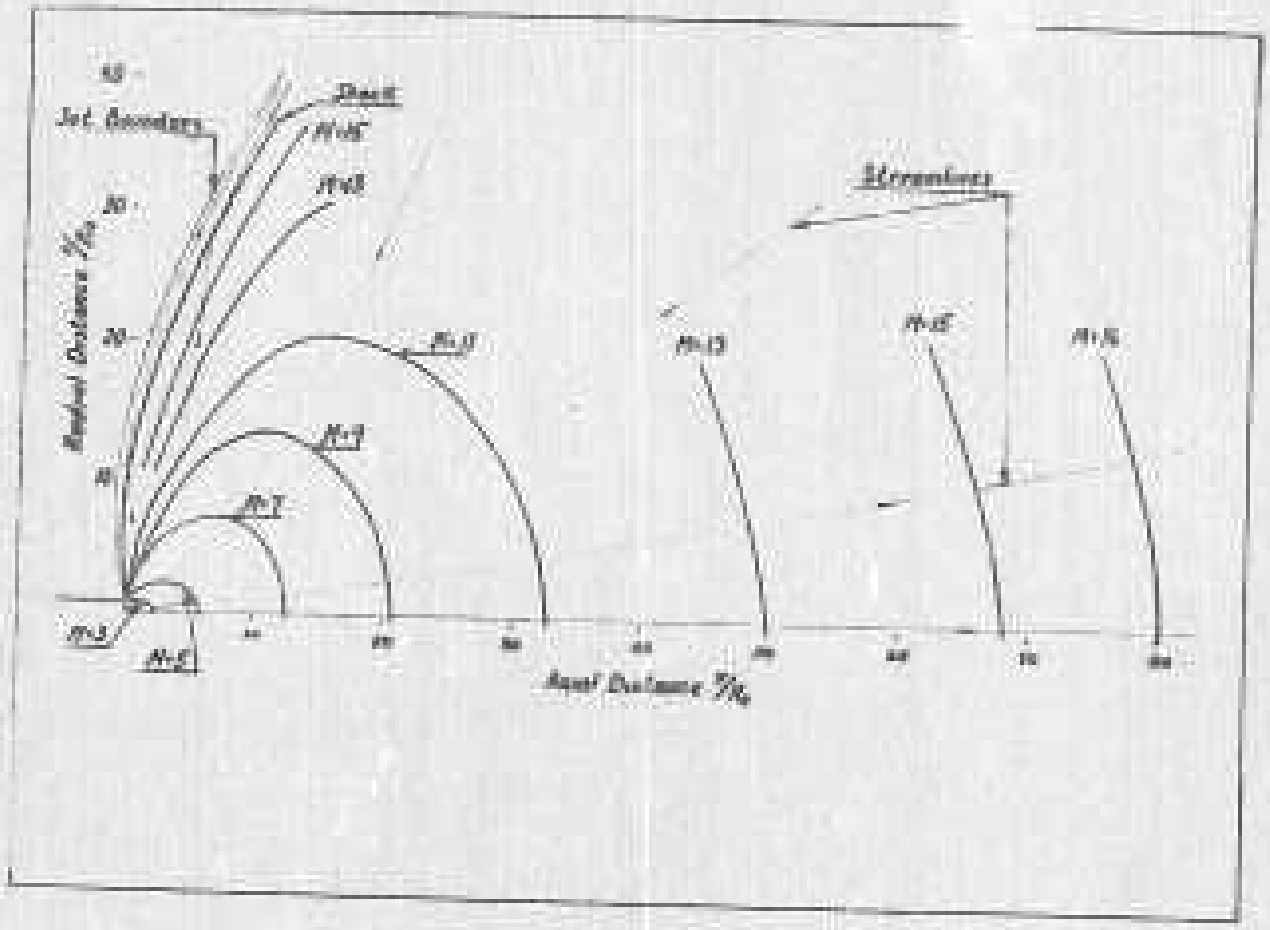

Figure 3 Streamlines, Iso-Mach Lines, Shock, and Jet Boundary Geometry

"NOTICE: When Government or other drawings, specifications or other data are used for any purpose other than in connection wit a definitely related Government procurement operation, the U.S. Government thereby incurs no responsibility, nor any obligation whatsoever; and the fact that the Government may have formulate furnished, or in any way supplied the said drawings, specifications or other data is not to be regarded by implication or otherwise a in any manner licensing the holder or any other person or corpor tion, or conveying any rights or permission to manufacture, use or sell any patented invention that may in any way be related theret

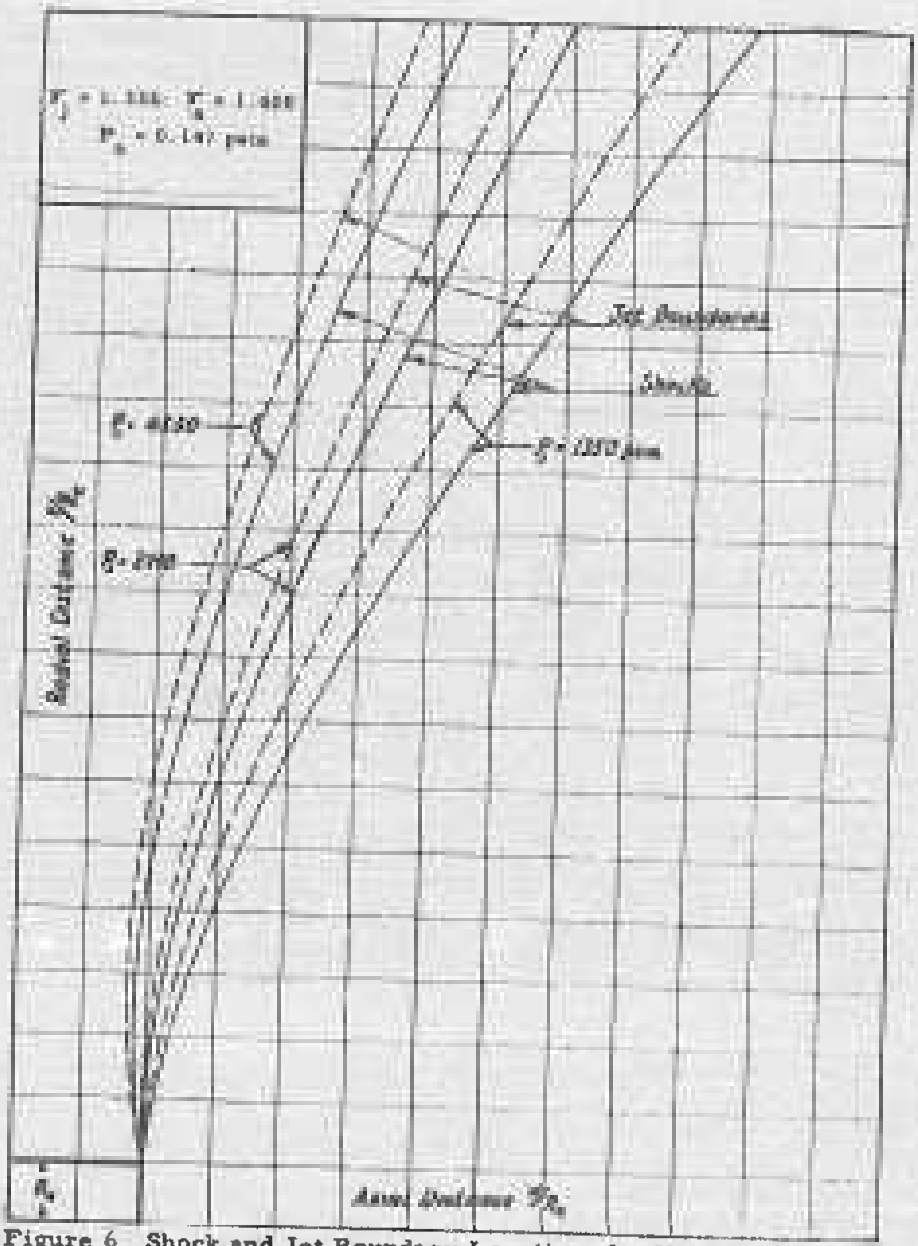

Figure 6 Shock and Jet Boundary Locations for Various Initial Jet Static Pressures

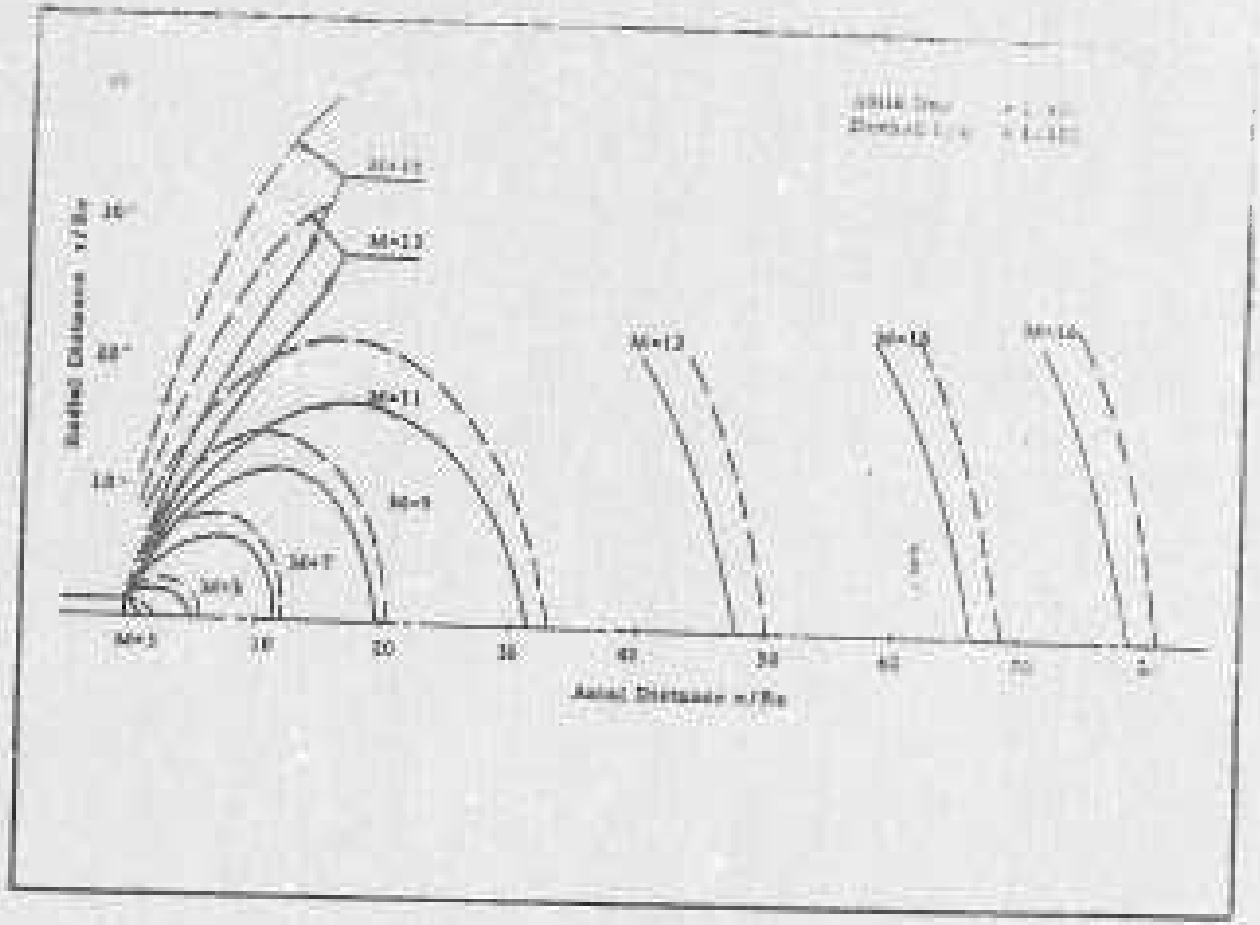

Figure 7 Iso-Mach Lines for $\gamma = 1.332$ and $\gamma = 1.400$

AN EXPLOSIVE DRIVEN CONICAL SHOCK TUBE FOR THE STUDY OF SPHERICAL SHOCK WAVES*

William S. Filler
U. S. Naval Ordnance Laboratory

INTRODUCTION

This paper describes a method for generating spherical blast waves using only a small fraction of the amount of explosive normally required for generating such blasts. From a fundamental and military viewpoint such shocks are of great interest. Indeed, substantial effort, as past symposia indicate, has gone into simulating individual characteristics of explosive blasts. Two conspicuous examples are the decaying pressure behind the front and the development of large peak overpressures. The work which has been done with spherical shock generators of the non-high-explosive type -- the glass sphere experiments at Toronto University and the pyramidal tube used by Campbell (Reference 1) -- have been concerned with weak shocks.

The conical tube described below is generically related to Campbell's device. His tube is a pyramidal cone in shape with its compression chamber at the apex end. The compression and expansion sections are separated by a diaphragm which is ruptured to generate a shock. The tube described in the present paper has the shape of a circular cone and the blast wave is generated by detonating a small quantity of high explosive under heavy confinement at the apex, (Figure 1).

Consider a sphere of high explosive intercepted by a cone. The apex of the cone is at the center of the sphere and the conical surface extends far beyond the spherical surface of the explosive. Detonation of the spherical sector of the explosive within the cone should result in a blast wave comparable to the blast from the free air detonation of the full explosive sphere, assuming no energy is lost to the cone wall. In a device patterned after this model, a given quantity of explosive may be used to produce blast waves characteristic of much larger charges. The ideal amplification factor for the conical shock tube is defined as the ratio of the volume of the full sphere of explosive to the volume of the spherical sector (or the ratio of their weights).

EXPERIMENTAL DESIGN

The experiment performed was intended to demonstrate the feasibility of an explosive driven conical shock tube. Consequently, in the design of the cone, chief emphasis was placed on the use of the minimal quantity of explosive that would provide a blast wave that would be measurable with available pressure transducers and high speed recording equipment.

*This work was supported by the Navy Bureau of Ordnance.

To start with, in place of the idealized spherical segment of explosive discussed above, we chose a convenient and readily available commercial electric detonator. It was of the plastic-cased variety which would minimize the damaging effects of fragments. The explosive load in this detonator was calculated to have the estimated equivalent heat of explosion energy of 0.5 grams of TNT and was the sole source of driving energy for the tube.

The cone was designed to have an ideal amplification factor of 110; that is, it was designed to produce a shock wave simulating that from the detonation of a 55 gram sphere of TNT. A total cone angle of 22 degrees was calculated to produce the desired amplification factor. The entire conical tube was about 4 feet long with a base diameter of 1.5 feet. The main cone body was rolled from 1/8-inch sheet steel. Near the apex, a cylindrical mild steel firing block 3-1/4 inches in diameter by 5 inches long was bolted to the main cone body. The firing block was drilled to provide a snug sliding fit for the detonator.

In the firing position (Figure 2), the cone axis was vertical with the firing block resting on the ground. Explosive loading was accomplished by lowering the detonator from the open end of the cone down into the firing block. Wires were left trailing out of the open end. After seven shots the volume of the detonator hole in the firing block had increased by about one third. No other deformation of the cone was noticed.

INSTRUMENTATION

As may be seen in Figure 3, the characteristic shape of a typical explosive blast pressure wave is the well known discontinuous shock front followed by a rapid decay which, in the case of a 55 gram charge (the simulated amount anticipated in our cone experiment), returns to ambient pressure again in about 500 microseconds. In order to detect and record such pressure transients with reasonable accuracy, the instrumentation must have a rise time capability of the order of 10 microseconds. Instrumentation with this capability was available for this cone experiment from other programs. Such programs involving the measurement and study of blast waves from high explosives have been a continuing activity at the Naval Ordnance Laboratory.

Two types of piezoelectric transducers made by the Atlantic Research Corporation were used to obtain pressure-time histories of the blast. One, a flush type gage, model LD-60, was set in the wall of the tube; the other, a pencil type gage, model LC-13M, was mounted in the flow. The sensing elements of the gages were tubes of lead zirconate, 1/4 inch in diameter. The length of the pencil gage sensing element in the direction of shock propagation was 1/8 inch. The length of the nose or baffle ahead of the sensing element in the pencil gages was 8 times the diameter of the gage. This baffle minimizes disturbing effects at the sensing element caused by the presence of the gage in the flow. The baffle design is based on interferometric diffraction studies of long, slender bodies in shock tube flows (Reference 2).

Gages were calibrated by exposing them to shock waves whose peak pressures were accurately known. This was done by means of free field firings of a standard explosive. Sensitivity could be determined from recordings of the shock wave obtained with a particular gage. Recording was by means of 304H Dumont oscilloscopes and drum cameras capable of providing a one millisecond per inch time resolution of the film.

QUALITATIVE RESULTS

Figure 3 shows records obtained with the cone and how they compare with a typical record from a full spherical charge. Figure 3a is a set of records obtained from one cone shot. Records 2, 3 and 4 were from type LC-13M pencil gages mounted in the flow and compare favorably in over-all character with record 5 in Figure 3b of a free field blast from a 55 gram spherical charge. Record 1 is from the type LD-60 gage mounted flush in the cone wall. The noise is due to vibration transmitted up to the tube wall from the detonation. The simple mounting arrangement used for this gage was not adequate to insulate it from such vibrations. In the case of records 2, 3 and 4 the higher frequency noise was filtered out by rubber insulation which was incorporated in the pencil gage mount. Imperfections that are still present in these records may be real and may result from disturbance to the flow at wall irregularities especially at welded joints of the cone sections. Exacting cone shape tolerances were not specified for this model.

QUANTITATIVE RESULTS

Quantitative evaluation of the performance of the cone was made by measuring the peak pressure (P), positive impulse (I), and positive duration (T) of the shock wave (Figure 3) that was recorded at several distances (R) from the apex of the cone. The positive impulse of the shock wave is defined by the expression

$$I = \int_0^T P \, dt$$

This integral is evaluated numerically by determining the area under the pressure-time curves such as are shown in Figure 3. The results for peak pressure and positive impulse are presented in Table 1.

Table 1 Conical Shock Tube Results

Average Peak Pressure Data, Positive Impulse Data, and Computed Effective Charge Weight (ECW)

R ft	$P_{average}$, psi	$I_{average}$ psi-msec	$ECW_{pressure}$ gm	$ECW_{impulse}$ gm
1.5	62	6.2	30	41
1.8	38	5.7	29	46
2.8	16	3.5	34	38

By using known data for the blast wave from a sphere of TNT fired under free field conditions and applying the scaling laws for the effect of the weight of explosive on the blast wave parameters, one is able to compute the weight of a full sphere of explosive, fired under free field conditions, required to produce peak pressures and impulses at a given distance equal to those produced by the explosive driven cone. These results are presented in Tables 1 and 2 as the Effective Charge Weight (ECW) for the cone and cone charge configuration employed. It was computed separately from peak pressure and positive impulse data. No significant difference is apparent between the ECW results for the flush page (1.5 feet) and the pencil gages in the flow.

Table 2 Cone Performances

	From Pressure Results	From Impulse Results
Effective Charge Weight (average)	31 gm	42 gm
Amplification Factor	62	84
Efficiency Factor	0.56	0.75

The amplification factor in Table 2 is the ratio of the effective charge weight calculated above to the actual charge weight used in the cone (in the present case 0.5 gm.). The efficiency factor in Table 2 is the ratio of the amplification factor to the ideal amplification factor (in the present case, 110). The efficiency factor indicates the extent of the energy losses at the source as well as losses by the shock wave along the tube walls.

Data on the positive duration of the cone blast wave are presented in Table 3.

Table 3 Average Positive Duration Data

R ft	T_{cone} msec	$T_{std.}$, msec
1.5	0.32	0.37
1.8	0.46	0.43
2.8	0.59	0.61

The data in colume T_{cone} are averages of measured cone positive duration times.

If the wave shape of a cone blast is to correspond to that of a free field spherical blast, then the effective charge weight for positive duration data should be the same as that for peak pressure data. No direct method is available for computing the effective charge weight from positive duration data. However, the effective charge weight for peak pressure (31 grams) and positive duration data may be shown to be the same by the agreement in Table 3 between the duration of the blast in the cone (T_{cone}) and that from a

31 gram spherical TNT charge in free air (T_{std}). Consequently, the shape of the cone wave does correspond with the wave shape from a full 31 gram sphere of TNT.

DISCUSSION

Differences of the order of 25 per cent in effective charge weights, amplification factors and effeciency factors are apparent in Table 2 between results based on peak pressure data and impulse data. No explanation can be given for this at present. Further work and more data should help clarify this discrepancy.

The estimate of 0.5 gram of TNT as being equivalent to the explosive charge of the detonator is subject to uncertainty. This directly affects the efficiency calculation. The use of larger quantities of secondary type explosives with better known properties than the initiator type materials used in detonators will be of much value.

How the efficiency factor will change for cones of higher amplication is an important question. This will determine the practical upper limit of amplification attainable from explosive driven conical shock tubes. A two-degree cone with a theoretical amplification factor of 10,000 is being designed to explore this matter.

POSSIBLE APPLICATIONS

Many applications of this device appear worthy of consideration even at this early stage of development. Basically it provides a means of studying blast waves over their full range of pressures and a wide range of durations using relatively small quantities of explosive. The ability to provide field scale blast waves using only gram sized quantities of explosive offers a great stimulus, from an operating point of view, to develop the use of such a device provided the objective of a program may be fulfilled within the limitations of the blast cone. The study of the reflection of spherical shocks from rigid boundaries is an example of a suitable cone problem.

The simulation of very large charge blasts using substantial quantities of explosive as the driving means has interesting possibilities. This would require the development of a suitable firing block technique as well as a very long cone.

Where reduced ambient pressures or gases other than air are of interest as the propagating medium, the explosive driven cone would require only a fraction of the gas handling equipment required by large scale firing chamber facilities now being used or planned. Blast propagation studies in cones containing water or other liquids seem feasible. Underwater field operations are much more difficult than air blast field work and the possible benefits of a laboratory operated blast cone compared with sea-going operations appear great for suitable problems.

Finally, when the operating characteristics of the blast cone have been more accurately determined, it could be used as a simplified means for direct blast wave calibration of piezoelectric gages.

REFERENCES

1. R. Gordon Campbell, "Initial Wave Phenomena in a Weak Spherical Blast", Journal of Applied Physics, Vol. 29, No. 1, pp 55-60, January 1958.

2. W. Bleakney, D. R. White, W. C. Griffith, "Measurements of Diffraction of Shock Waves and Resulting Loading of Structures", Journal of Applied Mechanics, Vol. 17, December 1950, pp 439-445.

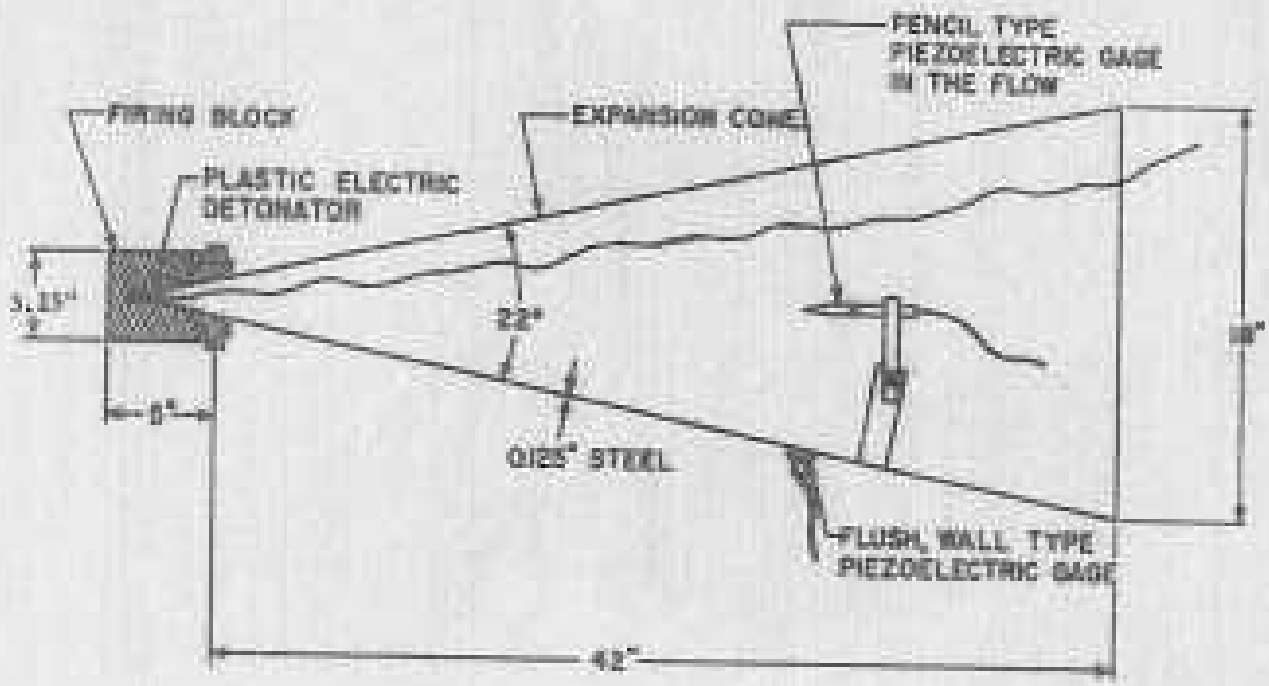

Figure 1 Diagram of Explosive-Driven Conical Shock Tube

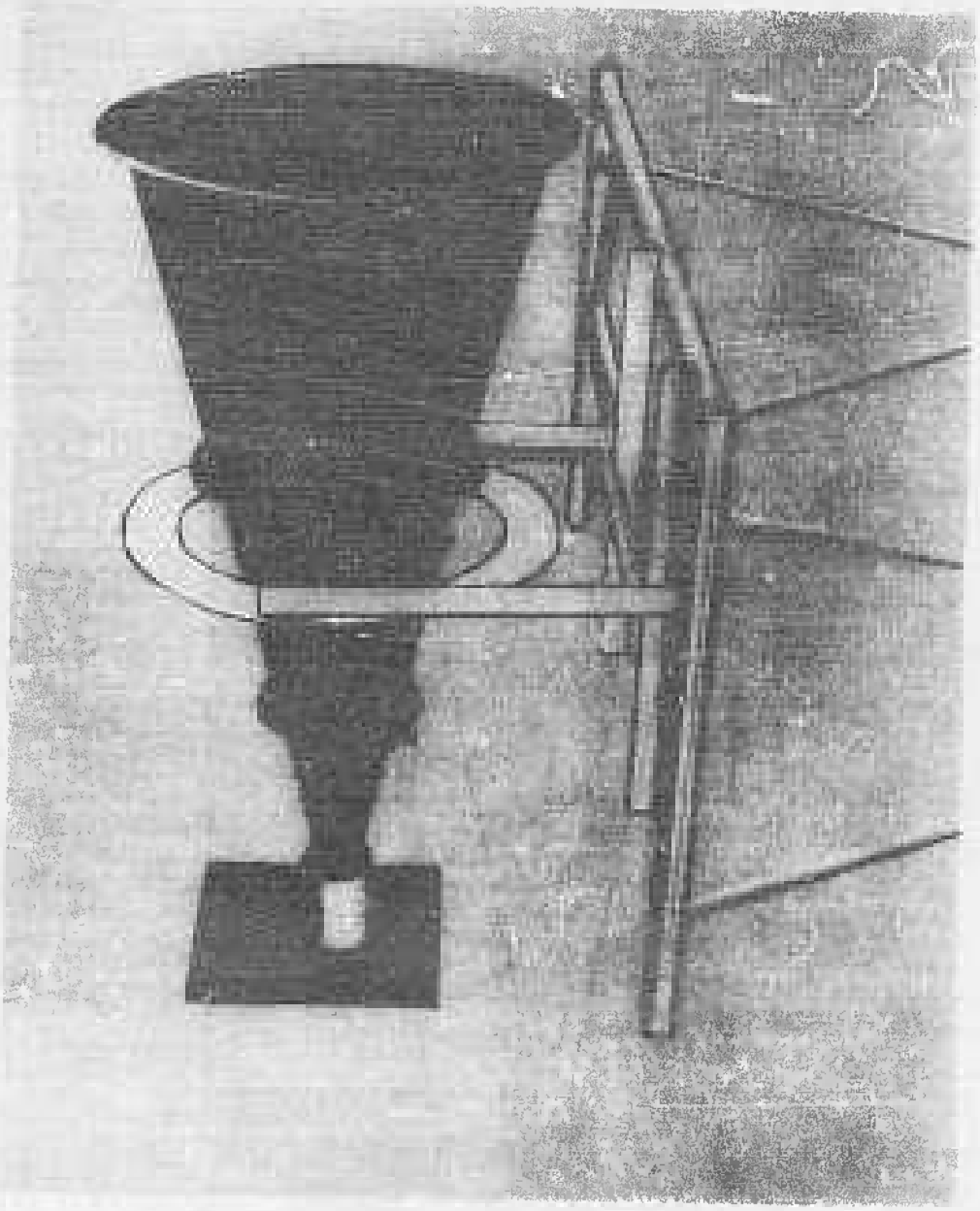

Figure 2 Explosive Driven Conical Shock Tube

RECORD NO.	DISTANCE (FEET) FROM GAGE ELEMENT TO CONE APEX OR CHARGE CENTER
1	1.5
2	1.8
3	2.8
4	2.8

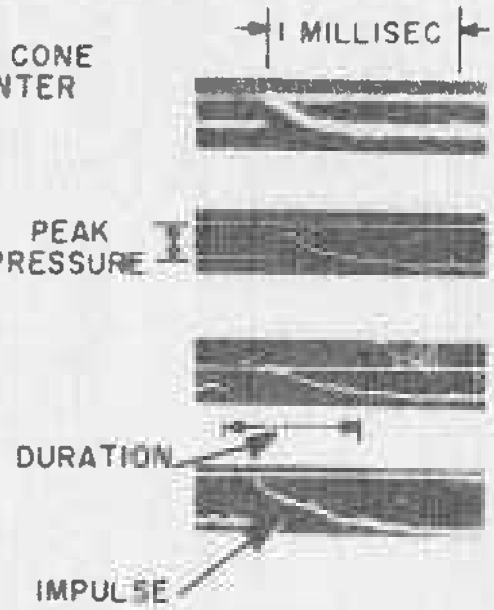

a. CONE SHOT RECORDS WITH 1/2 gm CHARGE

5	2.6

b. AIR SHOT RECORDS WITH 55gm SPHERICAL CHARGE

Figure 3 Records Obtained

KINETICS OF HYDROGEN RECOMBINATION IN A CHEMICAL SHOCK TUBE*

C. V. Metzler and W. H. Moberly
North American Aviation, Inc.
Rocketdyne Division

INTRODUCTION

The shock tube is one of the most promising tools developed in recent years for the study of high-temperature gas phase reactions. This tool is particularly useful for the study of the kinetics of chemical reactions which take place at such rapid rates that conventional experimental techniques are inadequate. One advantage of the shock tube in reaction kinetics studies is its ability to bring a gas sample to the desired high temperature and pressure conditions extremely rapidly. Another advantage is that the reaction can be conducted under almost completely homogeneous conditions. In addition, gas temperatures can be produced which are far in excess of those obtainable by conventional methods. The very short duration of the high temperature pulse results in practically no interaction with the tube wall and the necessity of utilizing ultra-high temperature materials can be eliminated.

The conventional shock tube consists of two chambers separated by a diaphragm. Prior to a test, one chamber is filled with a gas at high pressure (driver gas) and the other chamber is filled with a low pressure gas (driven or reactant gas). When the diaphragm separating the two chambers is ruptured, the driver gas expands rapidly into the low pressure chamber, generating a shock which travels down the length of the driven chamber.

The study of chemical kinetics in a shock tube began with the work of Davidson and his associates at the California Institute of Technology on dissociation reactions (Reference 1 and 2). In these studies, gases (N_2O_4, I_2) were dissociated by shock waves and the kinetics of the dissociations were followed by optically observing the change of gas opacity with time. Greene (Reference 3) and associates at Brown University and Penner and associates (Reference 4) at the California Institute of Technology have also employed optical techniques for studying gaseous reactions immediately behind a shock front.

However, optical studies of chemical kinetics behind shock waves are not without difficulties. In many cases the high reaction velocities which imply short duration of the kinetic phenomena and the low absorption and/or emission of the chemically reacting species pose data recording problems that seriously limit the application of such techniques. Also some species such as hydrogen absorb only in the vacuum ultraviolet region, which would be very difficult to handle with a shock tube. For these reasons the chemical shock tube was developed, which permits sampling at the end of a test.

*This work was supported by the United States Air Force Propulsion Laboratory, Wright Air Development Center, Air Research and Development Command under contract number AF33(616)-5551.

Chemical shock tubes differ from the conventional shock tubes by the addition of a vacuum chamber at the opposite end of the high pressure section from the driven chamber. The vacuum chamber is separated from the high pressure chamber by a second burst diaphragm which is ruptured after the primary diaphragm, but before the expansion wave generated by the bursting of the first diaphragm has traveled through the driver chamber.

A diagram of the chemical shock tube is shown in Figure 1. The function of the vacuum chamber is to trap secondary reflected shock waves and to generate a very strong expansion or rarefaction wave, which travels down the tube behind the incident shock, thereby cooling the reaction gas sample. The cooling rate of an expansion wave generated by a vacuum tank is greater than the cooling rate of the expansion wave in a conventional shock tube of the same geometry. This produces a single high temperature pulse caused by the reflected shock.

It is therefore possible to subject a sample of gas to a single high-temperature pulse of known temperature and duration. For the study of reactions which can be frozen by rapid cooling the progress of a reaction can be readily followed by sampling and analyzing the gas in the shock tube at the conclusion of each test. A series of tests utilizing variations in pulse time and temperature provides sufficient data to study the kinetics of such a reaction.

A typical wave diagram for a shock generated in a chemical shock tube is shown in Figure 1.

DESCRIPTION OF APPARATUS

The shock tube built for this program was patterned after a chemical shock tube designed by the Cornell Aeronautical Laboratory. The chemical shock tube was utilized by Cornell to study the reaction:

$$N_2 + O_2 \rightleftharpoons 2\,NO$$

The results of this study (References 5 and 6) demonstrated the usefulness of the chemical shock tube as a tool for the study of high temperature reactions.

The shock tube was fabricated from 3-inch inside diameter, schedule 40 stainless steel pipe jointed together by flanges with O-ring seals. The expansion chamber was fabricated from schedule 10 stainless steel pipe and was 24 inches in diameter and 48 inches long. The driver and driven sections of the shock tube were hydrostated to 2000 psi and the expansion chamber to 35 psi. The entire tube was rail mounted on three separate moveable trucks in order to simplify disassembly of the tube for replacement of the diaphragms and for varying the tube length.

Driver section lengths 4, 6, 8, and 10 feet long were used in the experiments. Four sections of 1, 2, 3, and 6 feet were used for the driven or reactant chamber so that any length from 1 to 12 feet could be used. All tests conducted during this program used the full length (12 feet) reactant

chamber. The flanged joints of the reactant sections were carefully boxed and fitted in order to make the sections interchangeable and to eliminate any rough spots that could cause reflected shock waves.

Commercially available prebulged stainless steel rupture discs (Black, Sivalls and Bryson, Inc., Kansas City, Mo.) were used for the two burst diaphragms. All of the tests were conducted with diaphragms rated at a burst pressure of 1000 psi. The discs were ruptured at 900 psi by plungers to assure reproducibility of the driver pressure, and to provide accurate control of the time delay between the rupture of the two diaphragms. The plungers were timed to provide the necessary delay by means of an auxiliary shock tube. The auxiliary shock tube consisted of a high pressure chamber separated by a diaphragm from two lines, one going to each of the shock tube diaphragms. The rupture of the auxiliary diaphragm generated a shock wave which traveled down each tube and drove plungers through the diaphragms. The time delay was provided by adjusting the lengths of the two lines leading to the plungers.

The control valves and gages for the pneumatic system were mounted on a central control panel. The pressures in each section of the shock tube were adjusted by means of Grove loaders mounted on the control panel. Pressures above atmospheric were measured by accurate Heise gages, A Wallace and Tiernan absolute vacuum gage and a mercury manometer were used for vacuum measurements.

Instrumentation was provided on the shock tube to make measurements of shock wave velocity, shock pressure, and delay time between the rupture of the primary and secondary diaphragms. The shock wave velocity was measured by two blast gages (Atlantic Research Corp., Alexandria, Va.) spaced 6 inches apart. A microsecond timer (Berkely Division of Beckman Instruments, Inc.) was started by the signal from the first gage and stopped by the signal from the second. A high response pressure transducers (SLM gage, marketed by Kistler Instrument Co., North Tonawanda, New York) was used to obtain a pressure-time trace of the passage of the incident and reflected shock waves. The pressure pulse was fed into an oscilloscope and recorded with a Polaroid Land Camera.

CHEMICAL KINETICS

The rate constant for the recombination reaction

$$H + H + M \xrightarrow{k_1} H_2 + M \qquad (1)$$

where M is H_2, is reasonably well established at low pressure and at room temperature as $1.0 + 0.1 \times 10^{16}$ cc. ^{2}mole^{-2} sec.$^{-1}$, although one investigator has reported a value closer to 10^{14} (References 7, 8, and 9). The dissociation reaction is expressed by the following equation.

$$H_2 + M \xrightarrow{k_1} H + H + M \qquad (2)$$

and its rate constant k_1 is related to the recombination rate constant by the thermodynamic equilibrium constant K:

$$K = k_1/k_1' \tag{3}$$

The rate of reaction (1) is not known at high-temperatures and high pressures. For other atom recombinations, notably the recombinations of bromine and iodine, the rate constants analogous to k_1' decrease by a factor of 10 to 100 between room temperature and 2000°K (Reference 10). The collision rate increases as $T^{1/2}$, but the duration of the collision lifetime of the intermediate complex goes down with increasing temperature in a manner depending on the Van der Waals attractions between the atom and the third body. Since the parameters for the latter process are not accurately known, one cannot predict whether k_1 increases, decreases, or remains essentially constant with temperature. For this reason, measurements in the shock tube were undertaken to evaluate k_1 at as high a temperature as possible.

The dissociation of hydrogen is difficult to study by either in-situ or sampling techniques. Optical in-situ methods, for instance, are not suitable because of the low concentration of hydrogen atoms and the fact that the vacuum ultraviolet region would have to be employed. Direct sampling methods cannot be used because of the recombination of atoms before and after sampling. Electron paramagnetic resonance techniques are not feasible because of the high-temperature of the reaction zone. It was desirable therefore, to find an additive to H_2 which would react at a known rate and in a known manner with H but not react directly with H_2. The additive selected was D_2, which forms HD in the presence of atoms by the well known reactions (Reference 11):

$$H + D_2 \xrightarrow{k_2} HD + D \tag{4}$$

$$D + H_2 \xrightarrow{k_2} HD + H \tag{5}$$

The amount of HD formed in time t is a measure of the value of k_1 as shown in the Appendix. Complete equilibrium for isotopic exchange may be expressed by the over-all reaction:

$$H_2 + D_2 \longrightarrow 2\,HD \tag{6}$$

The equilibrium constant for this reaction is approximately 4 and is essentially independent of temperature above 800°K (Reference 11). Thus HD_∞ (HD after complete exchange) can be evaluated for any initial mixture of H_2 and D_2. The ratio HD/HD_∞ characterizes the degree of reaction in the shock tube. Various degrees of reaction for constant time at high-temperatures are plotted in Figure 2 assuming the following values for the rate of association of H atoms: $k_1' = 10^{16}$, 10^{15}, and 10^{14} $cc^2 mole.^{-2} sec.^{-1}$. The following parameters were used for plotting

these curves: a total pressure in the reaction zone of 700 pounds per square inch, and a contact time of 5 milliseconds. A calculated curve for HD formation as a function of time at one temperature is shown in Figure 3. It is noted that even if k_1 varies by a factor of 100, the transition from no exchange to complete exchange occurs over a fairly restricted range of temperature, 1200-1600°K. By experimental determination of the amount of exchange at various temperatures in this range, values of k_1 can be evaluated by the shock tube method at different temperature. The value thus obtained, together with the known constant at room temperature, should provide data for reliable extrapolation to higher temperatures.

PROCEDURE

Mixtures containing argon, hydrogen, and deuterium were prepared and allowed to remain for at least 24 hours in order to insure uniformity of reactants. The reactant chamber was evacuated to about 30 microns and a sample added. The amount of the sample was determined by measuring the pressure in the reactant chamber and utilizing the perfect gas law.

Conventional shock tube theory was utilized for the calculation of the various conditions in the shock tube during and after the passage of the incident and reflected waves. The calculation of temperature involved using the Mach number, calculated from the original pressure ratio, and applying the Rankine-Hugoniot normal shock relations (References 12 and 13). These relations, which are based on the principles of conservation of mass, momentum and energy, were also used to predict the pressure produced by the incident and reflected shocks. The close agreement between the predicted initial pressures and those measured by the pressure pick-up served as a check on the temperature calculations.

The sampling procedure at the conclusion of a test was as follows: a one cubic foot sample was taken to insure that the entire sample between the end of the shock tube and the interface with the helium driver gas was removed; a second sample was taken to check whether the first sample removed all the reactant gases. As will be discussed later, it appears that this sampling procedure may have caused additional complications.

The concentrations of hydrogen, argon, deuterium and hydrogen deuteride at the end of each run must be known. Two methods of analysis were attempted. The first analytical method investigated was gas chromatography. It was found that by this method of argon, hydrogen and deuterium could be determined; however, the determination of hydrogen deuteride in the presence of hydrogen and deuterium was not possible.

It was then necessary to investigate the use of mass spectrometry for this analysis. The mass spectrometer was found to resolve the masses of all the materials in the sample, in which deuterium and helium which are both nominally mass four but actually differ slightly. The mass spectrometer used for these analyses was a Consolidated Electrodynamics Corporation Model -21-103C.

Blast gages and a microtimer were also employed to determine directly the Mach number; however, this method was not found to be sufficiently accurate or reliable.

RESULTS AND DISCUSSION

Above 2000°K, (Table 1) the experimental equilibrium constant for the over-all exchange reaction (6), based on the final concentration of H_2, D_2 and HD, was not four but was found to be between two and three. If all the H_2 and D_2 had been subjected to these temperatures for the observed time (1.82×10^3 sec), these results would be thermodynamically and kinetically impossible. A reasonable explanation appears to be that some mixing of hydrogen and deuterium with helium occurred at the interface as the membrane was broken. Emrich and Wheeler have actually reported the occurrence of such mixing in shock tubes (Reference 14). The contact surface between the cold helium and the hot reactant gases was thus ragged, and a considerable fraction of the hydrogen and deuterium was never heated at all. In sampling these high-temperature runs, large samples were taken and sufficient time was allowed to attain sample uniformity. This turned out to be a disadvantage, as it permitted the unheated portion to enter the sample bomb.

Another possibility that should be considered in high temperature operation is that the rate of cooling may not be fast enough to prevent reversal of the reaction and approach to the equilibrium composition of lower temperatures. It was computed that below 1500°K, the reaction should be frozen; but that above this temperature, a shift in the composition occurs during the cooling period. This was also verified by experiment.

Between 1000-1330°K several runs were made with fast sampling; a second sample was taken after waiting, so that the second sample of this series is comparable to the first sample in the high temperature series. As can be seen in Table 1 there was a large difference in apparent exchange between the first sample and the second sample. Several "first samples" were obtained with less than 10% helium. The second samples in these cases contained three to four times as much helium as the first. It may be expected, therefore, that the conversions found in the first samples are more representative of the condition of the shock tube. The first samples may not have been completely free from the difficulties caused by a ragged contact surface; however, since some helium was present. Subsequent runs were made with even faster sampling and samples free of helium were obtained. This indicates that sampling fast enough to eliminate the effect of the ragged interface is possible.

From the theoretical curve relating conversion to temperature (assuming a constant k_1' of 10^{16}), it is seen that the ratio of $\frac{HD}{HD_\infty}$ is extremely sensitive to temperature above 1200°K; for instance, this ratio increases from 0.3 to 0.8 over only a 50° temperature range. Since the experimental error in calculating the temperature for the shock tube experiments is of the order of ±15°, the lack of precision may be largely due to inaccuracies in temperature determinations. This difficulty can be resolved

by measuring the Mach number of the shock wave with very precise blast gages, which have only recently become available, and by operating below 1200°K where conversion is less sensitive to minor temperature variations.

There also appears to be another difficulty which is particularly apparent in the low temperature runs. The degree of exchange was appreciable in all the runs; it was over 40% even at 1000°K. This situation may be brought about by traces of oxygen (mass spectrometer readings on initial reactant samples indicate about 0.15% oxygen relative to about 50 to 60% H_2 and D_2). The initial reaction of oxygen would be:

$$H_2 + O_2 \longrightarrow HO_2 + H$$

followed by reactions (4) and (5). Such a sequence of reactions would account for the fact that no value for $\frac{HD}{HD_\infty}$ was less than 0.35. Since the kinetics of the hydrogen-oxygen reaction is not well known, it does not appear possible to draw any qualitative conclusions from the data about the effect of oxygen. The shock tube vacuum system has been redesigned to yield vacua of 3×10^{-3} mm Hg (previously 1.5×10^{-2} mm Hg). It is believed that further improvements can be made.

This investigation has shown that the kinetics of hydrogen atom recombination can be studied in the chemical shock tube using the hydrogen-deuterium exchange method. A mass spectrometer analysis technique has been developed which resolves the peaks of all the reactants and products including deuterium and helium. A fast sampling technique was worked out which eliminates products from the "ragged" interface section of the reactant chamber. Small amounts of oxygen have been found to affect the exchange reaction and therefore it is necessary to eliminate traces of air from the shock tube and mixing systems.

ACKNOWLEDGEMENT

The authors greatfully acknowledge many helpful discussions with Professor Harold S. Johnston.

REFERENCES

1. T. Carrington and N. Davidson, J. Phys. Chem 57, 418-27 (1953).

2. Britton, Davidson, and Schatt, Discussions Faraday Soc. 17, 58 (1954).

3. E. F. Greene, J. Am. Chem. Soc. 76, 2127 (1954).

4. Penner, Harshbarger, and Voli, Cal. Tech. Jet Propulsion Center Report AD 95210 AFOSR-TN-56-334, June 1956.

5. Glick, Squire, and Hertzberg, 5th International Symposium on Combustion, pp. 393-402, New York, Reinhold Publishing Co. (1955).

6. Glick, Klein, and Squire, J. Chem. Phys. 27, 850-57 (1957).

7. H. M. Smallwood, J. Am. Chem. Soc., 51, 1985 (1929).

8. W. Steiner, Trans. Faraday, Soc., 31, 623 (1935).

9. Senftleben and Hein, Physik, zeit, 35, 985 (1934).

10. Careri, et al, J. Chem. Phys. 24, 783 (1955).

11. Wolley, Scott, and Brickwedde, National Bureau of Standards, Research Paper, R P 1932 Vol. 41, Nov. 1948 p 379.

12. Shapiro, " The Dynamics and Thermodynamics of Compressible Fluid Flow", Vol. II, New York, the Donald Press Co. (1954).

13. Rudinger, "Wave Diagrams for Non-Study Flow in Ducts", New York, D. Van Nostrand, Inc. (1953).

14. Emrich and Wheeler, Physics of Fluids, 1, 14 (1958).

APPENDIX

DERIVATION OF INTEGRATED RATE EQUATION

A. Reaction Mechanisms:

(1) $M + H_2 \xrightarrow{k_1} 2H + M$

(2) $M + 2H \xrightarrow{k_1/K} H_2 + M$

(3) $M + D_2 \xrightarrow{k_1} 2D + M$

(4) $M + 2D \xrightarrow{k_1/K} D_2 + M$

(5) $H + D_2 \xrightarrow{k_2} HD + D$

(6) $D + H_2 \xrightarrow{k_2} HD + H$

(7) $D + HD \xrightarrow{1/2\ k_2} D_2 + H$

(8) $H + HD \xrightarrow{1/2\ k_2} H_2 + D$

(9) $M + HD \xrightarrow{k_1} H + D + M$

(10) $M + H + D \xrightarrow{k_1/K} HD + M$

Where M can be any of the atoms or molecules present.

The above rate constants are based on the assumption that isotopic effects are negligible and that the rate constant for forward exchange is twice that for backward exchange.[1,2]

B. Calculation for (H)

From the above mechanisms the rate of formation of hydrogen atoms can be expressed by:

$$(1)\ \frac{d(H)}{dt} = 2k_1(M)(H_2) - 2^{k}1/K(M)(H)^2 + k_1(M)(HD) - {}^{k}1/K(M)(H)(D) + k_2(D)(H_2) - k_2(H)(D_2) + 1/2\ k_2(D)(HD) = 1/2\ k_2(H)(HD)$$

---

[1] Woodley, Scott, and Breckwedde: Journal of the National Bureau of Standards, 41, 379, 1948.

[2] Boato, Careri, et al: Journal of Chemical Physics, Vol. 24, No. 4, 783-791, April 1956.

It is assumed that

$$\frac{(H)}{(D)} = \frac{(H_2)_o}{(D_2)_o} = \alpha$$

This is approximately true since (atoms) << (molecules). Equation (11) can then be simplified to:

$$\frac{d(H)}{dt} = k_1(M)\left\{2(H_2) + (HD)\right\} - k_{1/K}(M)(H)^2(2 + 1/\alpha) \qquad (12)$$

Since $(H_2) + H_{2_o} - 1/2\ (HD)$ Equation (12) can be expressed as:

$$\frac{d(H)}{dt} = 2\,k_1\,(M)(H_2)_o - k_{1/K}(M)(H)^2(2 + 1/\alpha) \qquad (13)$$

Separation of variables yields:

$$\int_o^{(H)} \frac{d(H)}{(2k_1(M)(H_2)_o - k_{1/K}(M)(H)(2 + 1/\alpha)} = \int_o^t dt \qquad (14)$$

Integration gives:

$$(H) = (A/B)^{1/2} \tanh (AB)^{1/2}\, t \qquad (15)$$

where

$$A = 2\,k_1\,(M)(H_2)_o \qquad B = k_{1/K}(M)(2 + 1/\alpha)$$

C. Calculation for (HD)

The rate of formation of hydrogen deuteride can be expressed by:

$$\frac{d(HD)}{dt} = k_2\,(D_2)(H) + k_2(H_2)(D) - 1/2\,k_2\,(HD)(D) - 1/2\,k_2\,(HD)(H)$$

$$- k_1\,(M)(HD) + k_{1/K}\,(M)(H)(D) \qquad (16)$$

Assume:

$$\left\{k_1\,(M)(HD)\right\} \quad \text{and} \quad \left\{k_{1/K}\,(M)(H)(D)\right\}$$

are negligible because k_1, (H), and (D), are very small under shock tube conditions. Substituting the value of (H) given in Eq. (15) yields:

$$\frac{d(HD)}{dt} = k_2\,(A/B)^{1/2}\left\{\tanh (AB)^{1/2}\, t\right\}\ \left\{2(D_2)_o - (1 + 1/\alpha)(HD)\right\} \qquad (17)$$

Separation of variables gives:

$$\int_0^{(HD)} \frac{d(HD)}{2(D_2)_o - (1 + 1/\alpha)(HD)} = \int_0^t k_2 (A/B)^{1/2} \tanh (AB)^{1/2} t \; dt \qquad (18)$$

Integration yields:

$$(HD) = \frac{2(H_2)_o}{1+\alpha} \left\{ 1 - \frac{1}{(\cosh (AB)^{1/2} t)^N} \right\} \quad \text{where } N = k_{2/B} (1 + 1/\alpha) \qquad (19)$$

Substitution for A, B, N, and α yields:

$$(HD) = \frac{2(H_2)_o (D_2)_o}{(H_2)_o + (D_2)_o} \left\{ 1 - \frac{1}{\left[\cosh k_1(M) \left\{ 2/K \left[2(H_2)_o + (D_2)_o \right] \right\} t \right]^{\frac{k_2 K \{(H_2)_o + (D_2)_o\}}{k_1(M)\{2(H_2)_o + (D_2)_o\}}}} \right\} \qquad (20)$$

Since the value of (HD) can be determined experimentally, and the initial concentrations, equilibrium constant, exchange reaction constant, and reaction time are known, the value of k_1, the dissociation rate constant can be calculated by an iteration technique. The value of k_1', the recombination rate constant, can be calculated from the relation $k_1' = k_{1/K}$.

Nomenclature

k	Appropriate rate constant
K	Appropriate equilibrium constant
( )	Concentration (gram-moles/cc)
$( )_o$	Initial concentration (gram-moles/cc)
t	time (seconds)

Table 1 Shock Tube Results

Temp	Time	Initial Concentration Mole %			Final Concentration, Mole. %										Extent of Exchange			
					First Sample					Second Sample					First Sample		Second Sample	
0° K	Msec	Argon	H_2	D_2	Argon	H_2	D_2	HD	He	Argon	H_2	D_2	HD	He	R*	$\frac{HD}{HD_{eq}}$	R*	$\frac{HD}{HD_{eq}}$
2000	1.6	65	17.5	17.5	20.4	2.8	2.8	3.7	70.3	3.7	0.26	0.46	0.26	95.2	1.72	0.795	0.54	0.546
2270	1.6	65	17.5	17.5	24.3	4.7	4.2	6.8	60.0	14.6	3.4	3.1	4.6	72.5	2.29	0.867	2.00	0.809
2680	1.8	65	17.5	17.5	13.4	3.1	2.0	2.7	79.8	21.3	3.5	3.2	5.0	67.0	1.81	0.794	2.27	0.855
2940	1.8	65	17.5	17.5	17.8	2.8	2.7	4.3	72.4	11.8	1.5	1.5	2.1	83.7	2.45	0.878	2.91	0.544
3760	1.8	65	17.5	17.5	27.7	4.7	4.3	6.7	56.6	16.6	2.6	2.6	3.5	74.7	2.17	0.854	1.92	0.803
3480	1.8	65	17.5	17.5	19.0	1.8	2.0	3.3	74.0	8.8	1.7	1.5	2.0	87.4	3.13	0.936	2.81	0.894
3640	1.8	65	17.5	17.5	15.6	3.1	2.7	5.1	73.4	12.1	2.1	2.0	3.4	80.4	3.12	0.937	2.70	0.907
1330	5	45.2	27.4	27.4	-	-	-	-	-	31.3	11.1	11.4	12.8	33.4	-	-	1.51	0.724
1330	5	45.2	27.4	27.4	33.8	14.1	13.3	23.5	15.3	33.1	10.4	11.5	14.9	29.9	2.97	0.743	1.81	0.806
1330	5	45.2	27.4	27.4	31.7	10.6	10.1	12.7	34.9	17.1	7.1	7.6	5.2	63.0	1.49	0.701	0.52	0.523
1330	5	41.3	33.7	25	22.6	11.8	6.8	9.2	49.6	8.7	4.6	3.3	2.2	81.2	1.05	0.685	0.32	0.453
1250	5	41.3	33.7	25	50.5	14.5	9.8	15.0	8.0	60.0	7.7	6.5	10.2	15.6	2.51	0.883	2.07	0.838
1150	5	36	44	20	23.5	22.3	6.8	8.2	39.2	12.2	10.3	3.4	2.6	71.0	0.45	0.377	0.16	0.356
1150	5	36	44	20	24.0	22.2	6.3	9.3	38.2	14.2	13.4	4.4	4.3	63.7	0.62	0.497	0.31	0.507
1150	5	36	44	20	33.9	34.2	7.0	20.2	4.7	29.8	32.5	7.2	16.9	13.6	1.73	0.816	1.25	0.747
1150	5	36	44	20	34.3	34.4	7.6	19.7	4.0	30.7	19.6	6.9	12.0	30.8	1.48	0.792	1.04	0.735
1000	1.8	37	53	10	32.6	45.8	4.7	7.0	9.9	24.2	34.4	4.0	4.0	33.4	0.23	0.497	0.12	0.389
1000	1.8	37	53	10	30.2	49.0	4.9	6.7	9.2	22.7	39.2	4.6	4.0	29.5	0.19	0.471	0.88	0.353

*R $\frac{(HD)^2}{(D_2)(H_2)}$

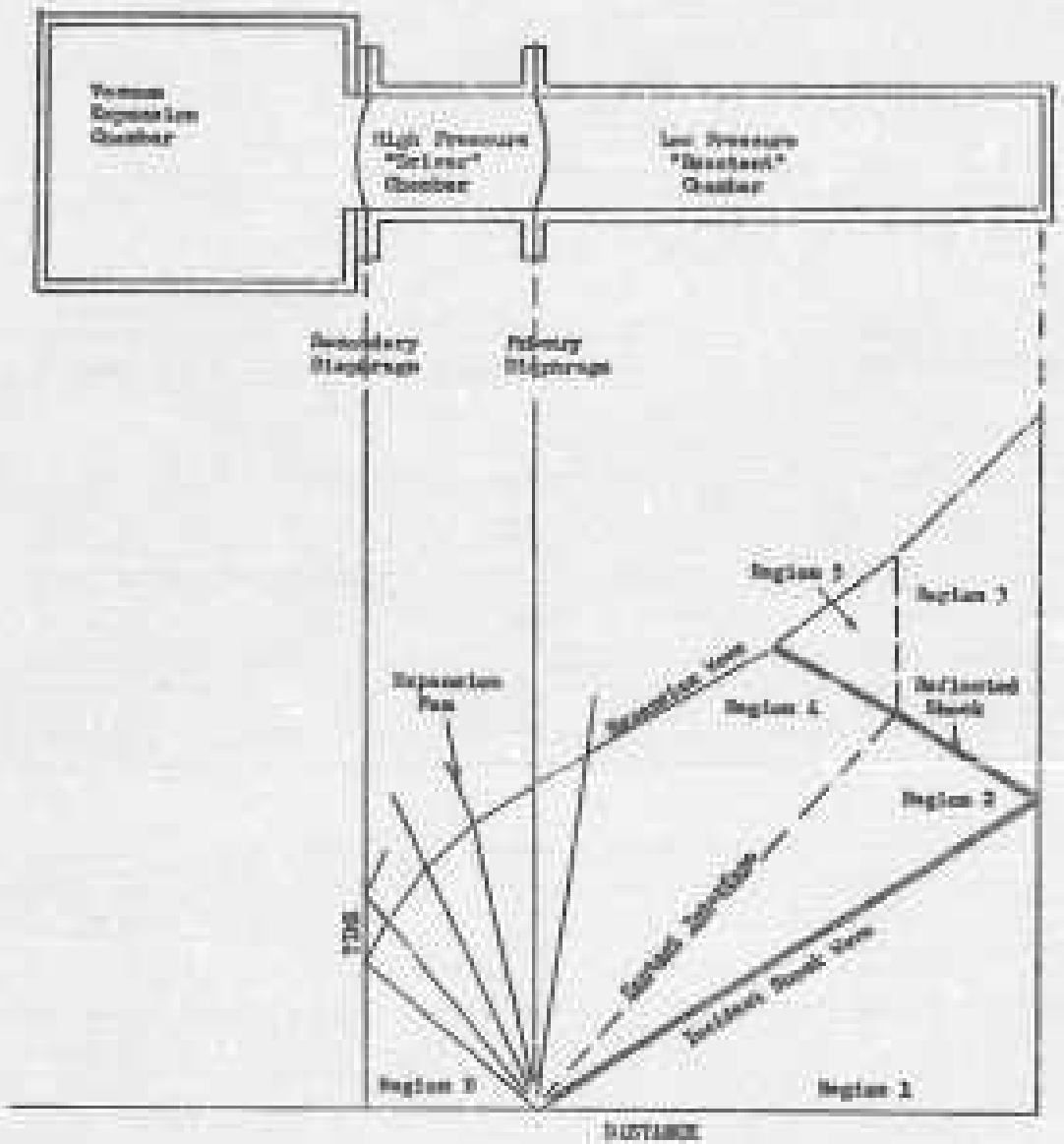

Figure 1 Configuration of Chemical Shock Tube and Typical Shock Wave Diagram

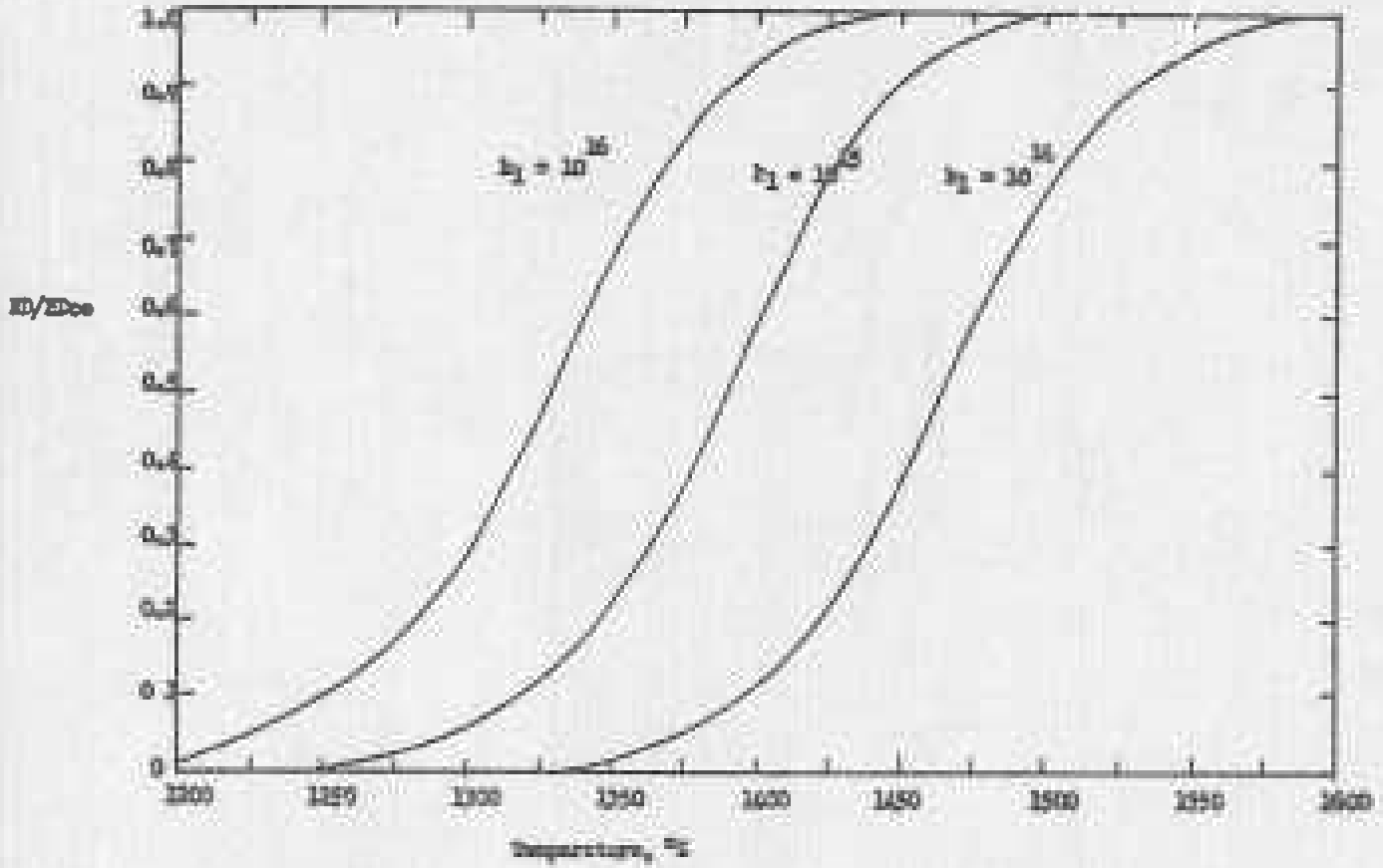

Figure 2 Theoretical Conversion after 5 milliseconds

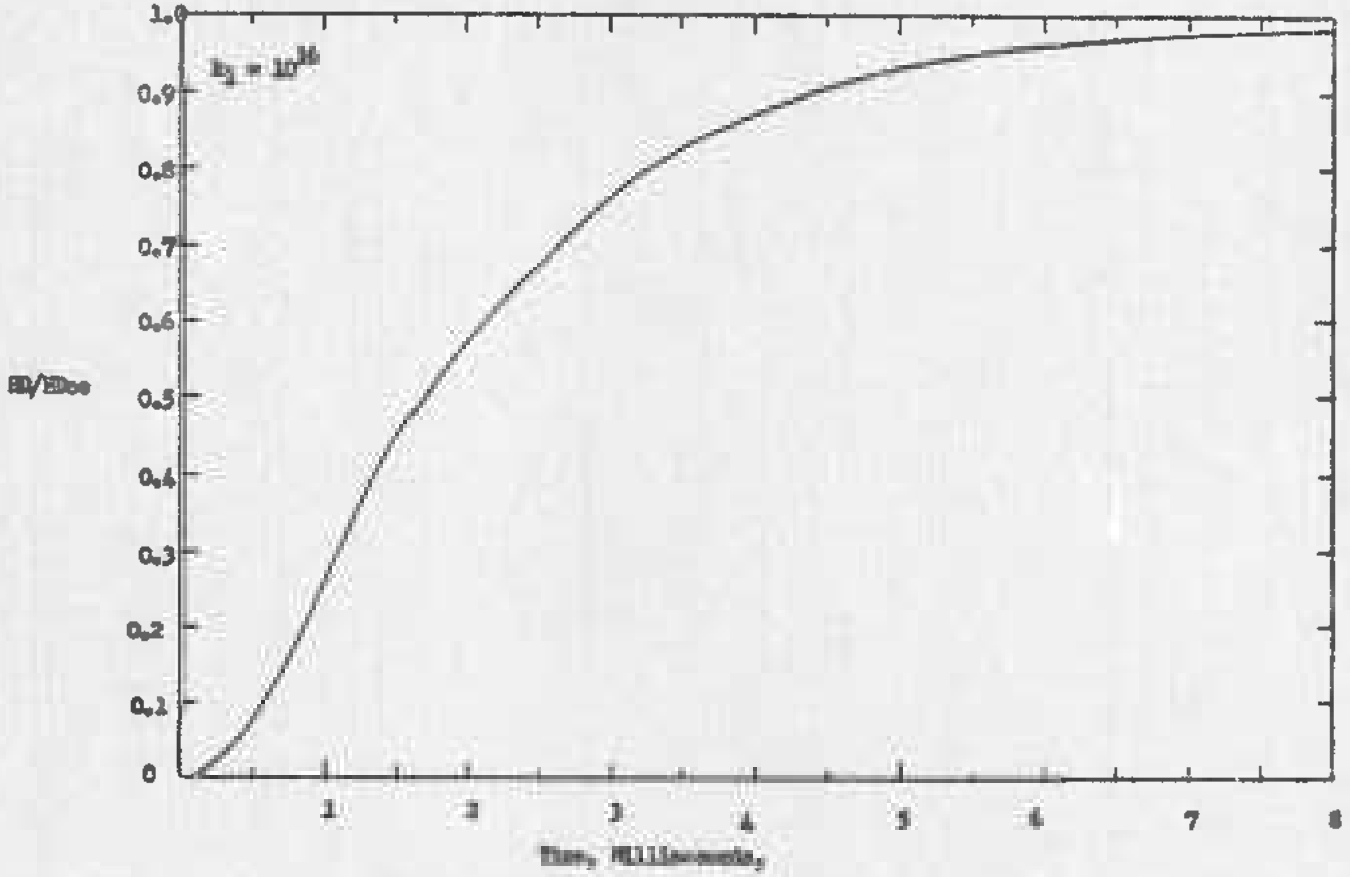

Figure 3 Theoretical Conversion at 1400°K

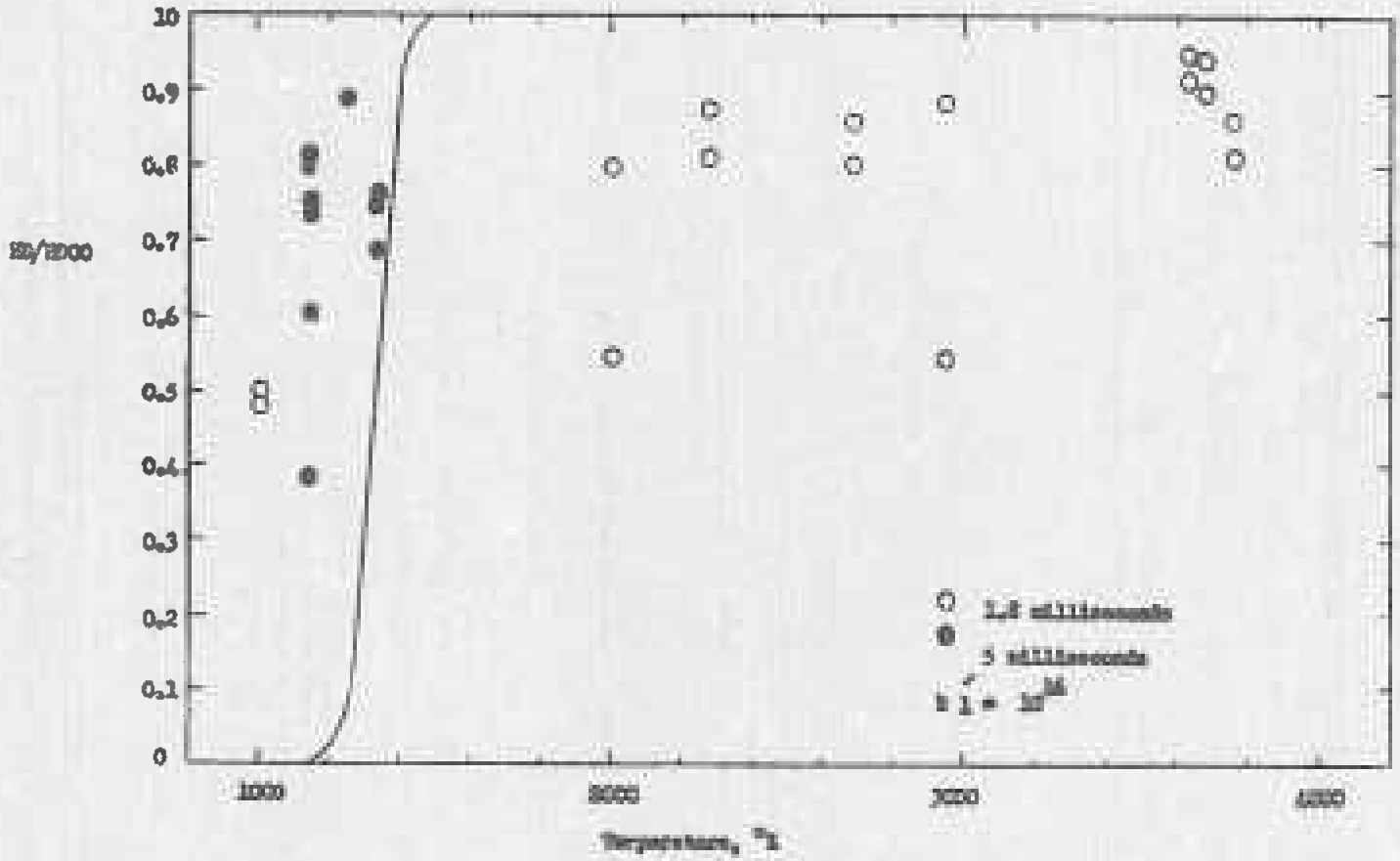

Figure 4 Shock Tube Results

MEASUREMENT OF O_2 CONCENTRATION BEHIND SHOCK WAVES USING AN ULTRAVIOLET ABSORPTION TECHNIQUE

John S. Evans and Charles J. Schexnayder
NASA Langley Research Center

In connection with studies of the effect of dissociation on gas properties and of the relaxation time for dissociation under various flight conditions, a method has been developed by the Langley Research Center for measuring the concentration of molecular oxygen as a function of time behind shock waves. The technique is based on the ability of the oxygen molecule to absorb ultraviolet light in the wavelength range 1,250 to 1,750 angstrom units, whereas atomic oxygen is transparent to these wavelengths. Work very similar to this has also been reported by the Avco Research Laboratory.

The main objectives of this paper are to describe the method and the equipment. It starts with a brief discussion of what is meant by absorption and in particular what sort of absorption occurs in oxygen - that is, how strong is the absorption of light in oxygen and how does the absorption coefficient vary with temperature and wavelength. A description of the shock tube and the instrumentation follows. Also a typical record is shown and is correlated with theoretical curves which show how light absorption should vary in the shock tube for various reasonable assumptions about the state of the gas behind a shock wave.

For the benefit of anyone who would like to be reminded of just what is meant by the term "absorption", Figure 1 shows the equation for absorption of monochromatic light in passing through a given thickness of gas. I/I_0 is the fraction of light which passes through the gas layer without being absorbed. The absorption coefficient k varies with temperature and the wavelength of light. Since it is defined in terms of gas at standard temperature and pressure an equivalent path length ℓ' is used in the equation instead of the actual path length ℓ. This equivalent path length is obtained by converting test conditions to standard conditions.

Figure 2 shows the absorption coefficient of molecular oxygen as a function of wavelength and temperature in the region of interest. It is the continuous absorption associated with the Schumann-Runge band system of oxygen and lies in the vacuum ultraviolet part of the spectrum - which, incidentally, is so named because spectrographs have to be highly evacuated to prevent complete absorption of all light by the oxygen present in the air. These absorption coefficient curves are calculated results obtained at the Langley Research Center. They are adjusted so as to match experimentally observed values which have been reported in the literature. Since all the literature data were taken at room temperature it will be interesting to check the high temperature curves experimentally with the shock-tube results. This can be done if conditions behind the shock front are known independently. For instance, if the shock Mach number is not too high little or no dissociation is present immediately behind the shock front and the other degrees of freedom,

such as translation, vibration, and rotation, are in equilibrium.[1] Thus temperature, density, and gas composition are known - leaving only the absorption coefficient to be determined from measurement of the change in transmitted light. Preliminary examination of the data in hand from this point of view has thus far proved satisfactory. Investigation of the temperature dependence of the absorption coefficient by this means will be continued.

Figure 3 shows a block diagram of the experimental setup used. Ultraviolet light from a pulsed hydrogen discharge tube passes through a 1-inch absorption path and a grating monochromator before it falls on a photomultiplier sensitized for ultraviolet light with sodium salicylate. Because of the oxygen present in air all light paths are in vacuum. The bandpass width of the monochromator is about 11 angstroms. A Polaroid Land camera is used to photograph the trace on a Tektronix 545 oscilloscope. The time resolution of the system is determined by the time required for the shock wave to cross the light beam and is approximately one-third of a microsecond. Ionization probes located 5 inches in front of a 5 inches behind the test section are used for the shock velocity measurements and to trigger the light source and scope sweep.

Two of the many discharge tube configurations which have been tried are shown in Figure 4. Since development work on the light source is still being carried on a general discussion of features common to all types tried will be given. The discharge takes place in flowing hydrogen at about 1 to 2 mm pressure. There is no window between the discharge and the lithium fluoride shock-tube window. Care is taken to insure the cleanliness of the glass and metal surfaces exposed to the discharge, but no elaborate outgassing procedures are used. The current pulse is of the order of 2,000 amperes and is obtained from an artificial transmission line made up of 20 condensers and 20 coils. The use of an artificial transmission line for energy storage gives the light pulse a long duration and a flat top. A heavy duty hydrogen thyratron is used to hold off the discharge until a triggering pulse is received from the shock tube.

The shock tube used (see Figure 5) has been described in the Journal Aeronautical Sciences (August 1958 issue) by Schexnayder. It is a double diaphragm type with a 16 to 1 area contraction just before the second diaphragm. The buffer chamber is filled with helium and the high pressure chamber is filled with helium or hydrogen-helium mixtures, depending on the Mach number desired. The high-pressure diaphragms are 1/16-inch scribed steel plates. The low-pressure diaphragms are Mylar film. The high-pressure diaphragm is broken by pressure. The low-pressure diaphragm is broken by the reflection of the primary shock wave at the contraction. The pressure in the 1-inch-diameter portion of the shock tube is always determined by the partial pressure of O_2 necessary to give a convenient amount of ultraviolet light absorption. For pure O_2 this pressure is about 0.3 mm and for a 10 per cent O_2 in argon mixture is about 3 mm. The low-pressure section is always pumped to 20 microns before filling and is raised to the desired initial pressure by admitting the gas mixture through a leak valve while continuing the pumping. Thus the runs are taken in a slowly flowing

[1] Avco's studies show that, while this statement is true for oxygen, it is not true in air. The time required for vibrational equilibrium in nitrogen is of the same order of magnitude as the dissociation time of O_2. (Avco Research Report 22).

mixture. The effects of residual vapor pressures and small air leaks are minimized by this procedure. The leak rate of the shock tube when closed off from the pump is 1 or 2 microns per minute.

Figure 6 illustrates a typical record obtained from a shock-tube run. The shape of the ultraviolet light pulse used as background for absorption is indicated by the dotted line. The sudden decrease in light intensity as the shock enters the absorption beam indicates that the amount of molecular oxygen in the path has increased. This is because of the increase in gas density across the shock front. The further decrease in light intensity shows that the amount of molecular oxygen increases still more as the dissociation proceeds. The useful part of the record is terminated by the arrival of the driver gas. It may seem paradoxical that the amount of molecular oxygen in the path should increase as a result of the dissociation of molecules into atoms. To make clear what happens look at the equation for absorption, which can be written like this:

$$\frac{I}{I_o} = e^{-\text{Constant}\,(1-\alpha)\,k_T\,\frac{\rho}{\rho_1}}$$

I/I_o is the fraction of light which gets through the shock tube without being absorbed. The degree of dissociation is indicated by α. The absorption coefficient is not a function of wavelength during a run because the monochromator is set at a fixed wavelength, but it is written in the equation as k_T to indicate its temperature dependence. The density ratio across the shock wave is ρ/ρ_1. Immediately behind the shock wave $\alpha = 0$ and $1 - \alpha = 1$. The density increase has a larger effect than the change in the value of k_T. Thus, as has already been stated, the increase in absorption noted when the shock front passes is primarily due to the density increase. In the relaxation zone behind the shock front the degree of dissociation is not zero but increases with distance from the shock front. The temperature falls as the dissociating molecules take up thermal energy, and the density ratio ρ/ρ_1 becomes larger. Under the conditions present for the record illustrated the density increase overpowers the other factors and causes increased light absorption even though the gas is dissociating. Note, however, that the density increase is not always predominant. Records are often obtained which show decreasing absorption as dissociation proceeds. Behind very strong shock waves the temperature is high enough to produce complete dissociation. In this case $\alpha \to 1$, $1 - \alpha \to 0$, and $\frac{I}{I_o} \to e^0 = 1$. Thus, there is no absorption of light at all when the oxygen molecules are all dissociated.

Some of these considerations are illustrated in Figure 7, which shows per cent transmission of light as a function of Mach number for various assumptions about the state of the gas. The horizontal line at the top marked "Initial" represents the amount of light being transmitted before the shock wave passes. The curve marked "Constant γ" at the bottom represents the amount of light transmitted after the shock passes if it is assumed that vibration and dissociation are both frozen. The "Frozen Dissociation" curve represents the amount of light transmitted if only the dissociation is frozen,

while vibration is assumed to be in equilibrium. The curve marked "Equilibrium" represents the amount of light transmitted when both dissociation and vibration are in equilibrium. For a given shock wave the per cent transmission at first lies on the "Initial" curve, drops to the "Frozen Dissociation" curve immediately behind the shock front and adjusts to the "Equilibrium" curve in the relaxation region. Note that this final adjustment may be in either direction - depending on the relative position of the two curves at the Mach number in question. Also note that for high Mach number the "Equilibrium" curve goes to 100 per cent transmission - indicating complete dissociation of the oxygen.

Figure 8 shows a plot like the one in Figure 7, but this time it is for a particular gas - namely pure oxygen at an initial pressure of 0.3 mm. The notation is the same as before. Experimental points are plotted on this figure for the gas in front of the shock, immediately behind the shock and at the end of the available testing time. These points agree fairly well with the theoretical curves, but better agreement is hoped for as the technique and equipment improve. The theoretical curves depend on calculated values of the absorption coefficient and may need revision if better values of the absorption coefficient are found.

It is evident that the relaxation time for dissociation of oxygen under condition actually present in the shock tube can be read directly from the records. The reaction rate for dissociation can also be evaluated from the records, but a rather careful analysis is necessary. The records we have are being analyzed to obtain the reaction rate. To date the results are preliminary and a bit rough. However, they are in substantial agreement with those published by Avco.

Summarizing quickly, an ultraviolet absorption technique has been tested and found suitable for studies of processes which involve rapid changes in the concentration of molecular oxygen. In particular, it has been applied to the study of the dissociation of molecular oxygen into atomic oxygen behind a shock wave. The time resolution is good - being about one-third of a microsecond for the equipment described.

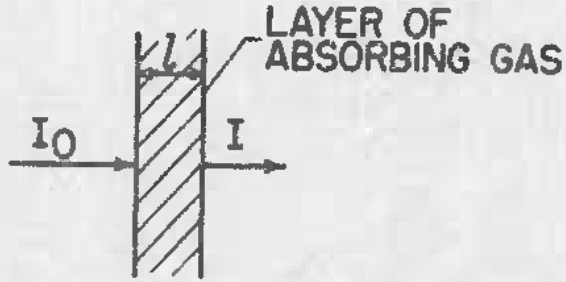

$$\frac{I}{I_0} = e^{-kl'}$$

I_0 = INTENSITY OF LIGHT ENTERING ABSORBING LAYER

I = INTENSITY OF LIGHT EMERGING FROM ABSORBING LAYER

k = ABSORPTION COEFFICIENT

l = ACTUAL PATH LENGTH

l' = EQUIVALENT PATH LENGTH AT STANDARD SEA LEVEL DENSITY

Figure 1 Light Absorption in Gas Layer. NASA

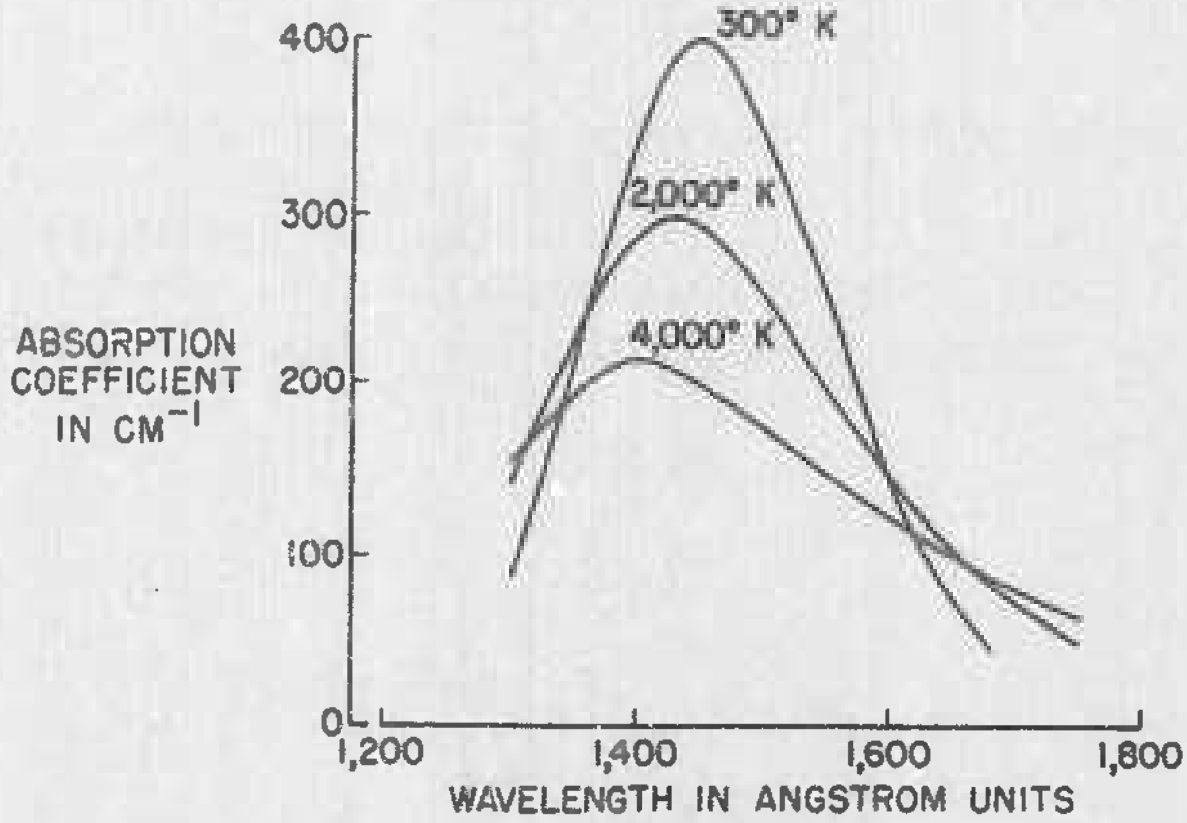

Figure 2 Absorption Coefficient of Molecular Oxygen As a Function of Wavelength and Temperature

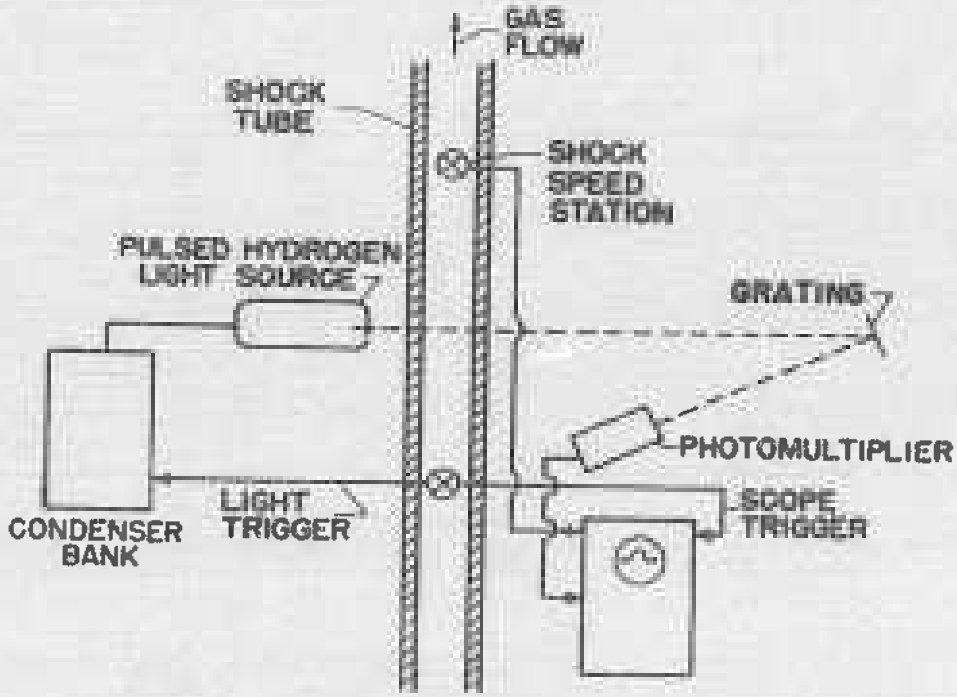

Figure 3 Schematic Diagram of Equipment

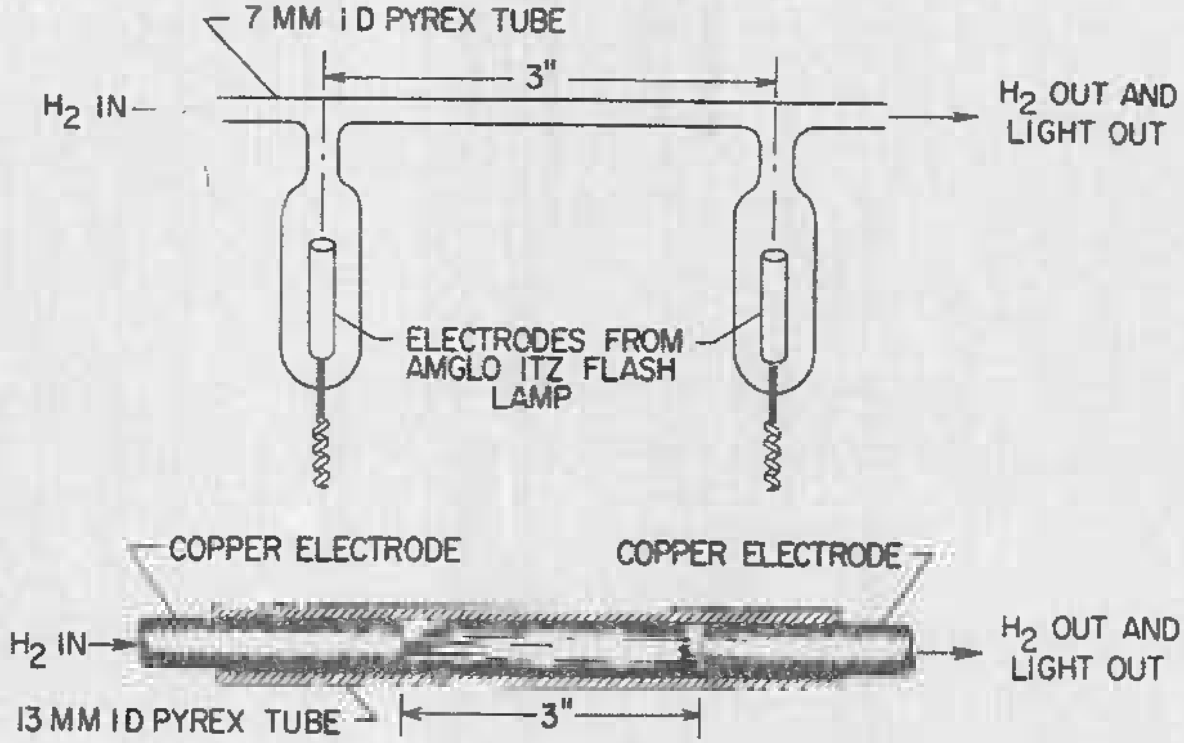

Figure 4. Two Hydrogen Discharge Tube Configurations

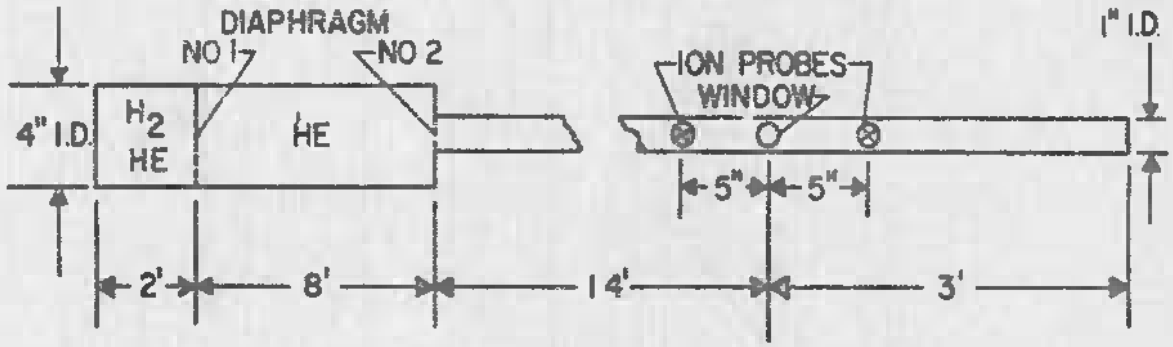

Figure 5 Double Diaphragm Shock Tube

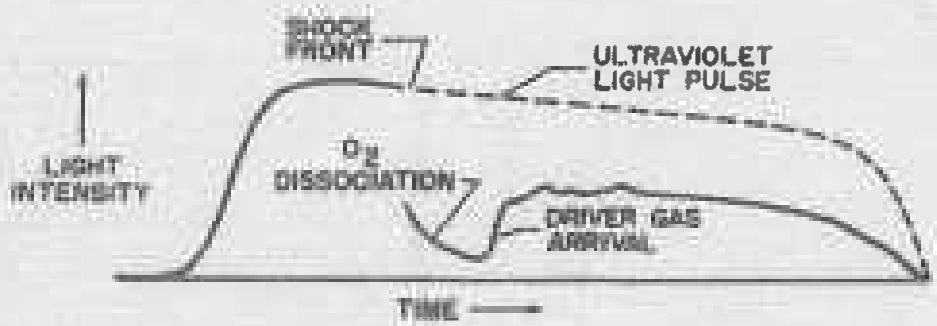

Figure 6 Oscillogram Showing Ultraviolet Absorption

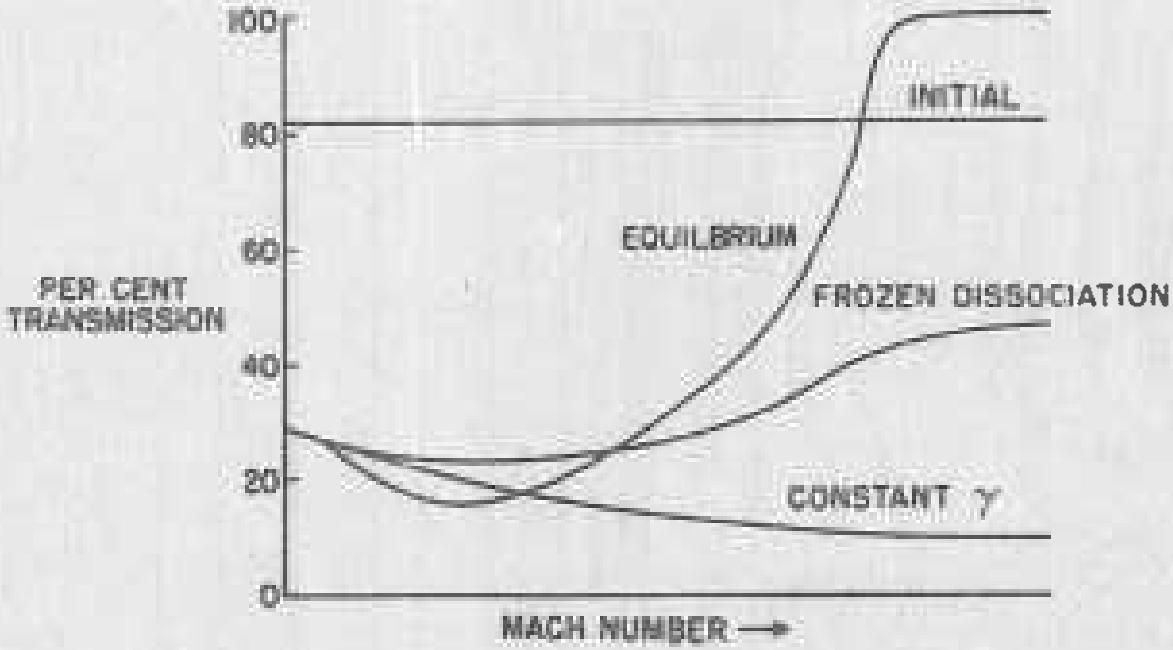

Figure 7 Per Cent Transmission of Ultraviolet Light Through Absorbing Gas Layer

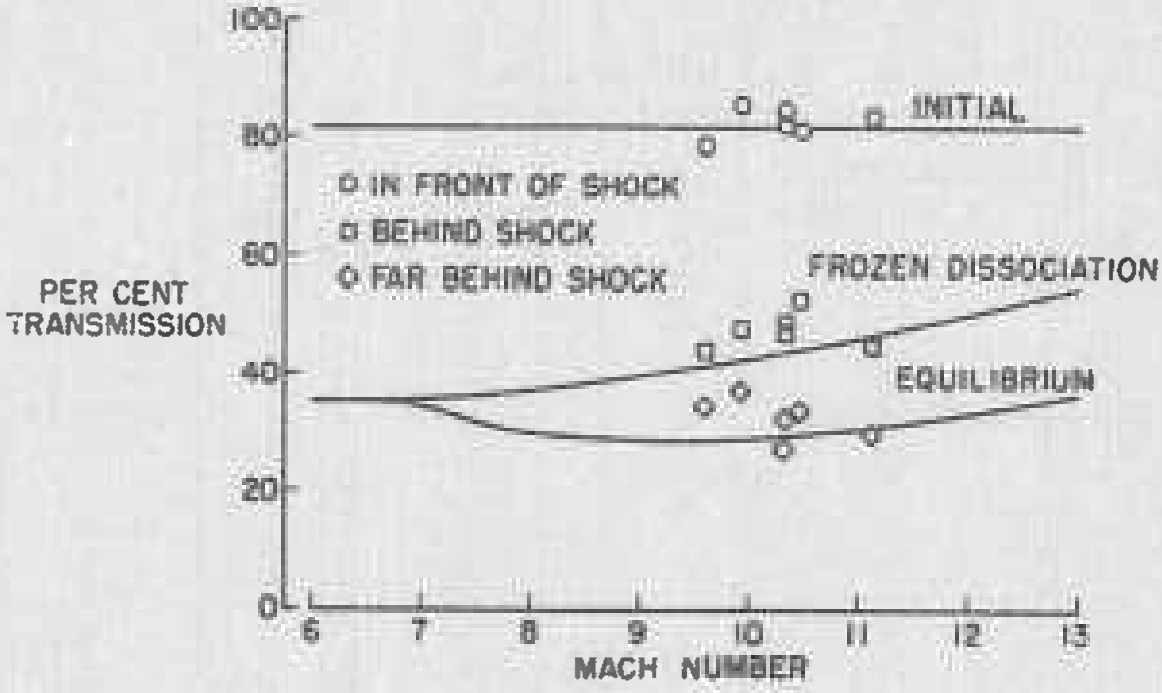

Figure 8 Per Cent Transmission of Ultraviolet Light Through Test Section Containing Pure Oxygen at 0.3 mm Hg

DIFFUSION EFFECTS ON SHOCK STRUCTURE IN A PLASMA

O. W. Greenberg and H. K. Sen
Air Force Cambridge Research Center
Bedford, Massachusetts

and

Y. M. Treve
Block Associates, Inc.
Cambridge, Massachusetts

ABSTRACT

Diffusion effects on the structure of a steady, plane shock in a proton-electron plasma have been studied using a simplified, two-fluid hydrodynamic model in which diffusion is the only shock broadening mechanism. Charge separations occur inside the shock because of the mass difference between protons and electrons. The shock is shown to have electric field and density oscillations as a function of distance through the shock. The peak electric fields are large; the peak electric field inside a weak shock of Mach 1.17 reaches 41,700 volts/cm for typical quiescent plasma conditions. The distance in which electric field changes occur is of the order of the Debye length of the quiescent plasma. The present work is limited to shocks of Mach number less than 2.

I. THE MODEL AND THE EQUATIONS

A. Simplified Two Fluid Model of the Shock

The model of a shock in a totally ionized medium considered here is an extension of a model considered by Cowling[1] in which the only dissipative mechanism broadening the shock is the relative diffusion between two different species. Following Cowling, we assume that the temperatures of the two species are equal at each point in the shock profile and that the mean free path, λ, for collisions which damp diffusion is constant through the shock.[2] Our extension of Cowling's model consists in allowing the two components to carry charges e and $-e$, where e is the magnitude of the protonic charge. We will carry through the discussion for a fully ionized proton-electron plasma, and will neglect the ratio of the electron mass, m_e to the proton mass, m_p, in comparison to 1, throughout. The extension of this work to a system in which the components carry charges $Z_1 e$ and $-Z_2 e$ and both masses are comparable, is straightforward. We will assume that the proton and electron gases obey the ideal gas law, and that both gases have the specific heat ratio 5/3.

Two effects occur because of the charges in the plasma: first, electric fields are generated because of charge separation inside the shock wave, and secondly the shock carries a current in the case that the electric field does not vanish at the end points of the shock.

The purpose of this paper is to consider charge separation and electric field production in a shock wave in a plasma; it is for this reason that we have chosen diffusion as the shock broadening mechanism for this simplified discussion of the shock. The effect of the macroscopic electric field is taken into account exactly in this work, rather than being estimated after the shock structure has been determined.

B. Definitions and Kinematical Relations

In this subsection we define the variables which we will use in the paper, and derive useful kinematical relations between them. For easy comparison with Cowling, we use his hydrodynamic variables; however, to make this work self-contained we repeat the definitions of these variables.

We consider a steady, plane shock in the frame of reference in which the coordinate axis moves with the shock front velocity. We let the positive direction of x point toward the dense region behind the shock. The superscripts $'$ and $''$ refer to the limits as $x \to -\infty$ and $x \to +\infty$ ("in front of" and "behind" the shock) respectively. The subscripts p and e refer to the protons and electrons respectively.

We take u_p, u_e to be the flow velocities, and $u = \dfrac{m_p u_p + m_e u_e}{m_p + m_e} \approx u_p$ to be the mean flow velocity. The number densities of the components are n_p, n_e, and the total number density is $n = n_p + n_e$. The fractional concentration of protons is $f = n_p/n$. The mass density of the fluid is $\rho = m_p n_p + m_e n_e \approx m_p n_p$. The specific volume v is ρ^{-1}. The mass flux per unit area per unit time is $M = \rho u$. The hydrostatic pressure is p. The electric field strength is E. Finally the net charge density is $q = (n_p - n_e)e$, and the current carried by the shock is $J = (n_p u_p - n_e u_e)e$.

From the definitions of ρ and f,

$$\rho = m_p f n, \tag{1}$$

and

$$n_p = \frac{1}{m_p v}, \tag{2a}$$

$$n_e = \frac{1 - f}{m_p f v} \tag{2b}$$

Using the definitions of M, J and equations (2a, b), we find

$$u_p = Mv, \tag{3a}$$

and

$$u_e = \frac{(Me - m_p J) f v}{(1 - f) e} \tag{3b}$$

C. Boundary Conditions

We require that our shock model be steady (time independent), one dimensional (all variable quantities depend on x only), and uniform at large distances from the transition region (gradients of hydrodynamic variables and of the electric charge density and field vanish in front of and behind the shock). These conditions, for the hydrodynamic variables, are quite familiar. We add the remark that if no approximations are made, these conditions imply that the charge density and electric field vanish at both ends, and that the total current (which is conserved) vanishes throughout the shock. However, when the Joule heat can be neglected, the shock can carry a current, and then the electric field cannot vanish at either end, but -- together with the pressure and density -- obeys a set of extended Rankine-Hugoniot relations. The demonstration of these statements will be given below.

D. Shock Structure Equations

In order to verify the remarks above concerning the boundary conditions on the electrical quantities, we will write the equations to include the possibility of charges, currents, and fields at the endpoints. We will make free use of the formulas in subsection I(B) and of standard formulas for the transfer properties of a two fluid system.[3] With the continuity equations for each species taken into account, the shock structure equations for our model are

$$\frac{d}{dx}\left(p + M^2 v - \frac{E^2}{4\pi v}\right) = E q_0, \tag{4}$$

$$\frac{d}{dx}\left(\frac{M^2 v^2}{2} + \frac{5}{2} M p v f - \frac{5}{2} m_p p v f \frac{J}{e}\right) = EJ, \tag{5}$$

$$M v (1-2f) + m_p f J = \frac{3}{2}\sqrt{\frac{m_p}{10 m_e}}\, M p \lambda_e (1-f)\left\{\frac{1}{fp}\frac{dp}{dx} - \frac{1}{f(1-f)}\frac{df}{dx} + \frac{e(1-f)E}{m_p f p v}\right\}, \tag{6}$$

$$\frac{dE}{dx} = \frac{4\pi e (2f-1)}{m_p v f} = q_0, \tag{7}$$

where $M = \sqrt{\frac{3}{5}\frac{v^2}{p/\rho}}$ M is the Mach number of the shock. Equations (4) through (7) are the equations for momentum transfer, energy transfer, relative diffusion of the two species, and Poisson's equation respectively. The terms in q_0 in equations (4) and (7) allow for a non-vanishing charge density at either end. The fact that the charge density must be the same at the front and the back follows from the uniformity requirement on equation (7). The terms in J in equations (5) and (6) allow the shock to carry a non-vanishing current.

E. Charges and Currents at the Ends of the Shock

We now show that q_0 must vanish. The uniformity requirement on equation (7) in terms of f and v requires

$$\tau = \frac{v''}{v'} = \frac{(2f'' - 1)}{(2f' - 1)} \cdot \frac{f'}{f''} \tag{8}$$

where τ is the inverse compression ratio of the shock. The only solutions of (8) which allow $\tau \neq 1$ are $f' = f'' = 1/2$, and $f' \neq f''$. The first possibility implies $q_o = 0$, and, as will be shown below, is the only admissible solution. The second possibility forces $q_o \neq 0$, and from the uniformity requirement on (4) requires $E' = E'' = 0$. We now show that $E' = E'' = 0$ is inconsistent with $q_o \neq 0$ and thus eliminate this second possibility. If $E' = E'' = 0$, the uniformity requirement on (6) yields

$$J = \frac{Me\,(2f' - 1)}{m_p f'} = \frac{Me\,(2f'' - 1)}{m_p f''} \tag{9}$$

The only solution of (9) is $f' = f''$, which implies $q_o = 0$, and thus removes the second possibility above. We can now drop the terms in q_o in equations (4) and (7); and equation (4) can be integrated once to give

$$p + M^2 v - \frac{E^2}{8\pi} = A, \tag{4'}$$

where A is a constant determined by the boundary conditions.

We now discuss the possibility of the shock carrying a current. The uniformity requirements on equations (5) and (6) are

$$E' J = E'' J = 0, \tag{10}$$

and

$$J = \Sigma' E' = \Sigma'' E'', \tag{11}$$

where

$$\Sigma() = \frac{3}{2} \frac{1}{\sqrt{10\, m_p^3\, m_e}} \frac{M}{m} \frac{e^2}{p()\, v()} \lambda,$$

is the electrical conductivity at either end. The only solution of (10) and (11) is $E' = E'' = J = 0$, and thus shocks which are exactly uniform at the end-points cannot carry a current, and must have vanishing electric fields at both ends. However, we note that there are conditions in a plasma in which the Joule heat EJ is small. If we neglect the term EJ, then it is possible for the shock to carry a current.[4] In this case, the electric field at the end points will not vanish but will be related to the current by equation (11), which is another way of writing Ohm's Law. We can now integrate equation (5) once to get

$$\frac{M^3 v^2}{2} + 5\, Mp\, v\, f - 5\, m_p\, p\, v\, f \frac{J}{e} = B \tag{5'}$$

where B is a constant determined by the boundary conditions. Equations (4'), (5'), (6) and (7) are the shock structure equations which determine the space variations of pressure, specific volume, composition, and electric field for this model.

F. Extended Rankine-Hugoniot Conditions

When the shock can carry a current, the boundary conditions on the electric field are coupled to the boundary conditions on the hydrodynamic variables through a set of extended Rankine-Hugoniot relations. There are different ways of writing these Rankine-Hugoniot conditions, depending on which variables are specified and which are then derived from the conditions. One way to write the conditions is to choose the parameters, M, J as well as the quiescent hydrodynamic variables p', v'. Then equations (4'), (5') and (6), each taken at both endpoints, give six equations for the remaining six quantities p'', v'', E', E'', A, B. These equations are:

$$p^{(\,)} + M^2 v^{(\,)} - \frac{E^{(\,)2}}{8\pi} = A \tag{12}$$

$$\frac{M^3}{2} v^{(\,)2} + \frac{5}{2}\left(M - m_p \frac{J}{e}\right) p^{(\,)} v^{(\,)} = B \tag{13}$$

$$J = \Sigma^{(\,)} E^{(\,)}, \tag{14}$$

where each of (12), (13) and (14) is to be taken for both the primed and double primed sets of variables.

G. Dimensionless Shock Structure Equations

For further analysis of the shock structure equations it is convenient to write them in dimensionless form. The remainder of this paper is concerned only with shocks which carry no current; we write down the dimensionless shock structure equations for this case only.

The dimensionless equations are:

$$\pi + \phi - \mathcal{E}^2 = a = \frac{4}{5}(1 + \tau) \tag{4d}$$

$$\phi^2 + 10\pi h\,\phi = 2b = 4\tau \tag{5d}$$

$$\frac{\zeta(1-2h)}{1-h} = \frac{3}{2}\sqrt{\frac{m_p}{10m_e}}\,\frac{1}{m}\left[\frac{\xi}{h\pi}\frac{d\pi}{dz} - \frac{\xi}{h(1-h)}\frac{dh}{dz}\right] + \frac{\sqrt{3}}{20}\sqrt{\frac{m_p}{m_e}}\,\frac{1}{m^2}\,\frac{\lambda}{\lambda_D}\,\frac{\mathcal{E}}{\pi h^2} \tag{6d}$$

$$\frac{d\mathcal{E}}{dz} = -\frac{\sqrt{30}}{60}\,\frac{1}{m}\,\frac{\lambda}{\lambda_D}\,\frac{2h-1}{h\,\xi} \tag{7d}$$

where the reduced variables are

$$\pi(z) = \frac{p(x)}{M^2 v'}, \quad \phi(z) = \frac{v(x)}{v'}, \quad \mathcal{E}^2(z) = \frac{E^2(x)}{8\pi M^2 v}, \quad h(z) = f(x), \quad z = \frac{x}{\lambda}.$$

The relevant lengths in the problem are λ, the mean free path for proton-electron collisions, and λ_D, the Debye shielding length. The ratio of these lengths, λ/λ_D, characterizes the static properties of the plasma in front of the shock.[5] The Mach number, m, gives the shock strength and is related to the inverse compression ratio, τ by

$$m^2 = \frac{3}{4\tau - 1} \tag{15}$$

II. STUDY OF THE SHOCK STRUCTURE EQUATIONS IN A PHASE PLANE

A. Continuous Solutions

The shock structure equations (I, 4d) through (I, 7d) are equivalent to a pair of first order, non-linear equations in the reduced specific volume, ϕ, and electric field, $\mathcal{E}$:

$$\frac{d\phi}{dz} = \phi\left\{\frac{2}{3}\sqrt{\frac{10m_e}{m_p}}\, m\,(2h-1)(2b-\phi^2) + \sqrt{\frac{10}{3}}\,\frac{1}{m}\,\mathcal{E}\right\}\left[9\phi^2 - 2b\right]^{-1} \equiv g_1(\phi, \mathcal{E}), \tag{1}$$

$$\frac{d\mathcal{E}}{dz} = \frac{\sqrt{30}}{60}\,\frac{1}{m}\,\frac{\lambda}{\lambda_D}\,\frac{2h-1}{h\phi} \equiv g_2(\phi, \mathcal{E}), \tag{2}$$

where

$$h = \frac{2b - \phi^2}{10\,\phi\,(a - \phi + \mathcal{E}^2)} \tag{3}$$

This subsection summarizes the phase plane analysis of equations (1) and (2). The details of this analysis are given in the appendix. The phase plane[6] in $\phi, \mathcal{E}$ is shown in Figure 1, in which are illustrated those isoclines of zero and infinite slope of

$$\frac{d\mathcal{E}}{d\phi} = \frac{g_2(\phi, \mathcal{E})}{g_1(\phi, \mathcal{E})}$$

that are important for the physical results. There are two singular points of importance, the points F and B, which correspond to the front and back of the shock respectively. The point F is always a saddle point; for λ/λ_D finite, the point B is either a focus or a node for the shocks of low Mach number which we will consider in this paper.[20] The critical value at which B changes from focus to node is

$$\left(\frac{\lambda}{\lambda_D}\right)_{N\text{-}F} = \frac{5}{24}\,\frac{m_e}{m_p}\,\frac{(m^2-1)(5m^2-1)(m^2+3)^2}{m^2\,(-7m^2+27)}, \tag{4}$$

where foci occur for $\frac{\lambda}{\lambda_D} > \left(\frac{\lambda}{\lambda_D}\right)_{N\text{-}F}$ and nodes for $\frac{\lambda}{\lambda_D} < \left(\frac{\lambda}{\lambda_D}\right)_{N\text{-}F}$. It can be shown (see Appendix) that there are solution curves

$$\phi = \phi(z) \quad \text{and} \quad \mathcal{E} = \mathcal{E}(z)$$

which join the points F and B, and along which the distance parameter z

varies from minus to plus infinity. These solutions give the values of the specific volume and electric field inside the shock transition. Typical focal and nodal solutions are shown in the phase plane in Figure 2, and in space in Figures 3a, b. The node-focus condition is plotted in Figure 4.

The oscillatory (focal) solutions occur when there is little dissipation (large λ/λ_D); while the damped (nodal) solutions occur when there is a large amount of dissipation (small λ/λ_D). These oscillations in electric field as a function of distance through the shock wave are roughly analogous to the oscillations of the current as a function of time in a discharging R-C circuit. In the latter case, oscillations also occur when there is little dissipation (large C/R), and damped solutions occur when there is a large amount of dissipation (small C/R).[20] Note that for this shock wave in a plasma, the density always overshoots the final Rankine-Hugoniot condition density in back of the shock. The non-monotonic density transition in this shock differs from the monotonic one which occurs in a shock in a single component, neutral gas.[7]

B. Discontinuous Solutions

The present model of a shock broadened only by diffusion (or, equivalently, broadened only by a finite conductivity) does not allow a continuous shock transition for all Mach numbers. This feature is shared by Gowling's model of a neutral, diffusion-broadened shock.[1] Mathematically, the discontinuity in the shock transition is associated with the critical line in the phase plane (see Figure 1). The families of solution trajectories on opposite sides of the critical line either both point towards the critical line, or both point away from it; thus a solution which reaches the critical line cannot cross this line, and must suffer a discontinuity.[8] The physical reason for the occurrence of discontinuous solutions is the neglect of some of the dissipative mechanisms. Solutions which have a discontinuity also occur, above some Mach number, in the classical theory of neutral shocks when only the thermal conductivity is included as a broadening mechanism.[9] In this classical case, inclusion of the dissipation due to viscosity allows a solution which is everywhere continuous for all Mach numbers. We expect that inclusion of viscous dissipation in the present model will have the same effect. In the present paper, we only discuss the continuous (weak) shock transitions. We defer the stronger shocks to a later work in which viscosity will be included. The Mach number, $\mathcal{M}_1$, above which discontinuous solutions occur, as a function of λ/λ_D, has been found numerically using a 650 IBM machine. The result is shown in Figure 5, which indicates that for values of $\lambda/\lambda_D > 50$, such as are found in a hydrogen plasma under most conditions, the solutions are continuous up to Mach number 1.169, and have a discontinuity at some point inside the shock for greater Mach numbers.

III. INTEGRATION OF THE SHOCK STRUCTURE EQUATIONS

A. Method of Integration

The simultaneous equations (II.1, II.2), have been integrated numerically using a 650 IBM machine. An outline of the method of solution follows. The solution is uniquely determined at the front, i.e. at the point F:(1,0). However, it is not possible to start the integration of the equations

(II.1, II.2) from F, since at F the parameter $z = -\infty$. However, the equation $\frac{d\mathcal{E}}{d\mathcal{V}} = \frac{g_2(\mathcal{V},\mathcal{E})}{g_1(\mathcal{V},\mathcal{E})}$ can be integrated in the phase plane starting from F to determine a single point G away from F. This point G was found very accurately, (to accuracy of 10^{-5} or 10^{-6}). The integration of (II.1, II.2) was started at G with the value $z = 0$ arbitrarily assigned to G. The Runge-Kutta method was used for the integration. The integration was carried out so that the computed values of $\mathcal{V}$ and $\mathcal{E}$ are accurate to at least 1%.

B. Numerical Results

A series of 18 continuous solutions of the equations was found numerically. Six values of λ/λ_D varying by four powers of 10 were used,[10] and at each value of λ/λ_D the integration was performed for three Mach numbers. The results are shown in Tables 1, 2, and 3. Table 1 shows whether the solutions are foci or nodes, and gives the ratio of the maximum electric field energy density to the pressure at that point in the shock, and the maximum fractional electron concentration. Table 2 gives the ratios of the half widths $\Delta_\mathcal{E}$ and $\Delta_\mathcal{V}$ of the single oscillations in $\mathcal{E}$ and $\mathcal{V}$ to the mean free path and Debye length for the focal solutions, and gives the $\Delta_\mathcal{E}$ ratios and the ratios of the hydrodynamic shock thickness $\delta_\mathcal{V}$ (in place of those of $\Delta_\mathcal{V}$) for the nodal solutions. These widths are illustrated in Figure 6. Table 3 gives the maximum magnitude of the electric field strength in volts/cm, and the maximum net charge density (charge separation) for typical conditions of the quiescent plasma.

C. General Features of the Shock Structure

The results of the numerical integrations indicate some general features for the shock structure. The ratio $E^2_{max}/8\pi p$ for fixed λ/λ_D, varies rapidly with m. Starting from zero for $m = 1$, $\frac{E^2_{max}}{8\pi p}$ reaches the value 0.004 even for weak shocks of $m = 1.169$. For typical plasma conditions, these electric fields are very large, even for these weak shocks. As indicated in Table 3, the electric field reaches 41,700 volts/cm for a Mach 1.169 shock.[11] This rapid increase with m is in accord with the fact that some of the kinetic energy of the flow in the supersonic region is converted, via charge separation inside the shock front, into electric field energy. The value of $E^2_{max}/8\pi p$, for fixed m, is roughly independent of λ/λ_D for $\lambda/\lambda_D > 1$, and decreases more and more rapidly as λ/λ_D decreases below 1. This feature is in accord with the idea that the full amount of charge separation (and electric field production) permitted by the Debye shielding mechanism is attained when $\lambda > \lambda_D$, and that $\lambda < \lambda_D$ inhibits the charge separation. The relevant length for a single electric field oscillation is of the order of λ_D for our case of small Mach number.[18] For the focal solutions, the relevant length, δ, for the decay of the electric field and the hydrodynamic oscillations is proportional to λ but independent of λ_D. We expect that for strong shocks δ will be of the order of λ; however, we have been unable to demonstrate this fact here because of the occurrence of discontinuous solutions. For the weak (continuous) shocks, the shock width is much larger than λ. Using the equations of first approximation to (II.1, II.2) near the back, we have calculated

the width

$$\delta = \frac{1}{4}\sqrt{\frac{m_p}{10\,m_e}}\,\frac{27-7\,m^2}{m(m^2-1)}\,\lambda, \qquad (1)$$

where δ is the distance in which the electric field decays to $1/e$ of its greatest absolute value.[12] For the nodal case, however, the numerical solutions indicate that the shock width is of the order of the Debye length, not the mean free path. Finally, we note that for all the solutions, the density at some point inside the shock exceeds the final density given by the Rankine-Hugoniot conditions. This density overshoot is in contrast with the monotonic density transition in shocks in a neutral, single component gas.[7] The oscillatory structure of the shocks in the plasma is analogous to the structure found recently in hydromagnetic shocks in a plasma.[13]

IV. CONCLUSIONS

The simplified two fluid model of a steady, plane shock in a plasma studied in this paper leads to two kinds of shock transitions; one (focal) in which the electric field and density oscillate going through the shock (λ/λ_D large), the other (nodal) in which the electric field has a single minimum and the density a single overshoot going through the shock (λ/λ_D small).[20] The electric fields produced by charge separation inside the shock can be very large even for relatively weak shocks, electric fields of 41,700 volts/cm are generated in Mach 1.169 shocks under typical quiescent plasma conditions. The distance in which electric field changes occur is of the order of the Debye length. It is expected that the total shock width of the focal transitions for strong shocks is the mean free path; but this has not been shown in the paper because of the occurrence of discontinuous solutions. It has been shown that for weak shocks, for which the shock width is much greater than the mean free path, this width is proportional to the mean free path and independent of the Debye length. The shock width of the nodal solutions is the Debye length.

We would like to note that our results differ from those of other authors who have considered this problem,[14,15,16] and to indicate briefly the source of the differences. These authors find neither oscillatory shock structure, nor large electric fields. The work of Jukes[14] is most similar to ours, in that he uses a hydrodynamic model. Jukes' primary interest is in finding the effect on the shock structure of the great difference between the proton and electron masses. He finds that, for strong shocks, the large value of m_p/m_e results in density, velocity, and proton temperature changes which occur in one or two mean free paths for momentum transfer between protons in the shocked gas, while the electron temperature change occurs in the large mean free path for energy transfer between electrons and protons. Jukes' calculation is valid for distances not greatly smaller than these mean free paths. However, Jukes neglects the electric field energy density, the charge separation, and the diffusion equation (generalized Ohm's law) during his calculation. These approximations eliminate the Debye length from the calculation, and thus for a plasma where $\lambda_D \ll \lambda$, Jukes' calculation is not valid for distances of the order of λ_D. Thus Jukes' estimate that

$$\frac{E^2}{8\pi p} \sim \left(\frac{\lambda_D}{\lambda}\right)^2$$

inside a strong shock should be taken as a statement about the magnitude of the average electric field extending over distances of the order of λ. This result is not then in conflict with our conclusion that

$$\frac{E^2}{8\pi p} \sim 35\left(\frac{\lambda_D}{\lambda}\right)^2$$

inside a weak shock, since our electric field reverses direction in a distance of about $5\lambda_D$, and would have a much smaller value if averaged over a distance comparable to a mean free path. Thus the present work appears to give a fine structure to Jukes' calculation.[19]

We will not make any detailed comments about the papers of Tidman[15] and Krook[16] which use the Mott-Smith[17] kinetic theory shock model; we only remark that Krook's work shows that the electric field vanishes for a low order approximation of the generalized Mott-Smith method. It will be interesting to see if higher orders of Krook's method give an oscillatory fine structure similar to that found here.

In the present paper we have omitted all shock broadening mechanisms except diffusion. We think that this omission is responsible for the discontinuous solutions which limit our discussion to low Mach number shocks. We expect that the inclusion of viscosity will lead to a continuous transition for shocks of all Mach numbers. We plan to carry out such a calculation, including viscosity, and perhaps other dissipative mechanisms. The main objects of such a calculation would be to find out the magnitude of the electric fields inside strong shocks, and if, for high Mach number shocks, the fine structure of the electric field is governed by a length significantly different from the static Debye length.

There may be some question in our use of an hydrodynamic model to describe effects which occur in a distance which is a small fraction of a mean free path. Since there is already a good deal of literature[7, 9, 17] discussing the validity of hydrodynamic models in shock wave theory, we will make only two comments about the hydrodynamic model here. First, it is well known that hydrodynamic models can be derived from kinetic theory via the Boltzmann equation by taking certain moments of the distribution function. Many discussions of shock waves using the Boltzmann equation also use some finite set of moments of the distribution function as part of a scheme to obtain an approximate solution of the kinetic equations. Thus the hydrodynamic and kinetic theory approaches to the shock structure are not qualitatively different; rather these approaches differ by employing different kinds of approximations to the distribution function. Secondly, as a matter of experience, both approaches lead to similar results for the shock thickness and other features of the shock transition, and the agreement is particularly good for low Mach number shocks.[7, 9]

Table 1

$\frac{\lambda}{\lambda_D}$	m	Node or Focus	$\left(\frac{E^2}{8\pi}\right)_{max}/P$	h	$\frac{\lambda}{\lambda_D}$	m	Node or Focus	$\left(\frac{E^2}{8\pi}\right)_{max}/P$	h
89.82	1.169	F	0.00426	0.560	0.8982	1.169	F	0.00414	0.549
	1.122	F	0.00174	0.520		1.122	F	0.00167	0.519
	1.074	F	0.000259	0.507		1.074	F	0.000233	0.507
17.96	1.169	F	0.00418	0.560	0.08982	1.169	F	0.00351	0.525
	1.122	F	0.00171	0.520		1.122	F	0.00146	0.513
	1.074	F	0.000231	0.507		1.074	F	0.000222	0.505
8.982	1.169	F	0.00425	0.559	0.008982	1.753	N	0.0113	0.423
	1.122	F	0.00173	0.520		1.291	N	0.00198	0.479
	1.074	F	0.000228	0.507		1.074	N	0.000932	0.498

h is the fractional proton concentration at greatest deviation from neutrality.

Table 2

$\frac{\lambda}{\lambda_D}$	m	$\frac{\Delta_E}{\lambda_D}$	$\frac{\Delta_E}{\lambda}$	$\frac{\Delta_g}{\lambda_D}$	$\frac{\Delta_g}{\lambda}$	$\frac{\delta_g}{\lambda_D}$	$\frac{\delta_g}{\lambda}$
89.82	1.169	4.70	0.0500	1.78	0.0190	-	-
	1.122	5.57	0.0620	3.26	0.0363	-	-
	1.074	7.49	0.0834	4.77	0.0530	-	-
17.86	1.169	4.41	0.246	1.50	0.0835	-	-
	1.122	5.54	0.308	3.16	0.176	-	-
	1.074	7.49	0.417	5.45	0.303	-	-
8.982	1.169	4.60	0.490	1.82	0.195	-	-
	1.122	5.35	0.618	3.26	0.363	-	-
	1.074	7.15	0.796	4.77	0.531	-	-
0.8982	1.169	4.49	4.90	1.95	2.09	-	-
	1.122	5.27	5.87	3.19	3.55	-	-
	1.074	6.47	7.20	5.11	5.68	-	-
0.08982	1.169	4.49	50.2	2.75	29.4	-	-
	1.122	5.57	62.0	3.56	39.7	-	-
	1.074	6.13	68.2	5.11	56.8	-	-
0.008982	1.753	3.96	441.	-	-	0.657	73.1
	1.291	5.32	593.	-	-	1.91	213.
	1.074	8.17	910.	-	-	4.51	502.

Table 3

Typical plasma conditions:

$\eta_e = 1.50 \times 10^{15}$ cm^{-3}
$T = 3.00 \times 10^{4}$ °K
$\lambda = 5.28 \times 10^{-2}$ cm
$P = 1.24 \times 10^{5}$ dynes·cm^{-2}
$\lambda_D = 5.88 \times 10^{-4}$ cm
$\rho = 2.51 \times 10^{-8}$ gm·cm^{-3}
$\frac{\lambda}{\lambda_D} = 89.82$

γ_m	E (volts/cm)	$\eta_p - \eta_e$ (10^{16} cm^{-3})
1.169	41,700	+0.537
1.122	25,300	+0.155
1.074	11,500	+0.0446

$\eta_p - \eta_e$ is given at greatest deviation from neutrality.

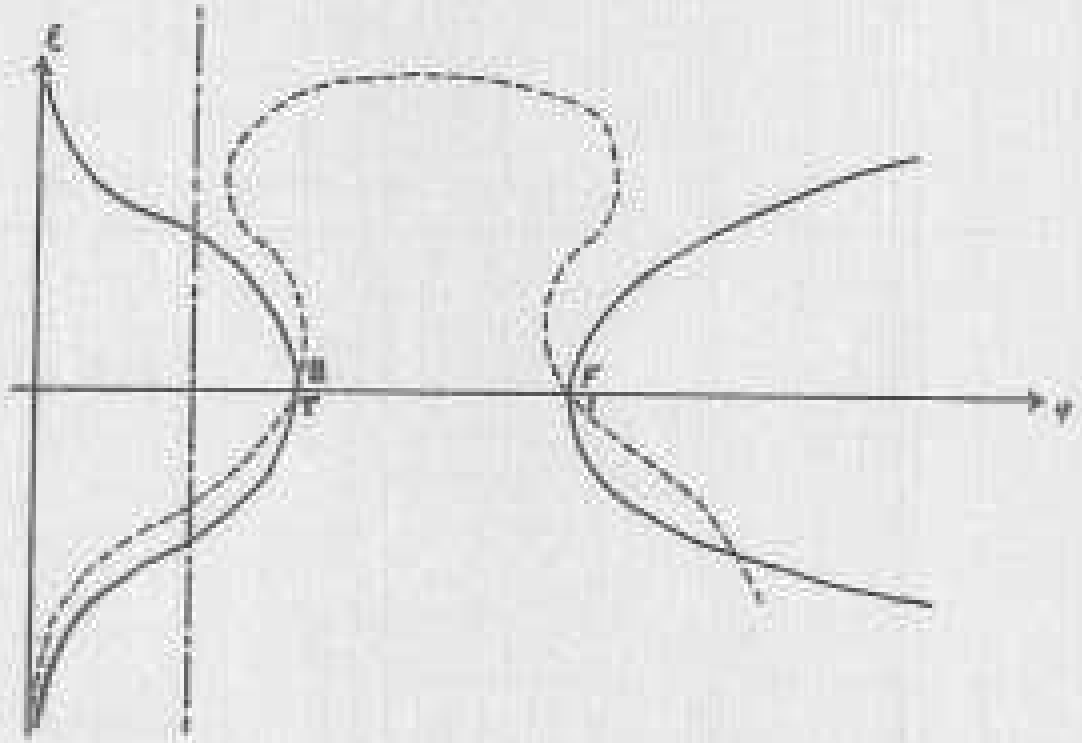

locus of slope $+\infty$ [locus where $g_1(\psi, \xi) = \xi$]

locus of slope $-\infty$ [locus where $g_2(\psi, \xi) = \xi$]

critical line of slope σ [locus where $g_\sigma(\psi, \xi) = \sigma$]

F: $(1, \sigma]$ corresponds to the front of the shock and is reached at $x = -\infty$

B: $[F, \sigma]$ corresponds to the back of the shock and is reached at $x = +\infty$

Figure 1

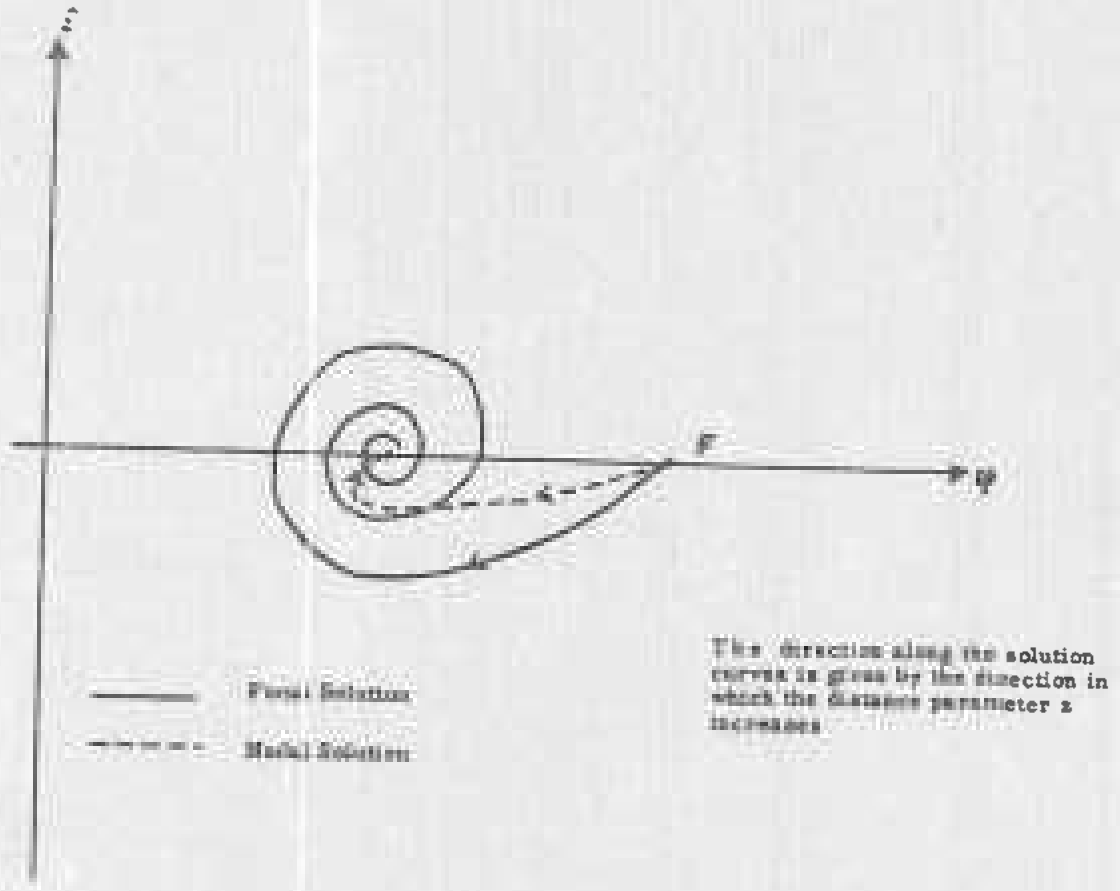
F
Focal Solution
Radial Solution
The direction along the solution curves is given by the direction in which the distance parameter s increases

Figure 2

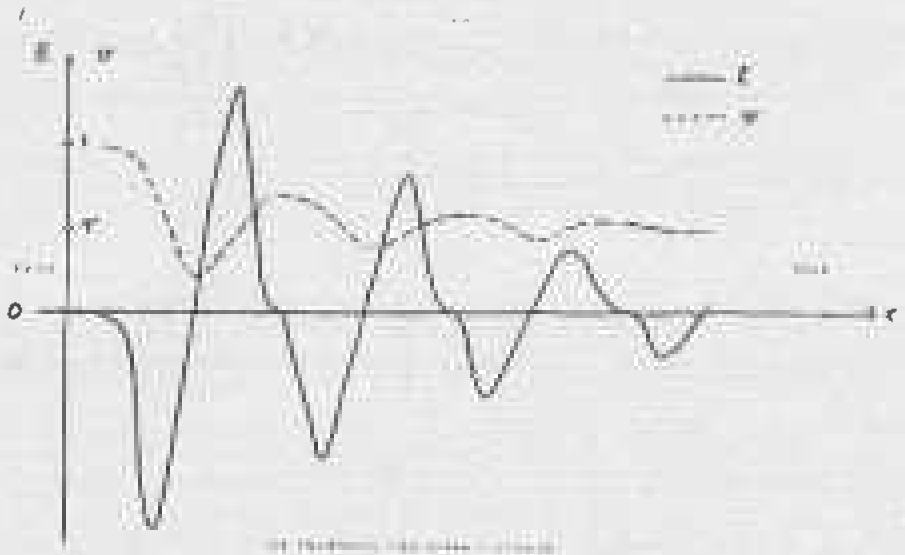

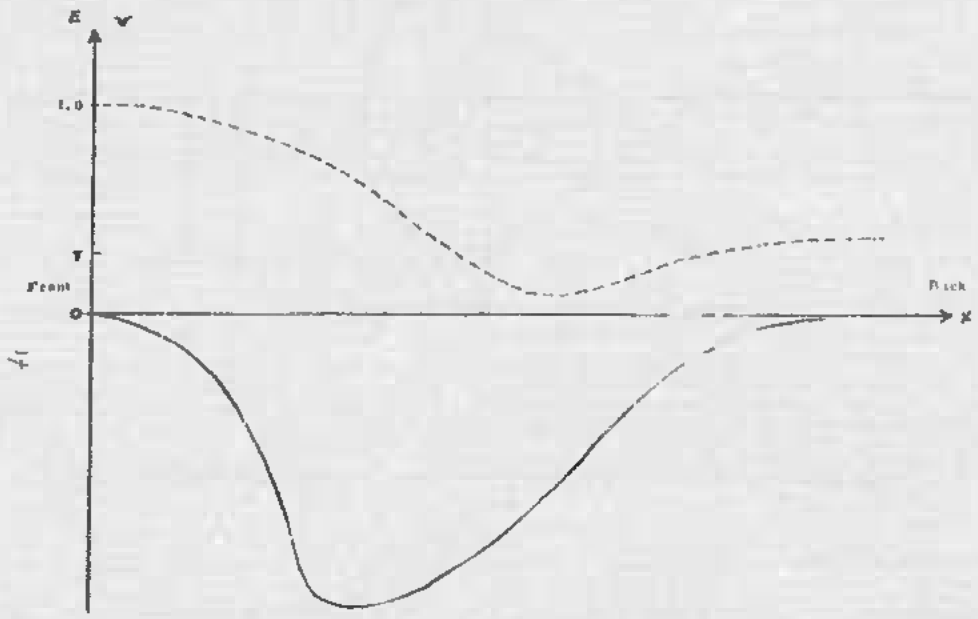

(b) Damped Solution (node at back)

Figure 3

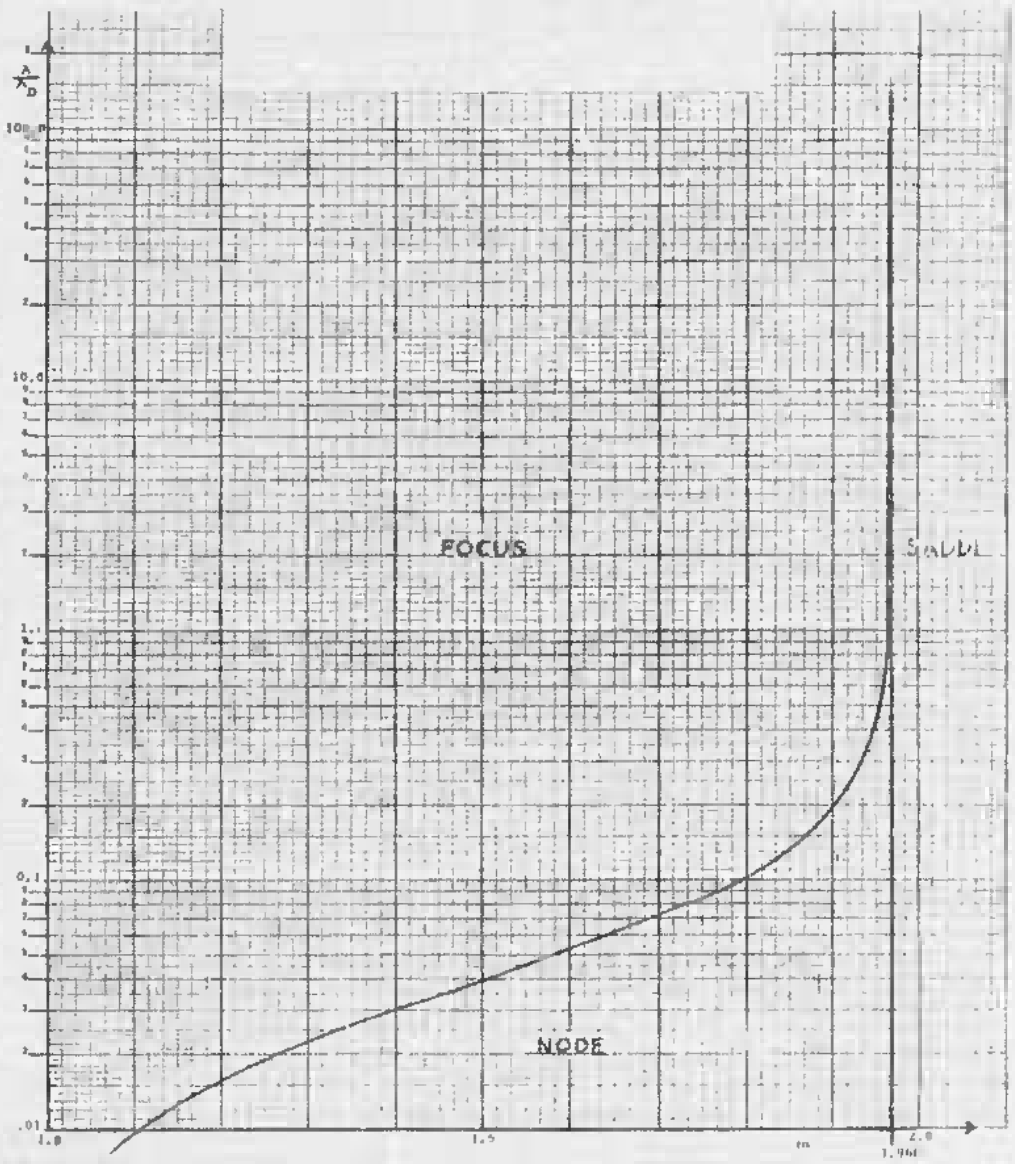

Figure 4 Condition for Node, Focus or Saddle at the Back

"NOTICE: When Government or other drawings, specifications or other data are used for any purpose other than in connection wi a definitely related Government procurement operation, the U.S. Government thereby incurs no responsibility, nor any obligation whatsoever; and the fact that the Government may have formulat furnished, or in any way supplied the said drawings, specifications or other data is not to be regarded by implication or otherwise a in any manner licensing the holder or any other person or corpo tion, or conveying any rights or permission to manufacture, use or sell any patented invention that may in any way be related there

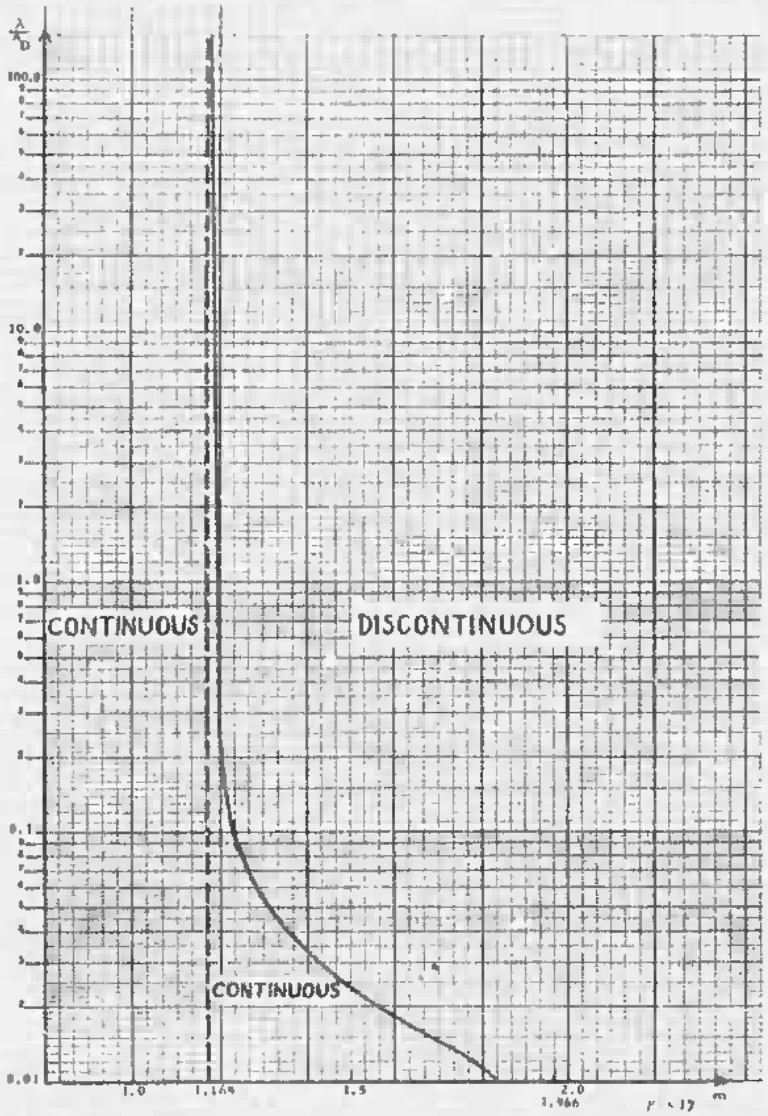

Figure 5 Condition for Continuous Versus Discontinuous Solutions (Found from 650 Calculations)

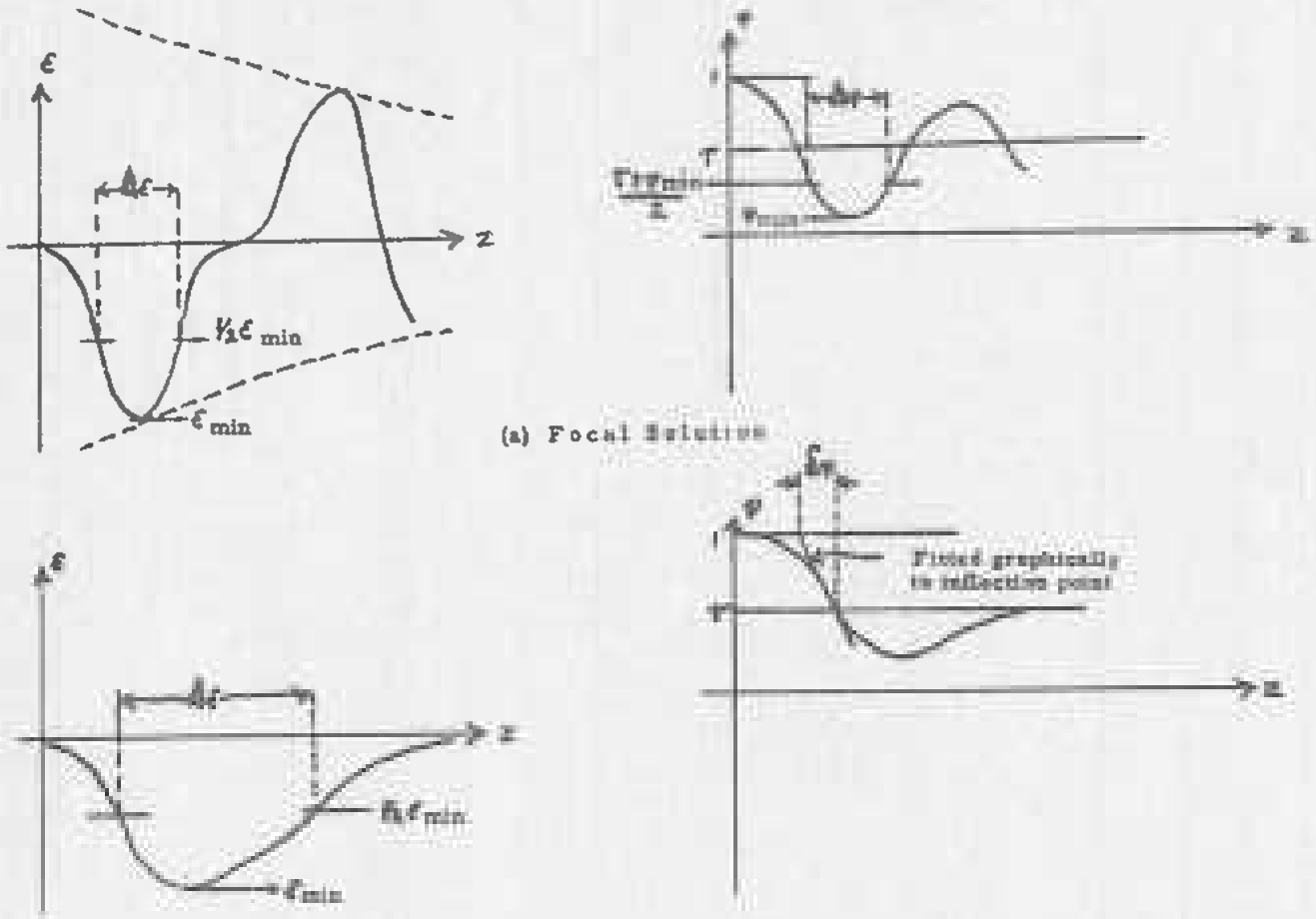

(a) Focal Solution

(b) Nodal Solution

Figure 5 Widths of Electrical and Hydrodynamic Variations

APPENDIX

MATHEMATICAL ANALYSIS

The system of equations (II.1, II.2) may be written

$$\frac{d\mathcal{E}}{dy} = \sigma \frac{2h - 1}{\vartheta h} \tag{1}$$

$$\frac{d\vartheta}{dy} = \frac{\vartheta \left[(2h - 1)(4\tau - \vartheta^2) + 20\sigma\xi\right]}{g\vartheta^2 - 4\tau} \tag{2}$$

where

$$h = \frac{4\tau - \vartheta^2}{10\vartheta\left[\frac{4}{5}(1 + \tau) - \vartheta + \mathcal{E}^2\right]} \tag{3}$$

$$y = \frac{M}{D'} x$$

$$\sigma = \frac{e D' \sqrt{2\pi}}{m_p M^2 v'^{3/2}}$$

More explicitly, after replacing h by this expression:

$$\frac{d\mathcal{E}}{dy} = g_2(\vartheta, \mathcal{E}) = 2\sigma \frac{4(\vartheta - 1)(\vartheta - \tau) - 5\vartheta\mathcal{E}^2}{\vartheta(4\tau - \vartheta^2)} \tag{4}$$

$$\frac{d\vartheta}{dy} = g_1(\vartheta, \mathcal{E}) = \frac{(4\tau - \vartheta^2)\left[4(\vartheta - 1)(\vartheta - \tau) - 5\vartheta\mathcal{E}^2\right] + 100\sigma\vartheta\mathcal{E}\left[\frac{4}{5}(1 + \tau) - \vartheta + \mathcal{E}^2\right]}{5(g\vartheta^2 - 4\tau)\left[\frac{4}{5}(1 + \tau) - \vartheta + \mathcal{E}^2\right]} \tag{5}$$

We will show that there exist continuous, bounded and single-valued functions $\vartheta(y)$, $\mathcal{E}(y)$ satisfying this system and the boundary conditions:

$$\begin{cases} \mathcal{E}(-\infty) = \mathcal{E}(+\infty) = 0 \\ \vartheta(-\infty) = 1, \ \vartheta(+\infty) = \tau \end{cases} \tag{6}$$

and such that i) the pressure $\pi = \frac{4}{5}(1 + \tau) - \vartheta + \mathcal{E}^2$ remains positive;

ii) the ion concentration h stays in the range $0 \leq h \leq 1$.

We confine our study to the continuous solution for which $\frac{4}{g} < \tau < 1$.

A. Phase-portrait

In order to obtain a qualitative picture of the solutions to this problem, we begin by applying the standard procedure of investigating the nature of the various isoclines in the phase-space of the variables ϑ and $\mathcal{E}$.

From equations (4) and (5) one obtains the differential equation of the trajectories (T) in the ϑ, $\mathcal{E}$-plane:

$$\frac{d\mathcal{E}}{dy} = 10\sigma \cdot \frac{g\vartheta^2 - 4\tau}{\vartheta(4\tau - \vartheta^2)} \times \frac{\left[\frac{4}{5}(1+\tau) - \vartheta + \mathcal{E}^2\right]\left[4(\vartheta-1)(\vartheta-\tau) - 5\vartheta\mathcal{E}^2\right]}{(4\tau-\vartheta^2)\left[4(\vartheta-1)(\vartheta-\tau) - 5\vartheta\mathcal{E}^2\right] + 100\sigma\vartheta\mathcal{E}\left[\frac{4}{5}(1+\tau) - \vartheta + \mathcal{E}^2\right]} \tag{7}$$

The above condition i) implies that (T) stays to the left of the parabola (P) defined by the equation

$$\frac{4}{5}(1+\tau) - \vartheta\mathcal{E}^2 = 0 \tag{8}$$

(see Figure A1). The conditions ii) is then satisfied if: $4\tau - \vartheta^2 > 0$, i.e, if (T) stays in the intersection of the half-plane $\vartheta < 2\sqrt{\tau}$ with the region defined by

$$h \leq \frac{4\tau - \vartheta^2}{10\vartheta\left[\frac{4}{5}(1+\tau) - \vartheta + \mathcal{E}^2\right]} \leq 1. \tag{9}$$

This region is bounded to the left and to the right by the branches (C_1') and (C_1'') of the cubic (C_1) along which $h = 1$.

Let R be the region just defined where conditions (i, ii) are satisfied inside R there are three isoclines of interest:

1. A cubic (C_2) (with two branches, C_2' and C_2'') along which $\frac{d\mathcal{E}}{d\vartheta} = 0$, whose equation is

$$4(\vartheta-1)(\vartheta-\tau) - 5\vartheta\mathcal{E}^2 = 0 \tag{10}$$

and which corresponds to $h = \frac{1}{2}$. The curve is real outside the strip $\tau < \vartheta < 1$, admits the of the $\mathcal{E}$-axis as an asymptote, and intersects the parabola (P) at the points α and β for $\vartheta = 2\sqrt{\tau}$. Notice that $h > \frac{1}{2}$ in the regions bounded by the branches (C_1') and (C_2'), and (C_1''), and (C_2'') respectively, whereas $h < \frac{1}{2}$ in the region between (C_2') and (C_2'').

2. A straight line (Δ) along which $\frac{d\mathcal{E}}{d\vartheta} = 0$, defined by $\vartheta = \frac{2}{3}\sqrt{\tau}$ and lying to the left of the point $B(\tau, 0)$ but never intersecting (C_1'). Let $J(\frac{2}{3}\tau, 0)$ denote the foot of (Δ) on the ϑ-axis.

3. A curve (Γ) along which $\frac{d\mathcal{E}}{d\vartheta} = \infty$, defined by

$$(4\tau - \vartheta^2)\left[4(\vartheta-1)(\vartheta-\tau) - 5\vartheta\mathcal{E}^2\right] + 100\sigma\vartheta\mathcal{E}\left[\frac{4}{5}(1+\tau) - \vartheta + \mathcal{E}^2\right] = 0. \tag{11}$$

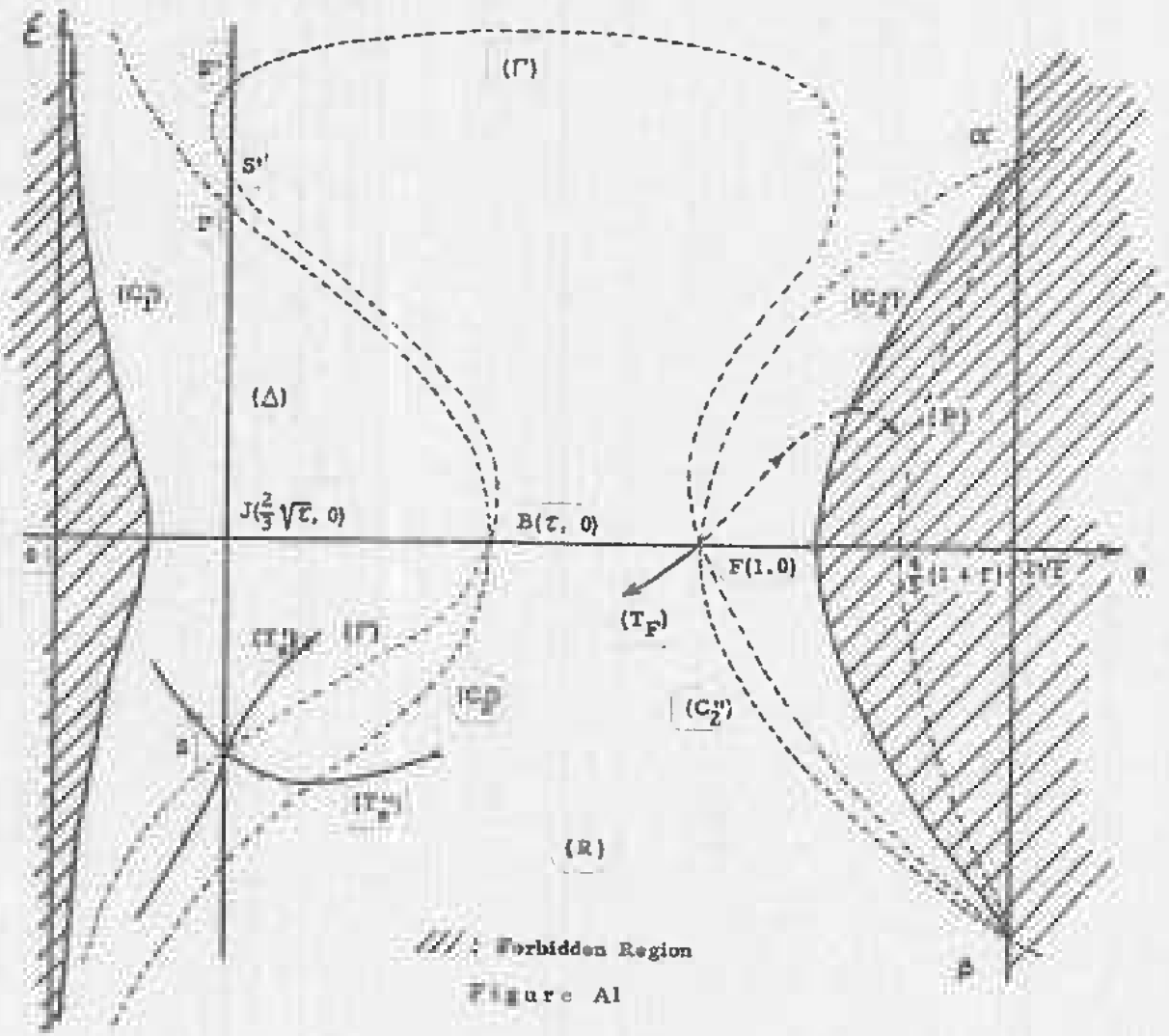

///: Forbidden Region

Figure A1

The form of (Γ) as shown on Figure A1 has been qualitatively derived using the following method:

Eq. (11) is equivalent to the pair of equations

$$\mathcal{E}(\vartheta, h) \equiv -\frac{4\tau - \vartheta^2}{20\sigma}(2h - 1) = \mathcal{E} \tag{12}$$

and

$$h(\vartheta, \mathcal{E}) \equiv \frac{4\tau - \vartheta^2}{10\vartheta\left[\frac{4}{5}(1+\tau) - \vartheta + \mathcal{E}^2\right]} = h. \tag{13}$$

The ordinates of the points of intersection of a straight-line $\vartheta = \vartheta_0$ with (Γ) are equal to those of the points of intersection of the curve (γ) defined by $h(\vartheta_0, \mathcal{E}) = h$ defined by $\mathcal{E}(\vartheta_0, h) = \mathcal{E}$. Therefore, by drawing the families of curves (γ) and straight-lines (δ) for various ϑ_0 it is possible to construct (Γ). We now proceed to investigate the nature of the singular points, i.e., the points at which $d\mathcal{E}/d\vartheta$ takes the form $0/0$.

Singular Points

We see at once that the isoclines (C_2), $(\frac{d\mathcal{E}}{d\vartheta} = 0)$, and (Γ), $(\frac{d\mathcal{E}}{d\vartheta} = \infty)$, intersect each other at the points $F(1.0)$ and $B(\tau, 0)$ which are therefore singular points. There are three other singularities at the intersection of (Γ) with (Δ). Applying the method outlined above it is possible to show that one of them, S say, always lies on the segment IJ of (Δ) (see Figure A1) whereas the two others S' and S'', when real, stay above the intersection I' of (Δ) and (C_2'). For reasons which will be given later S' and S'' cannot affect the topological aspect of the trajectories (T) and therefore will be disregarded.

Singularity F(1.0): By expanding the functions $g_1(\vartheta, \mathcal{E})$ and $g_2(\vartheta, \mathcal{E})$ about F and neglecting terms in $(\vartheta - 1)$ and $\mathcal{E}$ of degree ≥ 2, one obtains a linear approximation of the system, valid in a small neighbourhood about F:

$$\frac{d\vartheta}{dY} = \frac{8\sigma - (1 - \tau)}{4\tau - 1}(\vartheta - 1) \tag{14}$$

$$\frac{d\mathcal{E}}{dY} = \frac{4(1 - \tau)}{8 - 4\tau}(\vartheta - 1) + \frac{160\sigma}{8 - 4\tau}\mathcal{E}. \tag{15}$$

Applying the standard procedure[6], the nature of the singularity is determined by the reality and the sign of the roots S_1 and S_2 of the characteristic equation:

$$S^2 - \frac{4(1 - \tau)}{8 - 4\tau}S - \frac{160\sigma^2(1 - \tau)}{(8 - 4\tau)(4\tau - 1)} = 0. \tag{16}$$

Since by assumption $\frac{4}{8} < \tau < 1$, we have for any σ : $S_1 S_2 < 0$. Hence the roots are real and of opposite signs. Therefore F is a saddle point through which pass two trajectories, F being approached for $Y \to +\infty$ along one of them, for $Y \to -\infty$ along the other.

Since F corresponds to the front of the shock, only the latter trajectory is of interest. Its slope in the phase-plane is found to be

$$-\frac{1-\tau}{\sigma}\left[1-\sqrt{1+\frac{40\sigma^2(g-4\tau)}{(1-\tau)(4\tau-1)}}\right], \tag{17}$$

and is therefore >0. It remains to be determined in which direction the solution must leave F in order to stay inside the region (R) previously defined. Looking at Figure A1, and noticing that:

i) $\frac{d\mathcal{E}}{d\vartheta} > 0$ in the region bounded by (C_2'') above, (Γ') below and (C_1'') to the right;

ii) $\frac{d\mathcal{E}}{d\vartheta} = 0$ along (C_2'') and (C_1'');

we see that the solution which leaves F above the ϑ-axis cannot cross (C_2'') and therefore must reach (C_1'') and enter the forbidden region. Thus this solution must be ruled out. This completes the proof that the solution is uniquely determined at F, and that the electric field $\mathcal{E}$ is negative at the front of the shock.

Singularity $B(\tau, 0)$: the first approximation to the system is

$$\frac{d\vartheta}{dy} = -\frac{8\sigma(1-\tau)}{\tau^2(4-\tau)}(\vartheta-\tau) \tag{18}$$

$$\frac{d\mathcal{E}}{dy} = -\frac{4(1-\tau)}{g\tau-4}(\vartheta-\tau)+\frac{10\sigma}{g\tau-4}\mathcal{E}, \tag{19}$$

which leads to the characteristic equation

$$S^2+\frac{4(1-\tau)}{g\tau-4}S+\frac{160\sigma^2(1-\tau)}{\tau^2(g\tau-4)(4-\tau)}=0. \tag{20}$$

Because we restricted our study to the case $\tau > \frac{4}{g}$, we see that $S_1 S_2 > 0$ for any σ, so that B is either a node or a focus, depending on whether the roots are real or complex, respectively. In either case, $S_1 + S_2 < 0$; hence B is approached for $Y \to +\infty$ in agreement with the fact that it corresponds to the back of the shock.

If $\sigma < \sqrt{\frac{\tau^2(1-\tau)(4-\tau)}{40(g\tau-4)}} = \sigma_1$ B is a node approached by an infinity of trajectories. In other words, through any point sufficiently close to B there passes a trajectory going directly to B. Furthermore, all these trajectories have a common tangent at B whose slope is found to be

$$\frac{1-\tau}{10\sigma}\left[1+\sqrt{1-\frac{40\sigma^2(g\tau-4)}{\tau^2(4-\tau)(1-\tau)}}\right] \tag{21}$$

and is therefore >0. If $\sigma > \sigma_1$, B is a focus, i.e. the solutions about B are spirals. It can be shown that if M is a point on one of these, the polar radius B M revolves clock-wise when its length decreases and tends to zero as $Y \to +\infty$.

Singularity S: Unlike F and B, S is not a point of equilibrium since $\frac{d\mathcal{E}}{dy} \neq 0$ at S. Due to the fact that the ordinate $\mathcal{E}_s$ of S_2 is a root of the equation of the third degree (11) where ϑ is set equal to $\frac{2}{3}\sqrt{\tau}$, the method usually applied to determine the nature of a singularity is not practical. This difficulty may be overcome by deriving the equation whose roots are the slopes λ_s' and λ_s'' of the trajectories passing through S. If $\vartheta_s (=\frac{2}{3}\sqrt{\tau})$, $\mathcal{E}_s$, π_s and h_s, are the respective values of the variables $\vartheta, \mathcal{E}, \pi$, h at S, this equation is:

$$g\,\lambda_s^2 - (10\,h_s^2\,\vartheta_s - 4h_s\vartheta_s - 10h_s^2\,\pi_s + \vartheta_s)\lambda_s - \frac{10\sigma(2h_s - 1)(\sigma - 2\,h_s^2\,\vartheta_s\mathcal{E}_s)}{h_s\,\vartheta_s} = 0 \quad (22)$$

But $h_s > \frac{1}{2}$ as indicated before and $\mathcal{E}_s < 0$; hence $\lambda_s'\lambda_s'' < 0$ and S is either a saddle point or a node. Now, the first order expansion of the numerator and denominator of $d\mathcal{E}/d\vartheta$ in series of powers of $(\vartheta - \vartheta_s)$ and $(\mathcal{E} - \mathcal{E}_s)$ would lead to an expression of the form

$$\frac{d\mathcal{E}}{d\vartheta} = \frac{c(\vartheta - \vartheta_s)}{a(\vartheta - \vartheta_s) + b(\mathcal{E} - \mathcal{E}_s)} \quad (23)$$

with no term in $(\mathcal{E} - \mathcal{E}_s)$ in the numerator, because the isocline $(\Delta)(\frac{d\mathcal{E}}{d\vartheta} = 0)$ has an infinite slope. Hence the characteristic equation would then be of the form: $S^2 - aS - bc = 0$, and the equation whose roots are the slopes of the tangents to the trajectories would be:
$\lambda_s^2 + \frac{a}{b}\lambda_s - \frac{c}{b} = 0$. But we have shown that $\lambda_s'\lambda_s'' < 0$; hence $-\frac{c}{b} < 0$ and $S_1S_2 = -bc < 0$. Hence S is a saddle point through which pass only two trajectories (T_s') and (T_s'')(see Figure A1).

We shall now prove that in the case when B is a node, the trajectory (T_s') which leaves S with a positive slope in the upward direction is bound to go to B. Let K be the intersection with (Δ) of the common tangent (θ) of the infinity of trajectories passing through B. (See Figure A2). If we show that at any point L of the segment KB the slope λ_L of the trajectory (T_L) passing through L is smaller than the slope of (θ), we may conclude that any (T_A) coming from a point A lying in the region (ρ) bounded by (Δ), (Γ') and (θ) is trapped between (θ) and $(\Gamma_\infty$: along which $\frac{d\mathcal{E}}{d\vartheta} = \infty)$, and therefore is bound to go to B.. This will be true for (T_s) also.

Let μ_s denote the slope of (θ). A straightforward method for proving that $\lambda_L < \mu_s$ at any L would be to use equation (6) and show that $\frac{d\mathcal{E}}{d\vartheta} < \mu_s$, ———. Unfortunately the inequality thus obtained is too

cumbersome to be worked out and we have to apply another method based upon the consideration of the family of isoclines (I_λ) inside (ρ).

The curves (I_λ) are defined by the equation

$$\frac{d\varepsilon}{d\vartheta} = \frac{g_2(\vartheta, \varepsilon)}{g_1(\vartheta, \varepsilon)} = \lambda \quad \text{or} \quad \lambda g_1 - g_2 = 0 \tag{24}$$

and therefore pass through S and B for any λ. No two curves $(I_{\lambda'})$ and $(I_{\lambda''})(\lambda' \neq \lambda'')$ intersect each other in (ρ) except of course at S and B, for if they did at a point N, say, there would exist two distinct trajectories passing through N with slopes λ' and λ'', which is impossible since (ρ) contains no singular point other than S and B. In particular, no $(I_\lambda)(\lambda \neq 0)$ intersects either (Δ) or (C_2') which both belong to the family (I_λ) and correspond to $\lambda = 0$, except at the points S and B. Therefore the curves (I_λ) behave in (ρ) as shown in Figure A2.

The derivation of the slope $\mu(\lambda)$ of the tangent at B to an arbitrary (I_λ) leads to the following expression

$$\mu(\lambda) = \frac{1 - \tau}{5\sigma} - \frac{2}{5} \cdot \frac{(1 - \tau)(g\tau - 4)}{\lambda \tau^2 (4 - \tau)}, \tag{25}$$

and it can be verified that $\mu(\lambda_1) = \mu_1 = \lambda_1$. In other words, the line (ϑ), of slope μ, (which is the common tangent to the solutions at B) is tangent at B to the isocline (I_{λ_1})(along which $\frac{d\varepsilon}{d\vartheta} = \lambda_1 = \mu_1$). Since $\mu(\lambda)$ is a monotonically increasing function of λ, if we restrict ourselves to λ', such that $0 < \lambda' < \lambda_1$, we shall have $\mu(\lambda') < \mu(\lambda_1) = \lambda_1$. Such an isocline $(I_{\lambda'})$ leaves B with a slope smaller than that of (ϑ). But we have shown that it stays in (ρ) and necessarily goes to S. Hence it must intersect KB at some point L. Therefore, if we continuously vary λ' from 0 to λ_1, the point L continuously describes the whole segment BK. It follows at once that the slope $\lambda_L = \lambda'$ of the trajectory passing through any point L of BK is smaller than λ_1, i.e., the slope of BK. Thus we have completed the proof that the trajectory (T_s') which leaves S in (ρ) necessarily arrives at B.

In order to complete the phase portrait it is useful to study how the trajectories behave when $\sigma \to +\infty$ and 0.

Limit Solutions for: $\sigma \to +\infty$: Dividing equation (2) by equation (1) one obtains

$$\frac{d\varepsilon}{d\vartheta} = \left[\frac{\vartheta^2 h (4\tau - \vartheta^2)}{\sigma (g\vartheta^2 - 4\tau)} + 20 \frac{\vartheta^2 \varepsilon}{(g\vartheta^2 - 4\tau)(2h - 1)} \right]^{-1} \tag{26}$$

If $\sigma \to +\infty$ the solutions of (26) tend uniformly to the solution of the equation:

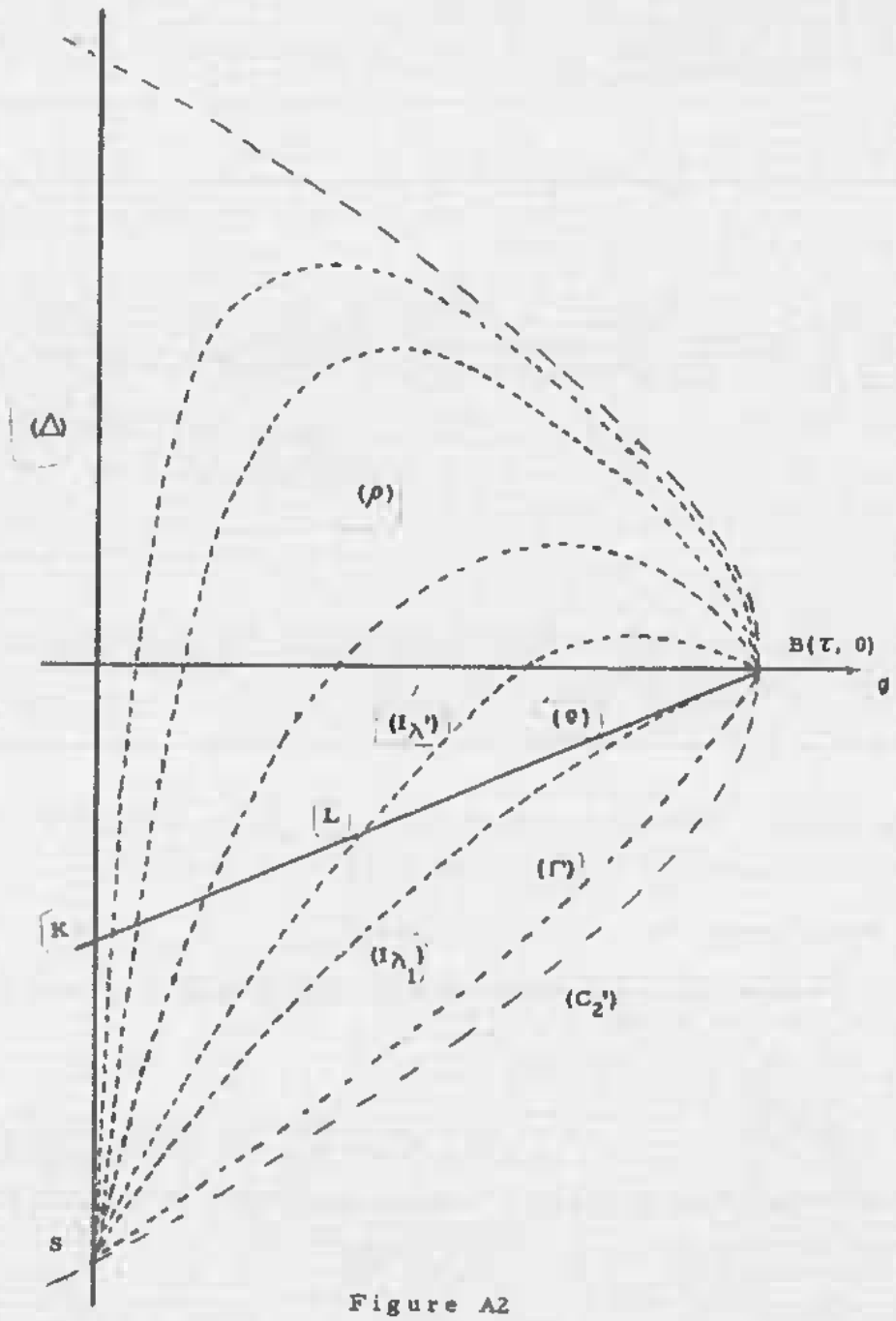

Figure A2

$$\frac{d\mathcal{E}}{d\phi} = \frac{(g\phi^2 - 4\tau)(2h-1)}{20\phi^2\mathcal{E}} \tag{27}$$

whose general integral is found to be exactly

$$10\phi\mathcal{E}^2 = C\phi^2(4\tau - \phi^2)^4 + g\phi^2 - 8(1+\tau)\phi + 4\tau \tag{28}$$

where C is the constant of integration. The curves (τ) defined by equation (28) are symmetric with respect to the ϕ-axis. The singular points F(1, 0) and $J(\frac{2}{3}\sqrt{\tau}, 0)$ are saddles and B $(\tau, 0)$ is a center surrounded by closed curves.[3] Figures A3a, A3b and A3c show the different aspects of the solutions. The critical value $\tau_c = 0.7985$ corresponds to the case where the particular trajectory (τ_F) which passes through the point F(1, 0) also passes through $J(\frac{2}{3}\sqrt{\tau}, 0)$.

Limit Solutions for $\sigma \longrightarrow 0$: In this case the system reduces to

$$\begin{cases} \dfrac{d\mathcal{E}}{dy} = 0 & (29.1) \\ \dfrac{d\phi}{dy} = \dfrac{\phi(2h-1)(4\tau - \phi^2)}{g\phi^2 - 4\tau} & (29.2) \end{cases}$$

The trajectories in the $\phi, \mathcal{E}$-plane are straight lines $\mathcal{E} = \mathcal{E}_0 =$ constant along which the representative point $M(\phi, \mathcal{E}_0)$ moves according to the parametrization defined by equation (29.2). In particular the trajectory which passes through F(1.0) is merely the ϕ-axis.

We are now in the position to complete the phase portrait and determine under which conditions there exist solutions satisfying the requirements of the problem. As mentioned before, at F, the only admissable trajectory (T_F) leaves F in the region $\mathcal{E} < 0$ with a slope:

$$-\frac{1-\tau}{10\sigma}\left[1 - \sqrt{1 + \frac{40\sigma^2(g-4\tau)}{(1-\tau)(4\tau-1)}}\right]$$

At the same point the slope of the trajectory (t_F) which is the solution of the reduced equation (27) (corresponding to $\sigma = +\infty$)) is found to be

$$\sqrt{\frac{2}{5} \cdot \frac{(g-4\tau)(1-\tau)}{4\tau - 1}}.$$

It can be easily shown that the latter is always greater than the former. If we define a region (R_1) as the subregion of (R) where $\phi > \frac{2}{3}\sqrt{\tau}$, we see that at a point $M(\phi, \mathcal{E}) \in (R_1)$ the term with σ in the right hand side of equation (26) is always positive, so that at such a point M the slope of the trajectory (T), solution of the given system, is smaller than the slope of the trajectory (t) solution of the reduced equation (27).

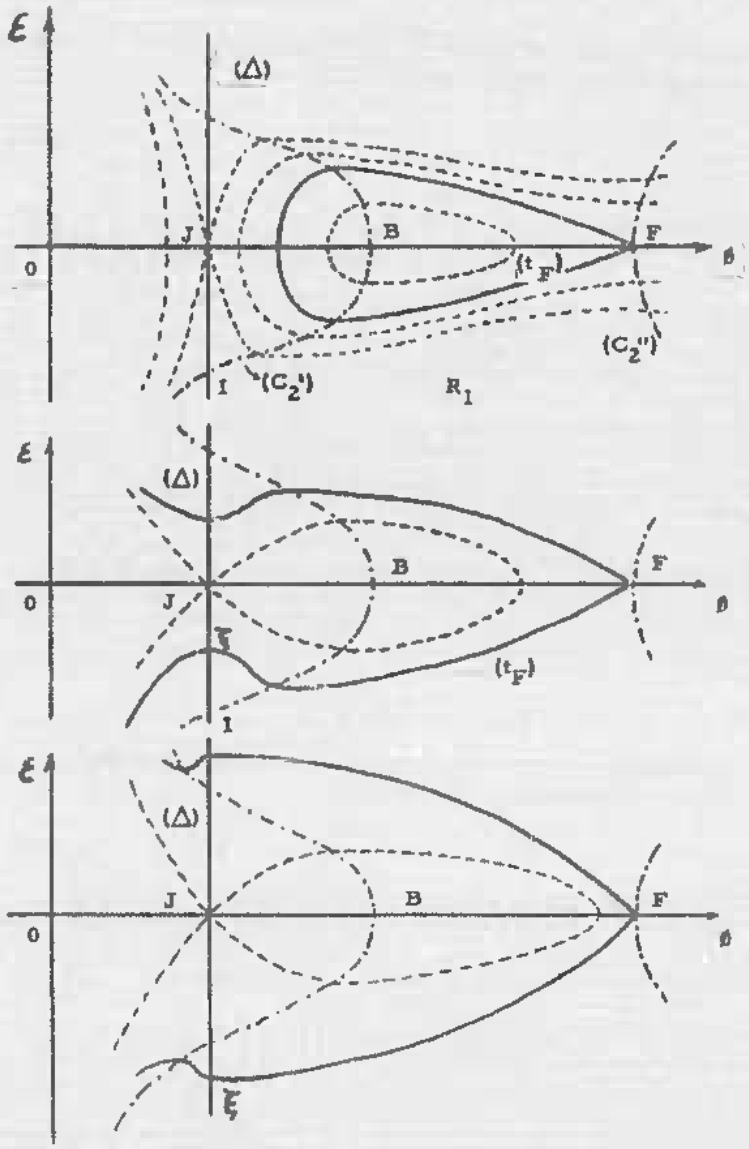

Fig. A3a -
Case I: $\tau_c < \tau < 1$

Fig. A3b -
Case II: $4/g < \tau < \tau_c$
(t_F) reaches (Δ) above I.

Fig. A3c -
Case II: $4/g < \tau < \tau_c$
(t_F) reaches (Δ) below I.

Figure A3

It follows that if $\mathcal{E}(\vartheta)_F$ and $\mathcal{E}_R(\vartheta)_F$ denote solutions of equation (26) and (27) respectively such that $\mathcal{E}(1)_F = \mathcal{E}_R(1)_F$ we have $|\mathcal{E}(\vartheta)_F| < |\mathcal{E}_R(\vartheta)_F|$ for $\frac{2}{3}\sqrt{\tau} < \zeta < 1$.

At this point we have to distinguish between two cases, I): $\tau > \tau_c$, the critical value already defined for which (t_F) connects F and J $(\frac{2}{3}\sqrt{\tau}, 0)$, _____ and, II): $\tau < \tau_c$.

Case I: $\tau > \tau_c$. Then (t_F) encloses $B(\tau, 0)$ and necessarily intersects the isocline $(\Gamma: d\mathcal{E}/dy = \infty)$ at some point η_t (see Fig. A4a, A4b. Hence, by the inequality $|\mathcal{E}(\vartheta)_F| < |\mathcal{E}_R(\vartheta)_F|$, (T_F) intersects (Γ) at some point η_T on the arc $\eta_t B$ of(Γ). From there on, a) If B is a node, (T_F) goes directly to B as proved before (Fig. A4a). b0 If B is a focus, (T_F) goes up, intersects the ϑ-axis at some point between $J(\frac{2}{3}\sqrt{\tau}, 0)$ and $B(1, 0)$ and begins spiraling about B, staying inside (t_F) (Fig. A4b). In both cases we may conclude that for any σ there exists one and only one solution satisfying the requirements of the problem. The behavior of the functions $\vartheta(y)$ and $\mathcal{E}(y)$ corresponding to these cases is pictured in Fig. 3a and 3b.

Case II: $\tau < \tau_c$: In this case the solution becomes discontinuous if σ is greater than a critical value σ_c, which is a function of τ. The discontinuous solutions occur when the solution curve starting from F reaches the line (Δ) before it reaches the curve (Γ).[21] Thus for the discontinuous solutions, the solution curve reaches (Δ) at some point ζ_σ below S_σ, the intersection of (Δ) and (Γ) (see Figure A5). We now consider the location of the points ζ_σ and S_σ as σ varies for fixed $\tau < \tau_c$, and show that for every such τ there is one critical $\sigma = \sigma_c$ below which the solutions are continuous. For $\sigma = \infty$, the solution of the reduced equation intersects (Δ) at ζ_∞ (it is irrelevant whether ζ_∞ is above or below I, the intersection of (Δ) and (C_2)). Since $\partial/\partial\sigma(d\mathcal{E}/d\vartheta) > 0$ in R_1, for any $\sigma > 0$ the point ζ_σ moves from ζ_∞ up (Δ) as σ decreases. However the point S_σ moves down (Δ) as σ decreases. Thus for some $\sigma = \sigma_c$, the points S_{σ_c} and ζ_{σ_c} coincide. For $\sigma < \sigma_c$, the solution curve reaches (Γ) between S_σ and B and thus the solution remains continuous and reaches B.

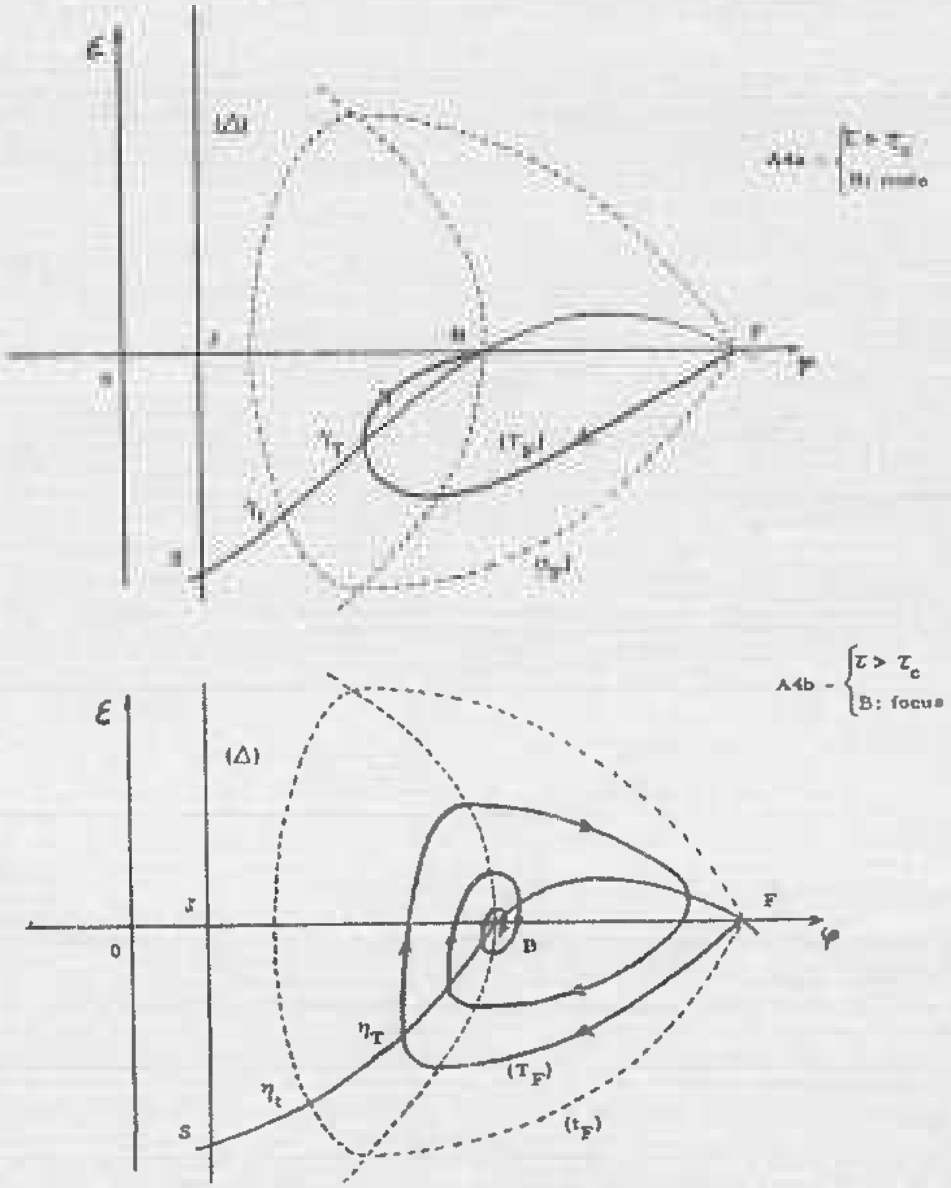

Figure A4

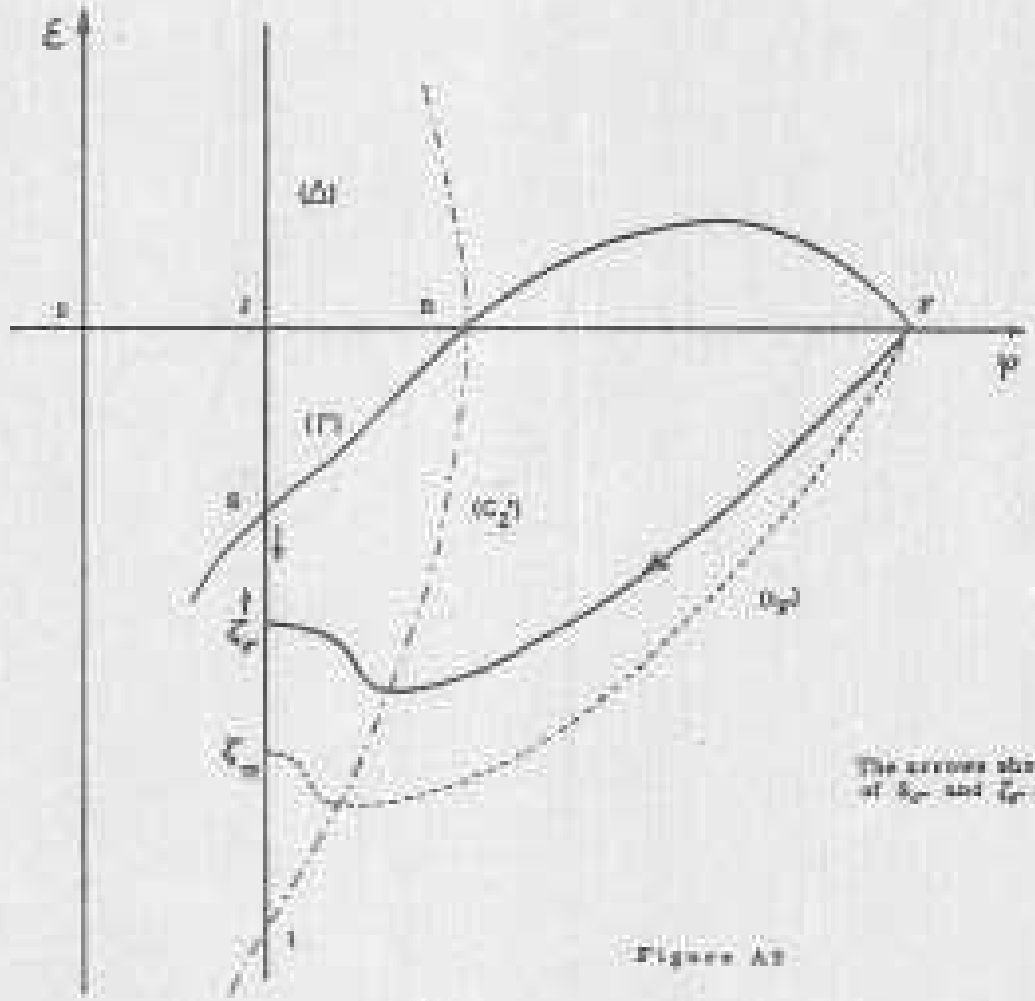
E
(Δ)
s
i
n
s'
P
(Γ)
s
(C_2)
(Γ_p)
ξ_p
ξ_m
1
The arrows show the motion of ξ_m and ξ_p as r decreases.

Figure A2

REFERENCES

1. T. G. Cowling, Phil. Mag. 33, 61 (1942).

2. The assumption that λ is constant does not affect the qualitative results obtained for weak shocks.

3. S. Chapman and T. G. Cowling, The Mathematical Theory of Non-Uniform Gases, Cambridge University Press (1953).

4. The neglect of the Joule heat here is similar to the neglect of the Joule heat in discussions of a steady current in a metallic conductor.

5. The characterization of the quiescent plasma by the dimensionless ratio λ/λ_D can be replaced by a characterization of the quiescent plasma in terms of the temperature, T, and electron density, η_e, by using the formulas (given by Chapman and Cowling):

$$\lambda = \sqrt{\frac{6}{\pi}} \left(\frac{kT'}{2e^2}\right)^2 \frac{1}{\eta_e} \frac{1}{\log\left(1 + \frac{2(kt')^3}{\pi e^6 n_e'}\right)},$$

$$\lambda_D = \sqrt{\frac{kT'}{8\pi n_e' e^2}}$$

6. N. Minorsky, Introduction to Non-linear Mechanics, J. W. Edwards (1947).

7. D. Gilbarg and D. Paolucci, J. Rat Mech. Anal. 2, 617 (1953).

8. See N. Minorsky, loc. cit. for a discussion of critical lines and discontinuous solutions.

9. H. Grad. Comm. Pure Applied Math. 5, 257 (1952).

10. The smaller values of λ/λ_D do not occur in a fully ionized hydrogen plasma. These values were considered here for two reasons: first, to understand the interplay of λ and λ_D in determining the shock structure, and secondly, because the smaller values of λ/λ_D may be reached in mixtures of plasma and buffer gases. Values of λ/λ_D larger than those considered here do not change the shock structure qualitatively.

11. We have obtained discontinuous solutions of the shock equations which indicate that $E^2_{max}/8\pi\rho$ continues to increase rapidly with Mach number for shocks stronger than those considered here, and that this ratio can be of the order of 0 4 for strong shocks. We give this indication of the trend of the results for high m, even though the present model is not reliable there.

12. Note that $\delta \to \infty$, $m \to 1$ as would be expected. The vanishing of δ for $m^2 = 27/7$ is a symptom of the occurrence of discontinuous solutions for $m^2 \geq 27/7$.

13. C. S. Morawetz, Institute of Math. Sci. N. Y. U. Report NYO-8677 (1959); L. Davis, R. Lüst and A. Schlüter, Bull. A.P.S. II, 4, 200 (1959).

14. J. D. Jukes, J. Fluid Mech. 3, 275 (1957).

15. D. A. Tidman, Phys. Rev. 111, 1439 (1958).

16. M. Krook, Annals of Physics 6, 188 (1959).

17. H. Mott-Smith, Phys. Rev. 82, 885 (1951).

18. The limiting wavelength, Λ, of the oscillations near the back of the shock (as $\alpha \to \infty$) is

$$\Lambda = 2\pi \sqrt{\frac{m_p}{10\, m_e}}\, \frac{\lambda}{m} \left\{ \frac{5^3 - 2^5}{5} \frac{m_p}{m_e} \frac{m^2 (m^2 - 1)}{(m^2 + 3)^2 (-7 m^2 + 27)(5 m^2 - 1)} \left(\frac{\lambda}{\lambda_D}\right)^2 - \frac{36 (m^2 - 1)^2}{(-7 m^2 + 27)^2} \right\}^{-1/2}$$

The limit, Λ_∞, for $\frac{\lambda}{\lambda_D} \to \infty$, is

$$\Lambda_\infty = \frac{\pi}{8\sqrt{3}} \frac{m^2 + 3}{m^2} \left(\frac{(-7 m^2 + 27)(5 m^2 - 1)}{m^2 - 1} \right)^{1/2} \lambda_D,$$

which exhibits the expected proportionality to λ_D.

19. It should be repeated that the present paper neglects the effects, calculated by Jukes and Tidman, of the different mean free paths for energy and momentum equilibrium between the proton and electron gases, as well as the different temperatures of the proton and electron gases inside the shock. Our λ corresponds more closely to Tidman's ℓ_v.

20. For the case of no dissipation ($\lambda/\lambda_D \to \infty$), the singular point at the back, B, becomes a center, and the trajectories in the phase plane are closed curves around B. This situation is discussed in the appendix under the heading $\sigma(\alpha \frac{\lambda}{\lambda_D}) \to \infty$. In particular, the solution starting from the front (which previously corresponded to the shock transition) returns to the front, and thus now corresponds to a finite amplitude solitary wave, rather than a shock wave. The solution for this case can be found in closed form and is given in the appendix.

21. On (Δ), $\frac{d\phi}{dy} = \pm\infty$ and $\frac{\delta\phi}{dy}$ has opposite signs on opposite sides of (Δ). Thus any curve passing through (Δ) corresponds to a solution $\phi(y)$ which is not single-valued. In this case there is no continuous solution to the shock problem; however, we expect that there will be a discontinuous solution[5] which can be obtained by considering the limit solutions, for vanishing viscosity, of the higher order set of equations in which viscosity is included. These discontinuous solutions will not be discussed in this paper.

TECHNIQUE OF PRESSURE MEASUREMENT ON AN AIRFOIL IN A SHOCK TUBE

J. Ray Ruetenik

INTRODUCTION

The measurement of the blast loading on airfoils has been underway at M.I.T. for the past 5 years.[1-9] At small angles of attack, good correlation of the lift measurements has been obtained with linearized indicial and gust theory at subsonic speeds, in both the diffractive[7] and post-diffractive periods;[1-7] and at sonic speed, in the diffractive and early post-diffractive periods.[3,7] At large angles, where stall occurs, large increases in the lift are observed due to strong vortices shed from the leading edge, followed by oscillations and subsequent reduced lift.[2] A program is currently underway at M.I.T. to study the latter condition of transient stall.

The measurements to date have been made primarily with the interferometer. But at large angles where stall occurs, the viscous effects on the upper surface are larger, so that the determination of the surface pressure is quite uncertain. Therefore direct pressure measurements are required.

The boundary layer on the shock tube wall also works against the interferometric measurements, which measure, of course, wall to wall. Unfortunately the boundary layer thickens with time, and the interacts with the flow over the airfoil more at large angles of attack, increasing the difficulty of measuring this stalled condition. By measuring the pressure near the midspan, the sensitivity to wall effects can be reduced. With finite span airfoils the pressure must necessarily be measured directly.

It is expected that pressure measurements will not displace interferometric measurements, at least for two-dimensional airfoils, but that the pressure transducer will measure at several points and the interferometer can fill in the details.

TRANSDUCER REQUIREMENTS

The basic requirements for a pressure transducer to measure airfoil pressure distributions in a shock tube, even as large as the M.I.T. 8 × 24-inch tube, are miniaturization, good low-frequency response, accuracy, and insensitivity to acceleration.

A 4-inch chord airfoil with a 10-per cent thickness ratio is about the maximum model size tolerable, which means a transducer must be about 0.1 inch high. Frequencywise, the test period extends from 0.2-50 milliseconds, so the transducer must be flat to one per cent from 0.03-4,000 cps. The accuracy problem is common to blast tests; at low particle speeds the shock overpressure is large compared to the dynamic pressure, e.g., at a particle Mach number behind the shock, M_2, of 0.4 the dynamic pressure is

only 25 per cent of the overpressure. Therefore, for a normal-force coefficient $c_N \approx 1$, to measure c_N to 10 per cent, the local overpressure must be measured to 1-1/4 per cent of the shock overpressure. At higher Mach numbers the accuracy requirement is not so severe. However, it is important to note that a differential transducer, one that measures the difference and is insensitive to the pressure level, would only have to measure to 10 per cent. An electrical differencing will be described later.

Acceleration sensitivity and signal from straining of the airfoil can be reduced by proper design. A considerable advantage of these crystals is their small size and mass involved.

There was no commercial pressure transducer that fulfilled the size and frequency requirement. Therefore, a pressure transducer was developed in this laboratory. The major portion of the development of this transducer is reported in reference 10. Since the work reported in reference 10 was completed, the pedestal has been redesigned and a series of measurements have been made of the acceleration sensitivity. These will be included in this paper.

CONFIGURATION

Barium titanate not only has the large open-circuit voltage sensitivity to pressure of quartz and tourmaline, but furnishes a significantly larger charge, about equivalent to Rochelle salt. This is important due to the capacitance of the lead and amplifier input. Barium titanate has several desirable mechanical features. The piezoelectric axes are easily aligned; it is a ceramic, so that it is readily formed into a variety of shapes; and the temperative effect is less than in Rochelle salt.

A sketch of the transducer is shown in Fig. 1. The barium-titanate element is a circular disc 0.125-in. in diameter. and 0.050-in. high. It is cemented to a steel pedestal, which will be described below. The pedestal and airfoil serve as the ground lead. The voltage to be measured is across the disc. The polystyrene disc insulates the disc electrically and thermally from the silver diaphragm. The pressure is applied through the silver diaphragm.

One of the early problems was the large thermal signal from the shock-compressed gas. A polyvinylchloride sheet is cemented to the outside of the silver, serving as an insulator. The little heat that does penetrate the plastic is largely conducted away by the silver, and finally the polystyrene disc is also a good thermal insulator. A balance must be reached between large thicknesses for thermal insulation and small thicknesses to keep the pressure signal large and for miniaturization.

The wire cemented to the crystal is teflon insulated to minimize signal from wire motion. The signal is fed to an electrometer tube in a cathode follower stage, and then to a conventional amplifier. By careful control of the charge leakage, the time constant can be extended without sacrificing the signal. The electrical aspects are described in detail in reference 10. Incidentally, it is possible to use other configurations of the barium titanate which produce somewhat larger signals, but the disc has the advantage of

mechanical simplicity and low charge leakage; actually a very large pressure sensitivity was obtained with this simple configuration.

AIRFOIL BENDING

The problems involved in the airfoil motion are shown in Fig. 2. The sensitivity to the airfoil bending and elongation arises from the sensitivity of the barium titanate element to a strain in any of the principal directions. Placing the element exactly on the airfoil centerline would eliminate the elongation, but it does not eliminate the bending effect, and as a matter of fact, the centerline cannot be found close enough to even reduce the elongation sensitivity sufficiently. Several isolation methods were attempted, but "standing the transducer on a pin", Fig. 2a, was the most satisfactory. The pedestal is necked to about 1/10th of the crystal diameter.

This method of isolating the element was tested as follows: One crystal was cemented directly to a bar, and a second crystal which was mounted on a pedestal was cemented to the same bar. In one test the bar was stretched, and in the second test it was bent in such a way that the outer skin of the bar was curved only. The sensitivity to both elongation and bending was reduced by the pedestal by more than a factor of 200, which is the minimum signal that could be measured.

With the transducers in the airfoil, and the airfoil mounted in the shock tube, a weight was placed on the airfoil equivalent to the load due to the maximum normal force which is 2.4 psi. The voltage across a transducer was measured when the load was applied. The sensitivity was set so that a signal equivalent to 1/1000 of the mean pressure difference across the airfoil could be detected. No signal was observed. Therefore it was concluded that the sensitivity to strain was negligible.

AIRFOIL ACCELERATION

Sensitivity to airfoil acceleration was more of a problem. The predominant acceleration is in the direction of the axis of the transducer. The method of compensation is to locate a second crystal, hereon called a compensating element, next to the transducer and isolated from the air pressure, Fig. 2. The compensating element is connected in parallel with the pressure element and polarized in the opposite direction, so that ideally the portion of the signal due to acceleration is cancelled.

The whole transducer was placed into a double-wedge airfoil, and set at an angle of attack where $c_N \approx 1$. The whole transducer was covered, so that it would not measure the air pressure. A shock was fired and the peak-to-peak signal from acceleration was 7 millivolts. The signal due to the mean pressure difference across the airfoil was about 100 mv., therefore the peak-to-peak acceleration signal was about 7 per cent of the signal from the pressure difference. The acceleration sensitivity was measured in a shaker test, and also calculated by assuming that the signal is essentially from acceleration of the barium titanate element. The two values of the acceleration sensitivity were about the same 0.2 mv/g, where the pressure sensitivity was 30 mv/psi. The aerodynamic load in the test gave about a 60-g acceleration to the airfoil, which is quite large.

Reducing the thickness of the barium titanate element by one-half reduces the fraction of the signal due to acceleration to one-fourth. Unfortunately this also reduces the sensitivity to pressure (not quite as fast as the reduction in thickness, depending upon the external capacitance). Eventually, as the thickness is reduced, the load from the wire, diaphragm, etc. on the crystal becomes predominate. The agreement of the calculated and measured values of the acceleration signal indicate that the mass accelerated was primarily the barium-titanate element.

Tests were made with the compensating element disconnected, to evaluate the reduction in acceleration signal by the element. The tests are as yet not conclusive, but in one test the compensating element appeared to reduce the acceleration sensitivity to one-third. The matching of the crystal dimensions and polarization must be improved in order to make a more conclusive statement.

The signal from the bending of the lead wire in the airfoil was tested by keeping everything intact and depolarizing the crystal. The signal was about 1 mv peak-to-peak when subjected to the same shock. These tests all indicate that a further reduction in acceleration signal by a factor of two or three is all that can be expected.

CALIBRATION

Since the response does not go down to D. C., the transducer must be calibrated dynamically. However, the charge leakage rate generally has a time constant of a minute or better, so a simple facility will serve.

The device used is a "reverse-dead-weight tester," Fig. 3. The airfoil is shown attached to the cell that fits in the wall of the shock tube. The section of a box beam is the calibration chamber, which fits over the airfoil in the shock tube, and is clamped in place by the second cell. The chamber is pressurized through a tee connnection to the manometer, and the latter serves as the dead weight. The procedure is to rapidly release the pressure in the chamber to the atmosphere by the large clamp, and measure the voltage jump on an oscilloscope. The box beam comes to atmospheric pressure in about 50 milliseconds (a constriction in the manometer hose throttles the air flow from the manometer).

A typical oscillogram is shown in Fig. 4a, which is termed "pneumatic", because air is the fluid. A calibration curve with the transducer shunted by a 1000 $\mu\mu$f. capacitor is shown in Fig. 5. The data all fell within one-per cent of the mean line. In fact, the silver diaphragm was removed from the transducer, a new diaphragm installed, and the lower calibration curve was obtained, which differs only slightly from the upper curve. The shock-tube measurement was made by firing a shock, knowing the shock strength and the local pressure coefficient. The shock-tube data are within two per cent of the calibration data.

An improvement in the technique was obtained by filling the box beam nearly full of water (hydraulic calibration). An oscillogram is presented in Fig. 4b. With this method the jump is nearly flat, whereas the pneumatic

calibration has the constant voltage followed by a drift. The difference is due to the cooling of the gas in the chamber by the expansion. Heat is transferred from the transducer, whereas in hydraulic calibration the temperature is constant.

For shock tests, the amount of thermal insulation necessary to reduce the thermal effect to a negligible magnitude was determined by increasing the thickness of the thermal insulation until any further increase in the thickness did not change the rise in signal at long delay times (50 milliseconds maximum). Actually no improvement was obtained over the minimum thickness of polyvinylchloride, 0.002-in., that was tested, so this thickness has been used on the transducers. Also, the silver diaphragm was 0.0005-in. thick in these tests. Pneumatic calibration has shown that a 0.001-in.-thick diaphragm reduces the thermal effect significantly. Therefore, as a safety factor a 0.001-in. diaphragm is now used.

APPLICATION

Two transducers were placed in a 10-per cent-thick symmetrical-double-wedge airfoil at the 35-per cent-chord station on the upper and lower surface. A pair of simultaneous pressure records is presented in Fig. 6, for a $M_2 = 0.4$ and $\alpha = 8.3$ deg. At 8.3 deg. stall first occurs on this airfoil. The larger oscillations in the upper-surface signal are attributed to the pressure fluctuations of the unsteady flow on this surface. The record of the lower surface was always smoother.

The errors in obtaining the difference in pressure between the two surfaces from two oscillograph traces are double, and at low Mach numbers it is the problem of a small difference between two large signals. Therefore a test was run wherein the signals were differenced electronically to give a single record. When the airfoil was calibrated the two signals were matched through a differencing amplifier to a single null signal at the output. The resulting difference signal, for the shock condition of Fig. 6 is shown, in the oscillogram of Fig. 7. The oscillations show that the uncertainty, at later times, of an average over several milliseconds is about $\pm$ 10 per cent of the difference signal. The difference agrees with interferometer measurements until the time when the first vortex from the leading edge passes over the transducer, between 2 and 3 milliseconds. After this the pressure difference measured by the transducer is about 20 per cent below the value measured by the interferometer. This is the direction in which the difference is expected.

CONCLUSION

The effort has been directed toward achieving a miniaturized pressure transducer which has good reliability. It is not believed to be the ultimate in miniaturization for the requirements stated above; present indications are that the transducer could be scaled down from the present height of 0.140 in. to about 1/16 in. This would reduce the acceleration sensitivity even further, and enable measurement of the pressure nearer edges of the airfoil. Some reduction in signal from the present 80 mv/psi (without a shunt capacitor) would occur. Further reduction is primarily limited by the pedestal height.

ACKNOWLEDGMENTS

This investigation was sponsored under contract to the Aircraft Laboratory of the Wright Air Development Center. The active cooperation of the Aircraft Laboratory has contributed materially to its success. The direction of Professor R. L. Bisplinghoff and Dr. E. A. Witmer is gratefully appreciated.

REFERENCES

1. Ruetenik, J. R., and Witmer, E. A., Transient Aerodynamics of Two-Dimensional Airfoils, Part I, Interferometric Measurements of Two-Dimensional Airflow Development About a Symmetrical Double-Wedge Airfoil in Shock-Initiated Subsonic Flow, M.I.T., WADC TR 54-368, Part 1, August 1956.

2. Ruetenik, J. R., and Witmer, E. A., Transient Aerodynamics of Two Dimensional Airfoils, Part 2, Interferometric Measurements of Airflow Development About an NACA 65-010 Airfoil in Shock-Initiated Subsonic Flow, Including Transient Stalling Effects, M.I.T., WADC TR 54-368, Part 2, March 1958.

3. Andrews, P. T., and Ruetenik, J. R., Transient Aerodynamics of Two-Dimensional Airfoils, Part 3, Interferometric Measurements of Airflow Development About an NACA 65-010 Airfoil in Shock-Initiated Transonic Flow, M.I.T., WADC TR 54-368, AD 209497, January 1959.

4. Hobbs, N. P., Indicial Downwash and Its Structural Effect on the Horizontal Tail, M.I.T., WADC TR 56-164, AD 97325, August 1956.

5. Hobbs, N. P., The Transient Downwash Resulting from the Encounter of an Airfoil with a Moving Gust Field, Journal of the Aeronautical Sciences, Vol. 24, No. 10, pp. 731-740, 754, October 1957.

6. Bisplinghoff, R. L., and Witmer, E. A., Blast Loading of Aircraft Structures, Sixth Anglo-American Aeronautical Conference, Folkestone, England, September 10, 1957.

7. Ruetenik, J. R., Blast Loading of Airfoils at Subsonic and Transonic Speeds, in preparation.

8. Witmer, E. A., Studies of Transient Air Forces on Two-Dimensional Airfoils, AFSWC First Shock Tube Symposium, February 1957.

9. Ruetenik, J. R., Development of the Shock Tube Facility for Airfoil Studies, AFSWC First Shock Tube Symposium, February 1957.

10. Ruetenik, J. R., Development of a Miniature Pressure Transducer for Application to Airfoil Studies in the Shock Tube, M.I.T., WADC TR 58-629, AD 206259, December 1958.

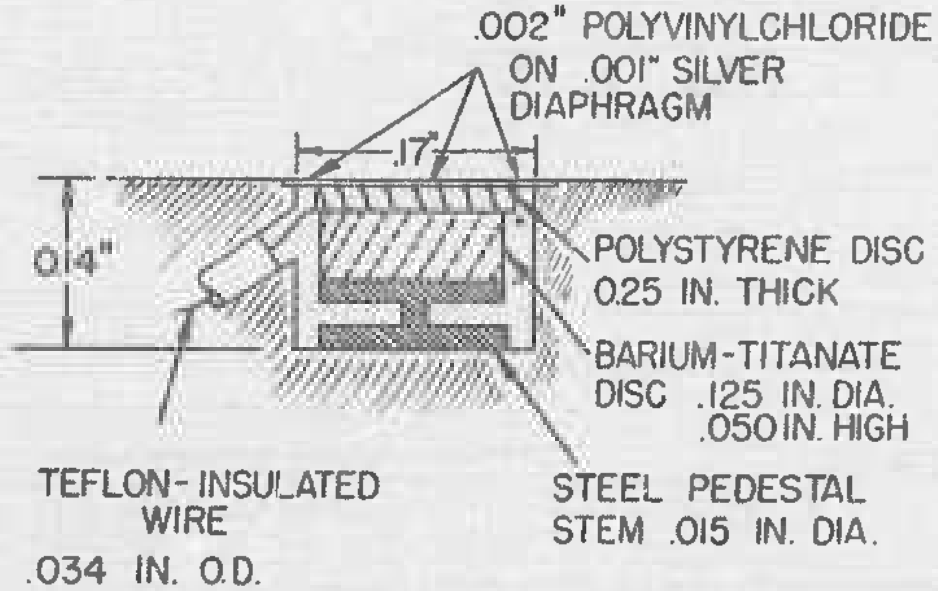

Figure 1 Sketch of Miniature Pressure Transducer

AIRFOIL STRAIN

ISOLATION METHOD

(a) BENDING AND/OR ELONGATION OF AIRFOIL AT BASE OF TRANSDUCER

AIRFOIL ACCELERATION

COMPENSATION METHOD

(b) ACCELERATION OF AIRFOIL

Figure 2 Methods of Correcting for Airfoil Straining and Acceleration

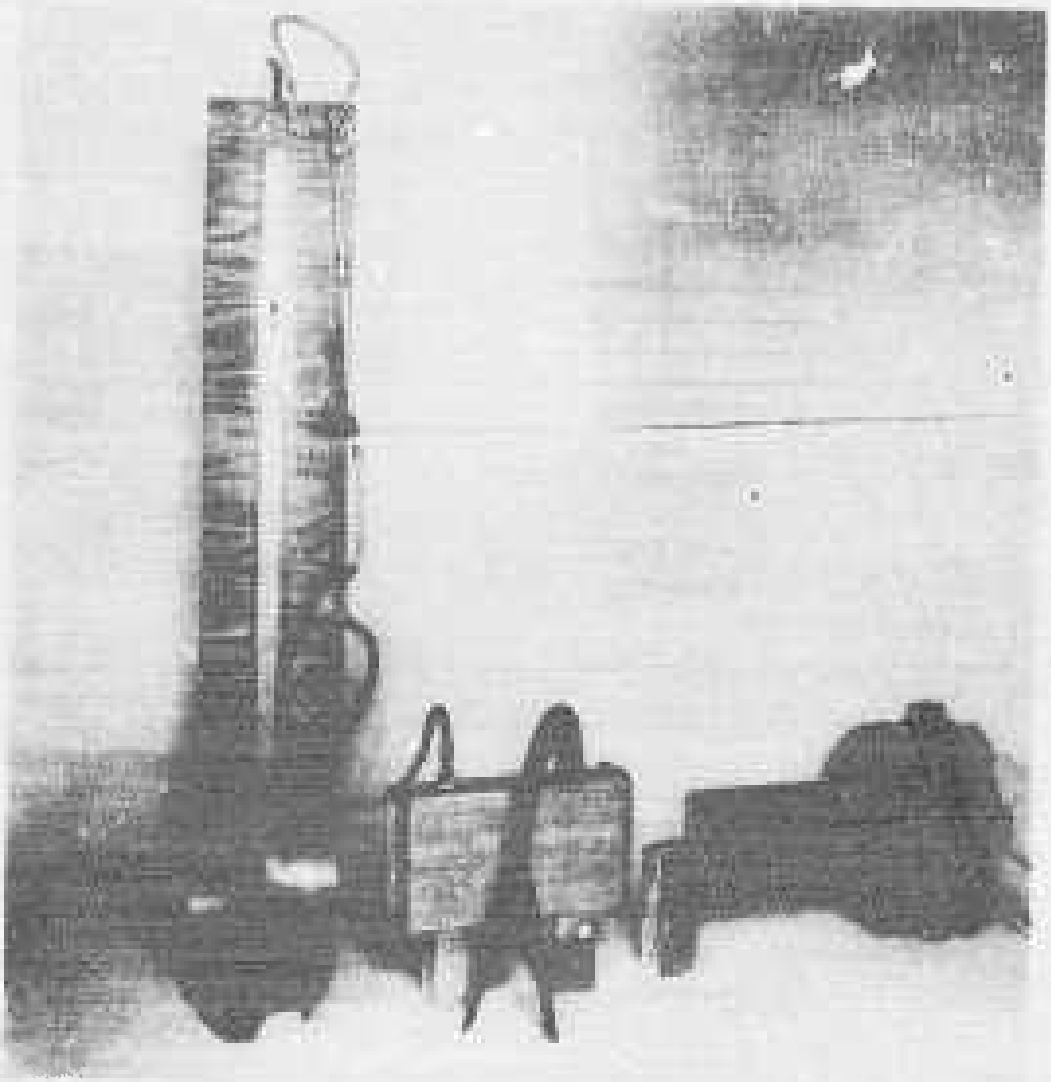

Figure 3 Photograph of Reverse-Dead-Weight Tester

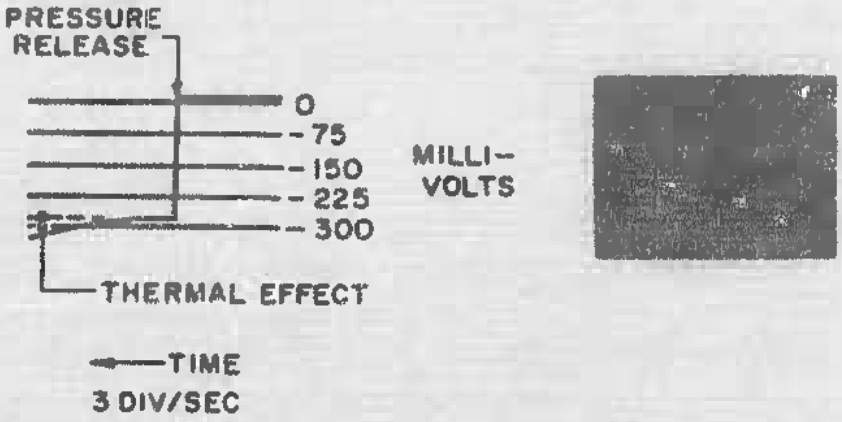

(a) PNEUMATIC CALIBRATION

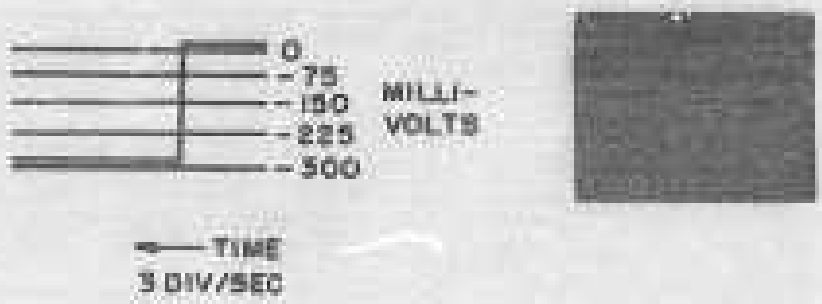

(b) HYDRAULIC CALIBRATION

Figure 4 Oscillograms of Transducer Calibration by Reverse-Dead-Weight Tester

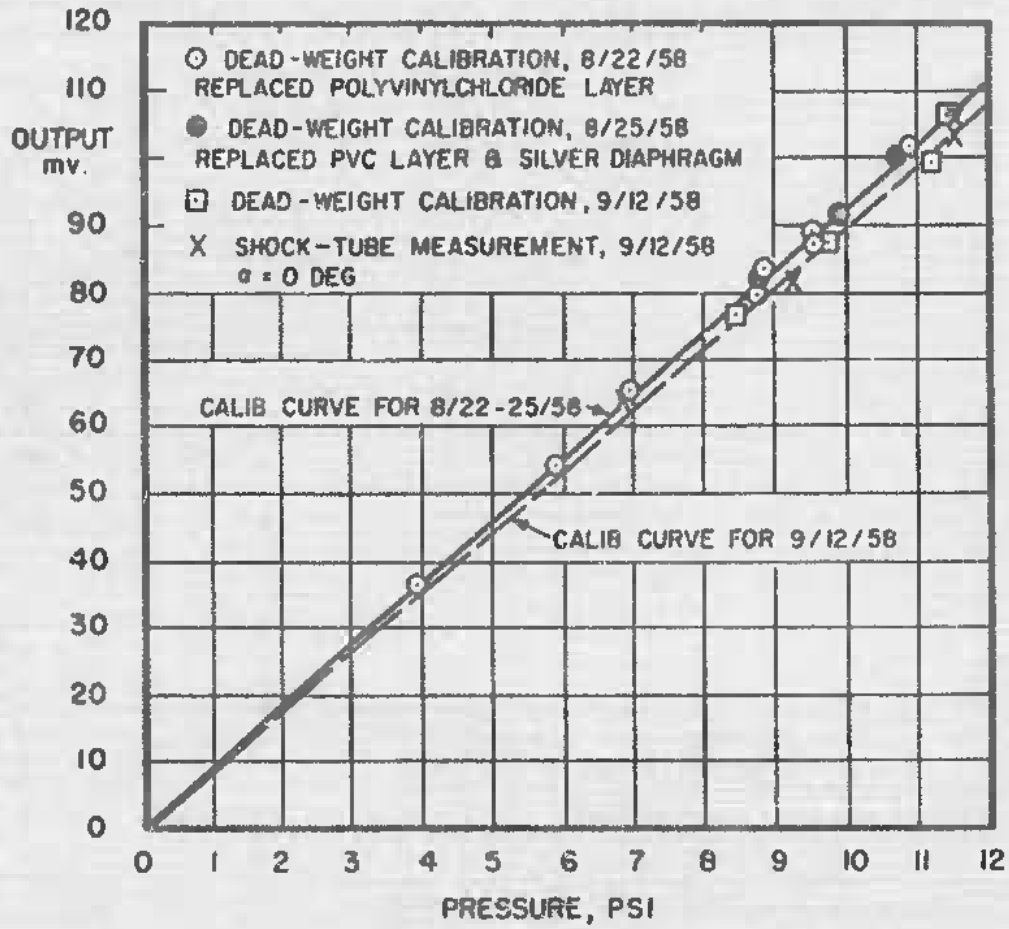

Figure 5 Calibration of Pressure Transducer

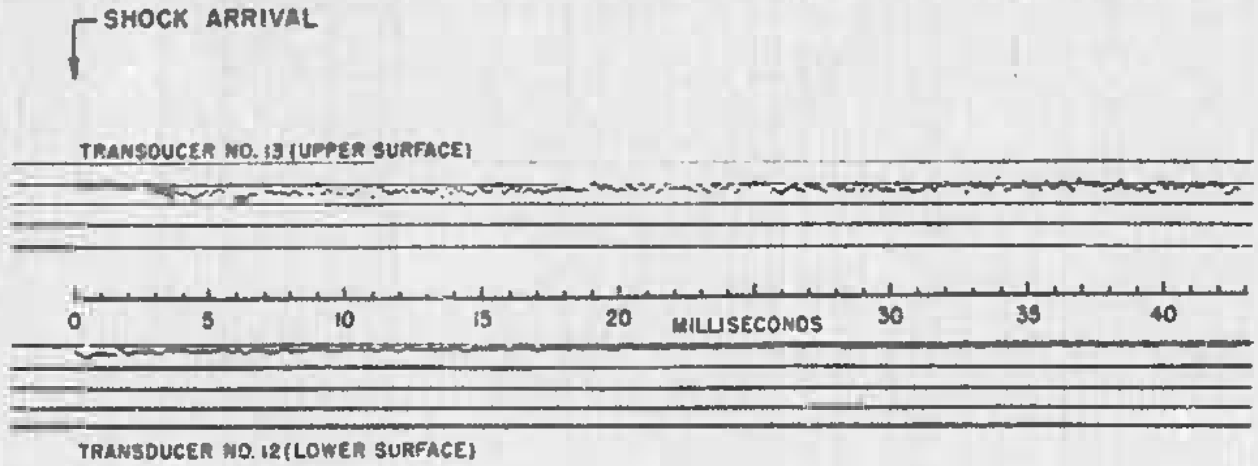

$M_2 = 0.4$

$p_2 - p_1 = 12.0$ PSI

RUN 129.8

Figure 6 Shock-Wave Pressure Records of Transducers No. 12 and 13
$\alpha = 8.3$ deg

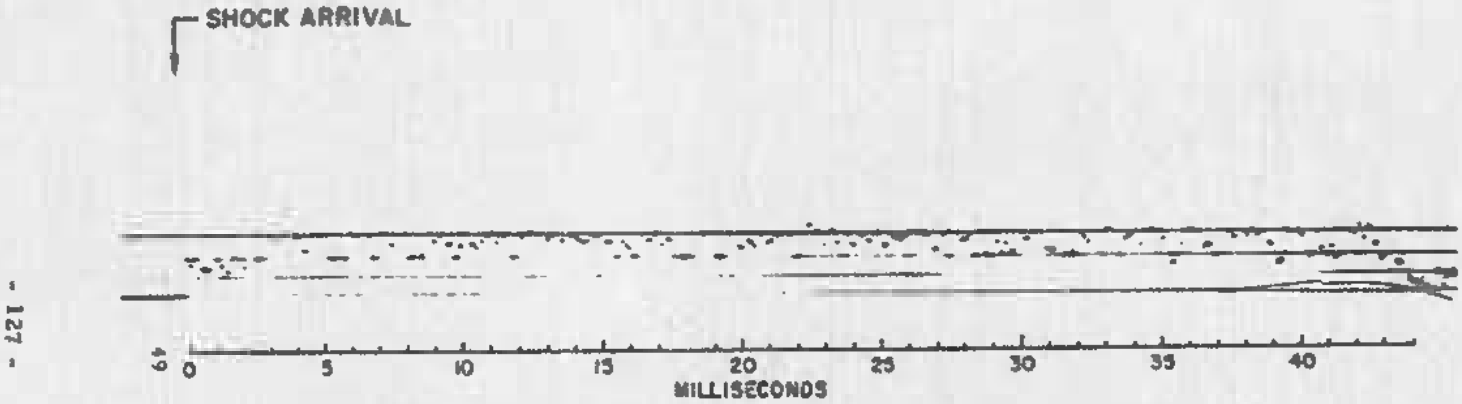

$M_2 = 0.4$

$p_2 - p_1 = 12.0$ PSI

RUN 129.5

Figure 7 Shock-Wave Record of Differential Pressure Measurement, Transducer No. 12 Minus No. 13, $\alpha = 8.3$ deg

THE APPLICATION OF PRESSURE AND FORCE TRANSDUCERS IN SHOCK TUNNEL AERODYNAMIC STUDIES

C. J. Harris and E. M. Kaegi
General Electric
Missile and Ordnance Systems Department

SUMMARY

Dynamic operating conditions and test section flow properties in a shock tunnel have imposed stringent performance specifications on the pressure and force instrumentation required for important ranges of tunnel operation. Available pressure sensing transducers and circuitry have been evaluated for application to shock tunnel facility and model measurements. Pressure and axial force measuring systems have been developed and techniques applied for accurately calibrating and using these systems.

NOMENCLATURE

SYMBOLS

A	Electronic Adder unit
C	Electronic constant coefficient unit
CV	Constant volume
D	Axial force
DIV	Electronic divider unit
L	Length of cavity-bleed hole
M	Flow Mach number
P, p	Pressure
R	Model cylinder or base radius
RC	Resistance X capacitance
Re	Reynolds number
S	Distance along model surface measured from the model stagnation point
T	Temperature
V	Volume of pressure gage cavity

f	Frequency
n	Ratio of base pressure to free stream pressure
r	Model nose radius
μ	micro (10^{-6})
ΔP_s	Change in model stagnation pressure
ΔP_M	Change in model surface pressure, other than at the stagnation point
ΔP	$P_2 - P_1$

SUBSCRIPTS

1	Driven tube initial conditions
2	Region behind the incident shock
3	Region behind the contact zone
5	Reflected region
c	Cylindrical portion of a blunt model
i	Initial conditions in the test section
m, ∞	Test section free stream
s	Model stagnation point

INTRODUCTION

To improve continuously on knowledge in the relatively new aerodynamic problem areas associated with hypersonic flight and atmospheric re-entry, several experimental laboratory tools have, in recent years, been developed and extended beyond their earlier capabilities. For example, the shock tube has proven to be a useful device for some types of re-entry testing, since it can provide high energy, low Mach number, quasi-steady flows for periods of time during which useful model data can be obtained. Another Laboratory facility - the shock tunnel - provides test flows that more closely simulate true flight environments than does the shock tube for many flight regimes. A 6-inch shock tunnel has been under development and operation for three years in the General Electric Missile and Space Vehicle Department and has been shown to be a satisfactory device for the study of many of the hypervelocity aerodynamic problems of current interest. (1) (2)*

Utilization of the shock tunnel and its application to hypersonic aerodynamic testing have required the solution of several instrumentation problems peculiar to this facility. The flow or testing interval in the MSVD shock tunnel is 1 to 6 milliseconds in duration depending upon the test configuration and conditions. During the test interval, equilibrium air temperatures as high as 5000 °K have been obtained at the stagnation point of a blunt model located in the expanded nozzle flow, and higher values are feasible.

This paper reports on recent work carried out in adapting fast response pressure and force instrumentation to aerodynamic model testing in the shock tunnel test flow environment. This includes measurements of model surface pressure, model axial force, and model lift and pitching moment. Heat transfer instrumentation problems and their solutions have been discussed previously. (2)

Attention is given also to pressure instrumentation required for the monitoring of such pertinent facility parameters as combustion driver pressure history, driven tube shock wave velocity and driven tube pressure histories. Accurate measurements of these parameters are required to determine the free stream test section flow properties reliably during shock tunnel model studies.

For the applications mentioned, it has been convenient to employ available transducers and circuitry in various combinations, paying particular attention both to the over-all measuring accuracy of the system and its frequency response and to the temperature characteristics, pressure sensitivity, loading and damping characteristics, physical dimensions, and dynamic calibration repeatibility of each transducer. These items are discussed where appropriate throughout the paper.

The paper is divided into four sections. The first describes the wide ranges of conditions encountered in shock tunnel testing and the pressure instrumentation techniques that have been developed to monitor the facility

---

*Numbers in parenthesis refer to references listed at the end of the paper.

parameters of interest. Section two is a description of the techniques used for the measurement of model surface pressures in the tunnel. In the third, calibration techniques for pressure measuring systems are discussed and evaluated. Section four is a summary of the force and moment measurement techniques that are now being used and developed.

FACILITY PRESSURE INSTRUMENTATION

The driver tube pressures are usually produced by the combustion of a mixture of 70% helium, 20% hydrogen, and 10% oxygen (mole percentages). Other mixtures have been used. In driver combustion studies conducted both at MSVD and at the G. E. Research Laboratory [3], it has been found that the 70% helium and mixture has a characteristic rise-time to peak pressure of between 10 and 20 milliseconds.

The strength of the normal shock wave in the driven section and, therefore, predictable shock tunnel operation is achieved when the combustion process is efficient and diaphragm rupture occurs close to or during peak combustion pressure. For satisfactory diaphragm rupture - no free pieces - it is also desirable to have the diaphragm break near the peak pressure value. The efficiency of the combustion process can be determined from combustion pressure-time history obtained both during constant volume conditions and during diaphragm rupture. The transducer required to monitor the changes in the driver environment during combustion must be capable of accurately detecting pressure changes from 500 to 10,000 psia, have a frequency response of 1000 cps (at least five times the highest frequency to be measured), be relatively temperature insensitive during the pressure recording interval, and be mechanically capable of withstanding erosion due to the products of combustion.

A transducer which to a large degree meets these specifications is a commercially available quartz crystal pressure gage. Figure 1 shows one of these transducers before and after use in the shock tunnel driver. Because of its rugged construction, it has been continuously used in 200 combustion driver tests without appreciable mechanical deterioration or change in its calibration constant. Without a high pressure adaptor, this gage is capable of measuring pressure changes to about 3000 psi. With a special adaptor, its range may be extended to 30,000 psi. Values as high as 12,000 psi have been measured with this gage.

The pressure pickup system using this gage is shown in Figure 2. The transducer is used in conjunction with a special low noise pickup cable and a piezocalibrator box. The piezocalibrator contains an electrometer tube circuit with an input impedance of 10^{14} ohms which matches the transducer output impedance. The quartz transducer is constructed with a composite membrane face which prevents the introduction of spurious pressure signals due to thermal and mechanical strains which may occur in the transducer housing. Further, no organic material is used inside the transducer so that it withstands high temperature satisfactorily.

High impedance transducer circuits of the type described operate readily in a shock tunnel facility. In a facility in which radiated electromagnetic fields cause electrical interference, the use of such high impedance instrumentation [4], [5] is not feasible.

The piezocalibrator box provides output signals compatible with oscilloscope or recorder pre-amplifier input circuits. A selector switch changes the input capacitance of the piezocalibrator in such a manner as to permit a fixed output voltage for different magnitudes of input electrostatic charge. The calibrator provides pulses of known voltage amplitude at its output. The magnitude of these pulses is controlled by a dial calibrated directly in psi. However, it is necessary to perform a calibration on each transducer and piezocalibrator as a set in order to obtain an accurate applied-pressure-change to dial-setting relationship. The calibration is carried out with the ammeter on the piezocalibrator set accurately at 1.00 milliampere. This is necessary since the voltage gain of this calibrator can vary from 0.96 to 0.23 as a function of calibrator voltage. [6] The quartz transducer may be calibrated statically and/or dynamically. The calibration methods are discussed in more detail in a later section.

To monitor the history of the combustion driver pressure, quartz transducers are flush mounted in 14mm tapped holes located along the 20-foot driver of the 6-inch shock tunnel. This driver, which is 8-inch in diameter, is shown in Figure 3 with the pressure instrumentation and spark plugs in position. The pressure transducer is sealed in position by means of a commercial spark plug gasket. Typical pressure-time histories obtained with this measuring system are shown in Figure 4. Shown here are a constant volume combustion record for a maximum pressure change of 2000 psia, and a typical 6-inch shock tunnel driver combustion record with a rupturing diaphragm. Other pressure-time histories shown were obtained in the 3-inch diameter driver of the 2-inch shock tunnel. This facility has been used in support of the larger tunnel program. The pressure change shown here is 4500 psia and the high pressure adaptor was applied. Also shown is the third of three successive constant volume combustion tests conducted using the same adaptor. It indicates that care must be taken in using the quartz transducer with its high pressure adaptor. While the transducer shows no ill effects due to the combustion process, the adaptor does tend to corrode quite rapidly and bind after repeated use. Better performance is obtained by removing the spring and fitting a small O-ring into the adaptor to prevent leaks.

Figure 4 also shows a driver pressure-time history which indicates that detonation rather than combustion of the mixture occurred. The peak pressure shown here is off scale and well over 6000 psia. The quartz transducers checked after such an incident are found to still function properly. When detonations are encountered and it has been possible to observe peak pressure values, the ratio of the peak pressure to initial driver load pressure is about fifty.

The shock tunnel may be operated as a shock tube, or with a straight-through nozzle or a reflected nozzle. Figure 5 shows these tunnel configurations. Pressures of the order of magnitude of the driver combustion pressure can be encountered in a portion of the driven tube of the reflected nozzle shock tunnel. The pressure in this portion, the reflected end of the driven tube, is one of several parameters which must be known accurately in order to determine test section flow conditions. The quartz transducers and associated circuitry are readily applicable for pressure monitoring here. The quartz transducer has a natural frequency of 48,000 cps while the piezo-

calibrator at full gain has a flat response up to 4000 cps and 40,000 cps at reduced gain. A piezoamplifier is available for use with the quartz transducer and this unit has a frequency response to 150,000 cps and a voltage gain of five.

To prevent adverse effects from mechanical vibration, the pressure transducer is placed in a housing and mounted with O-rings in the side wall of the shock tube reflected region. Figure 6 shows pressure records obtained with and without shock mounting. The present program being conducted with the 6-inch shock tunnel has required reflected region pressures of 3000 psia or less. The present shock tunnel mechanical design limits the reflected region pressure values to 5000 psia. Typical reflected region pressure-time histories are shown in Figure 7 for P_5 values of approximately 3000 psi and 250 psi. The former condition was obtained at a shock Mach number of 2. With a shock tunnel nozzle area ratio of 190 this gives a test section flow Mach number of 8, a test section Reynolds number of 9.4×10^5 per inch and a model stagnation temperature of 700°K. The latter reflected region pressure was achieved at a straight tube shock Mach number equal to 5. The nozzle area ratio used in this particular test was 22,500 and yielded a test section flow Mach number of approximately 20. Figure 8 gives an indication of the correlation achieved between experimental measurements obtained with the quartz transducer system and theoretical equilibrium air calculations for the reflected region. The parameters chosen are P_5/P_1 vs M_s where P_5 is the reflected region pressure.

The quartz crystal pressure transducer system is also used to monitor incident shock wave velocity. Shock mounted quartz transducers are placed along the side wall of the 112-foot driven tube. The shock wave arrival produces a step function type pressure rise. Pressure changes are of the order of 1 to 300 psia. The piezocalibrator selector switch permits operation of this system over this full range of side wall pressure changes.

The calibrator outputs are fed into three velocity recording systems. These consist of an electronic counter, a rotating drum oscillograph and a raster generator system. The counter and raster system require only a pulse signal upon shock arrival to yield the required shock velocity information. The oscillograph affords a complete pressure-time history at many positions along the driven tube downstream of the diaphragm. These pressure-time histories in addition to yielding shock velocity information also give an indication of how the shock is being formed. A typical oscillograph record obtained using the quartz transducers piezocalibrators is shown in Figure 9. The arrival of the reflected wave is also determined from this record. Shock velocity information obtained with the quartz gage system also affords a means of determining incident shock wave attenuation in the driven tube which can have important effects on model test data. [7]

MODEL PRESSURE INSTRUMENTATION

Measurement of model surface pressure in the 6-inch shock tunnel test section introduces problems not encountered in the previously referenced facility test regimes. Figure 10 indicates the test flow conditions that can be achieved in the G. E. 6-inch shock tunnel. [8] The points shown indicate test flow conditions where actual model studies have been conducted.

The model stagnation point pressure values and cylinder pressure values (based on the Modified Newtonian Prediction) for the given test flow condition is also indicated. Thus, it is seen that model pressure changes from less than 0.001 psia to greater than 100 psia can be obtained and must be accurately measured.

The duration of the useful test flow in the shock tunnel is generally between 1 and 6 milliseconds. Therefore, it is necessary to have pressure instrumentation with short response times (less than 100 μs) and high natural frequencies (above 10,000 cps).

The size of a gage is now an important factor. It is desirable to obtain maximum model surface coverage during one shock tunnel test. The quartz transducers have been successfully applied to the measurement of model surface pressure changes above 0.1 psia. However, the size of this transducer greatly limits the number of test points that can be obtained on a model of practical size. Typical model (Figure 11) diameter and length ranges are four to six inches and three to twelve inches respectively. It was therefore desirable to obtain a smaller transducer which would permit the accurate measurement of pressure changes to as low as 0.001 psia. Several transducers were considered and evaluated and are shown in Figure 12. Transducer A had attractive dimensions and a resonant frequency of 250,000 cps, but proved to be relatively sensitive to temperature changes and has a low voltage sensitivity (1/8 that of the previously discussed quartz transducer). Transducer B has a desirable resonant frequency and voltage output sensitivity. In addition, this transducer is available in an artifically cooled housing and therefore may be used in high temperature applications. However, its size is prohibitive for the conditions of interest. Transducer C, a strain gage type, is being evaluated in the Aerodynamics Laboratory now. The G. E. Research Laboratory has designed a barium titanate transducer (Transducer D) especially for shock tunnel model application. This transducer has been used extensively in the 4-inch shock tunnel at the Research Laboratory. Both C and D have desirable physical dimensions. An additional transducer, being evaluated now because of its small size, has an ammonium dihydrogen phosphate crystal as the active element; it is rated to have a pressure sensitivity ten times that of any other transducer tested at MSVD to date.

Transducer E (Figure 12) has been used successfully to measure model surface pressures changes of as low as 0.006 psia. This gage is composed of cylindrical tubes of either stabilized barium titanate or lead zirconate. The latter material has the better sensitivity stability with respect to temperature. For example, the Curie Point (the temperature at which spontaneous polarization of the piezoelectric crystal occurs) [9] for lead zirconate is above 300°C while it is only 100°C for barium titanate. Shock tunnel test section flow field studies involve high temperatures of a few millisecond duration. The effect of temperature on the pressure transducer response is dependent upon the heat transfer to the model surface during the test interval. [10] In one test regime (0.005 - 0.15 psi) where the barium titanate (Transducer E) is being applied the heat transfer rates are low-of the order of 10 BTU/ft^2-sec. This transducer is constructed so that the pressure sensing element is embedded in an isolating material which provides a good thermal delay. Thus, in shock tunnel testing the piezoelectric response of the transducer is over before the pyro-electric response takes place.

A portion of the thermal isolation system is an epoxy coating over the transducer face. This coating contributes to the damping of the sensitive element and insulates it from heat. The propagation time of the pressure wave through this coating and the sensitive element due to a face-on shock wave is of the order of a microsecond. The transducer is further designed to isolate the sensitive element from acceleration. The design figure of pressure sensitivity to acceleration sensitivity is 300. To reduce acceleration and mechanical vibration effects further, the transducers used in shock tunnel model surface pressure tests are mounted in a firm rubber sleeve (Figure 13). The model sting is isolated from the facility.

The low pressure system using the barium titanate transducers was initially limited to transducer voltage outputs below 100 millivolts by the pre-amplifier system. This pre-amplifier was modified so that the high input impedance barium titanate transducers could be coupled directly into its input circuit without losses in the over-all frequency response of the system. The impedance to ground at the pre-amplifier input was increased from 10 megohms to 120 megohms. The percentage frequency drop-off for a piezoelectric transducer is expressed by

$$\% = 1 - \left[\left(\frac{1}{2\pi f R C}\right)^2 + 1\right]^{-1/2}$$

The pre-amplifier input circuit was further modified so that the one system can be applied over the full model surface pressure range of interest. At extremely low pressure change conditions, oscillations due to model vibrations appear in the pressure record. An electrical narrow-band filter has been applied when necessary to filter out this noise.

The quartz gage model pressure measuring system is similar to that described previously under facility instrumentation techniques.

Examples of model surface pressure data obtained using the pressure systems discussed are shown in Figure 14. The model surface pressure distributions are generally expressed in ratio form with respect to the model stagnation pressure (P_s). Note the improvement in data scatter obtained during the development program. Actual data traces for these gages are shown in Figure 23.

Manual reduction of the model surface pressure data usually involves ratioing stagnation point values and pressure readings from at least three time positions within the test interval. To avoid the time, labor, and inaccuracies encountered in the manual system, an electronic analog technique has been applied, yielding a continuous read-out of the ratio of model surface pressure to stagnation point pressure during the full test interval. The analog system used is shown in Figure 15. The normal pressure model is instrumented to provide up to eight pressure stations per shock tunnel test.

To increase further the sensitivity of the various pressure systems for more accurate measuring in the 0.001 psia pressure change regime, efforts are being made to reduce attenuation of the transducer output signal

which results from excessive cable capacitance. The original cable required between the transducer and the impedance matching device was 30 feet in length. The cable capacitance is presently being reduced by reducing cable length to 6 feet and mounting the impedance matching device in the sting of the model system. Thus, the required electronic circuit will be within the shock tunnel dump tank during flow field tests. This so called sting pack consists of seven piezoamplifiers containing electrometer transistorized circuits. The whole sting pack is shock mounted in rubber within the sting of the model-support system. The sting pack (Figure 16) is 9-inches in diameter, and 15 inches in length.

PRESSURE TRANSDUCER CALIBRATION METHODS

The three previous sections have outlined many of the types of pressure data that must be obtained during the operation of a shock tunnel and described several systems and techniques that have been found to be useful in the different sections of the tunnel. Interest in using these transducer systems has led to the development of calibration techniques that satisfactorily evaluate the systems and predict their performance in the proposed environments.

The quartz transducers may be calibrated statically. This is possible because of: (a) the high leakage resistance obtained by the use of specially treated quartz crystals, (b) the use of special high resistance cable, (c) the very high input impedance of the piezocalibrator. To maintain this high impedance it is necessary to keep the cable connection to the transducer extremely clean.

Shock tube tests have shown that static* and dynamic calibration of each quartz transducer yields somewhat different results (Figure 17). Since shock tunnel model testing involves dynamic pressure changes of short duration, it is best to adopt a calibration technique that closely simulates the actual test environment. The discrepancies noted between static and dynamic calibration of the quartz transducer also have encouraged the adoption of detailed dynamic calibration techniques for all transducers used.

The pressure transducers are dynamically calibrated in a straight shock tube. The calibration is carried out in the Mach 2 to Mach 4 range where experimental normal shock wave results have been found to agree with shock tube theory. [11] [12] The accuracy of shock tube calibration in this regime is determined by the accuracy with which initial tube conditions are known and with which the incident shock Mach number is measured. A McLeod gage is used to determine P_1 to within a fraction of a micron of mercury. An electronic counter is used to determine shock velocity with an accuracy of $\pm$ 1%. The counter triggering system is comparable to the system detailed by Coulter. [13] Transducer voltage outputs for determining the signal strength of the gage systems per psi are displayed and photographed on calibrated oscilloscopes maintained at an accuracy of $\pm$ 0.2%.

*The calibration technique may be considered static when compared to shock tube calibration. The particular technique involved a pressure bomb and a quick opening valve.

Calibration of the transducer is carried out with the transducer located both along the side wall of a 2-inch round shock tube (Figure 18) and at the end of a 13-inch sting protruding along the axis of the tube from the rear end plate. Calibration in these two positions reasonably well simulates the test environment encountered during model testing in the expanded shock tunnel nozzle flow. Environmental conditions in the driver tube can be simulated (pressure and temperature values) in the reflected region of the shock tube. Along the side wall of the driven tube, as in the reflected region, the transducers are mounted in a hevi-met housing (Figure 19) which is shock mounted in the tube wall. The gage is also in a cavity. The effect of the cavity is to reduce the initial crystal loading rate in comparison to that of a flush mounted gage and this is believed to be responsible for the elimination of the erratic transducer performance experienced early in the development program.

This recessed hole also tends to protect the transducer from particle damage which is sometimes experienced after the useful portion of the tunnel test run.

The use of shock mounting in a cavity and a transducer with a high fundamental frequency reduces the problem of transducer ringing. This is inherent in low resonant frequency transducers where higher frequency components in the measured pressure change phenomena can excite the low resonant frequency of the transducer. When this happens the transducer rings and obscures basic pressure information. A transducer with at least a 30,000 cps resonant frequency is rated to give linear response up to 6,000 cps and is safe from excitation by higher harmonics in a relatively low frequency transient phenomena.

The comparison of transducer response with and without a cavity is shown in Figure 20. The improvement in calibration repeatibility due to applying the cavity technique is shown in Figure 17. The cavity used in calibration is designed to match the cavity incorporated into the pressure models used in tunnel testing. This cavity introduces a time delay in the pressure measuring system. The geometry of the cavity controls the duration of the time delay experienced. [14] It was observed that the general shape of the pressure-time history obtained using a cavity was quite similar to the shape of the voltage-time history obtained in a RC electrical circuit. An analogy between the two was constructed (Figure 21). Barium titanate pressure transducers were placed in cavities of accurately known geometry and pressure response curves were obtained during shock tube testing. Assuming the bleed hole to a resistance (with a slight capacitance to ground) and the cavity to be a capacitance, characteristic RC times were obtained. The analogous RC time occurs at 63% of the total voltage change, and 99% of the applied voltage change is achieved in five RC time increments. Therefore, for the cavity geometries plotted, a time delay of from 200 to 1000 microseconds may be expected. Based on these results, cavities used in pressure models are geometrically designed to yield the smaller time delay value $\left(\frac{LV}{A} = 0.1 \text{ to } 0.2\right)$.

The range of pressures required for calibrating transducers for use in model testing can be produced accurately in a shock tube with a pressure-break driver system. Two driver tube techniques are applied in the low pressure range. One involves the use of a scribed-mylar diaphragm and driver gas loads of helium and nitrogen mixtures to achieve diaphragm rupture. Driven tube initial pressures of the order of 100 microns of mercury yield pressure changes ($P_2 - P_1$) of approximately 0.02 psi at shock Mach numbers 4 or less.

A driver system using metallic foil and a plunger[15] to achieve diaphragm rupture yields comparable calibration pressure changes from 0.02 to 0.01 psi, but at normal shock wave strengths of little over Mach 1. Thus, the effect of temperature rise on transducer response may be studied. At these low pressures, mechanical vibrations introduce stability problems into the oscilloscope and counter triggering circuits. The use of the thin diaphragms and a pressure-break driver has helped to minimize this problem.

To achieve accurate calibration of the transducers at pressure changes below 0.02 psi, it is necessary to obtain driven tube initial pressures below ten microns of mercury. The original 2-inch shock tube facility is unable to achieve these driven tube conditions because of its physical volume and vacuum pump capacity, and because of the number of test ports located along the driven tube. A special low pressure calibration shock tube (Figure 22) was constructed to allow low pressure calibration. This is a simple shock tube consisting of only the driven section with four test ports along the side wall for mounting transducers. Cavities are built into the tube initially and the transducers may be mounted as in the pressure models. The tube uses a thin diaphragm and a fixed one-atmosphere driver.

Transducer response over a range of pressure changes are shown in Figure 23, with the calibration curves obtained on four barium titanate transducers in the 0.02 to 0.15 psi range.

The pressure transducers are calibrated as part of a fixed pressure measuring system. The system consists of the transducer, a particular output cable, an impedance matching device and an amplifier when necessary. This system is maintained as a unit during calibration and then applied as a fixed unit in shock tunnel model testing or shock tunnel facility measurements.

AERODYNAMIC FORCE MEASUREMENTS

The piezoelectric axial force balance is shown in Figure 24. The quartz crystal transducer is used as the force sensor because of its rugged construction.[16] A shaft, mounted on metallic flexures, has one end pre-loaded against the metallic face of the transducer. The other end of the shaft provides support for the model. The balance fits within the light-weight models generally used. Also shown in Figure 24 is the force-time history from the balance and the pressure-time history at the model stagnation point. The balance output records show that the application of the fast response quartz transducer yields a fast response force indicator. The low frequency oscillations which appear in the force-time record are due to the resonant frequency of the combined flexure-model mechanical

system. To reduce these oscillations, thin-walled magnesium models are now being used in place of the original aluminum models. The piezoelectric balance as shown, permits the flexures to be interchanged. For a given test condition, a set of flexures may be chosen to yield the desired sensitivity, resonant frequency and mechanical damping characteristics.

The magnitude of axial forces encountered during current shock tunnel testing range from 0.1 to 100 pounds. Experimental axial force data obtained on simple shapes using this balance are shown in Figure 25.

A strain gage balance has been used to obtain axial force measurements over an angle of attack range of 0° to 8°. Bonded strain gages are used. This system may be used at angle of attack by compensating for the initial un-balance in the strain gage bridge circuit. The response of this type of axial force balance is quite satisfactory for shock tunnel testing as shown by Figure 26. Here the force-time history of the strain gage balance and the pressure-time history of a quartz gage at the model stagnation point are compared. The lack of low frequency oscillations on the force-time history oscilloscope trace is due to the fact that the whole balance is potted in a foamy resin material. This technique has worked well in damping out mechanical oscillations using the strain gage system.

Several approaches have been investigated at MSVD and at other laboratories in developing a combined normal force and moment balance for use in shock tunnel aerodynamic testing. The problem is one of obtaining the short response times, which are required due to the short test flow duration with sufficient instrument sensitivity. A novel moment balance has been developed [17] which involves a model suspended in a magnetic field. High speed photography may also be used to study the motion of a model freely suspended in a short duration hypersonic flow field. This system is under development now at the Naval Ordnance Laboratory*. Also Wittlif and Rudinger have described an accelerometer balance that has been developed at the Cornell Aeronautical Laboratory. [18]

Efforts are continuing towards development of a mechanical moment and normal force balance using strain gages or piezoelectric gages as the sensing elements. The problem encountered in applying strain gages is that sensor members having stiffness high enough to respond quickly to the already short duration loading have insufficient sensitivity to yield accurate data. Improved strain gages and strain gage circuitry are presently being studied in an effort to overcome this problem. Other techniques also being studied are the free flight method and an internal strain gage balance system similar to that described by Perry and MacDermott. [5]

CONCLUSIONS

The developed pressure and force measuring system yield accurate experimental measurements in the 6-inch shock tunnel during studies of steady hypersonic aerodynamic problems. These measurements are obtained over ranges of flow conditions which simulate many aspects of hypersonic flight, ballistic missile re-entry, and satellite or glide re-entry situations.

*Seigel, A; private communications

Using available piezoelectric transducers, pressure measuring systems and techniques have been developed which permit the accurate determinations of shock-tunnel-driver tube pressure-time history, shock-tunnel-driven tube dynamic pressure, driven tube shock wave Mach number, and model surface pressure distributions. These dynamic pressure phenomena span a range from 10,000 psia to 0.001 psia. With the exception of the shock tunnel driver combustion process, the events of interest have a duration of 1 to 6 milliseconds and rise times to peak pressure of 1 to 2 microseconds. Relatively high gas temperatures and surface heat transfer rates exist during the test interval.

Static and dynamic calibration of the pressure systems have been evaluated and shock tube dynamic calibration techniques chosen and applied in such a manner as to simulate adequately the different test environments.

An analog computer concept, which has been applied as a pressure data reduction system, provides accurate model pressure data with a minimum of time and effort.

Both strain gages and piezoelectric transducers have been applied in force balance systems to yield accurate axial force measurements in shock tunnel hypersonic aerodynamic testing. Normal force and pitching moment balances, and free flight techniques currently being studied and developed appear feasible for application to shock tunnel testing.

A continuing effort is being maintained to improve these existing systems and to develop new pressure and force systems so as to extend the currently available measuring capabilities to wider ranges of operation.

ACKNOWLEDGEMENTS

The work reported herein represents the combined efforts of numerous persons and groups at the MSVD Aerosciences Laboratory over a time interval extending from June 1956 to the present.

W. R. Warren, H. W. Bousman, M. J. Engel and personnel immediately under their direction contributed extensively.

We wish to acknowledge the assistance of R. S. Robinson and W. Nickels in carrying out pressure and force investigations requiring use of the 2-inch shock tunnel and acknowledge the assistance of Misses B. L. Maguire, E. Miller and M. J. Hartmann in the reduction and tabulation of pertinent experimental 6-inch shock tunnel and 2-inch shock tunnel data.

REFERENCES

1. Warren, W. R., The Design and Performance of the G. E. Six Inch Shock Tunnel Facility; AFSWC Shock Tube Symposium, SWR-TM-57-2; Feb., 1957

2. Kaegi, E. M., Warren, W. R., and Vitale, A. J.; Experimentation with the General Electric Six Inch Shock Tunnel; Advanced Aerodynamics Lab. Tech. Memo #19, G. E., MOSD; April, 1958

3. Nagamatsu, H. T., and Martin, E. D.; Combustion Investigation in the Hypersonic Shock Tunnel Driver, G. E. Research Lab., Chemistry Research Department, Memo Report C-58-59; March 10, 1958

4. Mulkey, M. R., Earheart, Jr. W. T., and McAdams, Jr. E. E.; Pressure Measurement in an Arc-Discharge Wind Tunnel; AEDC-TN-58-16, ASTIA Document No. AD-152048; April, 1958.

5. Perry, R. W., and MacDermott, W. N.; Development of the Spark-Heated, Hypervelocity, Blowdown Tunnel-Hotshot; AEDC-TR-58-6, ASTIA AD-157138; June, 1958

6. Lederer, P. S., and Smith, R. O.; Performance Tests on Two Piezo-electric Quartz Crystal Pressure Transducer and Calibrator; NBS Report 4973; Feb., 1957

7. Rose, P. H., and Nelson, W.; On the Effect of Attenuation on Gas Dynamic Measurements Made in Shock Tubes; AFSWC, Second Shock Tube Symposium SWR-TM-58-3; March, 1958

8. Kaegi, E. M.; Maximum Free Stream Reynolds Number at Hypersonic Velocities in the G. E. 6-Inch Shock Tunnel, Advanced Aerodynamics Lab. TM #52, G. E., MSVD; Oct., 1958

9. Von Hippel, A. R.; Dielectric Materials and Applications, The Technology Press of M. I. T. and John Wiley & Sons, Inc.

10. Lees, L.; Laminar Heat Transfer over Blunt Nosed Bodies at Hypersonic Flight Speeds; ARS, Vol. 26, No. 4; April, 1956

11. Bleakney, W., Weimer, D. K., Fletcher, C. H.; The Shock Tube: A Facility for Investigations in Fluid Dynamics; The Review of Scientific Instruments; Nov., 1949

12 Lukasiewicz, J.; Shock Tube Theory and Application; National Aero. Estab. Canada, Report 15; 1952

13 Coulter, G. A.; Problems in the use of Piezo-Gages for Shock Tube Instrumentation; AFSWC Second Shock Tube Symposium, SWR-TM-58-3; March, 1958

14. Clark, R., Pressure-Time History in a Chamber Subjected to Shock Wave Filling Through an Orifice, AFSWC, Second Shock Tube Symposium, SWR-TM-58-3

15. Geiger, R. E., Proposed Investigation of Non-Equilibrium Effects in High Stagnation Enthalpy Flows Expanded to Low Density; Advanced Aerodynamics Lab. TM #75; G. E., MSVD; Feb., 1959

16. Harris, C. J., and Kaegi, E. M., Advanced Aerodynamic Testing with the G. E. 6-Inch Shock Tunnel, Advanced Aerodynamics Lab. TM #53, G. E., MSVD; Oct. 22, 1958

17. Tournier, M., and Laurenceau, P., Magnetic Suspension of a Model in a Wind Tunnel; "LaRecherche Aeronautique", De L'Office National D' Etudes Et De Recherches Aeronautiques, July-Aug., 1957

18. Wittliff, C. E., and Rudinger, G., Summary of Instrumentation Development and Aerodynamic Research in a Hypersonic Shock Tunnel; WADC TR 58-401; August, 1958

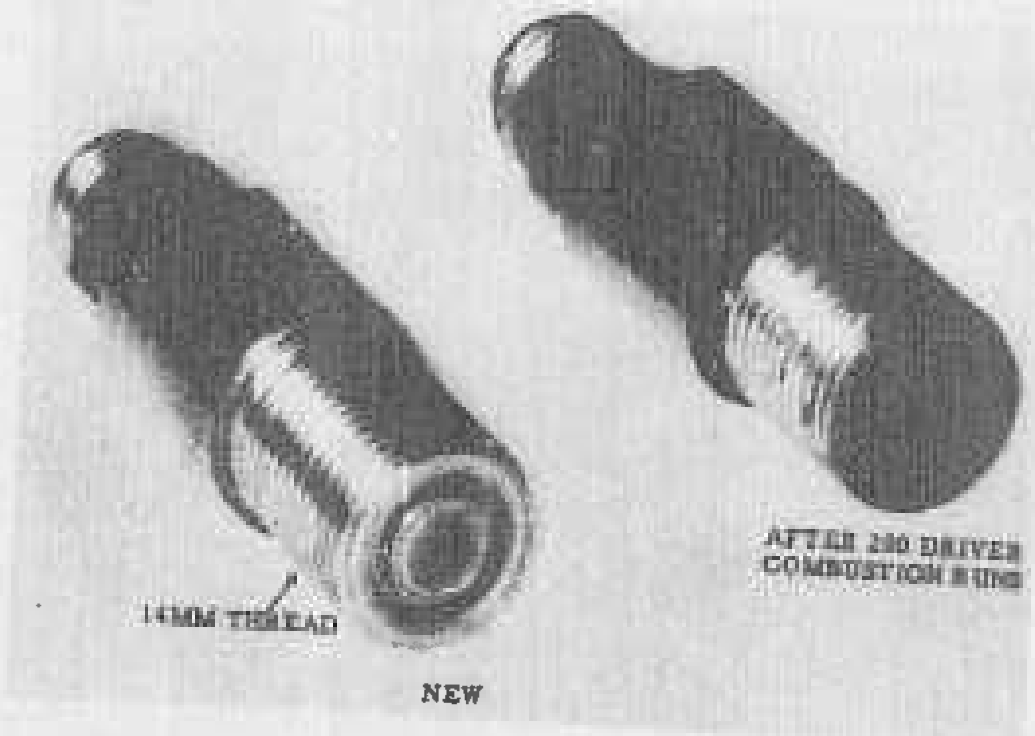

Figure 1 Quartz Pressure Transducer

Figure 2 Quartz Pressure System

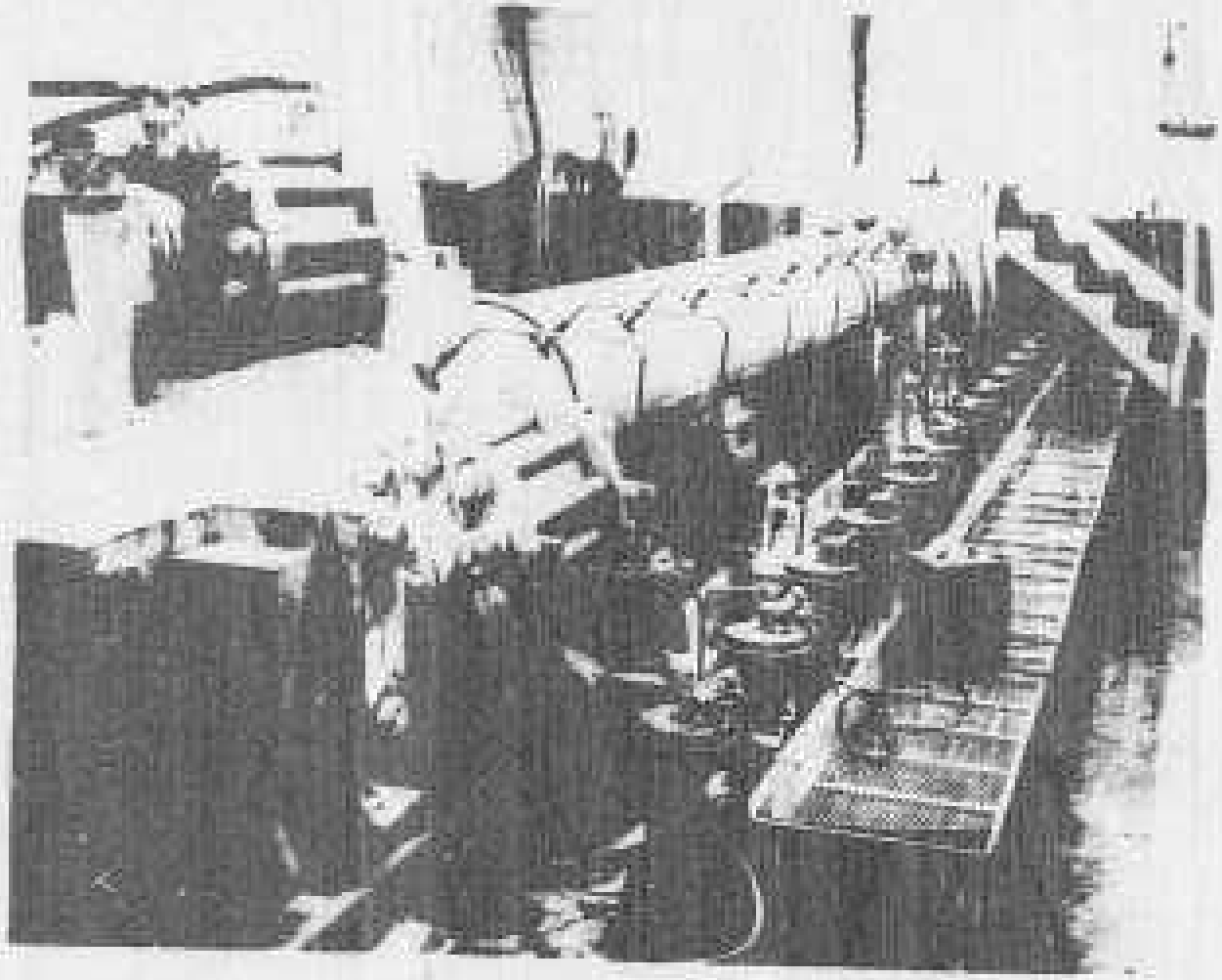

Figure 3 6-Inch Shock Tunnel Driver and Pressure Instrumentation

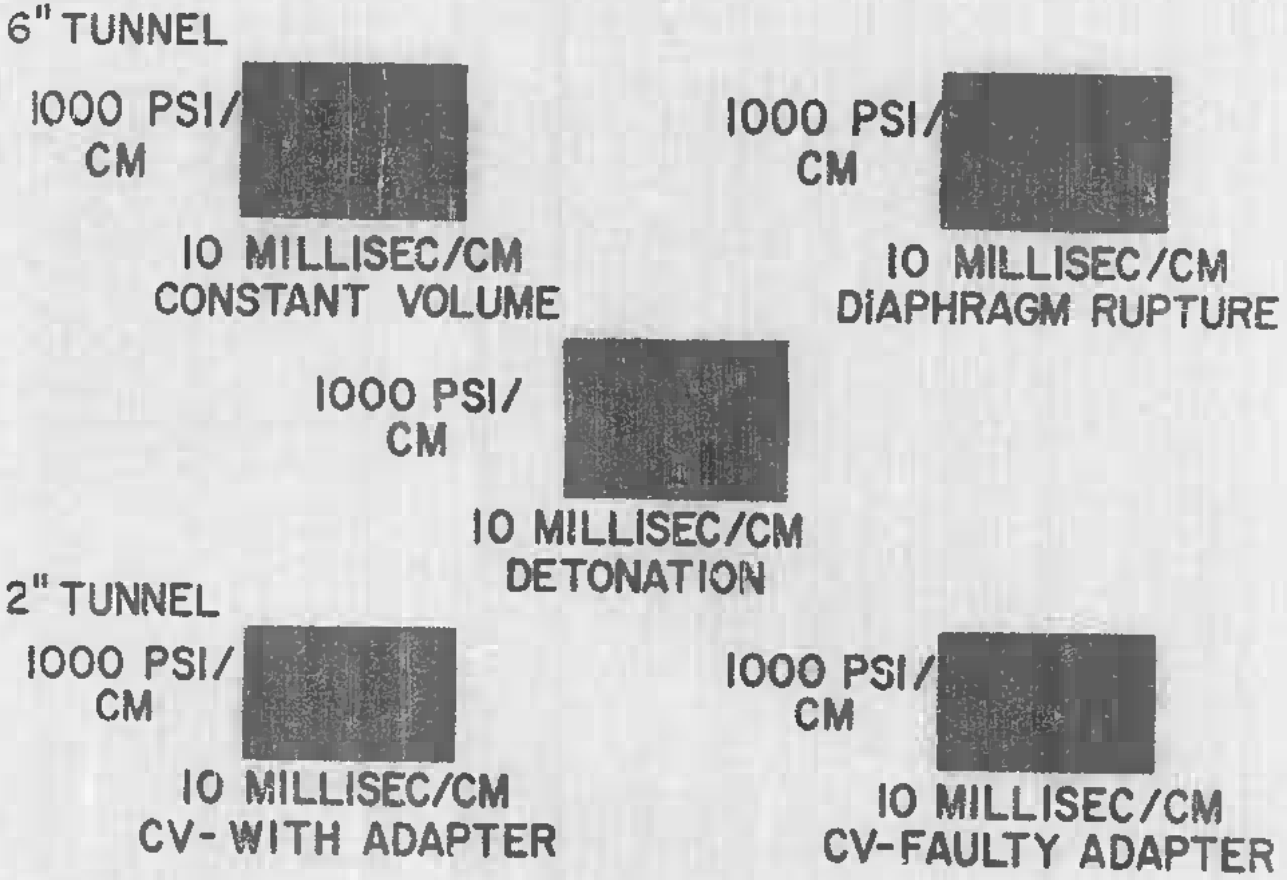

Figure 4 Shock Tunnel Driver Tube Pressure-Time History

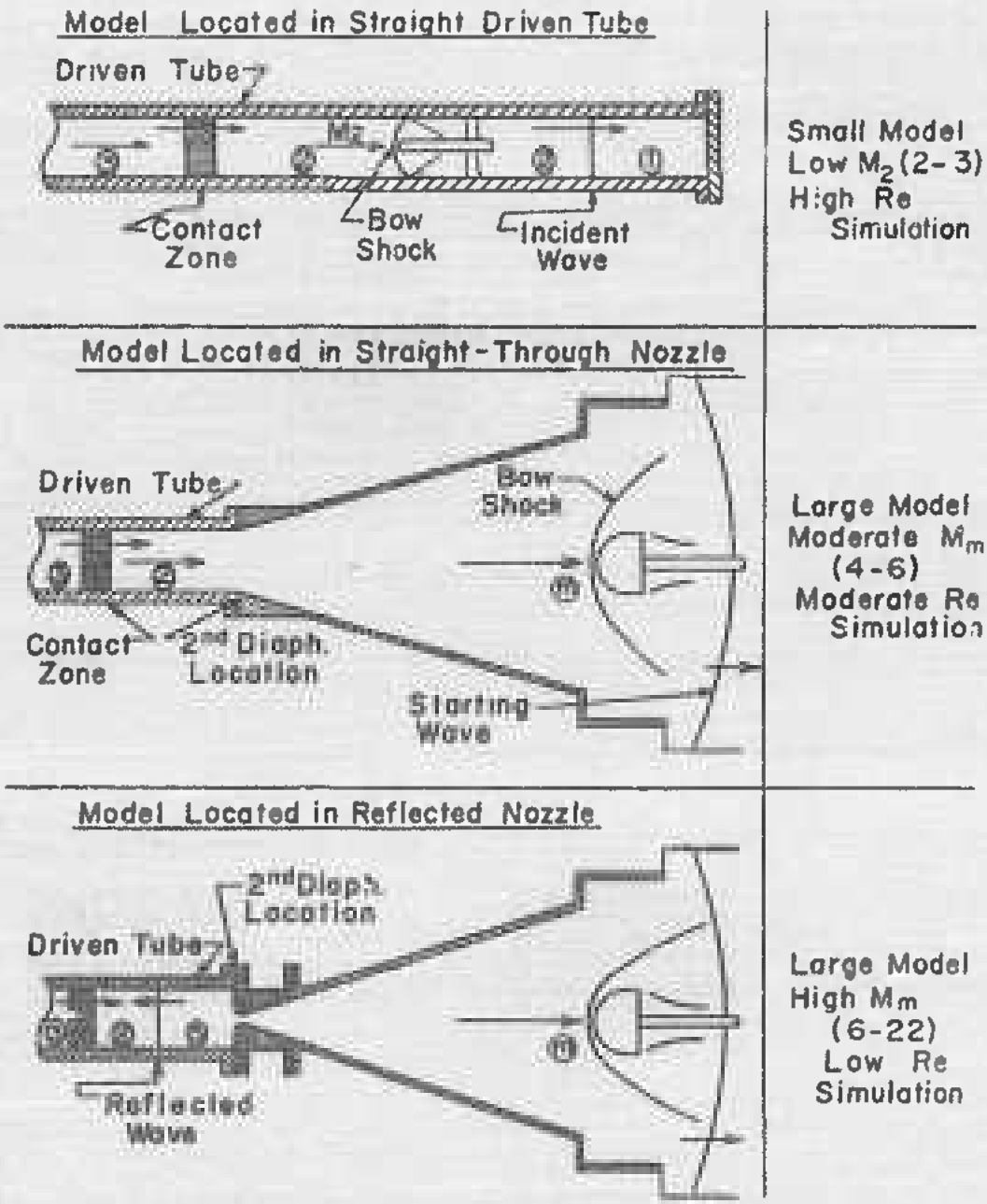

Figure 5 Regions Available for Aerodynamic Experimentation

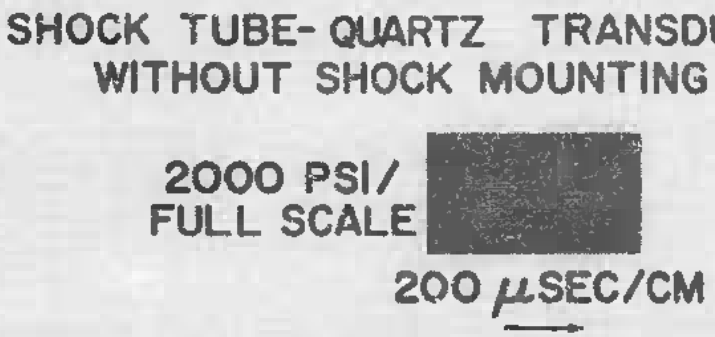

Figure 6 Reflected Region Pressure-Time Histories

Figure 7 Shock Tunnel-Quartz Transducer-Shock Mounted

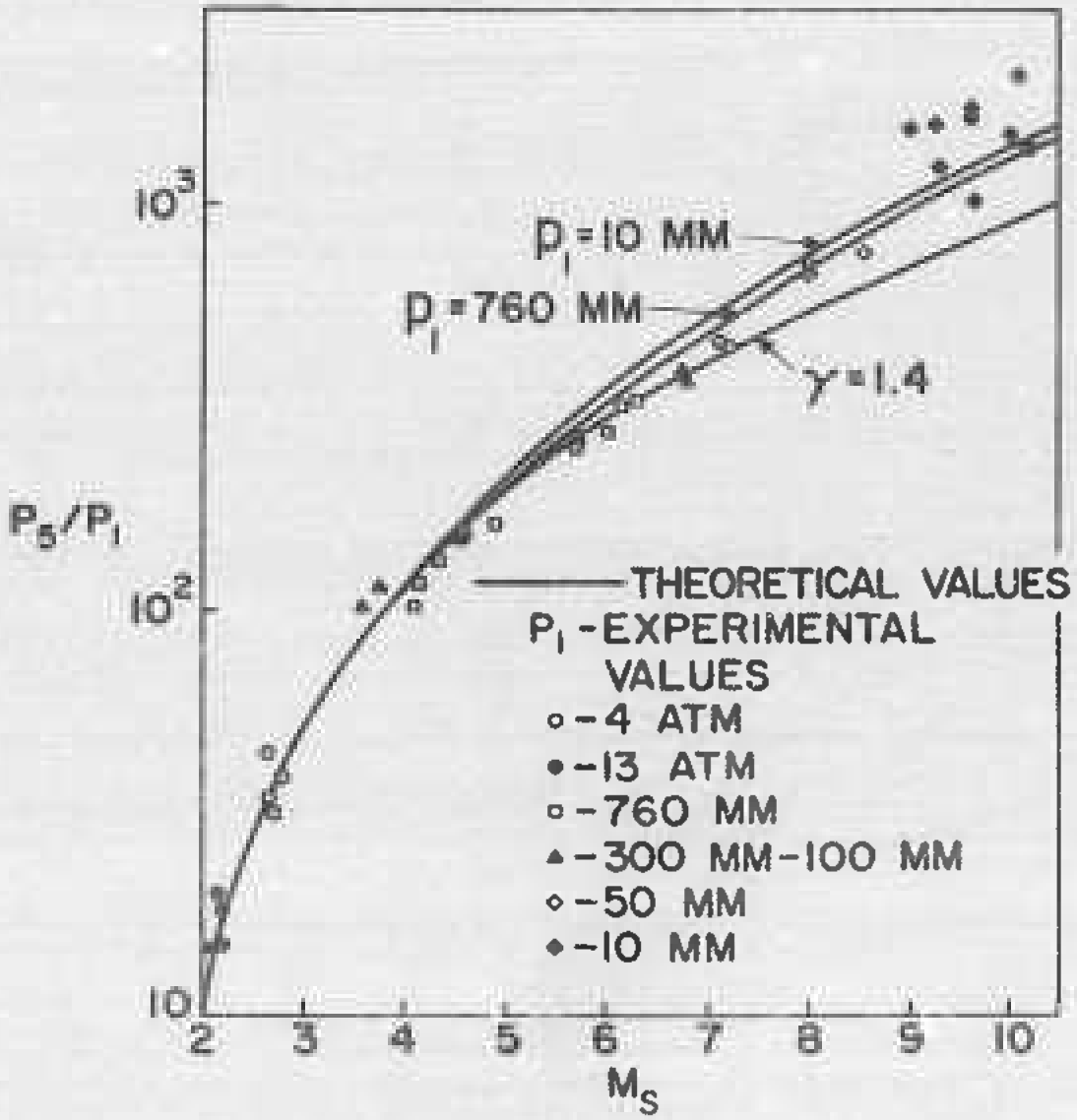

Figure 8 Reflected Region Pressure Ratio, P_5/P_1 Versus Shock Mach Number, M_s (6-Inch Shock Tunnel Experimental Values Versus Theoretical Values (T_1 = 530°R)

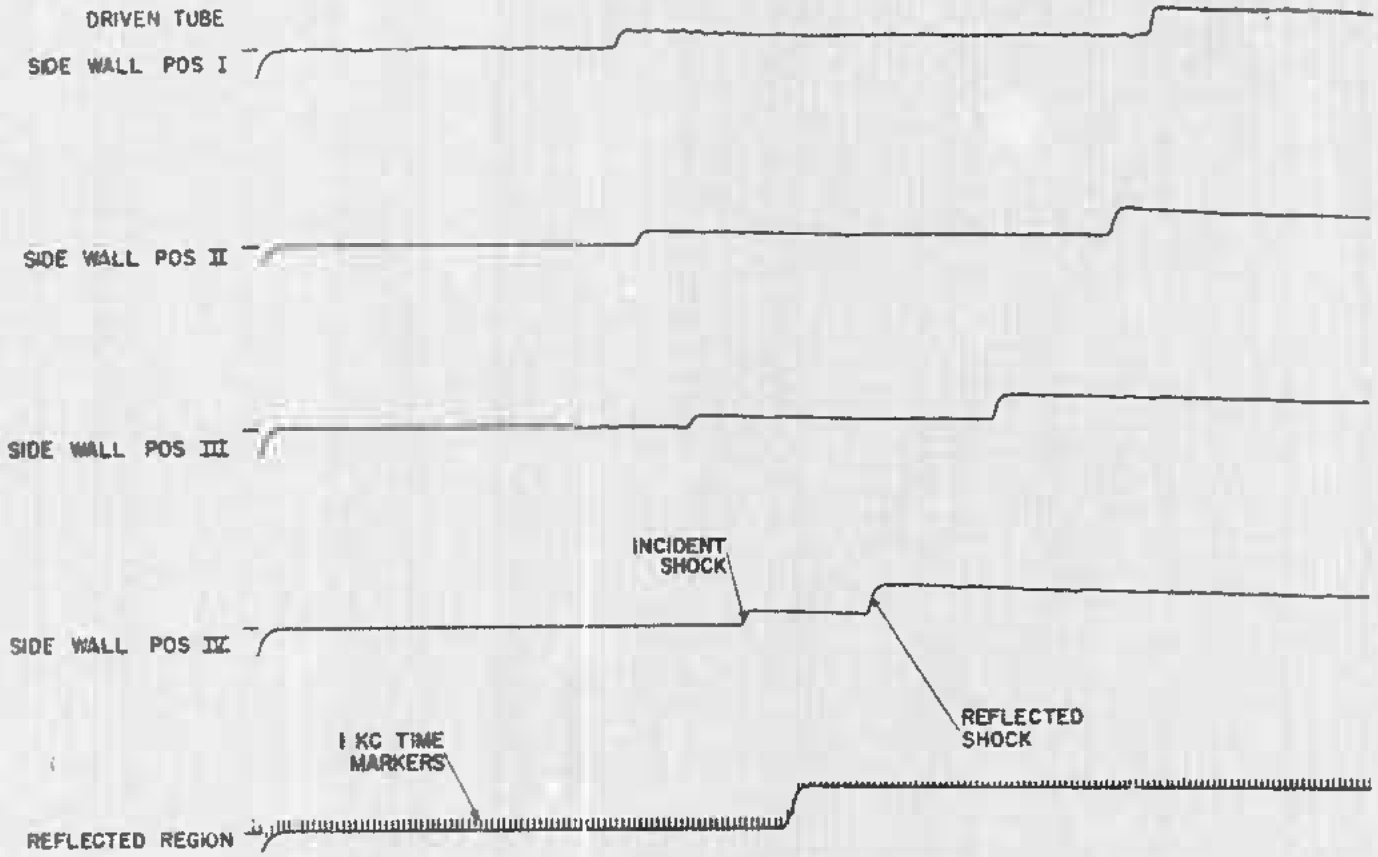

Figure 9 Shock Tunnel-Normal Shock Wave-Oscillograph Record

FREE STREAM RE/INCH

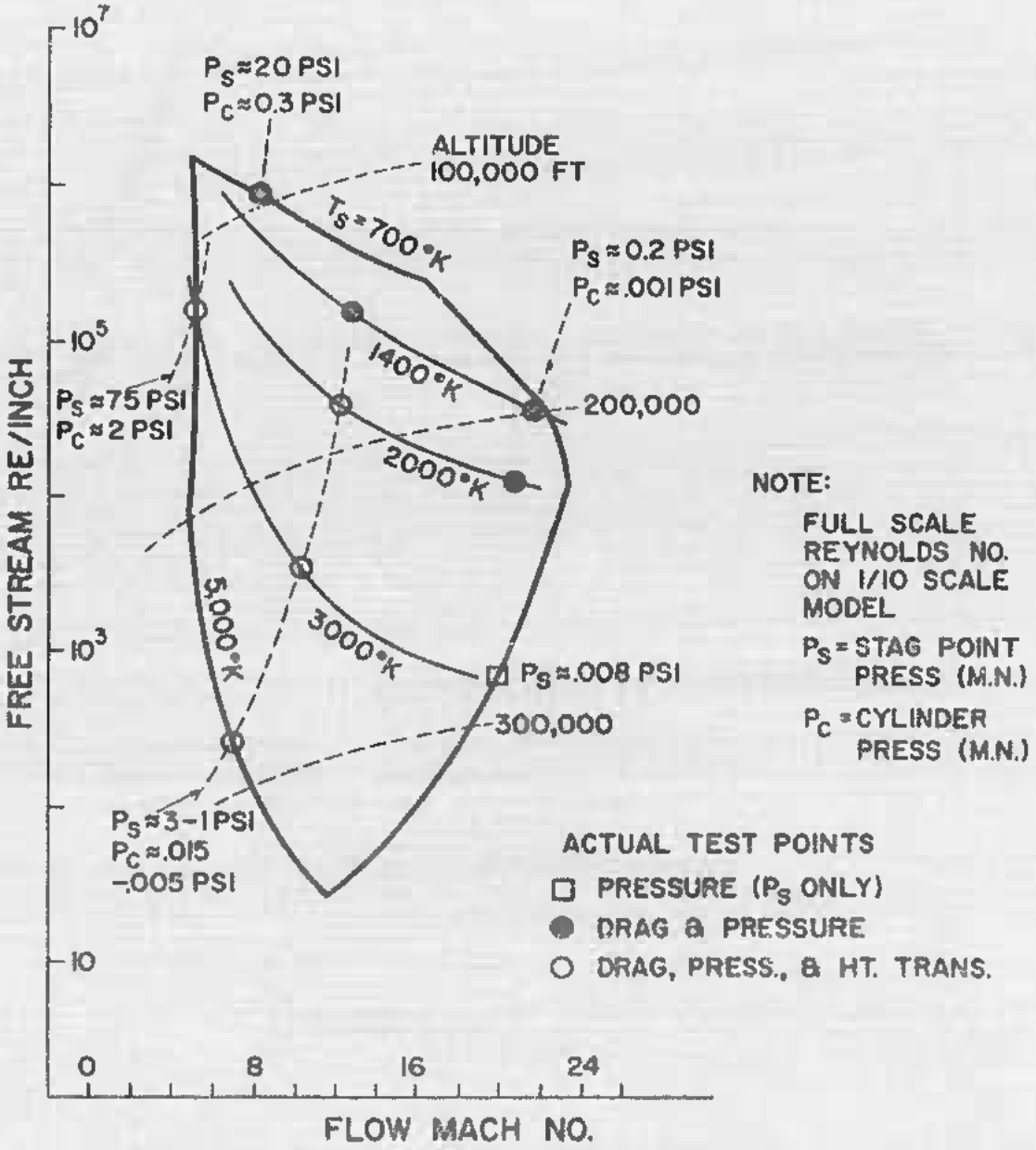

Fig re 10 Range of Test Flow Conditions for G. E. 6-Inch Shock Tunnel

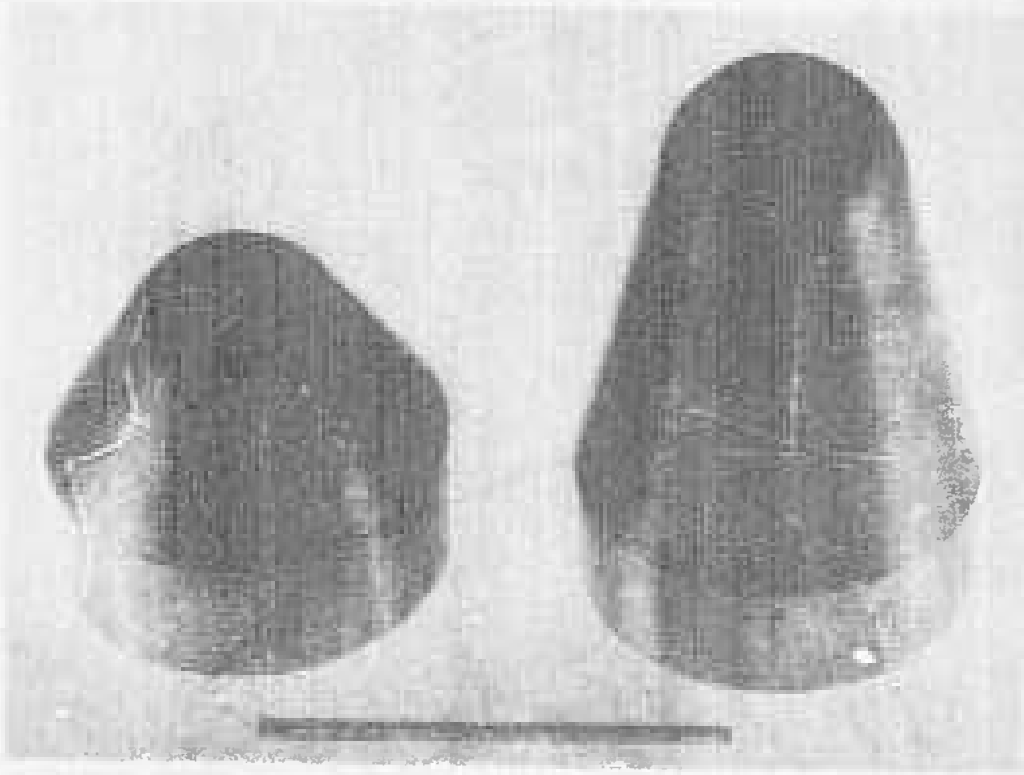

50° Blunt Cone

25° Blunt

Figure 11 Typical 6-Inch Shock Tunnel Pressure Models

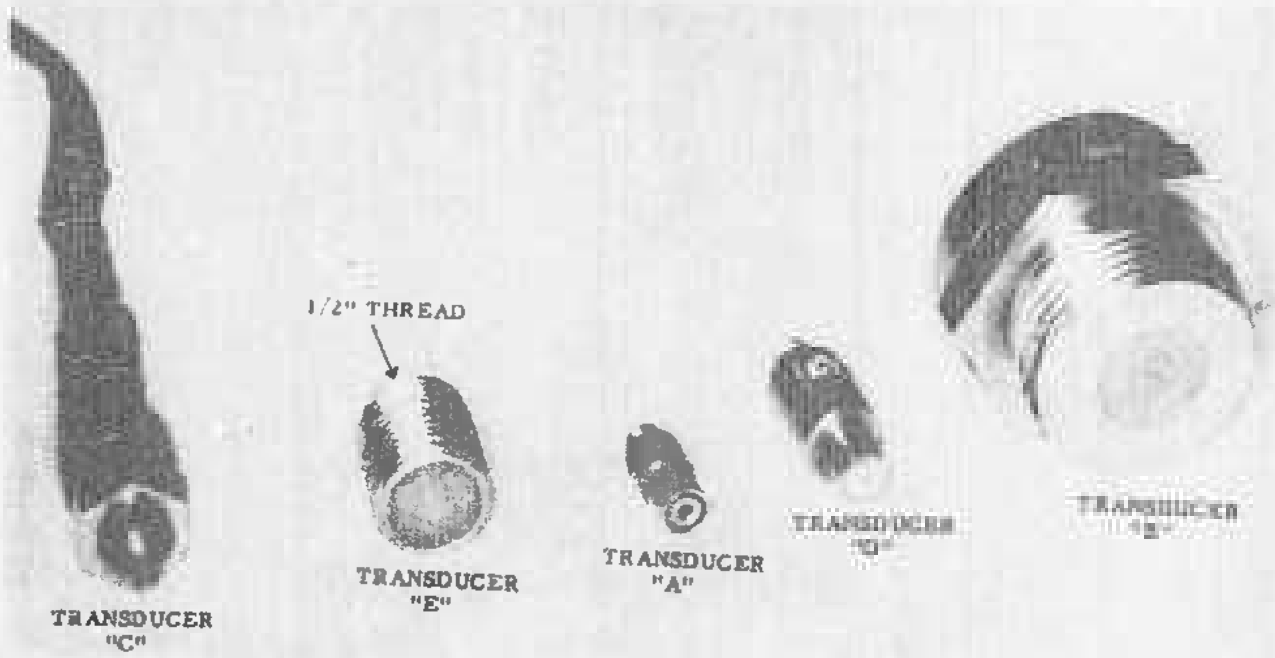

Figure 12 Pressure Transducers

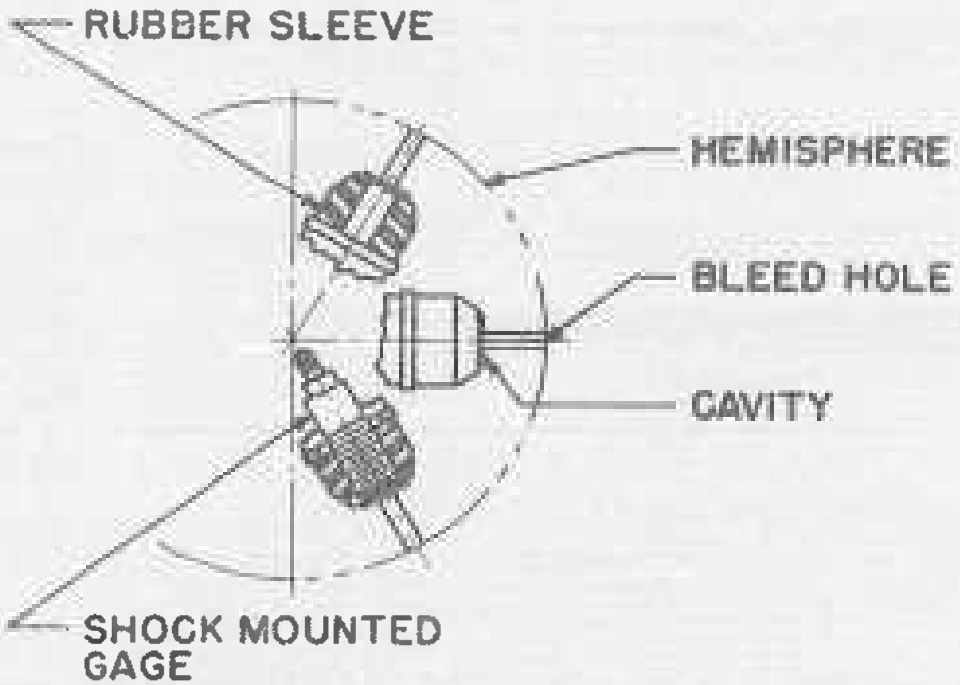

Figure 13 Model Mounting of Surface Pressure Transducers

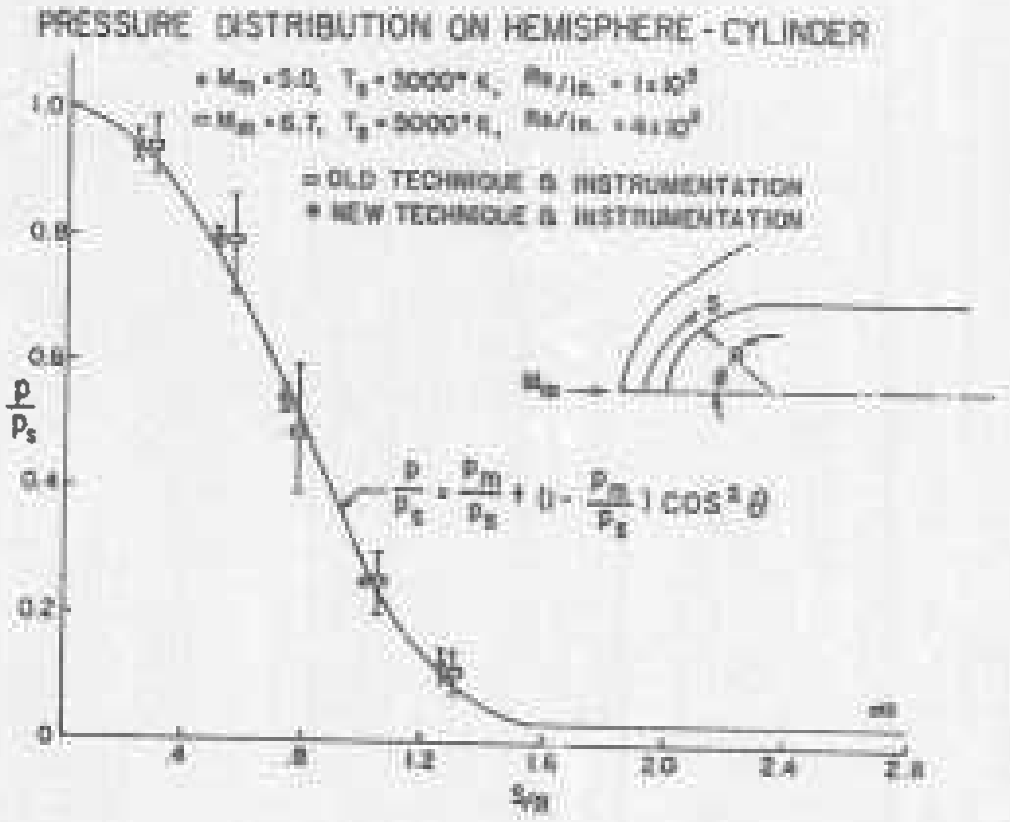

Figure 14(a) 6-Inch Shock Tunnel Experimental Model Pressure Distributions

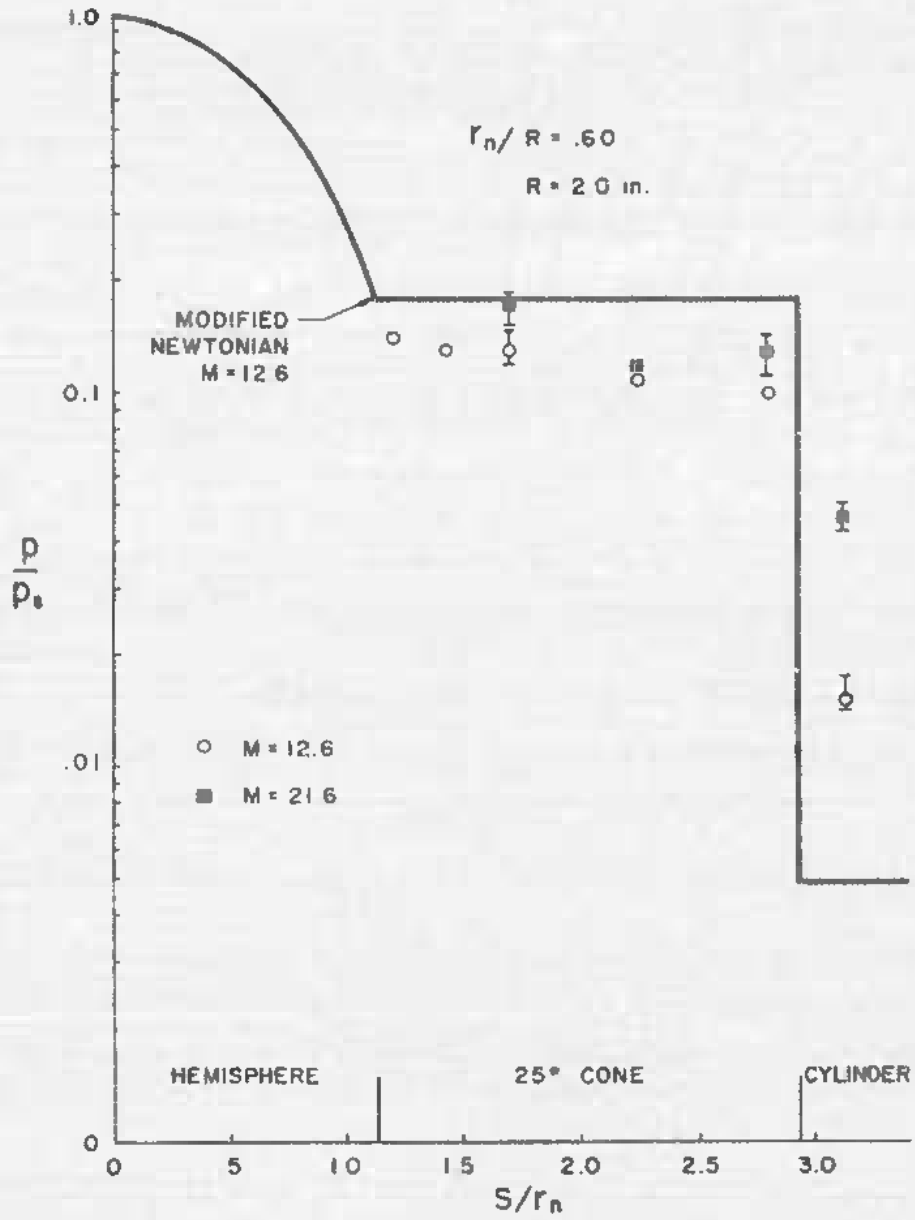

Figure 14(b) Pressure Distribution for 25-Degree Hemisphere - Cone - Cylinder

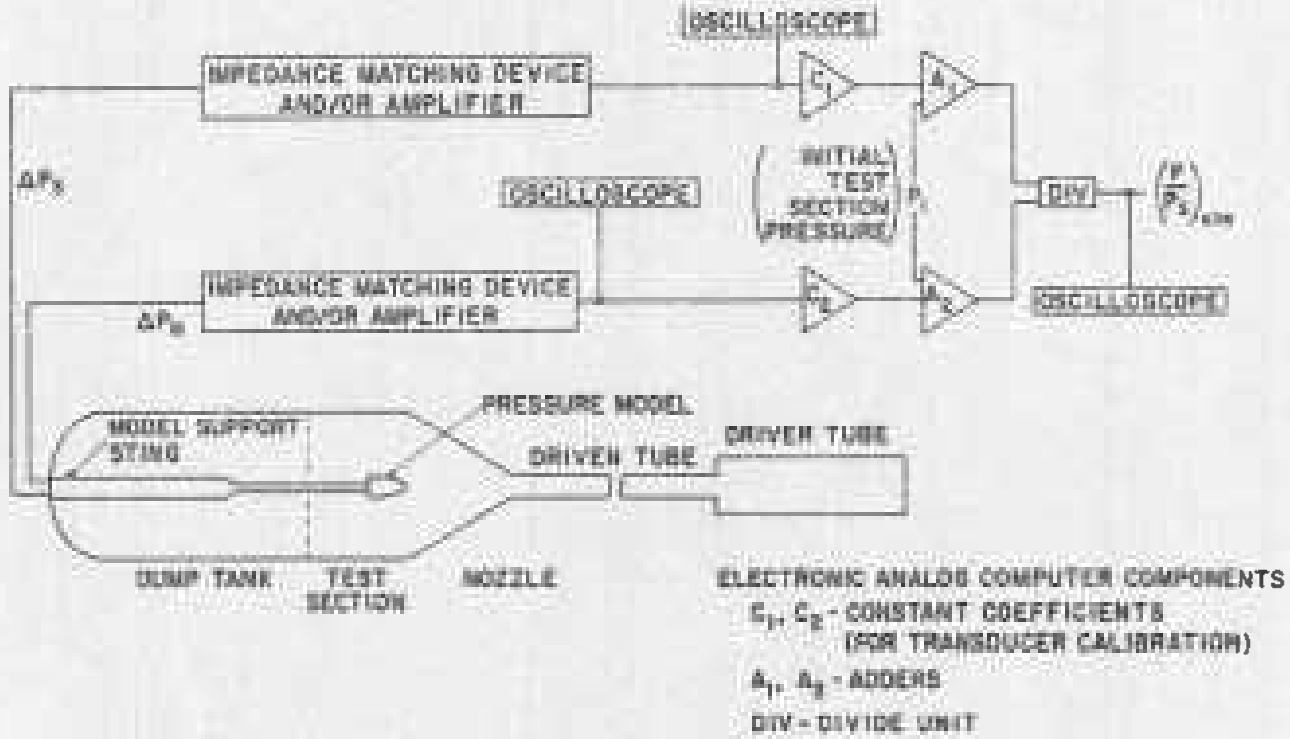

Figure 15 6-Inch Shock Tunnel - Electronic Data Processing System

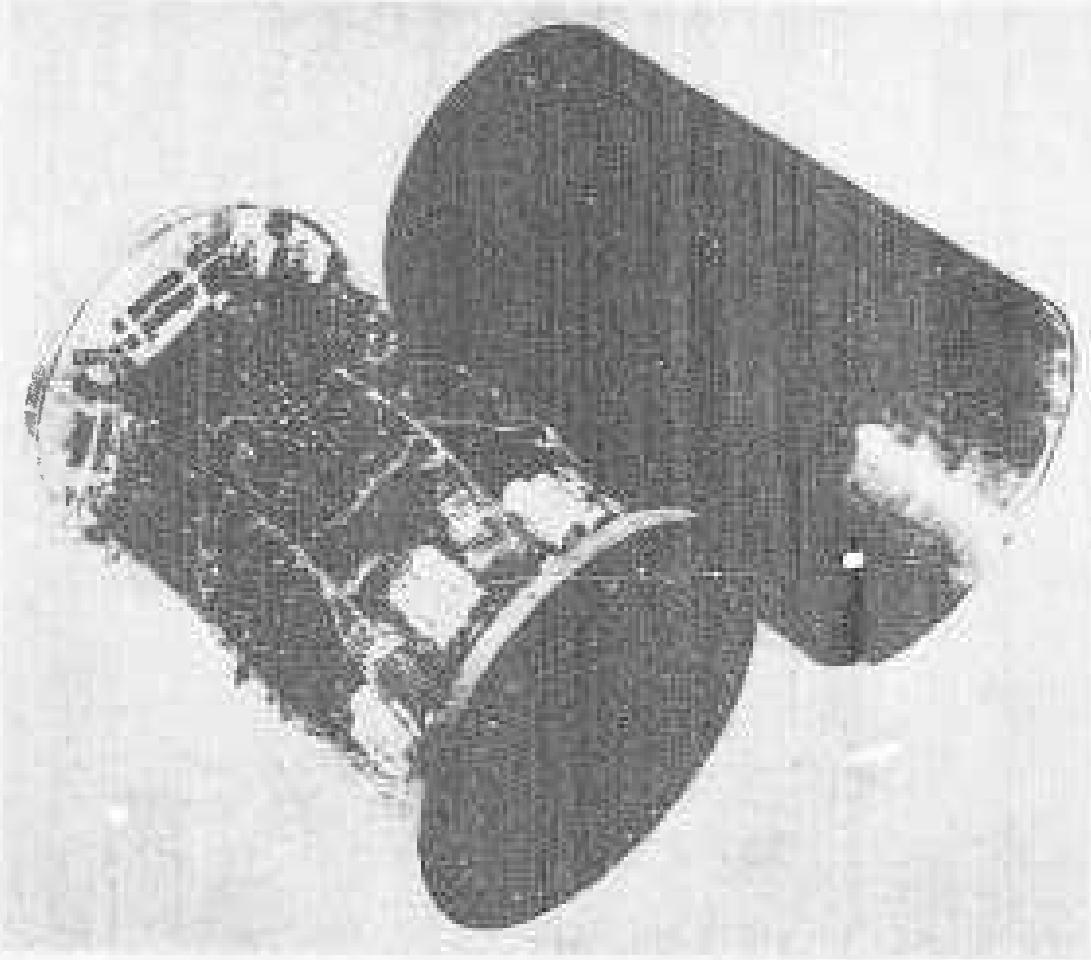

Figure 16 Transistorized Sting Pack

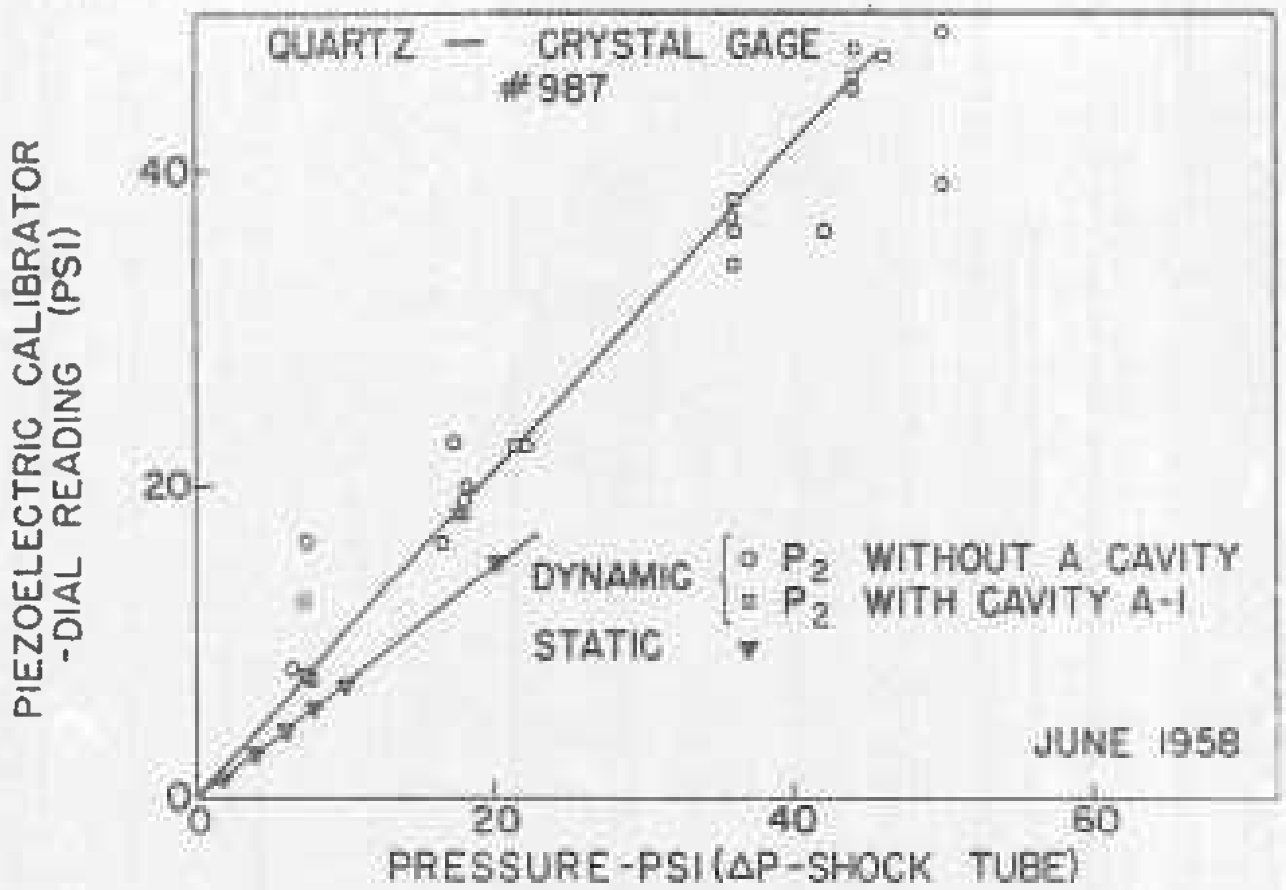

Figure 17 Calibration Curve

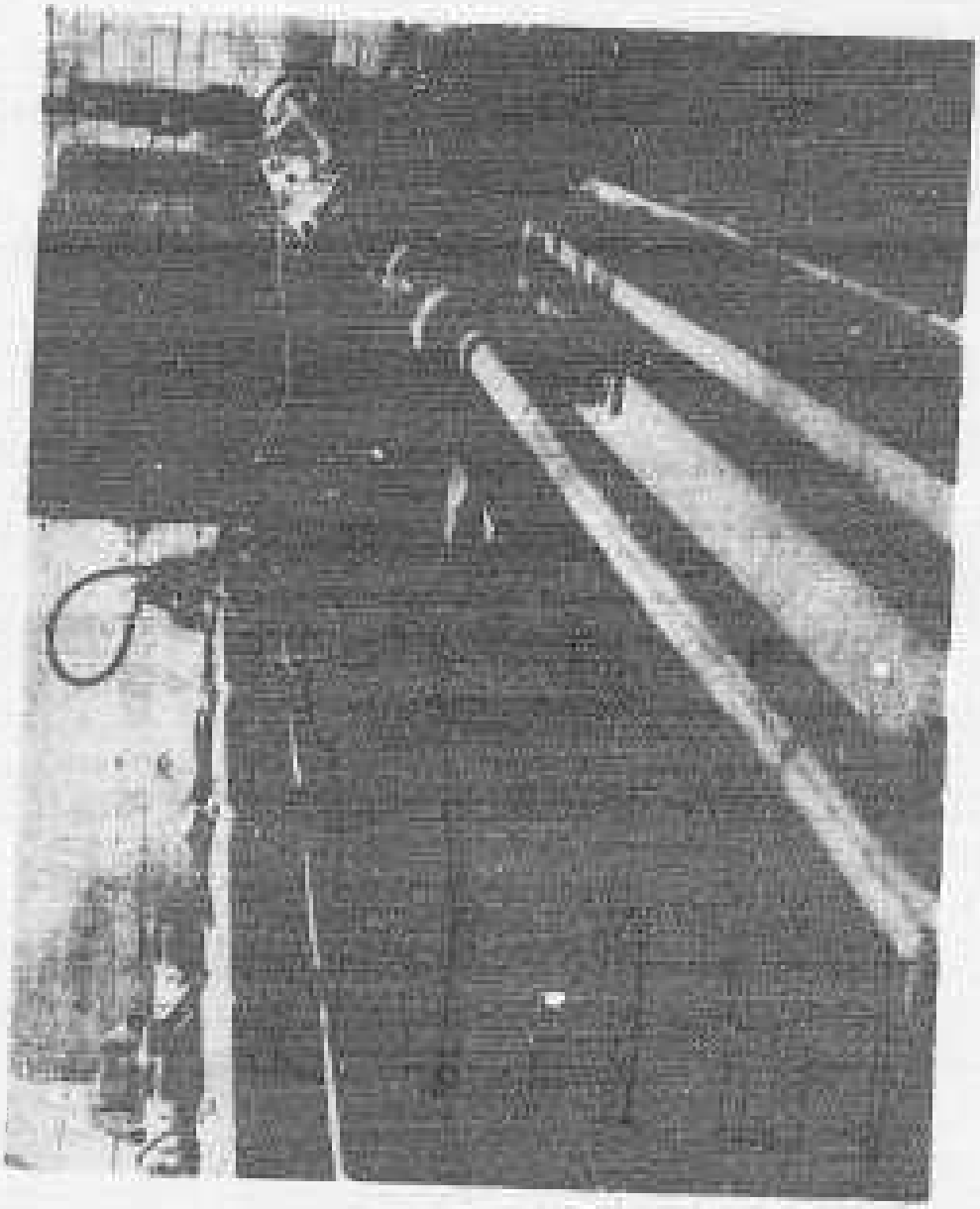

Figure 18 2-Inch Shock Tube - Tunnel

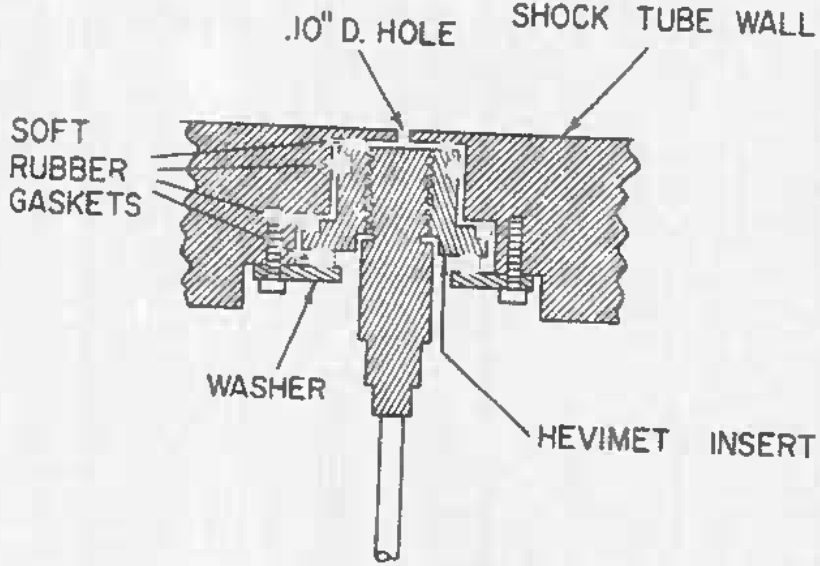

Figure 19 Recessed-Shock Mounted Pressure Gauge

WITH CAVITY

WITHOUT CAVITY

Figure 20 Model Surface Pressure-Time History With and Without A Recessed Cavity

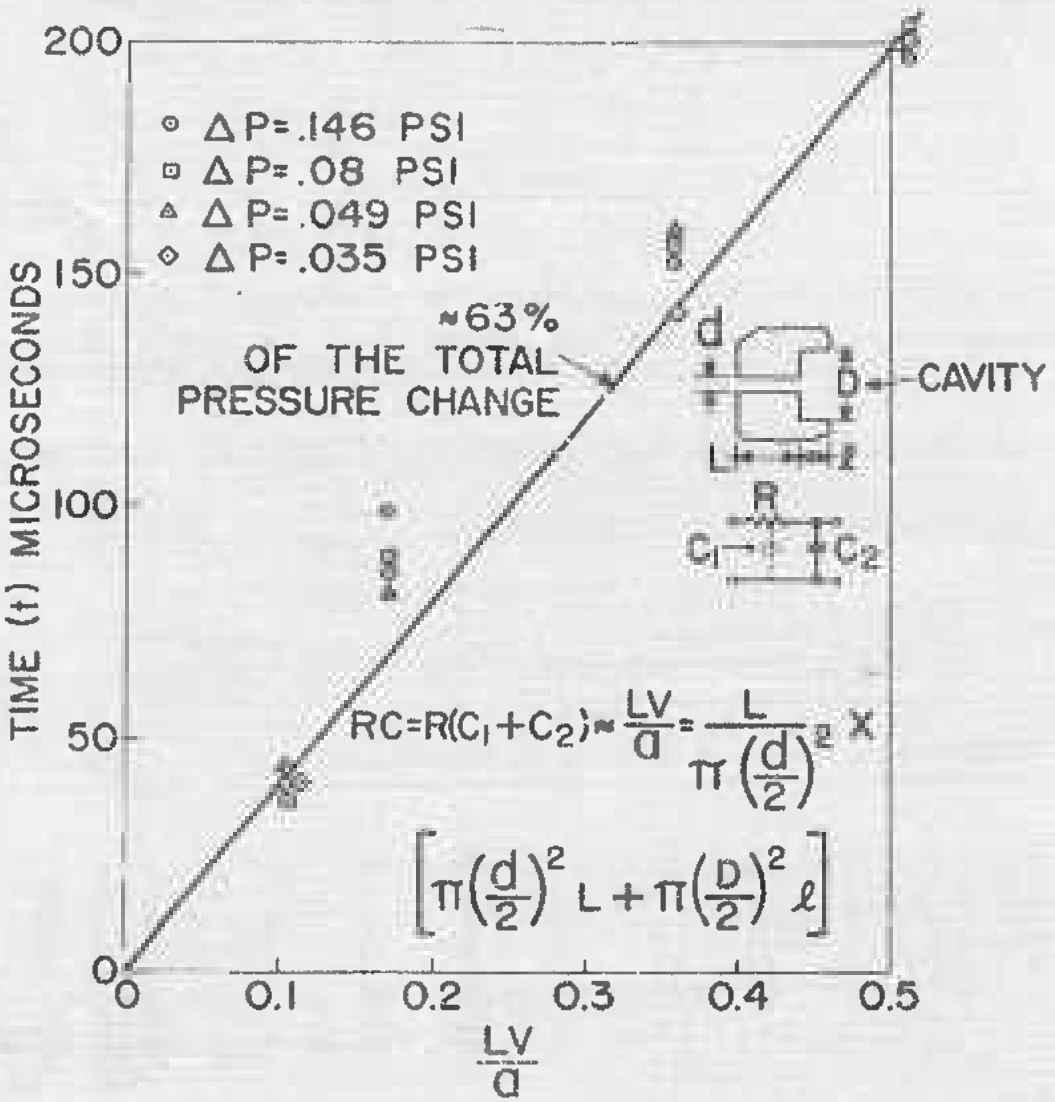

Figure 21 Experimental Time Delay Due To Cavity Filling For Recessed Pressure Transducers (2-Inch Shock Tube)

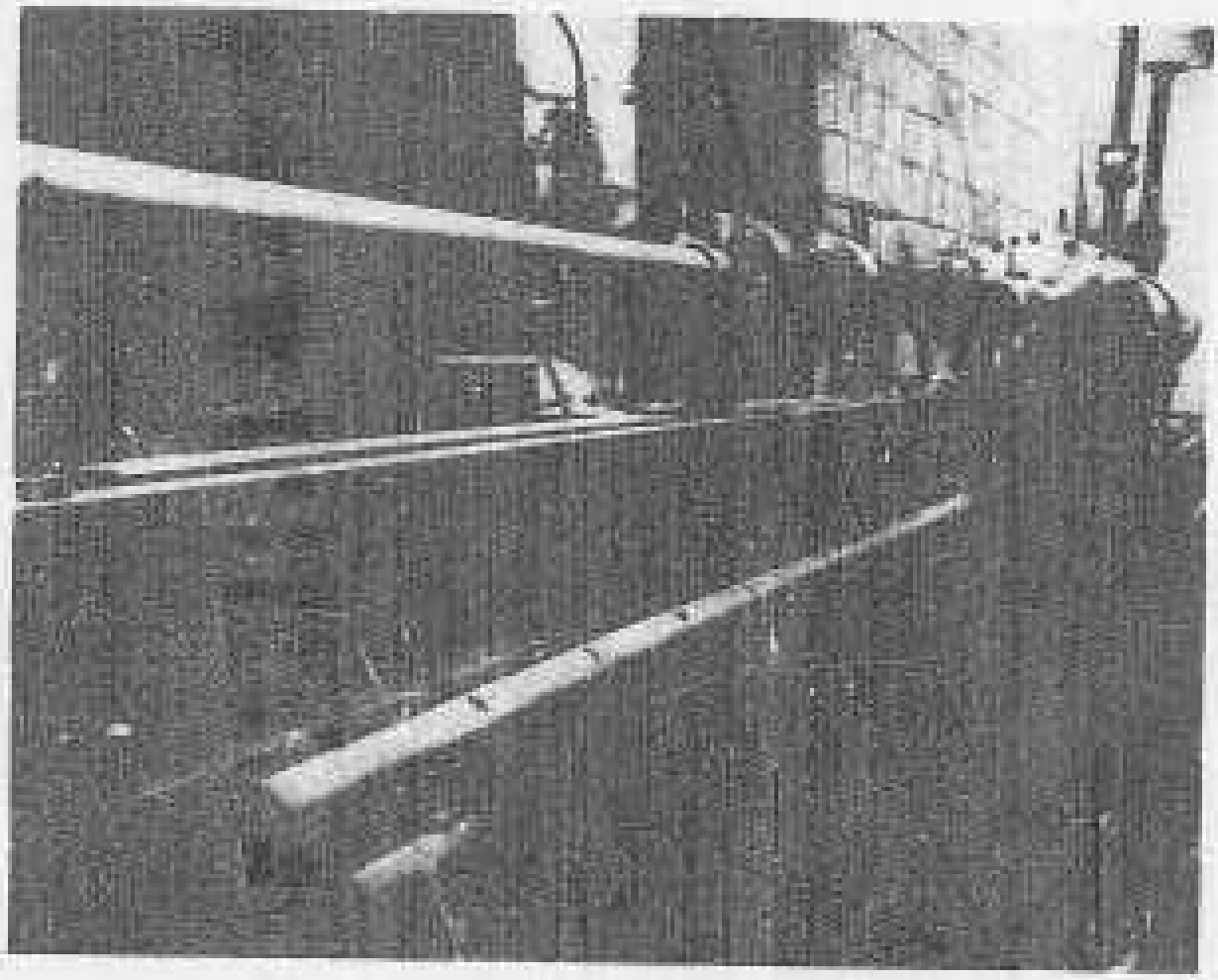

Figure 22 2-Inch Shock Tube - Low Pressure Dynamic Calibration

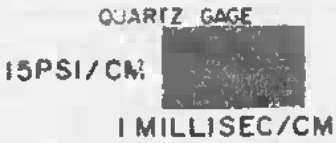

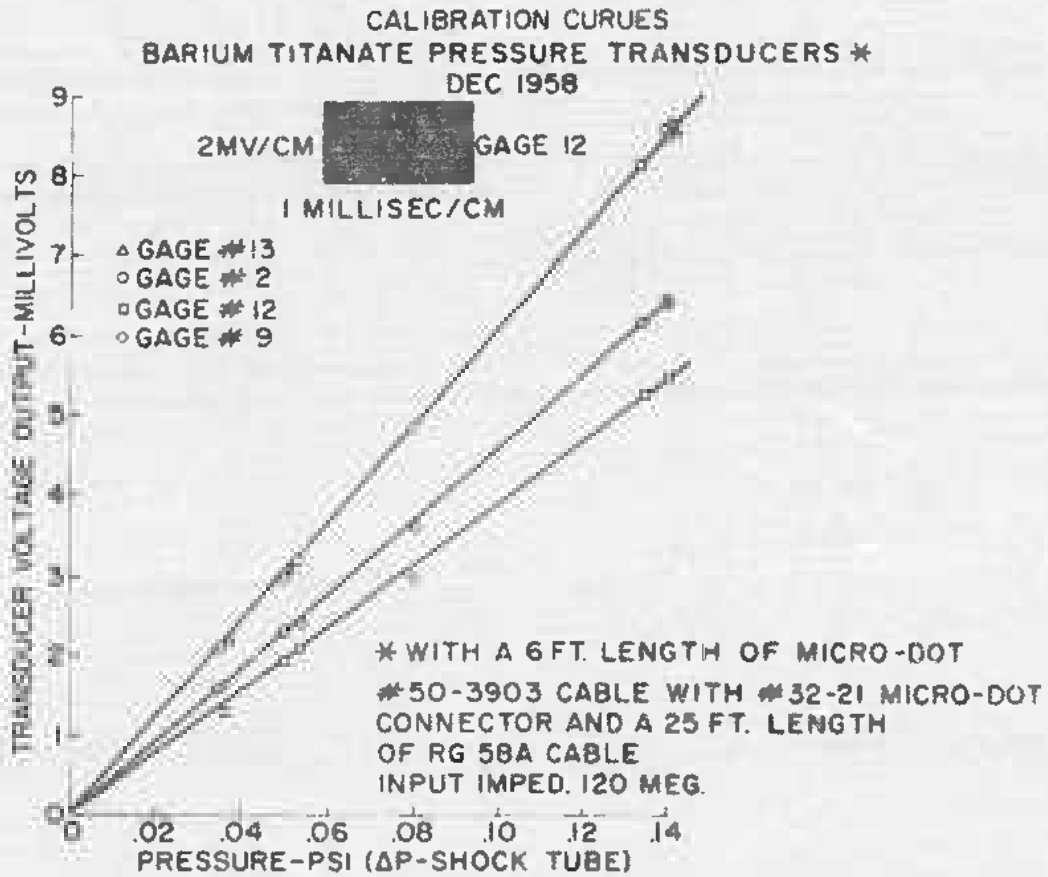

Figure 23 Model Stagnation Point Pressure-Time History

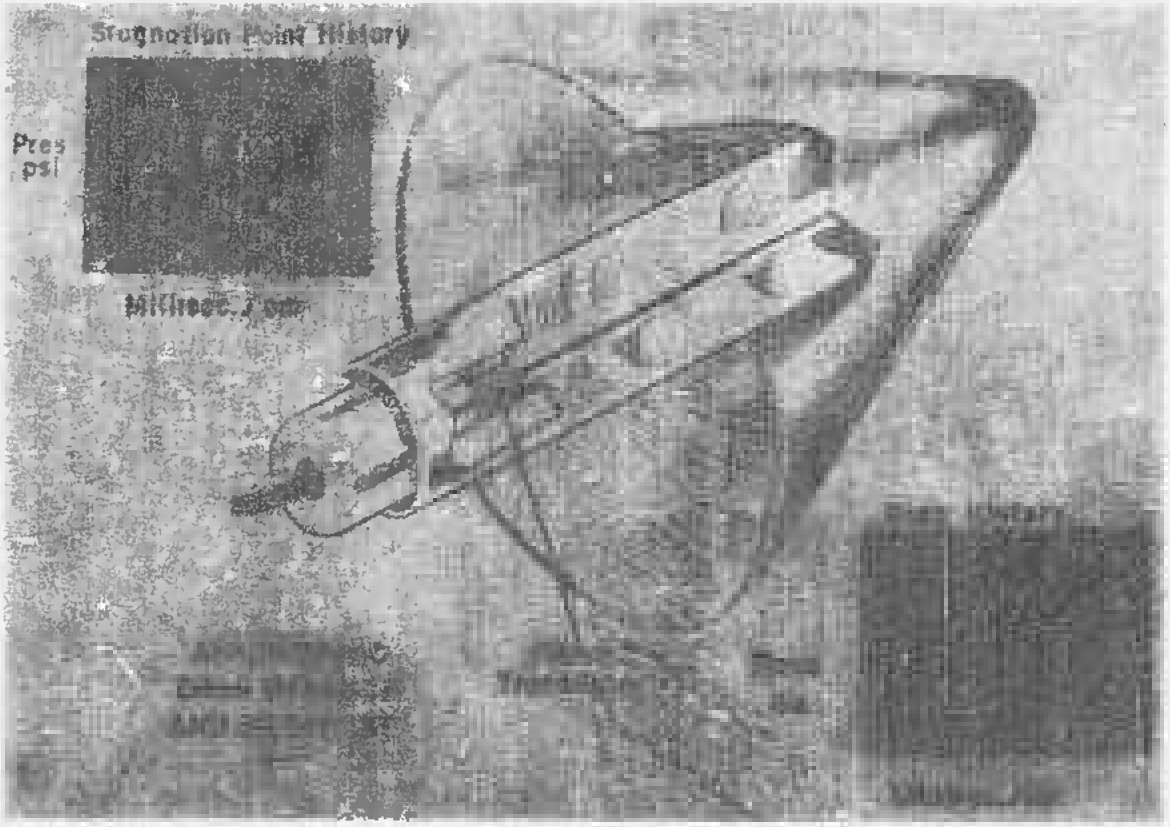

Figure 24 Piezoelectric Axial Force Balance,
Force Versus Time History From the Balance,
Pressure Versus Time History at the Model Stagnation Point.

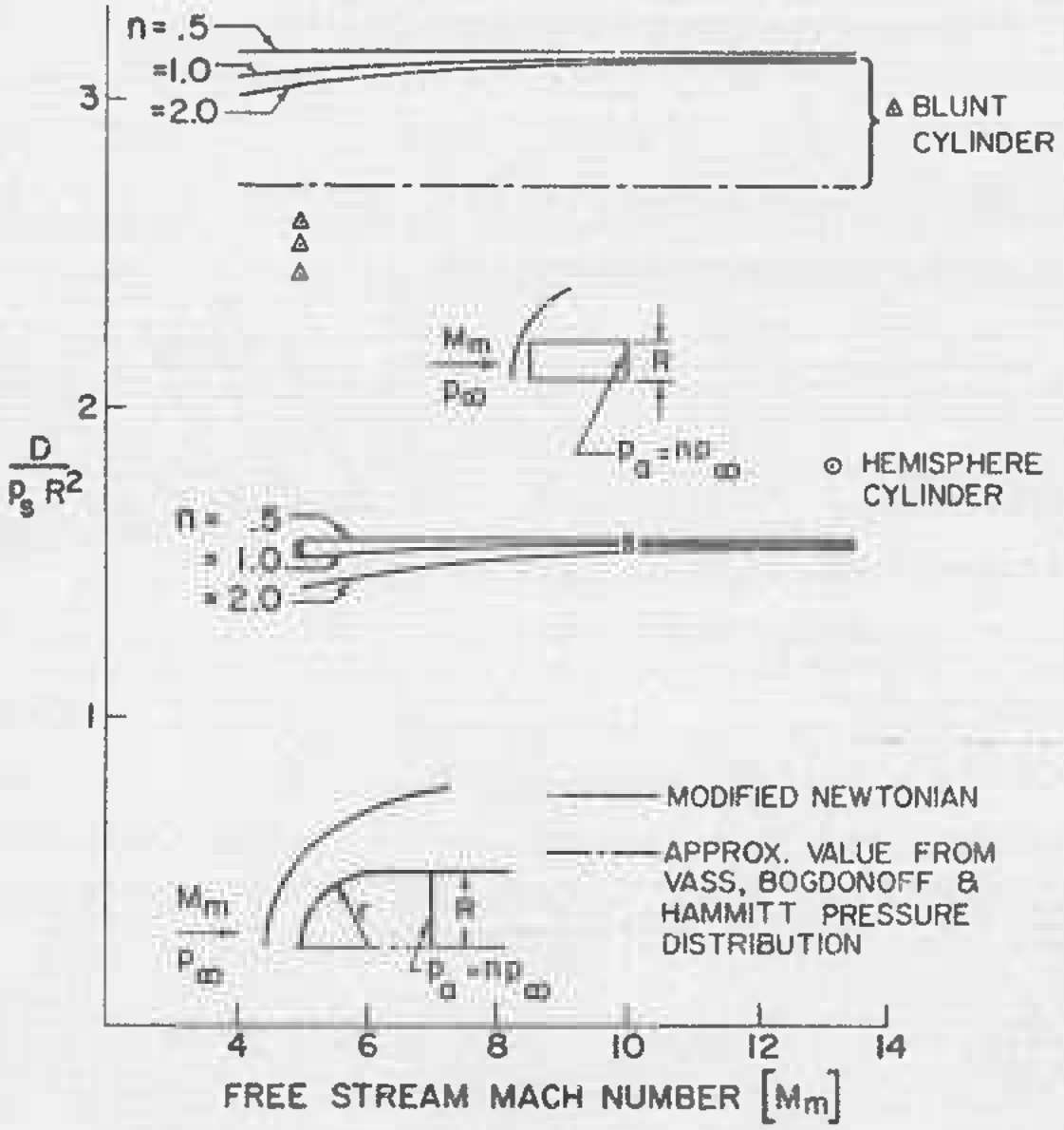

Figure 25 Experimental Drag On Basic Shapes Versus Mach Number

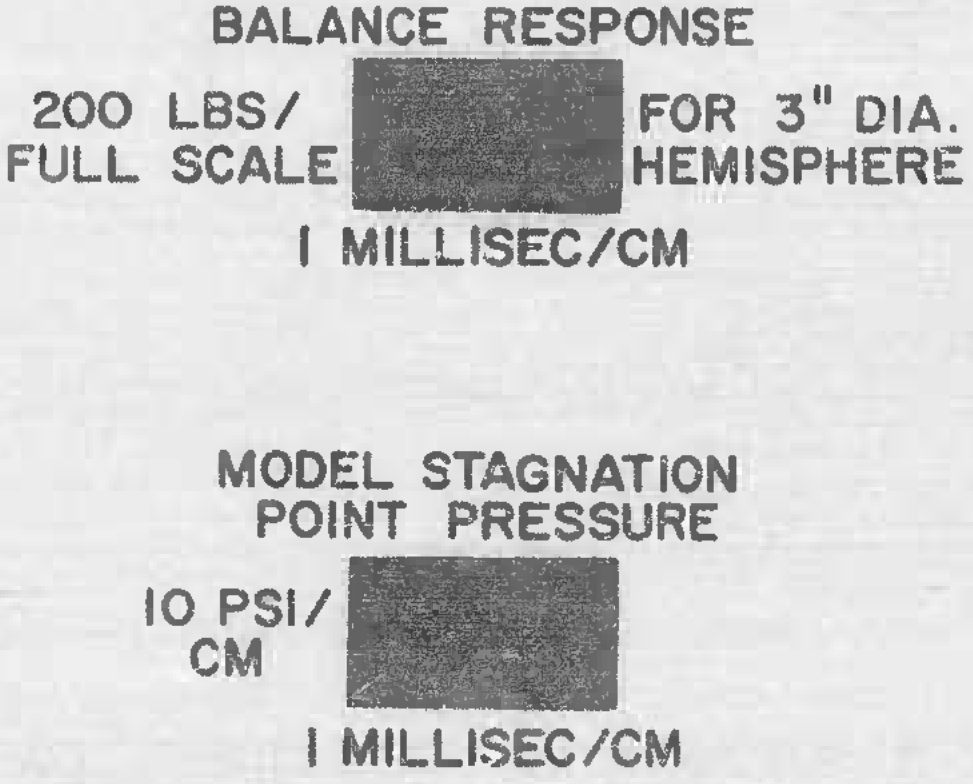

Figure 26 Typical Strain-Gage Axial Force Balance Output

SHOCK TUBE STUDIES OF THE EFFECTS OF SHARP-RISING, LONG-DURATION OVERPRESSURES ON BIOLOGICAL SYSTEMS*

D.R. Richmond, R.V. Taborelli, F. Sherping, M.B. Wetherbe, R.T. Sanchez, V.C. Goldizen, and C.S. White
Lovelace Foundation

INTRODUCTION

Shock tubes have been used successfully by a number of investigators to study the biological effects of variations in environmental pressures.(1, 2, 3) Recently an unusually versatile laboratory pressurization source became available with the capability of consistently reproducing a wide variety of pressure-time phenomena of durations equal to and well beyond those associated with the detonation of nuclear devices.(4) Thus it became possible to supplement costly full-scale field research in blast biology carried out at the Nevada Test Side(5, 6) by using an economical yet realistic laboratory tool. In one exploratory study employing pressure pulses of 5 to 10 sec duration wherein the times to max overpressure and the magnitudes of the overpressures were varied, a relatively high tolerance of biological media to pressures well over 150 psi was demonstrated.(7) In contrast, the present paper will describe the relatively high biological susceptibility to long duration overpressures in which the pressure rises occurred in single and double fast-rising steps.

METHODS

Shock Tube

The shock tube used to achieve variations in the pressure environment has been described in detail elsewhere.(4, 8) In brief, however, the apparatus consisted of a cylindrical pressure chamber 40.5 in. in diameter and 17 ft 5 in. long separated by a frangible diaphragm (Dupont Mylar) from an expansion chamber made up of sections of steel pipe 23-1/2 in. in diameter and 25 ft long. The reduction in diameter from 40-1/2 to 23-1/2 in. occurred over a 3-ft-long transition section upstream of the diaphragm station. The downstream portion of the shock tube was closed with a steel plate bolted to the end of the expansion chamber. See Figure 1. Following pressurization of the expansion chamber, which was accomplished by initiating rupture of the diaphragm with a .22 caliber bullet fired at an angle from a pistol mounted downstream of the diaphragm, high-pressure gas escaped through openings in the wall of the shock tube and thus determined the rate of pressure fall.

*This work was supported by contract with the Division of Biology and Medicine of the Atomic Energy Commission, and was carried out at the AEC-Lovelace Foundation Blast Tube Facility, Sandia Base, Albuquerque, New Mexico.

Animals and Cages

Four species of animals were exposed in metal-mesh cages having the dimensions noted in Table 1. The cages, shown in Fig. 2, 3, 4 and 5 were carefully sized to fit the animals snugly and thus served to minimize possible damage from displacement. The cages were either bolted against the inside of the end-plate of the shock tube or were fixed at varying distances away from the end-plate, e.g., 1, 2, 3, 6 and 12 in.

Table 1 Dimensions of the Animal Cages

Species	Dimensions of Individual Cage, in.	Number of Compartments	Division of Openings in Wire Mesh, in.
Mouse	1-1/2 × 1-1/2 × 3/4	5	1/4 × 3/4
Rat	2 × 2-1/4 × 8	5	1/4 × 3/4
Guinea Pig	3 × 3 × 8-1/2	3	1/4 × 3/4*
Rabbit	5 × 5 × 14	2	3/4 × 1-3/4**

*Approximately 60 per cent open area (diamond-shaped)

**Approximately 75 per cent open area (diamond-shaped)

Instrumentation

Pressure-time data were obtained using Wiancko pressure transducers and piezoelectric gauges appropriately integrated with amplifying equipment and recorders. The latter consisted of Consolidated galvanometers and an oscillograph for Wiancko data; and a Tektronix cathode ray oscilloscope mounting a camera to photograph the piezo gauge results.

Pressure-time Environment

Pressure gauges were located in the end-plate, face-on to the advancing shock front and side-on in the wall of the shock tube, 1 ft and 11 ft from the end-plate. The upper portion of Figure 6 shows a face-on pressure-time trace. The reader will note that the incident and reflected wave almost instantaneously activated the pressure transducer giving a sharp, fast-rising pressure pulse followed by a slow-rising crown. In contrast, the middle and lower records of Figure 6, taken with gauges located 1 ft and 11 ft from the end-plate of the tube, respectively, show two fast-rising steps in the pressure pulse followed by a crown. The first step was due to the incident shock, whereas the second was caused by the pressure reflection from the end of the tube. All overpressures were from 6 to 8 sec in duration.

Pressures to be reported later were read from the peak of the vertically rising portion of the record. The crown following the reflected shock represented only a small additional and slow rise over the pressure in the reflected shock and was considered unimportant biologically.

The secondary reflections in the latter portions of the traces in Fig. 6 were eliminated in some of the experiments by using the arrangement

shown in Fig. 7. As shown in the figure, the secondary pressure reflections were absent and, as will be indicated later, they were probably of no biological importance as far as the present study was concerned.

RESULTS

1. Animals Exposed Side-on Against the End-plate of the Shock Tube

Four species of animals, listed in Table 2 showing their numbers and body weights, were exposed side-on in cages bolted against the end-plate of the shock tube to reflected pressures of increasing magnitude. The mortality noted at 1 hr or less after exposure is detailed in Table 3, and plotted in Fig. 8. The latter shows typical sigmoid shaped mortality curves. The probit analysis of Finney [9] was applied to the data.

Table 2 Number and Species of Animals Used in This Study

Species	Body Weight (Mean, SE)	Age, months	Width in.	Number of Animals Exposed Against End-plate	Number of Animals Exposed At Various Distances from End-plate
Mouse (F) (Webster Strain)	18.5 ± 0.15 g	1-1/2	1	115	78
Rat (F) (Sprague Dawley)	192.0 ± 1.51 g	2 - 2-1/2	1-1/2	145	80
Guinea Pig (M&F) (English Breed)	436.7 ± 3.3 g	3-1/2 - 4	2	140	446
Rabbit (F) (New Zealand White)	1732 ± 35.8 g	2-1/2 - 3	4	55	38

Figure 9 shows a probit plot of the results and sets forth the reflected pressure in psi associated with 50 per cent mortality in each species (LD_{50}). As can be seen from the figure, the LD_{50} values arranged in ascending order were 29.8 (± 1.1), 33.4 (±1.2), 36.7 (±0.7), and 38.7 (± 0.6) psi for the mouse, rabbit, guinea pig, and rat, respectively. The standard errors of the means noted in parentheses above were encouragingly small.

Statistical tests showed that the LD_{50} value for the rat was significantly higher than those for the rabbit and the mouse, but not for the guinea pig. Though there was a significant difference between the guinea pig and the mouse, such was not the case when comparing the rabbit and the mouse or rabbit and guinea pig. Also, tests indicated the regression lines for the rat, guinea pig and rabbit were essentially parallel, but the slope of the regression line for the mouse was significantly different than those for the other three species of animals.

As previously mentioned, the multiple reflections returning secondarily from the compression chamber did not add to the mortality rate. For example, a group of 30 guinea pigs were exposed against the end-plate

Table 3 Mortality* as Related to the Magnitude of the Reflected Shock for Animals Exposed Side-on Against the Closed End of a Shock Tube

Overpressure in Reflected Shock psi	Number Killed Total	Mortality, per cent
Mouse:		
19.50	0/15	0
24.50	0/15	0
29.70	17/25	68.0
34.80	19/25	76.0
37.12	18/20	90.0
38.8	14/15	93.0
Rat:		
21.2	0/10	0
31.0	0/20	0
34.0	2/25	20.0
37.6	8/25	32.0
39.0	12/20	60.0
40.2	14/20	70.0
46.0	13/15	86.7
53.5	10/10	100
Guinea Pig:		
16.3	0/15	0
20.7	0/15	0
29.3	1/20	5.0
36.3	8/20	40.0
39.6	19/25	76.0
42.0	13/15	86.7
46.7	15/15	100
55.3	15/15	100
Rabbit:		
25.5	0/8	0
29.2	1/6	16.7
32.9	4/8	50.0
35.0	8/15	53.3
37.6	7/8	87.5
39.3	4/4	100
52.7	6/6	100

*Mortality at 1 hr or less.

to the pressure pulse that lacked the repeated reflections (Fig. 7). Fifty-seven per cent mortality was obtained with reflected shocks that averaged 39 psi. In the other arrangement where multiple peaks occurred (Fig. 6), initial reflected shocks of 38 psi produced 60 per cent mortality. The difference in mortality between the two groups was not significant.

2. Animals Exposed at Varying Distances from the End-plate of the Shock Tube

Guinea Pigs

Experiments similar to those described above were performed using guinea pigs except that the cages were located 1, 2, 3, 6 and 12 in. from the end-plate of the shock tube at the time of exposure. Mortality data for the several groups of animals are summarized in Table 4 which, for comparison, also includes results for animals exposed against the end-plate.

Probit analysis was performed on the data shown in Table 4. Mortality regression lines and the reflected pressures associated with 50 per cent mortality for the different cage positions are shown in Fig. 10. Attention is directed to the results which clearly indicate a rise in the LD_{50} values as the animals were moved away from the end of the tube being 36.7 + 0.7 psi against the end-plate and 40.8 ± 2.1, 48.3 ± 1.3, 52.8 ± 1.9, 58.6 ± 1.6 and 57.1 ± 1.1 psi for cage positions at 1, 2, 3, 6 and 12 in. from the reflecting surface, respectively. The reader will note that there was no essential difference in the results obtained at the 6 and 12 in. cage positions and that the rather large increase in pressure tolerance occurred at the 1 and 2 in. cage locations.

This somewhat remarkable finding occurred even though the time between the arrival of the initial incident pressure at the animal position and the subsequent reflected pressure was by measurement close to 1.4 msec for the 12-in. position and was much less at stations closer to the end-plate. Apparently the biological system can and does distinguish surprisingly short time intervals when stepwise pressure loading occurs with sharp-rising segments of the pressure pulse.

Mouse, Rat, Rabbit

To further explore the biological effects of step-loading, the experiments performed on guinea pigs described above were repeated using mice, rats, and rabbits with two alterations in procedure: (1) a series with animals exposed against the end-plate was included, and (2) the tube was operated at near constant compression chamber pressures of 58 psi. The latter yielded reflected pressures, which proved fatal for all animals exposed against the end-plate (which averaged 53 psi with a range from 48 to 56 psi).

Results obtained are tabulated in Table 5 in which are also included appropriate portions of the guinea pig data described in the previous section. A graphic presentation of the results are shown in Fig. 11. From a study of the figure at least two results are apparent. First, all animal species show a decrease in mortaility with increasing distance from the reflecting

Table 4 Mortality as Related to the Magnitude of the Reflected Shock Front for Guinea Pigs Exposed Side-on at Various Distances from the End-plate

Distance of Cage from End-plate, in.	Number of Animals	Reflected Overpressure, psi	Mortality* per cent
0	15	16.3	0
	15	20.7	0
	20	29.3	5
	20	36.3	40
	25	39.6	76
	15	42.0	86.7
	15	46.7	100.0
	15	55.3	100.0
1	21	31.1	14.3
	15	37.0	13.3
	15	42.0	40.0
	12	45.9	83.3
	12	52.0	100.0
2	12	39.3	8.3
	12	42.9	25
	18	48.8	55.6
	12	52.0	66.7
	9	58.0	77.8
	6	71.0	100.0
	9	77.3	100.0
3	9	37.7	0
	12	48.1	25
	15	50.6	26.7
	15	52.6	53.3
	9	56.7	77.8
	15	60.8	86.7
	12	73.5	91.7
6	9	35	0
	12	38	0
	18	47	5.56
	21	52.1	23.8
	15	59.2	60.0
	6	63.5	66.7
	9	68	77.8
	9	72.3	88.9
12	3	33	0
	6	37	0
	19	47.4	10.5
	9	52	22.2
	9	55.7	22.2
	9	58	55.6
	9	60	66.7
	15	62	80.0
	9	67.7	88.9
	12	72.5	100.0
	9	84	100.0

*Mortality at 1 hr or less.

Table 5 The Relation Between the Magnitude of the Reflected Shock and Mortality for Small Animals Exposed Side-on at Various Distances from the End-plate

Species	Number of Animals	Distance of Cage from End-plate, in.	Overpressure in Reflected Shock, psi*	Mortality, per cent
Mouse (5 per shot)	20	0	52 (52-52)	100
	24	1/2	55 (53-56)	63
	24	1	55 (54-56)	29
	15	2	54 (54-54)	0
	15	3	54 (54-56)	7
Rat (5 per shot)	15	0	52(48-55)	100
	10	1/2	53 (52-55)	100
	15	1	52 (50-53)	80
	15	2	52 (49-54)	13
	15	3	50 (48-52)	0
	15	6	48 (48-49)	0
	5	12	55 (55)	0
Guinea Pig (3 per shot)	20	0	48 (46-52)	100
	15	1	51 (49-53)	100
	18	2	51 (50-54)	72
	30	3	52 (50-54)	37
	21	6	52 (50-53)	24
	15	12	53 (50-54)	25
Rabbit (2 per shot)	12	0	42 (38-53)	100
	4	1	53 (52-53)	100
	8	2	54 (53-55)	88
	8	3	55 (53-56)	63
	6	6	52 (51-53)	17
	2	12	55 (55)	0

*Mean and range

surface, i.e., with increasing time between arrival of the incident and reflected waves. Secondly, the rate of decrease of mortality with increasing distance from the end-plate is greater for the smaller than the larger animals. Actually, the exploratory nature of the data do not justify further comment beyond pointing out that (1) only a trend in the behavior of biologic systems has been demonstrated, (2) the animals against the end-plate were over-shot, meaning that the reflected pressures were well above those required for 100 per cent mortality, and (3) lastly, the number of animals used to define each point were small, particularly in the case of the rabbit experiments.

DISCUSSION

General

From the practical point of view, when considering biological tolerance to overpressures of long duration, it is very important to distinguish between the incident and reflected pressures, the rate of pressure rise, the character of the rising portions of the pressure pulse and the geometry of exposure as it is interrelated with the above blast parameters. This is so because nuclear weapon effects data as presented in manuals showing the scaling laws for blast usually report the incident pressure[10] and say that 30 psi, when referring to the incident pressure, is a safe pressure for man. Such statements can have at least two inaccuracies. First, 30 psi incident in an appropriate geometry of exposure may result in sudden application of a reflected overpressure of 90 - 120 psi to a biologic target. Such reflected pressures of long duration applied as a single step would no doubt be fatal to man. Secondly, a 30 psi incident overpressure in another geometry of exposure might rise in two or more steep steps due to reflection, or might rise slowly to less than 30 psi in a time measured in several tens of milliseconds and produce no significant damage whatsoever. The point is that tolerance to pressure variations is a complex matter and considerable care must be observed in specifying safety criteria and in the design of protective structures.

Mortality from Single, Sharp-rising Overpressures

More specific consideration will now be given to the data comprising the present study, and a few comments regarding tolerance to single, fast-rising pressure pulses will be set forth.

First, in spite of large weight range there was little difference in the LD_{50} figures for the four species studied ranging from about 30 psi for the mouse to near 39 psi for the rat, with the rabbit and guinea pig in between.

Secondly, the range of the reflected pressure associated with 10 and 90 per cent mortality was quite small in the order of $\pm$7 to 12 psi on either side of the LD_{50} reflected pressure. What this can mean in terms of the incident pressure is indirectly illustrated by the data in Table 6 showing the relation between the incident (P_s) and reflected (P_f) overpressures as they occurred in the present study. The table shows that there is approximately a ratio of 3 between the P_s and the P_f which means that a variation of

Table 6 Reflected and Incident Overpressures Associated with 50 Per Cent Mortality for Animals Exposed Against the End-plate of the Shock Tube

Animal Species	Overpressure in psi		P_f/P_s
	Reflected (P_f)	Incident (P_s)	
Mouse	29.8	10.0	2.90
Rabbit	33.4	11.3	2.95
Guinea pig	36.7	12.1	3.03
Rat	38.7	12.6	3.07

Table 7 Reflected and Incident Overpressures Associated with 50 Per Cent Mortality of Guinea Pigs Exposed Against and at Various Distances from the End-plate of the Shock Tube

Distance from End-plate in.	Incident Overpressure (P_s), psi	Reflected Overpressure (P_f) (LD_{50}), psi	Difference (P_r), psi	Time between Steps, msec
0	12.1	36.7	24.6	~0
1	13.4	40.8	27.4	0.10*
2	15.6	48.3	32.7	0.20
3	16.9	52.8	35.9	0.30
6	18.7	58.6	39.9	0.63
12	18.2	57.1	38.9	1.36

*Estimated.

about ±7 to 12 psi in the P_f would require only a variation of near ±2 to 4 psi in the $\overline{P}_s$. Apparently the biological system is responding in what might be called an all-or-none manner to fast-rising overpressures. At least the range between near zero and 100 per cent mortality is small and those interested in protection should take careful note of this fact.

Thirdly, by way of speculation, it is doubtful that the LD_{50} reflected overpressures for fast-rising pulses of long duration applicable to the dog and to man are likely to be much above 40 - 45 psi if indeed they are that high. Though the present study supports such a guess, let it be clear that as yet there are no empirical data on which to base a firm opinion.

Animals Exposed at Varying Distances from the End-plate of the Shock Tube

It is now useful to note the relationships between the incident and reflected pressures that were associated with 50 per cent mortality of the guinea pigs exposed against and at various distances from the end-plate of the shock tube. Table 7 details the data.

The next to the last column of the table shows the difference between the incident and reflected pressures associated with equal biological response (50 per cent mortality). The last column shows the time between arrival of the incident and reflected pressures at the animal stations. When the incident and reflected pressures were applied almost simultaneously, a single, fast-rising increase in pressure of 36.7 psi was required for the LD_{50}. In contrast, progressively higher total reflected pressures were associated with the LD_{50} at increasing distances from the end of the tube up to the 6 in. position. At the same time, the magnitudes of the incident pressures for all groups were not near the LD_{50} value for a single pulse. Likewise, neither were the magnitudes of the second pressure steps applicable to the 1, 2, and 3 in. positions all near the single step LD_{50} figure (see the difference column in Table 7). One is forced to conclude that neither the incident nor reflected pulse alone was responsible for the mortality, rather that both were contributing.

In the case of the 6-in. and 12-in. stations, however, a comparison of Tables 6 and 7 show that the magnitude of the second stepwise rises in pressure - being about 39 - 40 psi - were above the single-step figure of near 37 psi associated with 50 per cent mortality. Were the second step alone producing death, a slightly higher mortality should have been obtained. That such was not noted, indicates that the presence of the initial shocks and associated pressures were giving the animals some protection from the second shocks and accompanying pressure rises through some adaptive mechanism not completely understood at the present time.

That such protection is very real is confirmed by Fig. 11 and Table 8 which was prepared from the guinea pig data given in Table 5 referable to mortality noted at different exposure positions with near constant reflected pressures. The actual incident and reflected pressures are shown, and in the last column are noted the mortalities that might be expected from the second step rise in pressure were they acting as single steps and alone

Table 8 Mortality Variations as a Function of Exposure Position for Guinea Pigs Exposed to a Near Constant Reflected Pressure But Showing the Incident and Reflected Pressure Data for Each Group (Data from Table 5)

Distance from End-plate, in.	Mortality, per cent	Incident Overpressure (P_s), psi	Reflected Overpressure (P_f) psi	Magnitude Second Step ($P_f - P_s$), psi	Time between Steps, msec	Mortality Expected from Second Step Alone
0	100	15.5	48	32.5	—0	
1	100	16.4	51	34.6		40
2	72	16.4	51	34.6	0.20	40
3	37	16.7	52	35.3	0.30	46
6	24	16.7	52	35.3	0.63	44
12	25	17.0	53	36.0	1.36	48

responsible for the mortality. Comparing the figures noted in the last column with those in the second given the observed mortality, shows that for positions at 0, 1 and 2 in., the observed mortality was higher than that expected on a single-rise basis. Therefore, the first and second steps were both contributing to the deaths noted. In contrast, for the 6-in. and 12-in. positions, the expected mortalities were well above those actually found, indicating that the initial pressure had existed long enough to allow the animal to adapt in a way that lent protection against the second rise in pressure.

While the problem is under study, it is not possible to offer any clear cut explanation to explain the facts noted above. In all probability, however, the pressure differentials which exist at various times between the air-containing lung and the external pressure are of critical importance. At least three factors could influence magnitude of the environment-lung pressure difference with time, e.g., (1) air could flow into the lung, (2) the volume of air-containing lung could change because the external pressure pushed the chest walls inward and the abdominal wall and diaphragm in and upward, respectively, and (3) fluid (blood and lymph) might migrate into the thorax and serve to reduce the air volume and hence reduce the pressure differential. Certainly, the speed with which these three adaptations could occur will vary and, in the absence of applicable experimental data, one can only remark that while the second possibility noted above looks more attractive for the time intervals set forth in Tables 7 and 8, all three factors no doubt contribute some to the adaptations which take place with overpressures of long duration.

SUMMARY

A closed-end shock tube was used to study the effects of single and step-wise, fast-rising overpressures of long duration on four species of experimental animals.

For animals exposed side-on against the end-plate to single, sharp-rising pressure pulses, the reflected pressures necessary to kill 50 per cent (LD_{50}) were as follows: for the mouse - 29.8 $\pm$ 1.1; rabbit - 33.4 $\pm$ 1.2; guinea pig - 36.7 $\pm$ 0.7; and the rat - 38.7 $\pm$ 0.6 psi.

Animals located at short distances away from the end-plate were loaded in a two-step manner. The steps correeponded to the incident and reflected shock fronts. With stepwise increases in pressure, animals tolerated much higher reflected overpressures than when the pressure load consisted of a single-sharp-rising pulse.

The importance of the time interval between step loads was pointed out and briefly discussed.

REFERENCES

1. B. Cassen, L. Curtis and K. Kistler, Initial Studies of the Effect of Laboratory Produced Air Blast on Animals, J. Aviat. Medicine, 21: 38-47 (1950).

2. H. Celander, C. Clemedson, U. Ericsson, and H. Hultman, The Use of Compressed-air-operated Shock Tube for Physiological Blast Research, Acta Physiol. Scand., 32: 6-13 (1955).

3. H. Schardin and O. Wünsche, Versuche an Kleintieren zur Bestimmung der Druckstossstödlichkeitsgrenze, Bericht V 17, Deutsche Versuchsanstalt für Luftfahrt E. V., January 1958.

4. D. R. Richmond and R. V. Taborelli, Some Results of a Shock Tube for Biomedical Investigation, pp. 56-69, "Proceedings of Second Shock Tube Symposium", Report SWR-TM-58-3, Air Force Special Weapons Center, March 5-6, 1958.

5. C.S. White, T.L. Chiffelle, D.R. Richmond, W.H. Lockyear, I.G. Bowen, V.C. Goldizen, H.W. Merideth, D.E. Kilgore, B.B. Longwell, J.T. Parker, F. Sherping, and M.E. Cribb, The Biological Effects of Pressure Phenomena Occurring Inside Protective Shelters Following Nuclear Detonation, Operation Teapot Report, WT-1179, October 1956.

6. D.R. Richmond, R.V. Taborelli, I.G. Bowen, T.L. Chiffelle, F.G. Hirsch, B.B. Longwell, J.G. Riley, C.S. White, F. Sherping, V.C. Goldizen, J.D. Ward, M.B. Wetherbe, V.R. Clare, M.L. Kuhn, and R.T. Sanchez, Blast Biology - A Study of the Primary and Tertiary Effects of Blast in Open Underground Protective Shelters, Operation Plumbbob Report, ITR-1467, September 1957.

7. D.R. Richmond, M.B. Wetherbe, R.V. Taborelli, T.L. Chiffelle, and C.S. White, The Biologic Response to Overpressure. I. Effects on Dogs of Five to Ten-second Duration Overpressures Having Various Times of Pressure Rise, J. Aviat. Medicine, 28: 447-460 (1957).

8. D.R. Richmond, The Biologic Response to Sharp-rising Pressures of Long Duration, presented before the meeting of the AEC AD Hoc Task Unit on Blast Biology, August 5, 1958, Albuquerque, N.M.

9. D. J. Finney, "Probit Analysis. A Statistical Treatment of the Sigmoid Response Curve," 2nd ed., Cambridge University Press, New York, 1952.

10. Armed Forces Special Weapons Project, Department of Defense, "The Effects of Nuclear Weapons" edited by Samuel Glasstone, U.S. Government Printing Office, Washington 25, D. C., June 1957.

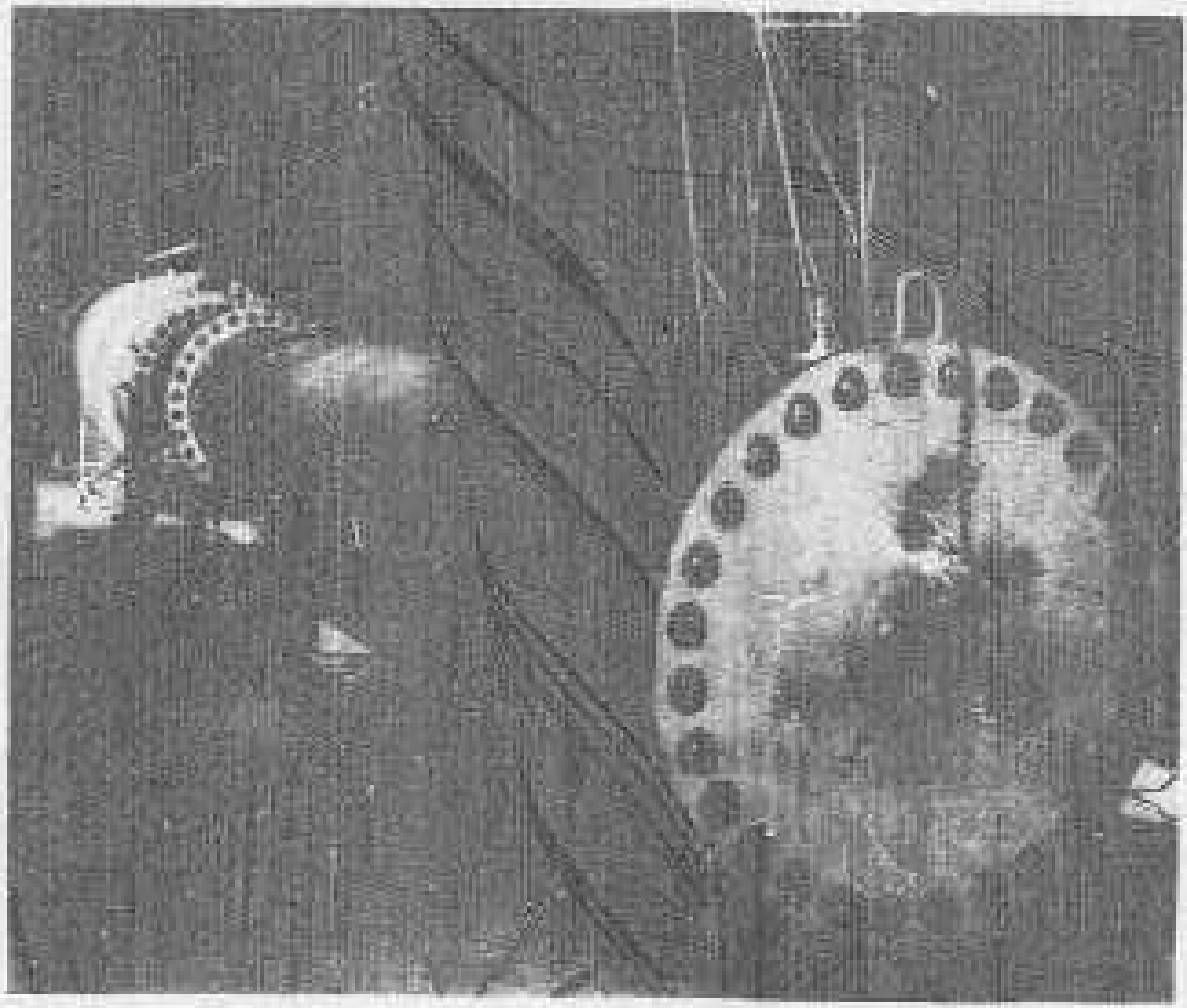

Figure 1 Shock Tube Viewed from the Closed End of the Expansion Chamber

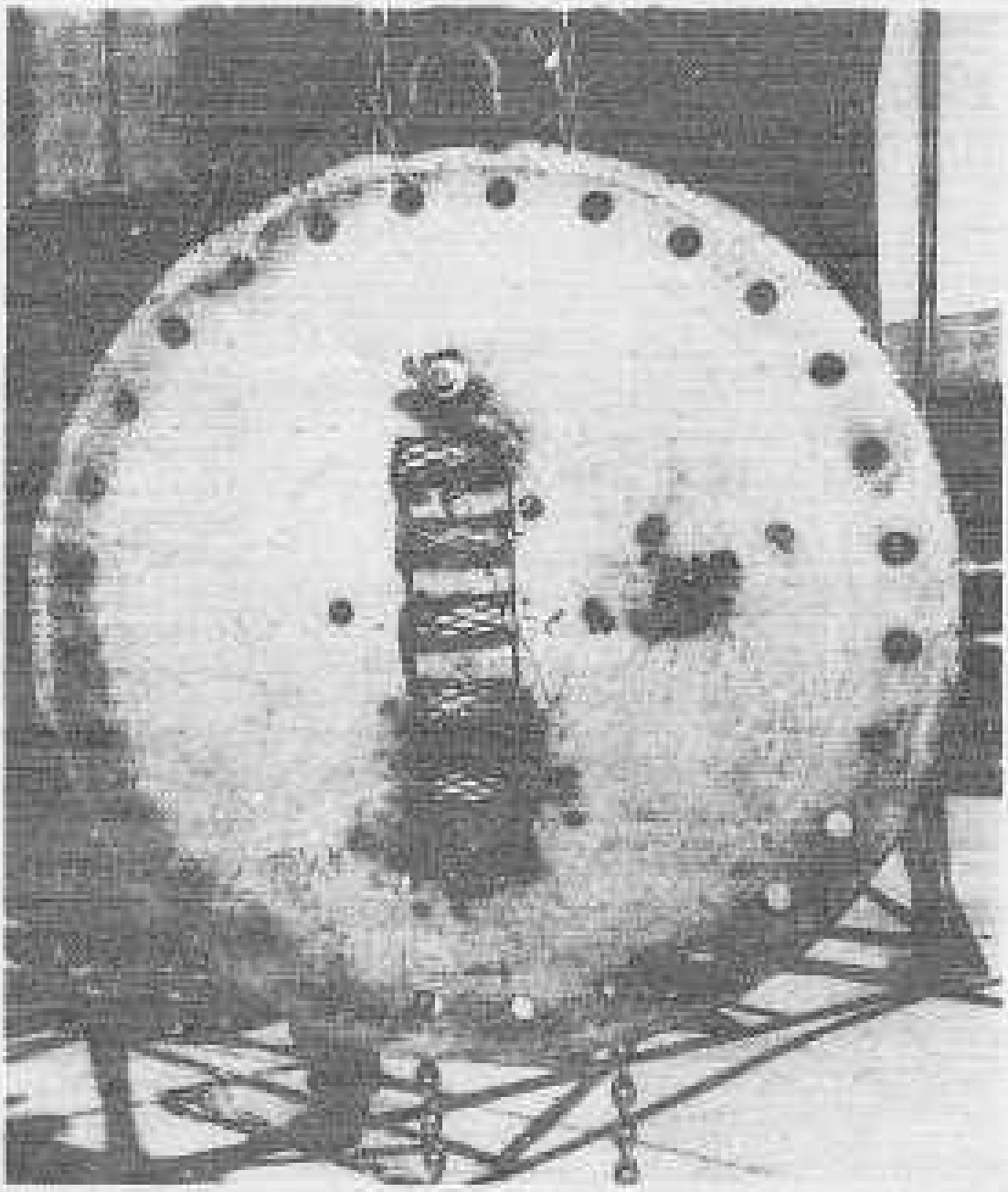

Figure 2 Mouse Cage Mounted Against the End-plate of the Shock Tube

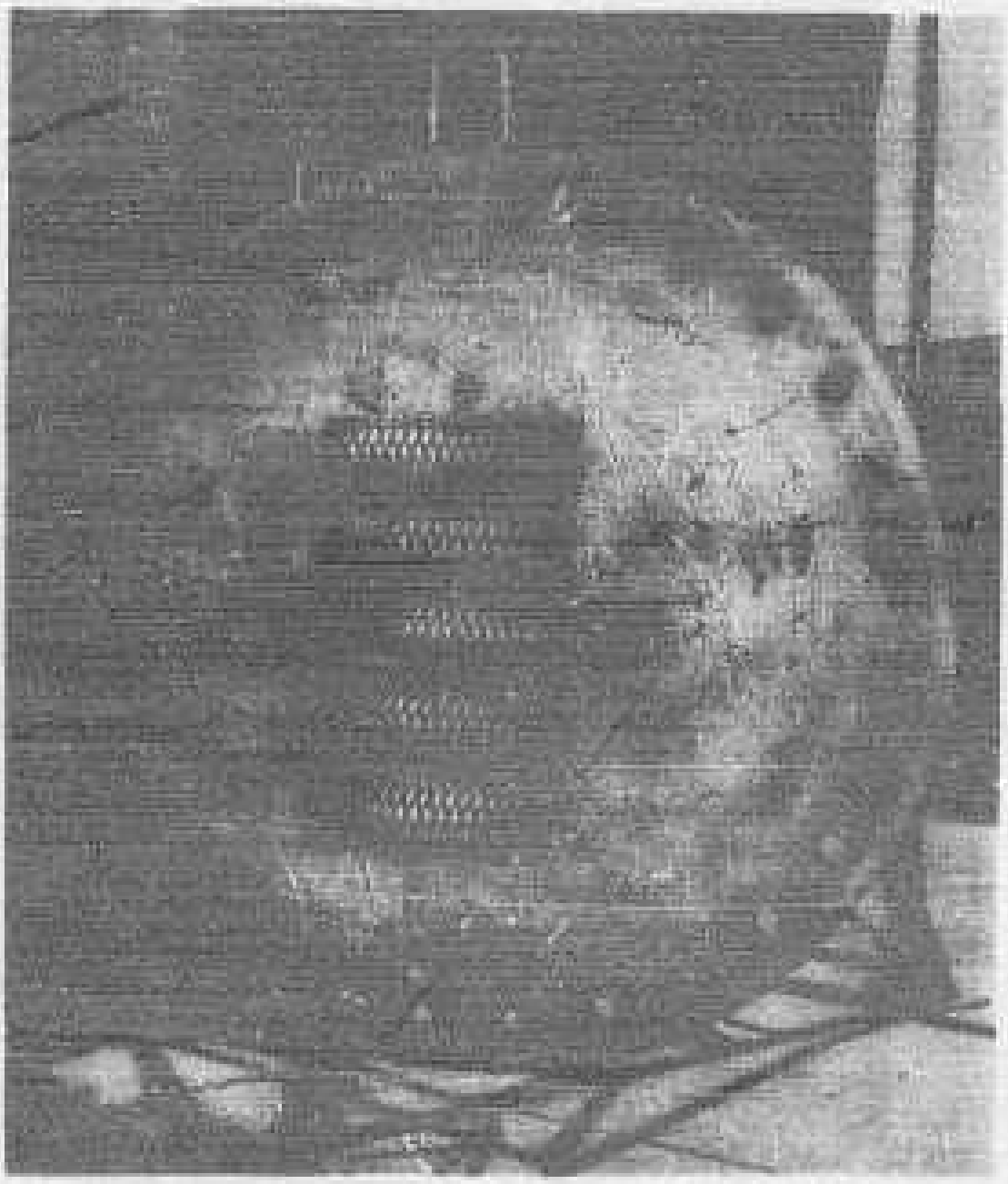

Figure 3 Rat Cage Mounted Against the End-plate of the Shock Tube

Figure 4 Guinea Pig Cage Mounted Against the End-plate of the Shock Tube

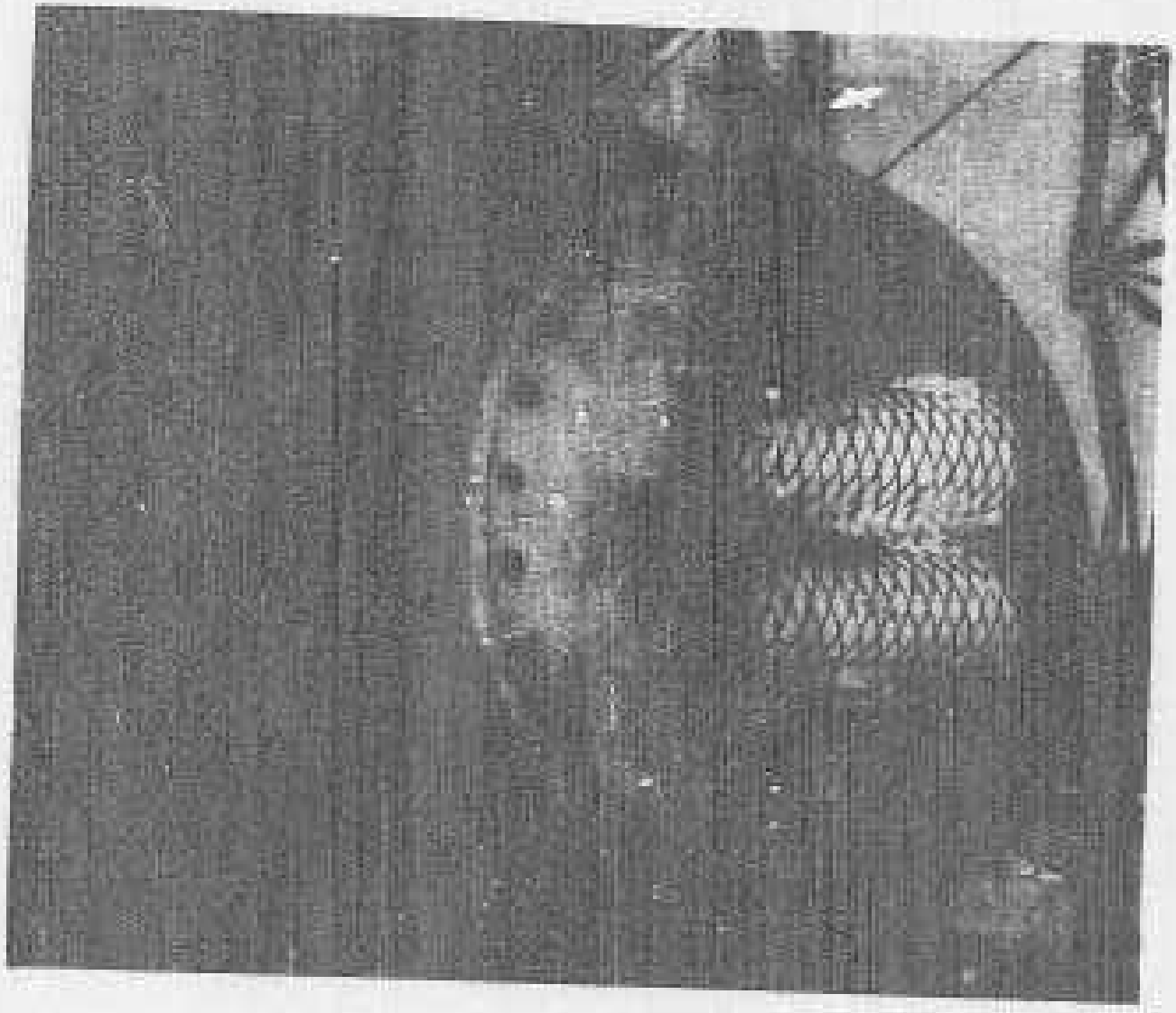

Figure 5 Rabbit Cage Mounted Against the End-plate of the Shock Tube

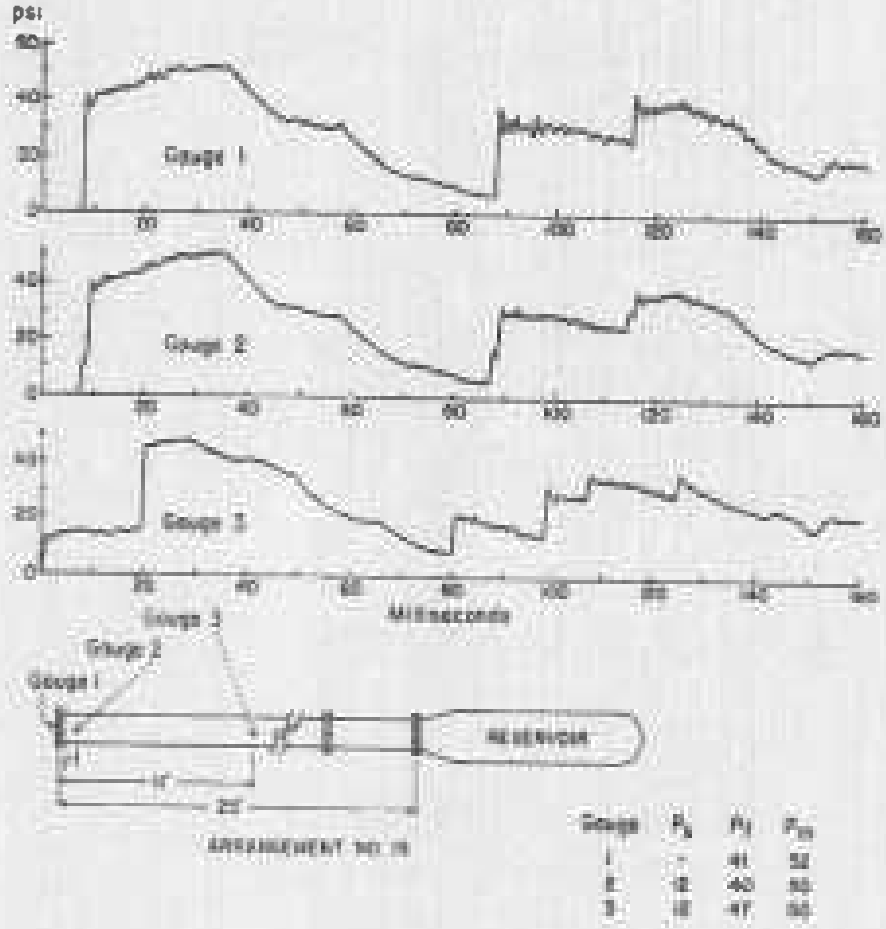

Figure 6 Pressure-Time Record Using Arrangement No. 15

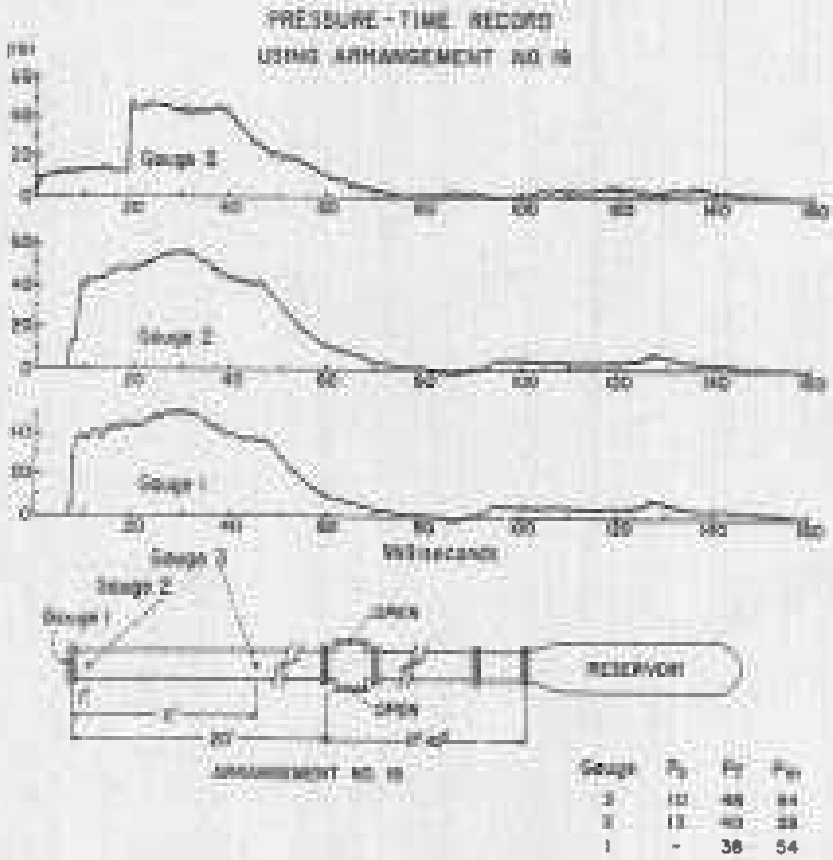

Figure 7 Records of Pressure-time Along Tube with Lateral Parts Open: Single Reflection

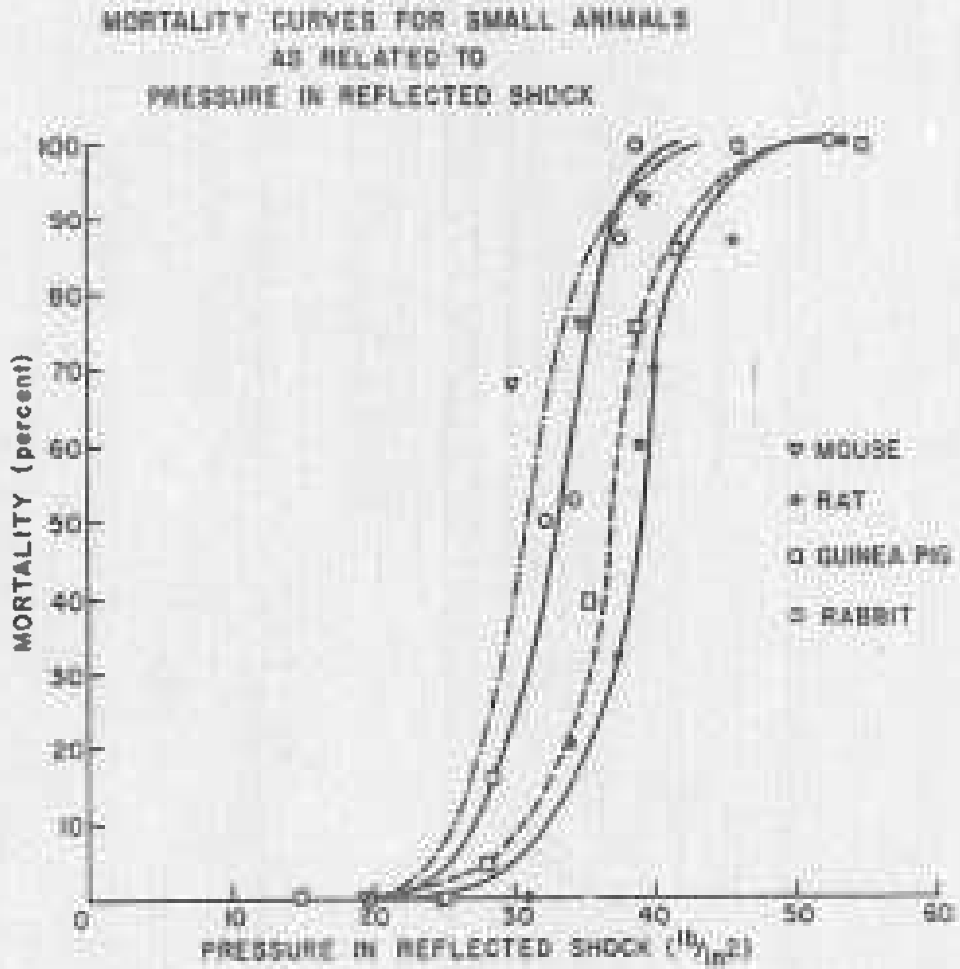

Figure 8 Mortality for Small Animal Species Exposed Against the End-plate of the Shock Tube as Related to the Pressure in the Reflected Shock

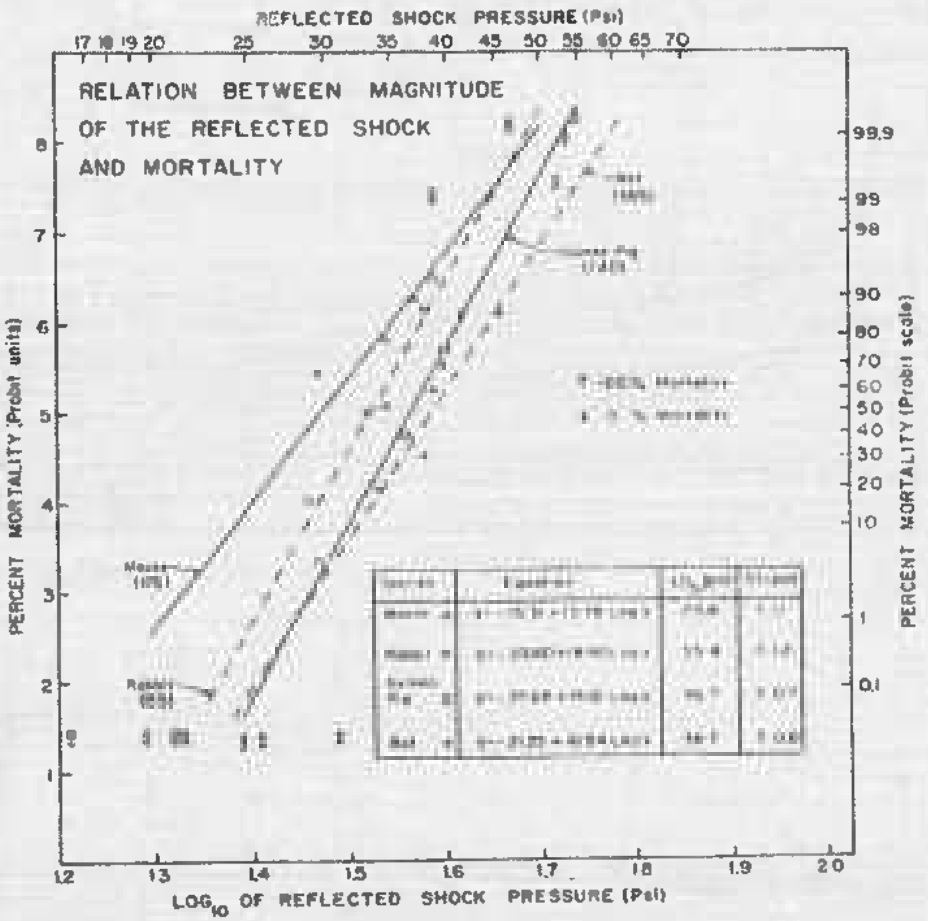

Figure 9 **Probit Regression Lines Relating Mortality for Animals Exposed Against the End-plate to the Reflected Shock Pressure**

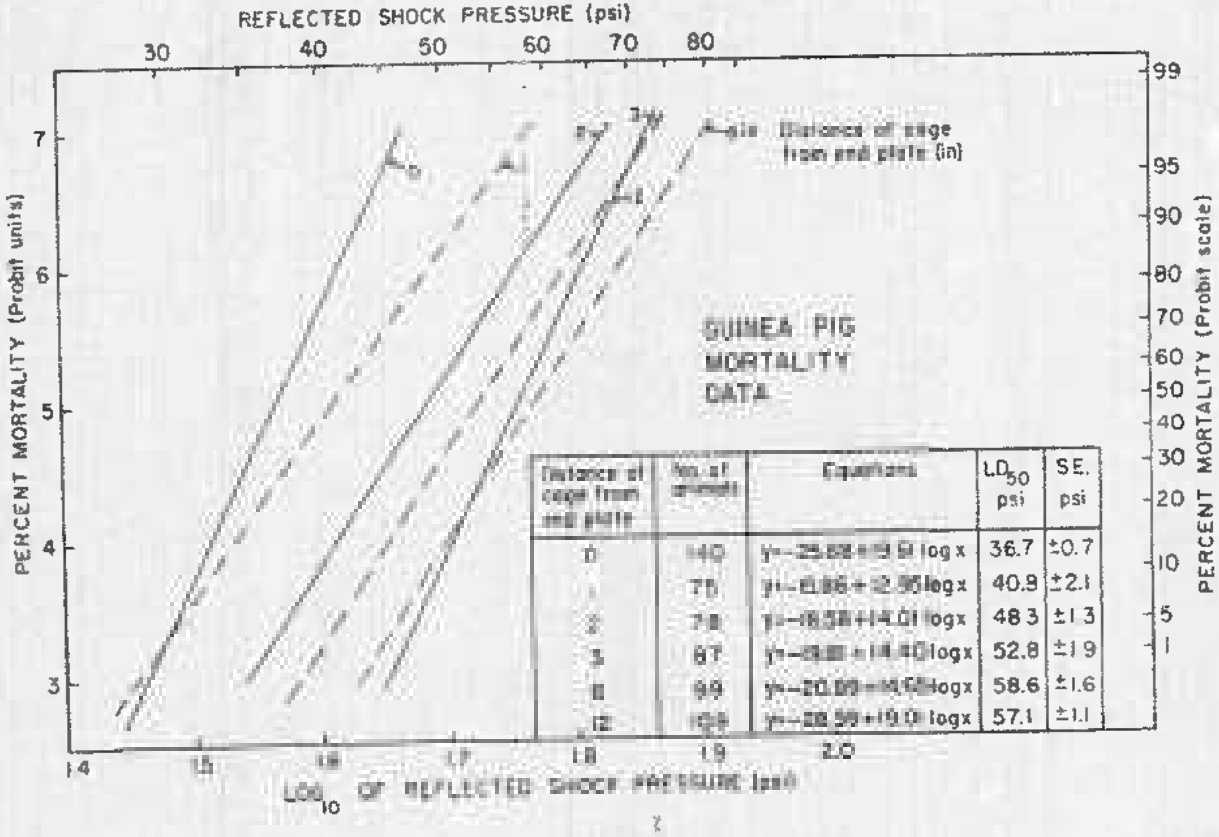

Figure 10 Probit Regression Lines Relating Guinea Pig Mortality at Various Distances from the End-plate to the Magnitude of the Reflected Shock

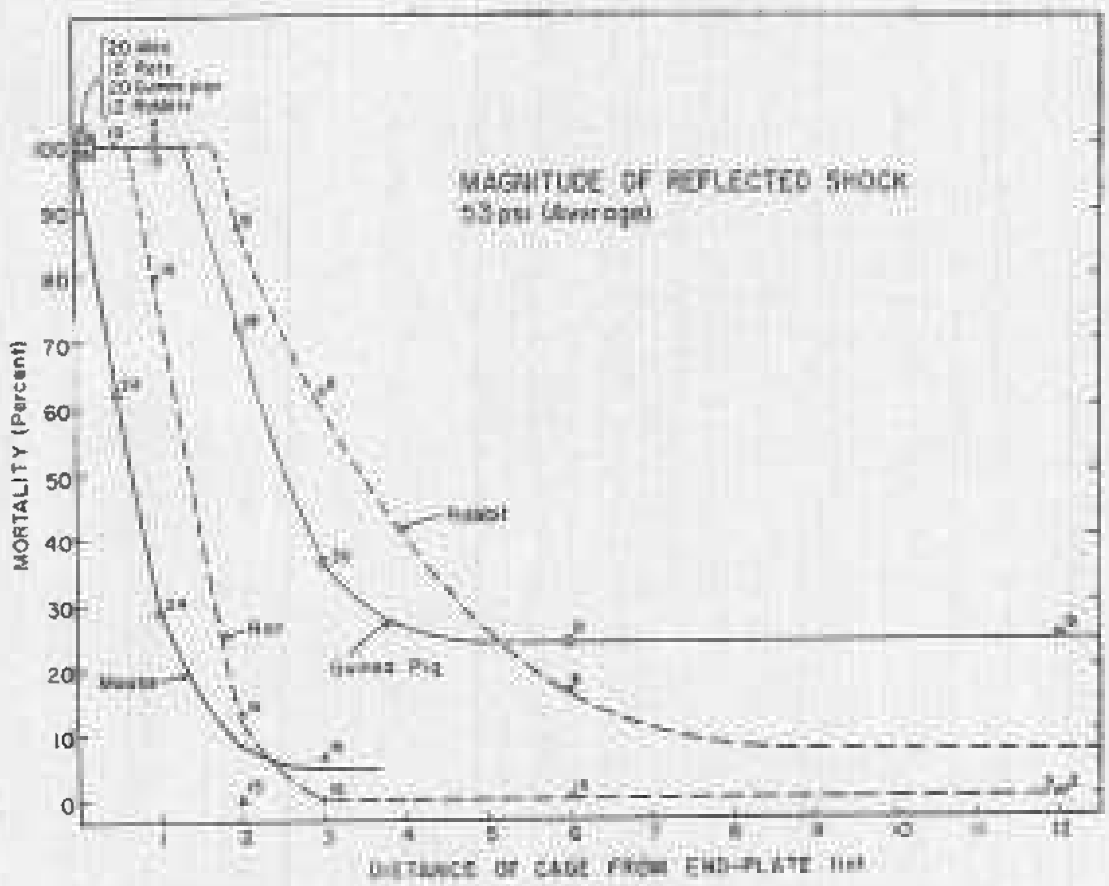

Figure 11 Mortality for Small Animals Located At Various Distances from the End-plate for Reflected Shocks Averaging 53 psi

PROGRAM FOR THE NCEL BLAST SIMULATOR

S. L. Bugg
Navy Civil Engineering Laboratory

GENERAL

Detailed descriptions of the NCEL Blast Simulator are contained in recent publications of the Society of American Military Engineers, American Society of Mechanical Engineers and the Society for Experimental Stress Analysis. Suffice it to say the simulator is a six-inch steel tube centered inside a 2-ft slotted tube which in turn is supported on four legs. Skirts eight inches apart are welded to the larger tube slot to direct the blast down upon the test specimen. The simulator is centered over a reinforced concrete pit 10 ft long, 9 ft wide, and 12 ft deep. Approximately 50 tons of steel and 175 tons of reinforced concrete were used in the construction of the simulator.

ENERGY SOURCE

The simulator depends primarily upon the use of Primacord as an energy source. Primacord is a high explosive detonating fuse which detonates at a rate of 20,000 ft per sec. One or more strands of the Primacord are centered in the 6-in.-diameter tube and exploded by the use of Composition C and two blasting caps. Very high pressures develop rapidly in the 6-in.-diameter tube and are vented to the 2-ft tube through 3000 holes drilled in the tube. Baffles at 15 in. intervals prevent reverberations in the tube. Intensity and duration of pressure in the large tube are controlled by the size of the charge, by the addition of nitrocellulose to the Primacord, and by the sequencing of 22 quick-opening valves on the simulator. These valves are solenoid operated and the orifice is one inch in diameter.

CRITERIA

The simulator was designed to produce pressures whose time of rise and of decay correspond to an atomic blast.

The design criteria for the simulator were as follows:

Time of rise to peak pressure	approx. 1 msec
Peak pressure	30 to 185 psi
Pressure decay	$P = P_o(1 - \frac{t}{t_o})e^{-\frac{t}{t_o}}$
Pressure duration	variable from 0.4 to 7.0 sec

Capabilities

The simulator was designed to test simple or fixed-end beams of 8 in. widths variable in depth from 8 to 12 in., and spans of 12-1/2 to 15 ft. Also, by utilizing the pit immediately beneath the simulator, 8-in.-wide frames with heights of 8 ft and spans of 12 ft may be tested for either vertical or lateral loads.

PROGRAM

Beams

Twelve 8-in.-by-10-in.-by-15-ft reinforced concrete beams have been tested for the following reasons: (1) to compare the results of previous small-scale beam tests (2) to learn more about the behavior under fixed-end conditions (3) to measure the response to uniform dynamic loading, (4) to determine the plastic hinge formation and diagonal tensile strength. Fortunately it was found that the simulator was sufficiently air tight to permit performing static control tests. The use of a Neoprene gasket and Teflon wipers produced almost no side friction and enabled the static and dynamic tests to be performed under identical support conditions.

In conducting these tests the results of the performance of the simulator and the test specimen are recorded by a 36-channel CEC oscillograph.

These tests demontrated the following:

1. Uniform loads were obtained in the simulator.
2. Good control was obtained over the time of pressure rise and decay.
3. 85 to 95% beam fixity was attained.
4. The dynamic magnification factor was 1.7.
5. The spring-mass system is valid for fixed-end beams.

CONNECTION TESTS

Approximately 40 specimens will be tested as a pilot program to determine the behavior of commonly employed connections under dynamic loading. Welded portal frame knees, beam-to-column connections, and column anchorages will be included. Portal frame members with square, curved, and haunched knees will be tested under both positive and negative moments. The beam-to-column connections will include shop-welded, bolted, and riveted specimens.

Instrumentation will include strain and acceleration records, plus reaction and deflection measurements.

FRAME TESTS

Twelve frame tests are planned. The prime purpose of these tests is the experimental verification of theoretical work already accomplished. Moment-rotation diagrams will be obtained for fixed and simply supported steel and aluminum frames with a span of 12 ft and a column height of 8 ft.

Some of the frames will be subjected to a uniformly distributed load on one column; others will be loaded on one column and on the beam. Deflections, pressures, accelerations, and strains will be measured.

ARCH TESTS

Dynamic loading of twelve arches is contemplated. These arches will have a span of ten feet. Uniform radial loading and lateral loading will be applied to arches of different stiffnesses and with various rise-to-span ratios. Instrumentation will be similar to that of the frame tests.

DYNAMIC RESPONSE OF SOILS TO AIR BLAST

It is desired to perform some basic studies on soils to determine their reaction to high intensity, rapidly applied loads. Initial dynamic tests will be made on dry, relatively cohesionless type soils. As the program progresses, the complicating influences of soil moisture and cohesiveness will be introduced into the program. The MIT Rapid Load Machine will be used to perform dynamic soil-shear-strength tests. It is believed that the NCEL simulator can be effectively used to determine the dynamic soil bearing capacity. Comparison will be made between the bearing capacity and modulus of reaction of soils as determined in field tests and in the dynamic tests made on a smaller dimensional scale in the rapid load machine and the blast simulator.

SOIL STRUCTURE MODEL TESTS

Utilizing information developed from previous tests, soil-structure models will be devised for testing in the blast simulator. Tests will be made on earth-covered models of rings, beams, and arches placed between the blast simulator skirts. Interaction of the models and the soil will be studied by means of high speed motion pictures made through transparent panels in the simulator skirts. Deflections, pressure, and other measurements will be recorded. The effects of the following variables will be investigated:

(1) Flexibility of structures

(2) Configuration of structure

(3) Ratio of structure span to depth of cover

(4) Soil environment.

This program has been planned to extend over a three-year period. Results to date warrant an optimistic outlook.

FACTORS IN THE DESIGN OF SHOCK TUBE FACILITIES

D. B. Singer
Armour Research Foundation
of Illinois Institute of Technology
Chicago, Illinois

The purpose of this paper is to discuss several of the factors which enter into the design of shock tube facilities. These factors can be grouped into four headings: structural integrity and economy, personnel comfort, utilities, and public relations aspects.

Structural integrity and economy can be achieved by carrying out a dynamic analysis of the foundation, and where the natural bearing capacity of the soil permits, to utilize the mass of the foundation mat for resistance to the extremely high impulse which develops when the tube is fired. To show in detail how this mass can be utilized, we give as an example a brief description of our experience with the foundations for the 6-foot shock tubes installed at the Air Force facility at Gary, Indiana and a projected design for a new facility.

The loads which develop as a result of shock tube firing are very high. Figure 1 shows two peak pressure-time loadings predicted for the tube in the new facility. The corresponding peak forces are 812,000 and 340,000 lb which are of the order of magnitude of thrusts developed in the launching of current long-range missiles and satellites. To the structural engineer such forces appear enormous in nature because, in the case of the higher load, the force developed is about as great as the wind load he might use in designing a 50-story skyscraper.

The designer's first inclination is to resort to batter piles, using a construction as shown in Figure 2. However, a dynamic analysis of the foundation should be conducted to determine whether or not a somewhat heavier mat would perform as well as pile construction. An analysis of this type was in fact performed for the installation at Gary and it was shown that the mat foundation would perform as well as a pile foundation, at a considerably lower price.

For this reason, the design of the projectiled facility was approached in terms of the spread mat. As in the case of the Gary facility, the behavior of the mat was represented by single mass acted upon by a dynamic load, and subjected to a constant resistance. Some of these assumptions will be discussed briefly.

The assumption of a single mass is based on the fact that stress waves in concrete will move at velocities given by the familiar

$$V = \sqrt{\frac{E}{\rho}}$$

which, for concrete, is somewhat less than 10,000 ft/sec. Assuming a mat 100 ft long, it turns out that a force applied at the middle will reach the ends in about 5 msec, which is considerably less than the durations of loading. For this reason we may consider that the entire mat, if it is tied together adequately from a structural point of view, can be regarded as a rigid body under the action of a single force.

The resistance to the motion of the mat was assumed to come from three sources: (a) the estimated frictional resistance of the mat developed at the mat-earth interface, (b) the so-called passive earth pressure of the mat at the end, and (c) the frictional resistance between the shock tube sections and the mat. These resistances are, for the most part, approximately constant throughout the life of the foundation. We would expect only that the passive earth pressures would not develop fully during the early firings of the tube, and that some compaction of the soil would take place. But after this initial compaction, the soil can be relied upon to develop the passive pressures it is given credit for. To minimize this compaction, it is recommended that specifications for the construction of such facilities be explicit in requiring that backfill around the foundation mat be carried out using good, clean soil materials having a high bearing capacity, and that proper consolidation and tamping procedures be employed.

Using the above assumptions it was possible to write the equation of motion for the mat, and to solve for its maximum displacement, starting with some assumption as to its initial mass. It becomes clear after a few trials that conventional mats simply would not work; the relatively low resistance furnished by friction and passive earth pressure resulted in such a high initial velocity of the mat that it had to move for an appreciable distance before the kinetic energy was dissipated. To decrease this movement without using expensive means, only one avenue seemed open: to bring into play greater passive earth forces. It was in this way that the idea of mat stems was born, a device that has proved itself in the Gary installation. Figure 3 shows a typical geometry for such stems. This device must be employed with care, because clearly spacing of the stems too close to each other will vitiate the tendency of the enclosed soil masses to react passively to the stems. Analytically, a measure of the spacing is provided by computing the lateral spread corresponding to a given height of naturally heaped soil. For a good bearing material such as sand, this lateral spread can be computed from the simple relation

$$L = 2H/\tan\phi',$$ as is

shown in Figure 4. ϕ' depends on the angle ϕ, which is known in soil mechanics as the angle of internal friction of a soil. For a 5-foot high stem, the distance L is about 11 ft. Using a somewhat high spacing, then, one is able to count reliably upon greater passive earth pressures and to prevent the mat from developing an excessive initial velocity. The table below shows the results of various trials of mat widths, thicknesses and stems, and the displacements computed for each combination (Figure 5). It should be noted here that the incremental volume of concrete required for the stems and thickened mat is on the order of 160 cubic yards of concrete, which can

be put in place for about $5000, which is less than the cost of a pile design for this foundation.

Structural integrity is also affected by the placing of steel reinforcement. Several points should be noted here. First, the longitudinal reinforcement in the central section of the mat should be substantial to provide for length-wise bending moments. Second, the stems should be reinforced in their vertical faces to permit them to act as cantilevers, the reinforcement being extended well into the mat. And finally, the toes of the stems and the lower face of the mat should be reinforced to resist transverse bending moments. Figure 6 shows this placement.

A second factor in the design of the tube is personnel comfort, or discomfort, in experiencing floor shocks. Psychologists have reported that for low frequencies up to about 8 cps, accelerations of 0.7g or less can be unpleasant, and even intolerable. These values apply to a person in the standing position facing the direction of acceleration, sideways tolerance is much lower.

Knowing the displacement-time history of the mat, one can compute the peak acceleration it is subjected to, and compare this with data on human comfort and discomfort as related to bodily acceleration. This comparison provides a guide to the choice of maximum permissible displacement. The slab is then proportioned to give a displacement not exceeding this amount.

The tube at Gary is being operated at loads somewhat higher than those contemplated in the original design. The slight movement of the slab which has been noticed, has been estimated to be between 1/16 and 1/8 in. The new tube is being designed to have essentially zero movement and consequently will have tolerably low accelerations.

A word about utilities. While a proper design should not result in appreciable longitudinal motion, it is entirely possible that some small motions and shocks may develop in the early life of the foundation. It is therefore desirable to attempt to bring in utilities, such as water, power, and sewage lines, in such a way that the longitudinal joints in these lines will bear the brunt of imposed shocks. Since such joints are usually designed to absorb small motions, no leaks in the system should result.

Finally, the noise which accompanies firing of the tube may constitute a nuisance from a public relations viewpoint. Two paths of action are open: first, one can consult acoustics specialists for their recommendations in abating the firing noise, or second, one can locate the tube at a remote site. This problem need not be a major problem in designing a tube facility, but some thought should be given to it.

We remark, in summary, that the design of a shock tube facility should be governed, among other things, by considerations of structural integrity and economy, psychological comfort levels, protection of utility connections, and noise abatement in the community. Dynamic analysis of the foundation provides a guide to a practical solution of these problems.

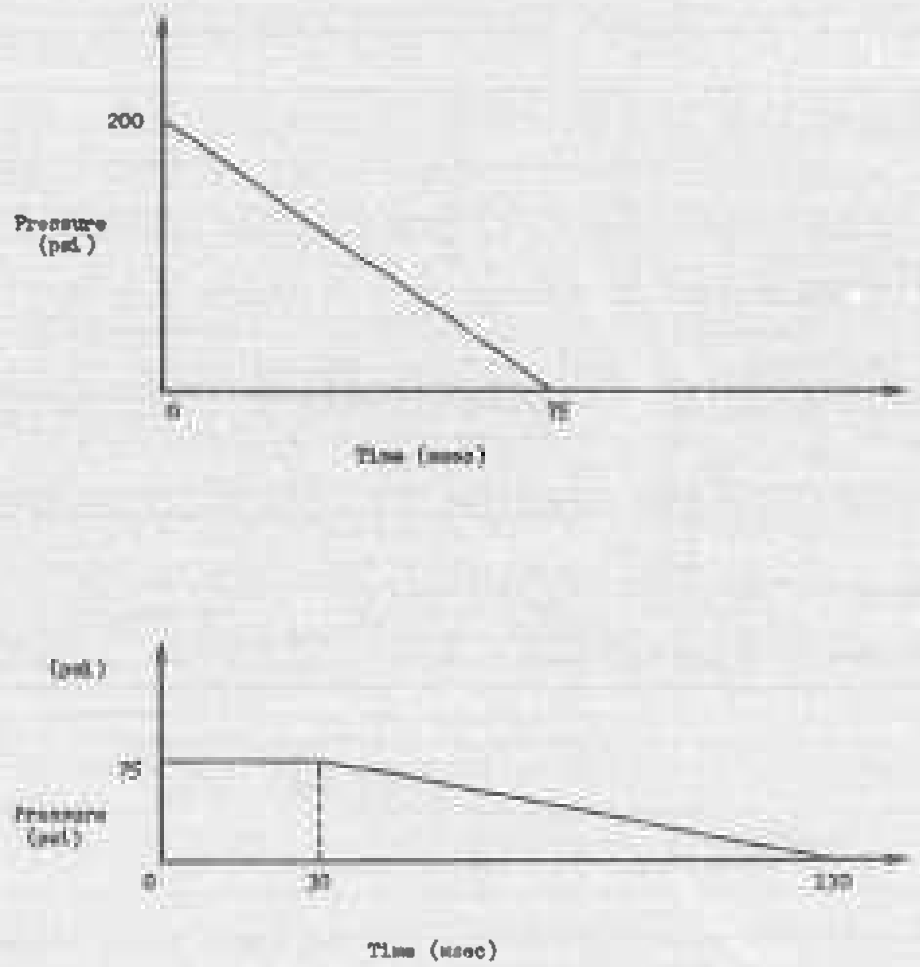

Figure 1 Peak Pressure-Time Loadings on Shock Tubes

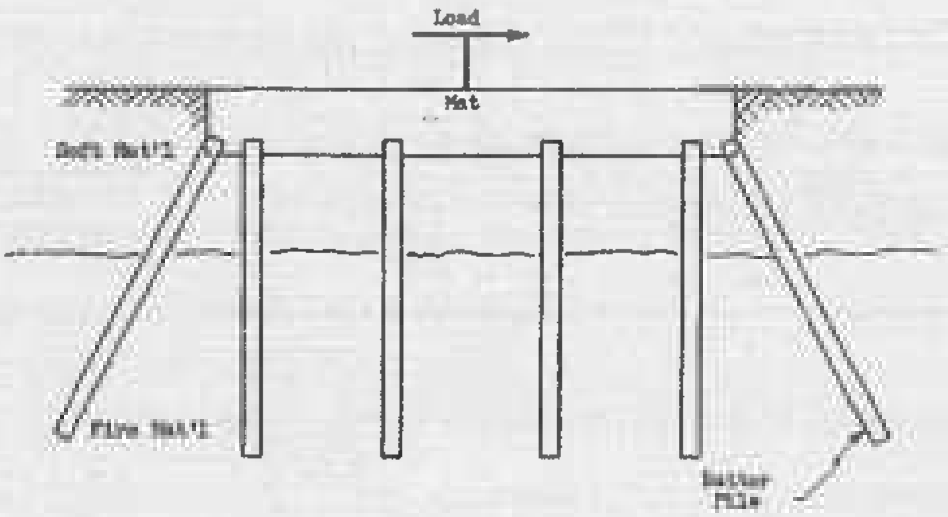

Figure 2 Conventional Foundation for Extreme Lateral Load

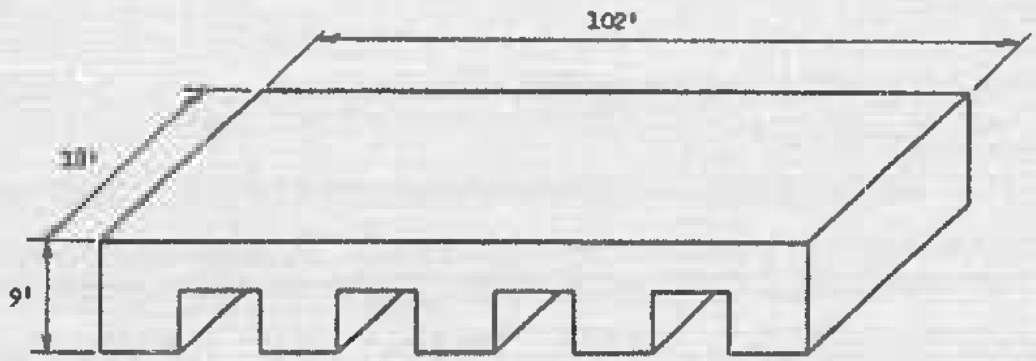

Figure 3 Geometry of Mat Using Stems

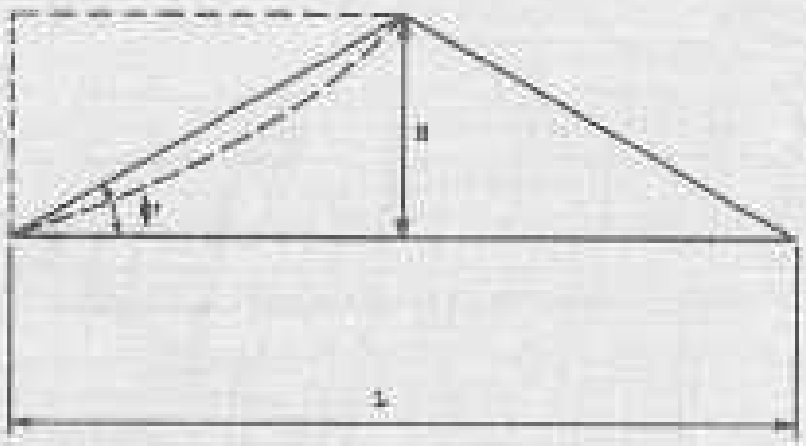

$$L = \frac{2H}{\tan \phi'} \qquad \phi' = \frac{\pi}{4} - \frac{\phi}{2}$$

Figure 4 The Geometry of Natural Heaping of Soil

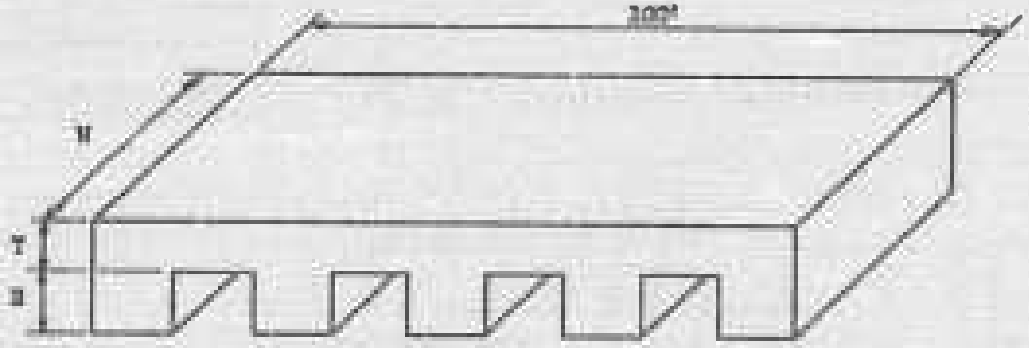

W (ft)	T (ft)	H (ft)	Vol (c.y.)	X max. (in.)
8	2	3	70	1 1/2
12	4	4	210	1/16+
12	5	4	260	1/32+
15	5	4	310	1/64-
18	5	4	370	.000+

Figure 5 Displacements Associated with Various Trial Mats

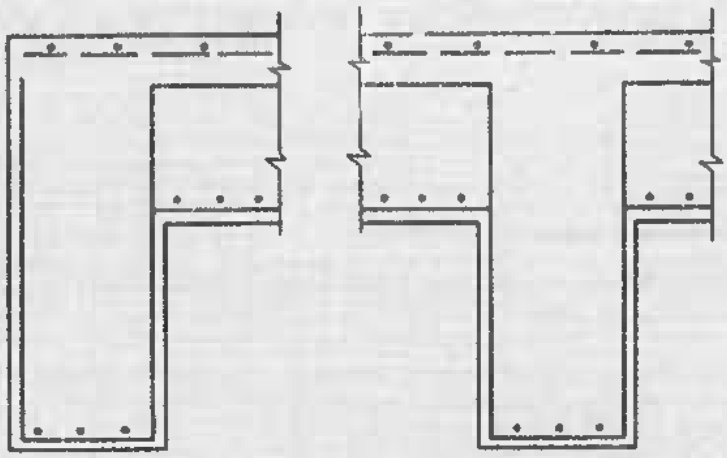

Figure 6 Placing of Reinforcement in Mat

THE SHOCK CHAMBER:

A DEVICE FOR PRODUCING HIGH STRENGTH, SPHERICALLY EXPANDING SHOCK WAVES

Kenneth Kaplan and A. B. Willoughby
Broadview Research Corporation

In studies of the loading of structures due to shock waves of high strength, it is desirable to subject the objects being studied to spherically expanding waves. While at the shock front the characteristics of shock interactions with reflecting surfaces can be determined with shocks from any source, behind the front, the overpressure and flow are dependent on the manner in which the shock wave is propagating. This dependence is especially important in the high shock strength region because of the importance of dynamic pressure loadings in this region. At a shock strength of only 5.6 (an overpressure of about 68 psi) dynamic pressure is already equal to overpressure, and at higher strengths exceeds the overpressure.

An obvious shock source for investigating the loading of structural models subjected to high strength spherically expanding shocks is that of spherical high explosives detonated in normal ambient conditions. However, there are certain practical limitations to the use of these sources. First, in scaling from certain full scale situations it is often necessary to use large quantities of TNT (order of hundreds of pounds) in order to achieve the proper relation between pulse length and model length even when using the smallest models which can be adequately instrumented. Second, any model which was subjected to shock from HE sources in normal ambient conditions would have to withstand the high actual overpressures associated with high strength shocks.

The subject of this paper, the Shock Chamber, is a research tool designed to overcome these limitations on the use of HE in normal air. It consists basically, of a steel vessel which can be evacuated, and in which small HE charges can be detonated. The resulting shock waves are then allowed to impinge on test models which are also in the chamber, and which are so located that wall reflections do not arrive at the models until after the time of measurement.

In effect, by detonating a charge in reduced ambient pressure conditions, the charge size is increased in direct ratio to the reduction in pressure. Thus, if 50 lb of HE are required to produce the proper loading on a given model in normal air, in the shock chamber operated at 0.01 atmosphere only 0.5 lb would be required to conduct the same tests. In addition, by using reduced ambient pressure conditions, a desired shock strength can be obtained without accompanying excessive actual overpressures. For example, a shock strength of 20 indicates an actual shock overpressure in free air of about 280 psi, but in an ambient pressure of 0.01 atmosphere the actual shock overpressure would be only about 3 psi. The effect is even more striking for reflected shocks (which would ordinarily determine peak model loadings). In the above example the strength of the reflected shock after a normal reflection would be

"NOTICE: When Government or other drawings, specifications or other data are used for any purpose other than in connection w a definitely related Government procurement operation, the U.S. Government thereby incurs no responsibility, nor any obligation whatsoever; and the fact that the Government may have formulat furnished, or in any way supplied the said drawings, specifications or other data is not to be regarded by implication or otherwise in any manner licensing the holder or any other person or corpo tion, or conveying any rights or permission to manufacture, use o sell any patented invention that may in any way be related there

about 122, corresponding to an overpressure of about 1780 psi in normal air, but to only 17.8 psi in 0.01 atmosphere.

The operating principle of the shock chamber is found in the ambient pressure scaling relationships due to Sachs (for which there already exists some experimental confirmation). These relationships are shown in Figure 1, along with the normal cube root scaling relationships.

Note that the quantity W/P_o in the Sachs scaling relationship appears in the same manner as does the charge weight W in the standard relationship. W/P_o has therefore been termed the effective charge weight.

From these relationships it can be seen that:

1) P/P_o = shock strength will remain constant if the charge distance divided by the cube root of the effective charge weight $\left[d/(W/P_o)^{1/3}\right]$ remains constant.

2) Time is unchanged if, in addition, the effective charge weight is unchanged.

Thus, both the shock strengths and pulse lengths from a charge of W pounds in a normal atmosphere would be duplicated in an ambient pressure of 0.01 atmosphere by a charge weighing only 0.01 W lb.

It is to be expected that this type of scaling will break down at positions close enough to the charge so that the expanding ball of detonation gases is close to the shock front. However this region is ordinarily not useful to us since the purpose of the device is to produce the high shock strength waves in air rather than in gaseous detonation products. We are therefore limited to that portion of the pressure pulse in front of the contact surface, that is, the surface between normal air and the gaseous detonation products.

PRETEST CHAMBER DEVELOPMENT TESTS

The development of the device is proceeding in two stages. During the first stage a small, pre-design test (or pretest) chamber was built. This was done for a number of reasons, but primary among them were: first, to verify the scaling relations at high shock strength; and second, to investigate the relationship between the shock front and contact surface. This chamber, at first constructed, is shown in Figure 2. It is a cylindrical vessel 5 feet in diameter and 9 feet long fitted with four nozzles (in addition to that used for evacuation). The vacuum pump is on the left, and the vacuum monitoring gauges are in the foreground. The nozzle on the right provides a port for charge insertion. The charge location can be varied over a range of about 2-1/2 to 5-1/2 feet from the right hand tank wall.

The pressures measuring probes are cylindrical and 1/4 in. and 1/2 in. in diameter where measurements were made. They are fitted with barium titanate ceramic pressure sensors both in the probe tips and along their sides. The sensors at the probe tips were to be utilized in the nozzle

directly opposite the charge to detect the contact surface separating shocked air from gaseous detonation products.

Difficulties were encountered, in these early tests, in acquiring satisfactory pressure records at ambient pressures of 0.1 atm and below. Unfortunately it appears that these difficulties were due to the simultaneous effect of a number of causes, (e.g. spurious ionization signals, and non-uniform charge detonation and reproducibility) making the elimination of them a somewhat lengthy operation. In previous tests under normal atmospheric conditions the same charges (27 gm of Comp A) as were used in the Pretest Chamber proved very reproducible and gave rise to clean sharp fronted shock waves. However by reducing ambient pressures, we (in a sense) moved much closer to our charge, where non-uniform shock generation is more likely to take place.

Investigation revealed that the best charge performance was obtained by making measurements on the axis of the detonator. At the end of this testing period about half of the charges were yielding sharp shock fronts and moderately smooth pulse shapes in the shock strength range from about 10 to 50. Typical pulses are shown in Figure 3.

In the tests conducted during this phase the arrival of the contact surface during the early portion of the pressure pulse was not detected even for shock strength of 40 to 50.

Following the initial tests, the pretest chamber was modified by the addition of a 2-foot diameter quick opening door and a stand on which to mount models. Several generalized topographic models of steel were fabricated which could be assembled in a number of ways and in particular as a 15-degree symmetrical valley, and as 15 and 30-degree symmetrical ridges. These models are shown in Figure 4. They are 24 inches wide (normal to the direction of shock propagation) and, for measurements made along their center line, are essentially infinite in width. Each slope is 3 inches long, and a flat portion 12 inches long in front of the shapes was provided for making monitoring measurements.

For convenience, throughout the test program, a single ambient pressure of 0.05 atmospheres (and therefore a single effective charge size) was utilized. Measurements were made both on the shapes themselves and on the 12-inch long flat portion, the latter serving both as monitor measurements and to provide flat terrain reference data. Charge reproducibility and the ability of the 27 gm charges to generate clean shocks appeared to have been improved so that approximately two-thirds of the detonations produced relatively clean shocks.

The reference data is shown on Figure 5, as a plot of equivalent free-air pressure (P/P_0) versus scaled distance ($d/(W/P_0)^{1/3} = d/W_e^{1/3}$). The standard deviation of the mean values of the measurements (as many as 16 observations were made at certain scaled distances) are also shown. For comparison, two similar curves from the literature have also been plotted, one arrived at in a manner similar to that used here (in that ambient pressure as low as 0.1 atmosphere were used). However, these were carried only to scaled distances

of 2. The second curve was published in 1956 after an extensive series of tests in normal atmospheric conditions with 1/2 to 8 lb spherical pentolite charges. It can be seen that the shock chamber derived curve follows the general trends of the others, agreeing particularly well at small scaled distances with that developed in a normal atmosphere.

For us, the most intriguing results of these tests were the effects which were observed on the back slopes of the ridge models. These effects were so striking that they could not be ignored, even though there was little time for their quantitative analysis. It was found that pressures throughout the shock waves, and the apparent positive durations of these waves were reduced to a very significant degree. Indeed the effects were large enough to be attributed, at first, to some sort of gauge deficiency. This no longer appears to be a possibility, however, for they were noted and appeared reproducible with a number of different gauges in various positions on the slopes. The effects are illustrated in Figure 6, which is a sketch of pressure-time readings taken during one shot at the center of the rising slope and at three locations of the falling slope. These readings have been normalized by dividing the measured pressures by predicted flat terrain pressures (from Figure 5) at the various stations.

At present we ascribe this pulse shortening to the formation and passage downstream of a vortex at the crest of the model, though further study would be required to validate this thesis.

Although further development work is needed in order to achieve maximum utility of the shock chamber, the experiments just described have demonstrated the utility of such a device.

At the present time the design of the final shock chamber has been completed. Its shape was originally thought of as hemispherical with the explosive charges detonated at the center of the plane surface. This shape, of course, is ideal for conducting tests with a large number of models. However, testing more than one or two models at a time seems unlikely because of the excessive instrumentation requirements for such testing; therefore, the hemispherical shape would be wasteful of space. Consideration was given also to using cone-shaped and truncated-cone-shaped vessels in which some wall reflections would be allowed. However, after analysis of these, it appeared that a vessel with walls far enough removed from the charge to prevent interference at the measuring station between reflected and primary waves would be most satisfactory. Such a vessel could, if economy of space were important, contain conical elements at locations in which reflections from them would not interfere with measurements, but the best shape from a standpoint of simplicity of construction and, therefore, of cost appears to be cylindrical. The dimension of the vessel for the desired scale factor and boundary conditions would be some 10 feet in diameter and about 20 feet long. A drawing of the proposed vessel is shown in Figure 7.

Reduced Ambient Pressure Scaling Relationships (Sachs 1946)	Normal Air Scaling Relationships
$\frac{P}{P_o} = f\left[\frac{d}{(W/P_o)^{1/3}}\right]$	$P = f\left[\frac{d}{W^{1/3}}\right]$
$\frac{I}{P_o(W/P_o)^{1/3}} = g\left[\frac{d}{(W/P_o)^{1/3}}\right]$	$\frac{I}{W^{1/3}} = g\left[\frac{d}{W^{1/3}}\right]$

Where:
- P = Shock Pressure
- P_o = Ambient Pressure
- d^o = Charge Distance
- W = Charge Weight
- I = Shock Impulse

Figure 1. Scaling Relationships

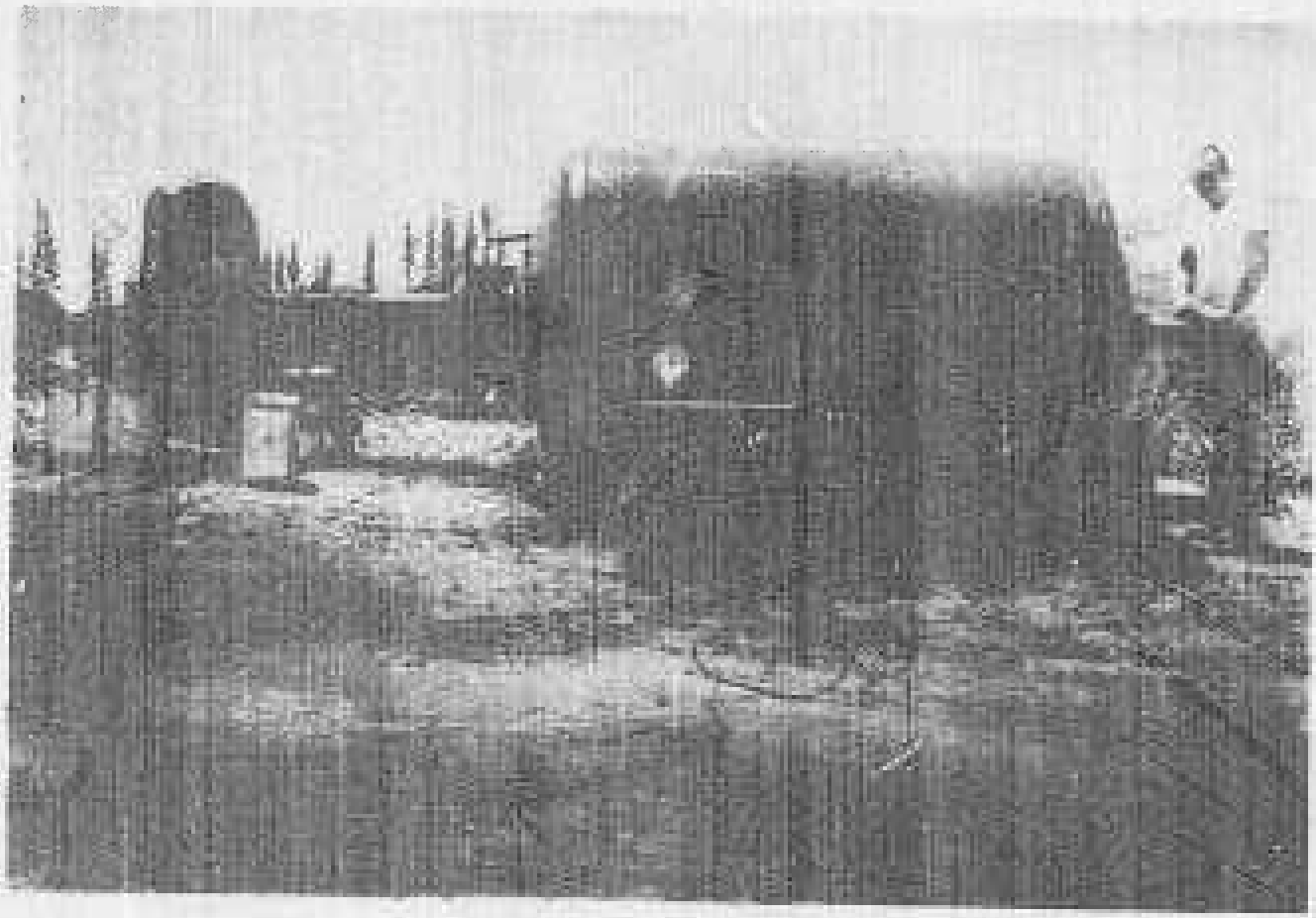

Figure 2 Pre-test Shock Chamber

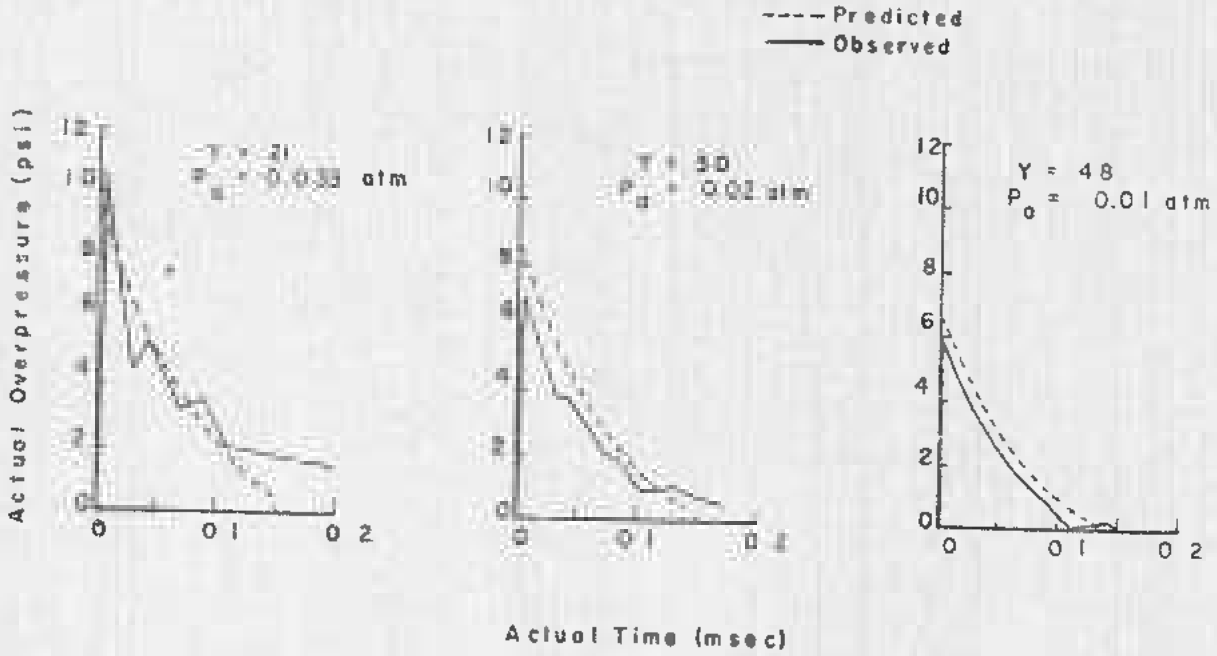

Figure 3 Typical Shock Chamber Pulse Shapes

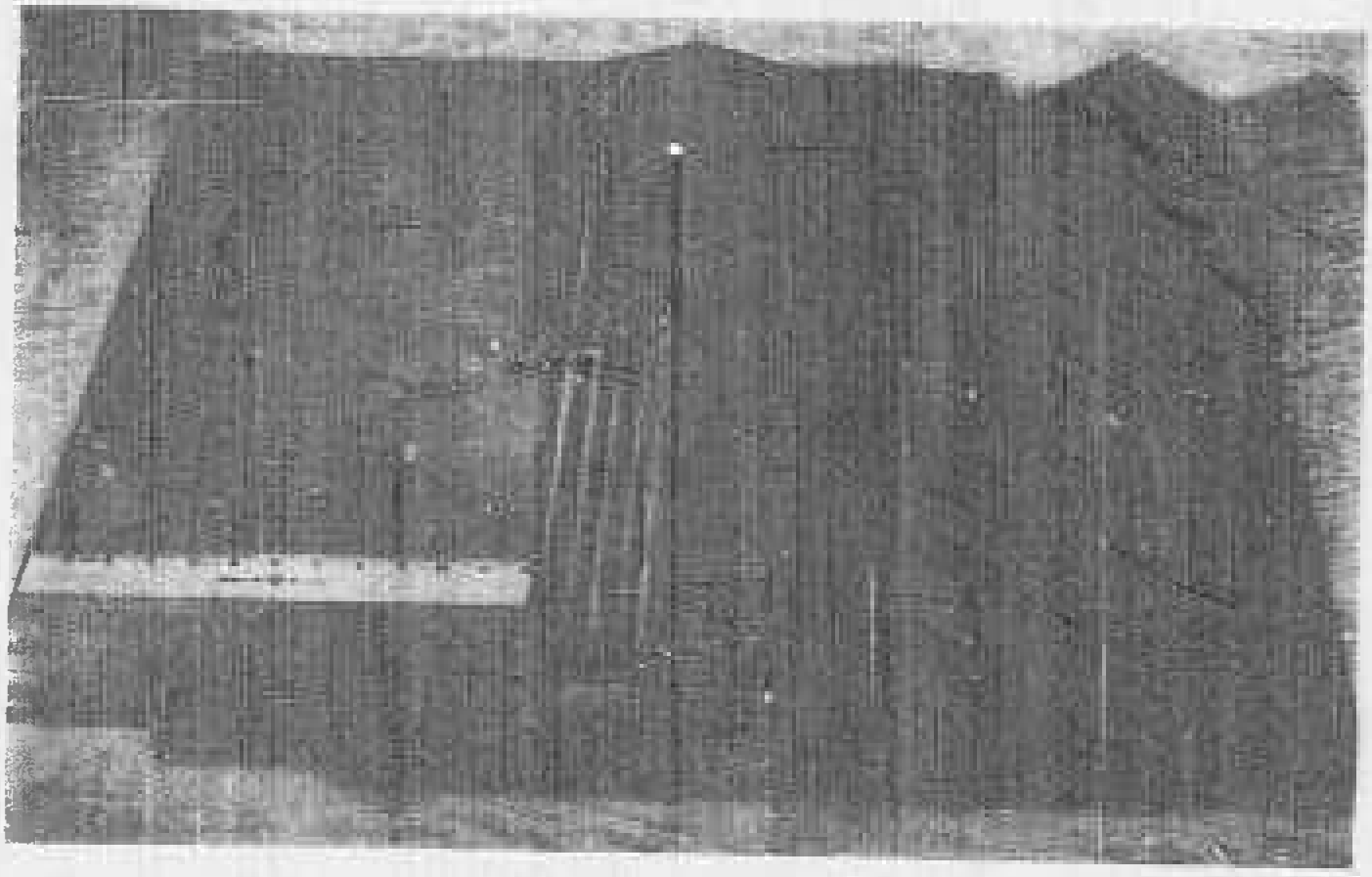

Figure 4 Model Assembled As for Test of 15-degree Symmetrical Ridge. On the Right is the Assembled 30-degree Symmetrical Ridge. The 15-degree Ridge Elements Were Also Used As 15-degree Symmetrical Valley Elements.

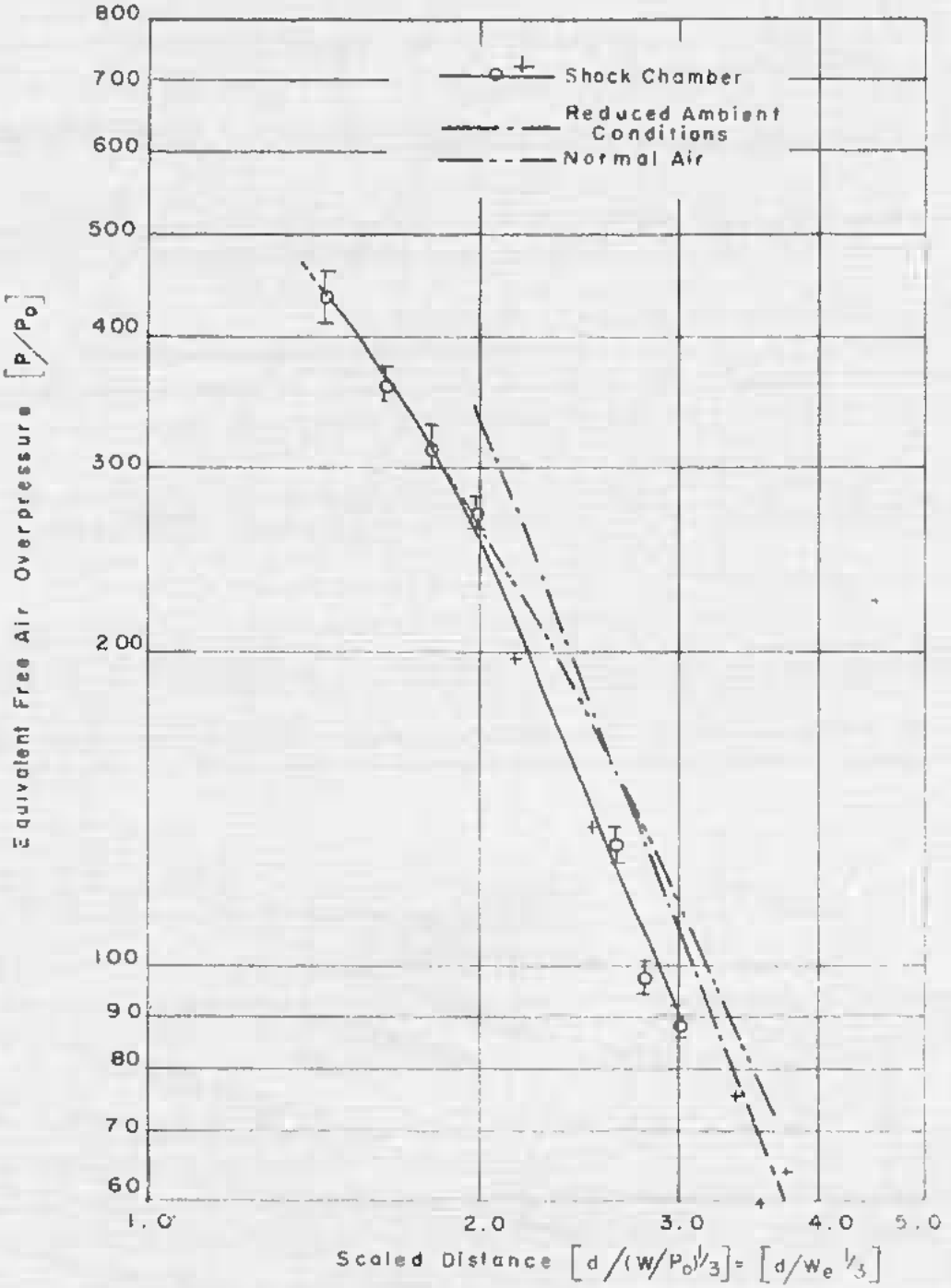

Figure 5 Equivalent Free Air Overpressure Versus Scaled Distance

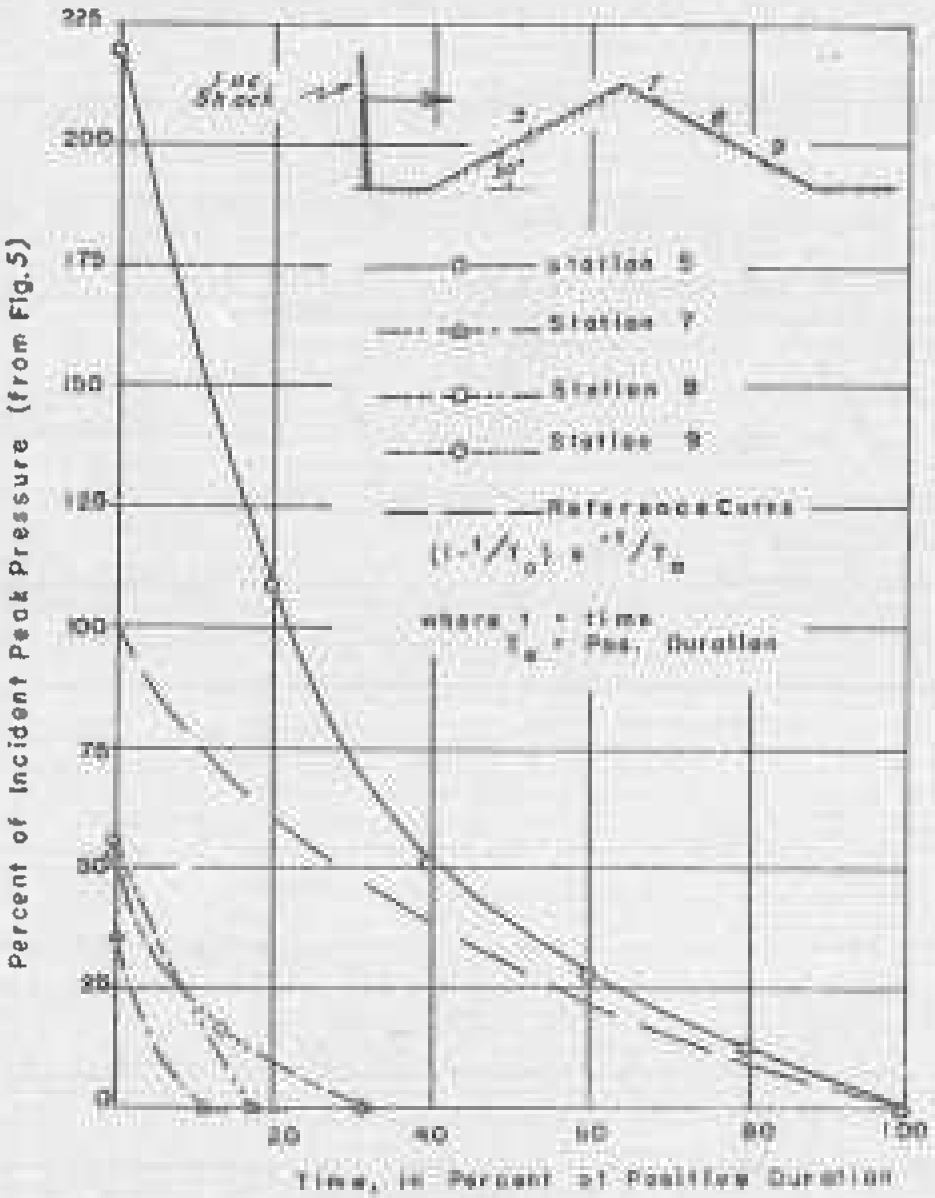

Figure 6 Approximate Pulse Shapes at Stations 5, 7, 8, and 9 of the 30-degree Ridge Model

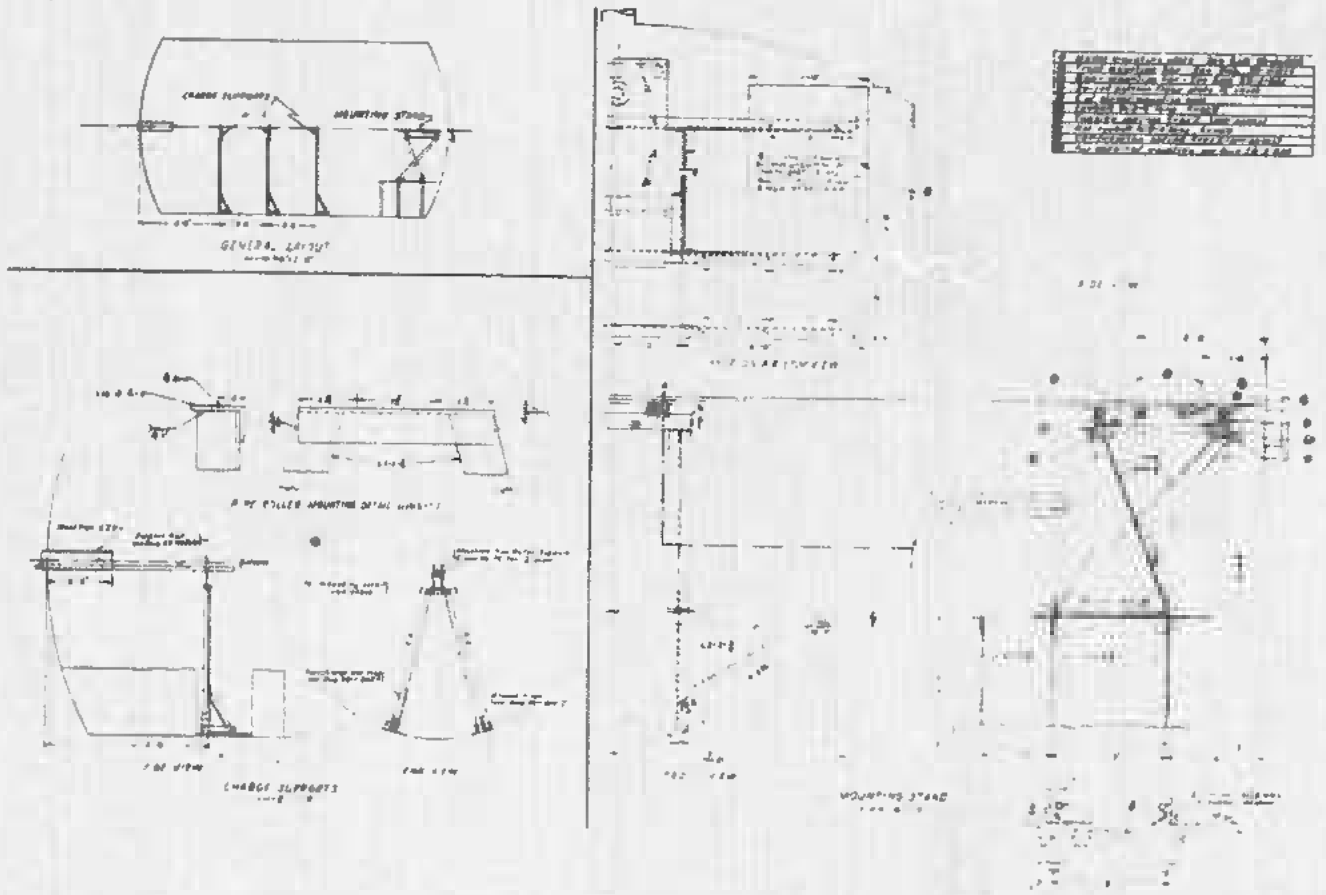

Figure 7 Final Shock Chamber Design

A ONE-INCH FORCE GAGE FOR DRAG MEASUREMENTS IN THE SHOCK TUBE

William G. Zuke
U. S. Naval Ordnance Laboratory

I. PURPOSE OF SMALL FORCE GAGE DEVELOPMENT

The Naval Ordnance Laboratory's participation in atomic field operations included measurements of drag force on simple model shapes. After the field data had been partially reduced and analyzed, it was necessary to conduct laboratory tests in shock tubes and wind tunnels to help understand and elaborate the field data. The field force gages ranged from 3 to 10 inches in characteristic dimension and the NOL shock tube, available for tests, had a 4-inch by 8-inch cross-section. To test the field gages, facilities such as the Ballistic Research Laboratory's 2-foot diameter shock tube or Armour Research Foundation's 6-foot diameter shock tube had to be used. When these facilities were used, each test series became a miniaturized field trip with the associated problems of scheduling, transportation arrangements, inability to repeat tests after data reduction and analysis, etc.

Because of these difficulties it was proposed that a small force gage be developed for use in the 4-inch by 8-inch shock tube at NOL. It is the purpose of this paper to describe the development and characteristics of that gage.

II. CHARACTERISTICS OF THE GAGE

A. General Design Characteristics

Gages used in the field were spheres, cubes, and circular and square cylinders. The square cylinder, or parallelepiped shape, was selected for the initial model primarily because the design and test problems for this shape would be less complicated than for other shapes.

The size of the gage was limited by the smallest practical size of the sensing element which could be used and by the size of the shock tube. The field gages had three orthogonal force sensing axes. The new gage was to have only one to measure the drag forces only. On the basis of size, strength, and sensitivity requirements, a four-pile tourmaline sensor made up of crystals 0.030-inch thick and 5/8-inch in diameter was chosen. To allow for sufficient strength of other gage parts, a gage size of 1 inch was chosen.

The gage design is very simple. There are only four main parts to the assembly. See Fig. 1. The parts are:

1. the sting or body of the gage, on which the other parts are mounted,

2. the force sensor, a plastic bonded, four-pile tourmaline element, which is bolted to the center of the sting,

3. the test section (on which drag force is measured) which is screwed to the sensor, and

4. a sleeve which is slipped over the sting in order to maintain a uniform aerodynamic shape over the length of the gage. A screw locks the sleeve in place.

Before the gage can be used in the shock tube, a pressure seal must be applied at the ends of the test section. This is necessary because the piezoelectric force sensor is also a pressure sensor. The external pressure field must, therefore, be isolated from the sensor.

In the shock flow a drag force is applied to the test section (and sting). This force pushes the force sensing test section into the rigidly mounted sting. This squeezes the force sensor mounted between the test section and sting. It is this squeezing of the sensor which causes a charge development by the sensor and thereby produces the force voltage signal. The basic design for the parallelepiped is adaptable for other two-dimensional shapes of similar size. A circular cylinder model has also been constructed.

B. Design of the Force Sensor

Initially, conventional four-pile tourmaline elements were used as the force sensor. These sensors were held together with solder which acted as an adhesive and as an electrode. Frequent breakage of the sensor occurred, and usually it was the solder bond which broke. This breakage was so common that, after a while, few good sensors were available. As an emergency procedure some of the broken sensors were bonded together with a plastic adhesive. It was noted that the repaired sensors did not exhibit the loss of sensitivity that had been expected. This was an interesting development because it introduced the possibility of using non-conducting adhesives which are much stronger than solder. It also showed that intimate electrical contact between crystals and electrodes was not necessary. The only modification for the design of plastic-bonded sensors was that separate electrodes were provided between crystals and at the end crystals. Appropriate leads were soldered to tabs on the electrodes. Figure 2 illustrates some of the steps for assembly of the force sensor.

Various plastic adhesives have been tried and the most satisfactory seems to be Fuller's Resiweld 105. It was among the strongest of the bonds tested (by impact testing) and it had relatively little effect on the over-all sensitivity of the sensor (the various bonds used did seem to affect the sensitivity of the sensor). Resiweld 105 must be cured at 150°C for 1-1/2 to 2 hours.

Another interesting adhesive that was tried was Eastman 910. It is not substantially stronger than solder but it cures almost immediately after the mating parts are brought together. Great care must be taken that parts are lined up properly when they are initially mated. The sensitivity of Eastman-bonded sensors showed least difference from solder-bonded

sensors. If additional strength over conventional solder-bonded sensors is not an important requirement, it seems reasonable to use Eastman 910. The assembly would be much quicker, easier, and cheaper and just as good as the soldered assembly. Care must be taken, however, not to overheat the electrodes when soldering leads on them as this weakens the bond. If feasible, leads may be soldered to the electrodes before assembly or perhaps mechanically fastened to electrodes after assembly.

For our purposes strength was an important factor; therefore, Fuller's Resiweld 105 was adapted for sensor construction.

C. Development Problem

Once the basic gage design had been accomplished; that is, the gage parts had been constructed, the assembled gage was subjected to several tests to determine its characteristics. The gage was calibrated and found to be linear (force versus output voltage) from 0 to 30 pounds of force (Fig. 3). The gage was then subjected to shock pressures in the shock tube. Figure 4 shows the gage in the shock tube test section. The resulting records were excessively noisy. The amplitude of the noise was many times the signal amplitude. Only by adding an electrical filter to the circuitry could the noise be reduced to approximately the amplitude of the signal. With a filter in the circuit, the noise/signal level was 0.61 at 10 psi shock pressure (4.4 lb force) to 0.75 at 5 psi (1.1 lb). Acceleration sensitivity was the immediate analysis; however, it was soon found that stress was being transmitted from the sting to the sensor also. When a load is applied to the test section of the gage, the sting bends slightly; and, since the sensor is in intimate contact with the sting, it also bends. This bending of the sensor resulted in a voltage signal. Since the bending or flexing occurred at the natural frequency of the sting system, corrective measures taken included beefing up the sting to increase the natural frequency, and the use of an electrical filter to eliminate these high frequencies. The mounting of the sensor was also changed so that the area of contact between the sensor and the sting was minimized (consistant with strength requirements). These measures helped to reduce the noise/signal level of 0.25 at 10 psi (4.4 lb) and 0.33 at 5 psi (1.1 lb). Figure 5 shows force-time records for various shock overpressures. Another results of these refinements was to increase the response time to 1-1/2 or 2 milliseconds for a step input.

The pressure sensitivity of the gage (the response to static overpressure) was checked by applying a static pressure step simultaneously to all sides of the gage. In the prototype gage a strong signal was observed. It corresponded to an 11% error at 20 psi and a 33% error at 5 psi. (These percentage errors are based on the drag forces expected at these pressure levels.*) The pressure seal was checked for leaks but found to be intact.

---

*Expected force is $F = AC_D q$ where A is the frontal area of the gage (one square inch), C_D is the drag coefficient (assumed to be 2 for the parallelepiped), and q is dynamic pressure defined as

$$q = P_o \frac{2.5 (P_s/P_o)^2}{7 + P_s/P_o}$$

where P_s is the shock overpressure and P_o is atmospheric pressure.

After some difficulty it was observed that the external pressure deformed the test section. When the test section was deformed, it was displaced from the sting and this resulted in a stretching of the pressure seal (a rubber membrane). Figure 6 illustrates this mechanism. The force due to the stretched membrane pulls the test section against the sensor, thus producing a positive force signal. To minimize the displacement caused by the pressure deformation, the front face of the test section was doubled in thickness (which theoretically should reduce bending by a factor of eight). This correction reduced the pressure sensitivity to much less than 1% of the expected force for all pressure levels from 5 psi to 40 psi.

The gage was next tested for temperature sensitivity. When the gage was heated slowly by bringing a lit match or cigarette in proximity to it, it was evident that the gage was sensitive to temperature changes. Since the gage would be subjected, in actual application, to shock wave temperatures for durations of only 15 milliseconds, a fast heat application method had to be found to evaluate the temperature response. A Sun Flash unit (used for flash pictures where a bright light of relatively short duration is needed) was flashed at the force gage. The record showed a step pulse at the time of the flash, then a decaying curve toward the original base line and beyond. The step pulse was not expected and was initially attributed to the electronics transients in the flash unit. (This is not unreasonable since there are large current surges at the time the sun flash is triggered.) Nevertheless the temperature response of the gage could not be evaluated because the thermal input at the gage was unknown. Finally the shock tube itself was used as a step temperature source. The approximate temperature changes in the shock tube could be determined from Rankine-Huguenot relationships. Since the gage response to temperature was desired, it was placed at the closed end of the expansion chamber where there would be reflected pressures but no flow and therefore no directed force. Since previous pressure sensitivity evaluation indicated that the pressure would have a negligible effect, any response could be attributed to temperature. Records of the gage response under these conditions showed initially a peaked signal in the direction of positive force then the decay to the base line and beyond. Figure 7 shows the temperature sensitivity records. The decay was explained in terms of thermal expansion of the crystals. The effect was therefore similar to that produced by tension on the crystal. The cause of the initial positive peak is not yet understood. It is the source of the large pressure-temperature error, being 7.1% after 2 milliseconds and 1.6% after 10 milliseconds.

III. OVER-ALL ACCURACY

A. Contributing Errors

Probably the most pertinent evaluation to be made of a gage is an estimate of its accuracy. The approach taken was to evaluate each of the contributing sources of error and then to combine these into an over-all figure of accuracy. Five contributing errors were considered.

(1) Time Constant. The nature of piezoelectric circuits, i.e., an RC loop, is such that there will be a decay associated with any signal. If the time constant (RC) is small, the decay will be fast and greater error

will result. The time constant for our gage circuit is about 1.0 second ($RC = 10^9$ ohms $\times 10^{-9}$ farads).

(2) Pressure and temperature sensitivities were determined by evaluation in the closed shock tube as described earlier. This test included both pressure and temperature changes even though the pressure effect was determined to be very small.

(3) Calibration uncertainty refers to the variation from linearity of the force-versus-output curve. It includes effects due to variability in electronics, variability in calibration forces applied and variability in the reading of calibration records.

(4) and (5) Calibration and force readability refer to the variability in the reading of the displacements of the voltage calibration step and the force step. Force readability is a large contributor to the over-all error because of the noise/signal level.

B. Over-all Error

The errors evaluated were both systematic and random. The systematic or consistent errors, time constant and pressure-temperature sensitivity, were such as to cause the force to be consistently high or consistently low. These errors if evaluated accurately over the whole range of conditions, may be used as corrections to the raw force data. It was believed that complete evaluation of pressure-temperature effects would be too time consuming. Since the time constant error amounts to about 1%, this would be too small a correction to be overly concerned with. The determination of these errors was considered sufficient for an estimate of over-all error.

The remaining errors are random, i.e., they have $\pm$ variation about some central value. With some injustice to statistical assumptions and procedures, the random errors were combined as the square root of the sum of the squares of each error estimate. (The individual error estimates did not come from the same population. Each error estimate is not equally reliable since the number of data points used in determining each is not necessarily the same, etc.).

The total error (Fig. 8) is the random standard error plus the absolute sum of the systematic or consistent errors.

$$\text{TOTAL ERROR} = \pm \left(\sqrt{e_3^2 + e_4^2 + e_5^2} + \left| e_1 + e_2 \right| \right)$$

The overaid accuracy of the force gage is considered to be better than 85% (less than 15% error).

IV. SUMMARY OF GAGE CHARACTERISTICS

Shape: cylinder of square cross-section.

Size: one-inch characteristic dimension.

Design simplicity: made in four units.

Design adaptability: basic design suitable for other two dimensional gages.

Stronger plastic bonded force sensor: has withstood shock pressures of 15 psi.

Sensitivity: 24 millivolts/lb with 1000 mmf across gage.

Linear over calibrated range: 0-30 lb.

Noise/signal level: 0.25 at 10 psi (4.4 lb) to 0.33 at 5 psi (1.1 lb).

Response to step pulse: 1.5 or 2 millisecond rise time.

Pressure sensitivity is less than 1% of expected force at all pressure levels.

Pressure and temperature sensitivity: 7.1% at 2 milliseconds to 1.6% at 10 milliseconds.

Over-all error: less than 15%.

A formal report concerning the force gage will be published late in 1959. It will be NAVORD Report 6211, A Piezoelectric Force Gage for Measuring Drag on Two-Dimensional Models in the Shock Tube, by William Zuke and Luther Slifer.

Figure 1 Force Gage

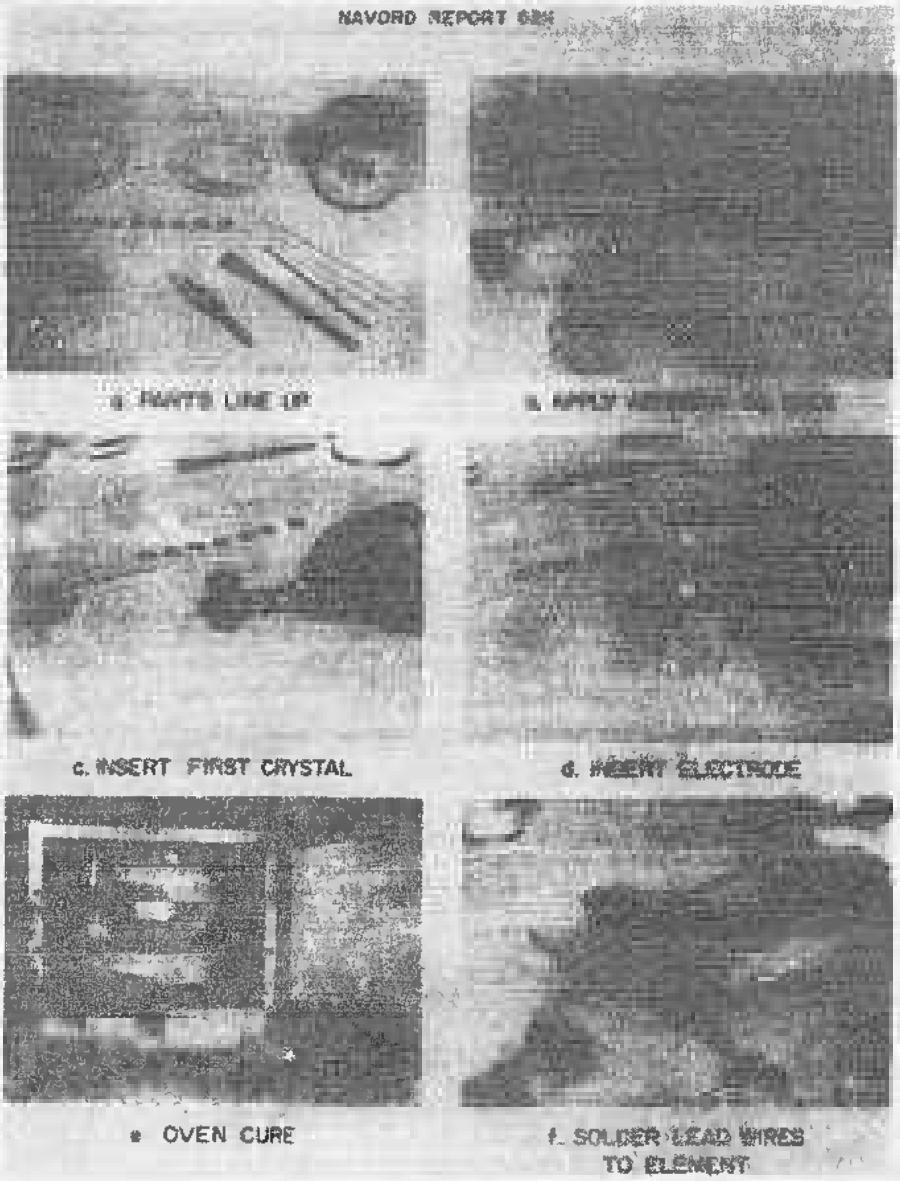

Figure 2 Force Sensor Assembly

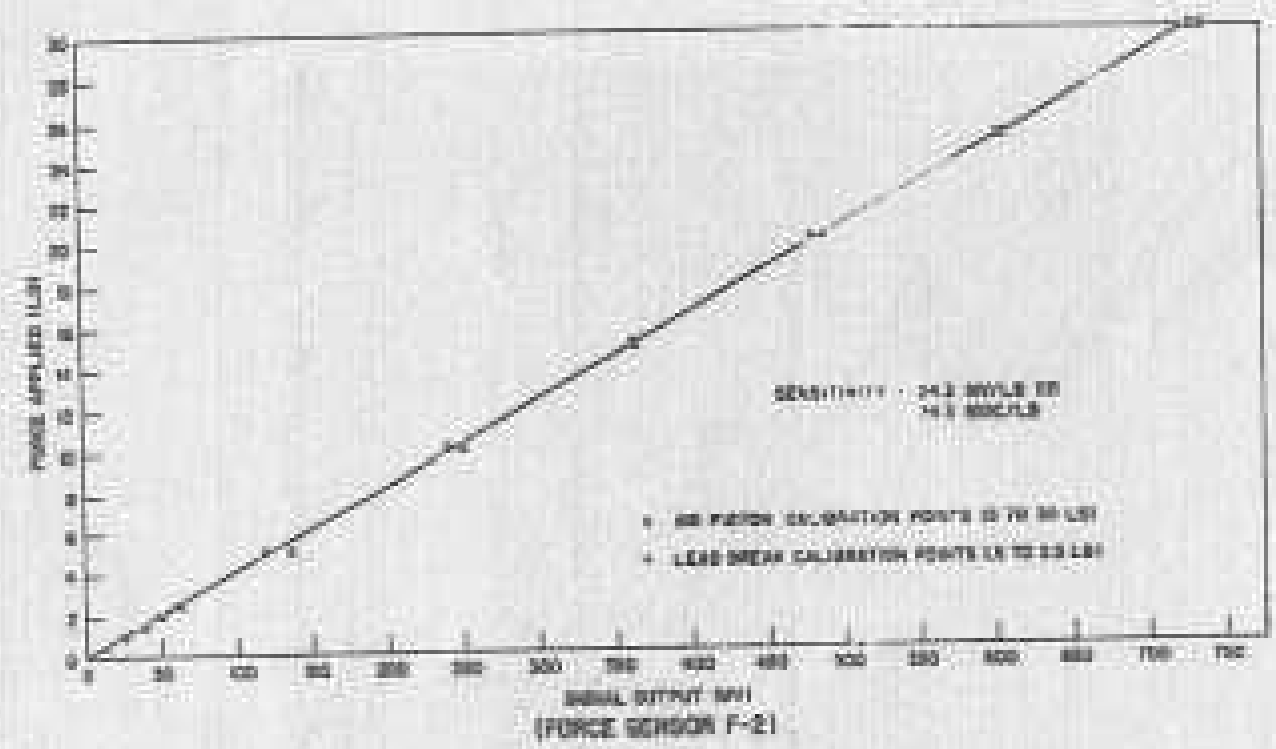

Figure 3 Calibration Curve

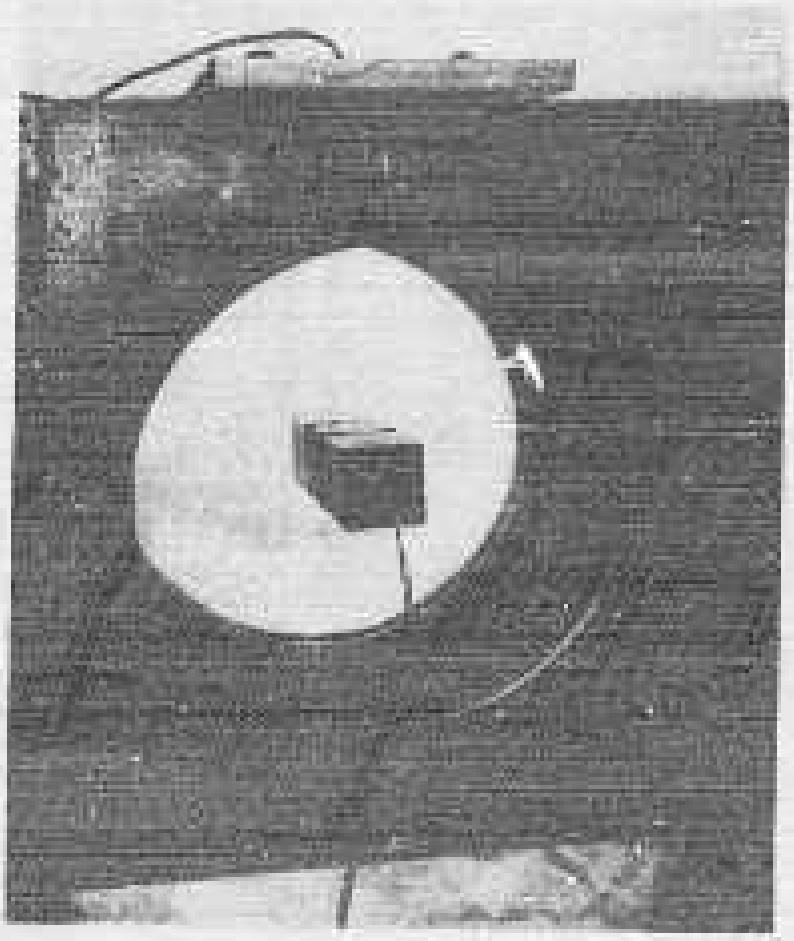

Figure 4 Force Gage in the Shock Tube

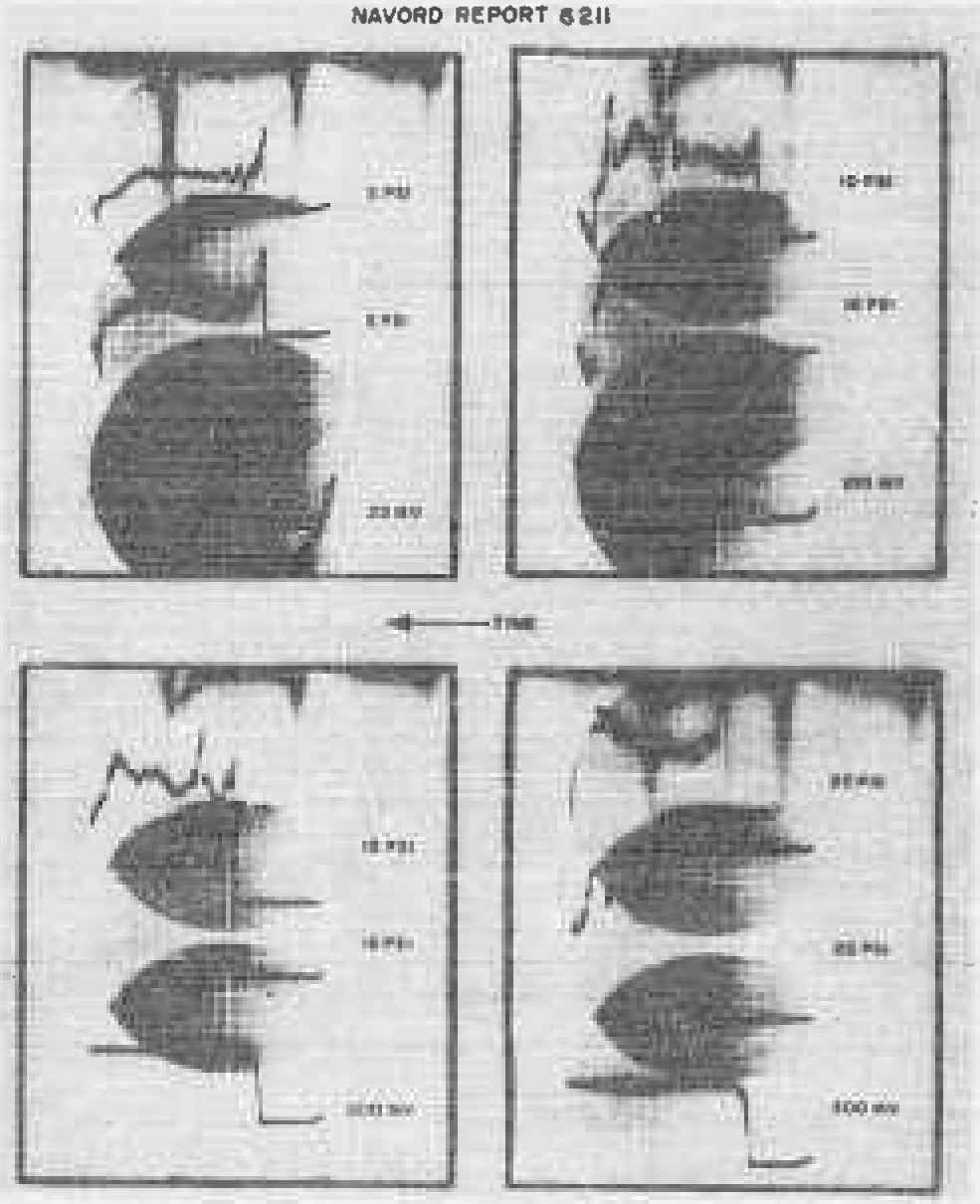

Figure 5 Shock Tube Force-Time Records

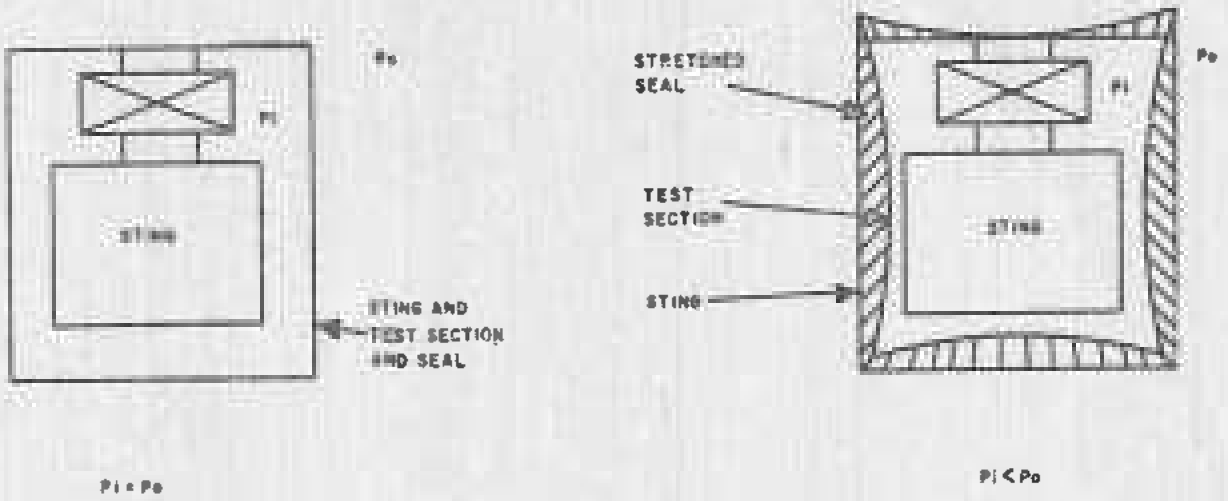

Figure 6 Deformation - Seal Effect

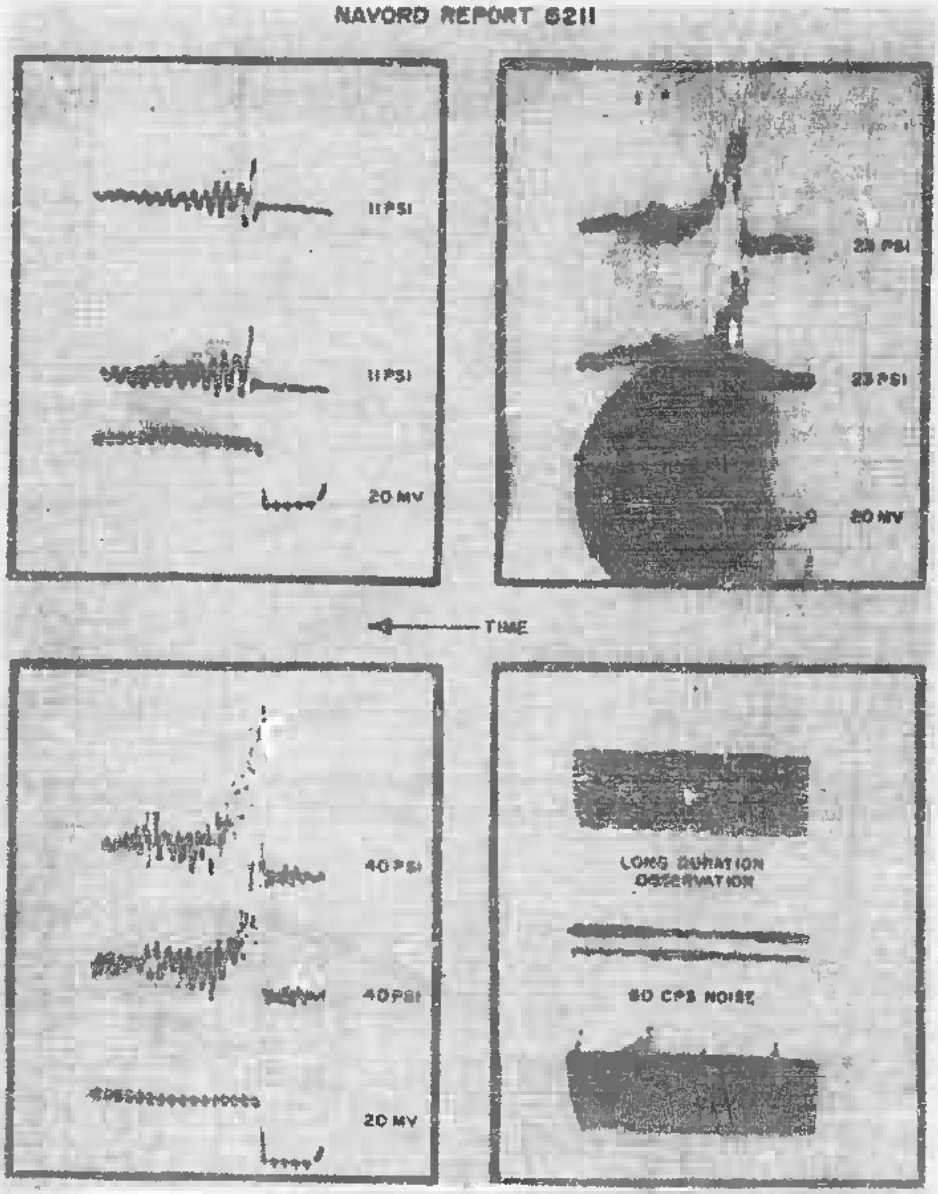

Figure 7 Temperature Sensitivity Records

	AT 5 PSI OR 1.15 LB		AT 20 PSI OR 16.7 LB	
	2 MS	10 MS	2 MS	10 MS
CONSISTANT ERROR	+6.9	+0.6	+6.9	+0.6
e_1 TIME CONSTANT	-0.2	-1.0	-0.2	-1.0
e_2 PRESSURE AND TEMPERATURE*	+7.1	+1.6	+7.1	+1.6
RANDOM STANDARD ERROR	$\pm$6.6	$\pm$6.2	$\pm$5.2	$\pm$5.4
e_3 CALIBRATION UNCERTAINTY	$\pm$2.0	$\pm$2.0	$\pm$2.0	$\pm$2.0
e_4 CALIBRATION REPEATABILITY	$\pm$1.6	$\pm$1.6	$\pm$1.6	$\pm$1.6
e_5 FORCE REPEATABILITY	$\pm$6.1	$\pm$5.6	$\pm$4.5	$\pm$4.7
TOTAL ERROR AS DEFINED BY $\pm\left(\sqrt{e_3^2 + e_4^2 + e_5^2} + \lvert e_1 + e_2 \rvert\right)$	$\pm$13.5	$\pm$6.8	$\pm$12.1	$\pm$6.0

*Average of Error Determined at 11 PSI (5.21 LB), 23 PSI (21.4 LB), and 40 PSI (62

Figure 8 Force Gage Error

CHANGES IN DRAG CAUSED BY SHIELDING

George A. Coulter
Ballistic Research Laboratories

ABSTRACT

Two shield-target model configurations are tested during the shock overpressure range from 5 to 30 psi. The difference of pressures measured on the front and rear surfaces of the target model are given for shields of heights one and two times the height of the target model. Families of curves are given for the two cases; differential pressure, considered to be drag pressure, is plotted as a function of the shield-target model spacing. These values of the drag pressure are compared to the values obtained for an unshielded target model.

LIST OF SYMBOLS

H	height of model perpendicular to wall of shock tube
L	length of model parallel to the flow direction
M_2	Flow Mach number
P_s	side-on shock overpressure
P_1	ambient pressure ahead of shock
P_2	pressure behind the shock front
Po_2	stagnation pressure of the shock
q_2	dynamic pressure
Re/L	Reynolds number per unit length
W	width of model across shock tube parallel to floor, perpendicular to flow

INTRODUCTION

At the request of AFSWP, the present shielding program was initiated at the Ballistic Research Laboratories Shock Tube Facilities to offer some explanation of certain field results obtained from a shielding experiment. Figure 1 illustrates these results by showing the comparative damage to vehicles resulting from translation caused by the flow following the shock wave.

The vehicles were placed side by side at the same ground distance from a nuclear test detonation. The input conditions of the shock waveform and pressure could, therefore, be expected to be the same at both prints. Figure 1-A shows the resulting damage to the unshielded vehicle; Figure 1-B shows the shielded vehicle with a minimum of damage.

The damage is clearly quite different for the two cases. Because of this great difference, the present shock tube experiment in shielding was devised to try to discover the shield-target configuration that would provide maximum protection to the target model. Only the drag pressure in the direction of the shock flow is studied in the present experiment. Other forces are not included in the study.

NATURE OF THE EXPERIMENT

The 20-inch square test section of the BRL 24-inch shock tube was chosen for the present experiment because here the models could be mounted directly to the walls of the test section. Since the experiment was designed to measure primarily the change in drag pressure caused by shielding, the many changes needed in the shield-target model spacing could be accomplished rather easily in the 20-inch test section.

A variation in shield height as well as in shield spacing was introduced into the experiment by the use of two shields with heights equal to one and two target model heights. The other dimensions of the shields were held constant throughout the experiment and were equal to those of the target model.

The shape of the target model chosen was a rectangular parallelepiped with dimensions 2-1/2 x 8 x 3 inches. A target model was designed so as to give some indication of the pressure variation on the front and rear surfaces of the model. This was done with the target model, or net force model, which is shown as a sectional view in Figure 2.

The many small holes on the front and rear faces of the target model were connected through small channels to two Consolidated Electrodynamics Pressure Transducers, Type 4-312, 50 psia. The net pressure available for model translation was assumed to be the difference between the recorded average pressures from the front and rear surfaces. This difference in pressure was assumed to be the drag pressure.

Small lengths of plastic tubing were used to physically couple the target model to the gages which were external to the model. This method of coupling removed unwanted vibration, but it set the limit for the rise time

at 2 or 3 milliseconds. Since only the steady drag pressure, after the diffraction phase was to be studied this response was assumed adequate. A 3 KC carrier amplifier system and a galvanometer-type oscillograph recorder complete the equipment.

Since the method of utilizing small holes in the net force model to measure pressure might lead to average pressures on the surfaces which did not represent the true average pressure, two preliminary checks were made. The first check consisted of measurements from small areas on each of front and rear surfaces of the net force model. These areas were obtained by masking the holes in the face plates. The unmasked area would then be the sensing area. The sensing area was then "moved" about the surface.

It was found by this method that an approximately uniform pressure, somewhat below the theoretical stagnation pressure for the shock wave, covered the front surface of the net force model. The rear surface did show some few per cent variation.

A second check was made with a strain gage force balance. See Reference 1 for a description of this type of balance. The values obtained for the unshielded target model using the strain gage balance were in fair agreement with those values obtained from the net force model with the holes. The values compared to within $\pm$ 15 per cent. It was felt that the net force model could be used as the target model for the shielding studies. A fairly accurate picture of the effect of shielding with variation in shield-target model configurations could be obtained, although there might be some doubt as to the absolute values of the drag pressure.

Before placing the shield-target model configurations, Figure 3, in the shock tube test sections preliminary shock input waveforms were obtained. One set of these records are shown in Figure 4. The upper trace is that of the side-on overpressure; the lower trace is that of the stagnation overpressure. For the measured side-on pressure, the corresponding measured stagnation pressure appears to be lower than the shock wave theory predicts. (Reference 2). The parameters for the input shock waves are given in Table 1.

Since the input waveforms all show an initial rise time from the baseline of 2 or 3 milliseconds, the records obtained from the shielding study were read beginning at 4 milliseconds. Because of the tendency for the input records to increase in pressure after about 35 milliseconds, no record was read after this time. These limits held the model study results to the interval 4 - 35 milliseconds. Average values for this interval were used from all the records.

RESULTS

The method above was used to obtain from the net force model the drag pressure for the unshielded target for the pressure range 5 to 30 psi. This range of pressures was repeated for each of the shield-target spacings from a distance of one-half to ten model lengths. (Spacing of 1-1/2 inches to about 30 inches). This was done for both of the shields. Figures

5, 6, and 7 show typical records obtained from the net force, with no shield, the 2-1/2-inch high shield and the 5-inch high shield. The shield-target spacing was 9 inches.

The results of shield-target data obtained are shown graphically in Figures 8 and 9. For similar curves of drag and shielding data see Reference 3 and 4. The families of curves of Figure 8 and 9 are for the two shields placed at distances upstream from the target model. The graphs show, then, the change in drag pressure (variation in the pressure difference between the front and rear surfaces of the net force model) as a function of the shield-target spacing for two shields.

Notice that in both cases the net pressures are initially negative for all shock pressures. As the spacing is increased a transition point is reached where the drag pressure is zero. This zero point is a function of shock pressure. These points occur at a shield-target distance of about three model lengths for the low shield and about five lengths for the higher shield. After the transition, or crossover point, the positive drag pressure increases.

The experiment did not permit shield-target model separation distances greater than 10 model lengths, however it can be inferred that if the separation distance were great enough the target model would be unshielded and the pressure difference value would be that of an unshielded target. At the 10-model-length separation distance the low shield permits the target to reach 70 per cent of the unshielded value, while the high shield permits the pressure to reach only 45 per cent of the unshielded value.

Figure 9 does not have either the 25 or 30 psi shock pressure values plotted. The recorded waveforms for these pressures become quite complex and hence invalidate the establishment of a single average.

CONCLUSIONS

A study of the drag pressure curves presented shows that protection is indeed afforded a shielded target model in the shock tube as it was in the field experiment. The curves also show that the drag pressure may be separated into a negative and positive phase as a function of shield-target spacing. The transition spacing where minimum drag occurs is a function of the shield height. For both shields studied, the transition occurred at a separation distance of about three times the shield height. This means that the higher shield did the better job of protecting the target model from the effect of the shock flow.

A more detailed analysis of the data could perhaps permit establishment of usable prediction techniques suitable for use under full scale conditions.

ACKNOWLEDGEMENTS

The author wishes to thank Mr. Benjamin Granath for his design suggestions of the net force model, also, to thank Mr. William Matthews for the tedious data reduction of the many records needed.

REFERENCES

1. Coulter, George A. and Matthews, William T., "Coefficients of Drag Measured With a Shock Tube Force Balance", Aberdeen Proving Ground, Maryland: BRL TN-1155, August 1957

2. Glass, I. L., "Part I: Theory and Performance of Simple Shock Tubes", University of Toronto: UTIA Review No. 12, Part I, May 1958

3. Hoerner, Sighard F., "Fluid-Dynamics Drag", 148 Busteed Driver, Midland Park, New Jersey: Published by the author, 1958

4. Johnson, M. R. and Bisshopp, F. E., "Net-Force Sensor Research", Chicago: American Machine and Foundry Company, AFSWC-TN-57-32(U), April 1958

Table 1 Shock Wave Parameters

P_s	P_2/P_1	P_{o_2}/P_1	M_2	q_2	$Re/Ft \times 10^{-6}$
5.1	1.34	1.38	0.21	0.62	1.7
10.6	1.71	1.88	0.37	2.44	3.6
15.6	2.05	2.42	0.49	5.12	5.3
20.1	2.35	2.93	0.57	7.96	6.8
25.2	2.69	3.61	0.66	12.2	8.4
30.9	3.07	4.41	0.74	17.6	10.1

Initial Conditions: $P_1 = 14.9$ psi

$T_1 = 535°R$

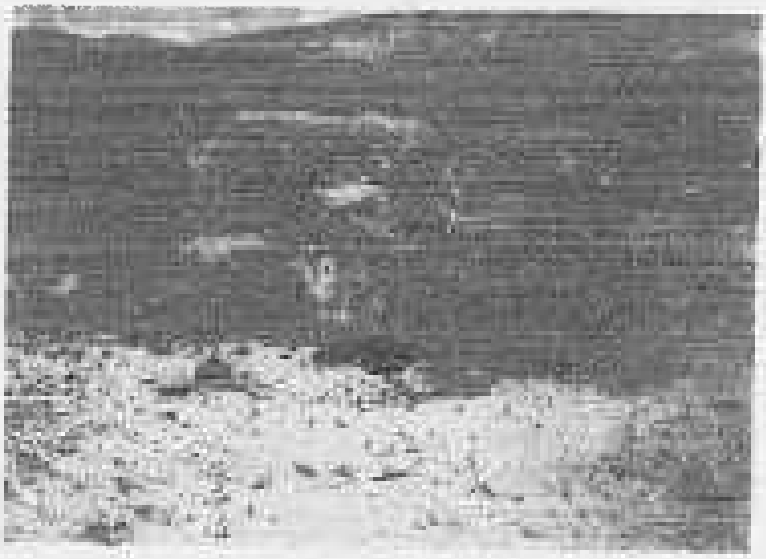

1a Unshielded Vehicle

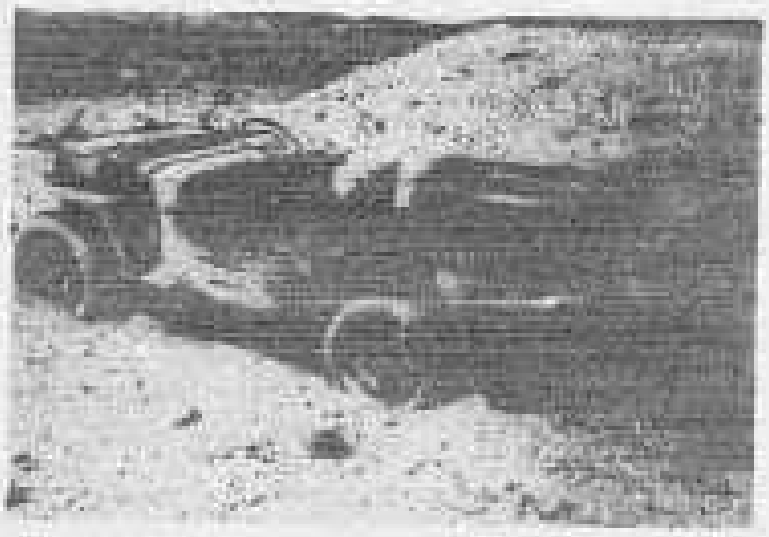

1b Shielded Vehicle

Figure 1 Comparative Damage for Shielded and Unshielded Vehicles

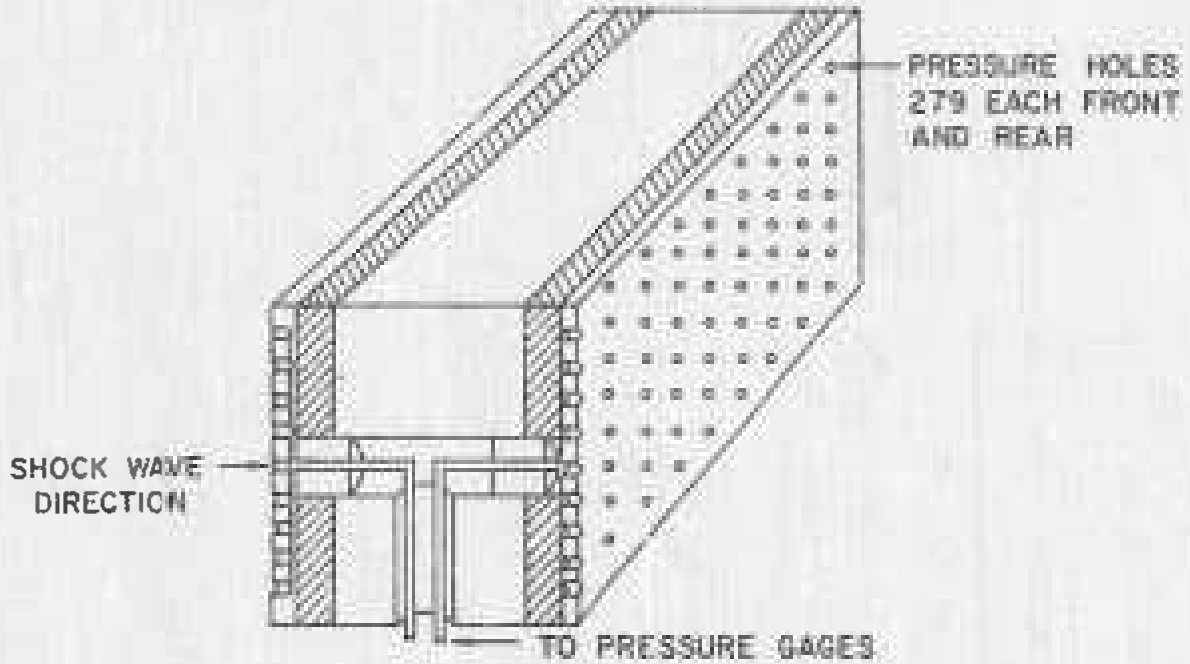

Figure 2 Sectional View of Net Force Model

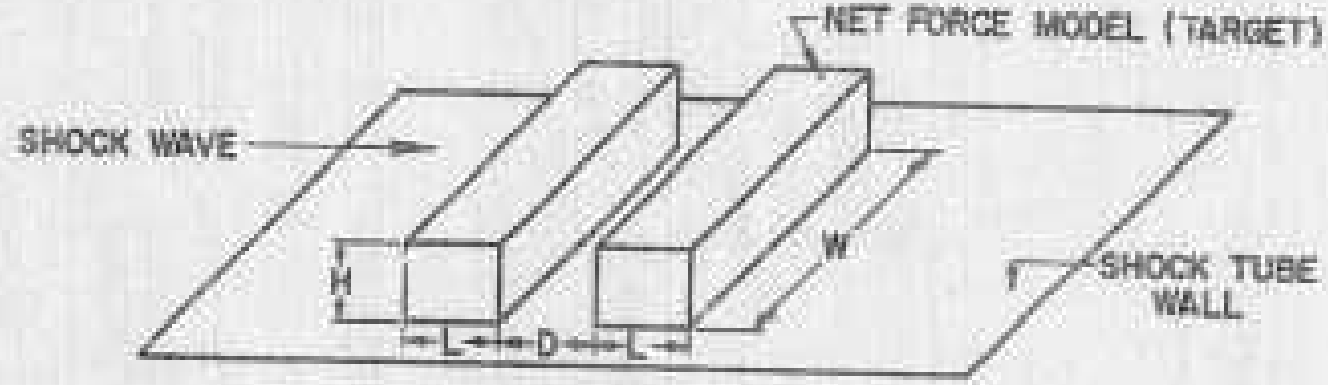

FIG. 3-A

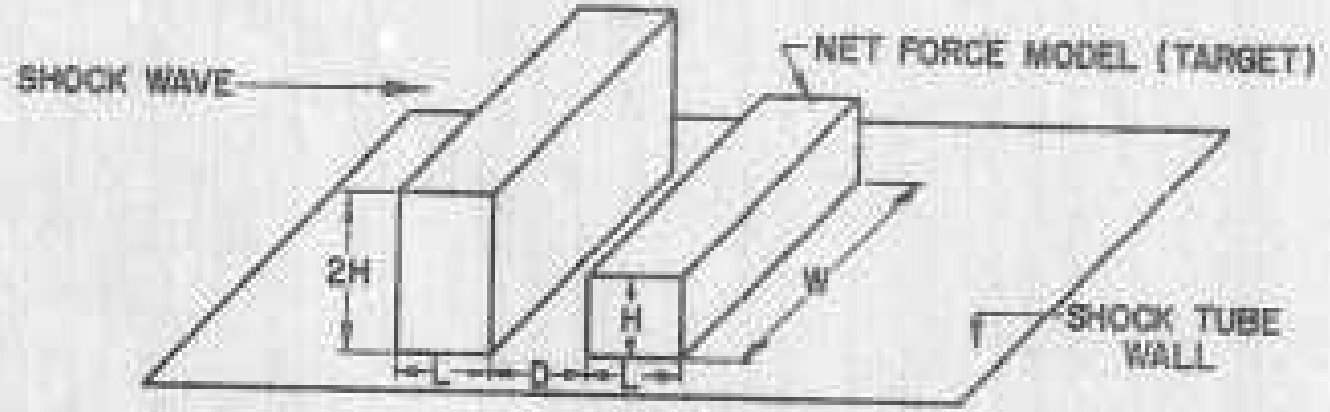

FIG. 3-B

Figure 3 Arrangement of the Shields and the Target Model

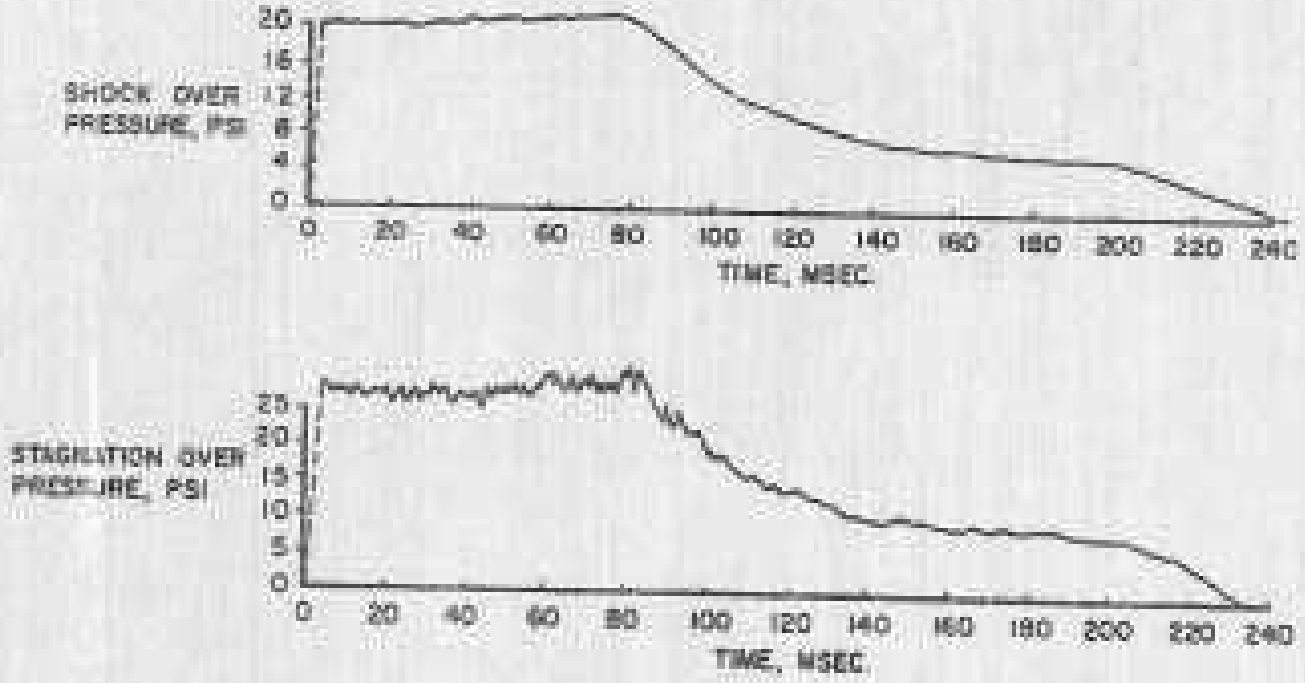

Figure 4 Typical Input Waveforms, 20 × 20 Inch Square Test Section

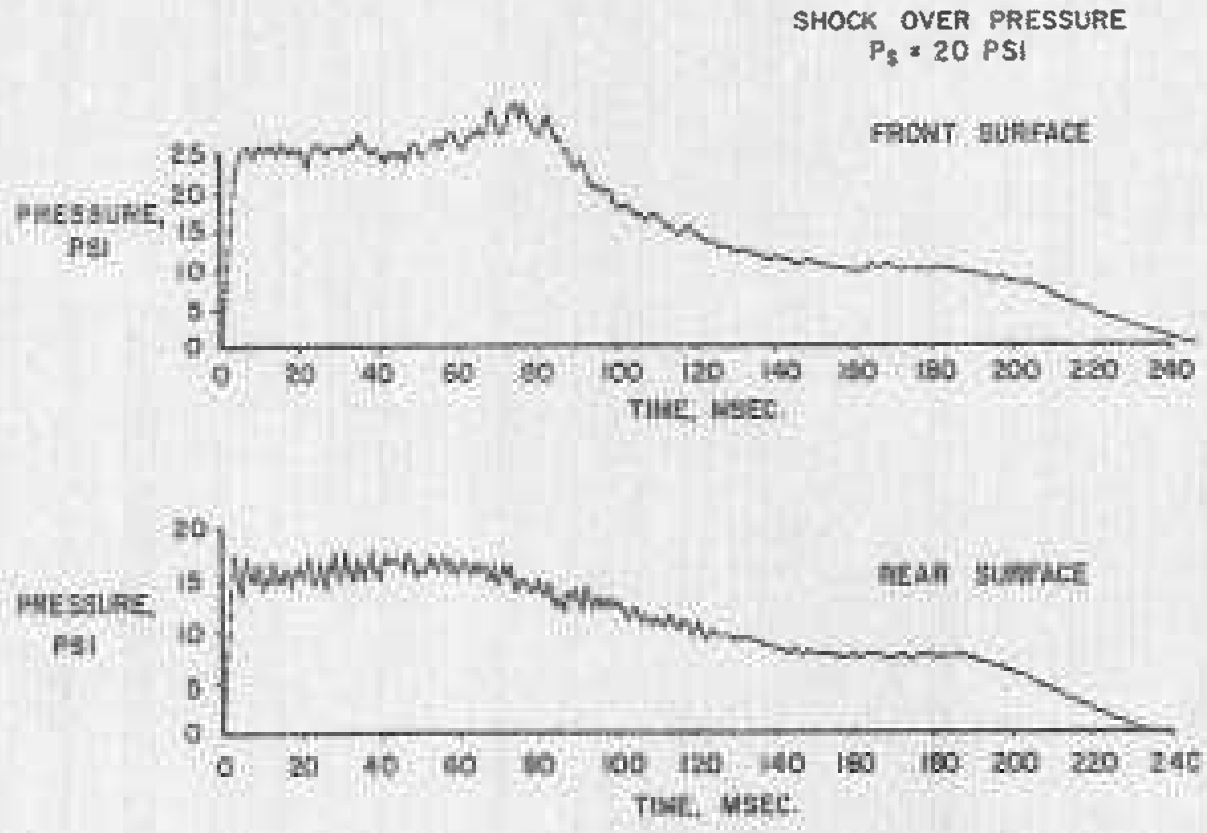

Figure 5 Typical Records from Unshilded Model

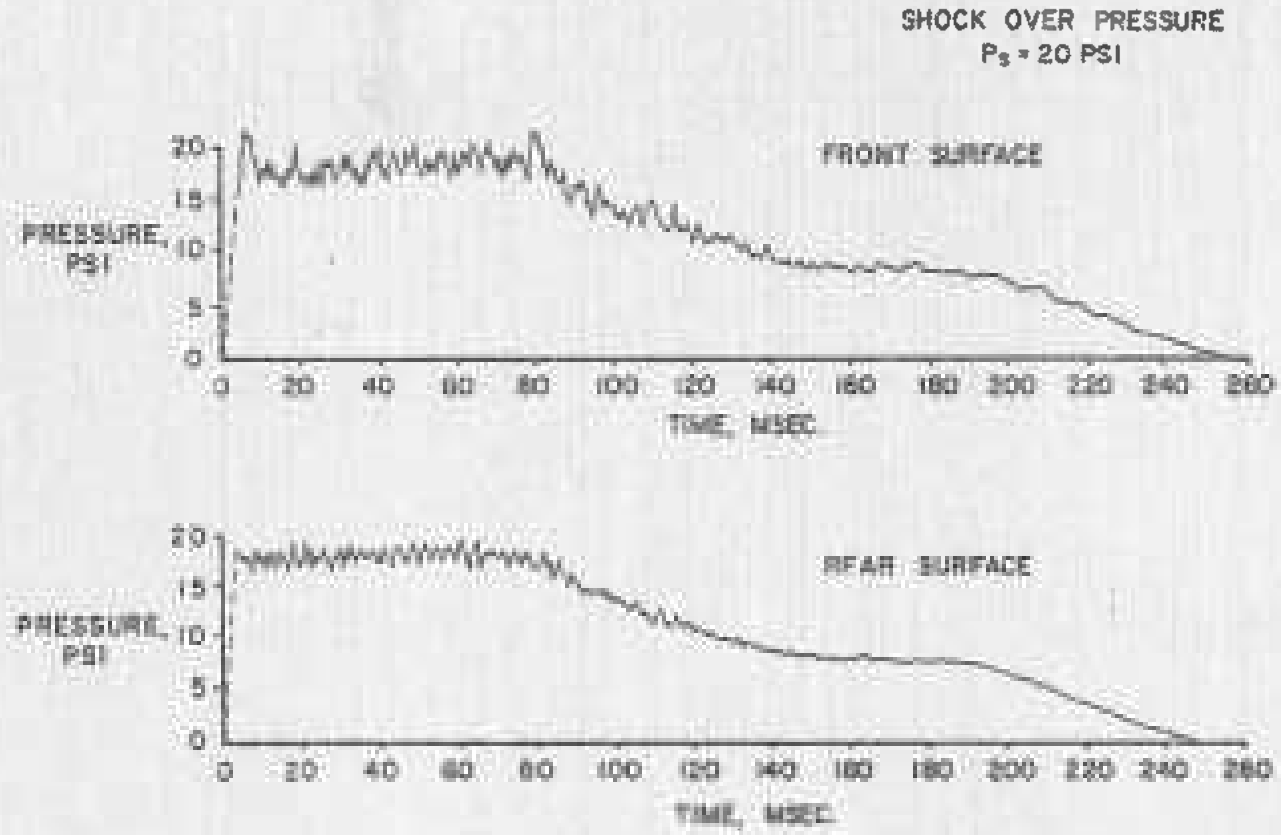

Figure 6 Typical Records from Model with 2-1/2 × 8 × 3 Inch Shield

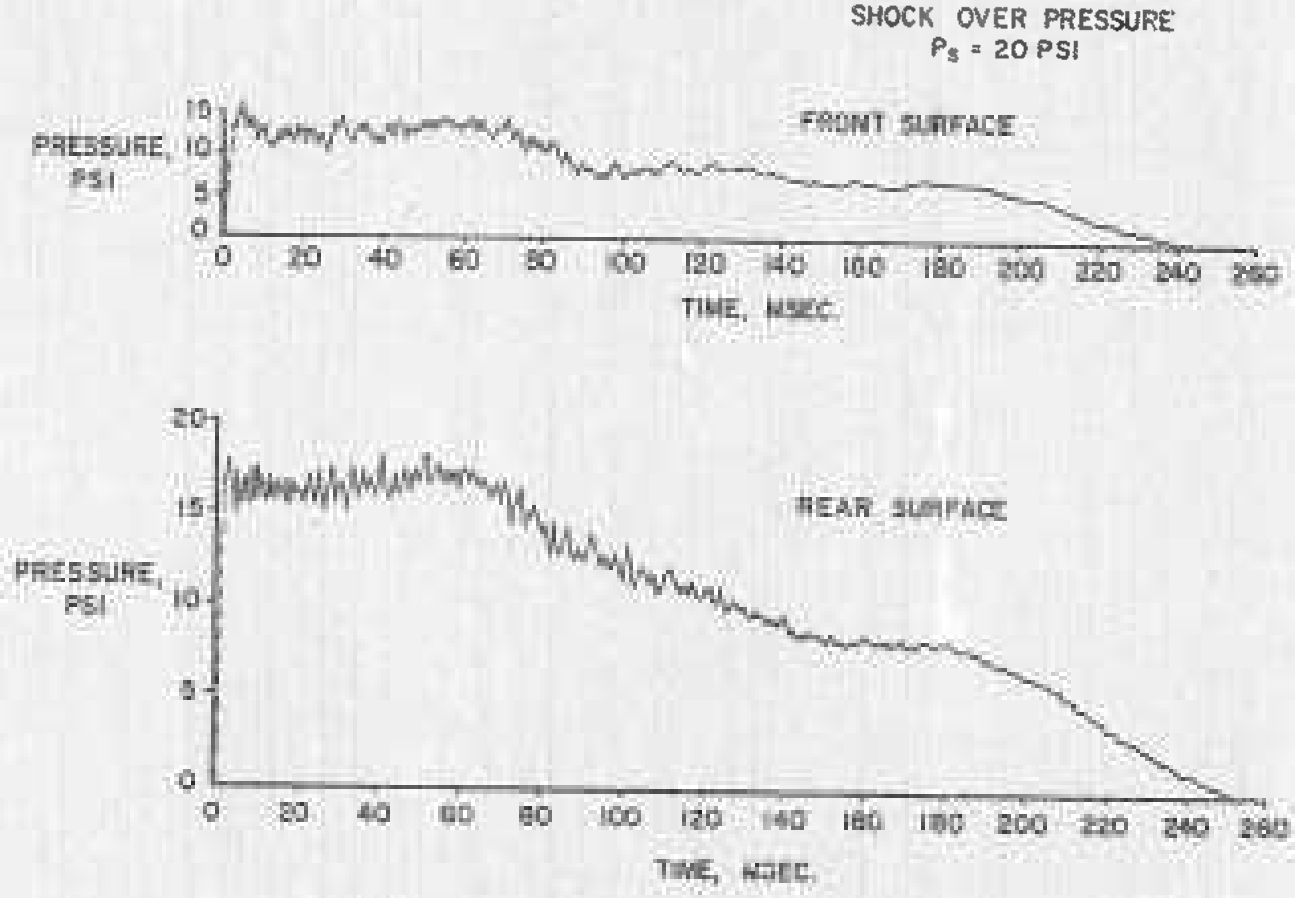

Figure 7 Typical Records from Model with 5 × 8 × 3 Inch Shield

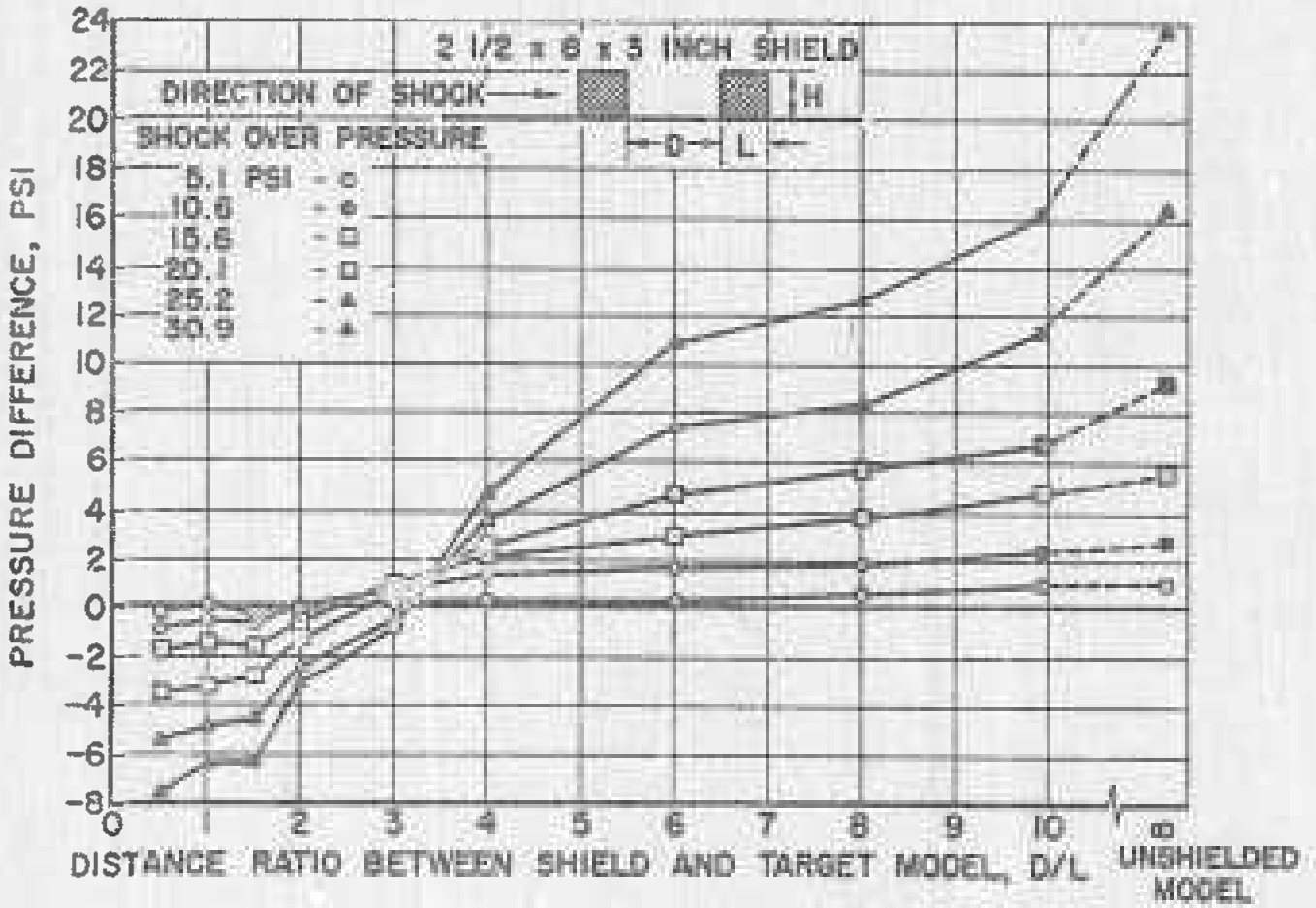

Figure 8 Pressure Difference as a Function of Shield Position

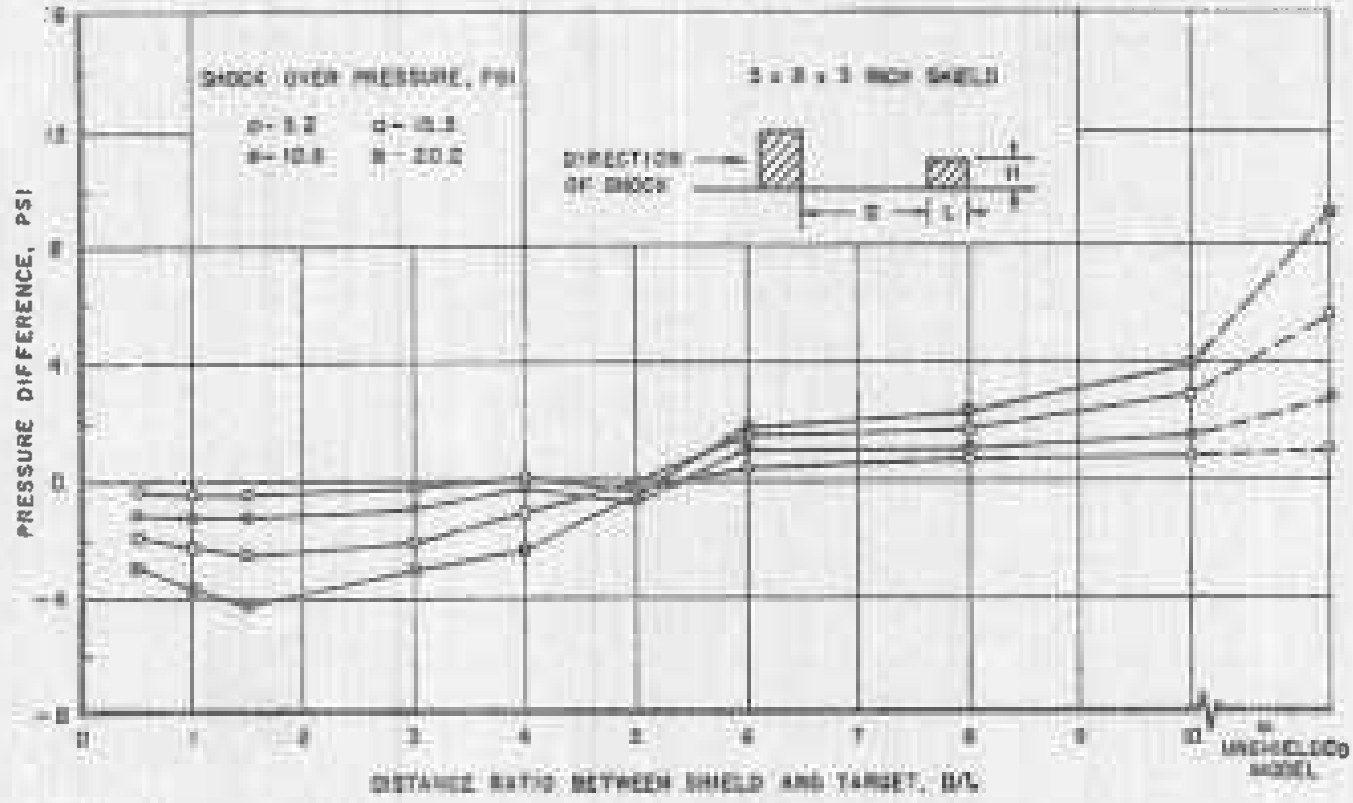

Figure 9 Pressure Difference as a Function of Shield Position

A COMPARISON OF PRESSURE COEFFICIENTS OBTAINED IN WIND TUNNELS TO SHOCK TUBE AND FIELD TESTS

Captain Marcus L. Whitfield
Armed Forces Special Weapons Project

ABSTRACT

Pressure coefficients for a 180-degree arch at Mach numbers 0.41, 0.51, 0.60, 0.71, 0.81, 1.18 and 1.75 and for a 90-degree dome at Mach numbers 0.48, 0.58, 0.70, 0.79, 0.90, 1.18, 1.57 and 1.75 with Reynolds numbers from 3.2×10^6 to 4.2×10^6 obtained from tests in the Naval Ordnance Laboratory supersonic wind tunnel are presented. A comparison is made between the wind tunnel coefficients, coefficients determined in the Air Force Six-Foot Shock Tube operated by Armour Research Foundation and coefficients derived from full-scale testing.

BACKGROUND

The purpose of this presentation is to describe some recent data on pressure coefficients over the surfaces of arches and domes and to compare this data with that obtained from shock tubes and full scale tests. The wind tunnel tests were performed by personnel at the Naval Ordnance Laboratory under the general supervision of the Air Ground Explosions Division.

Early investigators of air drag were only interested in the net translational effects on shapes, termed the drag coefficients. The aeronautical designer determined the net drag coefficient composed of parasitic and induced drag as a function of the speed of the plane in order to calculate the forces that must be overcome to permit flight. In recent years advanced design aircraft and missiles necessitated the determination of supersonic drag coefficients.

The advent of an atomic weapon initiated studies by structural analysts of means to adapt the wind tunnel drag coefficients to transient shock loadings. Also, the need for a diffraction history of this shock front resulted in interferometer and schlieren photography studies in shock tubes. With this knowledge the investigators designed full scale structures for tests under atomic weapons. Much of the full scale information obtained was at relatively low overpressures. For reliable pre-test loading information for prediction purposes at higher overpressures, it became evident that more than just a net drag coefficient was desirable for the design of the structural components and prediction of response, especially of arches and domes.

Present efforts are being directed toward the analysis of the loading on arches and domes by use of pressure coefficients. The pressure coefficient is defined by the equation:

$$C_p = \frac{P - Ps}{q}$$

where C_p is the pressure coefficient, P is the measured pressure, Ps is the side-on pressure, and q is the dynamic pressure. The pressure coefficient represents the drag coefficient over a unit area of surface and is primarily a function of particle velocity, size and density (especially in dust laden air), and Reynolds number of the flow and of the dynamic pressure wave form. Integration of the coefficients over the surface should represent the net drag coefficient.

Pressure coefficients on arches and domes were first provided through a limited study from the Air Force Six-Foot Shock Tube operated by Armour Research Foundation. With this knowledge the investigators designed full scale structures for testing in the environment of the blast from nuclear detonations. Correlation is difficult due to the non-ideal conditions and wave forms encountered in full scale tests which can not be reproduced in the shock tube; however, idealized diffraction phase loadings are now believed to be quite reliable. Shown here are the drag phase pressure coefficients published in "Blast Loading on Domes and Arches", AFSWP-522, by Major Ferd Anderson, formerly with AFSWP, who used data derived from full scale tests. Figure 1 represents the pressure coefficients from a non-ideal wave form versus the radial angle from the front edge for a 180-degree arch. This curve was extrapolated from full scale data on a 120-degree arch. Anderson noted that the C_d at 0 degrees is lower than C_d at 25 degrees because of the boundary layer near the ground surface and that, in certain cases, the value C_d equal to -0.4 will give unrealistic negative values for the loading scheme. Careful study showed that in no case did the loading go more than .3 or 4 psi below ambient and an adjustment is necessary when q(t) is large and p(t) small. Figure 2 represents the same plot for a 90-degree dome with the drag coefficients shown as pressure contours connecting points of equal values. The model used in this test had a height of 10 feet. Anderson calls attention to the fact that gage spacing precluded a study of the boundary layer effect; however, since C_d is decreasing rapidly with increased angle α, the boundary layer reduction of C_d would not be enough to be apparent. The previous note of caution pertaining to a value for C_d of -0.4 also applies to the dome. These coefficients represent an average, or weighted, value for the entire drag duration. Actually, as found in full scale data, this value may vary as illustrated by considering point A on the dome (Figure 2) which varies from + 0.4 to + 0.7; point B from 0 to - 0.5; and C from - 0.1 to - 0.5 under non-ideal loadings. Figure 3 presents a plot of the Mach flow to be expected in non-ideal high dynamic pressure waves.

To complement the full scale test results, an additional shock tube program was initiated at Armour Research Foundation to further define the diffraction and drag loadings at shock strengths of 1.3 to 7.0. Certain limitations are imposed on the comparison of this data with that from full scale. Only ideal shock waves of short duration are available in the shock tube. The dynamic pressures must be calculated from free stream overpressure and measured point pressures which may introduce large errors in the drag phase because of inherent instrumentation difficulties. Although the drag coefficients during the diffraction phase appears reliable, the drag phase coefficients computed may be open to question. Figure 4 shows the pressure coefficients for a 180-degree arch plotted as constant for the entire drag phase taken from a report "Air Blast Loading on Arches and Domes",

by E. V. Gallagher, ARF. Figure 5 shows the pressure coefficients on a 90-degree dome plotted as contours taken from the same report. Considering time of arrival of the shock wave at the pressure gage as zero, the time of initiation of the beginning for the drag phase is shown in ratios of height-to-time required for the shock wave to traverse the structure.

From the results obtained in the shock tube studies a requirement was developed for wind tunnel pressure coefficients at subsonic and supersonic Mach numbers. It was desired to relate the pressure coefficient to a given Mach, which under large duration blast waves might be used for response prediction methods and design of structures, especially arches and domes, to sustain loadings imposed by blast inputs. Arch and dome shapes were selected since these are the above ground structural configurations that can best withstand the high overpressures and dynamic pressures.

WIND TUNNEL TESTS

In order to use the wind tunnel data, certain assumptions had to be made. The Reynolds Number was computed, based on free stream condition, to be between 3.2×10^6 and 4.2×10^6 and its effect on the pressure coefficient was assumed negligible. Published data indicates that this assumption is reasonable for high subsonic, sonic and supersonic flows (Reference 4, 6 and 7). This is difficult to prove without a variable density wind tunnel. It was also assumed that a relationship between the dynamic force and Mach number could be established. This is only possible for the case of an ideal decay behind the shock front of blast wave parameters during which theoretical gas laws will hold. The random nature of the non-ideal blast wave is such that the relationship cannot be accurately predicted. The wind tunnel dynamic pressure is equal to $\frac{1.4}{2}$ times Ps times the Mach number squared:

$$\left(q = \frac{1.4}{2} P_s M^2\right)$$

The model designs were chosen to give the highest Reynolds Number possible without causing blockage and interference in the wind tunnels. The models were mounted on a smooth ground plane which bisected the tunnel test section, giving a flow over the plane equivalent to free tunnel flow except for boundary layer formation. Pressure taps were located so as to give the most practical information for plotting contours, and symmetry to the right and left of the flow axis was assumed. Dimensions and tap locations are shown in Figure 6, 7 and 8. Tests were conducted on 120- and 180-degree arches and on 60-, 90-, and 120-degree domes at Mach numbers from 0.4 to 1.75. Only the 180-degree arch and the 90-degree dome will be discussed here.

180-DEGREE ARCH

The 180-degree arch was tested at Mach numbers 0.41, 0.51, 0.60, 0.71, 0.81, 1.18 and 1.75 as shown in Figures 9 and 10. As the Mach number increases through Mach 0.81 the pressure coefficients are nearly constant. However, at Mach 1.18 there is a radical change as front face pressure coefficients increase from an average of + 0.4 to a value of +0.9

and a shift of the zero pressure coefficient from about 20 degrees to 65 degrees. There appears to be an increase in values on the rear face from -0.1 to a -0.6. At a Mach of 1.75 the front face value drops to + 0.6 and the rear face to - 0.2 and the zero coefficient moves to about 85-degrees. This variation is compared to that derived from shock tube and full scale tests in Figure 10. No explanation can be offered for the difference at this time.

90-DEGREE DOME

The 90-degree dome was tested at Mach Numbers 0.48, 0.58, 0.70, 0.79, 0.90, 1.18, 1.57 and 1.75. The pressure coefficients are plotted as contours and are shown in Figures 11 through 14. Note the increase in negative coefficient at the crown with increasing Mach in the subsonic region. Similar to the case of the arches, the loading changes considerably in supersonic flow. The pressure contours at Mach 1.57 most favorably compare with those obtained from full scale tests as shown in Figure 15. However, the pressure contours at Mach 1.18 compare very favorable with those obtained in the six foot shock tube as shown in the same figure. The wind tunnel data when compared to shock tube and full scale data showed reduced rear-face pressure coefficients at all Machs other than 1.18; in fact, a small positive coefficient was found on the lower rear face at all subsonic Mach numbers. The lowest pressure coefficients were found to exist at the highest Mach number. The latter was also true for rear face coefficients obtained from full scale tests; however, the front face coefficients at point A (Figure 2) on the dome increased from + 0.5 to more than + 0.7 with a change in Mach from 1.2 to 4.9.

SUMMARY

Further analysis of the wind tunnel data will be necessary before any positive conclusions can be made. Determination of the phase change from diffraction to drag in full scale blast waves is rather arbitrary; however, variations of pressure coefficients may furnish a reference for establishing the point of change. The contribution of the dust in the drag loading obtained from full scale testing has not been determined and could account for a portion of the deviation between full-scale and laboratory results. If the Mach-time history shown in Figure 3 is typical in that a variation about Mach 1 is indicated during most of the drag phase, then wind tunnel derived coefficients when corrected to full scale environmental conditions should be quite good for drag phase predictions, particularly for those involving large yield weapons. With a correlation of these coefficients and diffraction pressure coefficients determined from shock tube studies, a complete history of the loading can be defined where accurate loadings are necessary for laboratory computor investigations of response.

REFERENCES

1. Anderson, Ferd E. Jr., "Blast Loading on Domes and Arches", AFSWP-522, 21 July 1958 (Unclassified)

2. Gallagher, E. V., "Air Blast Loading on Arches and Domes", Report No. 15, Armour Research Foundation, Draft, September 1958 (Unclassified)

3. Rines, E.; Fergenson, M. and Kingery, C., "Air Blast Loading on Three Dimensional Scale Models of Dome Shape", AFSWP No. 773, BRL Memorandum Report No. 889, Ballistic Research Laboratories, Aberdeen Proving Ground, Maryland, 1955 (Unclassified)

4. Hoerner, Sighard F., "Fluid Dynamic Drag", published by the Author, Midland Park, New Jersey, 1958 (Unclassified)

5. Shapiro, Ascher H., "The Dynamics and Thermodynamics of Compressible Fluid Flow", Volumes I and II, The Ronald Press Company, New York, 1953 (Unclassified)

6. Lehnert, Richard, "Base Pressure of Spheres at Supersonic Speeds", NAVORD Report 2774, U. S. Naval Ordnance Laboratory, White Oak, Maryland, February 1953 (Unclassified)

7. Gowen, Forrest E. and Perkins, Edward W., "Drag of Circular Cylinders for a Wide Range of Reynolds Numbers and Mach Numbers", NACA TN 2960, Ames Aeronautical Laboratory, Moffett Field, California, June 1953 (Unclassified)

8. Oliver, Robert E., "An Experimental Investigation of Flow Over Simple Blunt Bodies at a Nominal Mach Numbers of 5.8", Memorandum No. 26, Guggenheim Aeronautical Laboratory, California Institute of Technology, Pasadena, California, July 1955 (Unclassified)

9. Levy, L; Lewis, S. D. and Parsons T. R., "Handbook of Normal Shock Relations", Contract AF 33(038)-8906. Massachusetts Institute of Technology, Cambridge, Massachusetts (Unclassified)

10. Bingham, H. H.; Weimer, D. K.; and Griffity, W., "The Cylinder and Semicylinder in Subsonic Flow", Technical Report II-13, Department of Physics, Princeton University, Princeton, New Jersey, July 1952 (Unclassified)

11. Smith, F. B., Jr.; Rines, E. G.; and Keefer, J. H.; "Air Blast Loading On Three Dimensional Scale Models of a Semi-Cylinder, AFSWP 1047, BRL Memorandum Report No. 1992, Ballistic Research Laboratories, Aberdeen Proving Ground, Maryland, July 1957 (Unclassified)

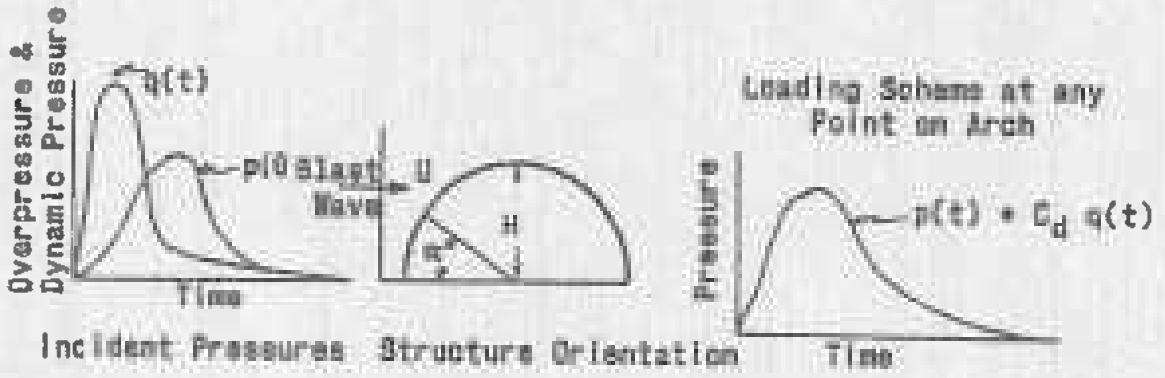

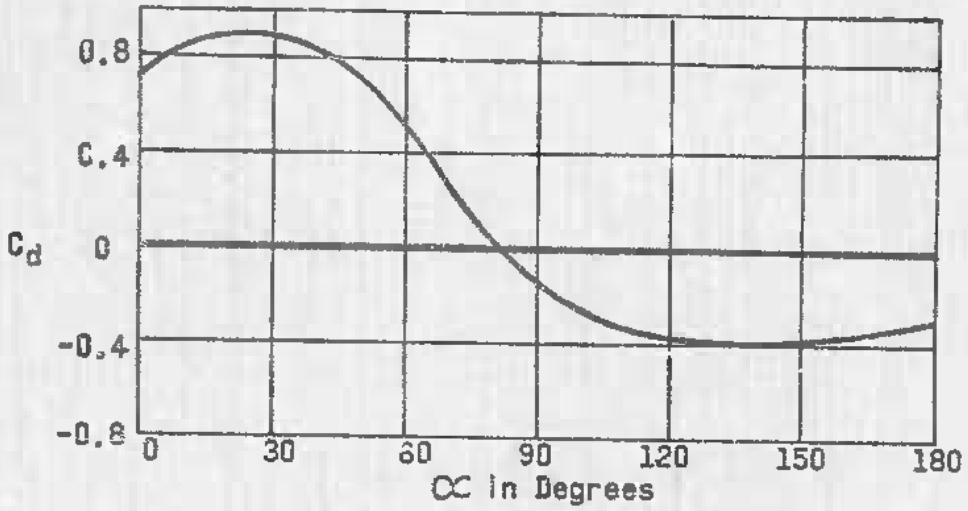

From "Blast Loading on Domes and Arches," by F. E. Anderson

Figure 1 Non-Ideal Loading Scheme for 180-Degree Arch for Peak Incident Overpressures of 100 psi or Less

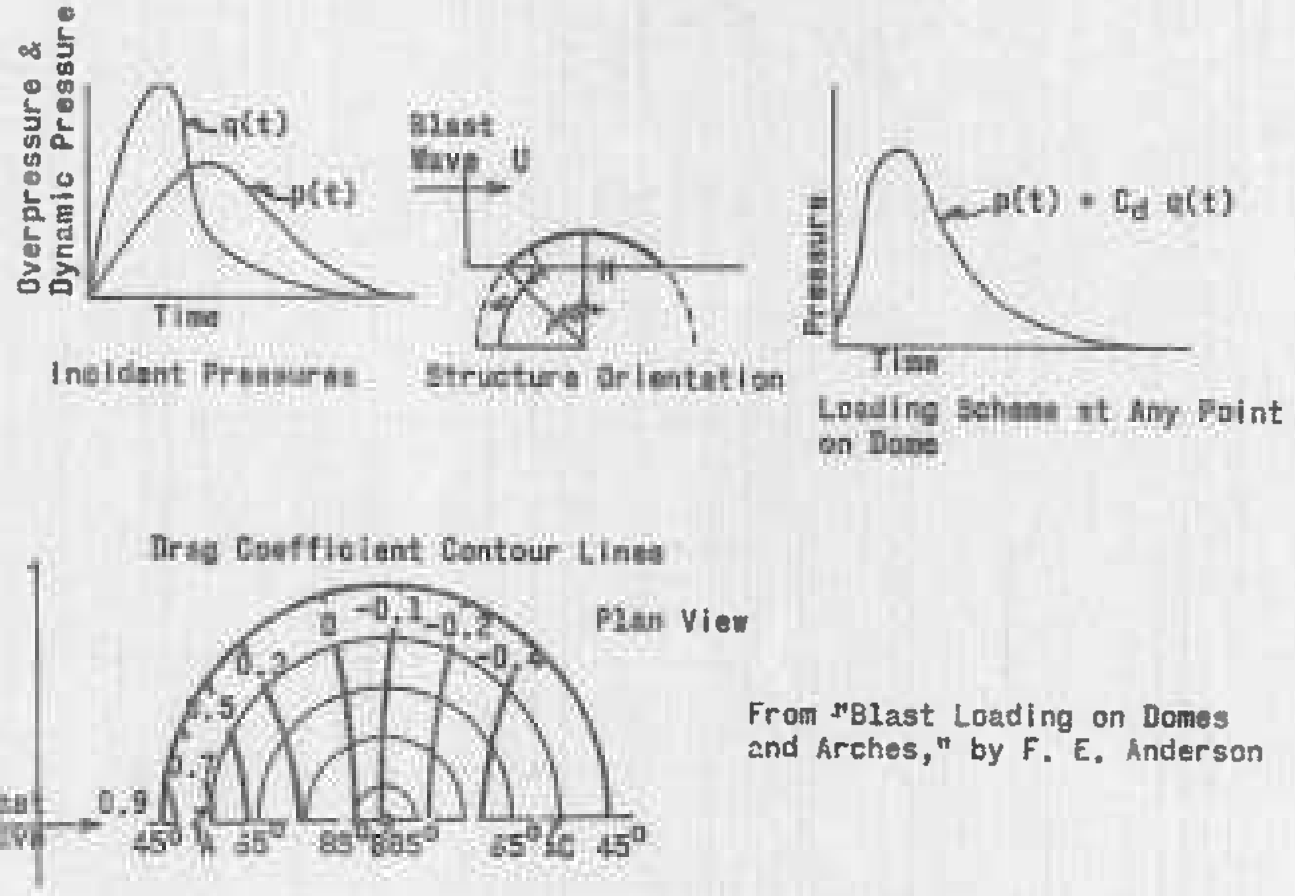

Figure 2 Non-Ideal Loading Scheme for 45-Degree (90-Degree) Dome for Peak Incident Overpressures of 100 psi or Less

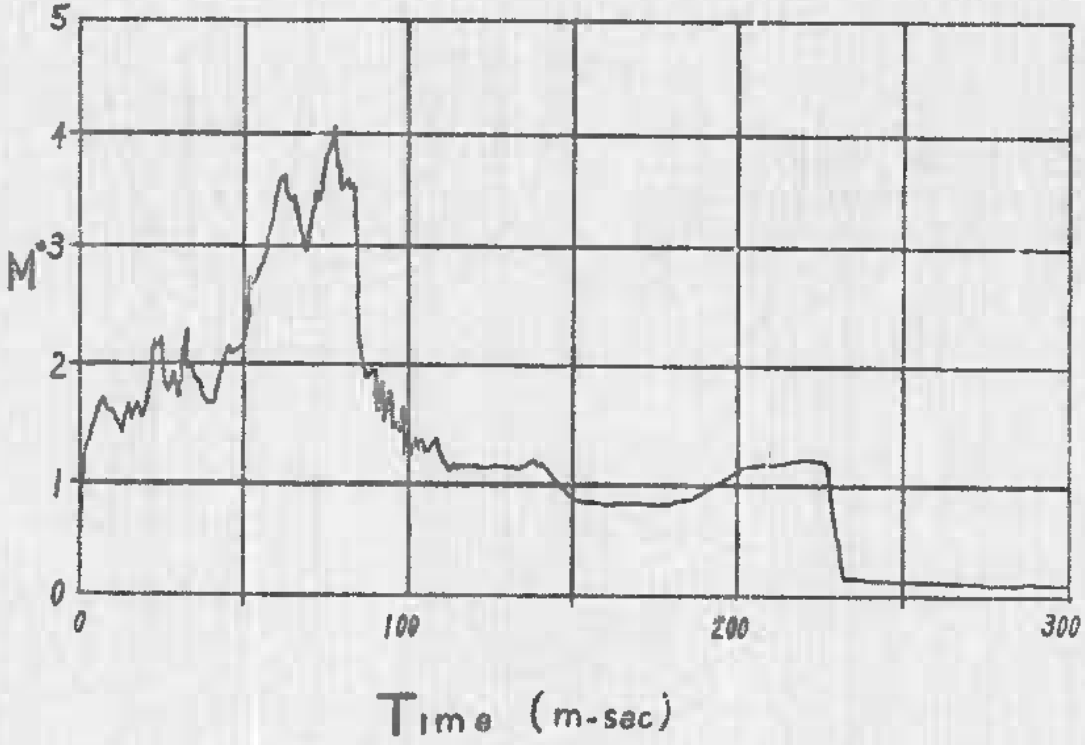

Figure 3 Typical Mach Versus Time Flow History for Non-Ideal Pressure Wave Forms

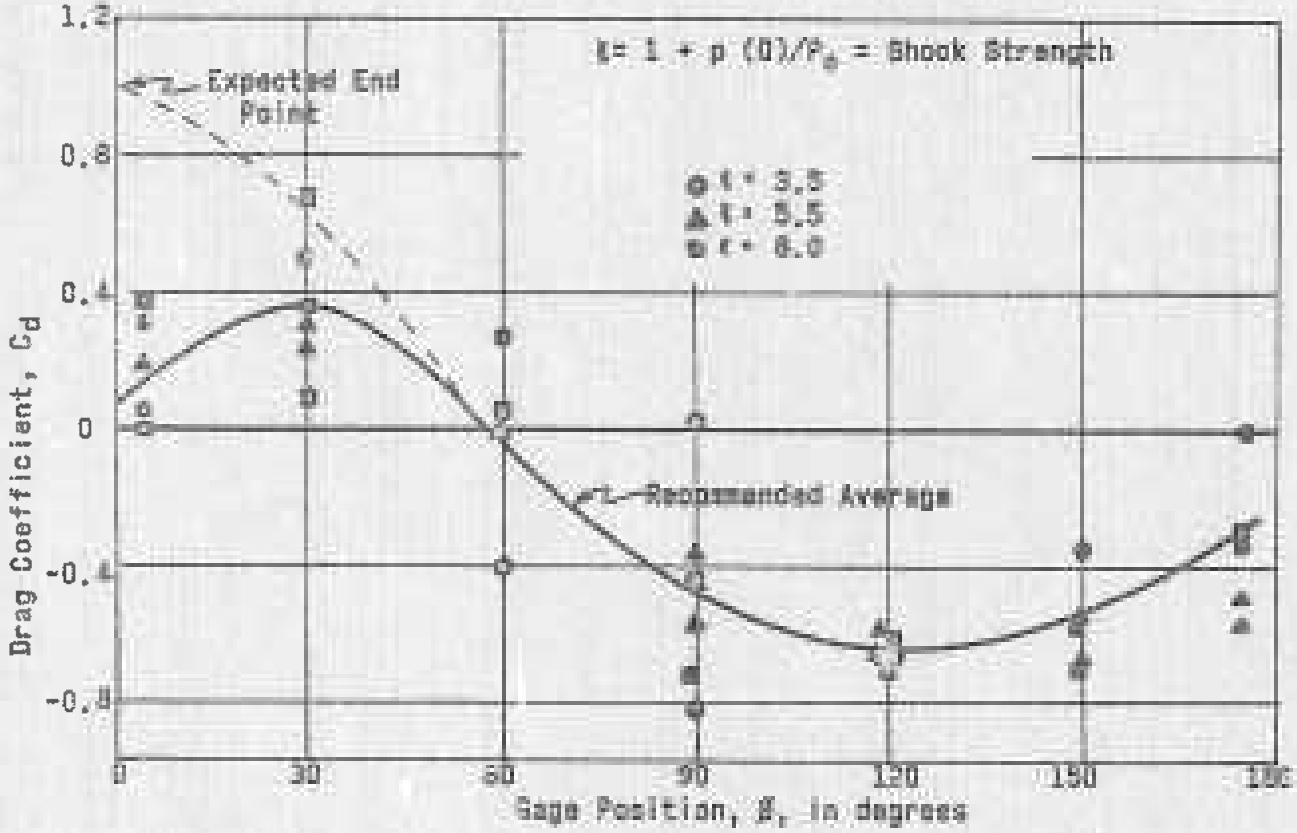

Figure 4 180-Degree Arch Drag Coefficient, C_d

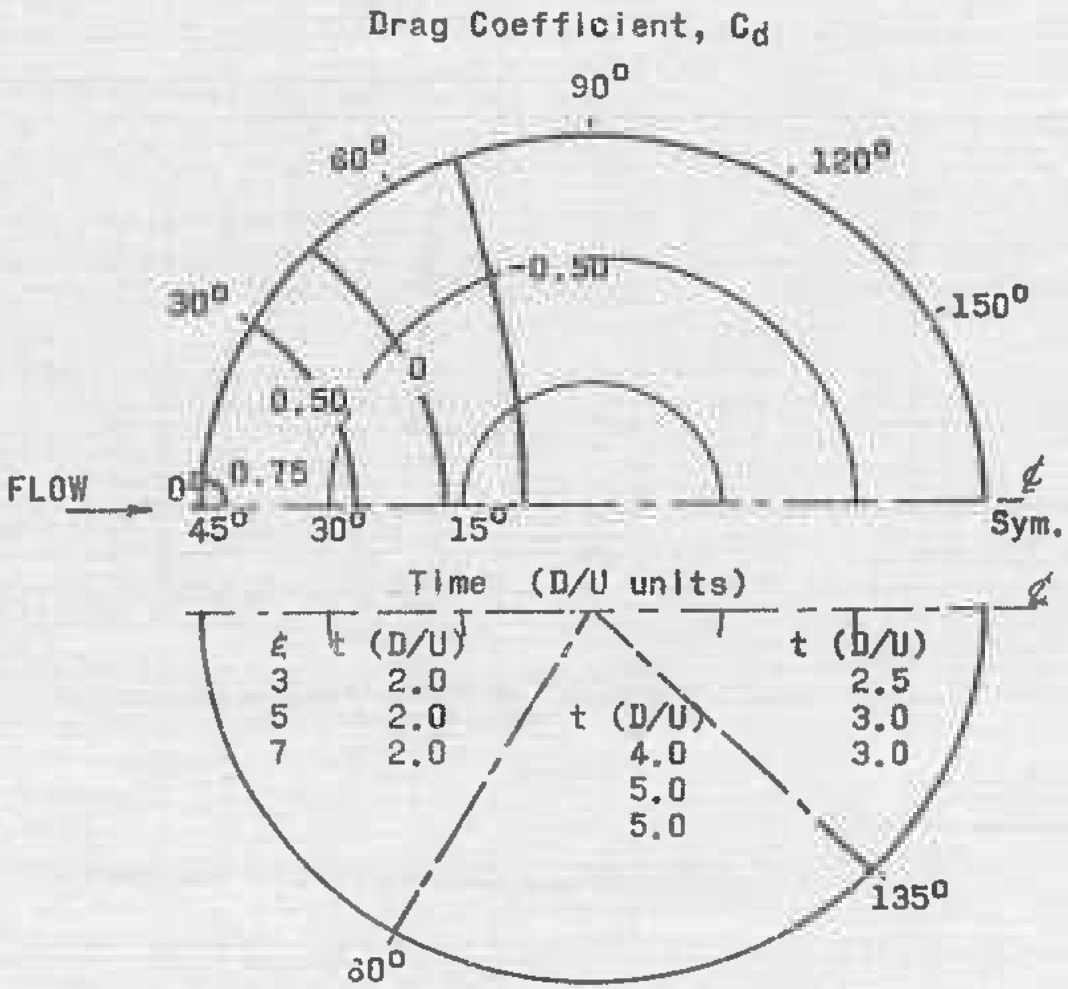

Figure 5 90-Degree Dome, Drag Coefficient, C_d, and Time From Shock Wave Arrival

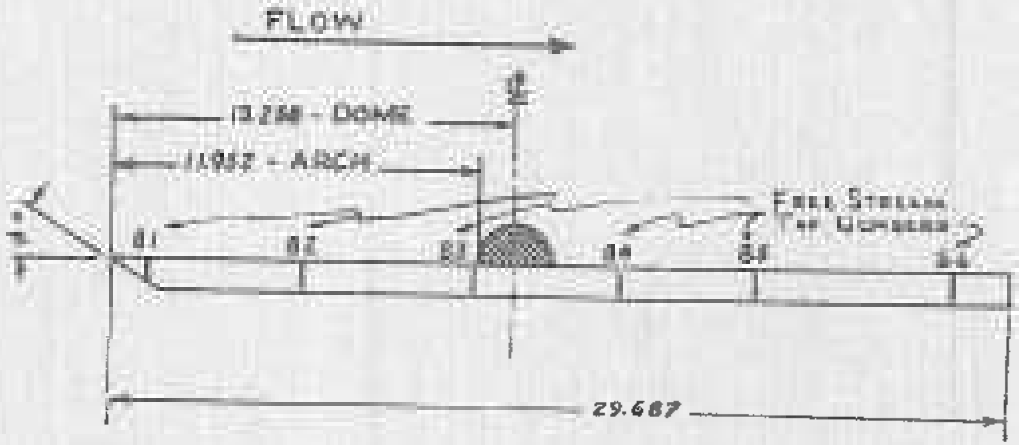

DIMENSIONS IN INCHES

Figure 6 Side View of The Wind Tunnel Ground Plane Showing Model and Free Stream Pressure Tap Locations

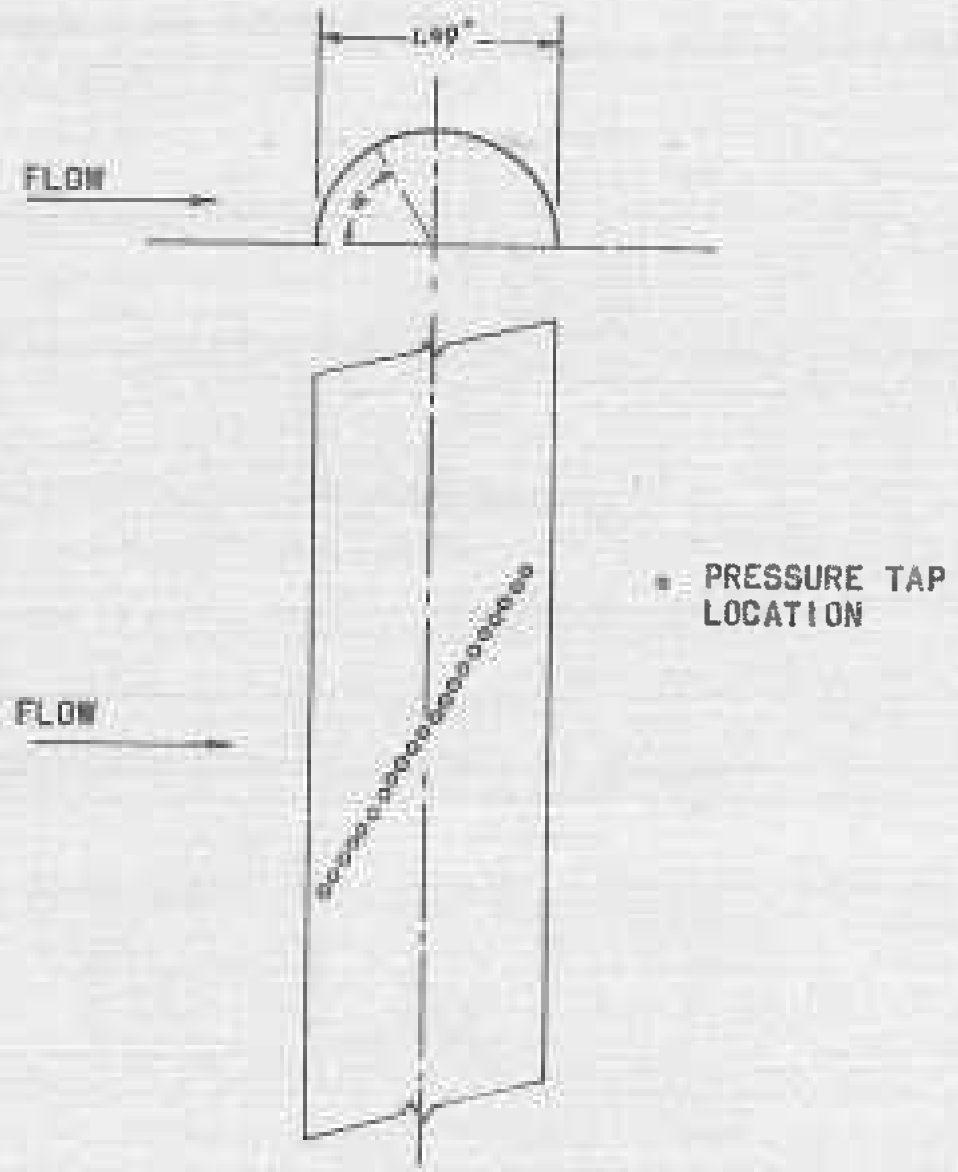

Figure 7 Pressure Tap Locations for Wind Tunnel Tests of 180-Degree Arch

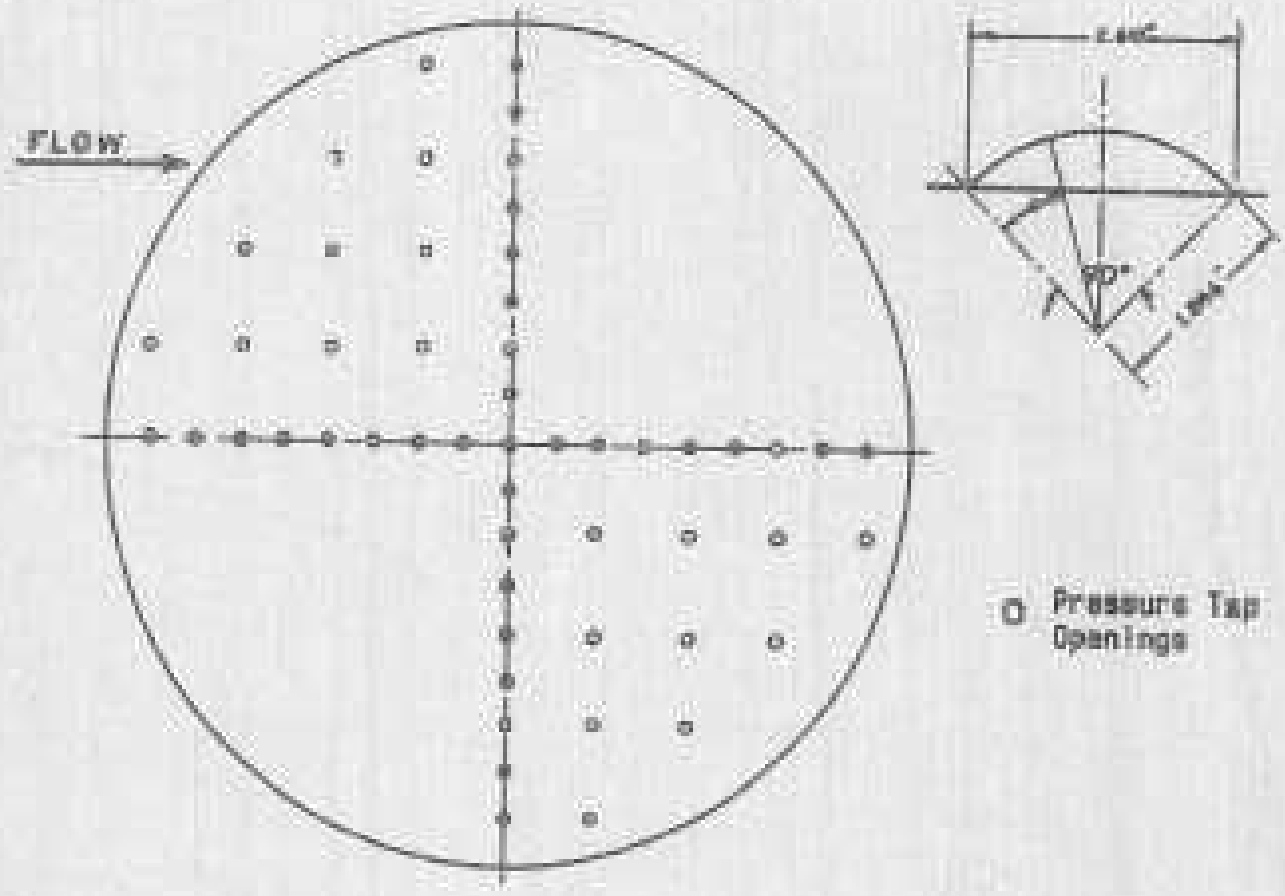

Figure 8 Pressure Tap Locations for Wind Tunnel Tests of 90-Degree Dome

"NOTICE: When Government or other drawings, specifications or other data are used for any purpose other than in connection wi a definitely related Government procurement operation, the U.S. Government thereby incurs no responsibility, nor any obligation whatsoever; and the fact that the Government may have formulat furnished, or in any way supplied the said drawings, specifications or other data is not to be regarded by implication or otherwise a in any manner licensing the holder or any other person or corpor tion, or conveying any rights or permission to manufacture, use or sell any patented invention that may in any way be related theret

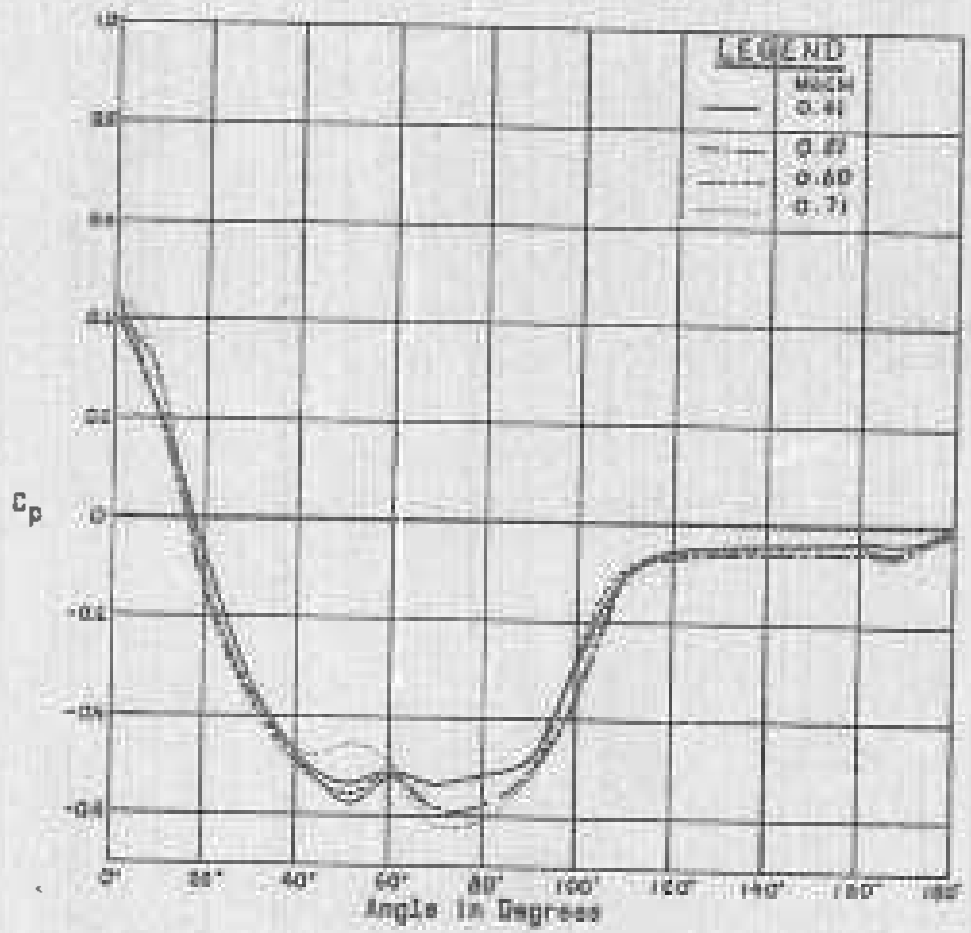

Figure 9 Pressure Coefficient Scheme From Wind Tunnel Tests of 180-Degree Arch

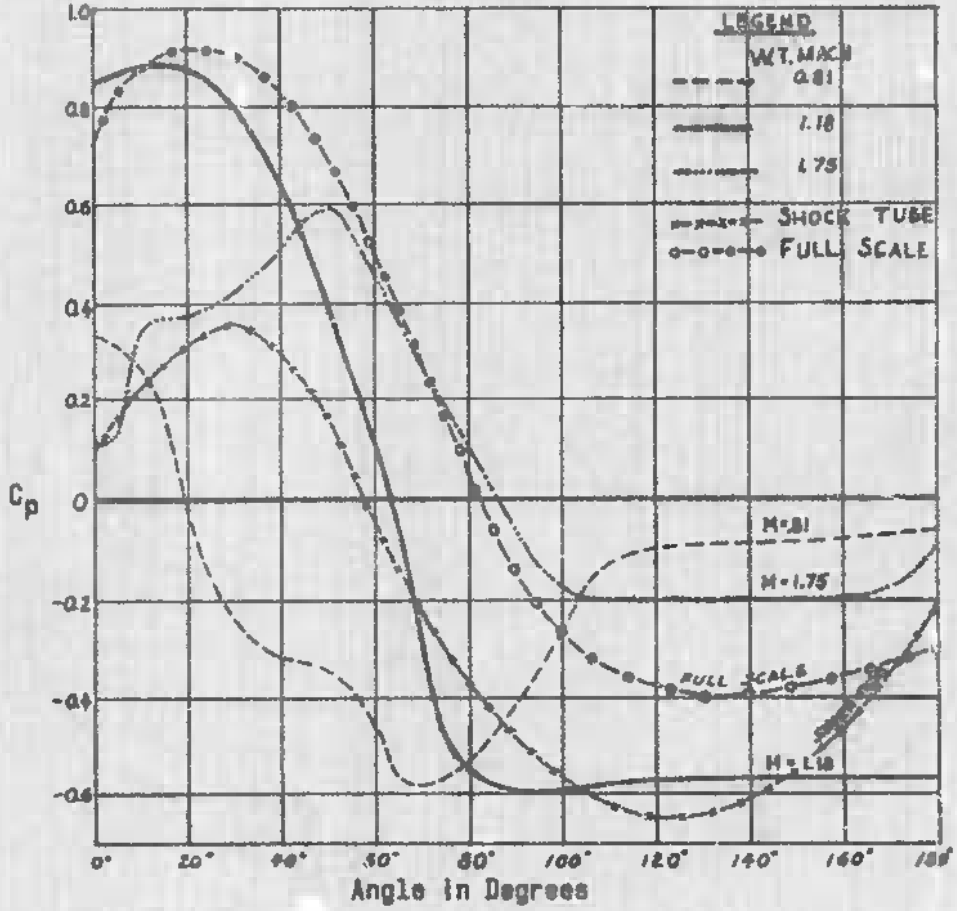

Figure 10 Comparison of Pressure Coefficient Schemes for 180-Degree Arch From Wind Tunnel, Shock Tube, and Full Scale Tests

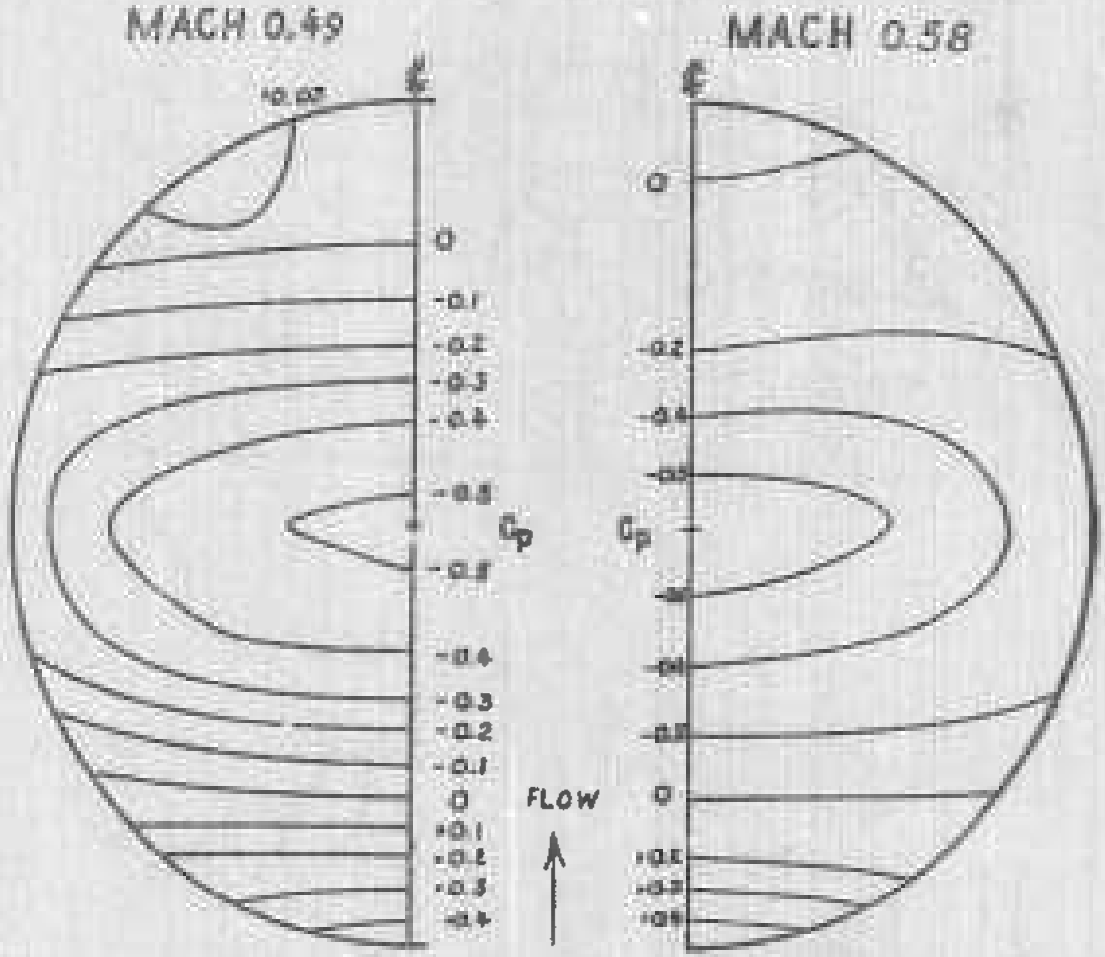

Figure 11 Pressure Coefficient Contours from Wind Tunnel on 90-Degree Dome

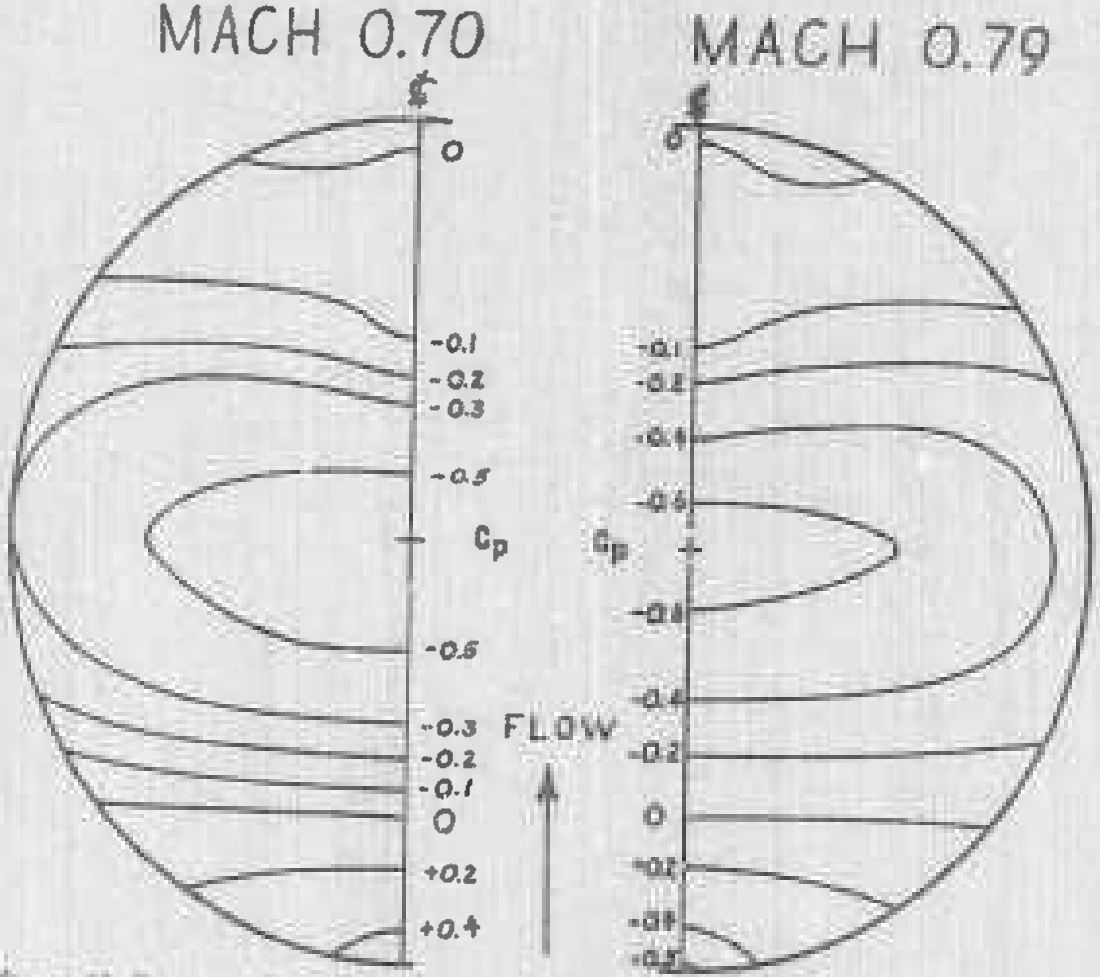

Figure 11 Pressure Coefficient Contours from Wind Tunnel on 90-Degree Dome

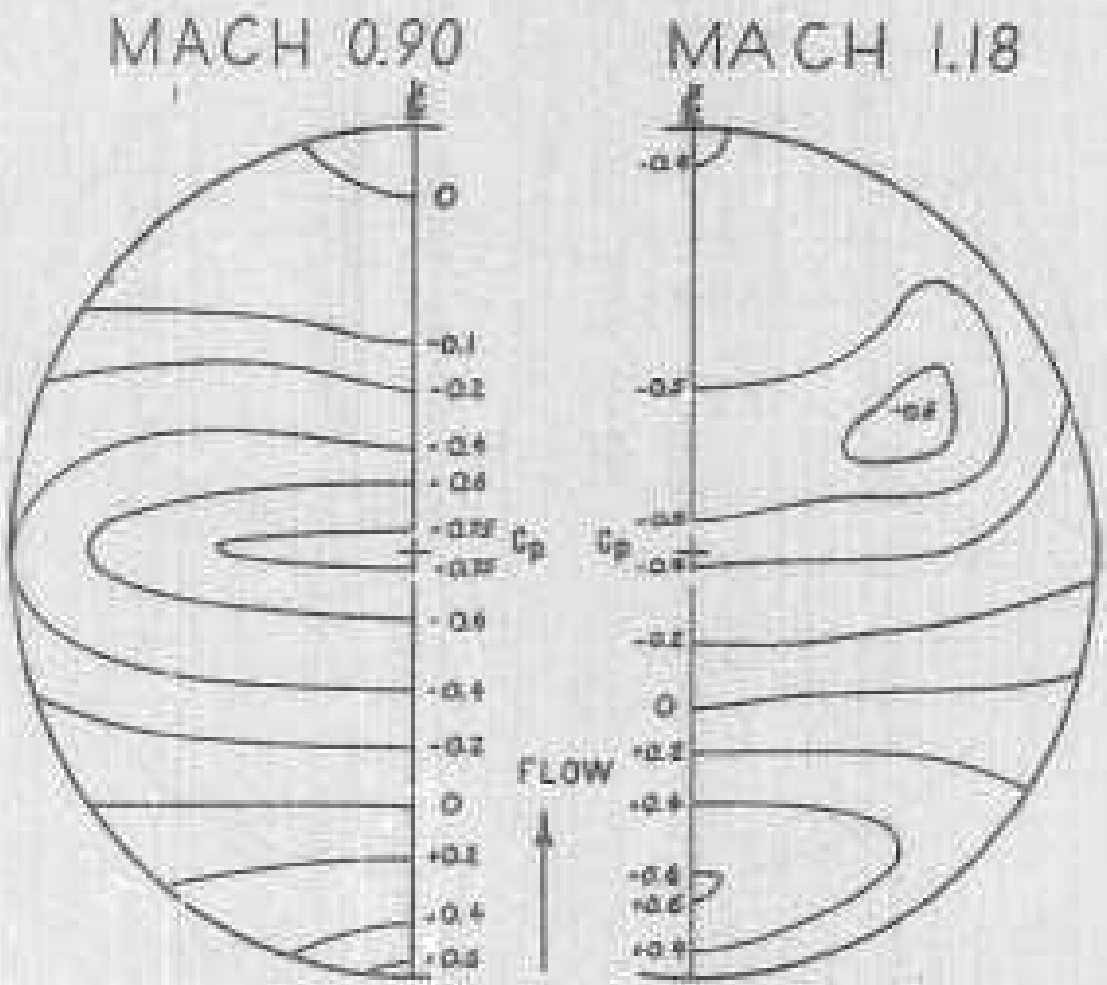

Figure 13 Pressure Coefficients from Wind Tunnel on 90-Degree Dome

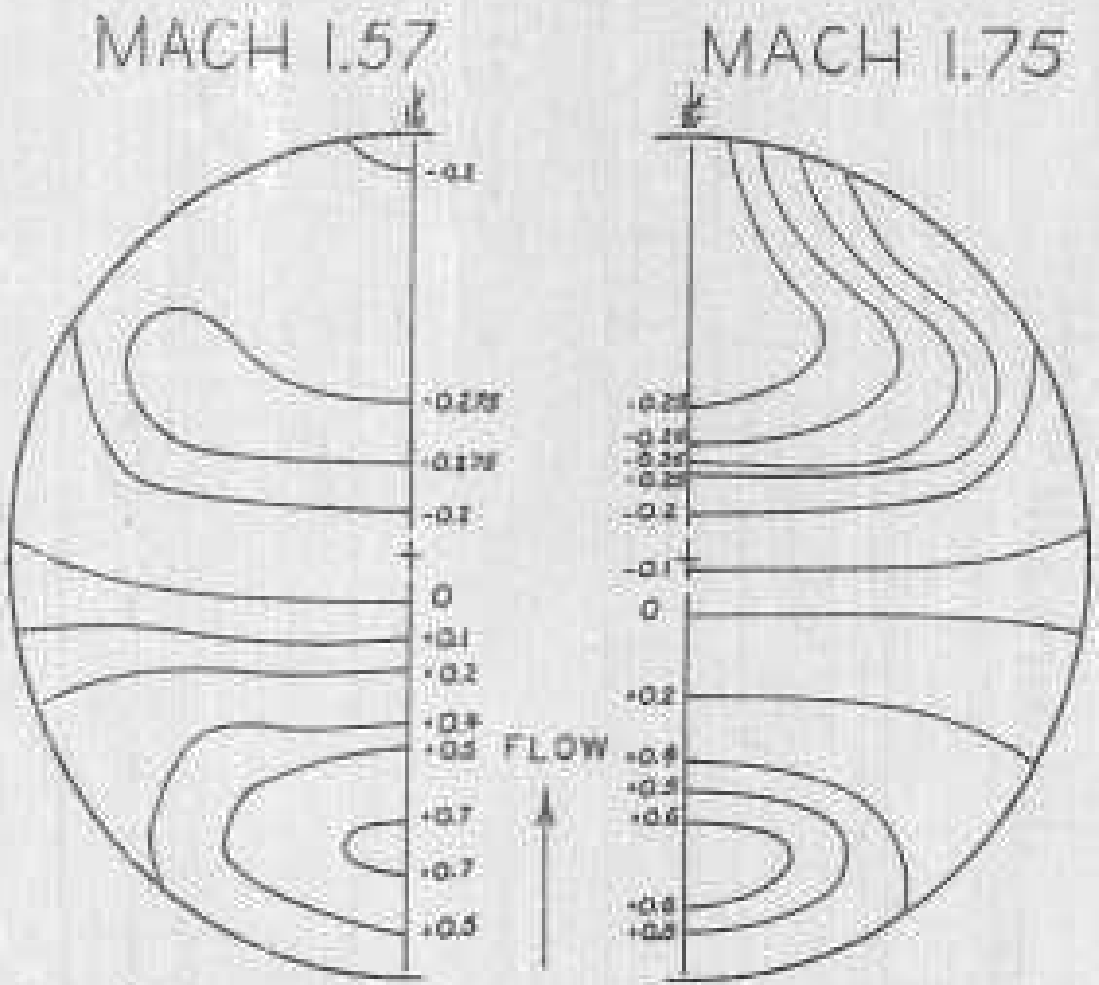

Figure 11. Pressure Coefficient Contours from Wind Tunnel on 90-Degree Dome

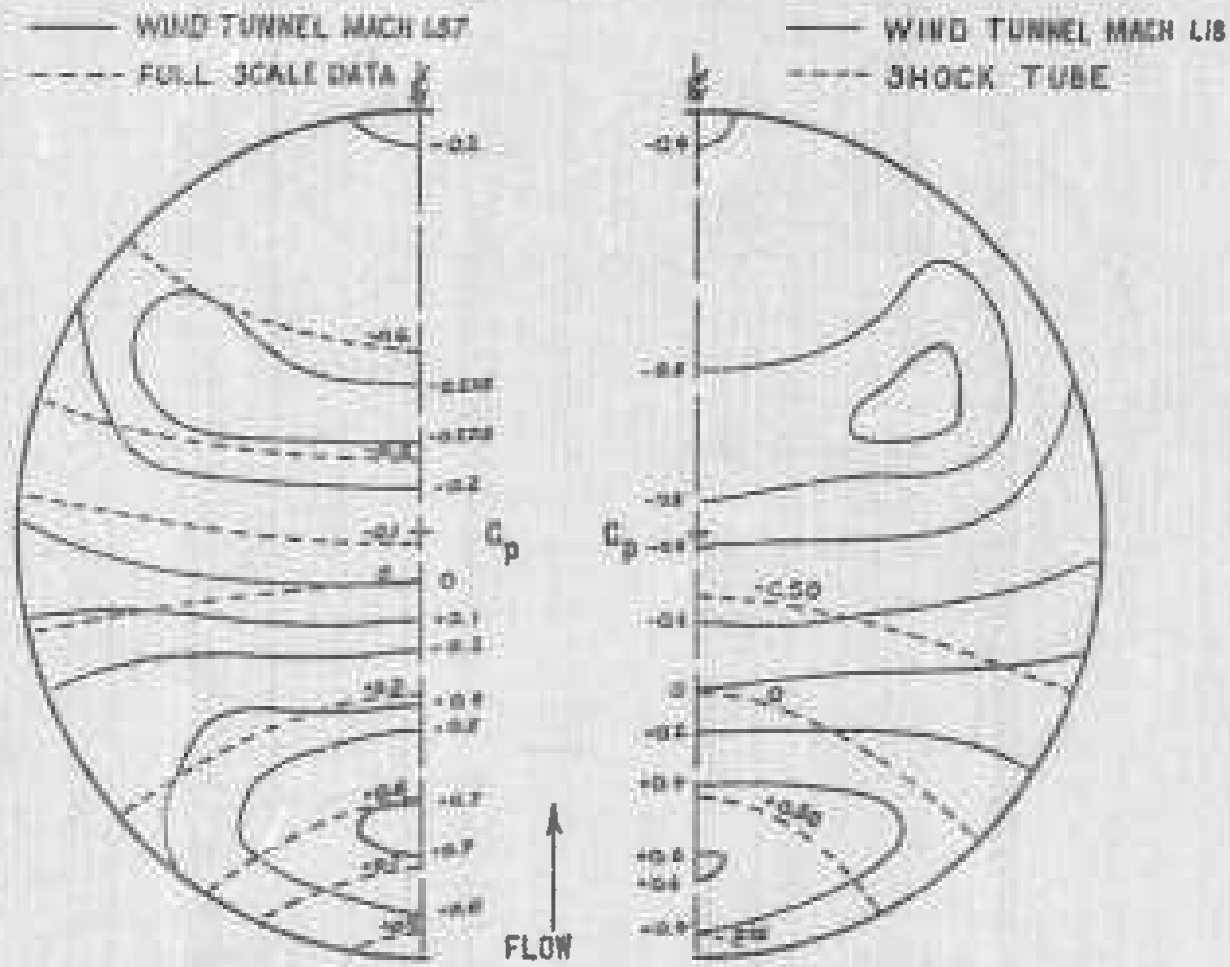

Figure 15 Comparison of Pressure Coefficient Contours for 90-Degree Dome From Wind Tunnel, Shock Tube, and Full Scale Tests

INTERACTION OF BLAST WAVES WITH WINGS
PART I. TEN-FOOT DIAMETER FREE JET SHOCK TUBE

Harold B. Pierce
NASA Langley Research Center

ABSTRACT

As part of the NASA studies on the problem of the loads experienced by an airplane subjected to blast-induced gusts, a shock tube facility has been constructed to simulate the flight conditions for model tests. The shock tube is 80 feet in length and 10 feet in diameter, the following diaphragm rupture, a free jet is obtained giving steady flow conditions for periods up to 50 or more milliseconds and up to Mach numbers of 1.0. This paper presents a discussion of the applications of the shock tube to blast loads studies and a description of the shock tube characteristics. The description covers the diaphragm rupturing techniques, the flow generation principles, and model testing procedures.

INTRODUCTION

For the past several years, the NASA has been investigating the interaction of blast waves with wings with particular emphasis on the loads caused by the blast-induced gusts. These studies were made with wings traveling at low speeds and involved two approaches. In one approach pressure-instrumented airplane models of about 6-foot span were launched into free flight at Mach numbers ranging from 0.1 to 0.2 and subjected to blast waves from actual explosions. The strength and position of the explosion were selected to impose angle-of-attack changes representative of two different operational conditions; the small angle change associated with the delivery of nuclear weapons, and the large angle change desired when blast waves are used as antiaircraft weapons. It was found that additional information was needed to explain the character of some of the measured pressure distributions. Accordingly, a second approach was instituted to examine the flow phenomena through use of small-scale schlieren studies. The next speaker will describe this second investigation as part of his talk. The results from both investigations have been published in classified NACA documents.

It was desired to extend the study of the effects of blast-induced gusts to the transonic and supersonic speed range and also to examine the loads produced during blast-wave diffraction. The experience gained with the free-flight testing technique at slow speeds showed, however, that this technique would be very difficult, time consuming, and expensive to apply at higher speeds. In order to overcome these shortcomings and also to permit more systematic testing, the NASA recently constructed the Ground Blast Apparatus at Wallops Island. This equipment utilizes a 10-foot-diameter free-jet shock tube and stationary model to provide flight simulation but continues with the use of actual explosions to provide the blast waves. This paper will point out some of the design considerations for this Ground Blast Apparatus and describe the operation of the shock tube.

DESCRIPTION OF APPARATUS

The elements comprising the Ground Blast Apparatus are shown in Figure 1 as they would appear during a test. The free-jet shock tube is shown shortly after a thin metal diaphragm mounted near the exit has been ruptured. The model is immersed in the flow of air issuing from the shock tube, and the blast wave from the explosion is rapidly approaching from the right. The flight condition simulated in this figure is that of an airplane in level flight being struck by the blast wave from an explosion directly below. Other flight conditions may be simulated by changing the explosion point or by changing the roll attitude of the model on its sting support.

Figure 2 shows the dimensions of the tube. It is 10 feet in diameter and the pressurized section is 80 feet long. A 5-foot extension downstream of the diaphragm prevents the ruptured diaphragm sections from opening too far and tearing off. The 10-foot diameter of the tube permits the use of models having a wing span up to 5 feet. An explosive such as Composition C-4 or HBX-1 produces the blast waves and the amount used depends on the speed range of the flow from the tube. In the Mach number range of 0.1 to 0.3, a charge weight of 150 pounds is chosen, while at flow speeds in the Mach 0.7 to 0.9 range, a charge weight of 600 pounds is used. The free-jet shock tube is currently undergoing calibration tests and has not been used with the airplane models to obtain research data.

An important part of the equipment not yet mentioned is the instrumentation used to measure pressure at the wing surface. The pressure instrumentation used previously in the free-flight tests had a response flat to 1 kc which was just adequate to provide measurements of the effects of the blast-induced gusts at the slow flight speeds. This response is not, however, high enough to measure these effects at the higher speeds nor to obtain information during the diffraction phase. Accordingly, the NASA developed a very small flush diaphragm pressure gage, together with a carrier amplifier system, which has a combined response flat up to 20 kc. This gage and the carrier amplifier are described in the appendix of this paper.

DESIGN CONSIDERATIONS

A general over-all description of the Ground Blast Apparatus has been presented. There are, however, several additional points concerning the shock tube and the selection of the proper model location that are of interest. The free-jet shock tube or shock tunnel is, in reality, a blowdown tunnel using a diaphragm as a quick opening valve. The flow issuing from the tube is actually the "cold flow" of the normal shock tube. That is, it is comprised of the air initially pressurized inside the tube which is accelerated out of the tube at steady velocity by the rarefaction wave formed on diaphragm rupture. The air continues to move out of the tube at constant velocity until the rarefaction wave, which initially moves into the tube, is reflected back to the exit. The Mach number of the flow depends on the initial pressure; for example, a pressure of about 2 pounds per square inch gives a Mach number of 0.1 while 38 pounds per square inch gives Mach 1, which is the maximum velocity attainable with the straight tube. For the 80-foot tube length, the flow duration ranges from about 0.15 second for Mach 0.1 down

to 0.10 second for Mach 1 although the actual useable portion of the flow is somewhat less as will be indicated later.

To avoid density changes between the boundary of the jet and the surrounding atmosphere which might hinder passage of the blast wave produced by the explosive charges, the pressurized air inside the tube is preheated by electric heaters. The preheat temperature is chosen so that on expansion of the air to atmospheric pressure in the free jet, the temperature will also be atmospheric.

Having indicated how the desired flow of air from the shock tube is produced, the next point is the proper location of the model during a test. Analysis showed that this location depends primarily on three considerations: (1) the mechanism by which the blast wave produces the desired angle-of-attack change on the model immersed in the jet, (2) the desire to locate the model away from the tube to avoid the local distortions of the blast wave which occur when it encounters the tube, and (3) the conflicting requirement that the model be placed close to the mouth of the tube to minimize the effects of the free jet mixing with the surrounding atmosphere. The two plan view sketches in Figure 3 have been prepared to illustrate the blast-wave effects. In the upper sketch, the conditions existing as the blast wave approaches the model are portrayed. The tube has been in operation long enough to provide steady flow over the model, and a blast wave chosen to produce a certain angle-of-attack change at the model is rapidly approaching the model from the side and, in this illustration, in a direction normal to the jet flow. The lower sketch shows the conditions a few milliseconds later when the blast front has just moved past the model. First, consider how the test location of the model depends on the way the blast wave changes the angle of attack. During passage through the jet, the blast wave deflects the particles of air it encounters into a new resultant flow direction which the model recognizes as the angle-of-attack change. This deflection of flow has moved the jet boundary through which the blast wave has passed but has not as yet affected the other boundary. To keep the model in the flow, then, it is necessary to locate it off center of the original jet flow in the direction of blast-wave passage.

The major distortions of the blast wave that result from the presence of the tube are also illustrated in the lower sketch. One, the reflection from the side of the tube, which could be a serious problem, has been trapped by a baffle aligned perpendicular to the blast front and prevented from arriving at the model until the test is completed. Nothing this simple could be devised, however, to prevent distortion of the blast wave on entering the open end of the tube and a resulting alteration of the flow field due to the expansion wave which is formed at this time and moves out toward the model. Naturally, to be sure that the conditions of the test are not altered, the model should be placed far enough from the tube exit that this expansion wave does not reach the model during the test period. It is felt, however, that since the initial portion of the expansion wave is quite weak, it may be possible to allow this portion of the wave to pass over the model location before the test is completed and not seriously affect the results. With a test duration of 10 milliseconds, which is the duration of the positive phase of the blast wave used in the tests, the model would be located about 15 feet out from the mouth of the tube.

OPERATIONS

As implied previously, the operations have thus far been limited to development tests with the tube proper. The major problems concerned the diaphragms, primarily because of their large size. These problems included selection of material, fabrication, clamping, and rupture. Steel diaphragms are currently being used for flow speeds in the region of Mach 0.7 to 0.9. For the lower speeds of Mach 0.1 to 0.3, diaphragms made of cloth and plastic are being developed. Since the major interest is felt to be in the higher jet speeds, only the development of the steel diaphragms will be discussed.

Because of the large size of the diaphragms, it was necessary to fabricate them by welding together several sheets of steel. The material presently used is 1010-1015 cold rolled annealed sheet steel. To avoid asymmetrical stresses, the weld pattern shown in Figure 4 was chosen. All welds are butt welds, and extreme care is taken since the material is only 1/32 to 3/64 of an inch thick.

The diaphragms are clamped in place between heavy flanges using 100 bolts, each 1-7/8 inches in diameter. To avoid slippage, the special clamping ring shown in cross section on Figure 5 is inserted between the flanges, downstream of the diaphragm. A 1/16- by 1/2-inch land is shown on the ring, and in the insert it can be seen that the surface of the land has been machined in a series of small sharp ridges. With the entire clamping force of the bolts concentrated on this small area, the ridges actually dig into the diaphragm metal and so far have prevented any slippage.

The 10-foot-diameter diaphragms presented a difficult rupture problem, particularly in preventing the diaphragm segments from going downstream following rupture. In addition, with the cold flow being used, it is particularly important that, following opening, the segments lie close to the tube wall in order to present a minimum obstruction to the flow. The method used was derived from experience with small circular shock tubes which indicated that satisfactory bursts would be obtained if the diaphragm were ruptured along predetermined lines into pie-shaped segments. Since scoring the 10-foot diaphragm and allowing it to self-burst would not be practical, tests were made in a 2-foot-diameter shock tube which showed that primacord could be used to cut the diaphragm. This method has the additional advantage for the Ground Blast Apparatus that the explosion of the primacord can be timed precisely with respect to the explosion of the charge producing the blast wave.

As with any new piece of apparatus, a number of unsatisfactory bursts have been made, however, just recently the proper combination of material with number of diaphragm segments was evolved so that the diaphragm opens quickly and no pieces fly downstream. As mentioned previously, low carbon steel proved satisfactory for the diaphragm material. The satisfactory number of pie-shaped segments in which to cut proved to be eight. In the course of the development tests, it was found that exploding the primacord on the inside or pressure side of the diaphragm substantially reduced the opening time, and Figure 6 shows a diaphragm with the primacord

so arranged. The eight legs of primacord are fixed together to the center of the diaphragm, and the explosion is initiated at this point. Since the diaphragm bulges out about 18 inches under pressure, it creates the problem of keeping the primacord in contact with the diaphragm. Since no excessive tension should be placed on the primacord, small wooden blocks with holes in them are fastened approximately every 6 inches along each leg to act as fair leads. With the primacord thus arranged on the inside, the opening time appears to be somewhere between 5 and 10 milliseconds. With it on the outside, the opening time is increased to 30 milliseconds.

Although rupturing the diaphragm by exploding primacord appears at present to be the best method, it has one serious disadvantage; namely, the blast wave it produces upon explosion.. The portion of this wave that moves out of the tube is not troublesome, but a strong shock wave also moves into the tube and superimposes itself on the normal shock tube processes. A qualitative view of the sequence of events, including the primacord effect, has been obtained from a total-head and a static-pressure probe mounted in the flow 15 feet in front of the tube, and this is presented in Figure 7. The ordinate is pressure increment, and the abscissa is time. The upper trace is derived from the total-head probe, and the lower from the static probe. The first disturbance to reach the probes is the combined shock wave from the diaphragm rupture and the explosion of the primacord, and the traces from both probes are similar. Just as this disturbance dies out, the slower moving cold flow which expands from behind the diaphragm reaches the probe location, and the pressure increment recorded from the total-head probe rises and levels out. Then follows the period of steady flow with the jet at atmospheric pressure during which a model would be subjected to a blast wave and the test results obtained. The next deflection of the records occurs when the portion of the blast wave from the primacord that initially moved into the tube is reflected back and strikes the probes. As with the beginning shock wave, both probes again show similar records. Shortly after this, the rarefaction wave returns to the tube exit and stops the flow. The early return of the primacord shock wave substantially reduces the period of steady flow, and its initial entry into the tube probably caused a delay in the start of the flow. Fortunately, the flow period remaining is of sufficient duration to conduct some of the blast tests. If a greater duration is required in the future, this can be obtained by increasing the length of the tube or by finding an equally effective means of rupturing this large size diaphragm without producing an added shock wave.

High-speed motion pictures of diaphragm opening have been taken, and a few enlarged frames from one of the movies are shown as Figure 8.

CONCLUDING REMARKS

The application of the 10-foot-diameter free-jet shock tube to blast loads studies has been discussed. Also presented were some of the design problems unique to this work, together with a description of the operations. Since calibration of the shock tube has not been completed, no research results could be presented.

APPENDIX

A POINT SOURCE TRANSIENT PRESSURE MEASUREMENT SYSTEM

Richard W. Morton

SUMMARY

A small electrical pressure gage has been developed at NASA Langley Research Center which is suitable for the measurement of shock tube and blast pressures. This gage evolved from previous designs that were intended for the carrier frequency range from 3 to 25 kilocycles (Reference 1). The present gage is approximately a point source at 20 kilocycles. To complement this gage, a two-channel carrier amplifier system of sufficient bandwidth was developed. The carrier frequency of this system was put at 120 kilocycles.

DESCRIPTION OF THE PRESSURE GAGE

The gage under discussion is a flush diaphragm inductance gage, details of which are shown in Figure 9. It has an outside diameter of 3/16 inch and a thickness of 1/10 inch. The length to the point of lead attachment is 0.281 inch. A coil of 125 turns of copper wire is placed around the pole piece. The diaphragm thickness for the 30-psi gage is 0.002 inch. The air gap is 0.004 inch. Full-scale pressure produces a deflection of 200 microinches.

Different full-scale pressure ranges may be had by changing diaphragm thickness. Doing this, of course, changes the natural frequency. A 0.0015-inch diaphragm has a full-scale range of 15 psi and a natural frequency of 42 kilocycles while a 0.002-inch diaphragm has a range of 30 psi and a natural frequency of 50 kilocycles.

The free diameter of the diaphragm is 0.120 inch. Estimating that the equivalent free piston is one-half of this, it can be said that the gage performs as a point source up to 20 kilocycles (Reference 2).

The linearity of the gage is ± 1 per cent of full scale and the output due to acceleration is 0.2 per cent per 100g's.

DESCRIPTION OF THE CARRIER AMPLIFIER

The inductance gage forms a single arm of a four-arm bridge. Figure 10 shows a block diagram of the system. The bridge is powered with 10 volts at 120 kilocycles. The bridge output is fed through a transformer and onto a coaxial cable. The cable then runs to the carrier amplifier proper. At this point all residual carrier voltage in the bridge output is balanced out by adding an equal and opposite bucking voltage. This bucking voltage is fashioned in a circuit containing two potentiometers and derives its 120-kc input from the carrier power supply. A signal will appear only when pressure is applied to the gage. The signal is now fed to an attenuator for gain control purposes. Next it enters a two-stage feedback amplifier. This

amplifier has a minimum feedback of 40 db over the band of interest. From the amplifier the signal is put through a bandpass filter, then into a similar amplifier, and a second bandpass filter. The function of the bandpass filters is to eliminate harmonics and reduce the effect of microphonics. Next, the signal is led to a phase-sensitive demodulator where it is converted to d-c. Finally, the signal is sent through a low pass filter and out into an oscilloscope.

In order to operate the demodulator, carrier voltage of adjustable reference phase must be provided. This is furnished by a resolver which converts the constant-phase, 120-kc, 10-volt supply to 10 volts at any desired phase. Being able to adjust the phase of the keying voltage has the operational advantage that the polarity of the carrier output may be reversed by a 180° rotation of the resolver shaft.

The carrier voltage is generated by a crystal oscillator which is amplitude stabilized with a pair of avalanche diodes. The oscillator output passes into a power amplifier which delivers 10 volts at 10 watts. The power amplifier is a feedback amplifier with 40 db of feedback.

RESPONSE OF SYSTEM

The linearity of the carrier amplifier is at least ± 0.5 per cent of full scale. Sensitivity to change in the 60-cps supply voltage is 0.03 per cent per volt at 100 volts. Figure 11 shows the variation of sensitivity with line voltage. Response to microphonics can simply be said to be good. Striking the most sensitive tube with a pair of pliers produces an output less than 10 per cent of full scale. This performance can be attributed to the bandpass filters.

The transient response of the system is limited by the output filter. Figure 12 shows the transient response. This filter cuts off at about 22 kilocycles.

CONCLUDING REMARKS

The combined linearity of the pressure gage and carrier system is approximately ± 1.5 per cent of full scale. The frequency response is sufficiently high considering the frequency at which the gage begins to depart from being a point source. The over-all system sensitivity to external disturbances is low.

It is felt that the described system is adequate to provide reliable measurements of transient pressures encountered in shock tube and blast work.

REFERENCES

1. Patterson, John L: A Miniature Electrical Pressure Gage Utilizing A Stretched Flat Diaphragm. NACA TN 2659, 1952.

2. Beranek, Leo L.: Acoustics. McGraw-Hill Book Co., Inc., 1954.

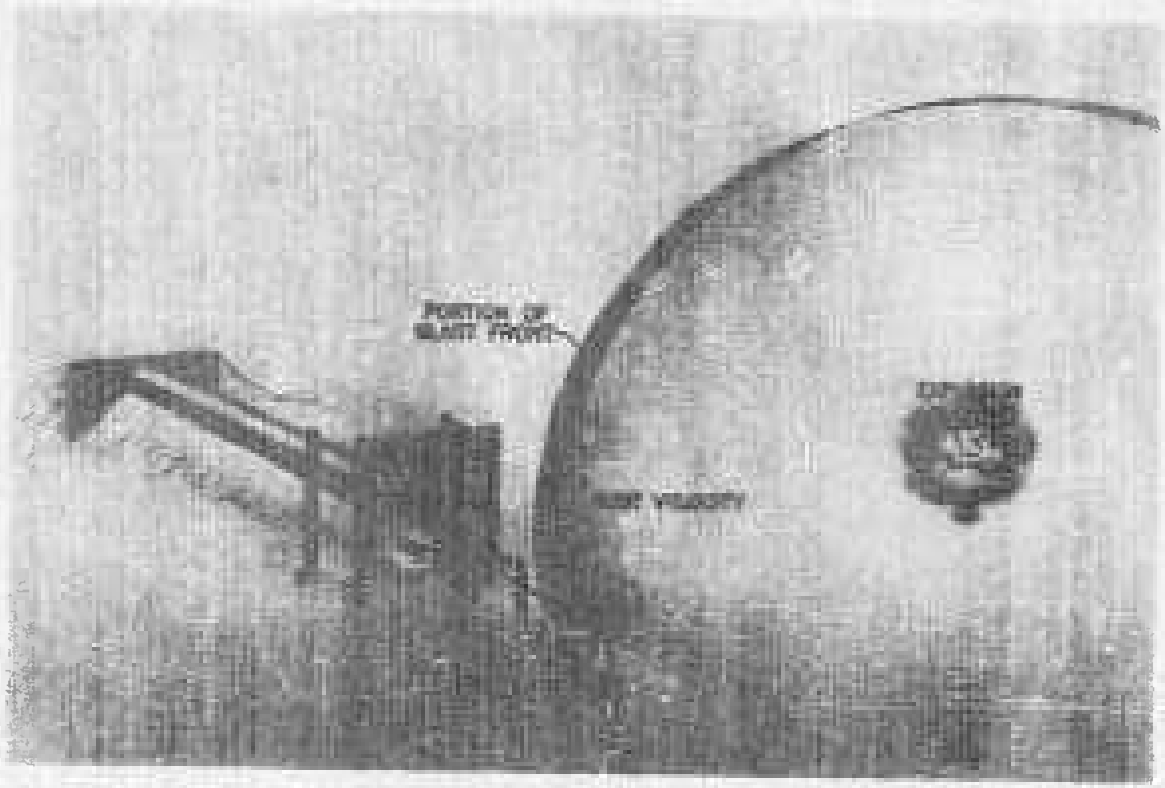

Figure 1 Blast Research with Fixed Model

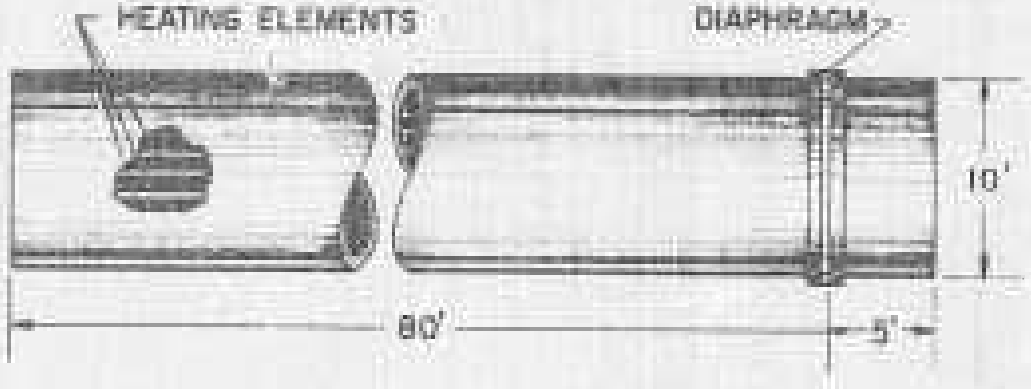

Figure 2 Ten-foot Free Jet Shock Tube

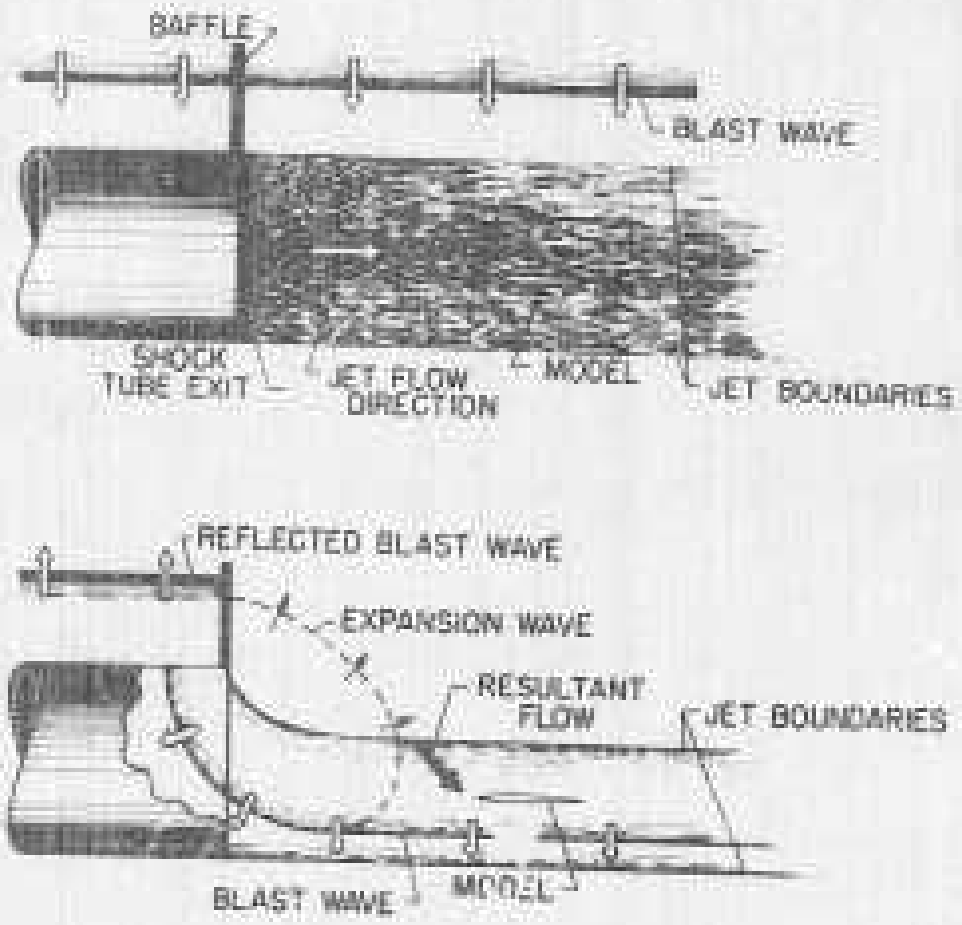

Figure 3 Blast Wave Distortions

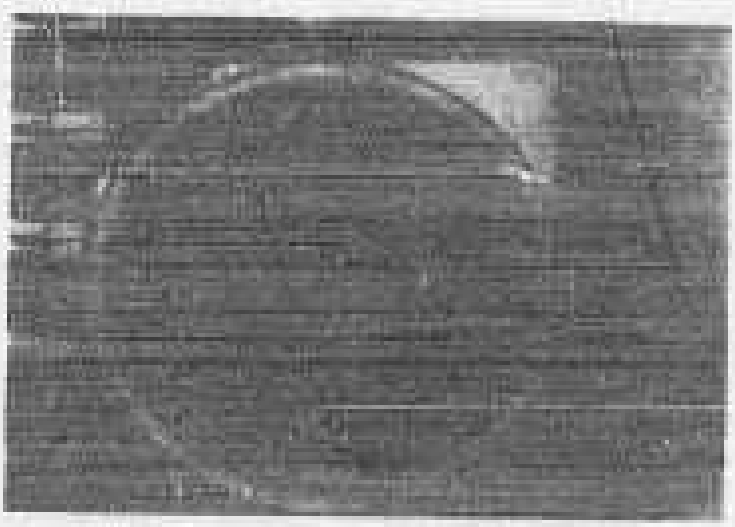

Figure 4 Diaphragm Fabrication Pattern

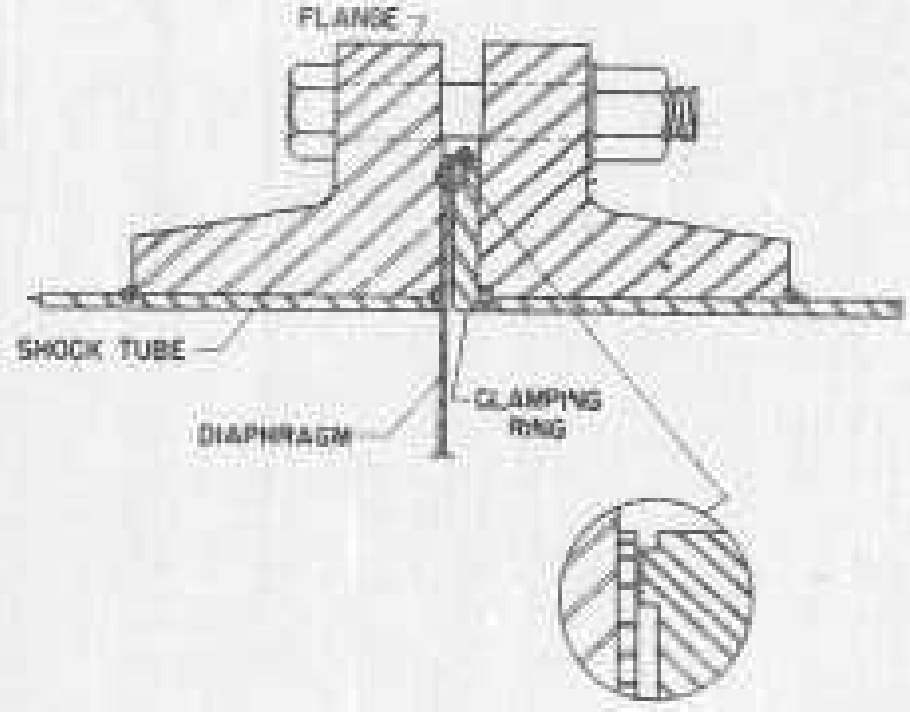

Figure 5 Clamping Ring Details

Figure 6 Primacord Arrangement

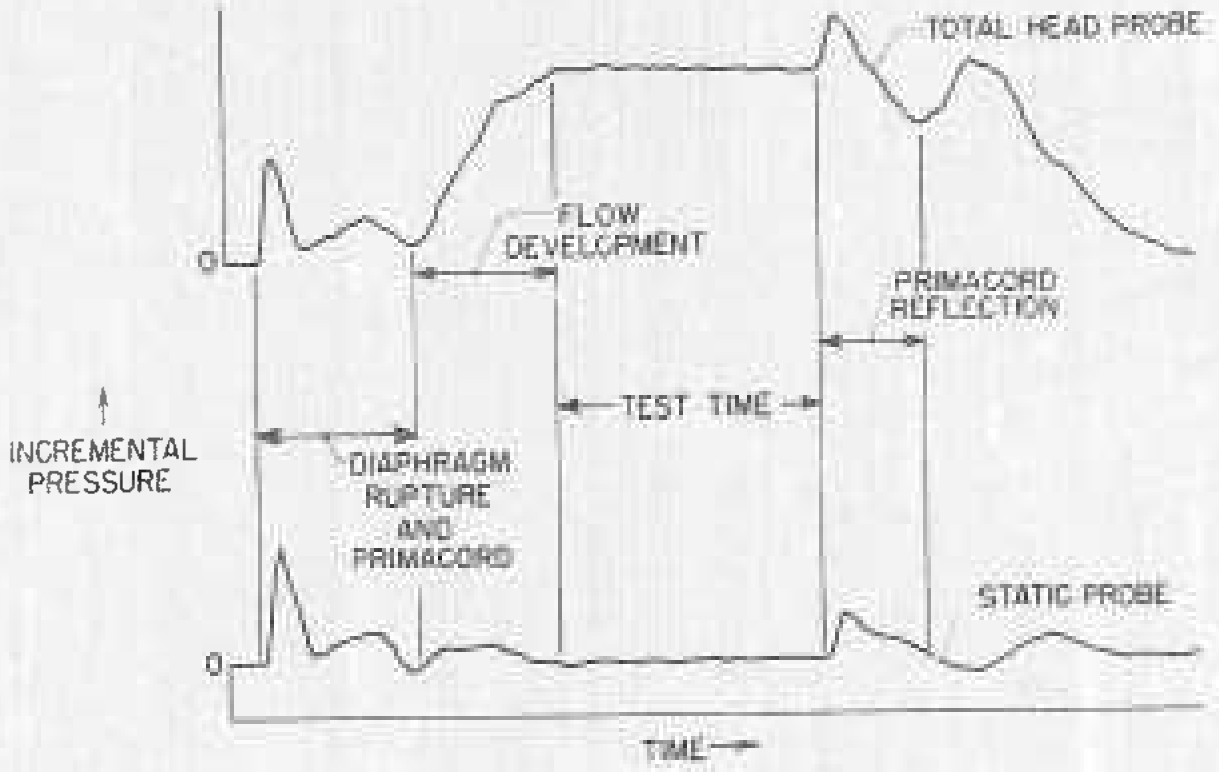

Figure 7 History of Flow Events

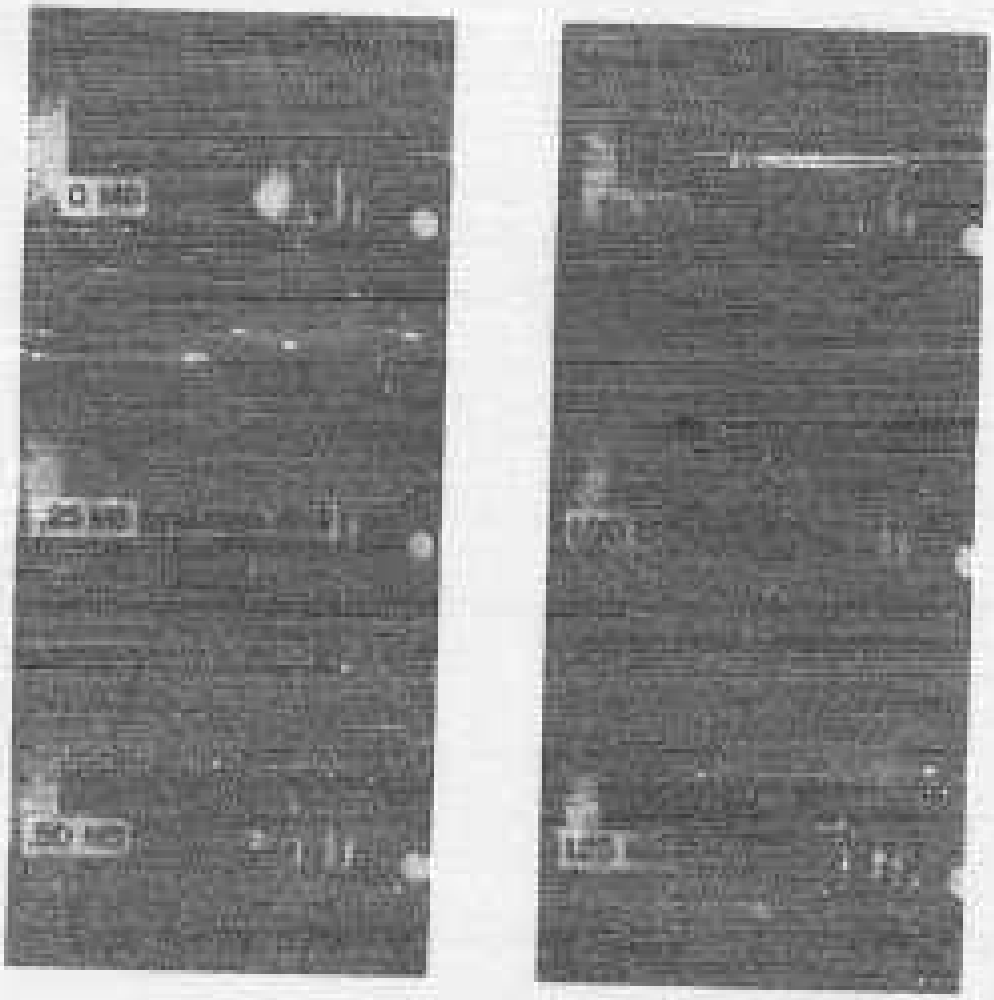

Figure 8 Initial Opening of Diaphragm

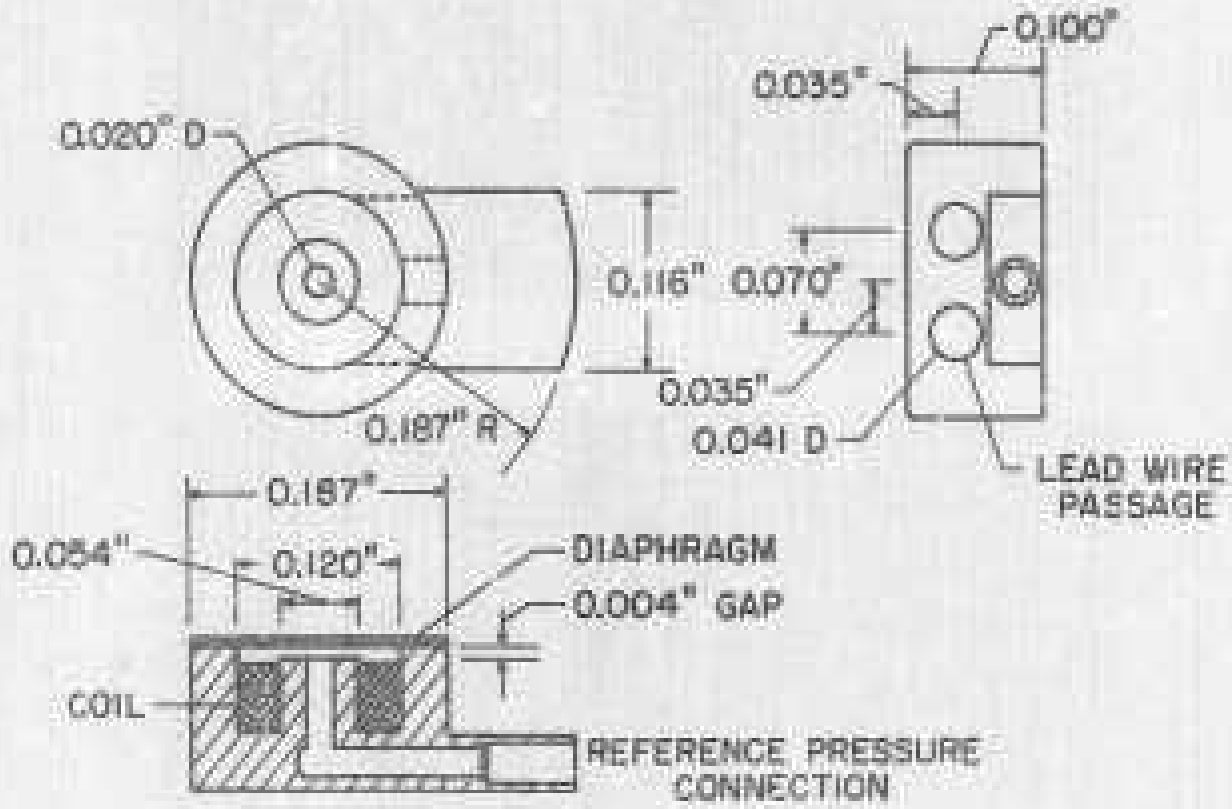

Figure 9 NASA Flush Diaphragm Inductance Pressure Cage

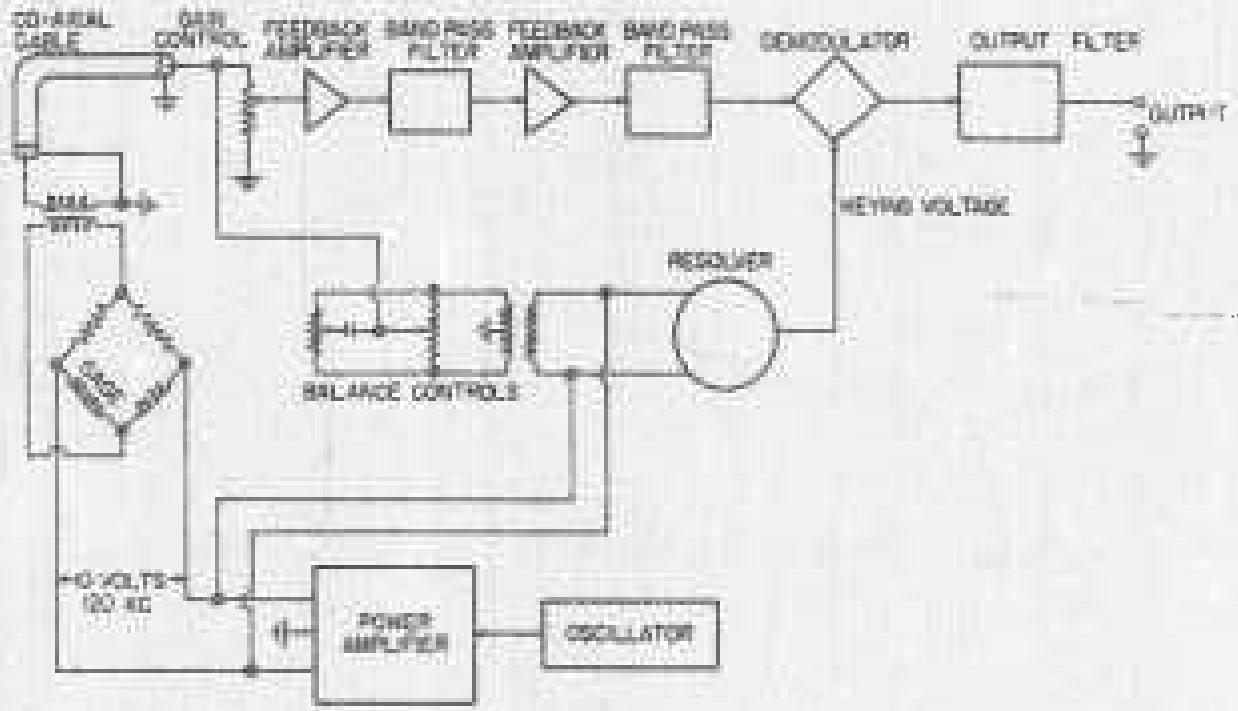

Figure 10 Block Diagram of 120kc Carrier Amplifier System

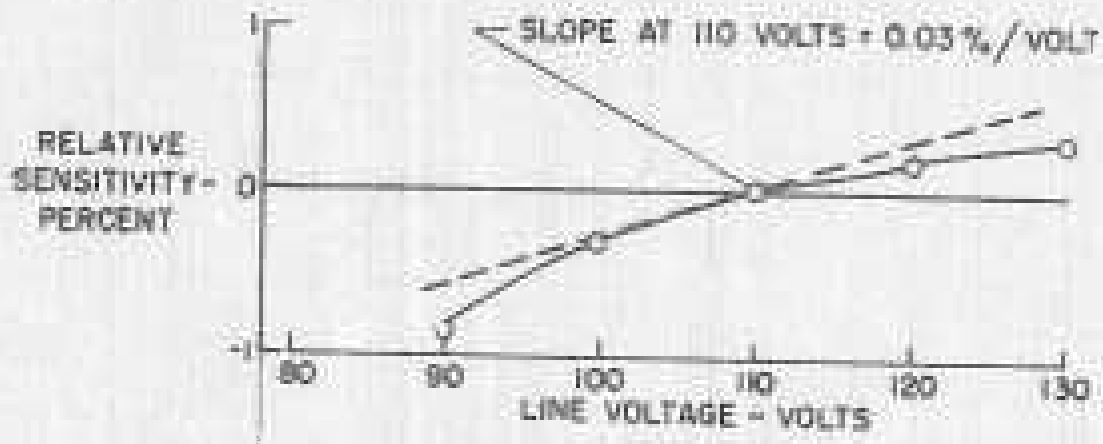

Figure 11 : System Sensitivity to Line Voltage

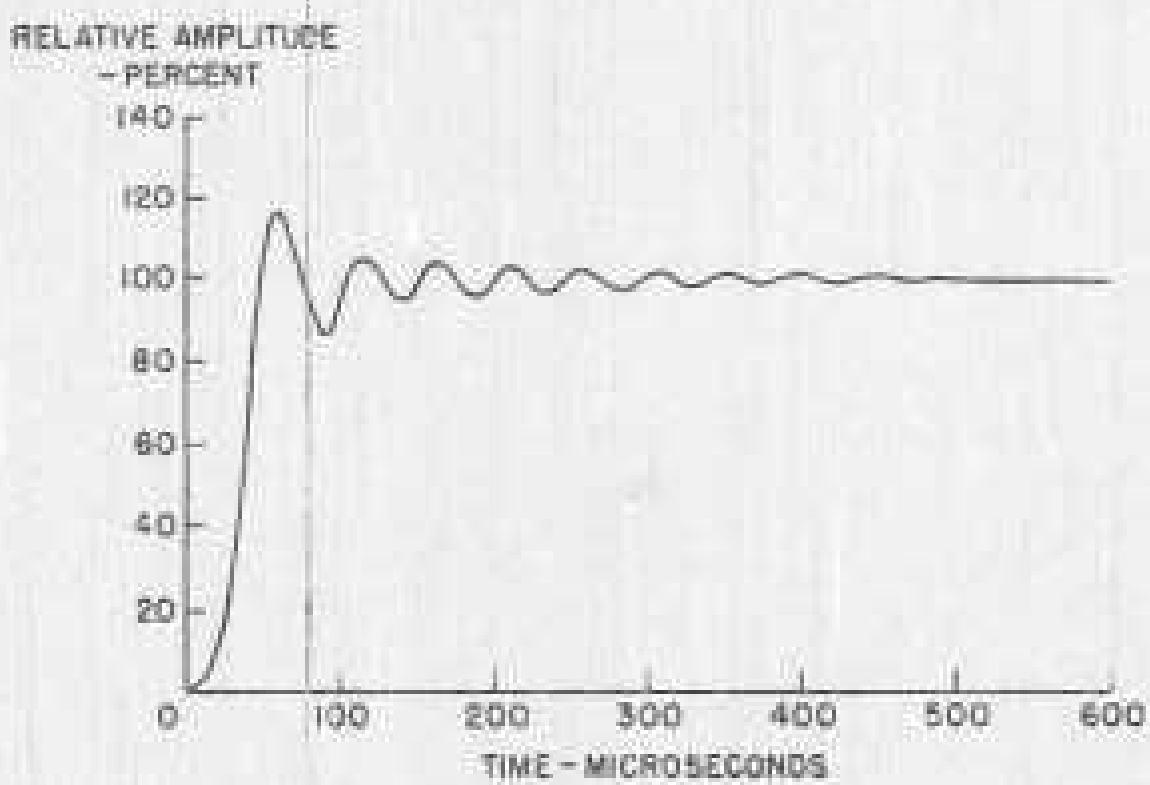

Figure 12 Transient Response of Output Filter

INTERACTION OF THE BLAST WAVE WITH WINGS
PART II. WAVE-TABLE STUDIES

Donald R. McFarland
NASA Langley Research Center

In one of the large rooms of the gas dynamics laboratory at the Langley Research Center there has been for some time a small-scale spherical blast-wave facility which we have called the wave table. This blast-wave table consists of a large flat steel surface, 12 by 15 feet, over which are detonated small, spherical bare high explosive charges. The spherical blast waves which are produced have proven to be very closely scaled and readily controllable laboratory versions of large high explosive and atomic blasts.

Various types of optical studies have been made on the wave table, including time-resolved measurements of Mach-stem formation and growth as a function of burst height, wave attenuation due to rough surfaces, and the transient flow field about bodies and wings. Because of the small scale of the bodies which have been used, the placement of pressure transducers has been generally limited to the table surface and used mainly for checks on the blast-wave pressure-versus-time characteristics and any wave reflections which may be present.

Because of the experience that had been gained in the use of the wave table in these types of studies, we have been involved in a combined program with the gust loads personnel on the study of the general problem of transient loads imposed on aircraft encountering blast waves.

Figure 1 shows the arrangement of an earlier investigation that was made by placing a small wing model in the air stream from a low-speed free-air jet located in the blast-wave table. This air jet simulated the forward motion of an aircraft in flight prior to encounter with a blast wave. The strength of the blast wave used was sufficient to change the angle of attack from 0° to 30° during which time the optical studies of the transient flow were made. Good correlation was obtained of the movement of vortices along the surface of the wing and the movement of the pressure load peak obtained by the gust loads group from their previous flying models.

Mr. Pierce has already told you of the ground facility involving a large shock tube which is to be used for extending these studies to higher velocities. In order to gain some preliminary insight into the feasibility of this idea as well as to obtain some optical data on the transient flow occurring at the higher Mach numbers, we installed a small scale version of this facility on our wave table, using a shock tube 6 inches in diameter.

Our small-scale facility arrangement is shown in Figure 2. The blast-wave table consists of a 2-inch-thick boiler plate approximately 12 feet by 15 feet, over which is detonated a small 15- to 50-gram bare pentolite charge. The shock tube tunnel is 4 feet long and 6 inches in diameter which is a one-twentieth scale of the large shock tunnel described by the previous speaker.

As pointed out in the previous talk, this type of shock-tube-tunnel operation uses the so-called "cold flow" of the shock tube. Normally, this part of the flow is not used for testing purposes in shock-tube work. Since all this "cold flow" must pass over the open diaphragm it is essential that the diaphragm pieces lay completely against the shock-tube wall to reduce any interference with the flow. Also, as was done in the large-scale facility, the air in the tube was preheated by electrically heating the shock-tube wall, in order to minimize reflections of the blast wave with this cold jet air stream. Diaphragms for the 6-inch-diameter tube were brass shim stock and were scribed in four pie sections. A remotely controlled hammer and plunger arrangement was used to burst the diaphragm at the desired pressure. Schlieren photographs were obtained at different blast-flow times by the use of a variable-delay generator triggered by the blast front which then fired the schlieren spark light source.

As I mentioned previously, a 0.10 Mach number steady free-air jet was used with the wave table prior to the use of the shock tube. To acquaint you with these low-speed data, some schlieren photographs of the vortex patterns are shown in Figure 3. The picture at the top of the figure shows the blast flow normal to the jet flow and of such strength as to produce an initial angle-of-attack change of 30°. This angle of attack, of course, decays as the blast flow decays with time. The first schlieren picture was taken shortly after blast front arrival. The second picture is in the order of 300 microseconds after blast arrival. In order to show the vortices somewhat more clearly, the model was set at a 30° angle of attack, to the blast flow with no initial flow that is, no jet flow over the wing model. The resultant flow velocity over the model is matched to that of the jet-flow case by moving the charge closer to the model, thus increasing the blast-flow velocity. It must be remembered here that although the resultant flow velocity is the same immediately after blast arrival, there are some important differences to be noted for the blast-alone case. There is no initial flow or flow field about the model prior to the blast, and there is also no change in angle of attack with time during the blast. Both the forward and normal components of the blast flow over the wing decay rapidly with time for this case, whereas only the blast velocity, or that velocity normal to the wing decays with time for the steady-jet-flow case. Despite these differences, there is good correlation between these two cases, if one relates the vortex movements to the free-stream fluid movement about the wing, rather than to the wing itself.

Figure 4 shows the photographs obtained from the present method and using the shock-tube flow at a forward Mach number of 0.35 which is an intermediate subsonic case. In the first picture the blast front can still be seen as it has just passed over the model. The vortex regions are still distinguishable, even though the shock-tube flow is not as clean as the flow in the previous case of the free-air jet. Here again the blast flow along at 30° angle of attack is shown for comparison.

The final figure shows a high subsonic Mach number where super-critical flow has already been set up on the wing model by the shock-tube jet flow before blast-wave arrival. The identity of the vortex seems to

be lost in the region of the compressibility shock, although the region of disturbance is still very evident. The blast-wave front shown in the first picture appears to be even more distorted than before. This is probably due to passing through a stronger mixing zone at the edges of the circular jet flow. With the blast flow alone, as in the previous case, the vortices seem to be more clearly defined, even at these higher velocity flows.

In conclusion, it is felt that these optical studies have provided a better insight into the nature of the transient flow over a wing at different Mach numbers, when the wing encounters a blast of sufficient magnitude to suddenly change the angle of attack by a large amount. These results should prove a useful supplement to the pressure loads investigations to be carried out in the large gust loads facility.

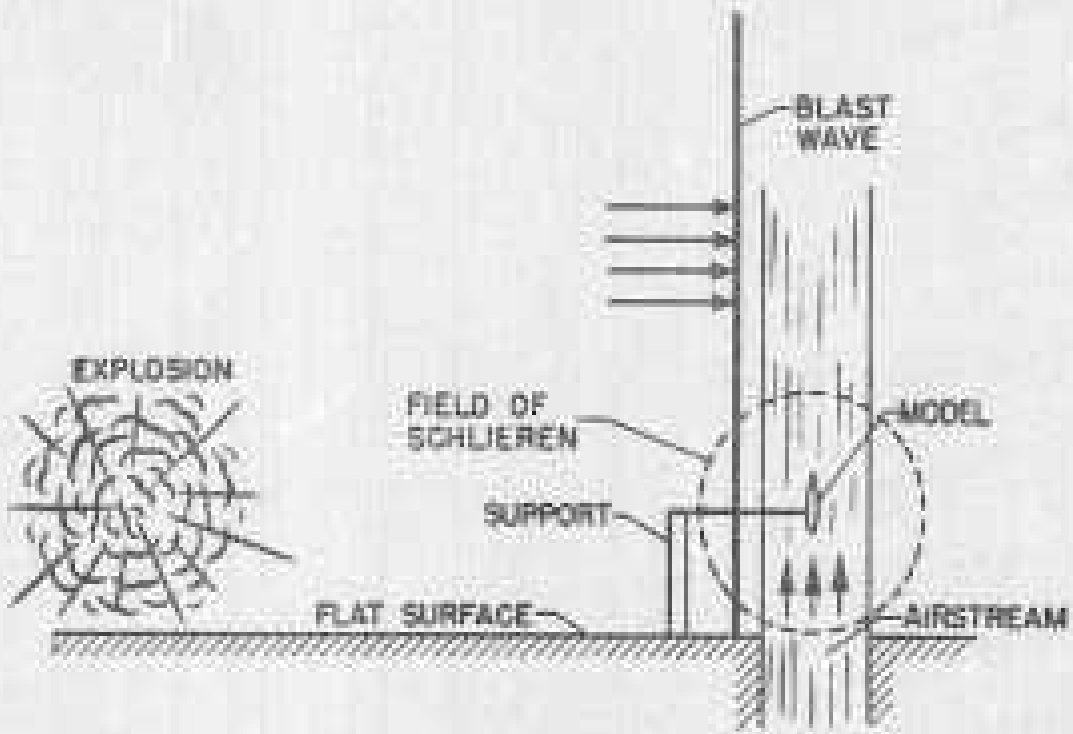

Figure 1 Arrangement of Low-speed Free Air Jet

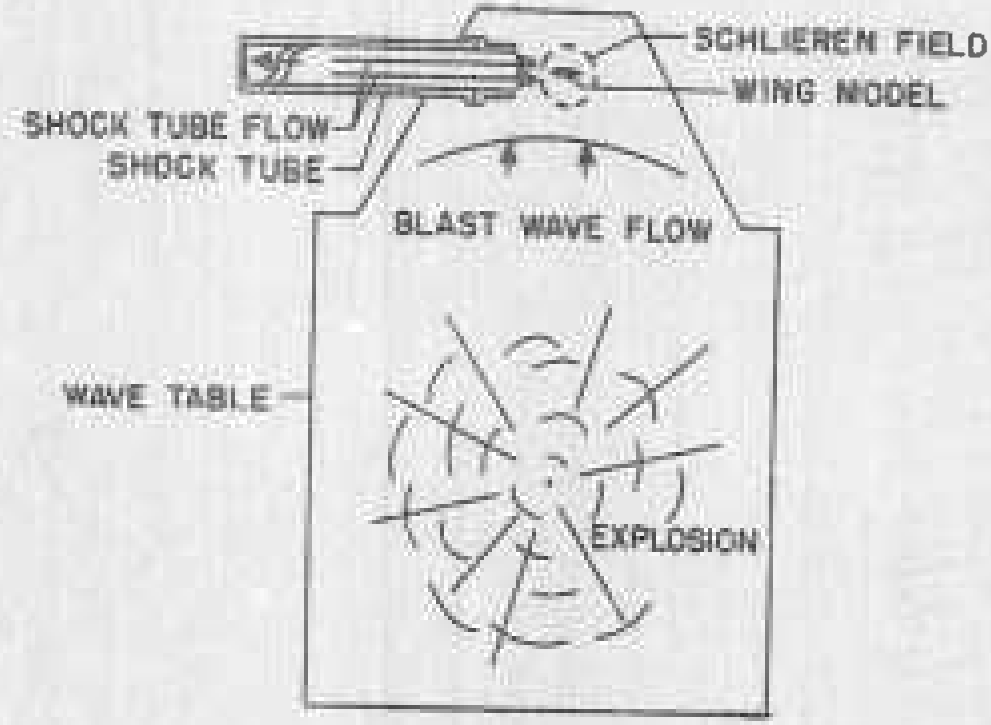

Figure 2 Schematic of Wave Table and Shock Tube

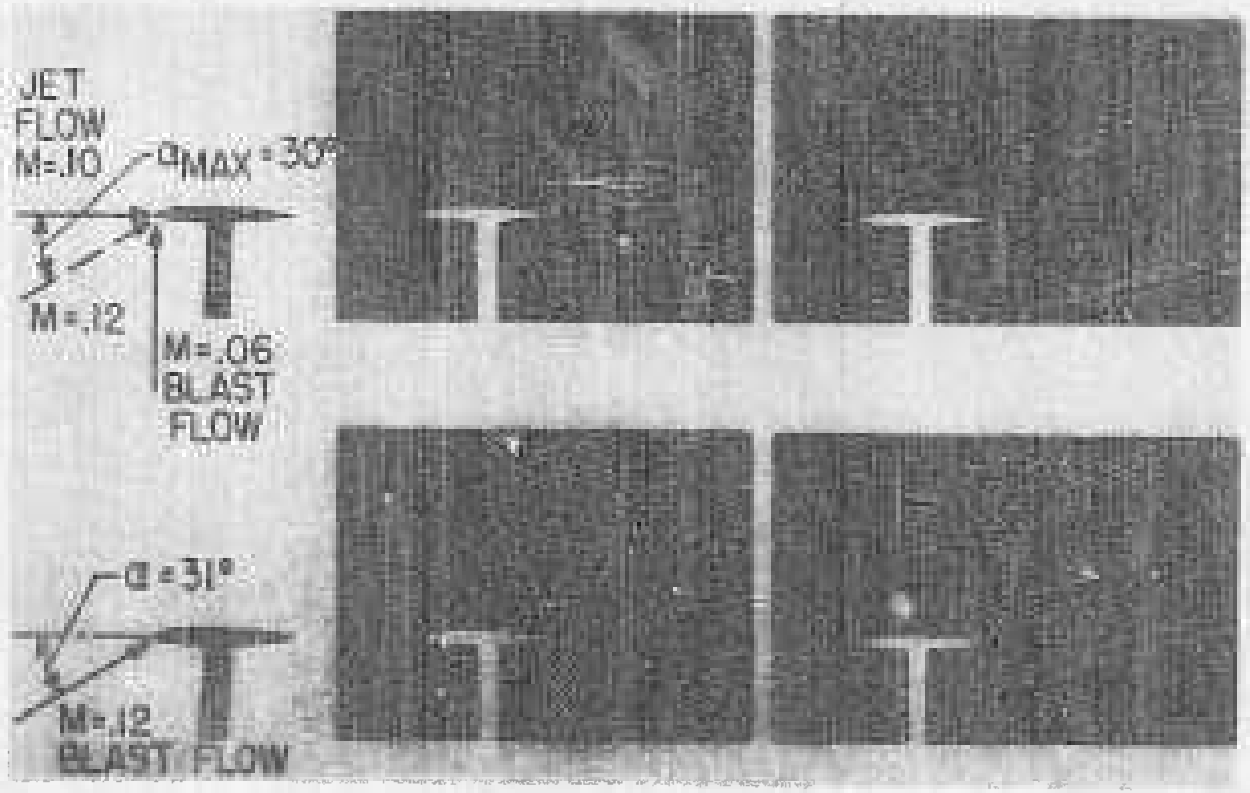

Figure 3 Sequence of Schlieren Photographs at M = 0.10

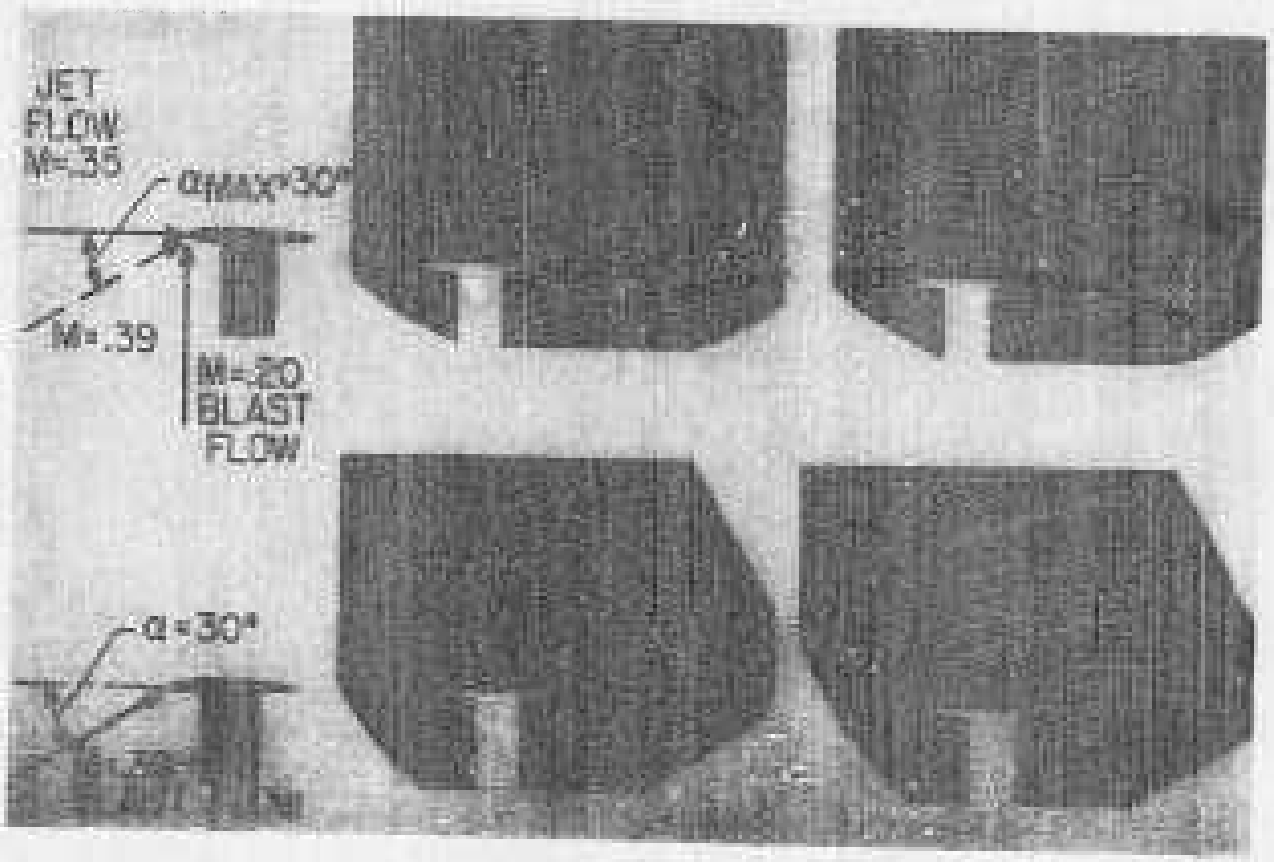

Figure 4 Sequence of Schlieren Photographs at M = 0.35

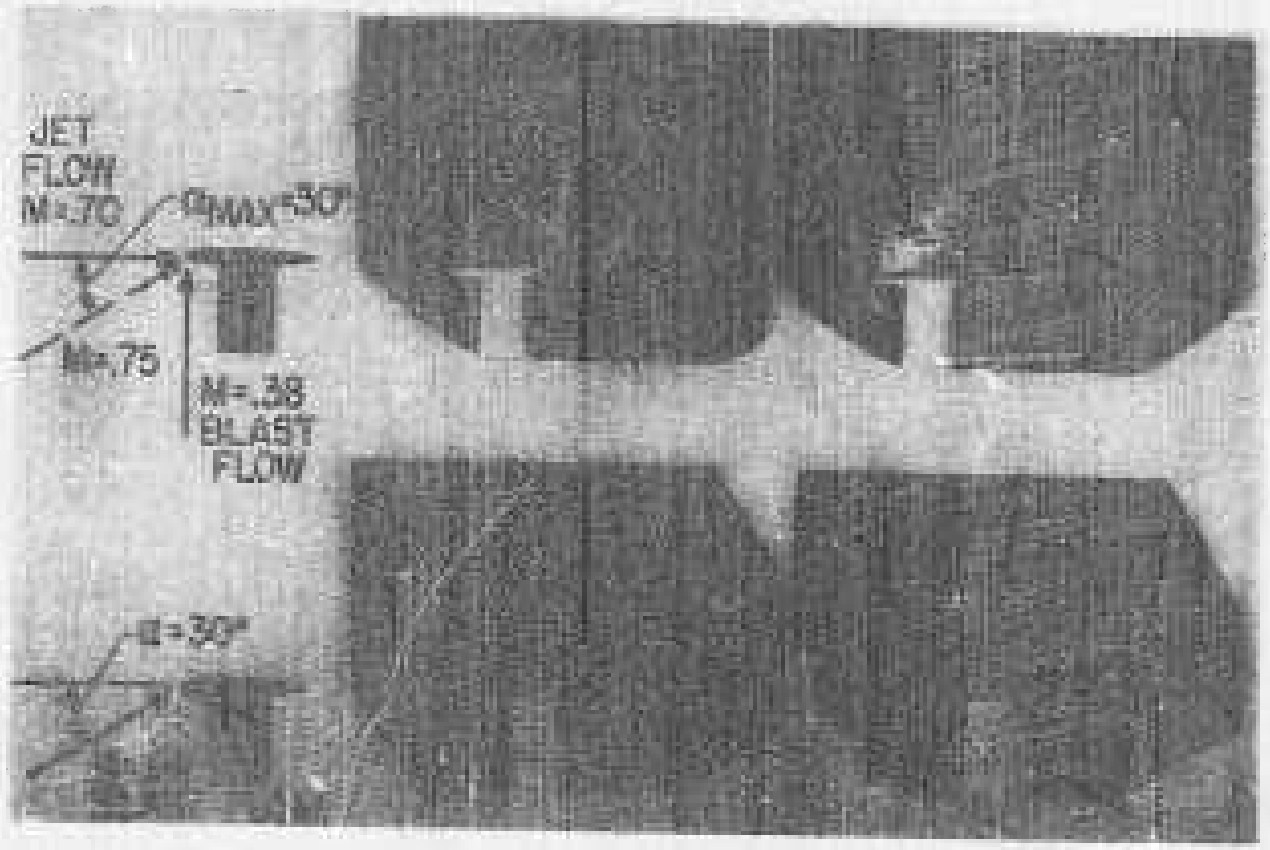

Figure 5 Sequence of Schlieren Photographs at M = 0.70

EXPERIMENTS AND THEORY ON EXPLOSIVE DECOMPRESSION IN THE SIX-FOOT SHOCK CHAMBER

T. H. Schiffman and A. H. Wiedermann
Armour Research Foundation

I. INTRODUCTION

The object of this paper is to solve the general decompression problem, and to apply this solution to calculation of the orifice area between two chambers for prescribed decompression rates, and to compare the theoretical rates with actual pressure-time records obtained in the six-foot shock tube which Armour Research Foundation operates for the Air Force.

Decompression rates can be classified as slow or fast depending upon the ratio of the sonic transit time (i.e., a characteristic dimension divided by sound velocity) to some characteristic time of the decompression process-the decompression duration, for example. If this ratio is small compared to unity (slow decompression) the local pressure gradients are negligible and a pseudosteady-state analysis is permissible. If this ratio is of the order of unity or larger, no pseudosteady-state analysis is permissible. The bulk of this paper deals with the slow decompression case.

II. STATEMENT OF PROBLEM

Consider the problem of two chambers separated by a nozzle or orifice. One chamber is initially at a higher pressure. The temperature of the gas in both chambers is initially near the same. At a given time the gas is allowed to flow through the nozzle. One would like to determine for the high pressure chamber the pressure-time history.

Assuming adiabatic-isentropic flow conditions, and neglecting heat loss through the chambers and across the nozzle, the problem can be presented as follows (see Fig. 1).

The quantities V_1, V_2, P_1', P_2', T_1', T_2' and A_o, shown in Fig. 1, and some other pertinent symbols utilized in this paper are defined as follows:

V_1, V_2 = Volume of Chambers 1 and 2

P_1', P_2' = Initial pressures in Chambers 1 and 2

$T_1' \approx T_2'$ = Initial temperature in Chambers 1 and 2

A_o = Area of nozzle or orifice

m_1', m_2' = Initial mass of gas in Chambers 1 and 2

$P_1(t)$, $P_2(t)$ = Pressure-time variation in Chambers 1 and 2

$T_1(t)$ = Temperature-time variation in Chamber 1

$\rho_1(t)$ = Density-time variation in Chamber 1

$m_1(t)$, $m_2(t)$ = Mass-time variation in Chambers 1 and 2

$W_o(t)$ = Mass rate of flow through nozzle

a_1' = Initial sound velocity in Chamber 1

III. BASIC EQUATIONS FOR THE SLOW DECOMPRESSION CASE

Assume a perfect gas, then

$$P_1(t) = \rho_1(t)\, R\, T_1(t) \tag{1}$$

where

R = Gas constant

And, for an isentropic flow process,

$$\frac{P_1(t)}{P_1'} = \frac{\rho_1(t)}{\rho_1} \tag{2}$$

where

k = Ratio of specific heats

Considering the gas properties to change slowly compared to the time required for a sound wave to travel several characteristic dimensions of the chambers allows the use of steady flow equations through the nozzle.

If $W_o(t)$ is the mass flow through the nozzle, the following two expressions are obtained for choked and nonchoked subsonic flow.*

(a) Choked flow in nozzle

$$W_o(t) = A_o \sqrt{\frac{k}{R}\left(\frac{2}{k+1}\right)^{\frac{k+1}{k-1}}} \frac{P_1(t)}{\sqrt{T_1(t)}} \tag{3}$$

*See, for example, A. H. Shapiro "The Dynamics and Thermodynamics of Compressible Fluid Flow", Vol. I, the Ronald Press Co., N. Y., 1953, pp. 83 to 85.

The Mach numer of the flow in the throat is sonic, $M_o(t) = 1$.

This condition exists when the pressure ratio across the nozzle is greater than the critical pressure ratio,

$$\frac{P_1(t)}{P_2(t)} \geq 1.89$$

(b) Subsonic flow in nozzle

When the pressure ratio across the nozzle drops below the critical pressure ratio, the flow will be subsonic. The mass flow through the nozzle is then given by

$$W_o(t) = A_o \sqrt{\frac{k}{R}} \frac{\frac{P_1(t)}{\sqrt{T_1(t)}}}{\left[\frac{P_1(t)}{P_2(t)}\right]^{\frac{k+1}{2k}}} \left\{ \left[\left(\frac{P_1(t)}{P_2(t)} \right)^{\frac{k-1}{k}} - 1 \right] \frac{2}{k-1} \right\}^{1/2} \tag{4}$$

The mass flow through the nozzle must be equal to the rate of change of mass of each chamber:

$$W_o(t) = -\frac{d\, m_1(t)}{dt} = \frac{d\, m_2(t)}{dt} \tag{5}$$

The volume V_2 is so large compared to V_1 that it can be considered infinite and, hence, the pressure rise in V_2 can be neglected. Thus, toward the end of decompression one, will actually obtain slightly higher pressures in V_1 than that indicated by the subsequent analysis.

IV. RESULTS

Normalizing the above equations by introducing the mass ratios

$$\frac{m_1(t)}{m_1'} = u_1(t) \tag{6}$$

and the pressure ratios

$$\frac{P_1(t)}{P_1'} = \pi_1(t) \tag{7}$$

one obtains, by manipulating Eq (1), (2), (3) and (5), the following differential equation:

(a) For choked flow

$$\frac{d\,u_1}{dt} = -\lambda u_1(t)^{\frac{k+1}{2}} \tag{8}$$

Subject to the boundary conditions

$$u_1(t) = 1 \text{ for } t = 0 \tag{9}$$

where one defines

$$\lambda \triangleq \frac{A_o}{V}\, a_1' \left[\frac{2}{k+1}\right]^{\frac{k+1}{2(k-1)}} \tag{10}$$

The solution of Eq (8) satisfying the boundary conditions (Eq (9)) is for the normalized mass ratio

$$u_1(t) = \left[1 + \frac{k-1}{2}\lambda t\right]^{-\frac{2}{k-1}} \tag{11}$$

The normalized pressure ratio is a more convenient quantity to compare for experimental observations and is obtained from Eq (2) as

$$\pi_1(t) = u_1(t)^k \tag{12}$$

(b) Subsonic flow

We again normalize in terms of $u_1(t)$ and $u_2(t)$ and define

$$P = \frac{P_1'}{P_2'} \tag{13}$$

and, by manipulating Eq (1), (2), (4) and (5), obtain a differential equation analogous to Eq (8) as

$$\frac{d\,u_1(t)}{dt} = -\lambda^* \left[u_1(t)^{k-1} P^* - 1\right]^{1/2} \tag{14}$$

where the starred quantities λ^* and P^* pertain to conditions at end of choking.

By introducing a quantity

$$\phi(t) = u_1(t)\, P^{*\frac{k-1}{k}} \tag{15}$$

one can separate the variables in Eq (14) and obtain a general solution for t explicity in term of ϕ and, hence, u_1 as

$$t = -\frac{P^{*1/k}}{\lambda^*}\left[\sqrt{\phi^2 - \phi}\left(\frac{\phi}{2} + \frac{3}{4}\right) + \frac{3}{8}\,\lg\left(\phi - \frac{1}{2} + \sqrt{\phi^2 - \phi}\right)\right] + \text{constant} \tag{16}$$

The constant in Eq (16) is evaluated from the boundary condition

$$u_1(t) = 1 \text{ (corresponding to } \phi = 1.2) \text{ for } t = 0 \tag{17}$$

(c) Solution match for choked and subsonic flow

The end of choking is again denoted by starred quantities. One obtains, by solving Eq (12) for the normalized time $[\lambda t]^*$ in terms of π_1^* and equating it to $[\lambda t]^*$ of Eq (16)

$$[\lambda t]^* = \frac{2}{k-1}\left[\pi_1^{*\frac{2k}{k-1}} - 1\right] \tag{18}$$

V. NUMERICAL EVALUATION OF MASS FLOW AND PRESSURE DECOMPRESSION

We shall illustrate the preceding theory with a numerical example of a slow decompression experiment (of the order of 1 second duration) which we performed for the Air Force. The full scale decompression event was performed in the shock tube by using a shock chamber bounded by a flange on the one end and by a heavy aluminum diaphragm on the other for the pressurized cabin. A decompression was initiated by puncturing a stressed plastic diaphragm which covered the appropriate orifice area. Installed in this chamber was equipment furnished by Sperry Gyroscope Company, (Fig. 5).

An explosive decompression event such as this would be experienced during high altitude flight if a pressurized cabin was suddenly vented as a result of enemy fire.

Incidentally, our program permitted the evaluation of the structural response of the unit.

Consider at this stage some of the prescribed end points, i.e., air with

$$k = 1.4$$
$$P_1' = 10.7$$
$$P_2' = 3.4 \qquad (19)$$

and hence

$$\pi_1^* = \frac{P_1^*}{P_1'} = \frac{1.89\, P_2'}{P_1'} = 0.6 \qquad (20)$$

corresponding to

$$u_1^* = \pi_1^{*\,1/1.4} = 0.695 \qquad (21)$$

and, by Eq (11),

$$\left[\lambda t\right]^* = 0.377 \qquad (22)$$

signifies the end of choking.

In order to utilize a common time scale for the choked and unchoked case, one calculates the rates $\frac{\lambda^*}{\lambda}$ for Eq (10)

$$\frac{\lambda^*}{\lambda} = 2.23\,\frac{a^*}{a_1'} = 2.23\,\pi_1^{*\,\frac{k-1}{2}} = 2.07 \qquad (23)$$

and Eq (16) becomes

$$\lambda t = -0.765\left[\sqrt{\beta^2-\beta}\left(\frac{\beta}{2}+\frac{3}{4}\right)+\frac{3}{8}\,\lg\left(\beta-\frac{1}{2}+\sqrt{\beta^2-\beta}\right)\right]+0.56 \qquad (24)$$

The end of decompression denoted by barred quantities is reached at the point where the pressure drops to P_2', corresponding to $\beta \longrightarrow 1$ in Eq (15) and (24) giving, for Eq (15),

$$\bar{u}_1 = 0.63 \qquad (25)$$

and from Eq (24)

$$\overline{\lambda t} = 0.76 \qquad (26)$$

The total dimensionless decompression duration is obtained from Eq (22) and (26) as

$$(\lambda t)_o = [\lambda t]^* + [\lambda t] = 1.137 \tag{27}$$

corresponding to

$$u_o = u_1^* \bar{u}_1 = 0.438 \tag{28}$$

and

$$\pi_o = u_o^{1.4} = 0.315 \tag{29}$$

where $[\lambda t]_o$, u_o, and π_o are the normalized durations, mass flow rates, and pressure values at the end of decompression.

The combined solution for the entire range of decompression for $u_1(t)$ and $\pi_1(t)$ are plotted in Fig. 2. Figure 3 is a replot of Fig. 2 with the pressures expressed in terms of psi absolute.

VI. CALCULATIONS OF CHAMBER SIZE AND ORIFICE (NOZZLE AREA)

In addition to the decompression end points specified by Eq (19) the following quantities are also fixed:

The volume $V_1 = 352 \text{ ft}^3$ (30)

The initial temperature $T_1' = 160°\text{F}$, (31)

corresponding to a sound velocity in air of

$$a_1' = 1225 \text{ ft/sec}, \tag{32}$$

and finally the desired decompression duration is taken as

$$t_o = 0.8 \text{ sec} \tag{33}$$

For the simulated decompression problem in the six-foot shock tube

$$V_1 = \frac{D^2 \pi}{4} L = 352 \text{ ft}^3 \tag{34}$$

which, combined with Eq (30) and

$$D = \text{diameter of shock tube} = 70.5 \text{ in.} \tag{35}$$

gives the chamber length, L,

$$L = 13 \text{ ft.} \tag{36}$$

From Eq (29) and (33) one obtains for the final decompression parameter:

$$\lambda_o = \frac{(\lambda t_o)}{t_o} = \frac{1.137}{0.8} = 1.42 \tag{37}$$

and, from Eq (10), (19), (30), (32) and (37), one calculates the orifice (nozzle area) A_o as

$$A_o = \frac{V_1}{a_1'}\left[\frac{2}{k+1}\right]^{\frac{k+1}{2(k-1)}} = 0.705 \text{ ft}^2 = 101.5 \text{ in.}^2 \tag{38}$$

Figure (4) presents the calculated pressure decompression time curve in terms of absolute pressure and time as obtained from Fig. 3, with $\lambda = 1.42$ together with the actual rate obtained experimentally by means of a Kistler pressure pick up at the center of the front face of the Sperry unit (Fig. 5). This point is roughly 4 ft behind the center of the diaphragm.

As seen from Fig. 4, the agreement between decompression predictions and measurement is quite satisfactory. Seven further measurements were taken at other points at the front, middle section, rear and interior of the Sperry unit which gave roughly the same result as shown in Fig. 4 indicating the pseudosteady-state approach was justified.

VII. THE FAST DECOMPRESSION CASE

The fast decompression case is illustrated in Fig. 6, 7, and 8.

Figure 6 indicates the conventional shock tube flow diagram, where now our area of interest is the high pressure region shown to the left of the diaphragm in Fig. 6.

The non-linear differential equations governing the one-dimensional, isentropic, non-steady-state gas flow can be expressed in operational form as

$$\left\{\frac{\partial}{\partial t} + (u + c)\frac{\partial}{\partial x}\right\}\left[c + \frac{k-1}{2}u\right] = 0$$

and

$$\left\{\frac{\partial}{\partial t} + (u - c)\frac{\partial}{\partial x}\right\}\left[c - \frac{k-1}{2}u\right] = 0 \tag{39}$$

leading to the solutions for the first of Eq (39) as

$$c + \frac{k-1}{2}u = \text{constant} = c_o \tag{40}$$

along

$$\frac{dx}{dt} = u + c \approx \frac{x}{t} \tag{41}$$

Figure 7 illustrates these Riemann invariants for various states, S.

The above Eq (40) and (41) can be solved with the adiabatic formula

$$\frac{c}{c_o} = \left(\frac{P}{P_o}\right)^{\frac{k-1}{2k}} \tag{42}$$

to give a relationship between the normalized pressure $\frac{P}{P_o}$ and normalized time $\frac{t\,c_o}{x_1}$:

$$\frac{P}{P_o} = \left\{\frac{k-1}{k+1}\left[\frac{x}{c_o t} + \frac{2}{k-1}\right]\right\}^{\frac{2k}{k-1}} \tag{43}$$

This relationship is plotted for the interval from the decompression starting point

$$\frac{P}{P_o} = 1, \quad \frac{t\,c_o}{x_1} = 1 \tag{44}$$

to the asymptotic value at infinity

$$\frac{P^*}{P_o} = \left(\frac{2}{k+1}\right)^{\frac{2k}{k-1}} \approx 0.279, \quad \frac{t\,c_o}{x_1} \longrightarrow \infty \tag{45}$$

This relationship is shown graphically in Fig. 8.

VIII. THE EXPERIMENTAL SET-UP

The Sperry Navigation Unit (Fig. 10 and 11) was installed in the Air Force Six-ft Shock Tube facility (Fig. 9) located at Gary, Indiana.

Kistler pressure gages and calibration units (Fig. 12) were used throughout the tests. This gage uses a quartz crystal as the sensing element and because of its very low output per psi must be used with a Kistler calibration unit.

The output of the calibration box was fed directly to a-c preamps for the fast decompression tests and to d-c preamps for the slow decompression tests. The output of the preamps was used to drive the oscilloscopes. A drum camera was used to photograph the faces of four CRT tubes. Most of this equipment is shown in Fig. 13.

IX. CONCLUSION

Closed solutions have been obtained for the general decompression problem. In the case of slow decompression, these solutions have been compared to actual decompression tests performed on Sperry Equipment installed in the Air Force 6-ft shock tube. Agreement between theory and experiment is satisfactory.

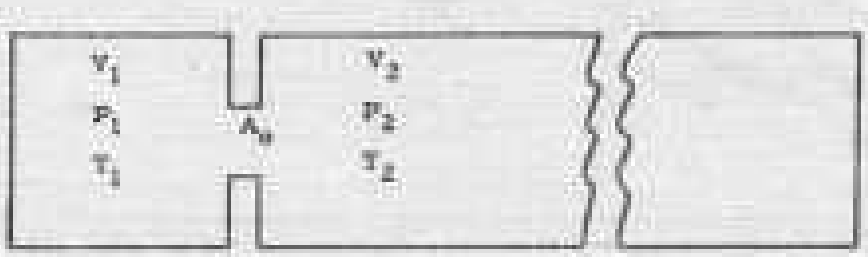

Figure 1 Compression and Decompression Chambers

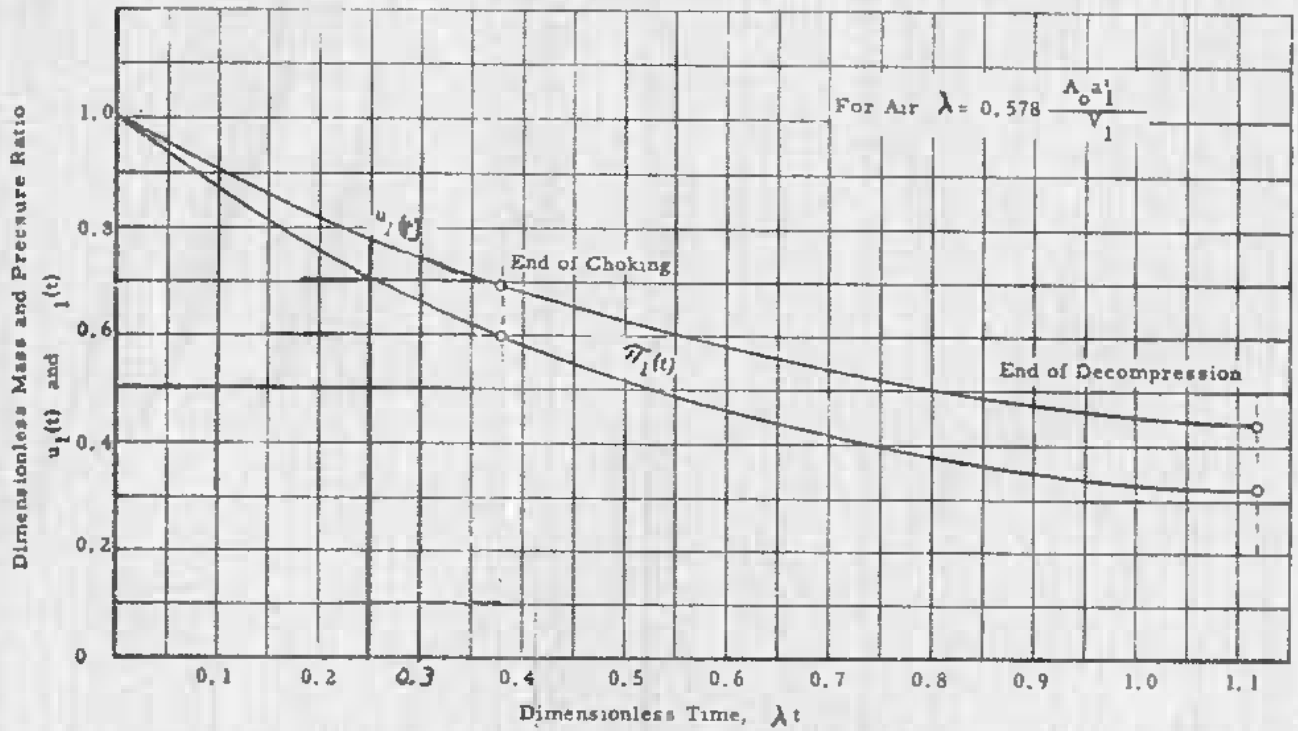

Figure 2 Matched Dimensionless Mass and Pressure Ratios Versus Dimensionless Time for Choked and Non-Choked Flow

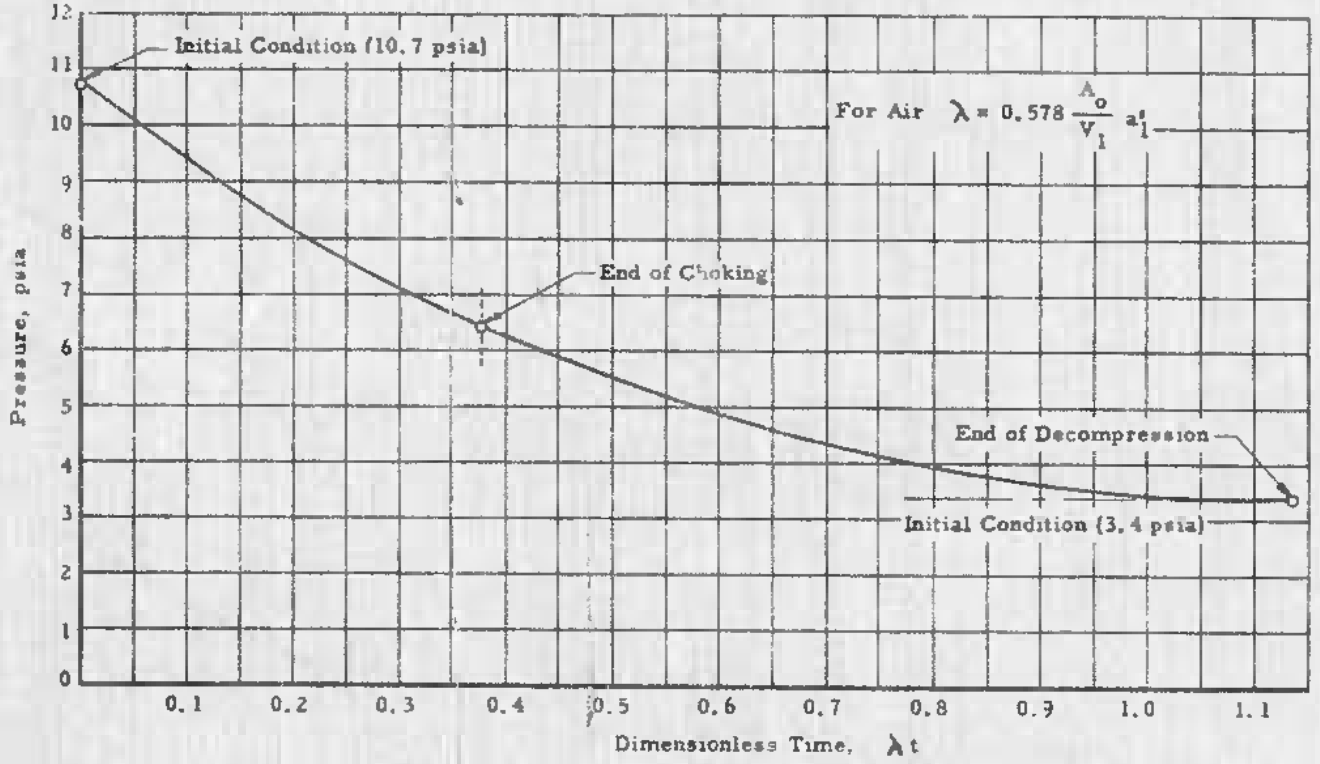

Figure 3 Complete Theoretical Pressure Decompression Curve Versus Dimensionless Time

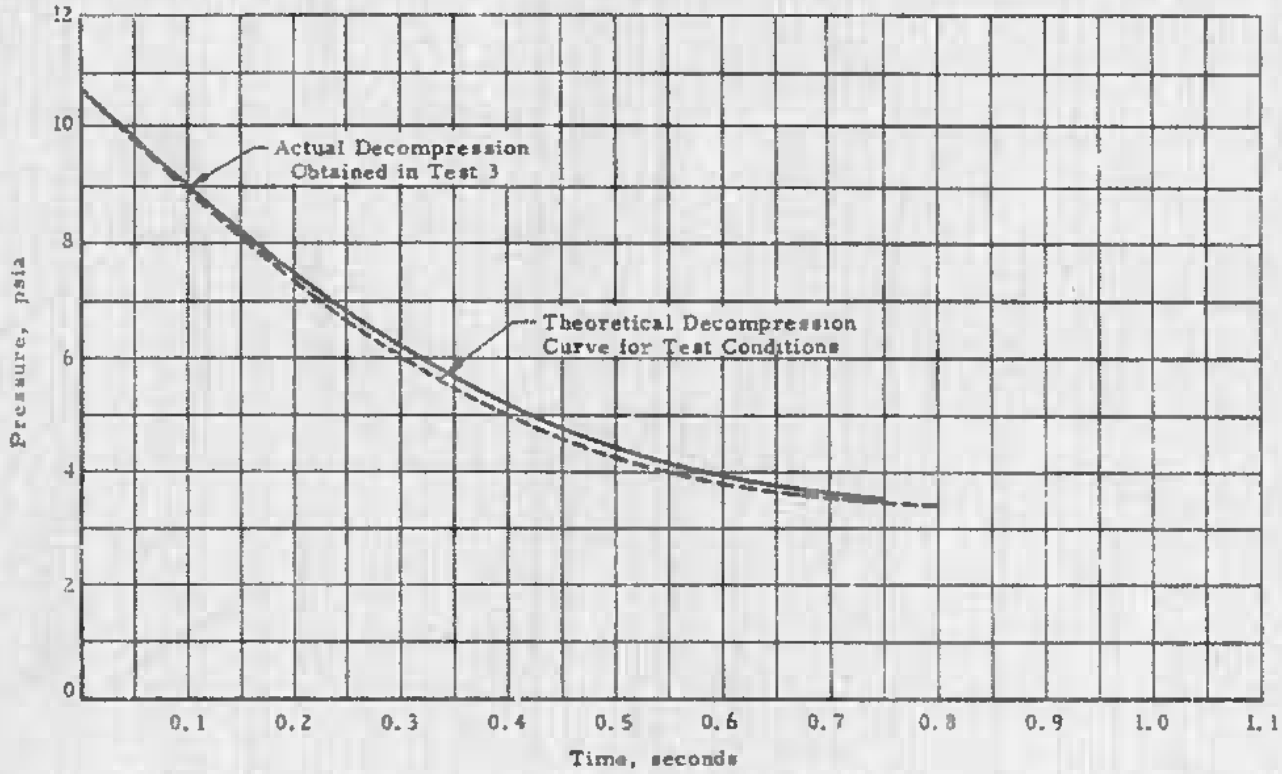

Figure 4 Comparison Between Theoretical and Actual Decompression Curves

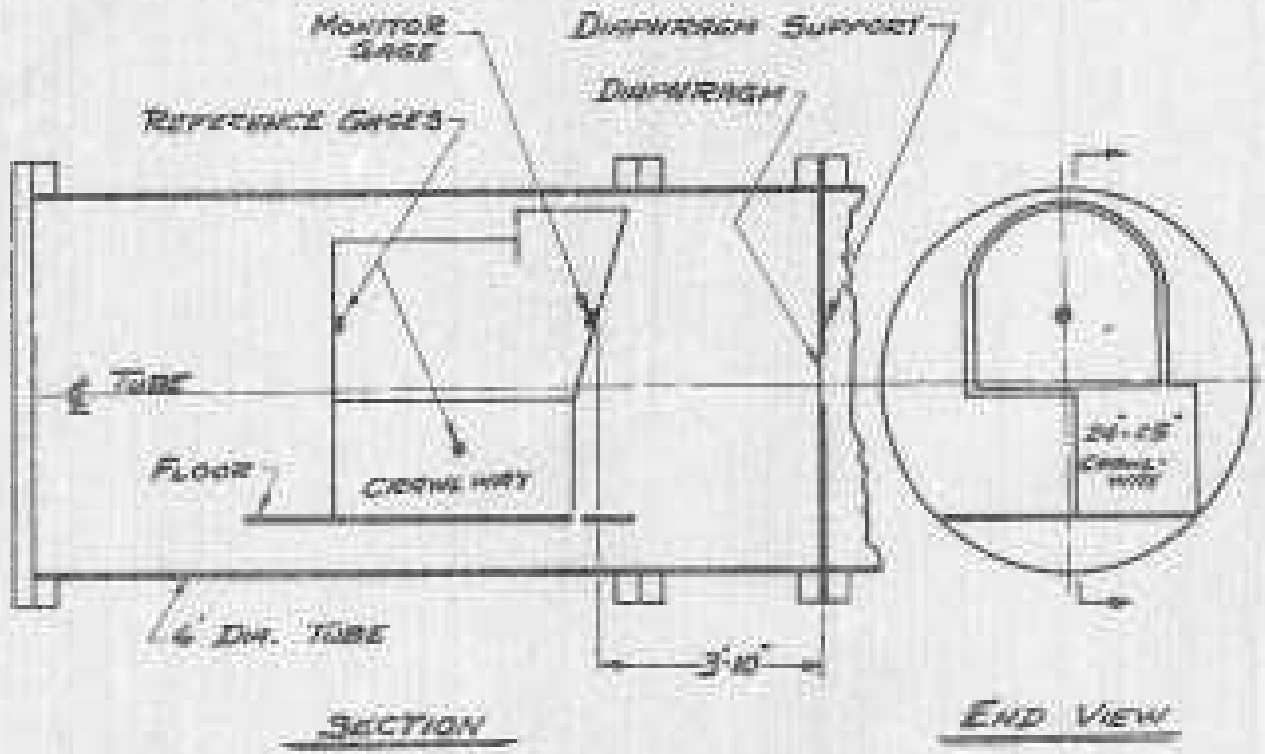

Figure 5 Navigation Unit Shock Tube

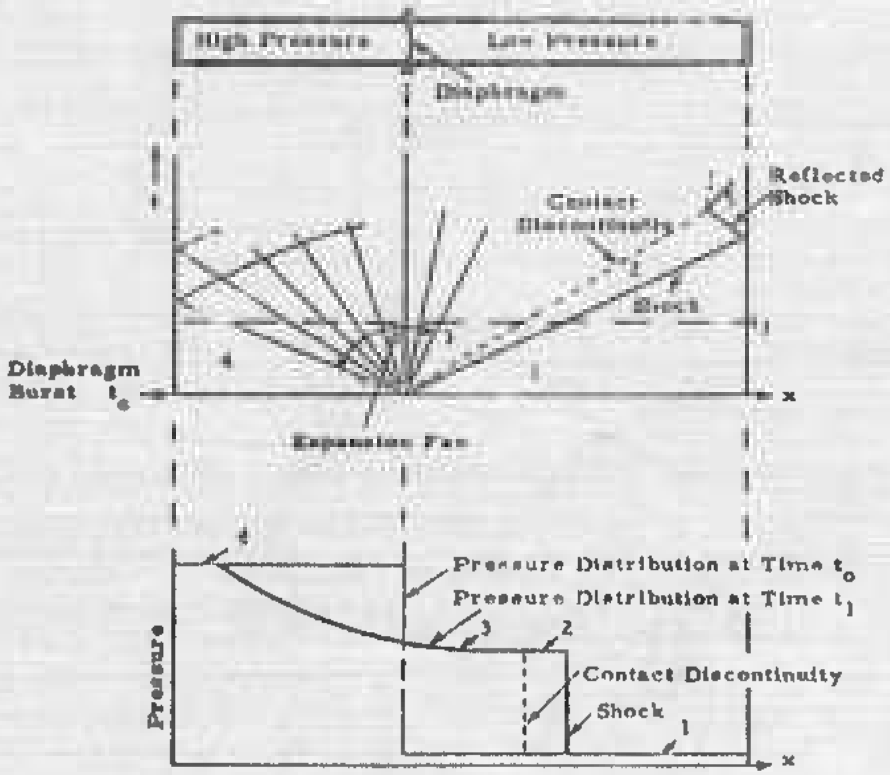

Figure 6 Schematic of Shock Tube Flow (x-t and p-t diagrams)

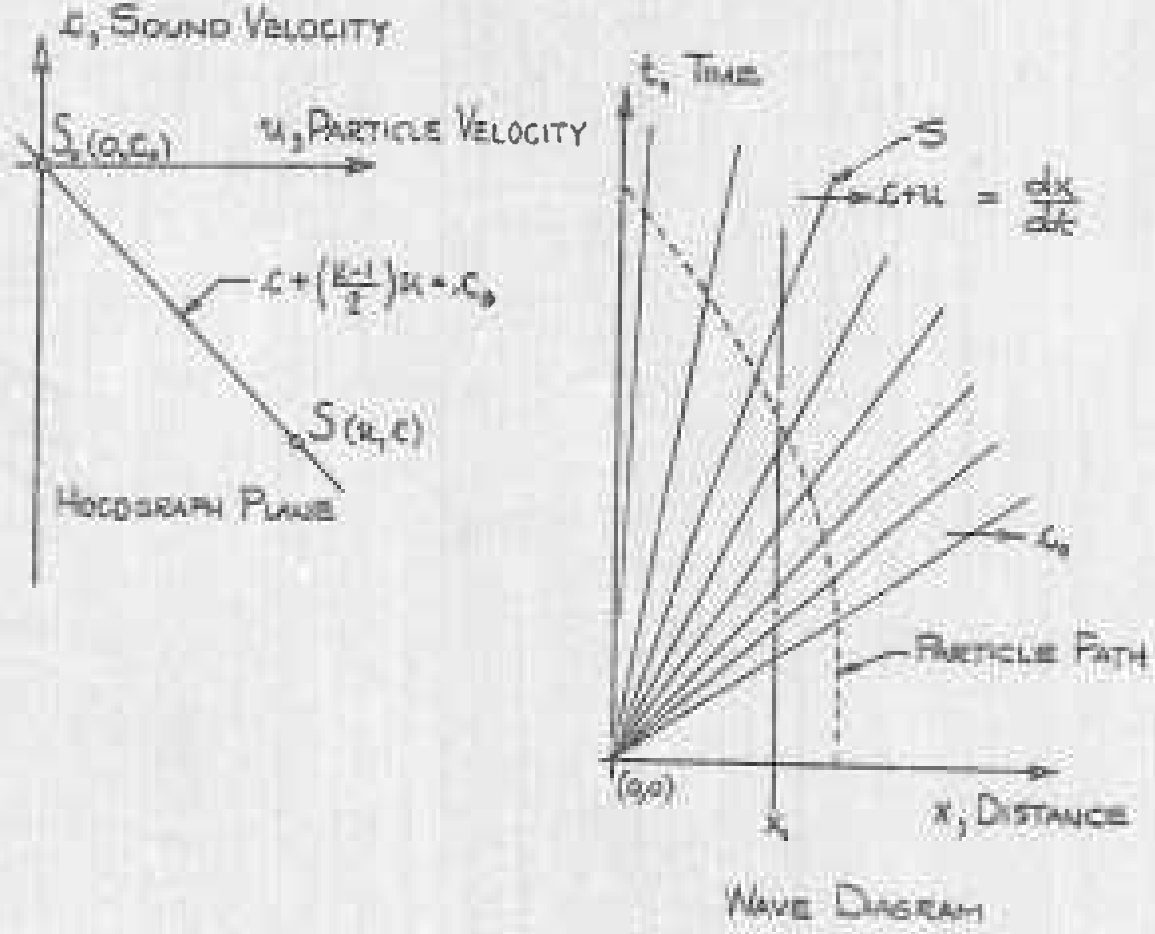

Figure 7 Fast Decompression Wave Diagram

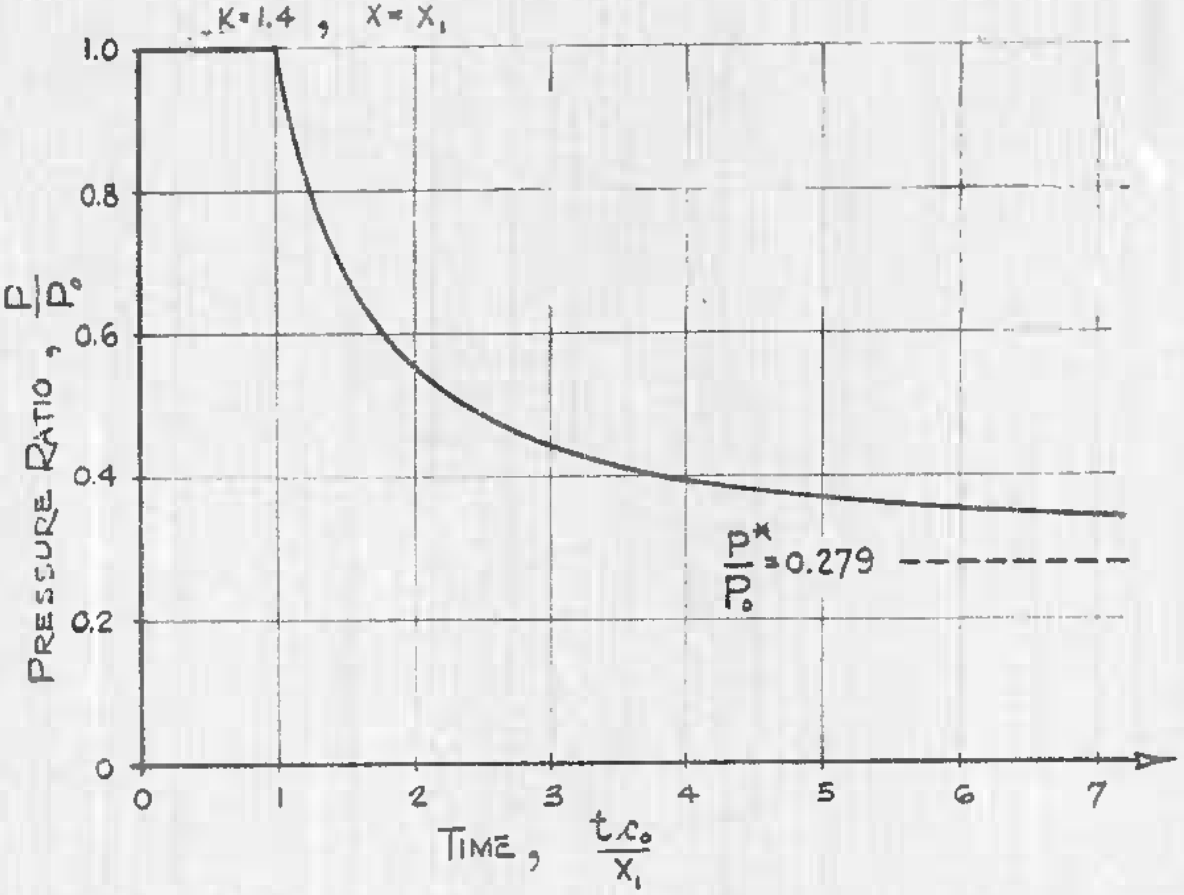

Figure 8 Theoretical Fast Decompression Dimensionless Pressure-Time Curve

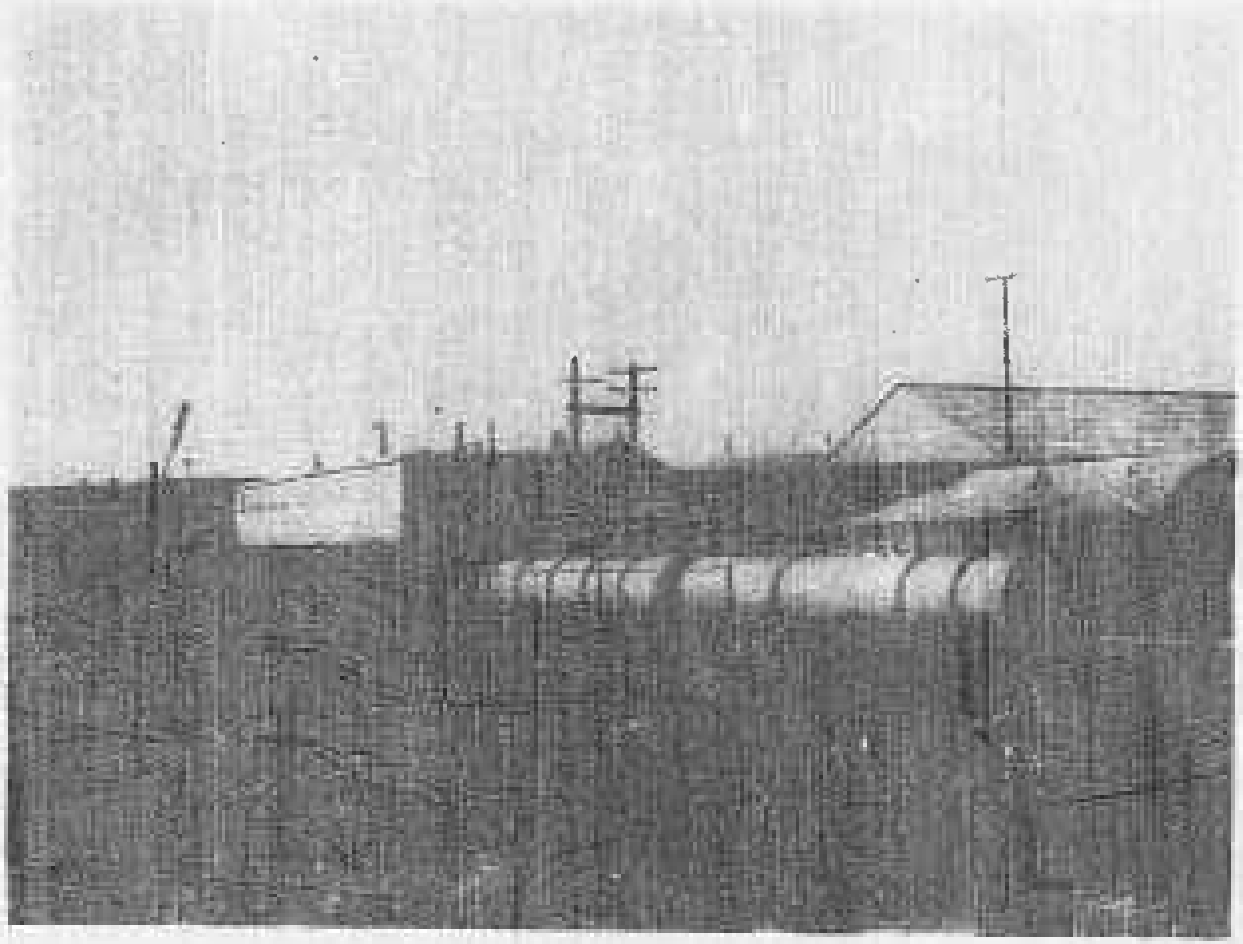

Figure 9 Air Force Six-Foot Shock Tube Facility

"NOTICE: When Government or other drawings, specifications or other data are used for any purpose other than in connection with a definitely related Government procurement operation, the U.S. Government thereby incurs no responsibility, nor any obligation whatsoever; and the fact that the Government may have formulated furnished, or in any way supplied the said drawings, specifications or other data is not to be regarded by implication or otherwise as in any manner licensing the holder or any other person or corporation, or conveying any rights or permission to manufacture, use or sell any patented invention that may in any way be related thereto

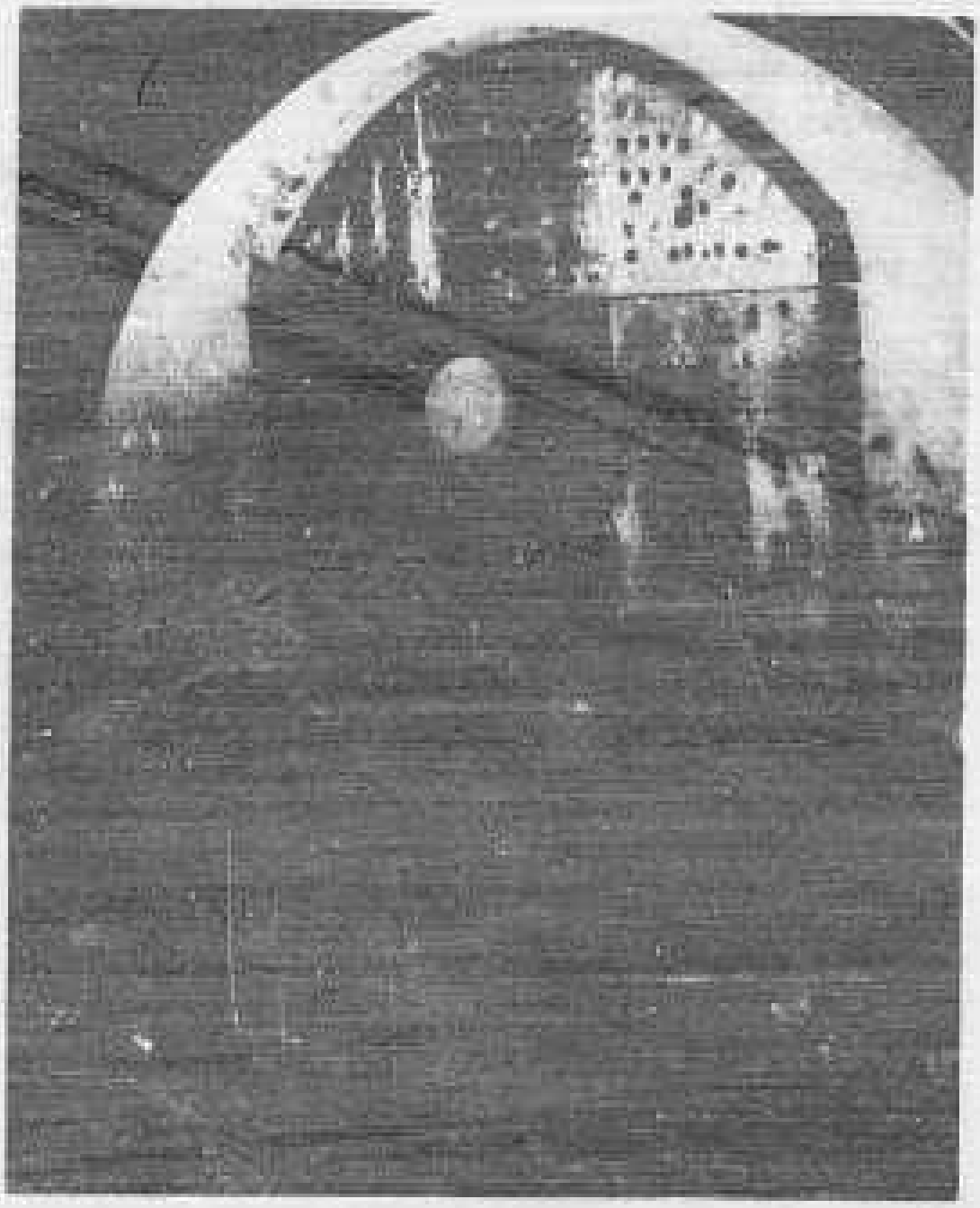

Figure 10 Sperry Navigation Unit in Compression Chamber

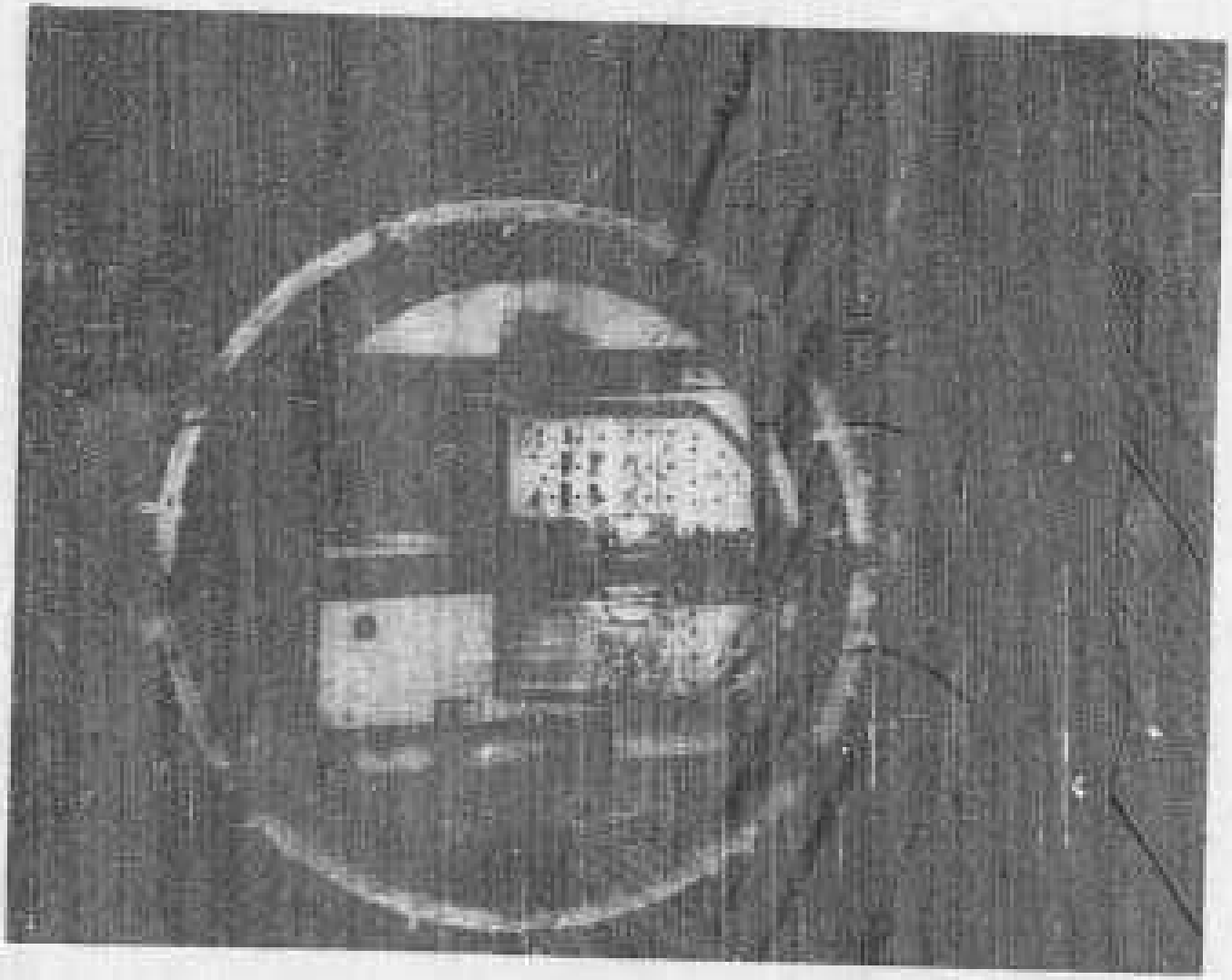

Figure 11. Survey Navigation Unit Related Positioning Device

Figure 12 Kistler Pressure Gage and Calibration Unit

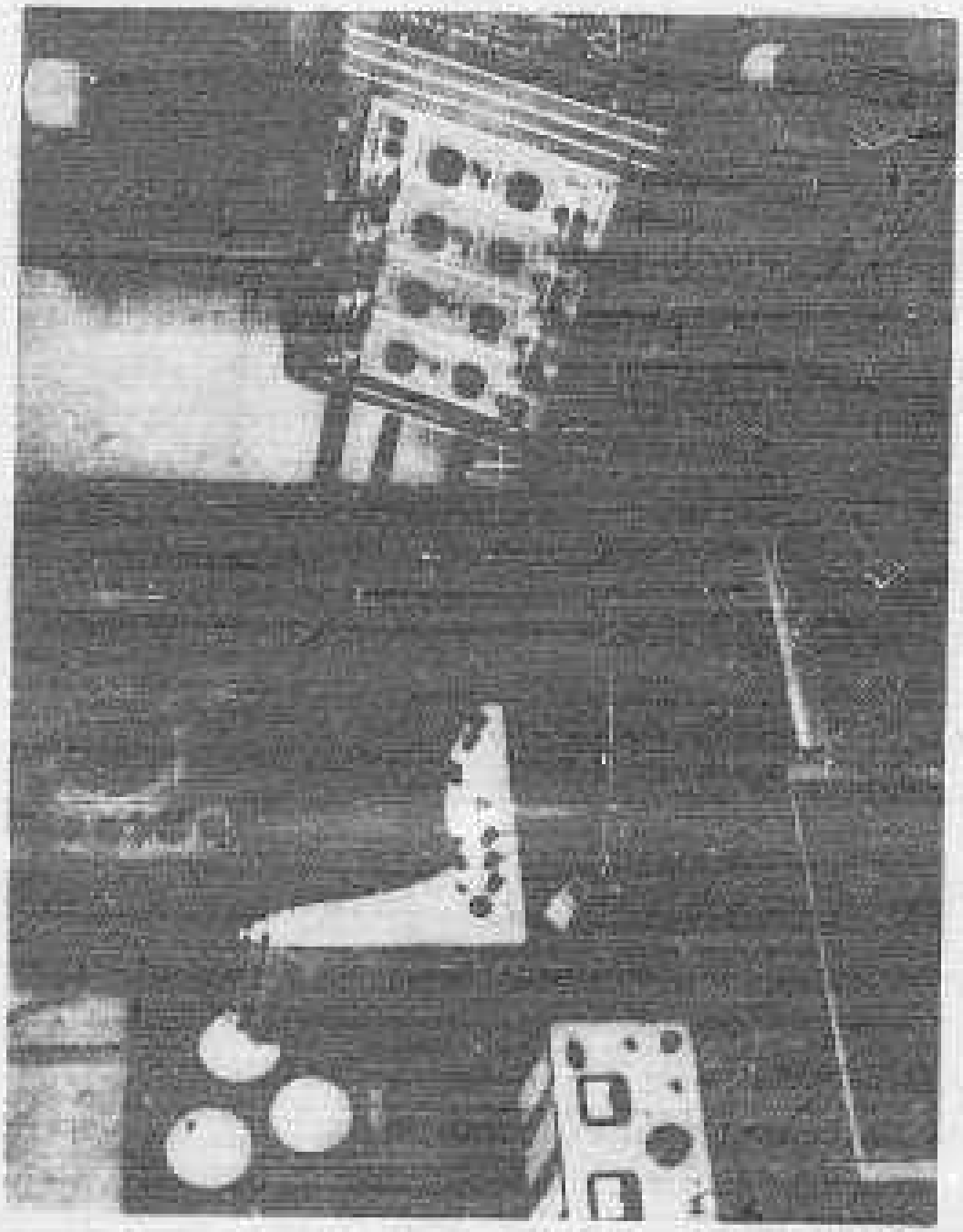

Figure 13 Instrument Room

THEORY OF FILLING PROCESS FOR CHAMBERS; SHOCK TUBE AND FIELD TESTS

A. H. Wiedermann
Armour Research Foundation

In this paper an analysis for the filling process of a chamber or cavity which is connected to the atmosphere by a channel or tunnel is presented. A blast wave propagating through the atmosphere sweeps past the entrance and initiates flow into the chamber configuration. The basic assumptions used in the analysis of two specific cases will be discussed and the result of the first case will be compared to experimental results obtained for essentially the identical conditions in the Air Force 6-foot Shock Tube Laboratory. Some comparisons will be made for the second case which duplicate a configuration tested in full scale field tests.

One aspect of weapon effects research is that of determining the transient forces or pressures acting on structures or objects of a wide variety of geometries. In general, the solutions of these gas dynamic problems are not obtainable by analytical means. The flow is governed by a system of non-linear equations which usually involve two or three special dimensions in addition to time. We are therefore forced to rely, to a great extent, upon experimental observations, either full scale field tests or scaled laboratory experiments, for the required information.

There exists a class of problems which are amenable to analysis, that is, those problems in which only one spatial dimension is involved can be solved analytically by the method of characteristics. Quite naturally then, geometries which consist of channels in which the length is long compared to the diameter (or some characteristic dimension of the section) fall into this category. This is the type of problem which will be discussed in this paper.

Slide 1 is a photograph of a model of a ship (guided missile frigate) in the Air Force 6-foot shock tube. The model was used to determine the forces acting on a ship when a blast wave interacts with it. Of course, an experimental approach was the only possible approach in this case. However, along with the interest in the loads on the exterior of ships, there exists some interest in determining the pressures in the boiler cavity of the ship, as well as in determining the pressures in the funnel which connect the cavity to the atmosphere. In connection with the experimental work on ships, some experimental results were obtained on a model which had an interior cavity and simulated a typical boiler-funnel configuration. A portion of the analysis presented herein is for this particular geometry and we will be able to make some qualitative comparison of the results. The second portion of this paper is concerned with the case of a personnel shelter connected to the surface by a tunnel.

Slide 2 illustrates the actual boiler funnel configuration. The significant features of the channel are the transition region where the cross-sectional area changes by approximately 60 per cent, the two bends and the slight flare at the cavity end. Illustrated also is the position (x) of the free field static pressure gage (σ^{∞}), two gages (1) and (2) in the channel, and a gage (i) in the cavity. In order to make the problem amenable, certain assumptions must be made. Solutions obtained by the method of characteristics are usually obtained by numerical methods (graphical in these examples) and changes in cross-sectional area are relatively easy to handle. In this example a single step change in area was used, thus resulting in the loss of some detail in the neighborhood of the transition. The slight flare in the funnel could be treated in a similar manner, but since the changes in area are small (as well as an increase in area) they were neglected. The bends in the funnel cannot be treated easily and therefore are neglected. However, in this example the bends are rather smooth (no sharp corners) and have a radius of curvature of the order of several funnel diameters so that the bends should have little if any effect on the problem. In the second example which I will discuss, there existed many sharp bends in the entrance tunnel. The effect of these bends was to superimpose many pressure fluctuations (the frequency of which were associated with the sonic transient time between bends) on the pressure records. These fluctuations could be ignored thus yielding the lower frequency fluctuations which are of interest to the effects analysts.

This analysis assumes that the gas is a perfect gas with constant specific heats and that the flow process is isentropic. This latter assumption is also valid across the existing shock wave of the first example since the strength of the shock wave is sufficiently weak that the change in static sound velocity can be neglected. The pertinent variables are presented in a dimensionless form in Slide 2 and are summarized in a list of symbols at the end of this paper. The pressure in the chamber is determined by monitoring the mass flow into the chamber and assuming that the pressure change in the chamber is due to an isentropic process. Thus the equation of continuity of mass must be used. This equation, together with the dimensionless form, are also given in Slide 2. The volume of the chamber normalized by some characteristic volume of the tunnel is a significant parameter in these filling problems. This parameter will be discussed briefly at the end of this presentation.

The basic theory of the method of characteristic as applied to one-dimensional non-steady flow problems in constant area channels will not be discussed here, since it is adequately presented in the open literature, rather then the application of this theory to this particular problem will be presented.

Slide 3 presents the "state plane" (i.e., the sound velocity-particle velocity plane) with some typical paths and a schematic of the entrance channel. S_b represents the state of the gas outside the funnel, S_a the state of the gas just inside the funnel, S and S' the states of the gas on either side of the area transition, S_c the state of the gas at the chamber end of the channel, and S_i the state of the gas in the chamber. The state of the gas, S_b, outside the funnel is a given boundary condition. The shock overpressure is given in a typical form as

$$p_{\sigma}(t) = p_{\sigma}(o)\, e^{-t/t_o}\,(1 - t/t_o) \qquad (1)$$

that is, the pressure increases suddenly (by a shock process) and then slowly decays to approximately the initial ambient pressure. The relationship between the states S_b and S_g, and S_c and S_i are similar in principle, provided that, in each case, the flow is in a similar direction (i.e., either "inflow" or "outflow"). For the case of "inflow" the assumption is made that the flow process is iso-energetic such that the State S_g (or S_e) lies on the curve given by the energy equation.

$$x^2 + \left(\frac{k-1}{2}\right)\phi^2 = \text{constant} \qquad (2)$$

The value of the constant is determined from the pressure of the gas at State S_b (or S_i) which, of course, varies with time. The effect of the dynamic pressure behind the shock wave (of State S_b) has been neglected. For weak shocks this simplification should introduce no error.

For the case of "outflow", two conditions can exist. When the flow at the end of the channel (State S_g or S_e) is subsonic, then the pressure must equal the pressure just outside the channel (State S_b or S_i). When the flow is sonic or supersonic, the pressure at the end of the channel can be greater than the outside pressure. If the flow at the end of the channel is accelerated due to a drop in the outside pressure, the flow will become "choked" at this point and the maximum Mach number of the flow will be unity. The supersonic State can only exist if it is due to the flow from within the channel. Such a condition exists, briefly, in the second example which will be presented here.

The relationship between the States S and S' must satisfy the equation of continuity of mass, viz,

$$A' x'^{2/k-1}\,\phi' = A x^{2/k-1}\,\phi\,. \qquad (3)$$

In addition to this equation we have assumed that the flow through the transition is iso-energetic and the energy equation must be satisfied. This is a reasonable assumption since the actual transition is smooth and gradual. Slide 3 illustrates the mapping of a characteristic of States A into the locus of States S' which satisfy the above conditions. When the flow of State S becomes choked (State S_1) the flow of State S' is illustrated by S_1'. It is possible that State S' must, due to the influence of the chamber, decrease in pressure. If this is the case (it occurs in the first example), then it is no longer possible for the flow to be iso-energetic, however, Eq (3) will be sufficient to determine the State of the gas of State S'. A standing shock wave will then exist within the transition zone. In handling this type of area change, it is possible to select something other than an assumption of iso-energetic flow, such as for example, a modified momentum equation which incorporates some flow losses.

Slide 4 presents the initial phase of the solution of the flow in the ship funnel. The increment in the sound velocity Δx used in this computation was 0.02. This value was selected because it yields a reasonable degree of resolution of the solution. The State S_∞ represents the ambient conditions in the funnel and chamber. The shock enters the funnel configuration at a time $t = 0$ and its strength is determined by satisfying simultaneously the Rankine-Hugoniot equations and the condition of iso-energetic flow. State S_{70} satisfies these conditions. When the shock wave reaches the transition it is transmitted, slightly weakened. A system of centered rarefaction waves propagates back upstream from the area transition position. State S_{60} satisfies the Rankine-Hugioniot equations and is related to State S_{73} by the equations governing the transition flow. The centered rarefaction wave interacts with the upstream boundary and results in the reflection of a compression wave such that the flow velocity increases (also the pressure) in the resulting flow State (State S_{83}). The slowly decaying outside pressure results in the propagation of a rarefaction wave down the funnel.

The shock wave which propagates down the funnel propagates out into the boiler chamber and reflects about within this chamber. Mass begins to enter the chamber and the average pressure in the chamber begins to increase. When the shock interacts with the downstream end of the funnel, a rather strong centered rarefaction wave is generated. The flow (State 66) is subsonic so that the pressure of the State is identical to the pressure in the chamber. As the pressure in the chamber increases, signals (compression waves) are sent upstream. Thus the pressure in the channel at the boundary end begins to increase (States S_{65} and S_{64}) and the flow velocity decreases. The strong centered rarefaction wave, which is moving upstream interacts with the area transition and transmits rarefaction waves until the flow in the smaller tube becomes choked at the transition position. The remainder of the strong centered rarefaction wave reflects at the area transition and decreases the pressure in the lower part of the funnel.

The wave diagram for a larger part of the solution is given in Slide 5. $\eta = 0$ refers to the chamber end of the funnel. A discussion of the details of the flow will not be given here, other than to note the time the flow remains choked in the transition (approximately $2 < \tau < 3$) and the generation of rarefaction waves at $\eta = 0$ which indicate the reduction of the outside static pressure. Also the generation of compression waves at $\eta = 1$ which indicate the buildup of the pressure in the chamber. At the time $\tau \cong 8$ (indicated by the arrow in Slide 5), the chamber pressure reaches a maximum and the flow reverses itself. Thereafter, rarefaction waves are generated at $\eta = 1$; these indicating the reduction in the pressure in the chamber.

The pressure variation (p_1 and p_2) at two stations in the funnel (indicated on the η axis by two arrows), the pressure variation in the chamber (p_3) and the blast wave overpressure $p_{\infty}(t)$ variation are shown in Slides 6 and 7. The analysis utilized a dimensionless presentation, however, for the purpose of comparison, the pressure and time scales are given in pounds per square inch gage and milliseconds respectfully so that a direct comparison could be made with the measurements observed in the experiments in the Air Force 6-foot shock tube.

Slide 8 presents the pressure records obtained in the shock tube. The pressure scale is not given since final calibration constants for the gage were not yet available. The shock overpressures used in this experiment were slightly larger than those used in the calculation, however, in this range of shock strength, no great change in shape of the pressure curves should occur. The time dots given on the uppermost time axis in Slide 8 are equivalent to one millisecond intervals. A detailed comparison of the computed and measured pressures indicates a very good qualitative comparison. The calculations based upon the above-outlined assumptions and theory yield a good prediction of both the gross behavior of the pressures in the system and some of the finer structure of the pressure variations.

The second example which was treated was that of a shelter subjected to considerably higher pressure and a somewhat distorted static pressure variation in the blast wave. Slide 9 presents the wave diagram for this case. $\xi = 1$ is the chamber end of the tunnel. This solution contains some phenomena which did not occur in the previous solution. The outside static pressure was sufficiently large so that the flow in the tunnel was accelerated to supersonic speeds. As a result the rarefaction and compression waves which were propagating upstream were at least temporarily swept back downstream. The compression (or weak shock) wave was actually swept out of the tunnel and into the chamber, such that a standing shock wave would exist momentarily at the end of the tunnel. As the flow velocity decreases in the tunnel due to the decay of the outside pressure, the standing shocks reform and propagate back upstream and eventually reach the surface end of the tunnel. The time of flow reversed occurs at approximately $\tau \cong 2.5$.

Slide 10 presents the pressure variation with time of the blast overpressure (P_∞), the chamber pressure (P_2), and the pressure variation (P_1) in the tunnel near the chamber end. The slide also includes a prediction of the chamber pressure (P_2') which was computed on the basis of quasi-steady flow using the conventional orifice equation for compressible flow and computing the mass flow rate as a function of the instantaneous pressure differences between the outside and chamber pressure. Such a computation does not allow for any time delay in the pressure buildup in the chamber and does not give any indication of the flow details in the entrance tunnel.

The above calculations demonstrate that the filling process for the chamber which are exposed to blast waves can be predicted with reasonable accuracy. The analyses are rather cumbersome in that numerical or graphical methods must be utilized to solve a specific case. In addition to the details of the flow process, the ratio of the peak chamber pressure to the peak outside pressure can be predicted. This ratio is significant in weapon effects research in that it is a measure of the protection obtained or the loads to be designed for in tunnel-chamber configurations. The Volume of the chamber, the tunnel length, and the duration of the blast wave are all important parameters which affect the chamber pressure. The ratio (V/LA) varied between the above two calculations, however, a direct comparison of the ratio of the peak chamber pressure to peak blast pressure is not meaningful due to the rather large difference in shape of the blast wave.

LIST OF SYMBOLS

P or p	pressure
ρ	density
R	gas constant
T	temperature
k	ratio of specific heats
c	sound velocity
x	dimensionless sound velocity
u	particle velocity
d	dimensionless particle velocity
t	time
L	length of tunnel
τ	dimensionless time
X	distance
χ	dimensionless distance
W	mass flow rate
A	tunnel cross-sectional area
M	Mach number
S	state of gas
A	constant

SUBSCRIPTS OR SUPERSCRIPTS

o or ∞	reference quantities
'	refers to chamber end of transition
e	refers to chamber end of tunnel
s	refers to surface end of tunnel
i	refers to chamber conditions
b	refers to outside (surface) conditions
σ	refers to a blast overpressure

Slide 1 Ship Model in 6-foot Shock Tube

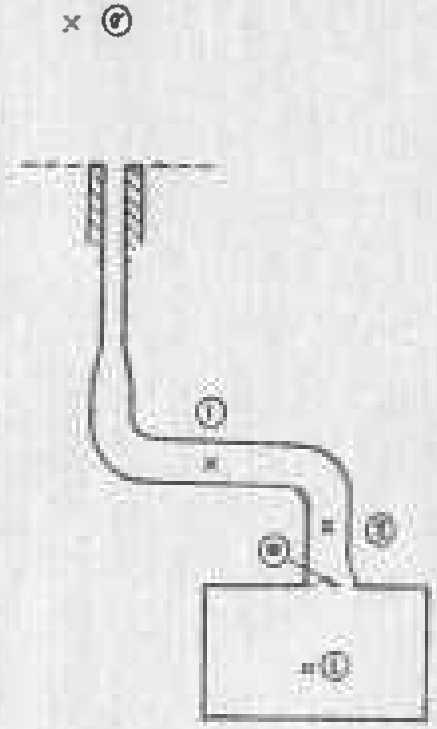

PERFECT GAS $P = \rho RT$

ISENTROPIC PROCESS $\frac{P}{P_0} = \left[\frac{\rho}{\rho_0}\right]^K$

DIMENSIONLESS VARIABLES:

$$\psi = \frac{c}{c_0} = \left(\frac{P}{P_0}\right)^{\frac{2K}{K-1}}$$

$$\varphi = \frac{u}{c_0}$$

$$\tau = \frac{t c_0}{L}$$

$$\zeta = \frac{x}{L}$$

CONTINUITY EQUATION:

$$W = \rho_e u_e A' = \frac{d}{dt}(\rho_i \forall)$$

OR

$$d\tau = \frac{\forall}{A'L}\left(\frac{2}{K-1}\right)\frac{\psi_i^{\frac{3-K}{K-1}}}{\varphi_e \psi_e^{\frac{2}{K-1}}} \cdot d\psi_i$$

Slide 2 Schematic of Boiler-Funnel Configuration

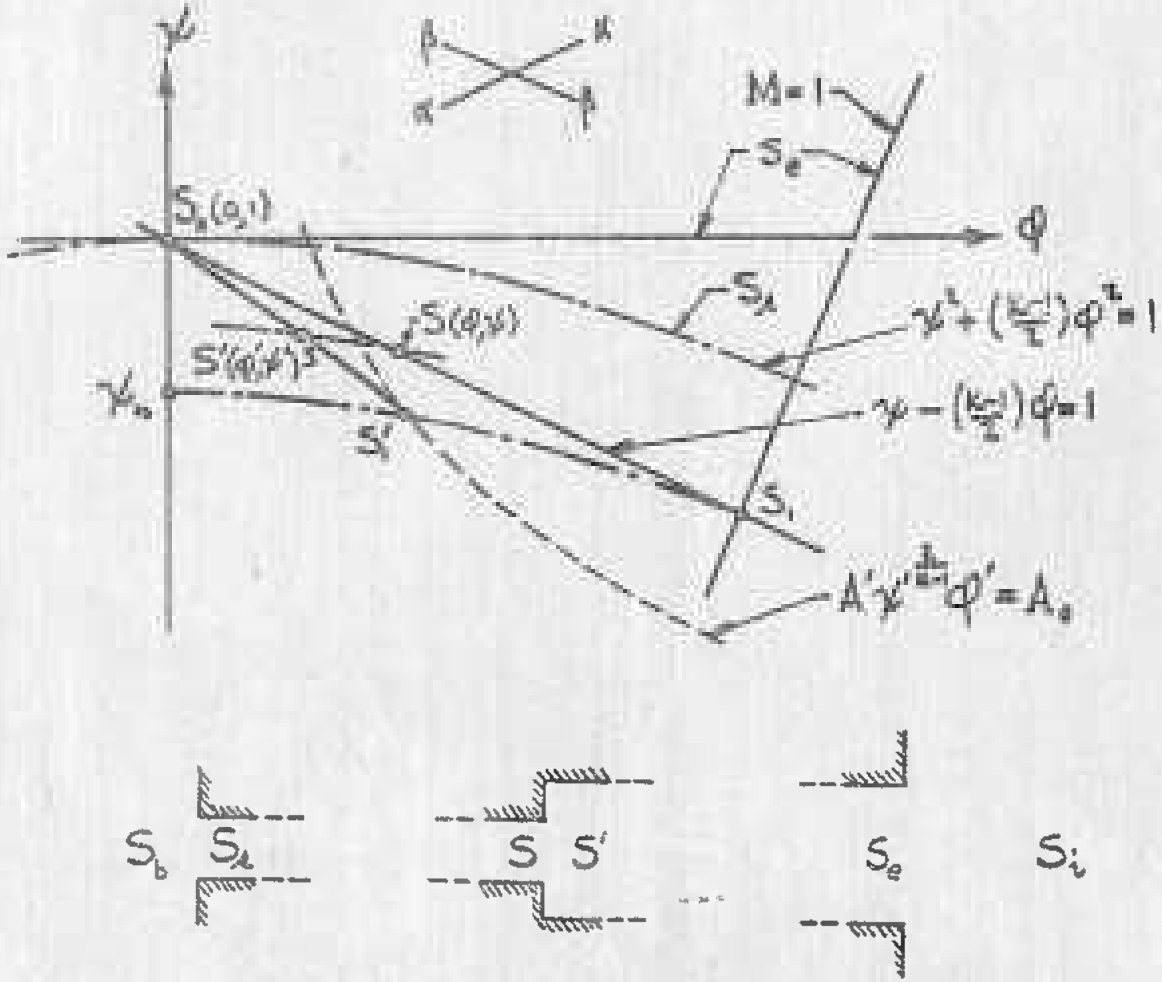

Slide 3 Schematic of State Diagram

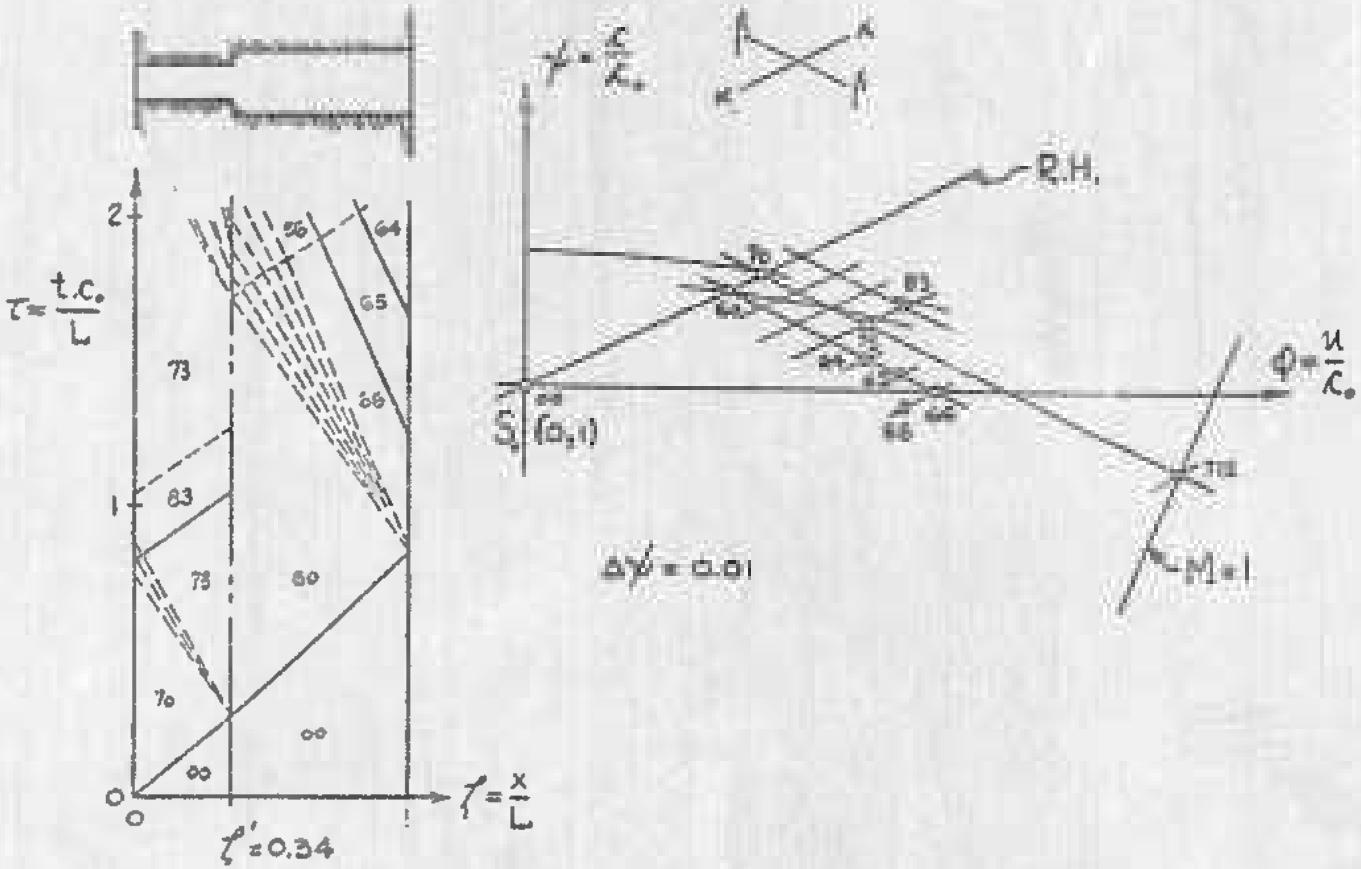

Slide 4 Initial Phase of the Flow in the Funnel

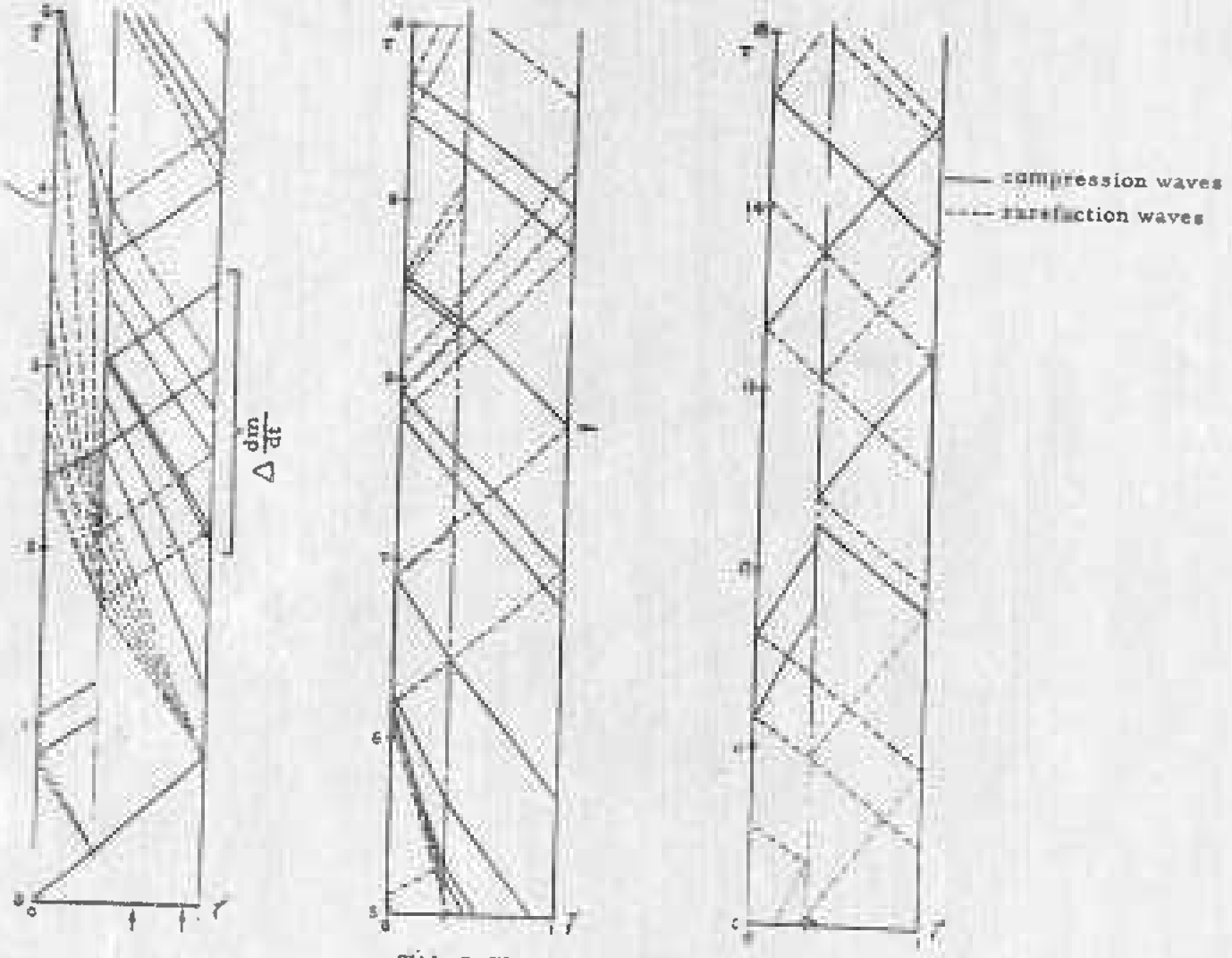

Slide 5 Wave Diagram for the Funnel

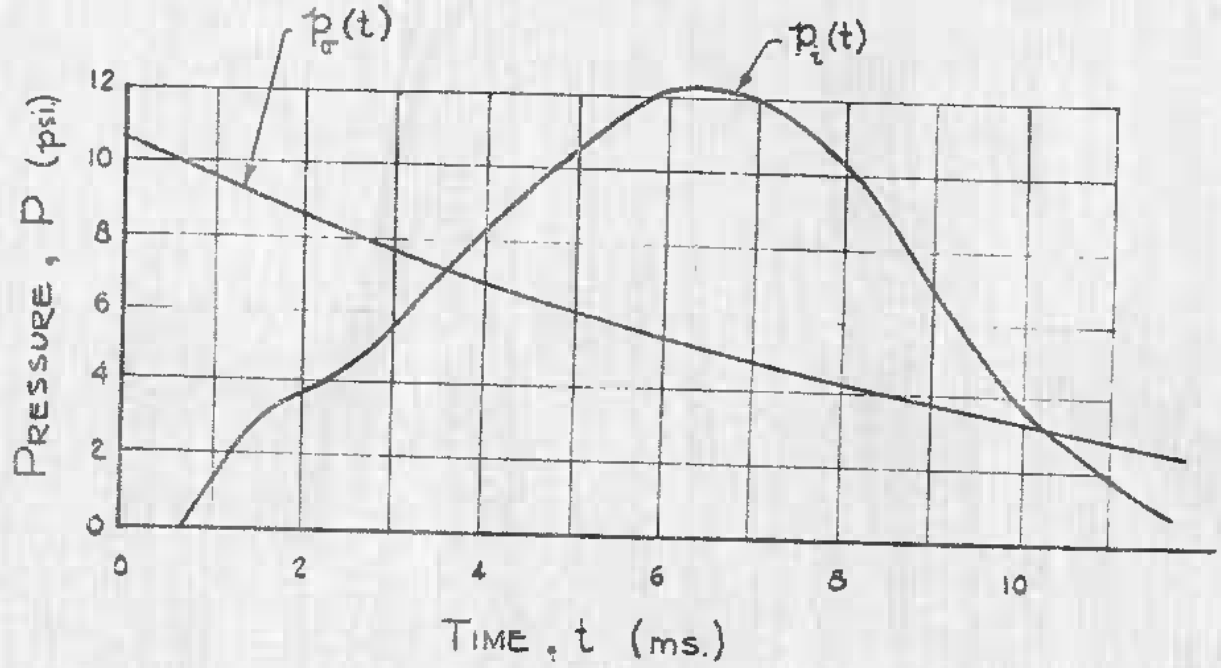

Slide 6 Pressure Variation - Chamber and Blast Pressures

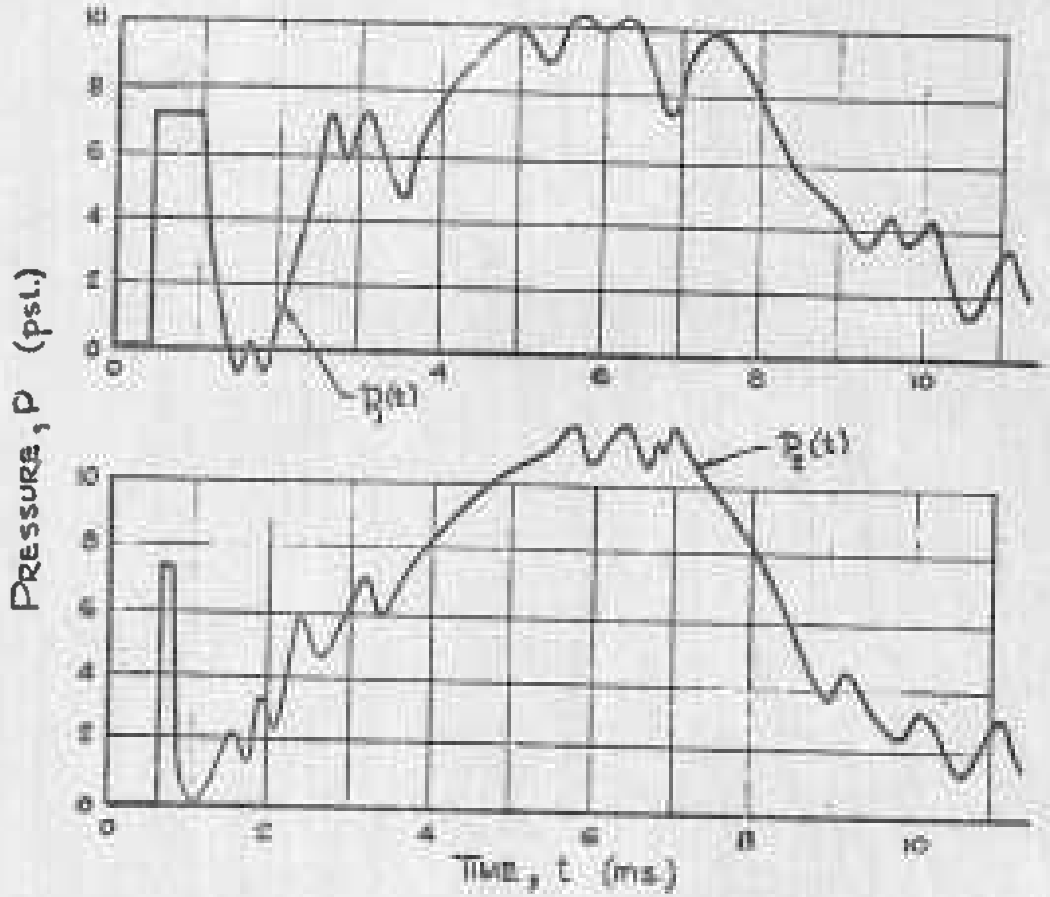

Slide 7 Pressure Variations in Funnel

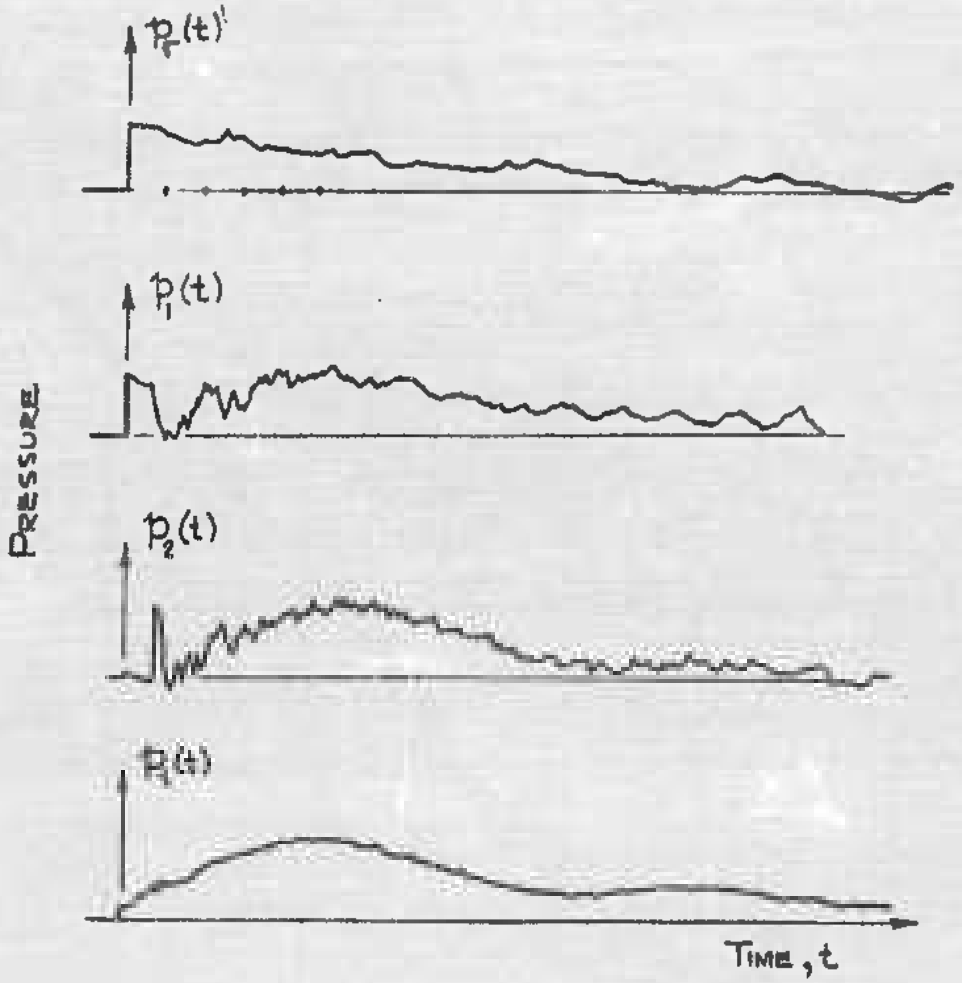

DH#3-8, $p_r(o) = 12.4$ psi.

Slide 8 Shock Tube Records

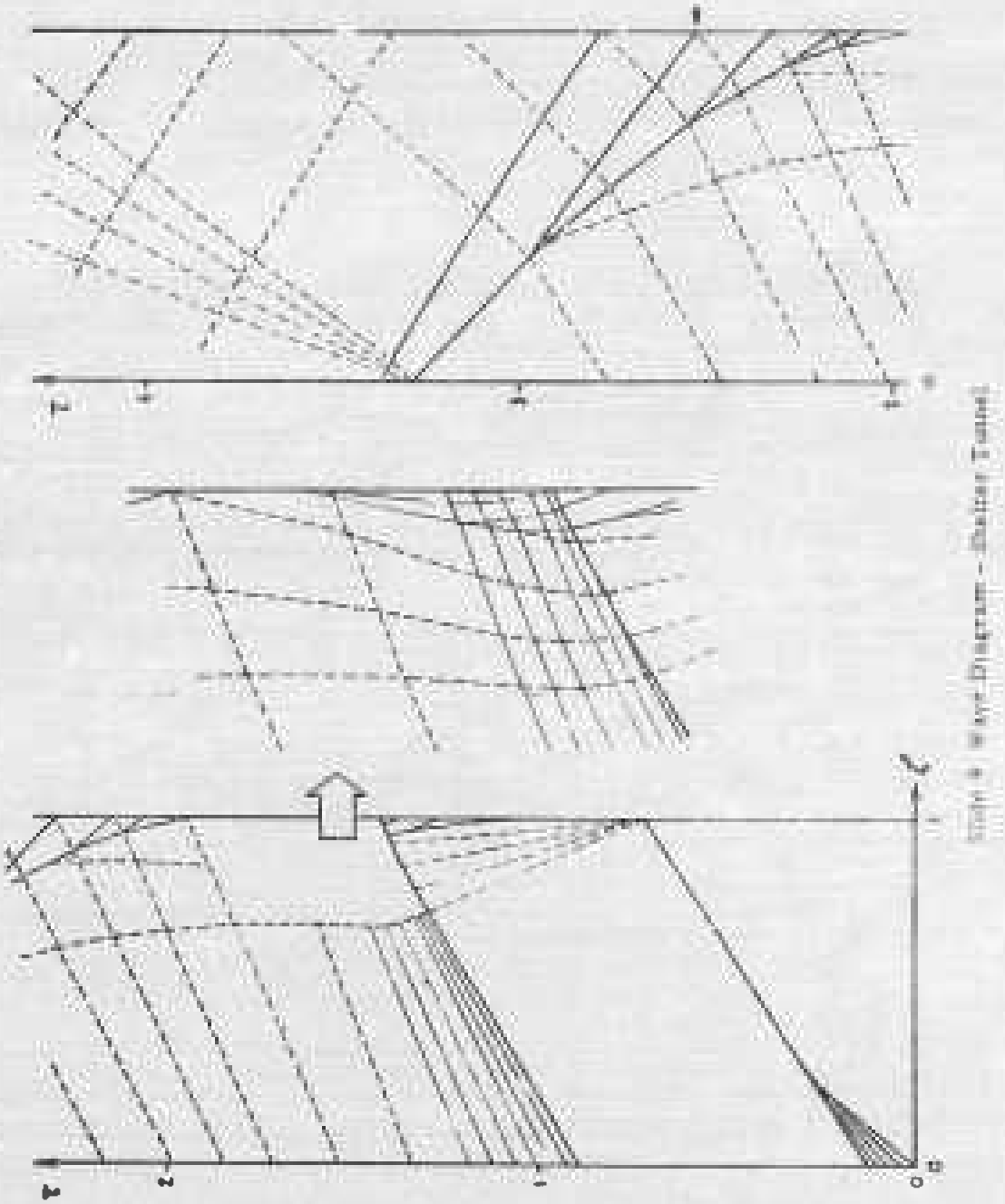

Stress Wave Diagram – Bolter Tunnel

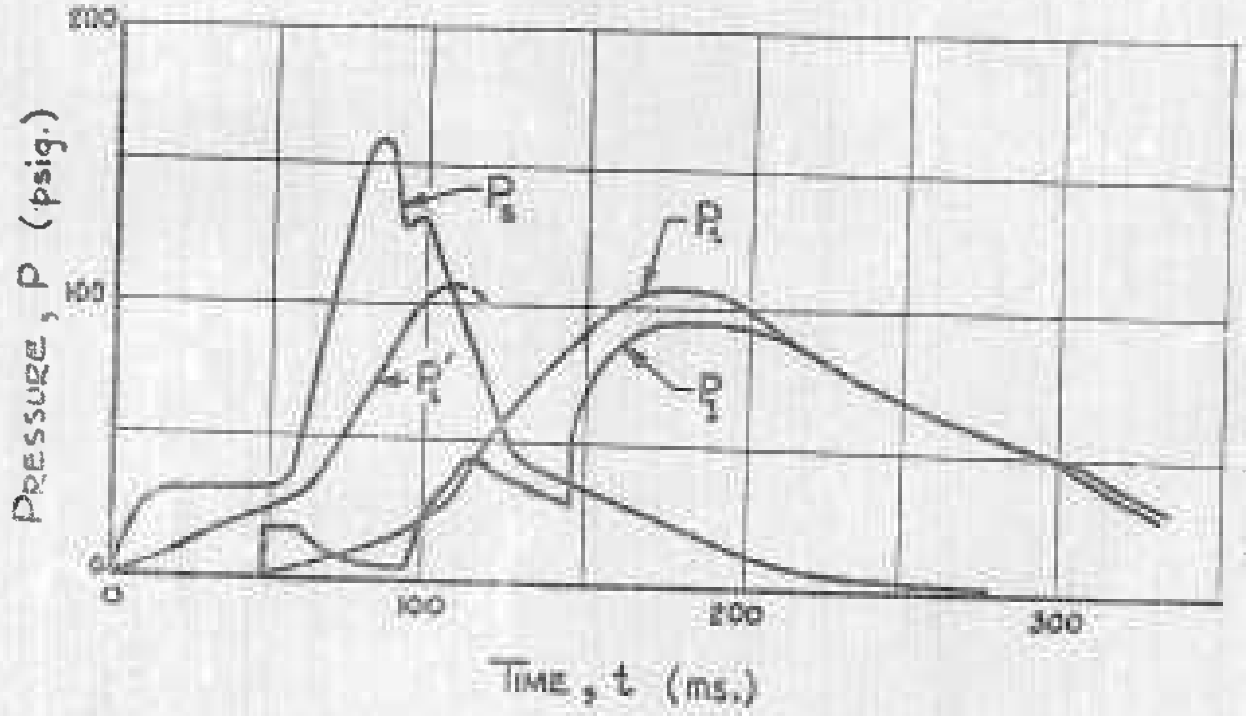

Slide 10 Pressure Variation in Shelter

DIAPHRAGM CALIBRATION TECHNIQUES IN A 2.00-INCH DIAMETER SHOCK TUBE

George H. Tweney
Boeing Airplane Company

ABSTRACT

Since the Second Shock Tube Symposium at Palo Alto, California, in March 1958, the Aerodynamic Test Group of the Pilotless Aircraft Division, Boeing Airplane Company, has designed, built, and operated a 2.00-inch inside diameter, cold-gas driver, shock tube.

Considerable operating experience has been gained in this facility during the past few months. In particular, a number of diaphragm materials and techniques have been tested, and good calibration data have been obtained. Heretofore, there has been a scarcity of published literature describing diaphragm burst techniques, with no results published in this country, and only one or two scattered references in British and Continental literature. Presented in this paper is a review of diaphragm experiences in this shock tube to date, including summaries of the behavior of various diaphragm materials for both low and high pressure ratios, different diaphragm holding techniques, manual and overload burst techniques, and illustrations of various type diaphragm failures. In particular, a new and somewhat unique method for the prescoring of metallic diaphragms is described. Numerous photographs of various diaphragm rupture patterns are shown. A brief description and photographs of the complete facility are also presented.

Diaphragm calibration data and burst techniques are given in a manner that should prove most useful to other facilities, and should save considerable time and cost in the design and development of suitable diaphragm techniques in other laboratories.

INTRODUCTION

A great deal of work has been done in the past few years on the design, development, and application of shock tube testing facilities. Considerable emphasis has been placed on the use of such facilities in both basic and developmental research, particularly in the field of gas dynamics. Despite the large volume of shock tube literature published in recent years (e.g. Reference 1), relatively little information of a systematic nature has been published on the behavior and bursting characteristics of various diaphragm materials. This has resulted in a critical lack of vital information, since the successful operation of any shock tube hinges largely on the bursting characteristics of the diaphragm. Developing suitable diaphragms during a test program is usually very time consuming, particularly when metallic diaphragms are used at large pressure ratios. No diaphragm results of any detailed significance have been published in the United States to this author's knowledge, (Reference 6 presents some data) and quantitative results have appeared in only a few European papers (References 2, 3, and 4).

This paper attempts to present a comprehensive review of diaphragm experiences in a small shock tube designed and constructed by the Aerodynamics Test Group of the Pilotless Aircraft Division of the Boeing Airplane Company.

This shock tube facility was designed and built with three basic purposes in mind:

1. Understanding and becoming familiar with the design characteristics of shock tubes in general

2. Becoming familiar with the characteristics of such tubes through actual operation

3. Providing a facility in as short a time as possible, which would be adequate for as wide a range of basic research and developmental testing as possible.

If is of interest to remark that the time interval for this facility, from the date of conception to the bursting of the first diaphragm, was exactly twelve working days. This included the preparation of all shop design drawings and complete fabrication of all the hardware.

This paper attempts to present diaphragm calibration data and a review of several bursting techniques in a manner that should prove of considerable help to other facilities.

The author is indebted to his co-worker, Mr. Floyd D. Jones, for much detailed assistance in the operation of the facility and the preparation of this paper.

DESCRIPTION OF THE FACILITY

A somewhat detailed description of the facility and its instrumentation is presented in Reference 5. A photograph of the complete installation looking downstream toward the driven end, is shown in Figure 1. A partial view, looking upstream toward the driver end, is shown in Figure 2.

The driver is six feet long, 3.25-inch inside diameter, with a wall thickness of 0.625 inch, and is made of No. 4340 Shelby seamless steel tubing. It is capped on the aft end, and at the forward end, is designed to fit into the diaphragm holder section which will be described later. The driver is mounted on a movable stand rolling on tracks, which allows it to be easily rolled back to facilitate changing diaphragms. Pressure is built up in the driver by connecting it to standard, commercial gas bottles, available up to maximum pressures of 2200 psi. Calibration runs and test runs made thus far have utilized nitrogen only, but the facility can also accommodate helium or other bottled inert gases. A bleed valve is provided on the driver section for purging the complete section after a blow is completed.

The diaphragm, which can be either metal or plastic, is securely held between two metallic rings (nicknamed the "cookie holder"), which in

turn, is threaded into the downstream end of the transition section. This enables a diaphragm assembly to be made on the bench, thus reducing the time lost between blows. Thus far, plastic, aluminum, and copper diaphragms have been successfully blown. This paper will present the results of considerable calibration work to determine the breaking characteristics of various type diaphragms over a range of thicknesses and with varying depths of scribe. Tests have been made by rupturing the diaphragm through overpressure only. A mechanical spear was installed at one time, but the results were none too satisfactory and it has since been discarded.

The transition section is shown in Figures 3 and 4. It is made of two large flanges machined from tool steel, one mounted on the driver and the other on the mating end of the driven tube, with the diaphragm holder between as described previously. Figure 3 shows the transition section open; the large gauge on the left is the P_1 Wallace-Tiernan indicator. Figure 4 shows a close up of the transition section looking toward the driven end flange. The two flanges are mated and secured with a Marman-type clamp arrangement prior to a blow. Future improvements will involve the eventual elimination of this clamp, and the insertion of the diaphragm directly in the transition section each time. The present diaphragm holder, disassembled, is shown in Figure 5. Phonograph grooves to help prevent diaphragm slippage are clearly visible.

The driven end of the assembly is made of 2.00-inch inside diameter × 0.25-inch wall 4130 seamless tubing. The total driven length is in three sections, an initial 16-foot section, plus two consecutive 8-foot sections, each securely joined by two flanges. This incorporates a certain flexibility in the driven section by allowing tests to be run with 16-foot, 24-foot, and 32-foot lengths of driven end. At present, the driven end is also capped, but plans are in process for incorporating an expansion-type, hypersonic nozzle on this end.

The driven tubes, and also the driver, are mounted on A-type frames which support the complete assembly at a convenient working level of three feet above the floor.

The driver, as described previously, is compressed by bottled gas and is instrumented with a Statham pressure transducer. The pressure buildup is continuously recorded on a Bristol strip chart recorder. This provides a permanent record of the rate of pressure rise and the maximum pressure at the time of diaphragm rupture. The only other instrumentation on the driver is a bleed valve for purging the system.

The driven end is evacuated to the desired evacuation pressure by a W. M. Welsh duo-seal vacuum pump. The evacuation pressure is continuously indicated on a Wallace-Tiernan pressure gauge. When the desired evacuation pressure is reached, this gauge can be locked out of the system, thus providing a continuous, visual record of the starting evacuation pressure and, at the same time, protecting the gauge from the pressure buildup in the system when the diaphragm ruptures.

Calibration instrumentation at the end of the driven tube consists at present of equipment suitable for measuring shock velocities and pressure impulses. Two Endevco piezoelectric pressure pickups are mounted at one-foot and at nine-foot distances from the downstream end of the driven tube. Each Endevco is wired to a cathode follower-amplifier, which, in turn, is wired into a Tektronix Model 545 oscilloscope equipped with a recording polaroid Land camera. Time intervals are measured and visually recorded on a Berkely Universal Eput and Timer. When the shock passes the upstream Endevco pickup, the first scope is triggered, the pressure impulse is photographed, and the timer is activated. When the shock passes the downstream pickup, the second scope is triggered, the pressure impulse is photographed, and the timer system is stopped, with the elapsed time permanently indicated on the Berkely timer.

The foregoing instrumentation has been provided only for the purpose of the initial calibration runs of the facility. Further refinements and improvements are contemplated as specific test programs are initiated. A set of Kistler gauges and amplifiers are now on order.

DIAPHRAGM CALIBRATION

Somewhat more than 300 blows have been made since the facility was completed. Approximately 200 of these were made specifically for calibration purposes. Much of the primary effort has been directed toward securing an acceptable diaphragm rupture. Various diaphragm materials have been experimented with, ranging from ordinary celluloid to metallic diaphragms made of aluminum, copper and stainless steel.

The primary problem in securing suitable rupture is involved in the type of scribing used to force the diaphragm to rupture into four uniform petals, at the same time preventing fragments from being blown into the driven end of the tube. Reference 4 suggests that no scribing is necessary, but experience in this facility has proven otherwise.

In order to develop a preliminary "feel" for the bursting characteristics of various diaphragm materials, a number of tests were run in a small bench facility known as the pot tester. This machine consists of a simple pressure tank of approximately one gallon capacity, with provision made for holding a diaphragm 1.5 inches in diameter, and building up a high pressure on one side of this diaphragm by means of laboratory compressed air. The maximum capacity of this tester is only 500 psi, but it does give an excellent visual indication of the burst characteristics of various materials. Some representative Mylar and celluloid samples are shown in Figure 6. Obviously, it is not feasible to scribe plastic diaphragms but the comparison between Mylar and celluloid as indicated in this Figure is quite marked. The Mylar diaphragms, regardless of the number of plies, rupture by combined deformation and tensile failure only, without ejecting any fragments downstream. On the other hand, the celluloid being much more brittle in nature, actually fails by separation and propels a large number of small fragments downstream into the driven end. This is undesirable from a testing point of view, as any such fragments would seriously erode test models mounted in the stream.

Aluminum diaphragm samples were also tried in the pop tester, and some experimenting was done here with various types of scribing. Figure 7 illustrates a number of these samples. It is obvious from the samples shown, that any attempt to scribe the diaphragm into many segments is not desirable, since it results in either a pinhole failure, or the actual loss of part of the diaphragm downstream. In these earlier bench tests, it was learned that double scribed lines oriented at 90°, thus dividing the diaphragm into four petals, gave the best results. Under some circumstances, satisfactory results may be obtained without scribing, but the risk of propelling fragments of metal downstream is greatly increased.

Various techniques have been tried in order to arrive at the best method of impressing the scribe lines. These have included hand scribing with a sharp tool, pantograph scribing, milling machine cutting, photo etching, and finally die stamping. None of these techniques have proven very successful except the photo etching and die stamping. Photo etching is an ideal process for copper diaphragms, and results in a smooth and precise scribe line, without any tearing or roughness, and with accuracies to 0.01 inch of scribe depth. Its only apparent disadvantage is the inability to prepare diaphragms right on the test site. For this reason, die stamping with a three-inch blade has been used in all the calibration data presented in these results. This is a very convenient technique, and can be done at the time of the test, with a degree of accuracy sufficient to provide reasonably reliable calibration data.

Figure 8 illustrates the range of diaphragm materials selected for calibration coverage in the tests. This figure is a bar chart arranged to show the per cent of material left after the scribe lines are made. This material remaining is defined in this paper as the effective thickness. The effective thickness is this the material thickness remaining after subtracting the depth of scribe from the original material thickness.

During the calibration runs, the shock tube was set up with the driven end 16 feet long. The test technique consisted of evacuating the driven end, and then pressurizing the driver until the rupture strength of the material was reached. Gauge pressure data were recorded at time of failure, for diaphragms with graduated amounts of effective thickness.

Before the diaphragm holder, as previously illustrated in Figure 5, was developed, it passed through several preliminary stages of design. Some of the earliest runs in the facility indicated that considerable difficulties could arise in attempting to hold the diaphragms so they would burst in the desired manner. Figure 9 illustrates some of the results obtained with the initial holder. The most apparent short-coming of the initial design was the narrow flange, and the tendency of the diaphragms to slip under high pressure. Typical failures resulting from this slip are illustrated in Figure 9. While it was possible to attain successful rupture in the initial holder, the repeatability was not good and the holder was redesigned into the final form shown in Figure 5. With one or two exceptions, there has since been almost one hundred per cent repeatability in more than several hundred blows. The major change involved in the redesign consisted of increasing the width of the flange in order to allow the O-ring seal to hold

completely. Some of the failures shown in Figure 9 are rather interesting in that a number of the diaphragms actually shattered and drove numbers of fragments down the tube with terrific force.

Figure 10 shows the results obtained with some Mylar diaphragms in the wide flange holder. As was determined in the preliminary runs made in the pop tester, celluloid was not at all suitable and it was not tried in the shock tube. All plastic diaphragm tests have concentrated on the use of Mylar. All the failures shown in Figure 10 are quite satisfactory and as far as could be determined, no fragments went downstream. Since it is not possible to prescribe a plastic diaphragm, the rupture patterns in Figure 10 may appear to be somewhat non-uniform but this is not deemed undesirable in a substance as elastic as Mylar. Undoubtedly, at the time of rupture, the Mylar was pressed tightly against the walls of the transition section, and did not obstruct rapid formation of the shock pattern. For low pressure ranges, possibly up to driver pressures of 200 psi, it would be difficult to improve on Mylar as a diaphragm material.

Figure 11 shows some typical wide flange, soft-copper diaphragm failures. The reverse flow failures are interesting, insofar as they illustrate how the diaphragm petals can be completely bent back on themselves when the shock goes through on the return journey. Even in the case of incomplete rupture, these petals can be severely bent in the reverse direction. On several occasions, ruptured petals have been found in the back end of the driver section. The underexpanded diaphragm shown in Figure 11 is typical of what can result when too strong a diaphragm is used for the driver pressure desired. An underexpanded diaphragm would obviously affect the shock formation, since the diaphragm petals are not completely expanded against the walls of the transition section. A scribed and an unscribed copper diaphragm failure are also shown in Figure 6.2.4 of Reference 6.

A similar series of wide flange, soft-aluminum diaphragms is shown in Figure 12. Some interesting reverse flow patterns are indicated here, and the lower group of four shows a nice sequence of progressively underexpanded diaphragms. Obviously, those shown on the left would have a very undesirable effect on the formation of the shock pattern. Several satisfactory examples are shown to illustrate the manner in which the four petals can be made to fully expand against the walls of the transition section. This expansion obviously takes place in a very short interval of time, with almost instant formation of shock. Studies of the time interval involved for shock formation have been reported in Reference 1. A photo of two unscribed aluminum diaphragm failures is shown in Figure 13 of Reference 4, to compare with those illustrated here.

Figure 13 presents a Mylar diaphragm burst-pressure calibration curve. Actual Mylar thickness (in this case, synonymous with effective thickness since there are no scribe lines), is plotted against driver pressure P_4. There is some scatter in the data, but this is to be expected at the low pressures involved. The single thickness diaphragms seem to present a fairly smooth curve, but there is a slight shift in the curve as multiple thickness diaphragms are introduced. Data are still somewhat inconclusive at

these very low pressures, but at the moment, there seems to be little justification for using multiple thickness plastic diaphragms.

A graph of effective thickness plotted against driver pressure for the soft-copper calibration diaphragms is shown in Figure 14. Inevitably, there will be some scatter in the data throughout the range of pressures for any given diaphragm thickness. Generally the scatter is reduced as the thickness and pressures are increased. At the upper ranges, repeatability is as good as 5%, while at the lower ranges, depending on diaphragm thickness, the scatter may be as high as 10% to 15%. It seems obvious from the curves shown in Figures 14 and 15 that, for a desired driver pressure, there is a band of the best effective thickness of the diaphragm for the pressure desired. For example, on Figure 14, one would not tend to select a diaphragm in 0.062-gauge at driver pressures of 800 psi or less. In this pressure range, one would prefer to drop down to an 0.046-gauge diaphragm.

Figure 15 shows a graph of effective thickness plotted against driver pressure for the soft-aluminum calibration diaphragms. It appears that the scatter in the data for aluminum is somewhat less than for the copper diaphragms. No explanation can presently be offered for this better agreement. However, it is likewise more evident in the aluminum curve, that there exists a most suitable diaphragm thickness for a given pressure range. As an illustration of this fact, consider the curve for 0.091-gauge between the driver pressures of 750 psi and 1750 psi. Between these ranges the curve is comparatively smooth, whereas, below 750 psi there is a substantial change in slope. Hence, for driver pressures below 750 psi, one would drop down to 0.071-gauge, or still further to 0.051-gauge.

Only a few stainless steel diaphragms have been tested in this program. Generally, they have not been too successful. The material is hard, lacks ductility, and has too great a tendency to release small, sharp particles downstream. Other experimenters have used cold rolled steel, even in multiple thicknesses, with some success (References 6 and 7), but present results show no apparent advantage to be gained in using steel instead of soft copper or aluminum. The latter appear preferable for their ductility, if for no other reason.

CONCLUSIONS

1. Burst patterns and calibration data have been presented for Mylar, soft-copper, and soft-aluminum diaphragms in a 2.00-inch diameter shock tube, up to driver pressures as high as 2000 psi.

2. Calibration curves for Mylar, copper, and aluminum show that there is a range of effective diaphragm thickness most suitable for a desired pressure range.

3. Both ordinary celluloid and stainless steel are considered unsuitable for diaphragm materials, because of their undue tendency to shatter and contaminate the air stream with sharp particles resulting in serious damage to models.

4. Several scribing techniques are described, and recommendations presented for photo etching and die stamping, which appear to be more practical and to produce more consistent results than other methods.

5. Recommendations are made for the bursting of diaphragms in a four-petal pattern, rather than any larger number, or with no petals at all.

6. Several unsuccessful and successful methods for the holding of diaphragms under high pressure have been described.

REFERENCES

1. Glass, I. I., Martin, W., Patterson, G. N., A Theoretical and Experimental Study of the Shock Tube. UTIA Report No. 2, November 1953, Institute of Aerophysics, University of Toronto.

2. Cox, S. G., Development of the R.A.E. 6-inch Diameter Shock Tube, Part I: Bursting of Diaphragms at 200 Atmospheres, R.A.E. Technical Note Aero 2510, May 1957, Royal Aircraft Establishment, Farnborough.

3. Freeman, A. J., Investigation and Development of High Pressure Burster Disks and Diaphragms. English Electric Company Limited, Report No. LM. U. 005, 1956.

4. Schultz, D. L., Henshall, B. D., Hypersonic Shock Tube Equipment at the National Physics Laboratory, U. K. AGARD Report 147, July, 1957.

5. Tweney, George H., 2.00 Inch Diameter Shock Tube, Pilotless Aircraft Division, Aerodynamics Test Group. Intra-PAD Memo Reference No. 5-7841/WT-47, June 9, 1958.

6. Hall, J. Gordon, Shock Tubes, Part II: Production of Strong Shock Waves, Shock Tube Applications, Design, and Instrumentation. UTIA Review No. 12, Part II, May, 1958, University of Toronto, Institute of Aerophysics.

7. Hufton, P. A., Hypersonic Facilities in the Aerodynamcs Department Royal Aircraft Establishment. AGARD Report 146, July 1957.

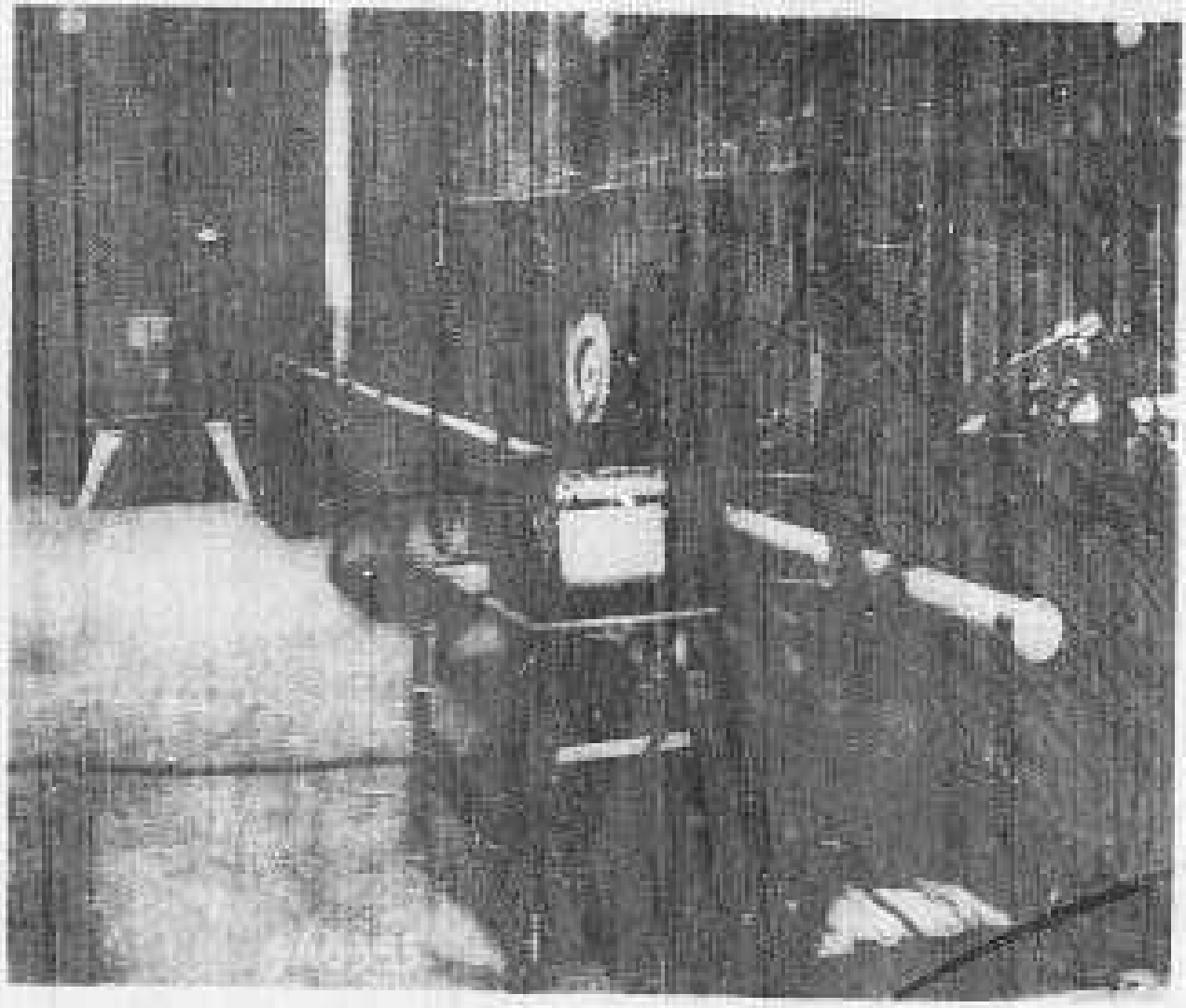

Figure 1 General View of PAD Shock Tube Facility Downstream Toward Driven End

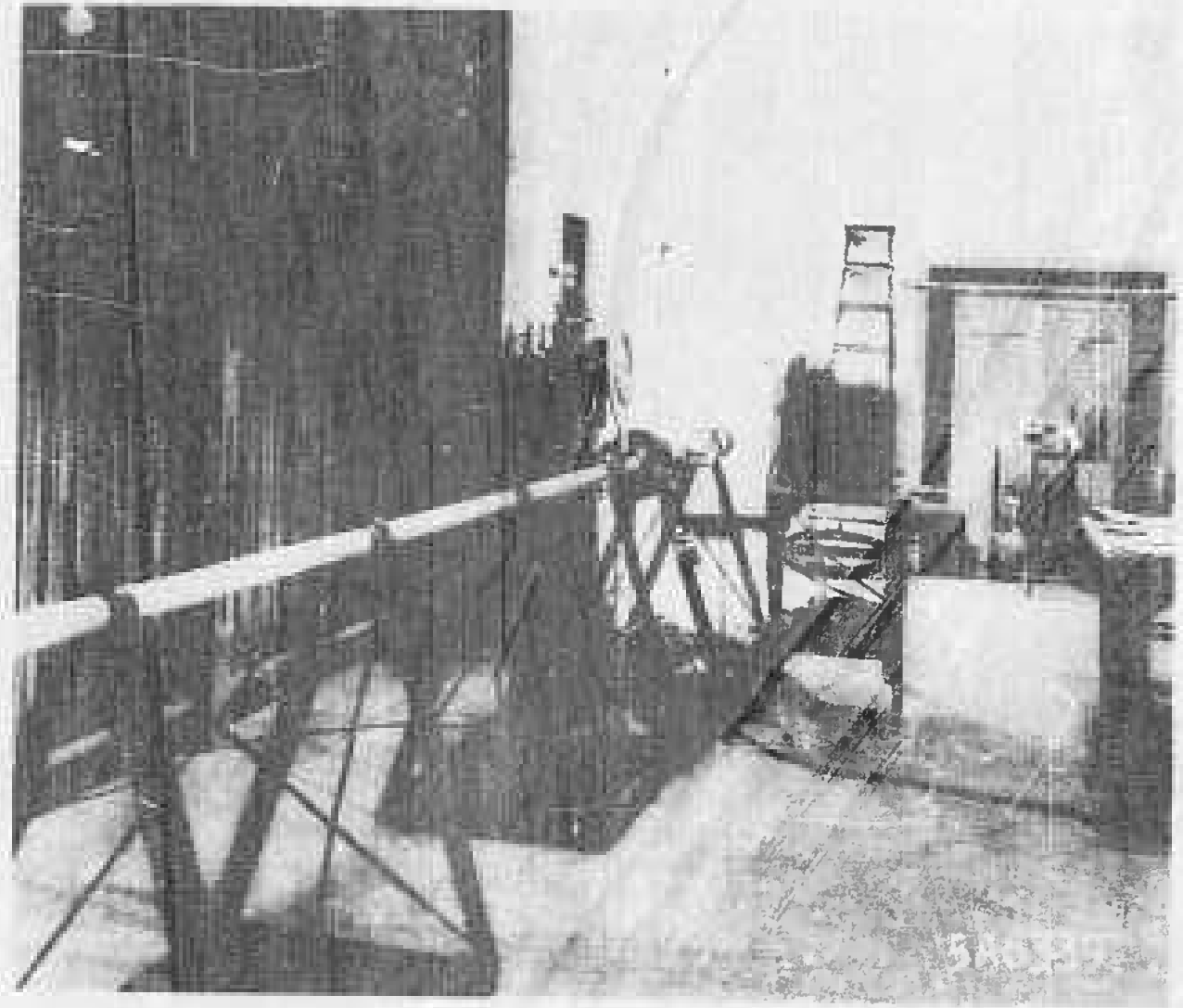

Figure 2 Partial View of PAD S[illegible]

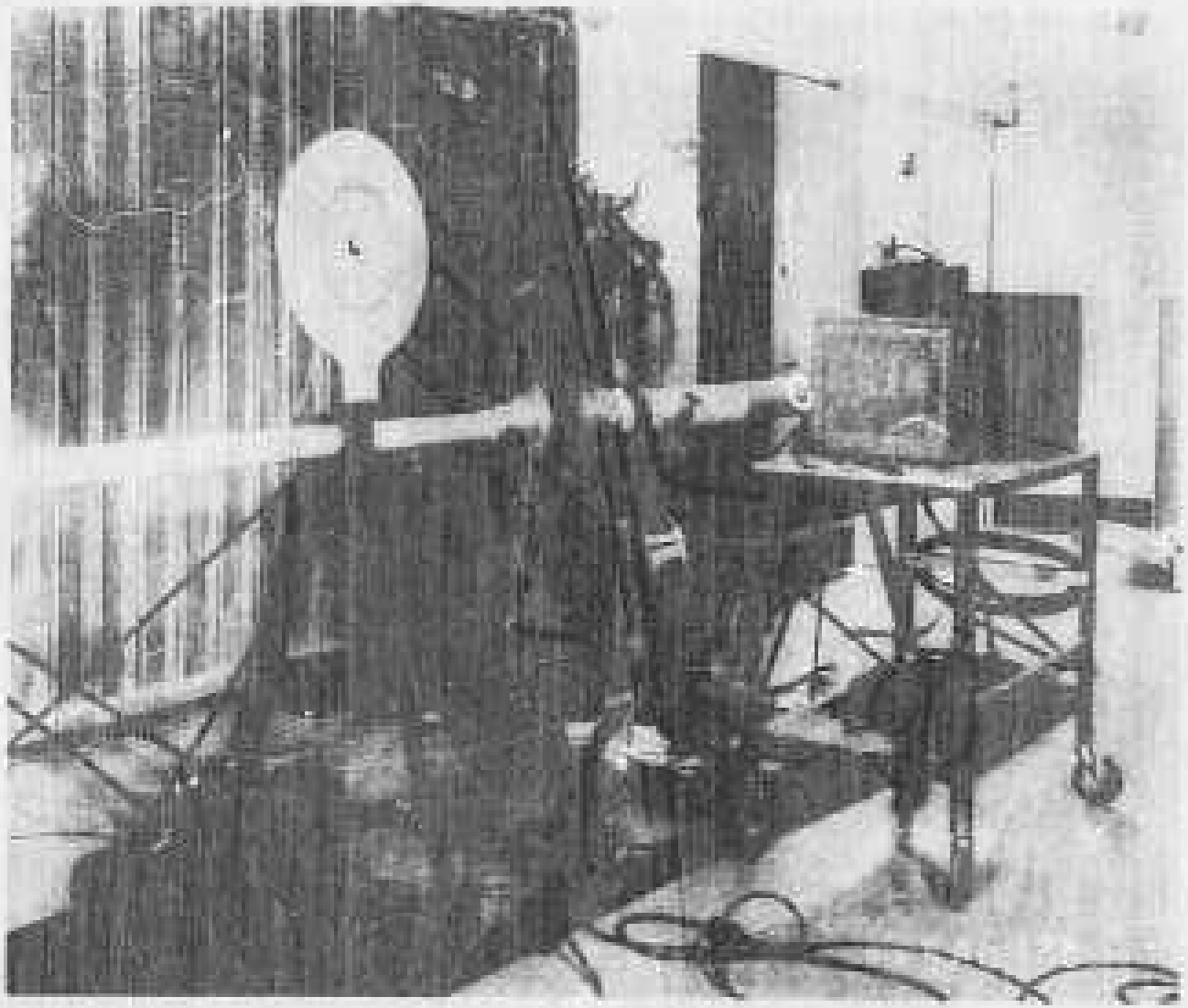

Figure 3 Transition Section (Shown Open) P_1 Wallace-Tiernan Gauge at Left

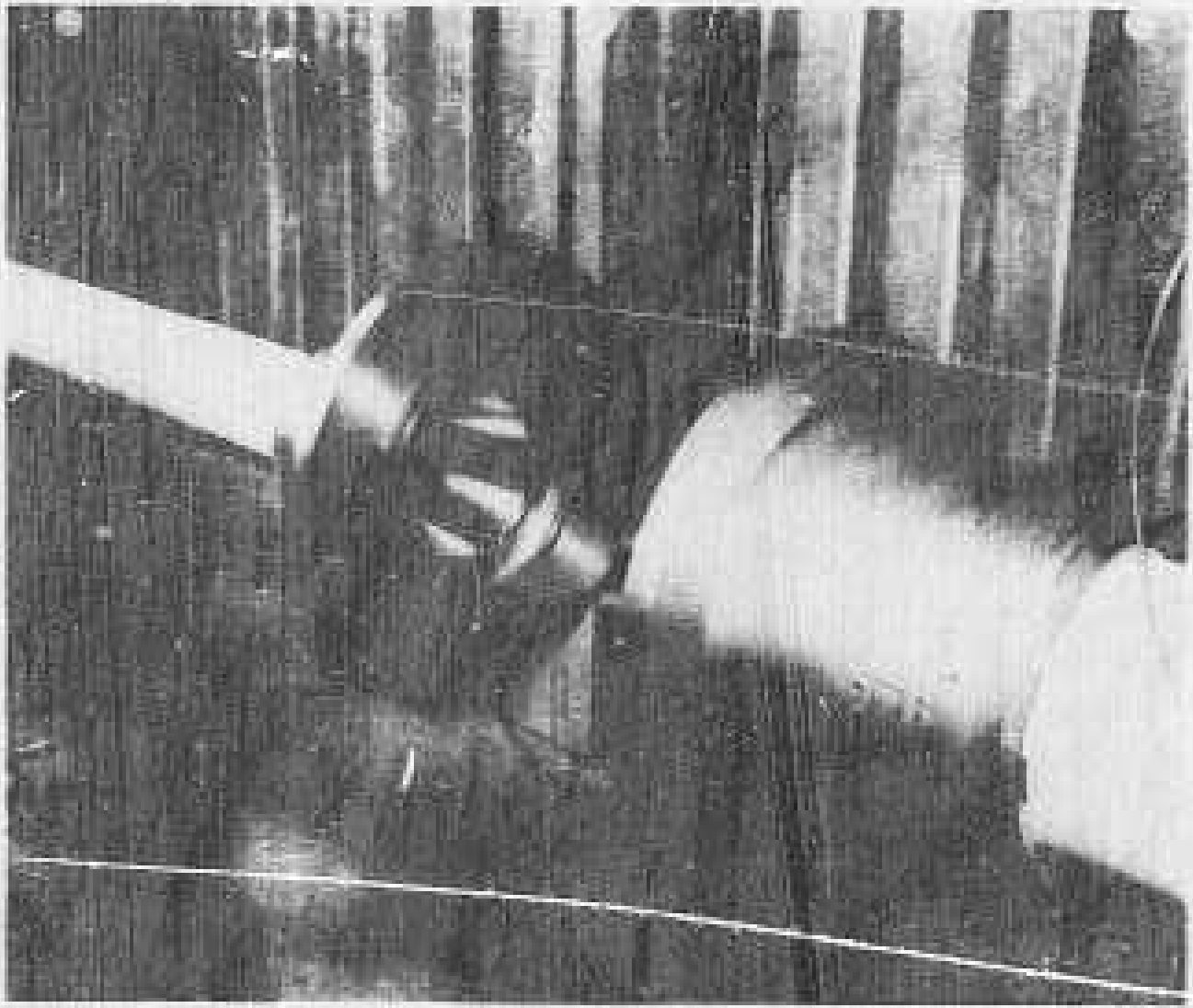

Figure 4 Close-up of Transition Section Showing Diaphragm Location at Driven End Flange

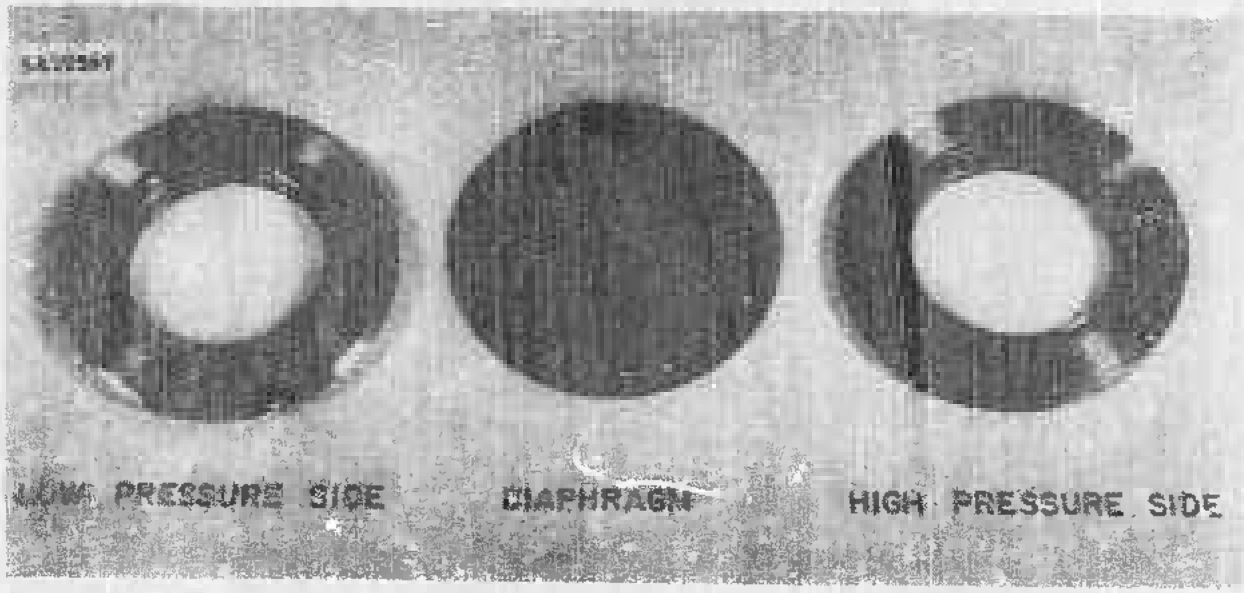

Figure 5 Shock Tube Diaphragm Holder
(Low Pressure and High Pressure Sides, Including Diaphragm)

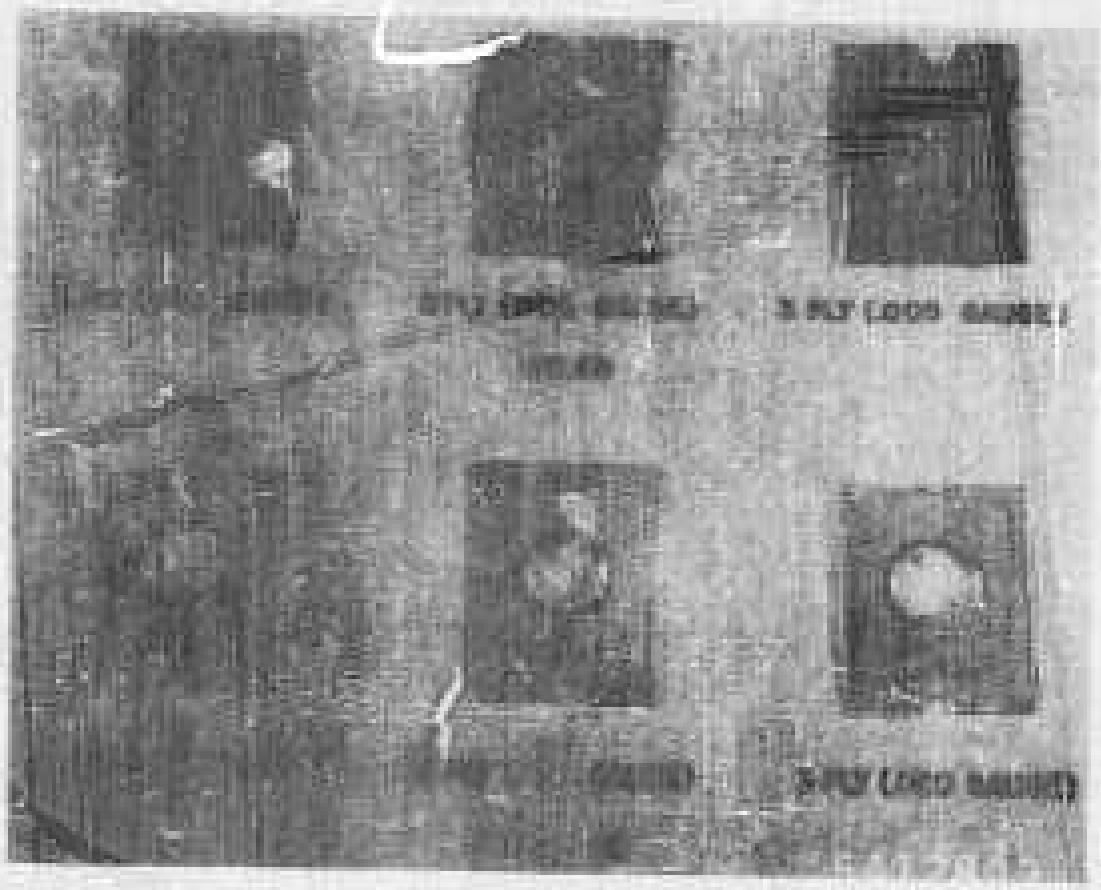

Figure 6 Pop Tester Samples, Mylar and Celluloid

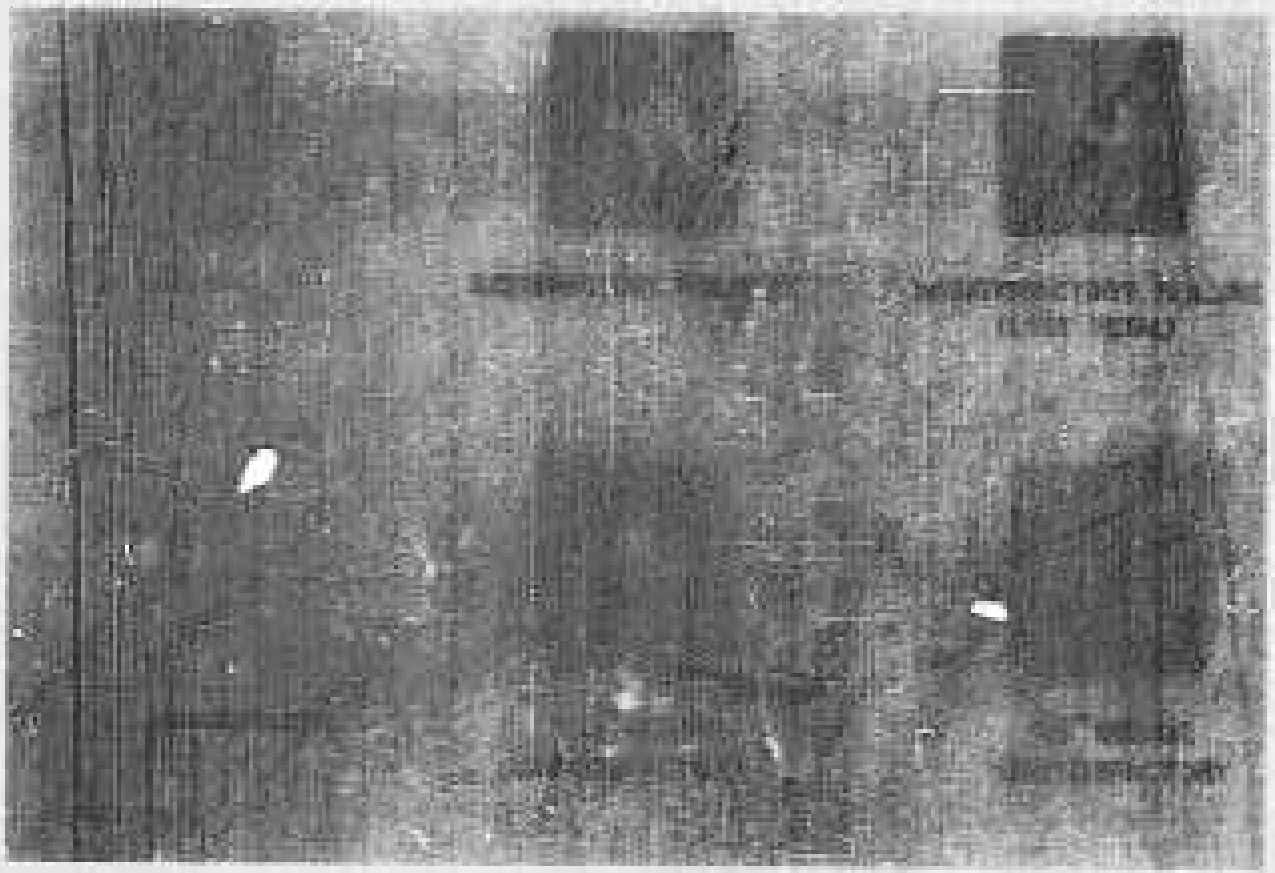

Figure 7 Pop Tester Samples, Aluminum

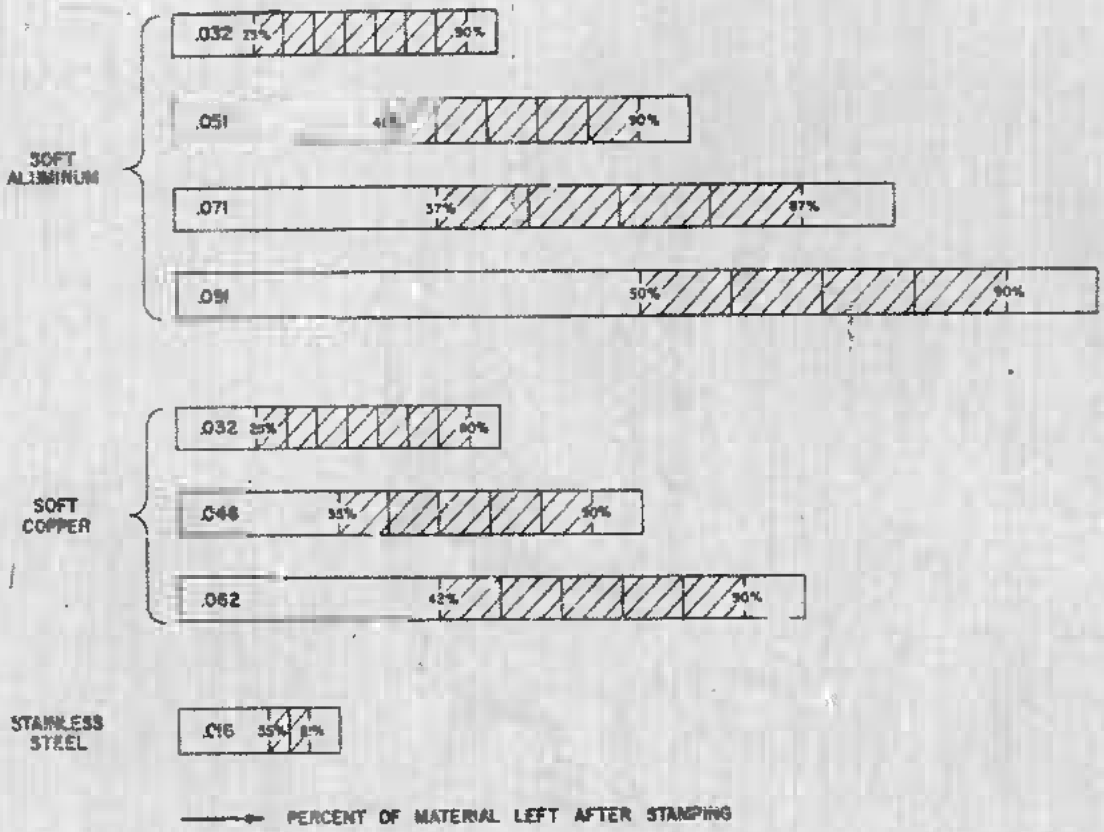

Figure 8 Range of Shock Tube Diaphragm Materials

Figure 9 Initial Diaphragm Results, Aluminum and Copper (Narrow Flange)

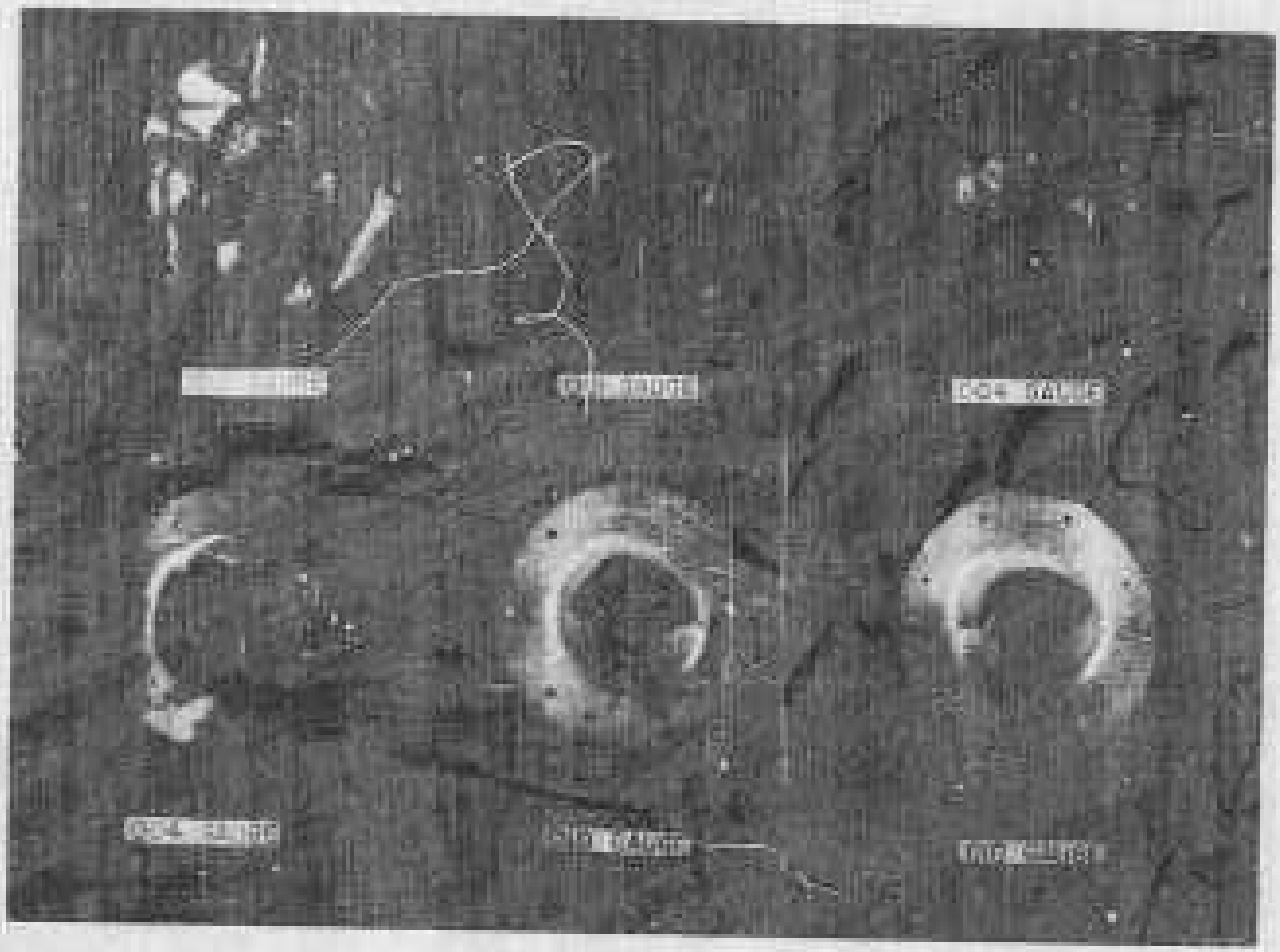

Figure 10 Wide Flange, Mylar Diaphragm Ruptures

Figure 11 Wide Flange, Soft-Copper Diaphragm Results

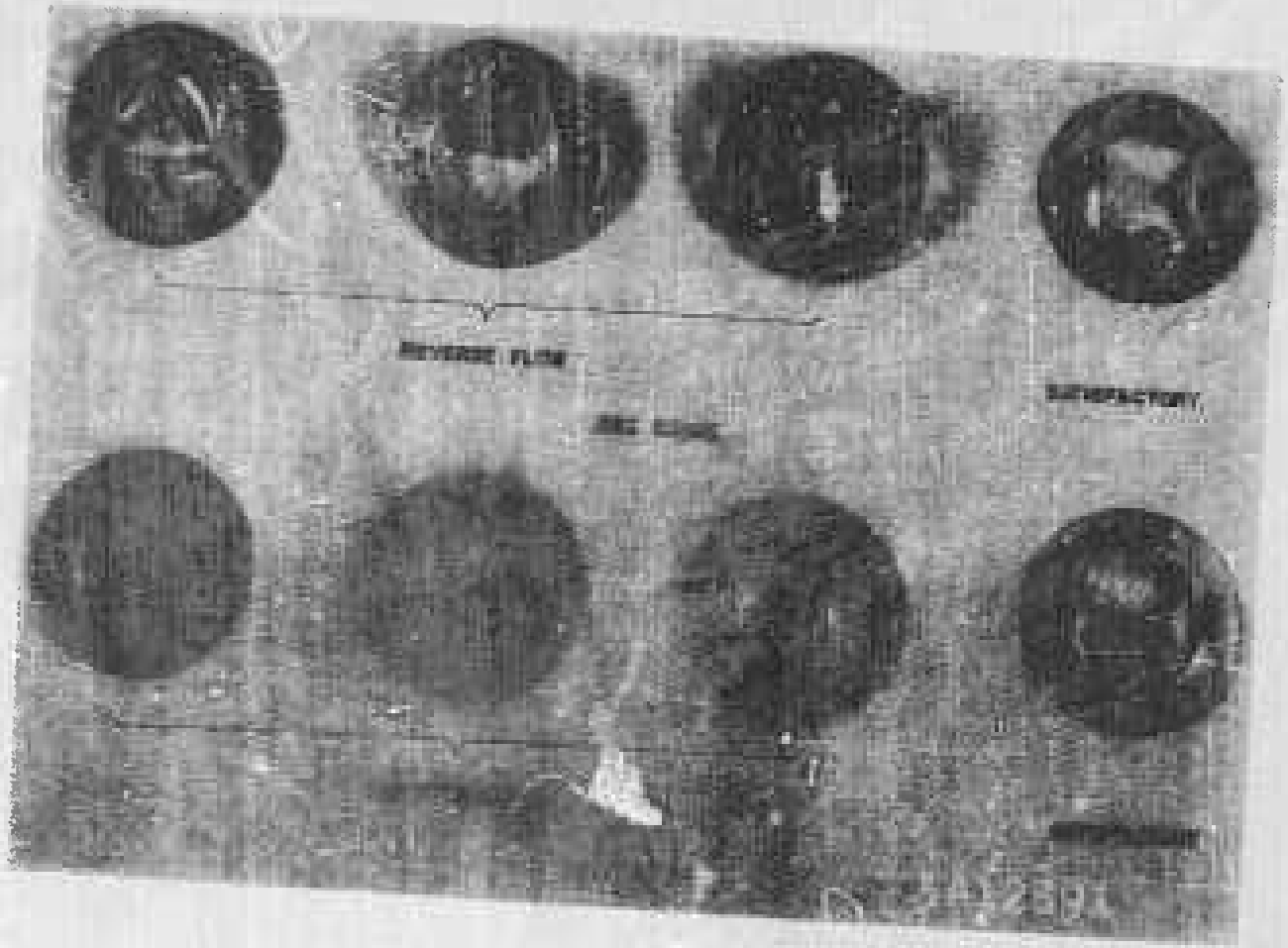

Figure 12 Wide Flange, Soft-Aluminum Diaphragm Results

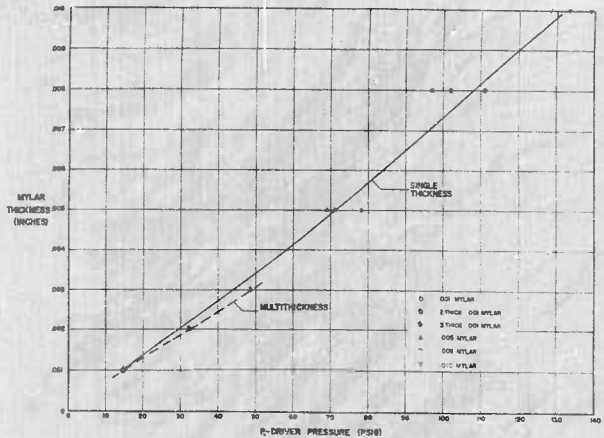

Figure 13 Mylar Diaphragm Burst-Pressure Calibration Curve

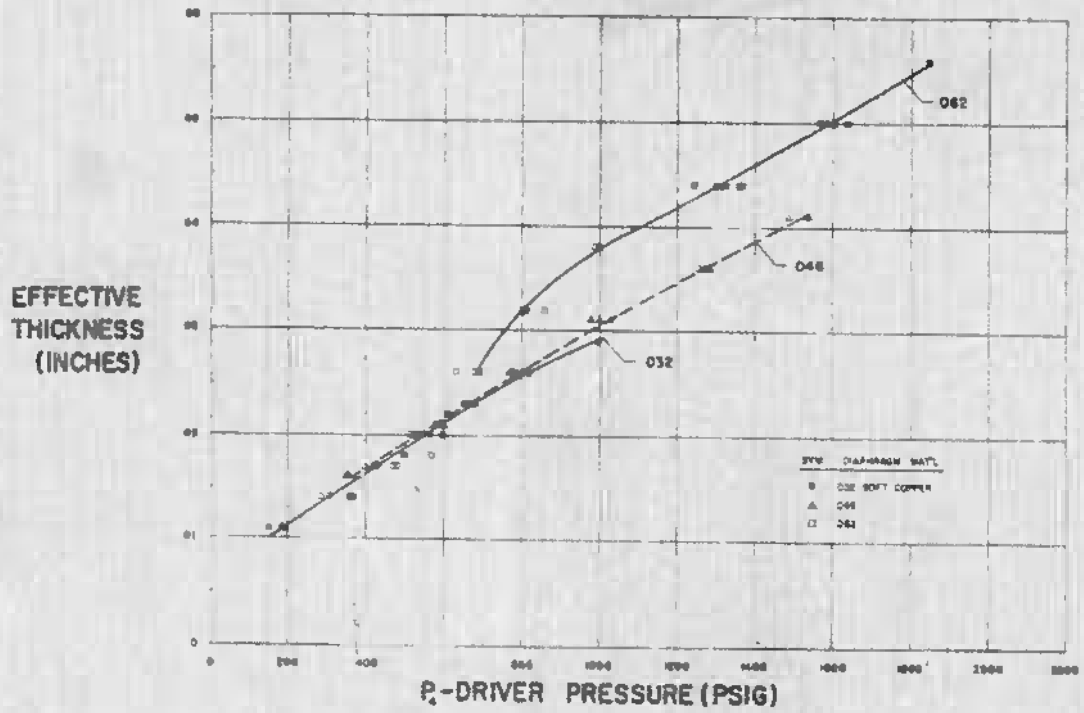

Figure 14 Soft-Copper Diaphragm Burst-Pressure Calibration Curve

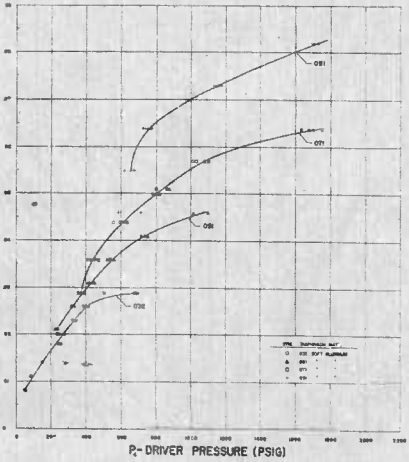

Figure 15 Soft-Aluminum Diaphragm Burst-Pressure Calibration Curve

CLOSING REMARKS

Roman R. Birukoff
Air Force Special Weapons Center

It was my duty and a privilege to organize all three Shock Tube Symposia for the Air Force Special Weapons Center, and I can't help but observe a gradually increasing interest in this yearly event. Since, to my knowledge, only a few organizations require a mandatory rehearsal for members presenting a paper elsewhere, I took the liberty requesting each participant in this Symposium to time and rehearse his topic beforehand. A marked improvement in timing and quality of presentation was obvious. Therefore, I suggest that all organizations follow this practice in the future.

In conclusion, in behalf of the Air Force Special Weapons Center, I wish to thank Jack Kelso of AFSWP and Jim Shreve of Sandia Corporation for assisting in conducting the Symposium, members of NASA for providing projection equipment, and participants and attendances, each and all, for taking part in this Symposium.